Journal of Experimental and Theoretical Physics, Vol. 101, No. 3, 2005, pp. 389–400.
Translated from Zhurnal Éksperimental'noĭ i Teoreticheskoĭ Fiziki, Vol. 128, No. 3, 2005, pp. 451–463.

ATOMS, MOLECULES, OPTICS

Four-Wave Mixing in a Liquid Suspension of Transparent Dielectric Microspheres

A. A. Afanas'ev, A. N. Rubinov, S. Yu. Mikhnevich, and I. E. Ermolaev
Stepanov Institute of Physics, National Academy of Sciences of Belarus, Minsk, 220072 Belarus
e-mail: lvp@dragon.bas-net.by
Received December 6, 2004

Abstract—The process of four-wave mixing in an artificial heterogeneous nonlinear medium—a liquid suspension of transparent dielectric microspheres—is considered. The dynamics of the concentration response to gradient forces that act on microspheres in the interference field of interacting waves are investigated on the basis of the Smolukhovskii equation. Kinetic equations for the amplitudes of light-induced concentration gratings that take part in the four-wave mixing are obtained with the use of the Fourier series expansion of the distribution function of microspheres. The ratios of the microsphere radius to the grating periods are obtained under which the resultant gradient force vanishes and, hence, a suspension of dielectric microspheres does not exhibit nonlinear properties irrespective of the intensities of the interacting waves. The kinetics of the process of four-wave mixing is investigated under efficient energy exchange between reference, signal, and reversed waves. It is shown that a liquid suspension of transparent dielectric spheres is a highly effective wideband nonlinear medium for reversing the wave front of low-intensity radiation of continuous-wave lasers. © *2005 Pleiades Publishing, Inc.*

1. INTRODUCTION

In this paper, we develop a theory of four-wave mixing in a liquid suspension of transparent microspheres (a heterogeneous medium) whose nonlinearity is associated with the variation of the concentration of microspheres under the action of gradient forces in the electromagnetic field of the interacting waves [1, 2]. It is well known [3] that, in a liquid suspension of microspheres, the gradient forces arising in the interference field of laser radiation draw microspheres with greater refractive index $n_0 > \bar{n}$ (where n_0 and $\bar{n}$ are the refractive indices of the microspheres and the liquid, respectively) into the region of maximal intensity (to the antinodes of the interference field). The increasing concentration of microspheres in the region with higher intensity of radiation leads to an increase in the refractive index of the suspension and to the corresponding decrease in the refractive index in the region of lower intensity (at the nodes of the interference field). In the opposite case, when $n_0 < \bar{n}$, the gradient forces draw microspheres into the region with lower intensity, thus increasing the refractive index of the suspension in the region with higher intensity of radiation. Therefore, irrespective of the ratio $\bar{m} = n_0/\bar{n}$, a liquid suspension of transparent microspheres—an artificial heterogeneous medium—behaves as a nonlinear self-focusing medium with a positive optical Kerr coefficient $n_2 > 0$ [3]. For the first time, a possible application of such heterogeneous structures as a nonlinear optical material was pointed out in [4].

The concentration nonlinearity of a heterogeneous medium associated with the spatial modulation of relatively large particles (microspheres) in a viscous liquid is characterized by much greater relaxation times compared with the nonlinearity of ordinary "atomic" media [5]. Since the size of microspheres is rather large (on the order of a few micrometers), their spatial modulation by gradient forces gives rise to abnormally large nonlinear coefficients. In [3], four-wave mixing experiments were carried out to determine the optical Kerr coefficient n_2 in a water suspension of latex microspheres of radius $a = 0.117$ μm with the use of argon laser radiation beams ($\lambda = 5145$ Å) with a power of about 100 mW. The optical Kerr coefficient was measured to be $n_2 = 3.6 \times 10^{-3}$ cm^2/MW for the concentration of microspheres $N_0 = 6.5 \times 10^{10}$ cm^{-3}, which turned out to be greater than the relevant coefficient in CS_2 by a factor of 10^5. The relaxation times of the concentration gratings of microspheres for a convergence angle of 6.4° between copropagating beams were greater than 100 ms. Due to the high values of the optical Kerr coefficient n_2, a liquid suspension of dielectric microspheres can be used as a highly effective wideband nonlinear medium for a low-intensity laser impulse of large duration.

In [6], a theory of four-wave mixing in liquid suspensions of small-size transparent microspheres was developed in a weak-field limit, when the saturation phenomena are neglected (the diffusion limit). In the diffusion limit, the gradient forces modulate the concentration of microspheres and produce two orthogonal

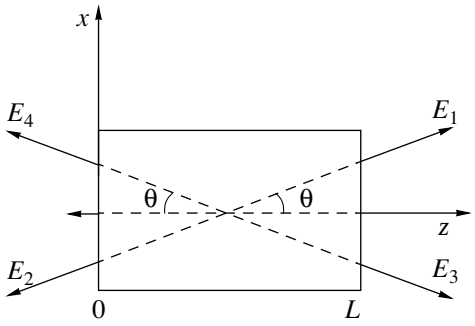

Fig. 1. Geometry of four-wave mixing: 2θ is the convergence angle of waves, and L is the length of the cell with a suspension.

concentration gratings; coherent scattering of radiation by these gratings leads to the formation of a reversed wave and the amplification of the test wave. In spite of the fact that only a small number of microspheres are involved in the four-wave mixing, the reflection coefficient of the reversed wave may reach significant values ($\eta > 1$). A factor that substantially restricts the application of the results of the theory developed in [6] is the approximation of small microspheres; in this approximation, the intensity of effective radiation inside microspheres is assumed to be constant irrespective of the position of the microspheres on the interference pattern of the field. In this case, the steady-state amplitudes of the gratings do not depend on the convergence angle of the interacting waves, and the coefficient of parametric coupling between these waves is proportional to the squared volume of a microsphere, i.e., to a value of a^6. In particular, we will show below that the theory of four-wave mixing developed in the approximation of constant intensity of radiation inside the microspheres [6] is valid in a very narrow interval of the microsphere radii, gives a considerably overstated value of the reflection coefficient η of the reversed wave in the region of $2ka \geq 1$ (k is the wavenumber), and does not predict the oscillating behavior of the function $\eta = \eta(a)$. In this paper, we develop a four-wave mixing theory that is free of these constraints; the results obtained here include the results of [6] as a particular case.

The theory developed below is based on a simultaneous system of truncated wave equations and the two-dimensional Smolukhovskii equation for the concentration of microspheres; a solution to the latter equation is represented as a Fourier series with time-dependent amplitudes of multiply periodic concentration gratings induced by the interacting waves. The gradient forces that arise in the interference field of co- and counterpropagating waves are calculated in the Rayleigh–Gans approximation. The amplitudes of the gradient forces, which are determined by the overlap integral of a microsphere and a periodically modulated intensity of the effective radiation that takes into account the nonuniform distribution of this radiation inside a microsphere, are obtained in the explicit form in spherical coordinates. The theory predicts the suppression of four-wave mixing due to the vanishing of the resultant components of gradient forces for certain dimensions of microspheres and the convergence angles of the interacting waves. We investigate the dynamics of the formation and relaxation of concentration gratings that are induced by the interacting light waves. We analyze the steady-state regime of four-wave mixing in the diffusion limit and determine conditions under which a parametric generation of a pair of mutually conjugate waves occurs with regard to the radiation loss due to the Rayleigh scattering by microspheres. We discuss the applicability scope of the results of [6] and the characteristic features of four-wave mixing in the diffusion limit, which are attributed to the nonuniformity of the effective radiation inside the microspheres. We present the results of the numerical simulation of the four-wave mixing process without any constraints imposed on the amplitudes of the interacting waves.

2. BASIC EQUATIONS

We will consider the process of four-wave mixing in a liquid suspension of transparent microspheres in the Rayleigh–Gans approximation [7]:

$$|\bar{m} - 1| \ll 1 \quad \text{and} \quad 4\pi a|\bar{m} - 1| \ll \lambda, \tag{1}$$

where λ is the radiation wavelength. Using inequalities (1), we can neglect the diffraction of radiation by microspheres [7], assuming that the effective field is specified; i.e., we can apply the so-called electrostatic approximation [8].

Let us represent the effective electromagnetic field as a sum of linearly polarized plane waves of frequency ω:

$$E = \frac{1}{2}\sum_{l=1}^{4} E_l(z, t)\exp[-i(\omega t - \mathbf{k}\cdot\mathbf{r})] + \text{c.c.}, \tag{2}$$

where $E_l(z, t)$ are the wave amplitudes and $\mathbf{k}_l$ are the wavevectors (see Fig. 1). We will assume that the interacting waves are polarized in the direction perpendicular to the plane zx.

During the four-wave mixing, the microspheres are in the field of two pairs of counterpropagating waves of comparable intensities. Therefore, one can neglect small radiative forces of light pressure in the theory in question [8, 9]. In this case, a key contribution to the light-induced formation of a concentration response is made by gradient forces, whose amplitude is given by [10]

$$\mathbf{F}_\nabla = \alpha_0 \int_V \nabla|\bar{E}|^2 dV, \tag{3}$$

where

$$\alpha_0 = \frac{3}{4\pi}\bar{n}^2\frac{\bar{m}^2-1}{\bar{m}^2+2} \quad (4)$$

is the specific polarizability of a microsphere,

$$\begin{aligned}|\bar{E}|^2 = \frac{1}{2}\{|E_0|^2 + [E_1E_2^*\exp(2i(k_z z + k_x x))\\ + E_3E_4^*\exp(2i(k_z z - k_x x))\\ + (E_1E_4^* + E_2^*E_3)\exp(2ik_z z) + (E_1E_3^* + E_2^*E_4)\\ \times \exp(2ik_x x) + \text{c.c.}]\}\end{aligned} \quad (5)$$

is the time-averaged intensity of the effective radiation, $|E_0|^2 = \sum_{l=1}^{4} U_l$, $V = (4\pi/3)a^3$ is the volume of a microsphere, $k_z = k\cos\theta$ and $k_x = k\sin\theta$ are the corresponding projections of the wavevector, $k = (\omega/c)\bar{n}$, and $U_l = |E_l|^2$. In fact, the integral in (3) is the overlap integral of a microsphere and the nonuniform intensity of the effective radiation.

We will assume that the products of complex conjugate amplitudes of the interacting waves are slowly varying functions of the longitudinal coordinate:

$$\frac{\partial|E_l E_{l'}^*|}{\partial z} \ll k_z|E_l E_{l'}^*|. \quad (6)$$

In this approximation, with regard to (5), the integral in formula (3) can be calculated in spherical coordinates exactly [11]. After the integration in (3), we obtain the following expression for the gradient force:

$$\mathbf{F}_\nabla = \mathbf{j}F_x + \mathbf{k}F_z, \quad (7)$$

where **j** and **k** are unit vectors;

$$\begin{aligned}F_\kappa = F_{\kappa 0}\exp[2i(k_z z - k_x x)]\\ + F_{\kappa 1}\exp[2i(k_z z + k_x x)] + F_{\kappa 2}\exp(2ik_\kappa \kappa) + \text{c.c.}\end{aligned} \quad (8)$$

are the components of the gradient-force vector $\mathbf{F}_\nabla$, and $\kappa = \{x, z\}$. The amplitudes of the harmonics of the components F_κ are defined by

$$\begin{aligned}F_{x0} &= -i\alpha_0 k_x E_3 E_4^* V_0 = -(k_x/k_z)F_{z0},\\ F_{x1} &= i\alpha_0 k_x E_1 E_2^* V_0 = (k_x/k_z)F_{z1},\\ F_{x2} &= i\alpha_0 k_x (E_1E_3^* + E_2^*E_4)V_x,\\ F_{z2} &= i\alpha_0 k_z (E_1E_4^* + E_2^*E_3)V_z,\end{aligned} \quad (9)$$

where

$$\begin{aligned}V_0 &= (a\Lambda_0)^{3/2}J_{3/2}(2\pi a/\Lambda_0),\\ V_\kappa &= (a\Lambda_\kappa)^{3/2}J_{3/2}(2\pi a/\Lambda_\kappa),\end{aligned} \quad (10)$$

$J_{3/2}(\xi)$ is the Bessel cylindrical function, and $\Lambda_0 = \pi/k$ and $\Lambda_\kappa = \pi/k_\kappa$ are the periods of the interference patterns of the corresponding pairs of waves. The constant coefficients V_0 and V_κ in (9) result from the integration of (3) and take into account the nonuniformity of radiation inside the microspheres. One can easily show that $V_0 = V_\kappa = V$ for $\xi \ll 1$. It is obvious that $|F_x/F_z| \propto \tan\theta$; hence, in the region of small angles $\theta \ll \pi/2$, the dominant role in the formation of the concentration response is played by the longitudinal (zth) component of the gradient force. It follows from (9) that, for certain ratios of the microsphere radius to the periods Λ_κ of the interference pattern of the field, namely, for $2\pi a/\Lambda_\kappa = \xi_i$ (where ξ_i are the roots of the Bessel cylindrical function $J_{3/2}(\xi)$, $i = 1, 2, \ldots$), the corresponding component of the gradient force vanishes irrespective of the positions of the microspheres. The so-called effect of "zero force" is attributed to the fact that the oppositely directed components of this field that act on the corresponding elements of a microsphere are equal. This effect was theoretically predicted independently in [8, 11]. It follows from (9) that, for certain values of the parameters of the system (for example, for $2k_x a = \xi_1$ and $2k_z a = \xi_2$), the components $F_{\kappa 2}$ of the gradient forces vanish (i.e., $V_\kappa = 0$) irrespective of the intensity of the effective radiation. Using the values of the first two roots of the Bessel function $J_{3/2}(\xi)$ [12], one can show that the condition $V_\kappa = 0$ is fulfilled for $a/\lambda = 0.709$ and

$$\tan\theta = \xi_1/\xi_2 \approx 0.58,$$

i.e., $\theta \approx 30°$. It is obvious that this condition is also satisfied for $\theta = 45°$ and $\sqrt{2}\,ka = \xi_i$. In this case, the minimal value of the ratio a/λ corresponds to $\xi_i = \xi_1$ and is equal to $a/\lambda = 0.506$. By virtue of inequalities (1), the conditions obtained above can be satisfied in suspensions with small values of the relative refractive index $|\bar{m} - 1| \le 10^{-2}$.

Thus, due to the zero force effect, the process of four-wave mixing, to which the main contribution is made by the components $F_{\kappa 2}$, can be nearly completely suppressed for appropriate values of the microsphere sizes and the convergence angle of the interacting waves. Note also that, depending on the radii of the microspheres, the amplitudes of gradient forces (9) are alternating functions. Therefore, the microspheres of appropriate sizes may be drawn either to the antinodes (when $J_{3/2}(\xi) > 0$) or to the nodes (when $J_{3/2}(\xi) < 0$) of the interference pattern of the field. This motion of microspheres can physically be explained by the tendency to cover a maximal number of antinodes of the interference pattern of the field [8, 11].

To determine the concentration response of microspheres induced by an electromagnetic field (see (1)),

we apply the two-dimensional Smolukhovskii equation[1] (see, for example, [13])

$$\frac{\partial N}{\partial t} = D\Delta_\perp N - b\left[N\left(\frac{\partial F_x}{\partial x} + \frac{\partial F_z}{\partial z}\right) + \left(F_x\frac{\partial N}{\partial x} + F_z\frac{\partial N}{\partial z}\right)\right], \quad (11)$$

where N is the concentration of microspheres (cm^{-3}), $D = k_BT/6\pi\nu a$ is the diffusion coefficient (cm^2/s), k_B is the Boltzmann constant, T is temperature (K), ν is the viscosity of the liquid, $b = D/k_BT$ is the mobility of microspheres, and $\Delta_\perp = \partial^2/\partial z^2 + \partial^2/\partial x^2$. Equation (11) is valid in the domain $t > t^*$ provided that the gradient force $\mathbf{F}_\nabla$ is a slowly varying function on the time t^* and space l^* scales defined by the relations [13, 14]

$$t^* = bm_0, \quad l^* = \sqrt{\frac{k_BT}{m_0}}t^*, \quad (12)$$

where m_0 is the mass of a microsphere. In particular, for a water suspension of latex microspheres of radius $a = 1.17 \times 10^{-5}$ cm with density 1 g/cm^3, which was used in the experiment in [3], we have $t^* \approx 3 \times 10^{-9}$ s and $l^* \approx 7 \times 10^{-9}$ cm at room temperature.

It is convenient to represent the solution to Eq. (11) as a harmonic series

$$N(x, z, t) = \sum_{m, n = -\infty}^{\infty} N_{mn}(t)\exp[2i(mk_z z + nk_x x)], \quad (13)$$

where $N_{00} = \langle N\rangle_{x,z} = N_0 = \text{const}$ is the initial concentration of microspheres, $\langle\ldots\rangle_{x,z}$ denotes spatial averaging, and $N^*_{mn} = N_{-m,-n}$. Substituting solution (13) into Eq. (11) and taking into account expression (8), we obtain the following system of kinetic equations for the amplitudes $N_{mn}(t)$ of concentration harmonics:

$$\left(\frac{\partial}{\partial t} + W_{mn}\right)N_{mn} = a_{mn}N_{m-1,n+1} - a^*_{mn}N_{m+1,n-1} + b_{mn}N_{m-1,n-1} - b^*_{mn}N_{m+1,n+1} + c_nN_{m,n-1} - c^*_nN_{m,n+1} + d_mN_{m-1,n} - d^*_mN_{m+1,n}, \quad (14)$$

where

$$W_{mn} = 4D[(mk_z)^2 + (nk_x)^2],$$
$$a_{mn} = 2\alpha_0 b(mk_z^2 - nk_x^2)E_3E_4^*V_0,$$
$$b_{mn} = 2\alpha_0 b(mk_z^2 + nk_x^2)E_1E_2^*V_0, \quad (15)$$
$$c_{mn} = 2\alpha_0 bnk_x^2(E_1E_3^* + E_2^*E_4)V_x,$$
$$d_{mn} = 2\alpha_0 bmk_z^2(E_1E_4^* + E_2^*E_3)V_z.$$

When the radii of the microspheres and the convergence angles of the interacting waves are small, i.e., $a \ll \Lambda_0$ and $\theta \ll \pi/2$, we can neglect the component F_x of the gradient force; then, the system of equations (14) is reduced to

$$\left(\frac{\partial}{\partial t} + W_{mn}\right)N_{mn} = 2\alpha_0 bVmk_z^2[E_3E_4^*N_{m-1,n+1} - E_3^*E_4N_{m+1,n-1} + E_1E_2^*N_{m-1,n-1} - E_1^*E_2N_{m+1,n+1} + (E_1E_4^* + E_2^*E_3)N_{m-1,n} - (E_1^*E_4 + E_2E_3^*)N_{m+1,n}]. \quad (16)$$

The nonlinear polarization of a suspension of microspheres induced by the variation of their concentration under gradient forces is defined by [6]

$$P = \frac{1}{2}\alpha_0 VN(x, z, t) \times \sum_{l=1}^{4} E_l(z, t)\exp[-i(\omega t - \mathbf{k}\cdot\mathbf{r})] + \text{c.c.} \quad (17)$$

Substituting formulas (2) and (17) into the wave equation, we obtain the following system of truncated equations for the amplitudes of the interacting waves:

$$\cos\theta\frac{\partial E_1}{\partial z} + \frac{1}{v}\frac{\partial E_1}{\partial t} = i\gamma(E_1 + \chi_{11}E_2 + \chi_{01}E_3 + \chi_{10}E_4) - \rho E_1,$$
$$-\cos\theta\frac{\partial E_2}{\partial z} + \frac{1}{v}\frac{\partial E_2}{\partial t} = i\gamma(E_2 + \chi_{11}^*E_1 + \chi_{10}^*E_3 + \chi_{01}^*E_4) - \rho E_2,$$
$$\cos\theta\frac{\partial E_3}{\partial z} + \frac{1}{v}\frac{\partial E_3}{\partial t} = i\gamma(E_3 + \chi_{01}^*E_1 + \chi_{10}E_2 + \chi_{1,-1}E_4) - \rho E_3, \quad (18)$$
$$-\cos\theta\frac{\partial E_4}{\partial z} + \frac{1}{v}\frac{\partial E_4}{\partial t} = i\gamma(E_4 + \chi_{10}^*E_1 + \chi_{01}E_2 + \chi_{1,-1}^*E_3) - \rho E_4,$$

[1] This equation is known as the Planck–Nernst equation in English-language literature [6].

where $v = c/\bar{n}$ is the velocity of light in the suspension,

$$\gamma = 2\pi\frac{k}{\bar{n}^2}\alpha_0 V N_0, \quad \chi_{mn} = \frac{N_{mn}}{N_0}.$$

In Eqs. (18), we took into account the equation $N^*_{mn} = N_{-m,-n}$ and phenomenologically introduced the amplitude coefficient of loss [6, 14]

$$\rho = \frac{8\pi}{3}N_0 k^4\left(\frac{\bar{m}^2-1}{\bar{m}^2+2}\right)^2 a^6, \tag{19}$$

due to the Rayleigh scattering by microspheres. Equations (18) imply that only two pairs of gratings from the spectrum of excited concentration gratings (13) take part in the process of four-wave mixing: one pair of orthogonal gratings,

$$N_\kappa \propto \cos(2k_\kappa \kappa), \quad \kappa = x, z,$$

leads to the parametric coupling of waves and the energy exchange among them, and the other pair,

$$N_\pm \propto \cos[2(k_z z \pm k_x x)],$$

leads to self-action phenomena. Due to the spatial averaging of the wave equations, other concentration gratings do not make a direct contribution to four-wave mixing. The indirect role of these gratings reduces to the influence on the values of the amplitudes of the main gratings N_κ and $N_\pm$.

The simultaneous system of wave equations (18) and kinetic equations (14) subject to the boundary conditions

$$\begin{gathered} E_1(0,t) = E_{10}(t), \quad E_2(L,t) = E_{20}(t), \\ E_3(0,t) = E_{30}(t), \quad E_4(L,t) = 0 \end{gathered} \tag{20}$$

and the initial conditions

$$\begin{gathered} N_{mn}(t=-\infty) = 0, \ m \neq 0, \ n \neq 0, \\ N_{00}(t=-\infty) = N_0 \end{gathered} \tag{21}$$

describes the process of four-wave mixing of waves of arbitrary intensities on the concentration nonlinearity due to the action of gradient forces on transparent microspheres.

3. KINETICS OF A CONCENTRATION GRATING OF MICROSPHERES

Based on Eqs. (14), we consider the kinetics of a concentration grating of microspheres induced by the interference field of two waves. Assume, for definiteness, that $E_2 = E_4 = 0$. Then, $a_{mn} = b_{mn} = d_m = 0$ and $c_n = 2\alpha_0 b n k_x^2 V_x E_1 E_3^*$; hence, the amplitudes N_{mn} of the concentration gratings and the relaxation constants W_{mn} depend only on the index n ($N_{mn} \equiv N_n$ and $W_{mn} \equiv W_n$). In this case, Eqs. (14) are significantly simplified and reduced to

$$\frac{\partial N_n}{\partial t} + W_n N_n = n(AN_{n-1} - A^* N_{n+1}), \tag{22}$$

where $W_n = 4Dn^2 k_x^2$ and $A = 2\alpha_0 b k_x^2 V_x E_1 E_3^*$.

For relatively weak waves, when higher order gratings ($n > 2$) can be neglected, Eqs. (22) yield

$$\begin{gathered} \frac{\partial N_1}{\partial t} + \Gamma N_1 = (AN_0 - A^* N_2), \\ \frac{\partial N_2}{\partial t} + 4\Gamma N_2 = 2AN_1, \end{gathered} \tag{23}$$

where $\Gamma = 4Dk_x^2$.

For rectangular pulses ($E_l(t) = E_l = \text{const}$ for $t \geq 0$, $l = 1, 3$), a solution to system of equations (23) can be obtained in the explicit form (see Appendix A). It follows from solution (A.3) that, due to the excitation of the second-order grating N_2, the amplitude of the main grating N_1 contains two components whose relaxation times are less than $t = 1/\Gamma$. The greater relaxation time of the main grating N_1 is estimated by the relation

$$\begin{aligned} \tau_1 &\approx \frac{1}{\Gamma}\left(1 - \frac{2}{3}\frac{|A|^2}{\Gamma^2}\right) \\ &= \frac{1}{4Dk_x^2}\left[1 - \frac{1}{6}\left(\frac{\alpha_0 b V_x}{D}\right)^2 U_1 U_3\right], \end{aligned} \tag{24}$$

which is valid for $U_1 U_3 < 6D^2/(\alpha_0 b V_x)^2$. Thus, in the approximation used, the relaxation time τ_1 of the main grating decreases linearly as the product of the intensities of the exciting waves increases. It follows from Eqs. (23) that the relaxation times $\bar{\tau}_n$ of the concentration gratings are determined by the diffusion coefficient and the periods of the gratings:

$$\bar{\tau}_n = 1/n^2\Gamma, \quad n = 1, 2.$$

In particular, for the parameter values $D = 1.88 \times 10^{-8}$ cm^2/s and $\Lambda_x = 3.5 \times 10$ cm^{-4}, which correspond to the experiment of [3], we have $\bar{\tau}_1 = 165$ ms; this result agrees well with the relaxation time $\bar{\tau}_1 = 140 \pm 40$ ms of the main grating N_1 measured in [3].

Figure 2 shows the time dependence of the normalized amplitude of the main grating, calculated from Eqs. (22), for various values of the intensities of the effective radiation. Figure 3 shows the relaxation time τ_1 of the main grating as a function of the radiation

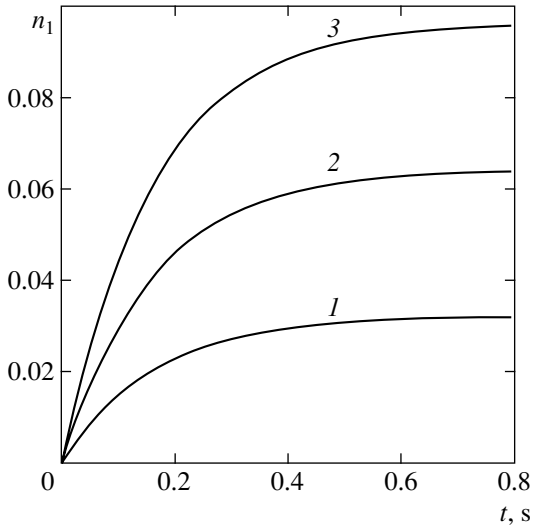

Fig. 2. Kinetics of the amplitude $n_1 = N_1/N_0$ of the main grating for $\xi = 2ka = 3.8$ and $\theta = 3.2°$ for the parameter values $|\mathscr{E}_0|^2 = 2\alpha_0 V\sqrt{U_1 U_2}/k_B T = 0.2 \times 10^{-7}$ (*1*), 0.4×10^{-7} (*2*), and 0.6×10^{-7} (*3*).

intensity $I = (c\bar{n}/8\pi)U_0$ and the convergence angle θ of the interacting waves. The analysis shows that, for the maximal value of the intensity of the interacting waves, it suffices to restrict the consideration to gratings with $n \le 8$ in Eqs. (22).

4. THEORY OF FOUR-WAVE MIXING IN THE DIFFUSION LIMIT

The diffusion approximation [6]

$$N(z, x, t) = N_0 + \bar{N}(z, x, t), \quad |\bar{N}| \ll N_0, \qquad (25)$$

imposes a constraint on the intensities of the interacting waves and corresponds to the situation when the terms proportional to the amplitudes of the concentration gratings N_{mn} ($m, n \neq 0$) on the right-hand sides of Eqs. (14) are neglected. In this case, Eqs. (14) imply the following relations for the components χ_{mn} that determine the process of four-wave mixing:

$$\left(\frac{\partial}{\partial t} + 4Dk_x^2\right)\chi_{01} = 2\alpha_0 V_x b k_x^2 (E_1 E_3^* + E_2^* E_4),$$

$$\left(\frac{\partial}{\partial t} + 4Dk_z^2\right)\chi_{10} = 2\alpha_0 V_z b k_z^2 (E_1 E_4^* + E_2^* E_3),$$

$$\left(\frac{\partial}{\partial t} + 4Dk^2\right)\chi_{11} = 2\alpha_0 V_0 b k^2 E_1 E_2^*, \qquad (26)$$

$$\left(\frac{\partial}{\partial t} + 4Dk^2\right)\chi_{1,-1} = 2\alpha_0 V_0 b k^2 E_3 E_4^*.$$

In the diffusion limit, the relaxation times

$$\tau_0 = \frac{1}{4Dk^2} = \frac{(\Lambda_0/2\pi)^2}{D} \text{ and } \tau_\kappa = \frac{1}{4Dk_\kappa^2} = \frac{(\Lambda_\kappa/2\pi)^2}{D},$$

of the concentration gratings do not depend on the radiation intensity and are determined by the diffusion coefficients and the periods of the interference pattern formed by the interacting waves. It follows from Eqs. (26) and (10) that, due to the nonuniformity of the radiation intensity inside the microspheres, the steady-state amplitudes of the concentration gratings depend on the convergence angle θ of the waves and take bounded values as the radius a of microspheres increases. Note that, for small radii of microspheres (for $V_0 = V_\kappa = V$) [6], the amplitudes of the concentration gratings do not depend on the angle θ and indefinitely increase as the microsphere radius increases.

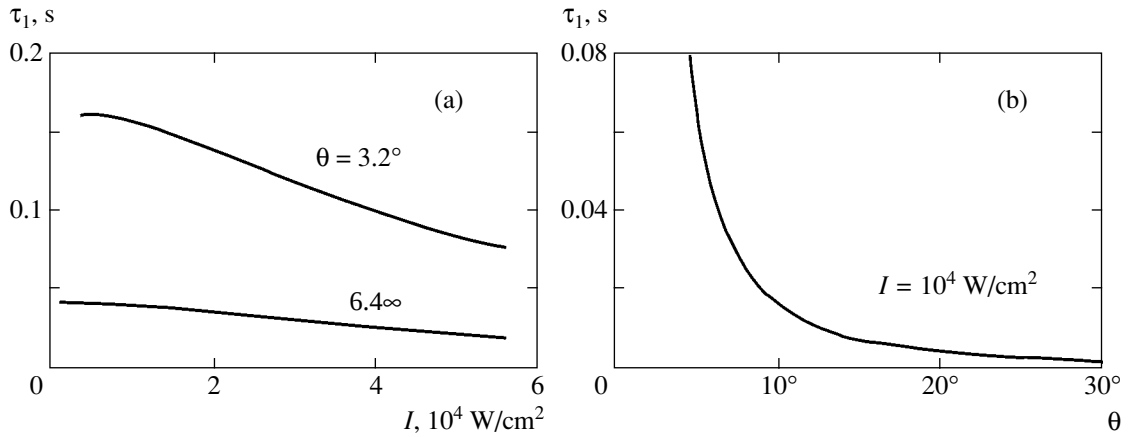

Fig. 3. Relaxation time τ_1 of the main grating as a function of (a) the intensity of effective radiation and (b) the convergence angle θ for $\xi = 2ka = 3.8$, $k = 1.6 \times 10^5$ cm^{-1}, $\alpha_0 = 5.3 \times 10^{-2}$, and $k_B T = 4.14 \times 10^{-14}$ erg.

In the steady-state regime (for $t \gg \tau_\kappa$), Eqs. (18) with regard to (26) are rewritten as

$$\begin{aligned}
\cos\theta\frac{dE_1}{dz} &= i\gamma\left\{\left[1+\frac{\alpha_0 b}{2D}(V_0U_2+V_xU_3+V_zU_4)\right]E_1\right.\\
&\left.+\frac{\alpha_0 b}{2D}(V_x+V_z)E_2^*E_3E_4\right\}-\rho E_1,\\
-\cos\theta\frac{dE_2}{dz} &= i\gamma\left\{\left[1+\frac{\alpha_0 b}{2D}(V_0U_1+V_zU_3+V_xU_4)\right]E_2\right.\\
&\left.+\frac{\alpha_0 b}{2D}(V_x+V_z)E_1^*E_3E_4\right\}-\rho E_2,\\
\cos\theta\frac{dE_3}{dz} &= i\gamma\left\{\left[1+\frac{\alpha_0 b}{2D}(V_xU_1+V_zU_2+V_0U_4)\right]E_3\right.\\
&\left.+\frac{\alpha_0 b}{2D}(V_x+V_z)E_4^*E_1E_2\right\}-\rho E_3,\\
-\cos\theta\frac{dE_4}{dz} &= i\gamma\left\{\left[1+\frac{\alpha_0 b}{2D}(V_xU_1+V_zU_2+V_0U_3)\right]E_4\right.\\
&\left.+\frac{\alpha_0 b}{2D}(V_x+V_z)E_3^*E_1E_2\right\}-\rho E_4.
\end{aligned} \tag{27}$$

Neglecting the reaction of weak waves E_3 and E_4 to the intense reference waves E_1 and E_2, from Eqs. (27) we obtain the following relations for $\rho = 0$:

$$\begin{aligned}
\cos\theta\frac{dE_3}{dz} &= i\{\bar\kappa_3E_3+\beta E_4^*E_{10}E_{20}\\
&\times\exp[i\bar\kappa_1\hat z+i\bar\kappa_2(\hat L-\hat z)]\},\\
-\cos\theta\frac{dE_4^*}{dz} &= -i\{\bar\kappa_4E_4^*+\beta E_3E_{10}^*E_{20}^*\\
&\times\exp[-i\bar\kappa_1\hat z-i\bar\kappa_2(\hat L-\hat z)]\},
\end{aligned} \tag{28}$$

where

$$\begin{aligned}
\bar\kappa_1 &= \gamma\left[1+\frac{\alpha_0 b}{2D}V_0U_2\right],\\
\bar\kappa_2 &= \gamma\left[1+\frac{\alpha_0 b}{2D}V_0U_1\right],\\
\bar\kappa_3 &= \gamma\left[1+\frac{\alpha_0 b}{2D}(V_xU_1+V_zU_2)\right],\\
\bar\kappa_4 &= \gamma\left[1+\frac{\alpha_0 b}{2D}(V_zU_1+V_xU_2)\right],
\end{aligned} \tag{29}$$

$\beta = (\gamma\alpha_0 b/2D)(V_x + V_z)$ is the coefficient of parametric coupling, $\hat z = z/\cos\theta$, and $\hat L = L/\cos\theta$. The solution to Eqs. (28) subject to the boundary conditions $E_3(0) = E_{30}$ and $E_4^*(\hat L) = 0$ has the form

$$\begin{aligned}
E_3(z) &= E_{30}\exp\left[i\left(\frac{\Delta}{2}+\bar\kappa_3\right)\hat z\right]\\
&\times\frac{2\Gamma\cos[\Gamma(\hat L-\hat z)]+i\Delta\sin[\Gamma(\hat L-\hat z)]}{2\Gamma\cos\Gamma\hat L+i\Delta\sin\Gamma\hat L},\\
E_4^*(z) &= 2i\beta E_{30}\sqrt{U_1U_2}\\
&\times\exp\left[-i\left(\frac{\Delta}{2}-\bar\kappa_4\right)\hat z+\bar\kappa_2\hat L\right]\\
&\times\frac{\sin[\Gamma(\hat L-\hat z)]}{2\Gamma\cos\Gamma\hat L+i\Delta\sin\Gamma\hat L},
\end{aligned} \tag{30}$$

where

$$\Gamma = \sqrt{\beta^2U_1U_2+\Delta^2/4} \tag{31}$$

is the increment of the parametric amplification of weak radiation and

$$\begin{aligned}
\Delta &= \bar\kappa_1-\bar\kappa_2-\bar\kappa_3+\bar\kappa_4\\
&= \gamma\frac{\alpha_0 b}{2D}(V_0+V_x-V_z)(U_2-U_1)
\end{aligned} \tag{32}$$

is the phase mismatch of the interacting waves.

It is obvious that the amplitude of the reversed wave E_4 is proportional to the coefficient β of parametric coupling. Using formulas (10), one can show that, for certain values of the microsphere radius a and the convergence angle θ of the interacting waves, the coef-

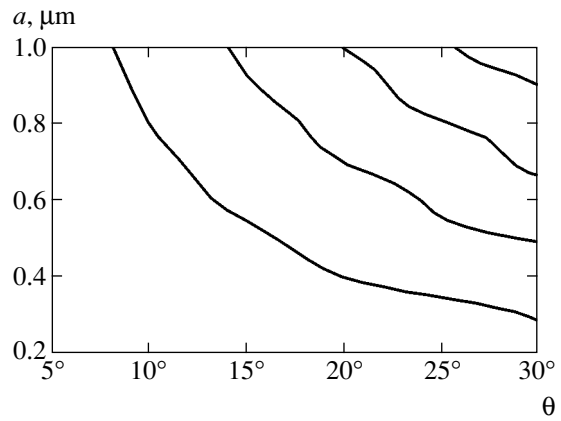

Fig. 4. Family of solutions to the equation $\beta(a, \theta) = 0$ for $k = 1.6 \times 10^5$ cm^{-1}.

ficient β vanishes. For these values of the parameters a and θ, due to the zero-force effect, concentration gratings with periods Λ_κ, which are responsible for the four-wave mixing, are not induced and hence a parametric generation of the reversed wave E_4 does not occur. Figure 4 represents a family of curves on the plane $a\theta$ that shows the values of the parameters a and θ at which the coefficient of parametric coupling vanishes ($\beta = 0$).

It follows from solutions (30) that the linear theory of four-wave mixing for $\Delta = 0$ ($\Gamma = \Gamma_0 = |\beta|\sqrt{U_1 U_2}$) imposes a constraint on the intensities of the reference waves; this constraint is associated with possible parametric generation of a pair of mutually conjugate waves E_3 and E_4^* with the threshold given by the condition [15]

$$\Gamma_0 L/\cos\theta = \pi/2. \tag{33}$$

Taking into account the definition of the coupling coefficient β from (33), we obtain

$$2kN_0\frac{\alpha_0^2 b}{\bar{n}^2 D}V|V_x + V_z|\sqrt{U_1 U_2}\frac{L}{\cos\theta} = 1. \tag{34}$$

It follows from (32) that the condition $\Delta = 0$ is satisfied in two cases: either when $U_1 = U_2$ or when $V_0 + V_x - V_z \equiv \bar{V} = 0$. Note that, $V_0 = V\kappa = V$ for small microspheres, $a \ll \Lambda_0$; hence, the condition $\Delta = 0$ is met, just as in the case of ordinary media with the Kerr nonlinearity [15], only for $U_1 = U_2$.

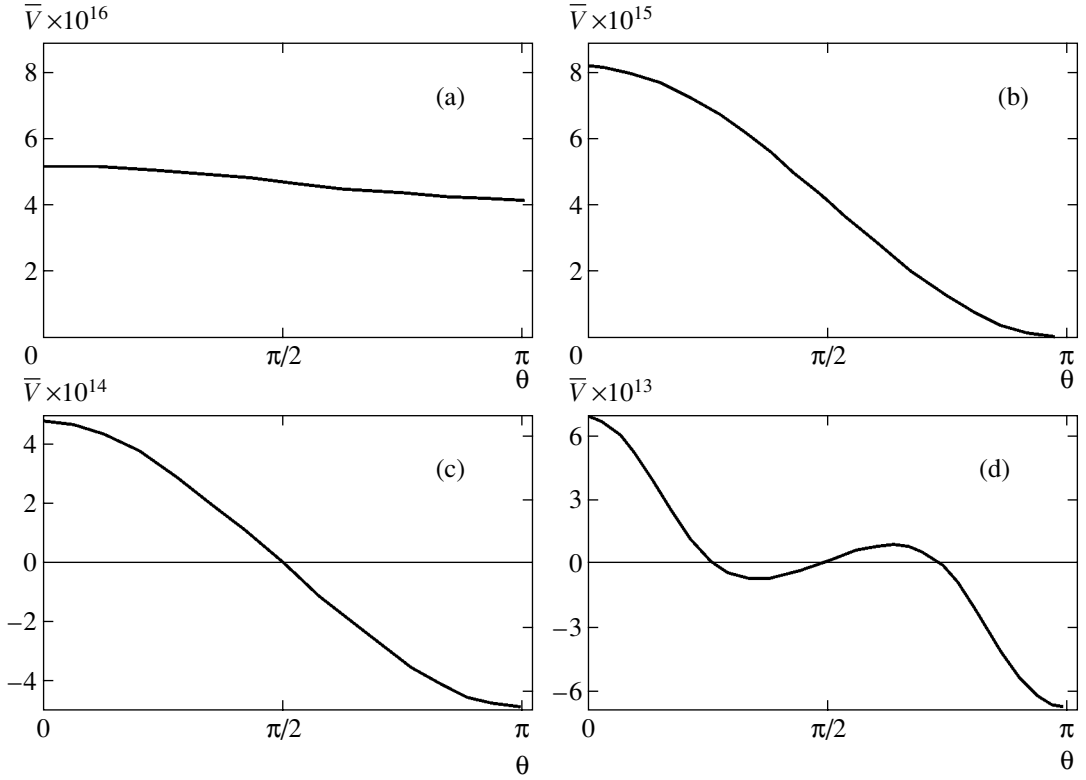

Fig. 5. Parameter $\bar{V}$ versus the angle θ for various values of the coefficient $\xi = 2ka$ for $k = 10^5$ cm^{-1}; (a) $\xi = 1.0$, (b) $\xi = 2.5$, (c) $\xi = 4.5$, and (d) $\xi = 10.9$.

Figure 5 presents the parameter $\bar{V}$ as a function of the angle θ for various values of the coefficient $\xi = 2ka$. One can see that the parameter $\bar{V}(\theta)$ may vanish in the region of $\xi \geq 2.5$. The threshold value of the coefficient $\xi = \xi_{thr} \approx 2.5$ at which $\bar{V} = 0$ corresponds to the angle $\theta = \pi/2$. When $\xi > 2.5$, the corresponding values of θ may be much smaller. Hence, in the region of $\xi > 2.5$ ($a > 0.2\lambda$), for appropriate values of the convergence angle θ, one can implement conditions under which weak radiation is generated parametrically at nonequal values of the intensities of the reference waves, $U_1 \neq U_2$. Note that, for relatively large values of $\theta \geq \pi/6$, Eqs. (18) must contain derivatives with respect to the transverse coordinate ($\sin\theta\partial/\partial x$).

A comparison of the results obtained in the diffusion limit with the similar results of theory [6] is illustrated in Fig. 6. This figure represents the reflection coefficient η of the reversed wave, calculated by the second equation in (30), as a function of the microsphere size for $U_1 = U_2 = U_0$ and for various values of the convergence angle θ of the waves. For comparison, the dashed line represents the reflection coefficient $\eta = \eta(\xi)$ calculated by the theory of [6]. One can see that the theory of [6], in which a gradient force is determined under the assumption that the intensity of radiation inside the microspheres is uniform, $\mathbf{F}_\nabla = \alpha_0 V \nabla |\bar{E}|^2$, predicts a significantly overstated value of ηand is valid in the region of small $\xi \ll 1$. Within the approximations used in [6], the coefficient η is independent of the convergence angle θ of the waves and hence is the same for any values of θ. One can see in Fig. 6 that, for relatively large values of θ, when the overlap of the microspheres with the interference pattern of the field becomes significant, the reflection coefficient $\eta(\xi)$ is a nonmonotonic function of the size of microspheres and vanishes at angles of $\theta = 30°$ and $\theta = 45°$ (at the points $\xi \approx 8.9$ and $\xi \approx 6.36$, respectively). As pointed out above, these values of the parameters correspond to the conditions under which the process of four-wave mixing is suppressed due to the vanishing of the resultant components $F_{\kappa 2}$ of the gradient force.

One can show that the consideration of linear loss ($\rho \neq 0$) in the case of $\bar{V} = 0$ leads to the following relation, which defines a threshold of the parametric generation of weak waves (see Appendix B):

$$\tan\hat{\Gamma}\hat{L} = -\hat{\Gamma}/\rho, \qquad (35)$$

where $\hat{\Gamma} = \sqrt{\beta^2 U_1 U_2 \exp(-2\rho\hat{L}) - \rho^2} > 0$.

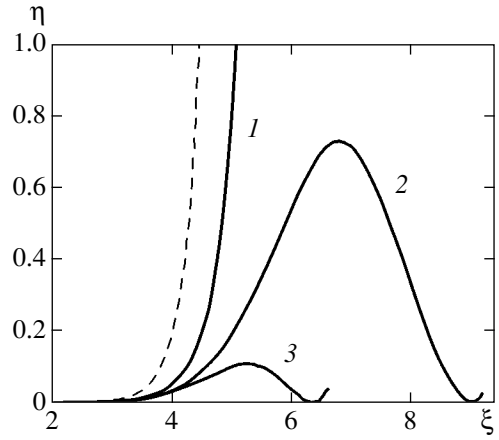

Fig. 6. Reflection coefficient η of the reversed wave as a function of the parameter ξ for $\gamma\alpha_0 V U_0 L/k_B T = 10^{-4}\xi^6$ and various values of the convergence angle θ: (*1*) $\theta = 3.2°$, (*2*) $\theta = 30°$, and (*3*) $\theta = 45°$; dashed curve is calculated by using the theory presented in [6].

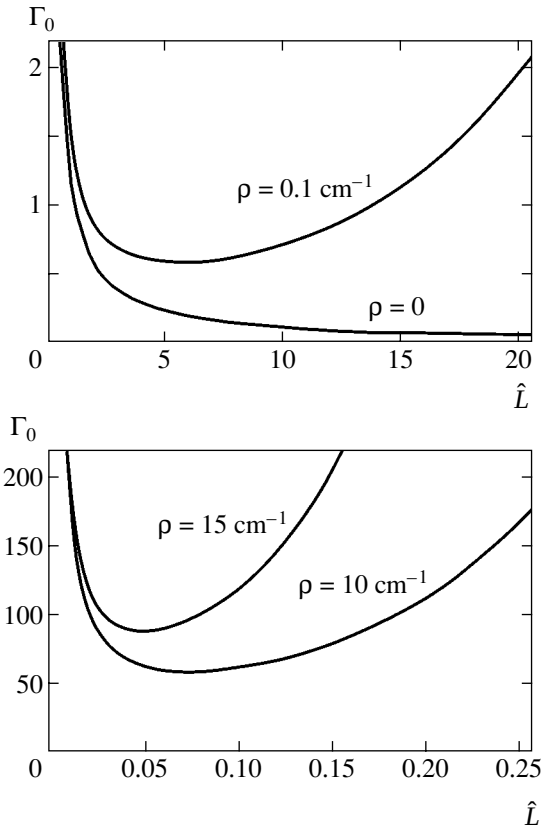

Fig. 7. Normalized threshold intensity Γ_0 of reference waves versus the length $\hat{L}$ for various values of the coefficient ρ.

Figure 7 shows the threshold value $\Gamma_0 = |\beta|\sqrt{U_1 U_2}$ as a function of the length $\hat{L}$ for various values of the amplitude coefficient of loss ρ. One can see that, for $\rho \neq 0$, the optimal value of $\hat{L}$ is equal to $(\rho\hat{L})_{opt} \approx 0.74$.

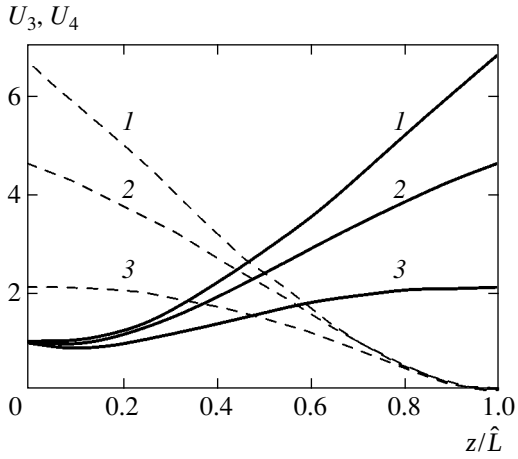

Fig. 8. Steady-state distributions of the intensities of the signal U_3 (solid lines) and reversed U_4 (dashed lines) waves for various microsphere sizes *a*: (*1*) 0.1 μm, (*2*) 0.11 μm, and (*3*) 0.12 μm.

For comparison, note that, for an ordinary medium with cubic nonlinearity, approximate analytic estimates yield a value of $(\rho\hat{L})_{\text{opt}} \approx 0.69$ [16].

5. CONCLUSIONS

The results obtained above show that, within the approximations used in [6], the concentration nonlinearity of a liquid suspension of transparent microspheres cannot be correctly calculated for a wide range of parameters. In particular, a rigorous calculation of the concentration nonlinearity yields much smaller values of the reflection coefficient of a reversed wave compared to those predicted by the theory of [6]. Nevertheless, estimates show that a liquid suspension of transparent microspheres—an artificial heterogeneous medium each of whose components taken separately does not exhibit nonlinear optical properties—may serve as a prospective wideband material for reversing the wave front of low-intensity radiation of continuous-wave lasers. The theoretical results obtained in the present paper are in good agreement with the experimental values measured in [3], of the reflection coefficient η of a reversed wave and the relaxation time τ_1 of a concentration grating versus the intensity of reference waves.

Figure 8 presents the spatial distributions of the intensities of the signal U_3 and reversed U_4 waves that is obtained by the numerical simulation of the simultaneous system of the wave (18) and kinetic (14) equations for the four-wave mixing of argon laser radiation ($E_{10}(t) = E_{20}(t) = E_0$ for $t \geq 0$, $E_{30}(t) = 1$) in a water suspension of latex microspheres [3] at room temperature: $n_0 = 1.59$, $\bar{n} = 1.33$, $N_0 = 6.5 \times 10^{10}$ cm^{-3}, $L = 10^{-2}$ cm, $\theta = 3.2°$, $D = 2.2 \times 10^{-13}a^{-1}$ cm^2/s, and the intensities $I = 7.5 \times 10^4$ W/cm^2 of the reference waves. One can see in Fig. 8 that, for the chosen range of the parameters, the efficiency of the four-wave mixing is quite sensitive to the size of microspheres. In this case, an increase in the microsphere radius by 20% leads to about a threefold increase in the reflection coefficient η of the reversed wave.

In this study, by analogy with [6], we have taken into account the radiation damping due to the Rayleigh scattering phenomenologically, by adding a linear loss factor $\rho \propto N_0$ to the wave equations (18). Strictly speaking, the spatial modulation of microspheres by the effective radiation leads to the dependence of the loss factor on the radiation intensity, $\rho = \rho(|E|^2)$. A rigorous consideration of the nonlinearity of the loss factor is guaranteed by an appropriate modification of formula (17), which has the form

$$P = \frac{\alpha_0 V}{2} N(x, z, t)\left\{1 + i\frac{8}{3}k\left(\frac{\omega}{c}\right)^2 \alpha_0 V\right\}$$

$$\times \sum_{l=1}^{4} E_l \exp[-i(\omega t - \mathbf{k}\cdot\mathbf{r})] + \text{c.c.}$$

in the general case. Hence, generally speaking, the processes of Rayleigh scattering also modulate the imaginary part of the dielectric constant of a suspension; i.e., amplitude–phase gratings are induced in the suspension whose amplitude component should be taken into account provided that $||\alpha_0|V \geq k^{-3}$.

Under relatively high intensities of the interacting waves, high concentrations of microspheres at the antinodes (nodes) of the interference field may lead to the formation of clusters even in a rarefied suspension [3]; naturally, this fact leads to a qualitative change in the process of four-wave mixing. Moreover, in this case, one should also take into account that the size of microspheres is finite, which restricts the limiting concentrations to $N_{\text{lim}} = 1/V$.

Thus, a further development of the theory of four-wave mixing in liquid suspensions of transparent microspheres should be carried out with regard to the nonlinearity of the imaginary part of the dielectric constant of the suspension, the formation of clusters of microspheres, and the saturation of the amplitudes of the concentration gratings due to the finiteness of the volume of microspheres.

APPENDICES

APPENDIX A

Upon the substitution of $N_n = \hat{N}_n \exp(-4\Gamma t)$, the system of equations (23) is reduced to the following second-order equation for $\hat{N}_1$:

$$\frac{d^2\hat{N}_1}{dt^2} - 3\Gamma\frac{dN_1}{dt} + 2|A|^2\hat{N}_1 = 4\Gamma A N_0 \exp(4\Gamma t). \quad \text{(A.1)}$$

A solution to this equation for $\lambda^2 = 9\Gamma^2 - 8|A|^2 > 0$ is given by

$$\hat{N}_1(t) = \exp\left(\frac{3\Gamma}{2}t\right)\left\{C_+\exp\left(\frac{\lambda}{2}t\right)\right.$$
$$+ C_-\exp\left(-\frac{\lambda}{2}t\right) + 8\frac{\Gamma}{\lambda}AN_0\int_0^t\exp\left(-\frac{3\Gamma}{2}t'\right) \qquad \text{(A.2)}$$
$$\left.\times\sinh\left[\frac{\lambda}{2}(t-t')dt'\right]\right\},$$

where $C_\pm$ are integration constants. The initial condition $\hat{N}_1(0) = 0$ implies the relation $C_+ = -C_-$. The coefficient C_+ is determined from the condition that

$$\hat{N}_2 \longrightarrow 0, \quad \hat{N}_1 \longrightarrow \frac{AN_0}{\Gamma}[1-\exp(-\Gamma t)]\exp(4\Gamma t),$$

as $A \longrightarrow 0$. It can easily be shown that this passage to the limit is attained for $C_+ = N_0A/3\Gamma$. Taking this fact into account, from (A.2) we find

$$N_1(t) = \frac{2AN_0}{3\Gamma}\exp\left(-\frac{5\Gamma}{2}t\right)$$
$$\times\left\{\sinh\left(\frac{\lambda}{2}t\right) + \frac{3\Gamma^2}{2\Gamma^2 + |A|^2}\right. \qquad \text{(A.3)}$$
$$\left.\times\left[\exp\left(\frac{5\Gamma}{2}t\right) - \cosh\left(\frac{\lambda}{2}t\right) - 5\frac{\Gamma}{\lambda}\sinh\left(\frac{\lambda}{2}t\right)\right]\right\}.$$

Similarly, for $N_2(t)$, the second equation in (23) yields

$$N_2(t) = 2A\int_0^t N_1(t')\exp[-4\Gamma(t-t')]dt'. \qquad \text{(A.4)}$$

APPENDIX B

For $\rho \neq 0$, the first two equations in (27) yield the following equations for the amplitudes of the reference waves:

$$\frac{dE_1}{d\hat{z}} = i\gamma\left(1 + \frac{\alpha_0 b}{2D}V_0|E_2|^2\right)E_1 - \rho E_1,$$
$$-\frac{dE_2}{d\hat{z}} = i\gamma\left(1 + \frac{\alpha_0 b}{2D}V_0|E_1|^2\right)E_2 - \rho E_2. \qquad \text{(B.1)}$$

A solution to these equations is given by

$$E_1(\hat{z}) = E_{10}\exp\left\{(i\gamma-\rho)\hat{z} + i\gamma\frac{\alpha_0 b}{2D}V_0|E_{20}|^2\right.$$
$$\left.\times\exp(-2\rho\hat{L})\int_0^{\hat{L}}\exp(2\rho z)dz\right\},$$
$$E_2(\hat{z}) = E_{20}\exp\left\{(i\gamma-\rho)(\hat{L}-\hat{z}) - i\gamma\frac{\alpha_0 b}{2D}\right. \qquad \text{(B.2)}$$
$$\left.\times V_0|E_{10}|^2\int_{\hat{L}}^{\hat{z}}\exp(-2\rho z)dz\right\}.$$

The substitution of solutions (B.2) into the last two equations in (28) yields

$$\frac{dE_3}{d\hat{z}} = i\{\bar{\kappa}_3(\hat{z}) + \beta E_{10}E_{20}E_4^*$$
$$\times\exp[(i\gamma-\rho)\hat{z} + i\varphi(\hat{z})]\} - \rho E_3,$$
$$-\frac{dE_4^*}{d\hat{z}} = -i\{\bar{\kappa}_4(\hat{z}) + \beta E_{10}^*E_{20}^*E_3 \qquad \text{(B.3)}$$
$$\times\exp[-(i\gamma+\rho)\hat{z} - i\varphi(\hat{z})]\} - \rho E_4^*,$$

where

$$\bar{\kappa}_3(\hat{z}) = \gamma\left\{1 + \frac{\alpha_0 b}{2D}[V_x|E_{10}|^2\exp(-2\rho\hat{z})\right.$$
$$\left.+ V_z|E_{20}|^2\exp(-2\rho(\hat{L}-\hat{z}))]\right\},$$

$$\bar{\kappa}_4(\hat{z}) = \gamma\left\{1 + \frac{\alpha_0 b}{2D}[V_z|E_{10}|^2\exp(-2\rho\hat{z})\right.$$
$$\left.+ V_x|E_{20}|^2\exp(-2\rho(\hat{L}-\hat{z}))]\right\},$$

$$\varphi(\hat{z}) = \gamma\frac{\alpha_0 b}{2D}V_0\left[|E_{20}|^2\exp(-2\rho\hat{L})\int_0^{\hat{z}}\exp(2\rho z)dz\right.$$
$$\left.-|E_{10}|^2\int_0^{\hat{z}}\exp(-2\rho z)dz\right].$$

The substitutions

$$E_3(\hat{z}) = \mathscr{E}_3(\hat{z})\exp\left(-\rho\hat{z} + i\int_0^{\hat{z}}\bar{\kappa}_3dz\right),$$
$$E_4^*(\hat{z}) = \mathscr{E}_4^*(\hat{z})\exp\left(-\rho(L-\hat{z}) + i\int_{\hat{L}}^{\hat{z}}\bar{\kappa}_4dz\right) \qquad \text{(B.4)}$$

reduce the system of equations (B.3) to the following second-order equation for the amplitude $\mathscr{E}_3(\hat{z})$:

$$\frac{d^2\mathscr{E}_3}{d\hat{z}^2} - [2\rho + i\Delta(\hat{z})]\frac{d\mathscr{E}_3}{d\hat{z}} + \beta^2|E_{10}|^2|E_{20}|^2\exp(-2\rho\hat{L})\mathscr{E}_3 = 0, \quad \text{(B.5)}$$

where

$$\Delta(\hat{z}) = \gamma\frac{\alpha_0 b}{2D}\bar{V}(\theta)\{|E_{20}|^2\exp[-2\rho(\hat{L}-\hat{z})] - |E_{10}|^2\exp(-2\rho\hat{z})\}.$$

It follows from (B.5) that, for $\bar{V}(\theta) = 0$, the roots of the characteristic equation

$$\lambda^2 - 2\rho\lambda + \beta^2|E_{10}|^2|E_{20}|^2\exp(-2\rho\hat{L}) = 0 \quad \text{(B.6)}$$

are given by

$$\lambda_\pm = \rho \pm i\sqrt{\beta^2|E_{10}|^2|E_{20}|^2\exp(-2\rho\hat{L}) - \rho^2} \equiv \rho \pm i\hat{\Gamma}. \quad \text{(B.7)}$$

Applying the boundary conditions $E_3(0) = E_{30}$ and $E_4^*(\hat{L}) = 0$, we determine the integration constants $C_\pm$ of the system of equations (B.3):

$$C_\pm = \pm E_{30}\frac{\lambda_\mp\exp(\mp i\hat{\Gamma}\hat{L})}{\lambda_-\exp(-i\hat{\Gamma}\hat{L}) - \lambda_+\exp(i\hat{\Gamma}\hat{L})}. \quad \text{(B.8)}$$

The condition $\lambda_-\exp(-i\hat{\Gamma}\hat{L}) - \lambda_+\exp(i\hat{\Gamma}\hat{L}) = 0$ implies formula (35).

ACKNOWLEDGMENTS

This work was supported by the ISTC, project no. B-479.

REFERENCES

1. G. A. Askar'yan, Zh. Éksp. Teor. Fiz. **42**, 1567 (1962) [Sov. Phys. JETP **15**, 1088 (1962)].
2. A. Ashkin, Phys. Rev. Lett. **25**, 1321 (1970).
3. P. W. Smith, A. Ashkin, and W. J. Tomlinson, Opt. Lett. **6**, 284 (1981).
4. A. J. Palmer, Opt. Lett. **5**, 54 (1980).
5. A. Yariv, *Quantum Electronics*, 2nd ed. (Wiley, New York, 1975; Sovetskoe Radio, Moscow, 1980).
6. D. Rogovin and O. Sari, Phys. Rev. A **31**, 2375 (1985).
7. H. C. van de Hulst, *Light Scattering by Small Particles* (Wiley, New York, 1957; Inostrannaya Literatura, Moscow, 1961).
8. P. Zemánek, A. Jonáš, and M. Liška, J. Opt. Soc. Am. A **19**, 1025 (2002).
9. S. A. Akhmanov and S. Yu. Nikitin, *Physical Optics* (Mosk. Gos. Univ., Moscow, 1998) [in Russian].
10. A. Rohrbach and E. H. K. Stelzer, J. Opt. Soc. Am. A **18**, 839 (2001).
11. A. A. Afanas'ev, A. N. Rubinov, and Yu. A. Kurochkin, Kvantovaya Élektron. (Moscow) **33**, 250 (2003).
12. G. A. Korn and T. M. Korn, *Mathematical Handbook for Scientists and Engineers*, 2nd ed. (McGraw-Hill, New York, 1968; Nauka, Moscow, 1973).
13. A. I. Akhiezer and S. V. Peletminskiĭ, *Methods of Statistical Physics* (Nauka, Moscow, 1977; Pergamon, Oxford, 1981).
14. L. D. Landau and E. M. Lifshitz, *Course of Theoretical Physics*, Vol. 8: *Electrodynamics of Continuous Media*, 2nd ed. (Nauka, Moscow, 1982; Pergamon, Oxford, 1984).
15. B. Ya. Zel'dovich, N. F. Pilipetskiĭ, and V. V. Shkunov, *Wave Front Reversal* (Nauka, Moscow, 1985) [in Russian].
16. B. Ya. Zel'dovich and T. V. Yakovleva, Kvantovaya Élektron. (Moscow) **8**, 1891 (1981).

Translated by I. Nikitin

Journal of Experimental and Theoretical Physics, Vol. 101, No. 3, 2005, pp. 401–409.
Translated from Zhurnal Éksperimental'noĭ i Teoreticheskoĭ Fiziki, Vol. 128, No. 3, 2005, pp. 464–475.

ATOMS, MOLECULES, OPTICS

Modified Phase Matching Conditions for Second Harmonic Generation in a Finite One-Dimensional Photonic Crystal near the Bragg Condition: Weak and Strong Diffraction

E. V. Petrov and B. I. Mantsyzov

Moscow State University, Moscow, 119992 Russia
e-mail: epetrov@genphys.phys.msu.ru; mants@genphys.phys.msu.ru

Received December 20, 2004

Abstract—Enhanced noncollinear second harmonic generation in a finite one-dimensional photonic crystal is analyzed theoretically under conditions of pump field localization near the Bragg reflection. It is shown numerically that phase-matched second-harmonic generation can be implemented in a finite one-dimensional photonic crystal that does not satisfy the conventional phase-matching conditions calculated for effective Bloch modes with narrow spectral lines. The intensity of the generated second-harmonic signal exceeds the second-harmonic intensity attained under the conventional phase-matching conditions by more than an order of magnitude. This phenomenon is explained by interference between Bloch modes having similar amplitudes, wavenumbers, and spectral widths. Since the spatial spectra of waves propagating in a bounded medium have finite widths, the broadened spectral lines of proximate effective Bloch modes resulting from Bragg diffraction of waves tuned to the first transmission resonances near the photonic bandgap edge overlap, merging into a spectral profile with center shifted relative to the original effective Bloch wavevectors. This effect leads to modified phase matching conditions for second harmonic generation in a finite photonic crystal, which are written for the centers of the spectral profiles resulting from modal overlap, rather than for individual effective wavevectors. Substantially different phase matching conditions are obtained for weakly and strongly diffracted beams, whereas conventional phase matching conditions hold only for transmitted signals in the case of weak diffraction. © *2005 Pleiades Publishing, Inc.*

1. INTRODUCTION

Recent development of new nonlinear optical materials, photonic crystals [1, 2], has motivated extensive studies of parametric conversion in periodic nonlinear structures [3]. Photonic crystal is an artificial structure with periodically modulated dielectric constant (in the general case, in three dimensions). When the modulation period is comparable to the optical wavelength, a light wave cannot propagate into the structure if its frequency or angle of incidence lies within a certain range called photonic band gap (PBG) [4]. Photonic crystals are characterized by strong localization of the energy of a pump (fundamental) beam whose frequency or angle of incidence corresponds to a PBG edge. The increase in pump energy density leads to higher amplitudes of polarization waves and, as a consequence, to higher intensities of Raman sidebands generated in parametric conversion processes. For one-dimensional photonic crystals, this effect was investigated in [5, 6]. We call it non-phase-matching enhancement. In [7], it was shown analytically that the energy of a localized pump wave can be proportional to the number of photonic-crystal periods cubed. Therefore, non-phase-matching enhancement provides a very efficient method for enhancing nonlinear wave interaction in periodically structured materials, whereas the intensities of signals generated in homogeneous media cannot increase faster than the sample length squared. It is well known that conversion of pump energy into Raman sidebands is efficient only when phase or group-velocity matching conditions are satisfied, as in birefringent crystals [8], artificial crystals with regular domain structure [9–11], or optical waveguides [12–14]. Since phase matching and non-phase-matching enhancement conditions are combined in photonic crystals [15–17], conversion efficiency can be additionally enhanced in photonic crystals as compared to homogeneous materials. For a photonic crystal about ten micrometers thick, the efficiency of energy conversion from fundamental into second-harmonic field can exceed 10% [18, 19], which is two orders of magnitude higher than the efficiency of nonlinear optical conversion in a homogeneous nondispersive medium of similar thickness. Strong spatial dispersion near the PBG edge [4] can compensate for the material dispersion in a photonic crystal, ensuring phase-matched interaction between fundamental and generated waves in nonlinear processes. We call this effect dispersion phase matching (DPM). Simultaneous fulfillment of the DPM and non-phase-matching enhancement conditions was predicted theoretically in [15] and demonstrated experimentally in [16] for second harmonic generation. Another mechanism of compensation of phase mismatch between interacting

waves in photonic crystals involves the reciprocal lattice vector and is known as quasi-phase-matching (QPM) [10]. QPM conditions are generally fulfilled for counterpropagating pump and signal waves, whereas DPM is characteristic of copropagating waves. Sum-frequency generation under QPM conditions combined with non-phase-matching enhancement conditions was demonstrated in [17]. Material dispersion can also be compensated for signals generated in nonlinear liquid crystals of certain types [20–22], which can essentially be treated as natural photonic crystals. However, the refractive-index modulation amplitude in these crystals is not sufficient for achieving significant non-phase-matching enhancement.

According to [15], second harmonic generation can be implemented in a photonic crystal under phase matching conditions for effective wavevectors [23] if the fundamental and second-harmonic frequencies are tuned, respectively, to the first and second transmission resonances relative to the corresponding PBG center frequencies. Experimental evidence of the corresponding second-harmonic intensity peak was obtained in [16, 24] for structures specially designed to meet these conditions. However, the efficiency of second harmonic generation under non-phase-matching enhancement conditions has never been analyzed for fundamental wave and second harmonic tuned to other transmission resonances. The parameters of periodic structures and pump beams corresponding to optimal efficiency of Raman sideband generation are generally calculated by using effective wavevectors [4, 23] in conventional phase matching conditions similar to those for waves propagating in infinite homogeneous media. In this method, the field propagating in a layered structure is represented as a superposition of Bloch modes characterized by effective wavevectors instead of Bloch vectors. However, a real photonic crystal cannot be treated as a homogeneous medium even approximately. The field inside a bounded crystal has a very complex structure consisting of Bloch modes with spectral widths $\Delta k \sim 2\pi/L$, where L is the sample length. Therefore, if the shift between two proximate Bloch modes with comparable amplitudes is approximately equal to Δk (when the pump is tuned near the PGB edge), then the corresponding spectral lines merge, and the resulting profile has a peak shifted relative to the effective wavevector. Accordingly, the phase matching conditions calculated for modes with finite spectral widths may be shifted relative to the phase matching conditions calculated by using effective wavevectors (corresponding to Bloch modes with narrow spectral lines), and the maximum shift is π/L. For example, the peak intensities and frequencies of the second-harmonic and sum-frequency signals measured in [17] were shifted relative to those corresponding to the exact phase conditions calculated for effective wavevectors.

In this study, we use a special noncollinear geometry to ensure non-phase-matching enhancement in a wide frequency range and apply the transfer matrix formalism [25] to demonstrate the possibility of efficient second harmonic generation in a thin one-dimensional photonic crystal when the fundamental-wave and second-harmonic first transmission resonances coincide. In this case, even though the conventional phase matching conditions calculated for effective wavevectors corresponding to Bloch modes with narrow spectral lines are not satisfied, the signal intensity exceeds that of the second harmonic satisfying the conventional phase matching conditions [15, 16]. This effect is explained by analyzing dynamics of coupled modes and taking into account the overlapping in both pump and signal spectra. We propose modified phase matching conditions written for the centers of profiles resulting from modal overlap in the spatial spectra of coupled waves. We show that optimal conditions for efficient coupling between the pump and signal waves are substantially different in the cases of strong and weak Bragg diffraction in a photonic crystal.

The paper is organized as follows. In Section 2, we formulate the problem, outline the method of solution, and describe the periodic structure to be examined. In Section 3, we analyze the spatial spectra of waves propagating through periodic structures. The results of Section 3 are used in Section 4 to explain the behavior of the frequency profiles of second-harmonic intensity obtained in the cases of weak and strong diffraction.

2. SECOND HARMONIC GENERATION NEAR THE EDGE OF THE PHOTONIC BAND GAP IN A BOUNDED PHOTONIC CRYSTAL

We consider second harmonic generation in a stack of N bilayers characterized by quadratic nonlinearity, with thicknesses d_1 and d_2 and complex frequency-dependent refractive indices $n_1(\omega)$ and $n_2(\omega)$, on an infinite substrate with complex refractive index n_{subs}. Their second-order susceptibilities $\chi_1^{(2)}$ and $\chi_2^{(2)}$ are assumed to be constant for simplicity (subscripts 1 and 2 refer to odd and even layers, respectively). Pump beams with frequencies ω_1 and ω_2 are incident from vacuum onto the crystal surface at arbitrary angles θ_1 and θ_2, respectively, to the normal vector. The z axis is aligned with the normal vector and directed into the crystal, the x axis is parallel to its surface, and the xz plane is the plane of incidence of the fundamental waves.

Owing to quadratic nonlinearity, a polarization wave with frequency $\omega_1 + \omega_2$ is created in the photonic crystal, which gives rise to a sum-frequency signal at $\omega_3 = \omega_1 + \omega_2$. The pump and sum-frequency fields inside the crystal, $\mathbf{E}_{1,2}(\mathbf{r}, t)$ and $\mathbf{E}_3(\mathbf{r}, t)$, and the sum-frequency output fields in vacuum and substrate are found by solving the nonlinear wave equation

$$\mathrm{rotrot}\mathbf{E} + \frac{1}{c^2}\frac{\partial^2 \mathbf{D}}{\partial t^2} = \frac{4\pi}{c^2}\frac{\partial^2 \mathbf{P}_{NL}}{\partial t^2}. \quad (1)$$

Here, $\mathbf{D}(\mathbf{r}, t) = n^2(\mathbf{r})\mathbf{E}(\mathbf{r}, t)$ is electric induction,

$$\mathbf{P}_{\mathrm{NL}}(\mathbf{r}, t) = \chi^{(2)} : \mathbf{E}(\mathbf{r}, t)\mathbf{E}(\mathbf{r}, t)$$

is the nonlinear polarization vector, and c is the speed of light in free space. In this study, the transfer matrix formalism [17, 25] is applied to solve Eq. (1) in the monochromatic plane-wave approximation for a prescribed pump field. This model is valid for pulses of duration up to 200–300 fs [6, 17] and weak nonlinearity. Under these assumptions, the transfer matrix formalism can be used to obtain an exact solution to Eq. (1) (with second spatial derivatives) describing the complex multiple-mode structure of localized fields in a thin photonic crystal.

Hereinafter, we consider the degenerate case of sum-frequency signal with $\omega_1 = \omega_2 = \omega$ and $\omega_3 = 2\omega$. To optimize the fundamental-wave parameters with respect to maximum generated signal intensity, we use the noncollinear beam geometry illustrated by Fig. 1a, which ensures fulfillment of the non-phase-matching enhancement condition in a wide frequency range. We vary ω and angle of incidence θ simultaneously to satisfy the non-phase-matching enhancement condition, i.e., to maximize the energy W of the field localized in the structure (Fig. 1b),

$$W = \int_0^L n^2(z)|E(z)|^2 dz,$$

where $z = 0$ and $z = L = N(d_1 + d_2)$ are the input and output surfaces of the photonic crystal. The mismatch parameters Δ_{DPM} and Δ_{QPM} corresponding, respectively, to dispersion phase matching and quasi-phase matching conditions, are expressed in terms of effective wavevectors as

$$\Delta_{\mathrm{DPM}} = (k_{1z}^{\mathrm{eff}} + k_{2z}^{\mathrm{eff}} - k_{3z}^{\mathrm{eff}})L, \quad (2)$$

$$\Delta_{\mathrm{QPM}} = (k_{1z}^{\mathrm{eff}} + k_{2z}^{\mathrm{eff}} + k_{3z}^{\mathrm{eff}} - Hl)L, \quad (3)$$

where k_{iz}^{eff} denotes the z components of the pump ($i = 1, 2$) and signal ($i = 3$) waves, $H = 2\pi/(d_1 + d_2)$ is the magnitude of the reciprocal lattice vector, and l is an integer called quasi-phase-matching order. Expression (2) is analogous to the phase mismatch for a homogeneous medium, while the term proportional to Hl in (3) takes into account the contribution of Bloch modes due to Bragg diffraction in a periodic structure. The parameters in (2) and (3) vary with ω and θ. Phase matching corresponds to

$$\Delta_{\mathrm{DPM}}, \Delta_{\mathrm{QPM}} \le \pi/2. \quad (4)$$

Since the fundamental waves have equal frequencies, the corresponding wavevectors are symmetric relative to the normal: $\theta_1 = +\theta_0$ and $\theta_2 = -\theta_0$, where the angle of incidence θ_0 ensures non-phase-matching enhancement for a particular ω. Since the tangential components of the electric field vectors are continuous across layer boundaries [23], the "angle of incidence" θ_3 for the second harmonic is zero for any ω.

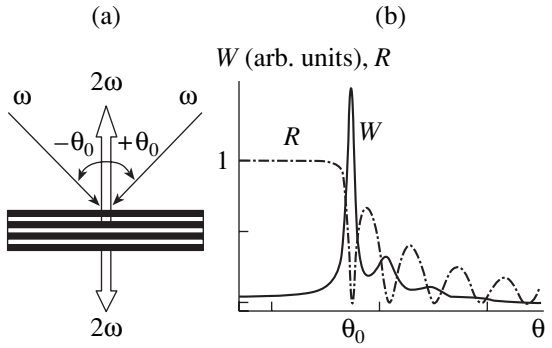

Fig. 1. Second harmonic generation: (a) noncollinear geometry; (b) reflectivity R and energy W of localized electric field of the pump beam vs. angle of incidence θ (θ_0 corresponds to non-phase-matching enhancement).

Figure 2a shows the intensities $I^{(+)}$ and $I^{(-)}$ of the transmitted and reflected second-harmonic signals in the geometry considered here versus normalized frequency for the stack of 15 bilayers with $n_1(\omega)$ and $n_2(\omega)$ corresponding to AlOx and AlGaAs (nonlinear optical material), respectively [16]. Here, $d_1 = \lambda_0/3n_1(\omega_0)$ and $d_2 = 3\lambda_0/4n_2(\omega_0)$, where $\lambda_0 = 2\pi c/\omega_0$ and ω_0 is a reference frequency; the substrate is vacuum. The intensity $I^{(\pm)}$ is normalized to that of the second-harmonic signal with frequency $2\omega_0$ generated in a homogeneous nondispersive medium of thickness $D = Nd_2$ with refractive index $n_2(\omega_0)$. Figures 2b and 2c show, respectively, the second-harmonic reflectivity and the phase mismatch parameters Δ_{DPM} and Δ_{QPM}, respectively. The phase matching order is $l = 4$, and all waves are s-polarized.

The second-harmonic intensity spectrum shown in Fig. 2a exhibits two peaks whose locations are indicated by vertical dash-dot lines A and B. The former corresponds to the zero of Δ_{DPM} associated with the second transmission resonance (relative to the second-harmonic PBG center frequency). The existence of this peak was demonstrated in [15, 16, 24]. The latter is associated with the first second-harmonic transmission resonance and is not related to any zero of Δ_{DPM} or Δ_{QPM}. This intensity peak is more than an order of magnitude higher than the former; i.e., the corresponding phase matching conditions cannot be formulated in terms of effective wavevectors corresponding to Bloch modes with narrow spectral lines, as in (2) or (3). Its location should therefore be explained by analyzing a multiple-mode structure in order to find phase matching conditions different from (2)–(4).

3. SPATIAL SPECTRA OF WAVES DIFFRACTED NEAR THE PHOTONIC BAND-GAP EDGE

In the model presented above, an effective wavevector $k^{\text{eff}}(\omega)$ is calculated to characterize the propagation of a wave with frequency ω through a multilayered stack [23]. The linear properties of a photonic crystal are characterized by the dispersion curve shown in Fig. 3 (right solid branch). Any layered structure generates a reflected (backward) wave. Since the magnitude of the corresponding wavevector is equal to that of the forward wave, the reflected-wave dispersion curve is symmetric to the forward-wave one relative to the ω axis (left solid branch in Fig. 3). However, Bragg diffraction in a periodic structure must give rise to a Bloch wave related to the incident wave by the Bragg condition $\mathbf{k}_2 = \mathbf{k}_1 + m\mathbf{H}$, where m is the number of the PBG responsible for diffraction; i.e., in addition to waves with wavevectors k^{eff} and $-k^{\text{eff}}$, there must exist Bragg-diffracted waves with $k^{\text{eff}} - mH$ and $-k^{\text{eff}} + mH$ (see Fig. 3). Thus, we must consider four waves propagating in a photonic crystal if diffraction is to be taken into account: two forward and two backward ones.

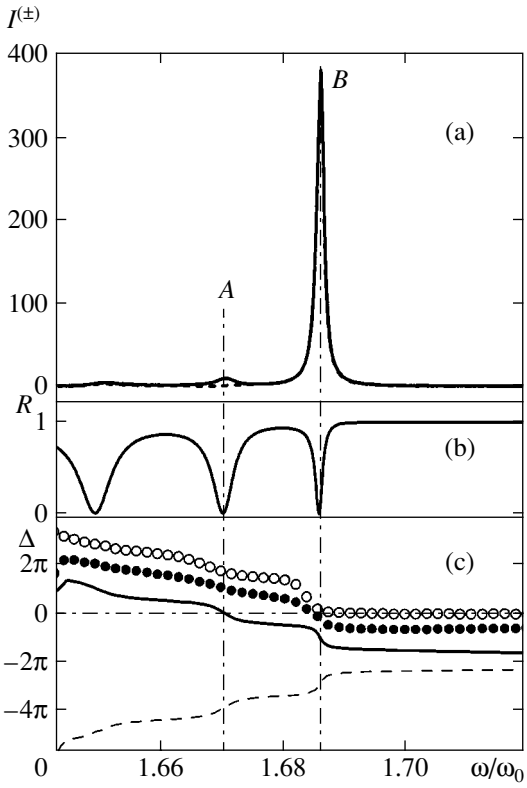

Fig. 2. Normalized frequency dependence: (a) normalized intensities $I^{(+)}$ and $I^{(-)}$ of the transmitted and reflected second-harmonic signals (solid and dashed curves, respectively); (b) second-harmonic reflectivity R; (c) phase mismatch parameters Δ_{DPM} (solid curve) and Δ_{QPM} (dashed curve); $\Delta^{(+)}$ (●) and $\Delta^{(-)}$ (○). Vertical dash-dot lines A and B indicate the peak second-harmonic intensities corresponding to the second and first transmission resonances, respectively.

The existence of waves with wavenumbers $k^{\text{eff}} - mH$ and $-k^{\text{eff}} + mH$ is easy to demonstrate for a structure with continuous dielectric constant $\varepsilon(z)$, because neither Fourier series expansion of solutions nor their matching at the points of discontinuity is required in this case. Since wave propagation in periodic structures is governed by qualitatively similar relations, we can consider a crystal with harmonically modulated dielectric constant:

$$\varepsilon(z) = \begin{cases} \varepsilon_0, & z \notin [0, L], \\ \varepsilon_0[1 + \mu\cos(Hz)], & z \in [0, L], \end{cases}$$

where ε_0 is the background dielectric constant, μ is the modulation depth, $H = 2\pi/d$ is the reciprocal lattice vector, d is the modulation period, $L = \Lambda N$ is the crystal length, and $z = 0$ and $z = L$ are the input and output ends of the modulated crystal. The electric field distribution $E(z)$ in a linear medium is found by solving Eq. (1) with zero right-hand side [23].

Within the interval $[0, L]$, the electric field of a plane electromagnetic wave with frequency ω can be represented as

$$E(r, t) = E_0(z)\exp[i(\omega t - k_x x)], \qquad (5)$$

where $k_x = k_0\sin\theta$ is the tangential component of the wavevector, $k_0 = \omega/c$ is the wavevector magnitude in free space, $k = k_0\sqrt{\varepsilon_0}$ is the wavevector magnitude in the medium, and θ is the angle between the wave prop-

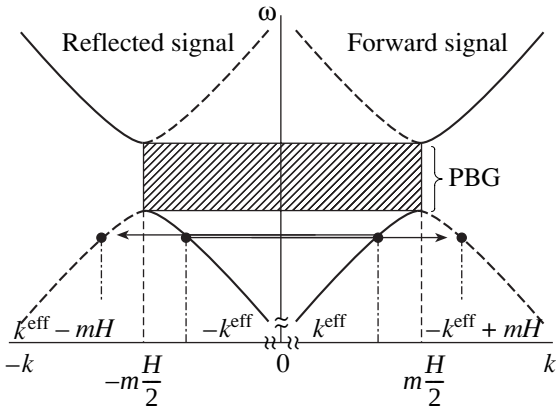

Fig. 3. Dispersion curves for forward (right) and reflected (left) signals in single-mode approximation (solid curves) and for diffracted signals (dashed curves). The hatched region corresponds to PBG. Dots on dispersion curves correspond to the wavenumbers of the forward (k^{eff}), backward ($-k^{\text{eff}}$), and Bragg-diffracted ($k^{\text{eff}} - mH$, $-k^{\text{eff}} + mH$) waves.

agation direction and the z axis. The complex amplitude $E_0(z)$ is expressed as

$$\begin{aligned} E_0(z) &= E_+(z) + E_-(z) \\ &= A_+(z)\exp(ik_z z) + A_-(z)\exp(-ik_z z), \end{aligned} \tag{6}$$

where $A_+(z)$ and $A_-(z)$ denote the amplitudes of the forward and backward waves, respectively, and

$$k_z = k_0\sqrt{\varepsilon_0 - \sin^2\theta}$$

is the z component of the pump wavevector. We assume that the dielectric-constant modulation depth is sufficiently small to satisfy the condition for slowly varying amplitudes,

$$\left|\frac{d^2A_\pm}{dz^2}\right| \ll \left|2k_z\frac{dA_\pm}{dz}\right|.$$

If the diffracted waves are tuned near the edge of the first PBG, then the parameter $\delta = k_z - H/2$ is a small quantity.

Substituting (5) and (6) into (1) (with $\mathbf{P}_{NL}$ set to zero), neglecting the fast-oscillating terms, and separating the terms containing $\exp(ik_z z)$ and $\exp(-ik_z z)$, we obtain the system of differential equations

$$\begin{aligned} \frac{d}{dz}A_+ &= i\frac{\mu k^2}{4k_z}A_-\exp(-2i\delta z), \\ \frac{d}{dz}A_- &= -i\frac{\mu k^2}{4k_z}A_+\exp(2i\delta z), \end{aligned} \tag{7}$$

subject to the boundary conditions

$$A_+(z=0) = A_+^0, \quad A_-(z=L) = 0,$$

where A_+^0 is the incident intensity on the left-hand boundary between the homogeneous and modulated media, and the latter condition means that no beam is incident on the right-hand boundary.

Substituting the solution to (7) into (6), we obtain the following expressions for the forward and backward electric field amplitudes:

$$\begin{aligned} E_+(z) &= \frac{\alpha\cos[\alpha(L-z)] - i\delta\sin[\alpha(L-z)]}{\alpha\cos(\alpha L) - i\delta\sin(\alpha L)} \\ &\quad\times A_+^0\exp\left(i\frac{H}{2}z\right), \end{aligned} \tag{8}$$

$$\begin{aligned} E_-(z) &= i\frac{\mu k^2}{4k_z}\frac{\sin[\alpha(L-z)]}{\alpha\cos(\alpha L) - i\delta\sin(\alpha L)} \\ &\quad\times A_+^0\exp\left(-i\frac{H}{2}z\right), \end{aligned} \tag{9}$$

where

$$\alpha = \sqrt{\delta^2 - \left(\frac{\mu k^2}{4k_z}\right)^2}.$$

We rewrite the real values of the electric field strengths given by (8) and (9) as

$$\begin{aligned} \mathrm{Re}[E_+(z)] &= \frac{1}{4\xi}\Bigg\{(\alpha+\delta)^2\cos(\beta_+ z) \\ &\quad + (\alpha-\delta)^2\cos(\beta_- z) - \left(\frac{\mu k^2}{4k_z}\right)^2\cos(2\alpha L) \\ &\quad\times[\cos(\beta_+ z) + \cos(\beta_- z)] \\ &\quad - \left(\frac{\mu k^2}{4k_z}\right)^2\sin(2\alpha L)[\sin(\beta_+ z) - \sin(\beta_- z)]\Bigg\}A_+^0, \end{aligned} \tag{10}$$

$$\begin{aligned} \mathrm{Re}[E_-(z)] &= \frac{1}{4\xi}\frac{\mu k^2}{4k_z}\{(\alpha-\delta)\cos(-\beta_+ z) \\ &\quad - (\alpha+\delta)\cos(-\beta_- z) + (\alpha+\delta)\cos(2\alpha L)\cos(-\beta_+ z) \\ &\quad - (\alpha-\delta)\cos(2\alpha L)\cos(-\beta_- z) \\ &\quad - (\alpha+\delta)\sin(2\alpha L)\sin(-\beta_+ z) \\ &\quad - (\alpha-\delta)\sin(2\alpha L)\sin(-\beta_- z)\}A_+^0, \end{aligned} \tag{11}$$

where

$$\xi = \alpha^2\cos^2(\alpha L) + \delta^2\sin^2(\alpha L),$$

$$\beta_+ = \frac{H}{2} + \alpha, \quad \beta_- = \frac{H}{2} - \alpha.$$

Expressions (10) and (11) demonstrate that the field propagating in medium with modulated dielectric constant consists of four waves, with wavenumbers β_+, β_- and $-\beta_+$, $-\beta_-$ corresponding to forward and backward waves, respectively, i.e., to k^{eff}, $-k^{\mathrm{eff}} + mH$ and $-k^{\mathrm{eff}}$, $k^{\mathrm{eff}} - mH$ with $m = 1$. Since any wave propagating in a bounded photonic crystal has a finite spectral width estimated as $2\pi/L$, the modes with spectral lines separated by Δk overlap and the lines merge into a profile with center shifted relative to their respective centers if

$$\Delta k \le 2\pi/L. \tag{12}$$

Let us show that the spectral components of a signal tuned to the first transmission resonance (relative to the PBG center frequency) satisfy condition (12).

The reflectivity R for a periodic structure is expressed as

$$R = \left|\frac{E_-(z=0)}{E_+(z=0)}\right|^2 = \frac{\sin^2(\alpha L)}{\left(\frac{4\alpha k_z}{\mu k^2}\right)^2 + \sin^2(\alpha L)}.$$

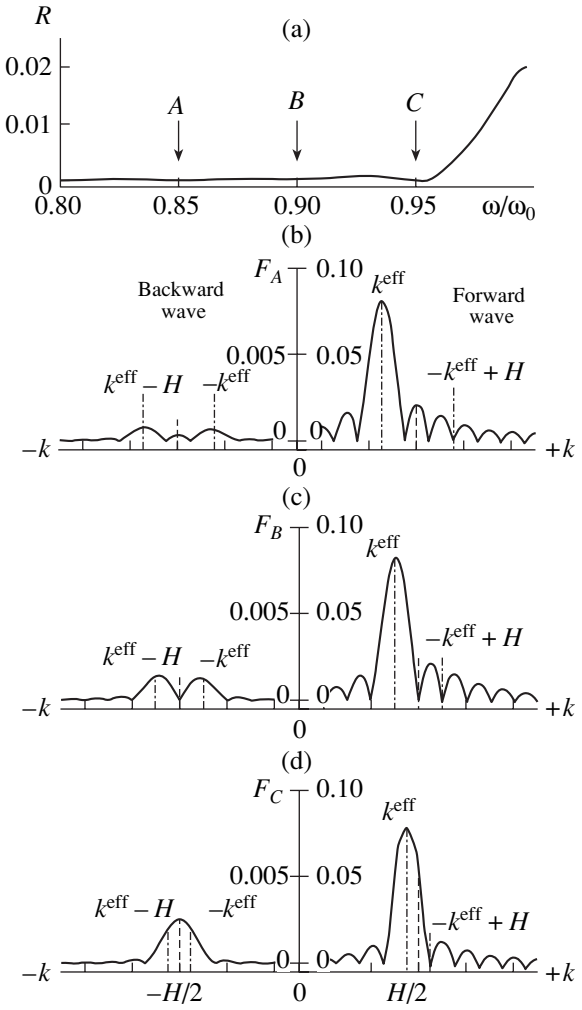

Fig. 4. Weak Bragg diffraction in a structure with cosinusoidally modulated dielectric constant: (a) reflectivity vs. normalized frequency. Spatial spectra of the forward and backward waves for pump beams tuned to (b) third, (c) second, and (d) first transmission resonances (*A*, *B*, and *C*, respectively). Vertical dashed and dash-dot lines indicate, respectively, $H/2$ components and the effective wavevectors of forward, backward, and diffracted waves calculated in the single-mode approximation.

Transmission resonances are defined by the condition $R = 0$, i.e.,

$$\alpha = \frac{\pi}{L}n, \quad n = 1, 2, 3, \ldots,$$

where n is the number of a resonance and the corresponding wavenumbers are

$$\beta_+ = \frac{H}{2} + \frac{\pi n}{L}, \quad \beta_- = \frac{H}{2} - \frac{\pi n}{L}.$$

Accordingly, $\Delta k = |\beta_+ - \beta_-| = 2\pi n/L$, which entails $\Delta k = 2\pi/L$ for the first transmission resonance, in agreement with condition (12). Thus, the modes centered at β_+ and β_- substantially overlap.

As an example, we consider second harmonic generation in the 20-period structure with $\Lambda/\lambda_0 = 0.25$, $\varepsilon_0 = 4$, and $\mu = 0.01$ (which corresponds to weak Bragg diffraction) in the case of normal beam incidence. Figure 4a shows the reflectivity plotted versus normalized wave frequency for this structure. The third, second, and first transmission resonances are indicated by *A*, *B*, and *C*, respectively. Figures 4b–4d show the spatial spectra

$$F(k) = \left| \frac{1}{2\pi L} \int_0^L \mathrm{Re}[E_\pm(z)] \exp(ikz) dz \right|$$

plotted versus k normalized to $2\pi/L$ for waves tuned to the resonances *A*, *B*, and *C*, respectively. Here, the spectra of $E_-(z)$ and $E_+(z)$ correspond to $k < 0$ and $k > 0$, respectively; vertical dash-dot lines, to $k^{\mathrm{eff}} - mH$, $-k^{\mathrm{eff}}$, k^{eff}, and $-k^{\mathrm{eff}} + mH$ with $m = 1$. Figures 4b and 4c demonstrate that the reflected-wave spectrum contains two lines of equal intensity centered at $k^{\mathrm{eff}} - mH$ and $-k^{\mathrm{eff}}$, owing to diffraction of the incident wave. The spectrum of the forward wave contains only the component centered at k^{eff}, whereas the one centered at $-k^{\mathrm{eff}} + mH$ (due to reflected-wave diffraction) is absent in the case of weak diffraction, because $|E_-(z)| \sim \mu$.

A totally different reflected-wave spectrum is obtained for diffraction near the first transmission resonance *C* (Fig. 4d). As shown analytically above, the lines corresponding to $k^{\mathrm{eff}} - mH$ and $-k^{\mathrm{eff}}$ overlap and merge into a single line. Figure 4d demonstrates that the resulting reflected-wave line is centered at $mH/2$, whereas the spectrum of the forward wave is still centered at k^{eff}.

To analyze the case of strong diffraction, we find the spatial spectra of waves propagating in a medium with cosinusoidally modulated dielectric constant having the parameters specified above, except for $\mu = 0.5$. The equations for slowly varying amplitudes are not applicable in this case, and the field distributions found numerically by using the transfer matrix formalism. Figure 5 shows the corresponding reflectivity and the spatial spectra of the backward and forward waves plotted in the same coordinates as those in Fig. 4.

Figure 5 demonstrates that the spectra of reflected waves are qualitatively similar in the cases of both weak and strong diffraction, differing only in amplitude, whereas the forward wave has a distinct component characterized by $-k^{\mathrm{eff}} + mH$ in the latter case. Its intensity at the transmission resonance *B* (Fig. 5c) is higher as compared to *A* (Fig. 5b), because Bragg reflection becomes stronger as the pump frequency is tuned closer to the PBG. Owing to the higher amplitude of the component with $-k^{\mathrm{eff}} + mH$, the center of the spectral profile resulting from modal overlap for a wave

tuned to the first transmission resonance C is shifted from k^{eff} in the direction of $mH/2$ (Fig. 5d).

The results of this section concerning the coupling efficiency in second harmonic generation can be summarized as follows. Due to the spectral shifts of the coupled waves involved in second harmonic generation near the corresponding PBG edge, phase matching conditions (2)–(4) do not hold for the reflected wave in the case of weak diffraction and for both reflected and forward waves in the case of strong diffraction. Thus, the degree of spectral overlap of the coupled waves should be taken into account in determining optimal conditions for second harmonic generation. Since the highest efficiency of coupling between the fundamental waves and the second-harmonic signal is attained when the sum of the wavenumbers of the strongest fundamental-wave components (i.e., the wavenumber of the nonlinear polarization wave) corresponds to the center of the second-harmonic spectral profile, the modified mismatch parameters

$$\Delta^{(\pm)} = (\bar{k}_1^{(\pm)} + \bar{k}_2^{(\pm)} - \bar{k}_3^{(\pm)})L \qquad (13)$$

expressed in terms of the centers of broadened spectral profiles should be used instead of (2) and (3), and the modified phase matching conditions are written as

$$\Delta^{(\pm)} \le \pi/2, \qquad (14)$$

where the superscripts (+) and (–) correspond to the forward and reflected pump ($i = 1, 2$) and signal ($i = 3$) waves.

In particular, the centers of the reflected-wave spectra in the case of strong diffraction of waves tuned near the first transmission resonance are given by the exact expression $\bar{k}_i^{(-)} = m_i H/2$, where m_i is the number of the corresponding PBG. Accordingly, the mismatch parameters defined by (13) can be written for both reflected and transmitted waves as follows:

$$\Delta^{(\pm)} = (m_1 + m_2 - m_3)\frac{HL}{2}.$$

Figure 2 illustrates strong diffraction near the PBGs with $m_{1,2} = 2$ and $m_3 = 4$, in which case we have $\Delta^{(\pm)} = (2 + 2 - 4)HL/2 = 0$; i.e., the phase matching conditions are satisfied exactly. This explains the existence of a second-harmonic intensity peak at the point B in Fig. 2a. Parameters (13) are shown as functions of frequency for the forward (closed circles) and reflected (open circles) waves in Fig. 2c, for which the centers of spectral profiles were determined directly from the computed spatial spectra. It is clear that phase matching conditions (14) for broadened spectral lines hold near the first transmission resonances.

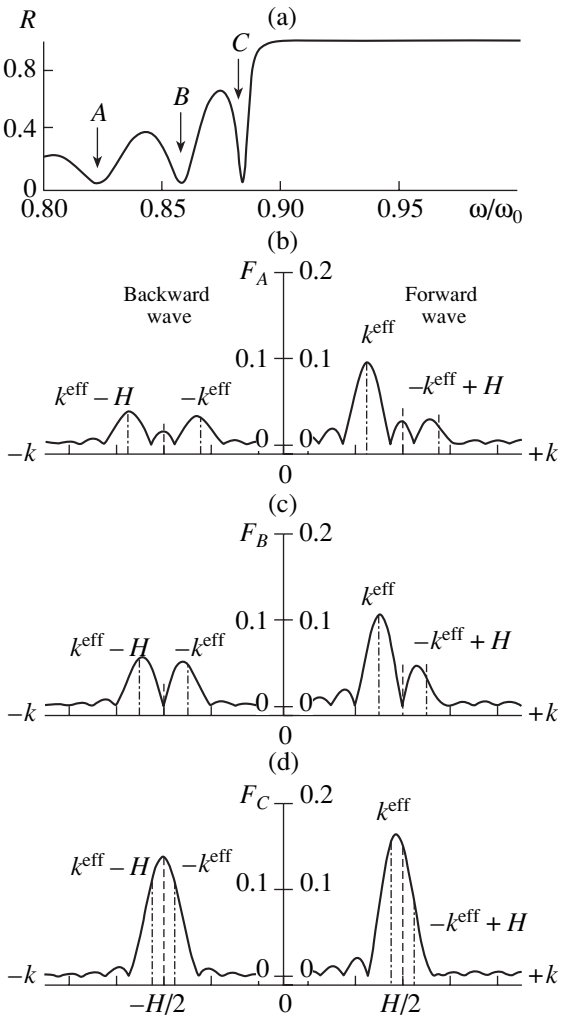

Fig. 5. Strong Bragg diffraction: (a) reflectivity vs. normalized frequency; (b)–(d) spatial spectra under the corresponding conditions specified in Fig. 4.

4. SECOND HARMONIC GENERATION NEAR THE POINT OF FORBIDDEN BRAGG REFLECTION: WEAK AND STRONG DIFFRACTION

Let us demonstrate that modified phase matching conditions (13), (14) hold for second harmonic generation near the point of so-called forbidden Bragg reflection, which is observed when $2\mathbf{k} = m\mathbf{H}$ for a wave propagating through a multilayer stack, whereas each individual layer can transmit light without reflection. In this case, total transmission occurs instead of the total reflection dictated by the Bragg condition. In particular, forbidden Bragg reflection is observed when a beam is normally incident on a stack of alternating layers of two types whose optical thicknesses are multiples of the beam half-wavelength λ: $d_i = p\lambda/2n_i$, where p is an inte-

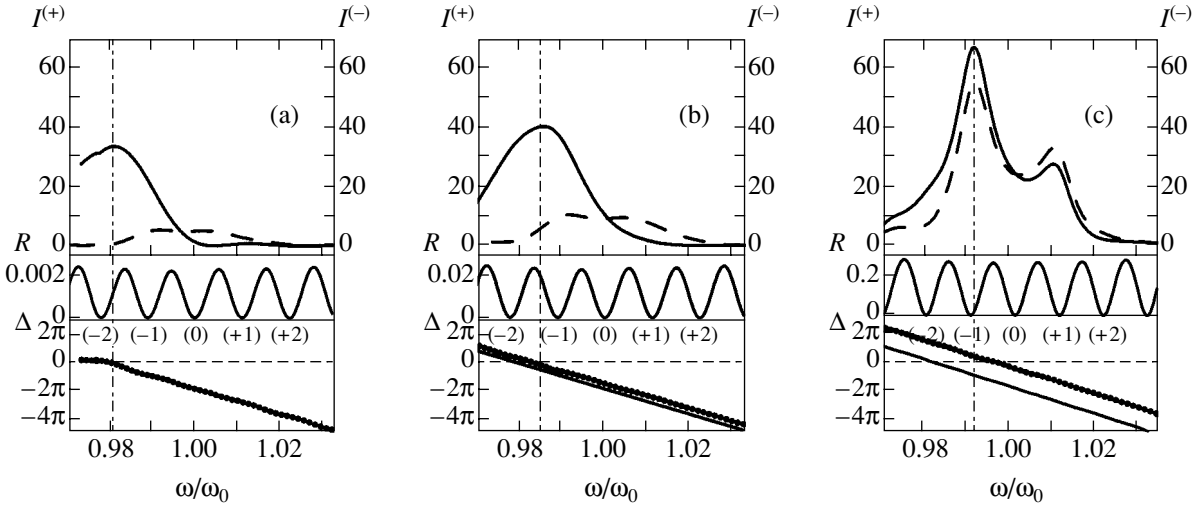

Fig. 6. Normalized intensities $I^{(+)}$ and $I^{(-)}$ of the transmitted and reflected second-harmonic signals (solid and dashed curves, respectively), second-harmonic reflectivity R, and phase mismatch parameters Δ_{DPM} (solid curves) and $\Delta^{(+)}$ (●) vs. normalized frequency for refractive-index contrast $\Delta n = 0.1$ (a), 0.3 (b), and 1.5 (c). Vertical dash-dot lines indicate peak intensities of transmitted second-harmonic signal.

ger and n_i (i = 1, 2) are the refractive indices of the layers.

Let us examine the variation of the intensity $I^{(\pm)}$ with increasing refractive-index contrast $\Delta n = |n_1 - n_2|$ for the second harmonic generated near the point of forbidden Bragg reflection for waves with frequency 2ω when the incident wave is tuned near the PBG edge. As an example, we consider noncollinear second harmonic generation (see Fig. 1) in the stacks of 15 bilayers with $d_{1,2} = 3\lambda_0/4n_{1,2}$, $n_1 = n_{subs} = 1$, and different n_2 for the nonlinear even layers in the absence of material dispersion.

Figures 6a, 6b, and 6c show the intensities $I^{(+)}$ (left ordinate axes) and $I^{(-)}$ (right ordinate axes) of the forward and reflected second-harmonic signals, the second-harmonic reflectivity R, and the mismatch parameters Δ_{DPM} and $\Delta^{(+)}$ given by (2) and (13) for n_2 = 1.1 (weak diffraction), 1.3 (intermediate case), and 2.5 (strong diffraction), respectively. The locations of peaks of $I^{(+)}(\omega)$ on the frequency axis are indicated by vertical dash-dot lines. The intensities are normalized as in Fig. 2. For the photonic crystal with the parameters specified above, forbidden Bragg reflection is observed if the second-harmonic frequency $2\omega_0$ corresponds to the central transmission resonance in the frequency dependence of R (denoted by (0) in Fig. 6). The first, second, etc., transmission resonances on its left and right (denoted by (–1), (–2), (+1), and (+2)) are analogous to those near the PBG in terms of both field distribution and spectral profiles.

In Fig. 6a, the point of maximum intensity of the forward second-harmonic signal coincides with the zeros of the mismatch parameters Δ_{DPM} and $\Delta^{(+)}$. By virtue of the beam geometry, the spatial spectra of both forward and backward waves are analogous to those in Fig. 4d. Accordingly, the spectrum of the forward wave is centered at $2k_{1z}^{eff}$, where k_{1z}^{eff} is the z component of the pump wavevector, and the curves of Δ_{DPM} and $\Delta^{(+)}$ coincide. The second-harmonic spectra at (±2) and (±1) are similar in form to those in Figs. 4c and 4d, respectively. Thus, modified phase matching conditions (14) hold for the forward signal near resonance (–2), where the strongest spectral components of the coupled waves overlap, and for the reflected signal near resonances (±1) and the point of forbidden Bragg reflection.

In the case of intermediate diffraction (see Fig. 6b), the reflected signal exhibits a qualitatively similar behavior, with a higher second-harmonic intensity due to stronger diffraction. The peak of the forward second-harmonic intensity is shifted to the right from the point where $\Delta_{DPM} = 0$, and the curves of $\Delta_{DPM}(\omega)$ and $\Delta^{(+)}(\omega)$ do not coincide. These changes are explained by appreciable contributions of the modes centered at $-k_z^{eff} + mH$ to the spectra of linear and nonlinear forward waves. The zero of $\Delta^{(+)}$ coincides with the point of maximum $I^{(+)}$.

In the case illustrated by Fig. 6c, the components centered at $-k_z^{eff} + mH$ strongly contribute to the spectra of the forward waves. The spectral profiles resulting from modal overlap at the fundamental-wave first transmission resonances are very similar in form to those shown in Fig. 5d, and their centers are located almost exactly at $mH/2$. Accordingly, the peak intensities of both forward and backward second-harmonic signals correspond to transmission resonances (±1).

5. CONCLUSIONS

Second harmonic generation is considered as an example to examine optimal conditions for nonlinear wave coupling in a finite one-dimensional photonic crystal in the cases of strong and weak Bragg diffraction. Special noncollinear beam geometry is used to meet the non-phase-matching enhancement conditions for the second-harmonic signal and determine the wave parameters corresponding to the most accurate simultaneous fulfillment of phase matching conditions. When the second harmonic is generated near the PBG or the point of forbidden Bragg reflection, the phase matching conditions for forward waves in the case of strong diffraction and for reflected waves in the cases of both strong and weak diffraction in a bounded medium differ from the corresponding conventional phase conditions. The modified phase matching conditions proposed here for a finite photonic crystal are written for the centers of the spatial spectral profiles resulting from the overlap of broadened lines, rather than for the effective wavevectors of individual Bloch modes. These modified conditions are used to explain the enhanced phase-matched second-harmonic generation predicted in this study in the case when the fundamental-wave and second-harmonic first transmission resonances coincide. The results obtained here can also be used to analyze conditions for efficient conversion by different mechanisms (parametric amplification, Raman scattering, etc.) in finite photonic crystals.

ACKNOWLEDGMENTS

This work was supported by the Russian Foundation for Basic Research, project no. 04-02-16866.

REFERENCES

1. E. Yablonovitch, J. Mod. Opt. **41**, 173 (1994).
2. K. Sakoda, *Optical Properties of Photonic Crystals* (Springer, Berlin, 2001).
3. *Nonlinear Photonic Crystals*, Ed. by R. E. Slusher and B. J. Eggleton (Springer, Berlin, 2003).
4. A. Yariv and P. Yeh, J. Opt. Soc. Am. **67**, 438 (1977).
5. M. Scalora, M. J. Bloemer, A. S. Manka, *et al.*, Phys. Rev. A **56**, 3166 (1997).
6. A. V. Balakin, D. Boucher, V. A. Bushuev, *et al.*, Pis'ma Zh. Éksp. Teor. Fiz. **70**, 718 (1999) [JETP Lett. **70**, 725 (1999)].
7. E. V. Petrov, V. A. Bushuev, and B. I. Mantsyzov, Izv. Ross. Akad. Nauk, Ser. Fiz. **66**, 1787 (2002).
8. J. A. Giordmaine, Phys. Rev. Lett. **8**, 19 (1962).
9. J. A. Armstrong, N. Bloembergen, J. Ducuing, and P. S. Pershan, Phys. Rev. **127**, 1918 (1962).
10. M. M. Fejer, G. A. Magel, D. H. Jundt, and R. L. Byer, IEEE J. Quantum Electron. **28**, 2631 (1992).
11. A. S. Chirkin, V. V. Volkov, G. D. Laptev, and E. Yu. Morozov, Kvantovaya Élektron. (Moscow) **30**, 847 (2000).
12. Y. Fujii, B. S. Kawasaki, K. O. Hill, and D. C. Johnson, Opt. Lett. **5**, 48 (1980).
13. Y. Ohmori and Y. Sasaki, Appl. Phys. Lett. **39**, 466 (1981).
14. G. P. Agrawal, *Nonlinear Fiber Optics* (Academic, New York, 1995; Mir, Moscow, 1996).
15. M. Centini, C. Sibilia, M. Scalora, *et al.*, Phys. Rev. E **60**, 4891 (1999).
16. Y. Dumeige, I. Sagnes, P. Monnier, *et al.*, J. Opt. Soc. Am. B **19**, 2094 (2002).
17. A. V. Balakin, V. A Bushuev, B. I. Mantsyzov, *et al.*, Phys. Rev. E **63**, 046609 (2001).
18. G. D'Aguanno, M. Centini, M. Scalora, *et al.*, Phys. Rev. E **64**, 016609 (2001).
19. B. I. Mantsyzov, E. V. Petrov, E. B. Tereshin, and V. A. Trofimov, Izv. Ross. Akad. Nauk, Ser. Fiz. **68**, 1710 (2004).
20. I. D. Olenik and M. Copic, Phys. Rev. E **56**, 581 (1997).
21. V. A. Belyakov, Pis'ma Zh. Éksp. Teor. Fiz. **70**, 793 (1999) [JETP Lett. **70**, 811 (1999)].
22. J.-G. Yoo, S.-W. Choi, H. Hoshi, *et al.*, Jpn. J. Appl. Phys., Part 2 **36**, L1168 (1997).
23. M. B. Vinogradova, O. V. Rudenko, and A. P. Sukhorukov, *The Theory of Waves* (Nauka, Moscow, 1990) [in Russian].
24. Y. Dumeige, P. Vidakovic, S. Sauvage, *et al.*, Appl. Phys. Lett. **78**, 3021 (2001).
25. D. S. Bethune, J. Opt. Soc. Am. B **6**, 910 (1989).

Translated by A. Betev

Journal of Experimental and Theoretical Physics, Vol. 101, No. 3, 2005, pp. 410–419.
Translated from Zhurnal Éksperimental'noĭ i Teoreticheskoĭ Fiziki, Vol. 128, No. 3, 2005, pp. 476–488.

ATOMS, MOLECULES, OPTICS

Off-Resonant Two-Photon-Assisted Electron Transfer between Quantum Dots

A. M. Basharov* and S. A. Dubovis**

Russian Research Centre Kurchatov Institute, pl. Kurchatova 1, Moscow, 123182 Russia
*e-mail: *bash@online.ru, basharov@gmail.com; **spiritt@list.ru*

Received February 8, 2005

Abstract—Electron transfer between bound states of remote quantum dots driven by an off-resonant electromagnetic pulse is analyzed. In the case of nearly equal energies of the states, a two-photon transfer mechanism related to the high-frequency off-resonant Stark effect is proposed. An equivalent transformation is used to derive an effective Hamiltonian that provides a basis for correct treatment of continuum (conduction-band) states. It is shown that optimal conditions for electron transfer correspond to quasi-resonant excitation of states near the lower edge of the continuum. The characteristics of the process are evaluated. © *2005 Pleiades Publishing, Inc.*

1. INTRODUCTION

One natural line of development in conventional semiconductor-based microelectronics is the miniaturization of individual elements, which includes extensive studies of quantum effects in nanosized objects and development of nanotechnologies. One of the most important tasks in this area is analysis of various regimes of interaction between electromagnetic field and nanostructures with a view to finding effective mechanisms for optical control of electron dynamics. In [1], the effect of electromagnetic field on a double quantum well was examined and conditions for electron confinement in one of the wells were discussed. In [2–9], the converse process of electron transfer between two identical quantum dots driven by an electromagnetic (optical) pulse was considered. It was shown in [2, 3] that photoinduced electron transfer between quantum dots in a double-dot system treated as a qubit can be used to implement quantum logic gates.

Most studies of photoinduced electron transfer have been focused on resonant (one-photon [2–8] or Raman [9]) transitions between discrete levels having substantially different energies. In particular, the analysis presented in [2] was the first study of photoinduced electron transfer between low-lying states of two identical quantum dots via a third level at the top of the potential barrier between the dots (Fig. 1a), with a driving field in resonance with the transition from the lower energy levels to the upper level in the three-level system. Note that this mechanism is difficult to validate experimentally, primarily because the preparation of two nearly identical quantum dots with prescribed properties is a complicated technical task.

This difficulty does not arise with regard to a Raman-resonant process of cyclic transition between states with energies E_1 and E_2 in a system driven by a bichromatic field with frequencies ω_1 and ω_2 such that $E_2 - E_1 \approx \omega_1 - \omega_2$ (Fig. 1b) [9] (see also [10–12]).

In this paper, we consider the case when $E_2 \approx E_1$ and the corresponding bound states are localized in remote quantum dots, which may not be identical (Fig. 2). In what follows, we show that electron transfer between the quantum dots can be implemented by driving the system with a monochromatic electromagnetic wave of arbitrary frequency. Thus, the phenomenon under analysis is a quite general off-resonant two-photon-assisted process related to the high-frequency Stark effect (atomic level shift due to virtual two-photon-assisted transitions) [10–12]. In the case of two particles (mod-

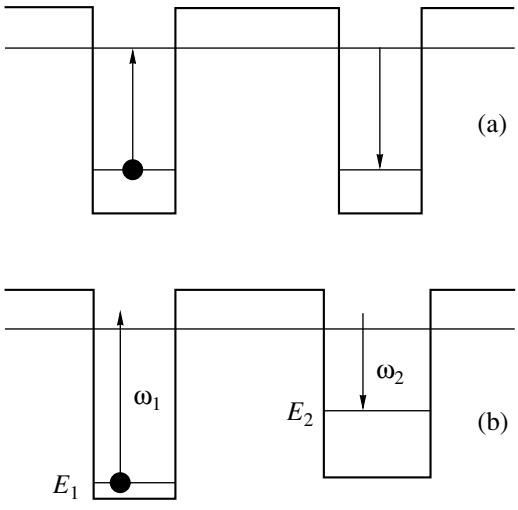

Fig. 1. Quantum-dot energy levels and driving frequencies in resonant electron transfer: (a) one-photon resonance in a three-level system; (b) Raman resonance between levels E_1 and E_2 with $E_2 - E_1 \approx \omega_1 - \omega_2$.

eled by quantum dots here), an analogous virtual transition causes not only an energy-level shift, but also a real transition between degenerate levels in separate quantum dots.

Effective electron transfer must involve quasi-resonant levels, and it is shown below that states near the lower edge of the continuum are best suited for quasi-resonant excitation. Note that continuum (conduction-band) electronic states have never been taken into account in analyses of photoinduced electron transfer [1–7, 9]. It should also be mentioned that most discussions of two-photon and multiphoton coupling mechanisms have focused on multiphoton transitions within a single quantum well [13, 14] and/or inter- or intraband transitions [15].

It is important that continuum states required to implement off-resonant two-photon-assisted electron transfer can be found for potential-energy profile of any form, whereas discrete states satisfying the requirements for three-level transfer [2–9] exist only in certain special cases. Moreover, the tuning to the lower edge of the continuum (which is optimal according to our analysis) does not require high precision, because a relatively broad range of energy levels is expected to contribute to the process. For these reasons, off-resonant two-photon-assisted electron transfer offers a more general model of various processes, in particular, in terms of scalability.

We show that the proposed mechanism is less specific with regard to both quantum-dot structure and driving parameters, as compared to previously analyzed schemes [2–9]. First of all, note that the condition that the energies of a pair of bound states be nearly equal is less restrictive than the requirement of identical quantum dots [2–8]. This condition can be satisfied, for example, by empirically adjusting the electrostatic potential applied to two-dimensional degenerate electron gas in order to create quantum dots [16].

Since the off-resonant two-photon-assisted electron transfer described here is a very general mechanism, it can be analyzed without taking into account individual characteristics of specific quantum dots. In our study, we rely only on the fact that the system has two nearly equal discrete energy levels (in separate dots) and a continuum (conduction band) defined by specifying its boundaries.

In the present analysis, we make use of a time-dependent equivalent transformation to derive an effective Hamiltonian that provides a basis for correct treatment of continuum states. The model considered here enriches the collection of problems that are easiest to solve by equivalent transformation of the Hamiltonian [11, 12].

The paper is organized as follows. First, we perform an equivalent transformation to derive an effective Hamiltonian for a double quantum dot system coupled to an electromagnetic wave. In particular, we show that the off-diagonal matrix elements corresponding to transitions between nearly equal quantum-dot energy levels do not vanish. Next, we obtain expressions for criteria quantifying the efficiency of two-photon-assisted electron transfer between the quantum dots. These expressions are then used to show that optimal conditions for electron transfer correspond to quasi-resonance between the driving frequency and transitions between the quantum-dot energy levels and the lower edge of the continuum. We also analyze the effect of single- and two-photon-assisted transitions to the continuum. Finally, we evaluate the characteristics of the process under analysis. In the Conclusions, we discuss possibilities of implementation of analogous processes in atomic and molecular systems.

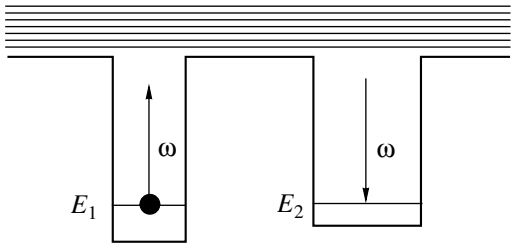

Fig. 2. Quantum-dot energy levels and driving frequency in off-resonant electron transfer between levels E_1 and E_2 with $E_1 \approx E_2$.

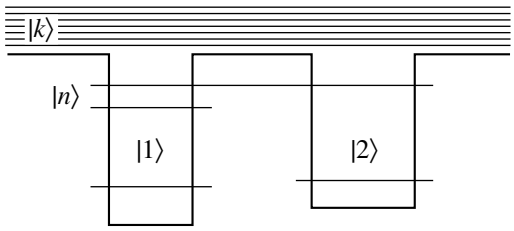

Fig. 3. Energy levels in the proposed model.

2. EFFECTIVE HAMILTONIAN OF A DOUBLE QUANTUM DOT SYSTEM DRIVEN BY AN OFF-RESONANT FIELD

We consider a system of two quantum dots with nearly equal bound states (see the quantitative criterion given below). We assume that the potential barrier between the dots is sufficiently high for these states to be treated as localized in the respective quantum dots. Thus, tunneling between the quantum dots on the time scale of the system can be neglected in the present analysis. Tunneling splits nearly equal energy levels. Detailed analyses of its role in photoinduced electron transfer were presented in [2, 8].

We seek optimal conditions for two-photon-assisted electron transfer between the states $|1\rangle$ and $|2\rangle$ in Fig. 3, denoting other bound states by $|n\rangle$ and continuum states by $|k\rangle$. Hereinafter, we use subscripts $i, j = 1, 2, n, k$ and

$\alpha, \beta = 1, 2$ to refer to the corresponding energy levels. Energy is measured from the lower edge of the continuum (conduction band).

Dynamics of an electron in this system driven by coherent electromagnetic field are described by the Scrödinger equation written in the dipole approximation (with $\hbar = 1$) as

$$i\frac{\partial \Psi}{\partial t} = (\hat{H}_0 - \mathbf{E}\cdot\hat{\mathbf{d}})\Psi. \quad (1)$$

Here, $\hat{H}_0$ is the unperturbed Hamiltonian whose eigenvalues correspond to the energy spectrum described above,

$$\mathbf{E} = \boldsymbol{\varepsilon}(t)e^{i(\mathbf{k}\cdot\mathbf{r}-\omega t)} + \text{c.c.}$$

is the electric field vector with slowly varying amplitude $\boldsymbol{\varepsilon}(t)$, and $\hat{\mathbf{d}}$ is the dipole moment operator. Assuming that the system's size is much smaller than the driving-field wavelength, we neglect the variation of the field in space:

$$\mathbf{E} = \boldsymbol{\varepsilon}(t)e^{-i\omega t} + \text{c.c.}$$

To derive a closed set of equations describing only transitions between $|1\rangle$ and $|2\rangle$, we perform an equivalent transformation of the state vector analogous to that used in [11, 12],

$$\Psi = e^{i\hat{S}}\tilde{\Psi},$$

to rewrite Eq. (1) as

$$i\frac{\partial \tilde{\Psi}}{\partial t} = \hat{\tilde{H}}\Psi \quad (2)$$

with the equivalent Hamiltonian

$$\hat{\tilde{H}} = e^{-i\hat{S}}\hat{H}_0 e^{i\hat{S}} - e^{-i\hat{S}}\mathbf{E}\cdot\hat{\mathbf{d}}e^{i\hat{S}} - ie^{-i\hat{S}}\frac{de^{i\hat{S}}}{dt}, \quad (3)$$

which is represented by the series

$$\hat{\tilde{H}} = \hat{H}_0 - i[\hat{S}, \hat{H}_0] - \frac{1}{2}[\hat{S}, [\hat{S}, \hat{H}_0]] - \ldots - \mathbf{E}\cdot\hat{\mathbf{d}}$$
$$+ i[\hat{S}, \mathbf{E}\cdot\hat{\mathbf{d}}] + \frac{1}{2}[\hat{S}, [\hat{S}, \mathbf{E}\cdot\hat{\mathbf{d}}]] + \ldots - ie^{-i\hat{S}}\frac{\partial}{\partial t}e^{i\hat{S}}.$$

The operators $\hat{S}$ and $\hat{\tilde{H}}$ are expanded in powers of electric field strength:

$$\hat{S} = \hat{S}^{(1)} + \hat{S}^{(2)} + \hat{S}^{(3)} + \ldots,$$
$$\hat{\tilde{H}} = \hat{\tilde{H}}^{(0)} + \hat{\tilde{H}}^{(1)} + \hat{\tilde{H}}^{(2)} + \hat{\tilde{H}}^{(3)} + \ldots, \quad (4)$$

where

$$\hat{\tilde{H}}^{(0)} = \hat{H}_0,$$

$$\hat{\tilde{H}}^{(1)} = -\mathbf{E}\cdot\hat{\mathbf{d}} - i[\hat{S}^{(1)}, \hat{H}_0] + \frac{\partial \hat{S}^{(1)}}{\partial t},$$

$$\hat{\tilde{H}}^{(2)} = \frac{i}{2}[\hat{S}^{(1)}, \mathbf{E}\cdot\hat{\mathbf{d}}]$$

$$-\frac{i}{2}[\hat{S}^{(1)}\hat{\tilde{H}}^{(1)}] - i[\hat{S}^{(2)}, \hat{H}_0] + \frac{\partial \hat{S}^{(2)}}{\partial t}.$$

Now, we construct an effective Hamiltonian with matrix elements $\tilde{H}_{ij} \sim \exp\{-(E_i - E_j)t\}$, so that Eq. (2) is equivalent to a system of equations for slowly varying amplitudes.

We assume that the driving frequency ω is not resonant with transition between $|1\rangle$ or $|2\rangle$ and any discrete level of the system. First, we consider the simplest case when $|E_a| > \omega$. Accordingly, we assume that the matrix elements of $\hat{\tilde{H}}^{(1)}$ corresponding to resonant one-photon transitions vanish: $\tilde{H}^{(1)}_{\alpha i} = \tilde{H}^{(1)}_{i\alpha} = 0$. Then, the equations for the matrix elements of $S^{(1)}$ have the following form:

$$\frac{\partial}{\partial t}S^{(1)}_{\alpha i} + i\omega_{\alpha i}S^{(1)}_{\alpha i} = \mathbf{d}_{\alpha i}\cdot(\boldsymbol{\varepsilon}e^{-i\omega t} + \boldsymbol{\varepsilon}^*\varepsilon^{i\omega t}),$$

where $\omega_{\alpha i} = E_\alpha - E_i$. Since $\boldsymbol{\varepsilon}(t)$ is a slowly varying function, we can write an approximate solution to this equation as

$$S^{(1)}_{\alpha i} = \mathbf{d}_{\alpha i}\cdot\left[\frac{\boldsymbol{\varepsilon}e^{-i\omega t}}{i(\omega_{\alpha i} - \omega)} + \frac{\boldsymbol{\varepsilon}^*\varepsilon^{i\omega t}}{i(\omega_{\alpha i} + \omega)}\right].$$

If the system has no bound states whose energies differ from $E_1 \approx E_2$ by 2ω (i.e., are two-photon resonant), then the nonzero matrix elements $\tilde{H}^{(2)}_{1j}$ and $\tilde{H}^{(2)}_{2j}$ are $\tilde{H}^{(2)}_{11}$, $\tilde{H}^{(2)}_{22}$, $\tilde{H}^{(2)}_{12}$, and $\tilde{H}^{(2)}_{21}$. Since $\omega_{i2} \approx \omega_{i1} = \omega_{i\alpha}$, they can be expressed as

$$\tilde{H}^{(2)}_{\alpha\alpha} = -|\varepsilon|^2\sum_i |d_{i\alpha}|^2\left(\frac{1}{\omega_{i\alpha} + \omega} + \frac{1}{\omega_{i\alpha} - \omega}\right), \quad (5)$$

$$\tilde{H}^{(2)}_{\alpha\beta} = -|\varepsilon|^2\sum_i d_{\alpha i}d_{i\beta}\left(\frac{1}{\omega_{i\alpha} + \omega} + \frac{1}{\omega_{i\alpha} - \omega}\right), \quad (6)$$

where d_{ij} denotes the component of the corresponding matrix element parallel to the vector ε. Thus, the second-order term responsible for two-photon processes in the effective Hamiltonian contains off-diagonal matrix elements corresponding to transitions between $|1\rangle$ and $|2\rangle$. Accordingly, these transitions can be described by expansions (4) limited to the second order. (Higher

order terms are analyzed separately below.) In final form, the matrix elements of the effective Hamiltonian

$$\hat{H} = \hat{\tilde{H}}^{(0)} + \hat{\tilde{H}}^{(1)} + \hat{\tilde{H}}^{(2)}$$

describing two-photon-assisted transitions are written as

$$H_{\alpha\alpha} = E_\alpha + E_\alpha^{\mathrm{st}}, \tag{7}$$

$$H_{21} = \Lambda, \quad H_{12} = \Lambda^*, \tag{8}$$

$$H_{\alpha n} = H_{\alpha k} = 0, \tag{9}$$

where

$$E_\alpha^{\mathrm{st}} = -|\varepsilon|^2 \sum_i |d_{i\alpha}|^2 \left(\frac{1}{\omega_{i\alpha} + \omega} + \frac{1}{\omega_{i\alpha} - \omega} \right) \tag{10}$$

denotes Stark shifts and

$$\Lambda = -|\varepsilon|^2 \sum_i d_{2i} d_{i1} \left(\frac{1}{\omega_{i\alpha} + \omega} + \frac{1}{\omega_{i\alpha} - \omega} \right) \tag{11}$$

is the Rabi frequency.

3. EFFICIENCY CRITERIA FOR ELECTRON TRANSFER

To describe electron transfer between $|1\rangle$ and $|2\rangle$ and quantify the efficiency of the off-resonant transfer mechanism discussed here, we seek a solution to Eq. (2) as a superposition of the eigenstates of the unperturbed system:

$$\tilde{\Psi} = \sum_i a_i(t) e^{-iE_i t} |i\rangle.$$

The coefficients $a_i(t)$ satisfy the relations

$$i\dot{a}_j e^{-iE_j t} + E_j a_j e^{-iE_j t} = \sum_i a_i e^{-iE_i t} \tilde{H}_{ji}. \tag{12}$$

Substituting (7)–(9) into (12), we obtain a closed system of equations describing cyclic transitions between $|1\rangle$ and $|2\rangle$:

$$\begin{aligned} \dot{b_1} &= -ib_2 e^{-i\Delta t} \Lambda^*, \\ \dot{b_2} &= -ib_1 e^{i\Delta t} \Lambda, \end{aligned} \tag{13}$$

where

$$b_j \equiv a_j e^{iE_j^{\mathrm{st}} t},$$

$$\Delta \equiv (E_2 + E_2^{\mathrm{st}}) - (E_1 + E_1^{\mathrm{st}})$$

is the energy difference between the Stark-shifted levels, which plays the role of a detuning.

Treating Λ as a time-independent quantity and setting $b_1(t = 0) = 1$ and $b_2(t = 0) = 0$ (the electron is initially in the first quantum dot), we obtain

$$b_1 = e^{-it\Delta/2} \left(\cos \Omega t + i \frac{\Delta}{2\Omega} \sin \Omega t \right),$$

$$b_2 = -i \frac{\Lambda}{\Omega} e^{-it\Delta/2} \sin \Omega t,$$

where

$$\Omega = \sqrt{|\Lambda|^2 + \frac{1}{4}\Delta^2}.$$

The probability of transfer of the electron to the second quantum dot is

$$|b_2|^2 = \frac{|\Lambda|^2}{2\Omega^2} (1 - \cos(2\Omega t)).$$

Accordingly, the corresponding optimal pulse width for electron transfer is $T = \pi(1 + 2n)/2\Omega$, where n is an integer. The corresponding probability of electron transfer between the quantum dots,

$$|b_2(t = T)|^2 \equiv |b_2|^2_{\max} = \frac{|\Lambda|^2}{\Omega^2}, \tag{14}$$

is close to unity only if the detuning from resonance is small:

$$\Delta \ll |\Lambda|. \tag{15}$$

As an estimate, we use the expansion of (14) in powers of the small parameter defined by (15) up to the first nonvanishing term:

$$|b_2|^2_{\max} \approx 1 - \frac{1}{4} \frac{\Delta^2}{|\Lambda|^2}. \tag{16}$$

To facilitate further analysis, we represent the detuning as $\Delta = \Delta_0 + \Delta_{\mathrm{st}}$, where the time-independent energy difference $\Delta_0 = E_2 - E_1$ is determined by quantum-dot structure, while the Stark-shift difference $\Delta_{\mathrm{st}} = E_2^{\mathrm{st}} - E_1^{\mathrm{st}}$ increases as the field strength squared. Note that condition (15) does not necessarily imply that both Δ_0 and Δ_{st} are smaller than $|\Lambda|$. Moreover, additional electrostatic potentials can be applied to shift energy levels so that $\Delta_0 \approx -\Delta_{\mathrm{st}}$ if the driving field is held constant. However, to elucidate the proposed transfer mechanism and optimize its parameters, we must separately examine the conditions

$$\Delta_0 \ll |\Lambda|, \tag{17}$$

$$\Delta_{\mathrm{st}} \ll |\Lambda|. \tag{18}$$

4. OPTIMIZATION OF THE DRIVING FREQUENCY

Since the time-independent energy difference Δ_0 is determined by the quantum-dot structure and cannot therefore be reduced, condition (17) can be satisfied only by increasing the Rabi frequency Λ. This can obviously be done by increasing the intensity of the driving field, as well as by adjusting the driving frequency.

Analyzing expression (11) for the Rabi frequency, we note that it is determined only by states that are not localized in one of the quantum dots, because $d_{2i}d_{i1}$ vanishes otherwise. Thus, we must take into account only continuum states and, probably, some discrete states near the top of the potential barrier between the dots. Let us explore possibilities to increase Λ by using continuum states only, since they can be found for a potential energy profile of any form. A discrete spectrum of delocalized states exists only in certain special cases, and their influence on two-photon processes should be considered as a correction to the result obtained by taking into account continuum states.

Changing from summation to integration over the continuum in (11), we have

$$\Lambda = -|\varepsilon|^2 \frac{V}{(2\pi)^3}\int d_{2\mathbf{k}}d_{\mathbf{k}1} \times\left(\frac{1}{E_{\mathbf{k}}-E_{\text{res}}}+\frac{1}{E_{\mathbf{k}}-2E_1+E_{\text{res}}}\right)d\mathbf{k}, \tag{19}$$

where V is the system's volume and $E_{\text{res}} = E_1 + \omega$. Note that the matrix elements $d_{2\mathbf{k}}$ and $d_{\mathbf{k}1}$ are localized in separate quantum dots, and the dependence of the result on their geometry and relative position require a special numerical analysis. In the limiting case when these states are localized within a compact region, the integral in (19) was evaluated in [17]. Here, we deal with the general case of spatially separated quantum dots, following the simple analysis presented in [18].

As a first step, we consider only the case of $E_{\text{res}} < 0$, when the lower edge of the continuum is above an energy interval corresponding to quasi-resonance. It is clear from (19) that the sum in parentheses is a monotonically increasing function of the driving frequency when $E_1 < E_{\text{res}} < 0$ for arbitrary $E_k > 0$ and $E_1 < 0$. It follows from this observation alone that optimal conditions correspond to E_{res} near the lower edge of the continuum.

However, this value of the driving frequency should be used to increase the Rabi frequency for more substantial reasons. Since the complex factor $d_{2\mathbf{k}}d_{\mathbf{k}1}$ in (19) is characterized by an intricate oscillatory behavior, its contribution to the integral with respect to $\mathbf{k}$ reduces the Rabi frequency [18]. This effect will be suppressed when the driving frequency is such that $E_{\text{res}} \sim 0$, because the corresponding denominators in (19) are close to zero and the phases in $d_{2\mathbf{k}}d_{\mathbf{k}1}$ can be treated as equal for all states near the lower edge of the continuum. Therefore, the integral is dominated by the contributions of these states, which do not cancel one another. Thus, condition (17) will be fulfilled if the driving frequency is such that E_{res} is close to the lower edge of the continuum.

Now, we consider condition (18). Rewriting (10) as

$$\Delta_{\text{st}} = -|\varepsilon|^2 \frac{V}{(2\pi)^3}\int(|d_{\mathbf{k}2}|^2 - |d_{\mathbf{k}1}|^2) \times\left(\frac{1}{E_{\mathbf{k}}-E_{\text{res}}}+\frac{1}{E_{\mathbf{k}}-2E_1+E_{\text{res}}}\right)d\mathbf{k}, \tag{20}$$

we see that the oscillation of $|d_{\mathbf{k}2}|^2 - |d_{\mathbf{k}1}|^2$ as a function of $\mathbf{k}$ is slower than that of $d_{2\mathbf{k}}d_{\mathbf{k}1}$ in (19). Thus, as E_{res} approaches zero and the energy interval indicated above becomes narrower, Stark-shift difference (20) increases slower than Rabi frequency (19). Therefore, the tuning of E_{res} to the lower edge of the continuum is also optimal with regard to condition (18).

5. TRANSITIONS TO THE CONTINUUM

Since the results obtained above for $E_{\text{res}} < 0$ (when the lower edge of the continuum is above the quasi-resonant energy levels) show that the optimal driving frequency corresponds to a vanishing $E_{\text{res}} < 0$, we should check whether the condition $E_{\text{res}} \geq 0$ is better suited for electron transfer between quantum dots.

If $E_{\text{res}} \geq 0$, then the sums over all continuum states in (5) and (6) yield resonant terms, which formally tend to infinity. Following [8], we change from ω to $\omega \longrightarrow \omega + i\delta$, where $\delta = +0$ (which corresponds to an adiabatically switched driving field). Then, we have

$$\frac{1}{\omega_{i\alpha}-\omega-i\delta} = P\frac{1}{\omega_{i\alpha}-\omega} + i\pi\delta(\omega_{i\alpha}-\omega),$$

where P denotes an expression whose integral is interpreted in the sense the Cauchy principal value. Having performed the change, we write the matrix elements of the effective Hamiltonian as

$$H_{\alpha\alpha} = E_\alpha + E_\alpha^{\text{st}} - i\gamma_\alpha, \tag{21}$$

$$H_{21} = \Lambda - i\Gamma, \quad H_{12} = \Lambda^* - i\Gamma^*, \tag{22}$$

where

$$E_\alpha^{\text{st}} = -|\varepsilon|^2\sum_i |d_{i\alpha}|^2\left(\frac{1}{\omega_{i\alpha}+\omega}+P\frac{1}{\omega_{i\alpha}-\omega}\right) \tag{23}$$

denotes a Stark shift;

$$\Lambda = -|\varepsilon|^2\sum_i d_{2i}d_{i1}\left(\frac{1}{\omega_{i\alpha}+\omega}+P\frac{1}{\omega_{i\alpha}-\omega}\right) \tag{24}$$

is the Rabi frequency; and

$$\gamma_\alpha = \pi|\varepsilon|^2\sum_i |d_{i\alpha}|^2\delta(\omega_{i\alpha}-\omega),$$
$$\Gamma = \pi|\varepsilon|^2\sum_i d_{2i}d_{i1}\delta(\omega_{i\alpha}-\omega) \quad (25)$$

are non-Hermitian corrections representing decay of bound states into the continuum.

Substituting (21) and (22) into (12), we obtain

$$\dot{b_1} + \gamma_1 b_1 = -b_2 e^{-i\Delta t}(i\Lambda^* + \Gamma^*),$$
$$\dot{b_2} + \gamma_2 b_2 = -b_1 e^{i\Delta t}(i\Lambda + \Gamma), \quad (26)$$

where the notation used in (13) is retained. To simplify analysis of these equations, we consider the case of $\Delta = 0$ (exact resonance). Under this condition, Eqs. (26) reduce to

$$\dot{b_1} + \gamma_1 b_1 = -b_2(i\Lambda^* + \Gamma^*),$$
$$\dot{b_2} + \gamma_2 b_2 = -b_1(i\Lambda + \Gamma). \quad (27)$$

Again, assuming that $\varepsilon(t)$ is a slowly varying function, we treat $\gamma_{1;2}$, Λ, and Γ as constant parameters. Substituting $b_1, b_2 \sim e^{\mu t}$ into (27), we obtain

$$\mu_{1;2} = -\frac{\gamma_1+\gamma_2}{2} \pm \left\{\left(\frac{\gamma_1-\gamma_2}{2}\right)^2 + |\Gamma|^2 - |\Lambda|^2 - i\Lambda^*\Gamma - i\Lambda\Gamma^*\right\}^{1/2}. \quad (28)$$

The real part of this expression describes the decay of bound states into the continuum, and its imaginary part characterizes cyclic transition between bound states. Therefore, electron transfer between the states $|1\rangle$ and $|2\rangle$ will occur with a probability close to unity only if the real part of (28) is much less than the imaginary part, which requires that

$$\Lambda \gg \Gamma, \gamma_{1;2}. \quad (29)$$

This is a reasonable and expectable result, because the non-Hermitian corrections in (21) and (22) must be small as compared to the transition frequency of interest. Moreover, if the driving frequency is not tuned exactly to resonance, then effective electron transfer requires that condition (15) be satisfied.

First of all, we note that the non-Hermitian corrections in condition (29) are roughly proportional to the electron density of states $N(E_{res})$ in the quasi-resonant part of the continuum. As an estimate, we use $N(E) \sim \sqrt{E}$, which follows from the quadratic dispersion law for free-electron gas at the bottom of the conduction band. This assumption obviously implies that the rate of irreversible decay to the continuum increases with E_{res}; i.e., it can be minimized by tuning the driving frequency to the lower edge of the continuum.

Now, we consider the Rabi frequency defined by (24) as a function of E_{res}. Retaining only the second term in each summand (since it is much greater than the first one because of the resonant denominator), we have

$$\Lambda \sim |\varepsilon|^2\sum_{\mathbf{k}} P\frac{d_{2\mathbf{k}}d_{\mathbf{k}1}}{E_{\mathbf{k}}-E_{res}}. \quad (30)$$

As mentioned above, the value of Λ is mainly determined by the contributions of energy levels close to E_{res}, because the oscillating contributions of other terms cancel one another. Therefore, we can estimate the Rabi frequency given by (30) as

$$\Lambda \sim |\varepsilon|^2 d^2 \int_{E_{res}-E_0}^{E_{res}+E_0} P\frac{1}{E'-E_{res}} \times\left(N(E_{res}) + \frac{dN(E_{res})}{dE_{res}}(E'-E_{res})\right)dE',$$

where d is the dipole moment averaged over the energy interval between $E' \sim E_{res} - E_0$ and $E' \sim E_{res} + E_0$, whose width E_0 depends on the oscillation period of the function $d_{2\mathbf{k}}d_{\mathbf{k}1}$. Then, we have

$$\Lambda \sim \frac{dN(E_{res})}{dE_{res}}.$$

For a quadratic dispersion law, this yields

$$\Lambda \sim \frac{1}{\sqrt{E_{res}}}.$$

Even though this rough estimate is actually not valid for $E_{res} = 0$, we can conclude that the Rabi frequency decreases as E_{res} deviates from the edge of the continuum; i.e., conditions (15) and (29) are satisfied less accurately.

Thus, the applicability of the result obtained for $E_{res} < 0$ is not restricted by this condition: to optimize electron transfer between quantum dots, the driving frequency must be quasi-resonant with transitions between the bound states and energy levels near the lower edge of the continuum.

The optimal conditions for electron transfer that follow from the expressions obtained above are consistent with the theory of multiphoton processes, because ideal conditions correspond to a vanishing rate of irreversible decay to the continuum. Since the quasi-resonant states playing the key role in the process include the lowest levels in the conduction band, the efficiency of photoinduced electron transfer can only increase in the case of nonzero density of states at the lower conduction-band edge.

6. ANALYSIS OF HIGHER ORDER CORRECTIONS

Both general considerations and expression (11) suggest that the resonant two-photon Rabi frequency is proportional to the squared strength of the driving field. Therefore, condition (17) will be satisfied more accurately for stronger fields. However, since the analysis based on expansion (4) is valid for a relatively weak field, we should use (4) to derive quantitative criteria for its applicability.

Omitting tedious intermediate calculations, we present only the final results here. To demonstrate general trends, we consider only the matrix element

$$\tilde{H}_{11}^{(4)} \approx \sum_k \frac{|\varepsilon|^2 |d_{k1}|^2}{\omega_{k1} - \omega} \sum_p \frac{|\varepsilon|^2 |d_{p1}|^2}{(\omega_{p1} - \omega)^2} - \sum_{k,p,q} \frac{|\varepsilon|^4 d_{1k} d_{kp} d_{pq} d_{q1}}{(\omega_{k1} - \omega)(\omega_{q1} - \omega)} \left(\frac{1}{\omega_{p1} - 2\omega} + \frac{1}{\omega_{p1}} \right). \quad (31)$$

Again, we change from ω to $\omega + i\delta$ with $\delta = +0$ to allow for irreversible decay to the continuum. Assuming that E_{res} is below the lower edge of the continuum (or slightly higher, so that the corresponding density of states is negligible) and using the fact that two-photon resonant states correspond to $E_{\text{res}}^{(2)} = E_1 + 2\omega$, we rewrite (31) approximately as

$$\tilde{H}_{11}^{(4)} \approx -\tilde{H}_{11}^{(2)} \sum_k \frac{|\varepsilon|^2 |d_{k1}|^2}{(\omega_{k1} - \omega - i\delta)^2} - i\pi |\varepsilon|^4 \times \sum_{k,p,q} P \frac{d_{1k} d_{kp}}{\omega_{k1} - \omega} P \frac{d_{pq} d_{q1}}{\omega_{q1} - \omega} \delta(\omega_{p1} - 2\omega). \quad (32)$$

In what follows, we use the dispersion law for free-electron gas to show that

$$\sum_k \frac{|\varepsilon|^2 |d_{k1}|^2}{(\omega_{k1} - \omega - i\delta)^2} \quad (33)$$

goes to infinity at $E_{\text{res}} = 0$ and decreases as E_{res} deviates up or down from the edge of the continuum. The former trend can be interpreted as a departure from the dispersion law due to resonant coupling between the bound states and the edge of the continuum. Thus, the first term in (31) is the minimal detuning of E_{res} from the edge of the continuum for which the analysis presented above holds. The off-resonant mechanism of electron transfer must remain effective even in the case of sharper tuning to the edge of the continuum, but expressions (23) and (24) for Stark shift and Rabi frequency become inapplicable. We estimate below the minimal value of $|E_{\text{res}}|$ as that corresponding to (33) on the order of unity. Analysis of the case when (33) is substantially greater than unity is outside the scope of the present study.

It is obvious that electron transfer between quantum dots can be effective only if the second term in (31) (two-photon ionization) is small as compared to the Rabi frequency. In other words, there exists an upper limit for the driving field strength

$$\pi |\varepsilon|^2 \sum_{k,p,q} P \frac{d_{1k} d_{kp}}{\omega_{k1} - \omega} P \frac{d_{pq} d_{q1}}{\omega_{q1} - \omega} \times \delta(\omega_{p1} - 2\omega) \ll \sum_k P \frac{d_{2k} d_{k1}}{\omega_{k1} - \omega}. \quad (34)$$

If required, this condition can be reformulated as a restriction on the Rabi frequency.

7. EVALUATION OF THE RABI FREQUENCY

In accordance with the results obtained above, we assume that the quasi-resonance values of E_{res} are near the lower edge of the continuum, but (33) is much less than unity. To be specific, we assume that $E_{\text{res}} < 0$. Since the second term in (19) is negligible as compared to the first one, we have

$$\Lambda \sim |\boldsymbol{\varepsilon}|^2 \frac{V}{(2\pi)^3} \int \frac{d_{2\mathbf{k}} d_{\mathbf{k}1}}{E_k + |E_{\text{res}}|} d\mathbf{k}. \quad (35)$$

Using the dispersion law for free-electron gas and introducing $q = \sqrt{2m^*|E_{\text{res}}|}$, where m^* is an effective electron mass, we rewrite (35) as

$$\Lambda \sim |\boldsymbol{\varepsilon}|^2 \frac{V}{(2\pi)^3} 2m^* \int \frac{d_{2\mathbf{k}} d_{\mathbf{k}1}}{k^2 + q^2} d\mathbf{k}. \quad (36)$$

Since this integral is dominated by the contribution of states with energies close to E_{res}, and the corresponding wavefunctions are plane waves (distorted near the quantum dots) with wavelengths decreasing with increasing energy, the integrand in (36) is characterized by complicated oscillatory behavior due to two factors. First, the magnitudes of $d_{2\mathbf{k}}$ and $d_{\mathbf{k}1}$ are complicated functions of $\mathbf{k}$. Second, the integrand's phase exhibits a periodic variation that can approximately be represented as $d_{2\mathbf{k}} d_{\mathbf{k}1} = |d_{2\mathbf{k}}$ and $d_{\mathbf{k}1}| e^{ikL}$, where L is the characteristic distance between the quantum dots. Recalling that the quantum dots represented by localized states $|1\rangle$ and $|2\rangle$ are separated by a sufficiently large distance in the present model (as in real systems of this kind), we can assume that the oscillatory behavior is mainly determined by the second factor.

To obtain a rough estimate for (36), we restrict the limits of integration to the sphere of radius $k_{\max} = 1/L$ (where the first oscillation is localized) and use constant approximate values of both $d_{2\mathbf{k}}$ and $d_{\mathbf{k}1}$:

$$d_{2\mathbf{k}} \approx d_{\mathbf{k}1} \approx ea \sqrt{\frac{a^3}{V}}. \quad (37)$$

Here, a is the characteristic quantum-dot size, and the radical reflects the fact that the product of a wavefunction $\psi_{\mathbf{k}}$ normalized to V with a function $\psi_{1;2}$ localized in the neighborhood of the corresponding quantum dot reduces the domain of integration to a volume on the order of a^3. Under these assumptions, we estimate (36) as

$$\Lambda \sim |\boldsymbol{\varepsilon}|^2 \frac{V}{(2\pi)^3} 2m^* \frac{e^2 a^5}{V} 4\pi \int_0^{k_{\max}} \frac{k^2 dk}{k^2 + q^2}. \tag{38}$$

The estimate for (33) given below shows that E_{res} can be such that q^2 does not exceed $k_{\max}^2$. Recovering dimensional Planck's constant, we evaluate (38):

$$\Lambda \sim \frac{|\boldsymbol{\varepsilon}|^2 e^2 m^* a^5}{\hbar^2 L}. \tag{39}$$

For $a \sim 10$ nm, $L \sim 100$ nm, and $m^* \sim 0.1 m_e \sim 10^{-28}$ g (i.e., under unfavorable conditions with regard to the requirement of large transition energy), we obtain $\Lambda \sim 10^{-5}$ eV even for a relatively weak driving field with $|\boldsymbol{\varepsilon}| \sim 10^3$ V/cm. It should be noted here that the optimal range given in [2] was $\Lambda \sim 10^{-5}$–10^{-4} eV.

8. ESTIMATES FOR LIMITING CONDITIONS

The results obtained in the preceding section demonstrate that the proposed mechanism has a wide scope in terms of the energy (and therefore, time) required to transfer an electron between quantum dots. However, we should also estimate the upper limit for the driving field strength given by (34). Repeating the analysis presented in the preceding section and restricting the domain of integration to $1/a$, we obtain the following estimate for the right-hand side of (34):

$$\begin{aligned} &|\varepsilon|^2 \sum_{k,p,q} \frac{d_{1k} d_{kp}}{\omega_{k1} - \omega} \frac{d_{pq} d_{q1}}{\omega_{q1} - \omega} \delta(\omega_{p1} - 2\omega) \\ &\quad \sim |\varepsilon|^2 \left(dD \frac{Vm^*}{a} \right)^2 N(E_{\text{res}}^{(2)}), \end{aligned} \tag{40}$$

where d is the characteristic magnitude of the dipole moment corresponding to transitions between the bound states and continuum, D is an analogous quantity for transitions between continuum states, $E_{\text{res}}^{(2)} = E_1 + 2\omega$ corresponds to two-photon absorption, and $N(E_{\text{res}}^{(2)})$ is the corresponding density of states.

The matrix elements for transitions between continuum states are estimated as

$$D \sim e \int \psi_{\mathbf{k}}^* \mathbf{r} \psi_{\mathbf{p}} d\mathbf{r}. \tag{41}$$

The nonzero value of this integral is entirely due to the contributions of the neighborhoods of the quantum dots. The integral over the rest of the space vanishes, because the transitions between continuum states of interest here may not preserve quasi-momentum. Therefore, D is a very small quantity on the order of a^3/V. Note that matrix element (41) couples a state with energy $E_{\mathbf{p}}$ near the lower edge of the continuum to a state with $E_{\mathbf{k}}$ comparable to the driving-field energy quantum; i.e., the wavefunction $\psi_{\mathbf{k}}$ oscillates faster than $\psi_{\mathbf{p}}$. Therefore, the value of the integral in (41) is determined by the oscillatory behavior of $\psi_{\mathbf{k}}$, and the characteristic interval of variation of the integrand is

$$a_0 \sim \frac{1}{k} \sim \frac{1}{\sqrt{m^* \omega}}.$$

Hence, (41) can be estimated as

$$D \sim e a_0 \frac{a^3}{V} \sim e \frac{1}{\sqrt{m^* \omega}} \frac{a^3}{V}. \tag{42}$$

Note also that the density of states is

$$N(E_{\text{res}}^{(2)}) \approx N(\omega) \sim V (m^*)^{3/2} \omega^{1/2}. \tag{43}$$

Combining (37), (40), (42), and (43) and recovering dimensional Planck's constant, we reformulate condition (34) as follows:

$$|\varepsilon| \ll \frac{\hbar^{7/4} \omega^{1/4}}{e a^2 L^{1/2} (m^*)^{3/4}}. \tag{44}$$

Following [2], we set $\omega \sim 0.1$ eV and find that inequality (44) yields $|\varepsilon| \sim 10^4$ V/cm. Using expression (39), we obtain the limiting condition

$$\Lambda \ll \frac{a \hbar^{3/2} \omega^{1/2}}{L^2 (m^*)^{1/2}} \tag{45}$$

for the Rabi frequency, which yields $\Lambda \ll 10^{-3}$ eV for the characteristic values specified above. Since our estimates show that the restrictions due to two-photon ionization can be either irrelevant or essential, they should be taken into account more accurately. For example, two-photon ionization can be ignored when the system's parameters are such that $E_{\text{res}}^{(2)}$ lies in the band gap.

Now, we consider the restrictions due to the first term in (31). Performing an analysis analogous to (35)–(39), we obtain the following estimate for (33):

$$\sum_k \frac{|\varepsilon|^2 |d_{k1}|^2}{(\omega_{k1} - \omega)^2} \sim \frac{|\boldsymbol{\varepsilon}|^2 e^2 (m^*)^2 a^5}{\hbar^4 q} \sim \frac{|\boldsymbol{\varepsilon}|^2 e^2 (m^*)^{3/2} a^5}{\hbar^3 |E_{\text{res}}|^{1/2}}.$$

It is clear that, first, the sum is divergent in the case of sharp tuning to the edge of the continuum and, second, the sum is much less than unity if

$$|E_{\text{res}}| \gg \frac{|\boldsymbol{\varepsilon}|^4 e^4 (m^*)^3 a^{10}}{\hbar^6} \sim |\Lambda|^2 \frac{m^* L^2}{\hbar^2}. \tag{46}$$

It should be noted here that both condition (34) and estimates (44) and (45) impose physical restrictions on electron transfer due to two-photon ionization, whereas (46) only restricts the applicability of the analytical expressions used to describe off-resonant electron transfer, rather than its implementation. If $|\boldsymbol{\varepsilon}| \sim 10^3$ V/cm, then

$$|E_{\text{res}}| \gg 10^{-6} \text{ eV}. \quad (47)$$

Thus, the estimates obtained meet conditions (46) and (47). For example, if $|E_{\text{res}}| \sim 10^{-5}$ eV, then $q^2 \ll k_{\max}^2$, which justifies the derivation of estimate (39) from expression (38).

Finally, we evaluate condition (18), which imposes the most essential restriction on the mechanism of two-photon-assisted electron transfer. According to expressions (10) and (11), the Stark shift is $E_{1;2}^{\text{st}}$ is a quantity comparable to, or even greater than, the Rabi frequency Λ, irrespective of the driving field strength. Since identical quantum dots, for which condition (18) is obviously satisfied ($E_1^{\text{st}} = E_2^{\text{st}}$), cannot be created by using present-day technologies, we should analyze the effect of dissimilarity between quantum dots on the difference in Stark shift.

Following the derivation of (35)–(39) and using the estimate $d_{\mathbf{k}\alpha} \sim ea_0\sqrt{a^3/V}$, where $a_0(k) \sim \min(a, 1/k)$, we obtain

$$E_{1;2}^{\text{st}} \sim \frac{|\boldsymbol{\varepsilon}|^2 e^2 m^* a^4}{\hbar^2}. \quad (48)$$

We see that the Stark shift strongly depends on the quantum-dot size; i.e., condition (18) can be violated even the difference in geometry is relatively small. Let consider the unfavorable case when the quantum dots are similar in shape, but differ in size, i.e., $\delta a \equiv a_2 - a_1 \ll a$. Using estimates (39) and (48), we rewrite condition (18) as

$$\frac{\Delta_{\text{st}}}{\Lambda} \sim 4\frac{\delta a}{a}\frac{L}{a} \ll 1. \quad (49)$$

We note here that a condition less restrictive than (49) is obtained for quantum dots that are almost equal in volume, but dissimilar in shape. To extend condition (49) to arbitrary size and shape, we represent it as follows:

$$\frac{\Delta_{\text{st}}}{\Lambda} \sim C\frac{\delta a}{a}\frac{L}{a} \ll 1, \quad (50)$$

where $C \sim 1$–10 is a dimensionless constant characterizing the combined effect of geometric parameters.

In our estimates presented above, we assumed that $L \sim 10a$. Accordingly, condition (50) is satisfied if δa is smaller than a by at least two orders of magnitude, i.e., if $\delta a \sim 0.1$ nm, which is smaller than the thickness of an atomic layer. In other words, electron transfer between small quantum dots ($a \sim 10$ nm) will be suppressed even if they differ in size by only one atomic layer.

Let us now consider more favorable cases, comparing our results with those obtained for electron transfer in a double-dot system via a third bound state (Fig. 1a) in [3], where suppression due to the difference between the dots was analyzed. We assume that the driving field is sufficiently strong to ensure that $\Delta_{\text{st}} \gg \Delta_0$ and neglect the time-independent energy difference Δ_0. Following [3], we consider two cases.

Case 1:

$$a = 20 \text{ nm}, \quad \delta a = 0.2 \text{ nm}, \quad L = 80 \text{ nm}. \quad (51)$$

If two-photon ionization is negligible, then we can combine (50) with (16) to obtain the probability of electron transfer $|b_2|_{\max}^2 \approx 1 - 4 \times 10^{-4} C^2$. For C between 1 and 10, the transfer probability varies from 0.9996 to 0.96.

Case 2:

$$a = 60 \text{ nm}, \quad \delta a = 0.2 \text{ nm}, \quad L = 240 \text{ nm}. \quad (52)$$

In this case, $|b_2|_{\max}^2 \approx 1 - 4.4 \times 10^{-5} C^2$ varies from 0.99996 to 0.996.

We should note here that the parameter values in (51) were found to be totally unsuitable for electron transfer, while the electron-transfer probability corresponding to (52) amounted to 0.9. Thus, two-photon-assisted electron transfer is much less sensitive to difference between the quantum dots, as compared to the three-level mechanism analyzed in [2–8]. We also note that additional electrostatic potentials can be applied to shift energy levels so that $\Delta = \Delta_0 + \Delta_{\text{st}} \approx 0$. Under this condition, difference in quantum-dot geometry will be insignificant, whereas it is essential for a three-level system [3].

9. CONCLUSIONS

Off-resonant two-photon-assisted electron transfer between two quantum dots can be observed and utilized in various quantum-dot systems. However, it is very difficult to study in ordinary atomic and molecular systems, since the process strongly depends on the size of quantum dots and the distance between them. In particular, it cannot be observed in a weakly ionized atomic and molecular gases characterized by normal interatomic distances and depolarizing-collision frequencies. Prospects are somewhat better for Rydberg atoms, but the most important role can be played by this mechanism in magneto-optical trapping and cooling of atoms. In [19–21], it was shown that magneto-optically trapped atoms should be modeled by using an energy level system analogous to that illustrated by Fig. 1b, and atom transfer between traps with energy levels E_1 and E_2 driven by a bichromatic pulse was discussed under the Raman resonance condition $\omega_1 - \omega_2 \approx E_2 - E_1$.

However, continuum states have never been taken into account correctly in models of magneto-optical trapping of ultracold atoms. The off-resonant transfer mechanism proposed here can be extended to atom transfer between magneto-optical traps with $E_1 \approx E_2$. The key formulas obtained in this study will hold within the framework of a simple model of off-resonant atom transfer, but the corresponding numerical estimates will be different.

Analysis of off-resonant two-photon-assisted electron transfer in a liquid must allow for interaction between molecules and may require more accurate modeling of molecular terms. However, since the complicated pattern of intersecting molecular terms in electromagnetic field must be give rise to various nonadiabatic transitions, the transfer mechanism in question will hardly play any significant role.

REFERENCES

1. F. Grossmann, T. Dittrich, P. Jung, and P. Hanggi, Phys. Rev. Lett. **67**, 516 (1991).
2. L. A. Openov, Phys. Rev. B **60**, 8798 (1999).
3. A. V. Tsukanov and L. A. Openov, Fiz. Tekh. Poluprovodn. (St. Petersburg) **38**, 94 (2004) [Semiconductors **38**, 91 (2004)].
4. J. H. Oh, D. Ahn, and S. W. Hwang, Phys. Rev. A **62**, 052306 (2000).
5. T. H. Stoof and Yu. V. Nazarov, Phys. Rev. B **53**, 1050 (1996).
6. B. L. Hazelzet, M. R. Wegewijs, T. H. Stoof, and Yu. V. Nazarov, Phys. Rev. B **63**, 165313 (2001).
7. A. D. Greentree, J. H. Cole, A. R. Hamilton, and L. C. L. Hollenberg, Phys. Rev. B **70**, 235317 (2004).
8. A. M. Basharov and S. A. Dubovis, Opt. Spektrosk. **99**, 607 (2005).
9. U. Hohenester, F. Troiani, E. Molinari, *et al.*, Appl. Phys. Lett. **77**, 1864 (2000).
10. M. O. Scully and M. S. Zubairy, *Quantum Optics* (Cambridge Univ. Press, Cambridge, 1997; Fizmatlit, Moscow, 2003).
11. A. I. Maimistov and A. M. Basharov, *Nonlinear Optical Waves* (Kluwer Academic, Dordrecht, 1999).
12. A. M. Basharov, *Photonics. Method of Unitary Transformation in Nonlinear Optics* (Mosk. Inzh.–Fiz. Inst., Moscow, 1990) [in Russian].
13. A. V. Baranov, Y. Masumoto, K. Inoue, *et al.*, Phys. Rev. B **55**, 15675 (1997).
14. E. Yu. Perlin, Opt. Spektrosk. **91**, 777 (2001) [Opt. Spectrosc. **91**, 729 (2001)].
15. A. V. Fedorov, A. V. Baranov, and K. Inoue, Phys. Rev. B **54**, 8627 (1996).
16. L. Jacak, P. Hawrylak, and A. Wojs, *Quantum Dots* (Springer, Berlin, 1998).
17. P. N. Butcher, and D. Cotter, *The Elements of Nonlinear Optics* (Cambridge Univ. Press, Cambridge, 1990).
18. G. Kurizki and A. Ben-Reuven, Phys. Rev. A **36**, 90 (1987).
19. D. Jaksch, C. Bruder, J. I. Cirac, *et al.*, Phys. Rev. Lett. **81**, 3108 (1998).
20. A. I. Maĭmistov, Opt. Spektrosk. **97**, 981 (2004) [Opt. Spectrosc. **97**, 920 (2004)].
21. D. Jaksch and P. Zoller, Ann. Phys. (N.Y.) **315**, 52 (2005).

Translated by A. Betev

Journal of Experimental and Theoretical Physics, Vol. 101, No. 3, 2005, pp. 420–426.
Translated from Zhurnal Éksperimental'noĭ i Teoreticheskoĭ Fiziki, Vol. 128, No. 3, 2005, pp. 489–496.

NUCLEI, PARTICLES, FIELDS, GRAVITATION, AND ASTROPHYSICS

Discrete Quantum Gravity in the Regge Calculus Formalism

V. M. Khatsymovsky*

Budker Institute of Nuclear Physics, Siberian Division, Russian Academy of Sciences, pr. Akademika Lavrent'eva 11, Novosibirsk, 630090 Russia

**e-mail: khatsym@inp.nsk.su*

Received March 17, 2005

Abstract—We discuss an approach to the discrete quantum gravity in the Regge calculus formalism that was developed in a number of our papers. The Regge calculus is general relativity for a subclass of general Riemannian manifolds called piecewise flat manifolds. The Regge calculus deals with a discrete set of variables, triangulation lengths, and contains continuous general relativity as a special limiting case where the lengths tend to zero. In our approach, the quantum length expectations are nonzero and of the order of the Plank scale, 10^{-33} cm, implying a discrete spacetime structure on these scales. © *2005 Pleiades Publishing, Inc.*

1. INTRODUCTION

Interest in the formulation of general relativity (GR) in discrete form stems primarily from the complexity of the theory. In a classical aspect, rewriting the essentially nonlinear equations of the theory, the Einstein equations, in terms of a discrete set of physical quantities, i.e., discretizing them, facilitates the use of numerical methods for their solution. In a quantum aspect, discretization can be introduced, as in any other field theory, to regularize the originally divergent expressions. However, in the case of GR, we have the following two distinctive features. First, according to the standard classification, GR is a nonrenormalizable theory; therefore, the dependence of the result on the specific choice of regularization cannot be eliminated by renormalization. Consequently, in this case, discretization must be not only a mathematical approximation like a finite-difference approximation of the originally continuum theory, but be realizable physics specifying the form of the theory at small distances. Second, the covariance of the theory relative to arbitrary coordinate transformations is specific to GR, and this property is in poor agreement with the quantum theory, in which the time plays a prominent role. To overcome this difficulty, one can try to formulate GR in an explicitly coordinateless form.

In the Regge calculus suggested in 1961 [1], the exact GR deals with a special case of general Riemannian spacetime, the so-called piecewise flat manifolds, which are flat everywhere except for the subset of points of zero measure. Any such spacetime can be represented as consisting of flat 4-dimensional simplexes (tetrahedrons). In the n-dimensional case, n-dimensional simplexes σ^n are considered. An n-dimensional simplex σ^n consists of $n + 1$ vertices each of which is connected by the edges with the other n vertices. All the geometrical characteristics of the n-simplex are uniquely defined by the (freely chosen) lengths of its $n(n + 1)/2$ edges. The Regge spacetime geometry is defined by freely choosing the lengths of all its edges, i.e., 1-simplexes. The link lengths of the two n-simplexes sharing an $(n – 1)$-simplex as their common face must be equal on this face. If, however, we consider all the n-simplexes containing an $(n –2)$-simplex as an $(n – 2)$-dimensional face, then, in general, this manifold cannot be embedded in flat n-dimensional spacetime when the link lengths are chosen freely, since the sum of the hyperdihedral angles of all the n-simplexes meeting on this $(n – 2)$-dimensional face is $2\pi – \alpha$, where the so-called angle defect α is not necessarily equal to zero. In the case of parallel translation of a vector along a closed contour contained in the above n-simplexes and enclosing the $(n –2)$-simplex in question, the vector is rotated through the angle α. This corresponds to a δ-function curvature distribution with the support on $(n –2)$-simplexes proportional to the angle defects on these simplexes. The action for 4-dimensional Regge spacetime is proportional to

$$\sum_{\sigma^2} \alpha_{\sigma^2} |\sigma^2|, \tag{1}$$

where $|\sigma^2|$ is the area of triangle σ^2 (2-simplex), α_{σ^2} is the angle defect on this triangle, and the summation is over all the 2-simplexes σ^2. Friedberg and Lee [2] showed that action (1) could be obtained from the expression

$$\frac{1}{2}\int R\sqrt{g}d^4x, \tag{2}$$

to which the Einstein action is proportional, by passing to the δ-function limit of the curvature R distribution. Thus, the Regge calculus is GR in which all the degrees of freedom except a discrete number of them are frozen, i.e., the so-called minisuperspace theory for GR. In this way, the first of the requirements mentioned above

is satisfied; more specifically, a Regge manifold is a special (although partly singular) case of a general Riemannian manifold. In addition, the mutual arrangement of the vertices (0-dimensional simplexes σ^0) and, hence, the geometry are uniquely fixed by the freely chosen invariant lengths of the edges (1-simplexes σ^1), which, thus, act as field variables. Therefore, the second requirement, the possibility of a coordinateless description, is also fulfilled.

Although the Regge calculus is only a subset in the configuration superspace of GR, this subset is dense in this superspace. This means that each nonsingular Riemannian manifold can be approximated with an arbitrarily high accuracy by a properly chosen Regge manifold. Such a Regge manifold can be constructed by dividing, for example, a Riemannian manifold into fairly small regions topologically equivalent to the simplexes σ^4 whose edges are geodesics. As the sought-for piecewise flat manifold, we can take a manifold of this type with the same topology, vertex connection scheme, and link lengths as those for the above division of the Riemannian manifold. Feinberg *et al.* [3] showed that the Einstein action (2) is obtained as the limit of the Regge action (1) for approximating spaces where the typical edge length (triangulation length) tends to zero. A more general statement was proven by Cheeger *et al.* [4] for the *n*-dimensional case: the so-called Lipshitz–Killing curvatures converge to their continuum analogs in the sense of measures if the decomposition into 4-simplexes becomes increasingly fine; i.e. the integrals of the quantities under consideration over the spacetime regions converge. The volume of a spacetime region and the contribution of the region to the Einstein action and to the Gauss–Bonnet topological term are special cases of these integrals.

The Regge calculus has exact discrete analogs of many quantities that can be defined in the continuum GR. The Einstein equations whose discrete analog was obtained by Regge by varying action (1) over the link lengths serve as the first example. It turns out that varying α_{σ^2} in (1) makes no contribution, and the equation derived by varying the length of a specific edge σ^1 is

$$\sum_{\sigma^2 \supset \sigma^1} \alpha_{\sigma^2} \cot \vartheta(\sigma^1, \sigma^2) = 0. \quad (3)$$

Here, $\vartheta(\sigma^1, \sigma^2)$ is the angle in the triangle σ^2 opposite to the edge σ^1, and the summation is over all the triangles with σ^1 as a common edge. Evidently, the discrete coordinateless formulation in terms of physical quantities (lengths) is ideally suited for numerical simulations, and the Regge calculus was originally used precisely for a numerical analysis of the Einstein equations [5].

However, the Regge calculus aroused the greatest interest when applied to quantum gravity. In this aspect, the main problem consisted in constructing a Hamiltonian formalism analogous to the Arnowitt–Deser–Misner formalism in the continuum GR [6]. In accordance with their result, the GR Lagrangian can be reduced to

$$L = \sum_A p_A \dot{q}_A - \sum_\alpha \lambda_\alpha \Phi_\alpha(p, q) \quad (4)$$

with the canonical variables p_A and q_A and the variables λ_α acting during the variation as the Lagrange multipliers whose values and dynamics cannot be determined from the equations of motion. Thus, GR is a theory described by the set of constraints $\Phi_\alpha(p, q) = 0$ and a zero Hamiltonian. In the case of the basically coordinateless Regge calculus theory, we had to partly return to the coordinate description, but with regard to only one coordinate, the time *t*, to pass from the discrete field distribution (in our case, the lengths and their functions) to a distribution smooth in *t*. The passage to the so-called (3+1) Regge calculus (discrete three-dimensional space plus continuous time) has been undertaken in a number of papers [7–18]. In general, the authors of these papers tried to define in one way or another the discrete analogs of the variables s p_A and q_A and the constraints $\Phi_\alpha(p, q)$, with emphasis on the requirement that the algebra of the Poisson brackets for these constraints be close to that in the continuum GR. If we adhere to the strategy that requires dealing with a special case of a Riemannian manifold at each stage, then the (3+1) Regge calculus is obtained as the limit of the 4-dimensional Regge calculus when the sizes of the 4-simplexes tend to zero in a certain direction chosen as the direction of time. This passage to the limit was studied in [7, 8, 15, 16]. In particular, we see a source of difficulties that did not allow the formulated problem to be completely solved in the cited papers: it consists in the singular nature of the description of simplexes using the link lengths when the sizes along a certain direction tend to zero. As an illustration, one can imagine a triangle one of the edges of which is infinitesimal: infinitesimal variations in the two other (finite) edge lengths then lead to finite variations in the angles. As a result, not all of the degrees of freedom can be described in the chosen length-type variables in a nonsingular way, and, hence, not all of the discrete analogs of the constraints $\Phi_\alpha(p, q)$ can be found.

2. THE PROBLEM OF CONSTRUCTING THE QUANTUM MEASURE IN THE REGGE CALCULUS

Thus, the singular nature of the passage to continuous time is associated with the use of the lengths alone as a fundamental set of variables in the Regge calculus. As long as we are studying the quantum measure on a completely discrete Regge manifold, this circumstance is of no importance to us. However, the basic concept underlying the quantum theory that can be used to construct the quantum measure is canonical quantization; the latter is defined precisely in the continuous time. Therefore, the sought-for quantum measure should be

defined from the requirement that it tend, in a sense, to the canonical quantization measure (Feynman path integral) whenever the continuum limit is taken along any of the coordinates, with the coordinate chosen acting as the time. In other words, the continuous time limit serves as a probe for defining the quantum measure in a completely discrete Regge calculus.

The singularities in the continuous time limit can be bypassed by extending the set of variables via the addition of new ones that have the meaning of angles considered as independent variables. The finite rotation matrices, discrete analogs of the connections in the continuum GR, are such variables.

3. REPRESENTING THE REGGE CALCULUS IN TERMS OF THE FINITE ROTATION MATRICES AS INDEPENDENT VARIABLES

The situation considered is analogous to rewriting the Einstein action (2) in the Hilbert–Palatini form,

$$\frac{1}{2}\int R\sqrt{g}d^4x \Leftarrow \frac{1}{8}\int \epsilon_{abcd}\epsilon^{\lambda\mu\nu\rho}e^a_\lambda e^b_\mu[\partial_\nu + \omega_\nu, \partial_\rho + \omega_\rho]^{cd}d^4x, \quad (5)$$

where the tetrad e^a_λ and the connection $\omega^{ab}_\lambda = -\omega^{ba}_\lambda$ are independent variables; Eq. (5) is reduced to (2) in terms of $g_{\lambda\mu} = e^a_\lambda e_{a\mu}$ if we substitute the solutions of these equations of motion for these variables in terms of $e^a_\lambda = e^a_\lambda e_{a\mu}$ for ω^{ab}_λ. The Latin indices $a, b, c,\ldots$ are vectorial with respect to the local Euclidean frames introduced at each point x. The Regge calculus analog of representation (5) is obtained if the local Euclidean frame is introduced in each 4-simplex. The transformation matrices Ω_{σ^3} between the frames in two 4-simplexes σ^4 sharing σ^3 as their three-dimensional face defined on 3-simplexes σ^3 are then the analogs of the connections. These matrices are finite SO(4) rotations in the Euclidean case (or SO(3,1) rotations in the Lorentzian case), in contrast to the continuum connections ω^{ab}_λ, which are the elements of the Lee algebra so(4)(so(3,1)) of this group. In this case, it is important to specify the direction in which the connection Ω_{σ^3} acts (and, accordingly, $\Omega^{-1}_{\sigma^3} = \overline{\Omega}_{\sigma^3}$ acts in the opposite direction); i.e., the connections Ω are defined on oriented 3-simplexes σ^3.

We can also define the curvature matrix R_{σ^2} on each 2-simplex σ^2 as the product of the connections $\Omega^{\pm 1}_{\sigma^3}$ on the 3-simplexes σ^3 sharing σ^2 that act in a certain direction along a closed contour enclosing σ^2 once and contained in these 3-simplexes. The matrix R_{σ^2} should represent the rotation around σ^2 through the angle α_{σ^2}. Apart from the direction along the contour, it is necessary to specify the 4-simplex $\sigma^4 \supset \sigma^2$ in which the contour begins and ends, i.e., the simplex in the local Euclidean frame of which we define the matrix

$$R_{\sigma^2} = \prod_{\sigma^3 \supset \sigma^2} \Omega^{\pm 1}_{\sigma^3}. \quad (6)$$

Discrete analogs of the connection and curvature were discussed by Bander [19, 20, 21] as functions of length. Our approach is based on treating the connections as independent variables and studying a representation of the Regge calculus action (1) analogous to the Hilbert–Palatini form of the Einstein action (5). To write out this representation, let us define the dual bivector of the triangle σ^2 in terms of the vectors l^a_1 and l^a_2 of its edges defined in a 4-simplex containing σ^2:

$$V_{\sigma^2 ab} = \frac{1}{2}\epsilon_{abcd}l^c_1 l^d_2. \quad (7)$$

The discrete analog of expression (5) suggested in our work [22] then reads

$$S(V, \Omega) = \sum_{\sigma^2} |V_{\sigma^2}| \arcsin \frac{V_{\sigma^2} \circ R_{\sigma^2}(\Omega)}{|V_{\sigma^2}|}, \quad (8)$$

where for the two tensors A and B, we defined

$$A \circ B = \frac{1}{2}A^{ab}B_{ab}, \quad |A| = (A \circ A)^{1/2},$$

in particular, $|V_{\sigma^2}| = |\sigma^2|$ is the area of the triangle. It is important that V_{σ^2} and R_{σ^2} in (8) be defined in the same 4-simplex containing σ^2. As can be shown, if we substitute the actual rotations connecting the neighboring local Euclidean frames and corresponding to the actual Regge lengths in the equation of motion for Ω_{σ^3} with action (8) as the variables Ω_{σ^3}, we get a closure condition for the surface of the 3-simplex σ^3 (the sum of the bivectors of its 2-faces being equal to zero) written in the frame of one of the 4-simplexes containing σ^3, i.e., an identity. This means that (8) is an exact representation for (1).

4. THE NATURALNESS OF PASSING TO THE AREA TENSOR REGGE CALCULUS

In the representation based on the rotation matrices, we can pass to continuous time and develop the canonical formalism in the Regge calculus [23], which has

second-class (i.e., noncommuting) constraints. As a result, the Feynman path integral contains the determinant of the Poisson brackets of the second-class constraints as a factor which is singular in a flat geometry. The point is that the Regge manifold geometry generally changes at any variations of the edge lengths except for the flat case in which these variations are symmetry transformations. In other words, the division of the constraints into those of the first and second classes changes in the flat case. The 3-dimensional case constitutes an exception. Due to the local triviality of the 3-dimensional gravity, all the dynamical constraints are first-class ones, and, therefore, the path integral takes a simple form. In this case, the problem of constructing the discrete quantum measure formulated in Section 2 can be solved to yield a simple form of this measure [24].

The conditions imposed on the discrete measure in Section 2 are highly restrictive, and, in general, the existence of a solution is not obvious. The singularity of the path integral in 4 dimensions near a flat geometry per se is not an obstacle to the existence of a solution; the presence of the above determinant factor in the path integral is crucial. This factor depends on variables that are lattice artefacts connected with a specific coordinate along which the continuum limit is taken, and, therefore, it can not be obtained from a universal expression by assuming a continuous time limit.

Let us try to modify the 4-dimensional Regge calculus to resemble the 3-dimensional case in canonical structure. The 3-dimensional Regge calculus in a representation analogous to (8) has the edge vectors $\mathbf{l}_{\sigma^1}$ instead of the area tensors V_{σ^2}. The edge vectors are independent variables, thereby ensuring the local triviality of the 3-dimensional gravity. In contrast, the area tensors are not independent. For example, the tensors of the two triangles σ_1^2 and σ_2^2 with a common edge satisfy the relation

$$\epsilon_{abcd} V^{ab}_{\sigma_1^2} V^{cd}_{\sigma_2^2} = 0. \tag{9}$$

The idea is to construct the quantum measure first for the system with formally independent area tensors, i.e., to initially concentrate on the quantization of the dynamics, while kinematical relations of type (9) are taken into account at the second stage.

In the area tensor Regge calculus, the problem of constructing the discrete quantum measure can be solved to yield a simple form of this measure [25]. Let us consider the Euclidean case. Since the Einstein action is known to be not bounded from below, the Euclidean path integral itself requires a redefinition. In particular, the result of [25] for the vacuum expectations of the functions of our field variables V and Ω can be written using integration over imaginary areas by a formal replacement for the tensors of a certain subset of areas π over which the integration in the path integral is performed,

$$\pi \longrightarrow i\pi,$$

in the form

$$\begin{aligned}\langle \Psi(\{\pi\},\{\Omega\})\rangle &= \int \Psi(-i\{\pi\},\{\Omega\}) \\ &\times \exp\left(-\sum_{\substack{t\text{-like}\\ \sigma^2}} \tau_{\sigma^2} \circ R_{\sigma^2}(\Omega)\right) \\ &\times \exp\left(i\sum_{\substack{\text{not}\\ t\text{-like}\\ \sigma^2}} \pi_{\sigma^2} \circ R_{\sigma^2}(\Omega)\right) \prod_{\substack{\text{not}\\ t\text{-like}\\ \sigma^2}} d^6\pi_{\sigma^2} \prod_{\sigma^3} \mathcal{D}\Omega_{\sigma^3} \\ &\equiv \int \Psi(-i\{\pi\},\{\Omega\}) d\mu_{\text{area}}(-i\{\pi\},\{\Omega\}),\end{aligned} \tag{10}$$

where for the two tensors A and B, we defined

$$A \circ B = \frac{1}{2} A^{ab} B_{ab}.$$

The equation implies a certain structuring of our Regge lattice that suggests constructing it from leaves, structurally similar 3-dimensional Regge geometries. The leaves are numbered by the values of a coordinate t. The corresponding vertices in the neighboring leaves are connected by the t-like edges, and there are diagonal edges connecting the vertex with the neighbors of the corresponding vertex in the neighboring leaf. It is then natural to define the t-like simplexes and the leaf simplexes as simplexes that either contain a t-like edge or are completely contained in the leaf, respectively, as well as the diagonal simplexes as all others. Then, τ_{σ^2} is V_{σ^2} when σ^2 is t-like, and π_{σ^2} is V_{σ^2} when σ^2 is not t-like, i.e., the leaf or a diagonal simplex. In the Regge calculus with independent area tensors, π_{σ^2} can serve as dynamical variables, while τ_{σ^2} must be chosen as parameters.

In many respects, Eq. (10) resembles the intuitively expected expression for the quantum measure. In particular, the expected (from symmetry considerations) invariant (Haar) measure on SO(4) $\mathcal{D}\Omega$ arises in the formal path integral expression corresponding in the continuous time limit to the canonical quantization with the kinetic term $\pi_{\sigma^2} \circ \bar{\Omega}_{\sigma^2} \dot{\Omega}_{\sigma^2}$ in the Lagrangian (the connection variables in the continuous time limit Ω

naturally correspond not to the tetrahedra σ^3, but to the triangles σ^2).

The specific features of the quantum measure include, first, the absence of the inverse trigonometric functions arcsin in the exponential, while the Regge action (8) contains such functions. This is because the canonical quantization is used at the intermediate stage of the derivation: in gravity, this quantization is completely defined by the constraints, the latter being equivalent to those without arcsin (in a sense, on-shell). Second, there are no integrations over some of the tensors, τ_{σ^2}, and, thus, the symmetry between different triangles is incomplete. Nevertheless, this symmetry violation can be considered as spontaneous when some *a priori* arbitrary direction denoted by the coordinate t in (10) is singled out. The curvature matrices $R(\Omega)$ on all but t-like triangles can be chosen as independent variables; these matrices on the t-like triangles are then (via the Bianchi identities) functions of these variables. Integrations over all area tensors would lead to singularities of the type $[\delta(R - \bar{R})]^2$.

This specific feature of the discrete quantum measure, incomplete symmetry with respect to different coordinate directions, is consistent with the above conditions imposed on it in Section 2: In the continuous limit along some coordinate x (which does not necessarily coincide with t), the absence of integrations over the tensors of the t-like triangles implies some of the simplest kinds of gauge fixing in the limiting measure, namely, fixing the tensors of some subset of triangles [25].

Given the properties of the invariant Haar measure and with negligible values of τ_{σ^2}, we obtain factorization of the inferred quantum measure into "elementary" measures on separate areas (which precisely corresponds to the local triviality of the theory) of the form

$$\exp(i\pi \circ R)d^6\pi\mathcal{D}R. \tag{11}$$

In turn, we use the group property

$$SO(4) = SU(2) \times SU(2)$$

to split the variables (π and the generator of R) into self- and antiself-dual parts, in particular, π is mapped into two 3-vectors, ${}^+\boldsymbol{\pi}$ and ${}^-\boldsymbol{\pi}$, in the adjoint representation SO(3). As a result, measure (11) is the product of two measures each of which acts in the 3-dimensional configuration space of area vectors,

$$\begin{aligned}&\exp(i{}^+\pi \circ {}^+R)d^{3+}\boldsymbol{\pi}\mathcal{D}{}^+R\\ &\times \exp(i{}^-\pi \circ {}^-R)d^{3-}\boldsymbol{\pi}\mathcal{D}{}^-R.\end{aligned} \tag{12}$$

As a result, the expression for the expectation of any function of the triangle area reads

$$\begin{aligned}\langle f(\pi)\rangle &= \int f(-i\pi)d^6\pi\int e^{i\pi\circ R}\mathcal{D}R\\ &= \int f(\pi)\frac{\nu_2(|{}^+\boldsymbol{\pi}|)}{|{}^+\boldsymbol{\pi}|^2}\frac{\nu(|{}^-\boldsymbol{\pi}|)}{|{}^-\boldsymbol{\pi}|^2}\frac{d^{3+}\boldsymbol{\pi}}{4\pi}\frac{d^{3-}\boldsymbol{\pi}}{4\pi},\end{aligned} \tag{13}$$

$$\nu(l) = \frac{l}{\pi}\int_0^\pi \frac{d\varphi}{\sin^2\varphi}\exp\left(-\frac{l}{\sin\varphi}\right).$$

In particular, the expectations of the powers of the area squared,

$$|\pi|^2 = \pi\circ\pi = \frac{1}{2}({}^+\boldsymbol{\pi})^2 + \frac{1}{2}({}^-\boldsymbol{\pi})^2, \tag{14}$$

and of the dual product,

$$\pi * \pi = \frac{1}{2}({}^+\boldsymbol{\pi})^2 - \frac{1}{2}({}^-\boldsymbol{\pi})^2, \tag{15}$$

can be easily obtained by averaging the powers of $\pm\pi$,

$$\langle({}^\pm\boldsymbol{\pi})^{2k}\rangle = \frac{4^{-k}(2k+1)!(2k)!}{k!^2}. \tag{16}$$

5. RETURNING TO THE STANDARD REGGE CALCULUS

Thus, we obtained finite nonzero area expectation values in the area tensor Regge calculus. However, we need the length expectations in the ordinary Regge calculus, which is derived by imposing uniqueness conditions on the lengths calculated in different 4-simplexes. These conditions are equivalent to the continuity conditions for the metric induced on 3-dimensional faces. In the configuration space of the area tensor Regge calculus, these conditions separate out some hypersurface Γ_{Regge}. The quantum measure can be considered as a linear functional $\mu_{\text{area}}(\Psi)$ on the space of functionals $\Psi(\{v\})$ on the configuration space (for our purposes, it will suffice to restrict ourselves to the functional dependence on the set of area tensors $\{v\}$; the dependence on the connections is unimportant). The physical assumption is that we can consider the ordinary Regge calculus as a kind of state of a more general system with independent area tensors. This state can be described by the functional

$$\Psi(\{v\}) = \psi(\{v\})\delta_{\text{Regge}}(\{v\}), \tag{17}$$

where $\delta_{\text{Regge}}(\{v\})$ is the (multidimensional) δ-function with the support on Γ_{Regge}. The derivatives of δ_{Regge} have the same support, but these violate the positivity in our subsequent construction. To be more precise, the δ-function is a distribution rather than a function, but it can be treated as a function being regularized. If the measure on such functionals exists in the limit when

regularization is removed, this allows us to define the quantum measure on Γ_{Regge},

$$\mu_{\text{Regge}}(\cdot) = \mu_{\text{area}}(\delta_{\text{Regge}}(\{V\})\cdot). \quad (18)$$

The construction of δ_{Regge} is unique under the natural assumption that the lattice artefacts are at a minimum. Let the system be described by the metric $g_{\lambda\mu}$ that is constant in each of the two 4-simplexes σ_1^4 and σ_2^4 separated by the 3-face

$$\sigma^3 = \sigma_1^4 \cap \sigma_2^4$$

formed by three 4-vectors ι_a^λ. These vectors also specify the metric induced on the face,

$$g_{ab}^{\parallel} = \iota_a^\lambda \iota_b^\mu g_{\lambda\mu}.$$

The continuity condition for the induced metric can be expressed in terms of the δ-function of the metric variations,

$$\Delta_{\sigma^3} g_{ab}^{\parallel} \stackrel{\text{def}}{=} g_{ab}^{\parallel}(\sigma_1^4) - g_{ab}^{\parallel}(\sigma_2^4). \quad (19)$$

Naturally, δ_{Regge} itself is defined to within a factor, which is an arbitrary function nonvanishing at nondegenerate field configurations. In the spirit of the abovementioned principle of the lattice artefacts being at a minimum, it is natural to choose this factor in such a way that the resulting δ-function factor depends only on the hyperplane specified by the 3-face, but not on the shape of this face; i.e., it is invariant with respect to arbitrary nondegenerate transformations,

$$\iota_a^\lambda \mapsto m_a^b \iota_b^\lambda.$$

This requires multiplying the δ-function by the determinant $g_{ab}^{\parallel}$ squared to give

$$[\det(\iota_a^\lambda \iota_b^\mu g_{\lambda\mu})]^2 \delta^6(\iota_a^\lambda \iota_b^\mu \Delta_{\sigma^3} g_{\lambda\mu}) = V_{\sigma^3}^4 \delta^6(\Delta_{\sigma^3} S_{\sigma^3}). \quad (20)$$

Here, S_{σ^3} is the set of the squares of the edge lengths of the 3-face σ^3, and V_{σ^3} is the volume of this face.

Further, the product of the factors (20) over all 3-faces should be taken. As a result, for each edge, we obtain the products of the δ-functions of the variations in its length between the 4-simplexes taken along closed contours,

$$\delta(s_1 - s_2)\delta(s_2 - s_3)\ldots\delta(s_N - s_1),$$

which contain a singularity like the δ-function squared. In other words, the conditions equating (19) to zero on different 3-faces are not independent. A more detailed analysis allows us to cancel out this singularity in a symmetric (with respect to different 4-simplexes) way (thereby extracting the irreducible conditions); the resulting δ-function factor remains invariant with respect to arbitrary deformations of the faces of different dimensions keeping each face in the fixed plane defined by it [26].

Qualitatively, it is important that our δ-function factor (in the simplest case, (20)) automatically turns out to be invariant with respect to the overall length scaling. Recall, however, that the area tensors π_{σ^2}, but not τ_{σ^2}, are the dynamical variables to be averaged. A more detailed analysis shows that, having fixed the scale of the tensors τ_{σ^2} at a level of $\varepsilon \ll 1$, we can consider the δ-function factor to be also invariant with respect to the overall scaling of the dynamical variables π_{σ^2} alone. This implies finite nonzero length expectation values in the ordinary Regge calculus as long as the area expectation values in the area tensor Regge calculus are finite and nonzero [27].

Strictly speaking, when passing from the area tensor Regge calculus to the ordinary Regge calculus, we first need to impose conditions ensuring that the tensors of the 2-faces in each specific 4-simplex define a metric in this simplex. These conditions of type (9) can be easily written in general form if we take a vertex of the given 4-simplex as the coordinate origin and consider the edges emanating from it to be the coordinate lines λ, μ, ν, ρ, … = 1, 2, 3, 4. The (ordered) pair λμ then means the (oriented) triangle formed by the edges λ and μ. The sought-for conditions are

$$\epsilon_{abcd} V_{\lambda\mu}^{ab} V_{\nu\rho}^{cd} \sim \epsilon_{\lambda\mu\nu\rho}. \quad (21)$$

The 20 equations of (21) define the 16-dimensional surface $\gamma(\sigma^4)$ in the 36-dimensional configuration space of the six antisymmetric tensors[1] $V_{\lambda\mu}^{ab}$. The sought-for factor in the quantum measure is the product of the δ-functions with the support on $\gamma(\sigma^4)$ over all 4-simplexes σ^4. The covariant form of constraints (21) with respect to the world index means that these δ-functions are scalar densities of a certain weight with respect to the world index, i.e., scalars to within the powers of the volume of the 4-simplex V_{σ^4}. Therefore, introducing factors of the type $V_{\sigma^4}^\eta$, we can get the scalar at a certain parameter η. More specifically, the product of the factors

$$\prod_{\sigma^4} \int V_{\sigma^4}^\eta \delta^{21}(\epsilon_{abcd} V_{\lambda\mu|\sigma^4}^{ab} V_{\nu\rho|\sigma^4}^{cd} - V_{\sigma^4} \epsilon_{\lambda\mu\nu\rho}) dV_{\sigma^4} \quad (22)$$

at $\eta = 20$ is a scale-invariant quantity as required by the principle of the lattice artefacts being at a minimum (i.e., the sought-for factor should not depend on the size of the 4-simplex). As a result, the conclusion reached in the previous paragraph about finite nonzero length expectation values in the ordinary Regge calculus as long

[1] There are also linear constraints of the type $\sum \pm V = 0$ ensuring the closure of the surfaces of the 3-faces of our 4-simplex. It is implied that these constraints have already been resolved.

as the area expectation values in the area tensor Regge calculus are finite and nonzero remains valid [27].

6. CONCLUSIONS

Thus, our approach to quantizing the Regge calculus "from the first principles" includes the following steps and conditions.

(1) Constructing the quantum measure that reduces to a Feynman path integral corresponding to the canonical quantization in the continuous time limit irrespective of which coordinate is taken as the time.

(2) Using the exact representation of the Regge action in terms of the rotation matrices as independent variables.

(3) Extending the configuration space of the theory by considering the area tensors as independent variables (considering the so-called area tensor Regge calculus).

(4) Reducing the quantum measure from the area tensor Regge calculus to the hypersurface corresponding to the ordinary Regge calculus using the principle of the lattice artefacts being at a minimum, i.e., minimal dependence on the shape and size of the simplexes.

As a result, we obtained quantum Regge length expectations of the order of the Plank scale, 10^{-33} cm. If these length values were zero, this would just imply that the quantum measure is saturated by arbitrarily small Regge edge lengths, i.e., smooth Riemannian manifolds, and, in fact, we would return to the continuum GR. Here, a remarkable property of the Regge calculus appears: this is the minisuperspace GR theory, in other words, exact GR for certain (piecewise flat) spacetimes. Therefore, the Regge calculus in the quantum theory does not mean abandoning continuum GR (it contains this theory as the limiting point), but is rather a description of the system using an alternative set of variables, triangulation lengths. Our result, nonzero length expectations, implies that GR is adequately described precisely by these variables when GR becomes discrete on the Planck scale dynamically, i.e., via competition between the various contributions in the functional integral, including the contribution of smooth manifolds.

ACKNOWLEDGMENTS

I am grateful to I.B. Khriplovich for his attention to and discussion of the work.

REFERENCES

1. T. Regge, Nuovo Cimento **19**, 568 (1961).
2. R. Friedberg and T. D. Lee, Nucl. Phys. B **242**, 145 (1984).
3. G. Feinberg, R. Friedberg, T. D. Lee, and M. C. Ren, Nucl. Phys. B **245**, 343 (1984).
4. J. Cheeger, W. Müller, and R. Shrader, Commun. Math. Phys. **92**, 405 (1984).
5. C.-Y. Wong, J. Math. Phys. **12**, 70 (1971).
6. R. Arnowitt, S. Deser, and C. W. Misner, Phys. Rev. **117**, 1595 (1960).
7. P. A. Collins and R. M. Williams, Phys. Rev. D **7**, 965 (1973).
8. P. A. Collins and R. M. Williams, Phys. Rev. D **10**, 3537 (1974).
9. R. M. Williams, Class. Quantum Grav. **3**, 853 (1986).
10. J. L. Friedman and I. J. Jack, J. Math. Phys. **27**, 2973 (1986).
11. T. Piran and R. M. Williams, Phys. Rev. D **33**, 1622 (1986).
12. J. Porter, Class. Quantum Grav. **4**, 375 (1987).
13. J. Porter, Class. Quantum Grav. **4**, 391 (1987).
14. J. Porter, Class. Quantum Grav. **4**, 651 (1987).
15. L. Brewin, Class. Quantum Grav. **4**, 899 (1987).
16. L. Brewin, Class. Quantum Grav. **5**, 839 (1988).
17. P. A. Tuckey and R. M. Williams, Class. Quantum Grav. **5**, 155 (1988).
18. P. A. Tuckey, Class. Quantum Grav. **6**, 1 (1989).
19. M. Bander, Phys. Rev. Lett. **57**, 1825 (1986).
20. M. Bander, Phys. Rev. D **36**, 2297 (1987).
21. M. Bander, Phys. Rev. D **38**, 1056 (1988).
22. V. M. Khatsymovsky, Class. Quantum Grav. **6**, L249 (1989).
23. V. M. Khatsymovsky, Gen. Relativ. Gravit. **27**, 583 (1995); gr-qc/9310004.
24. V. M. Khatsymovsky, Class. Quantum Grav. **11**, 2443 (1994); gr-qc/9310040.
25. V. M. Khatsymovsky, Phys. Lett. B **560**, 245 (2003); gr-qc/0212110.
26. V. M. Khatsymovsky, Phys. Lett. B **567**, 288 (2003); gr-qc/0304006.
27. V. M. Khatsymovsky, Phys. Lett. B **586**, 411 (2004); gr-qc/0401053.

Translated by V. Astakhov

Journal of Experimental and Theoretical Physics, Vol. 101, No. 3, 2005, pp. 427–436.
Translated from Zhurnal Éksperimental'noĭ i Teoreticheskoĭ Fiziki, Vol. 128, No. 3, 2005, pp. 497–507.

ORDER, DISORDER, AND PHASE TRANSITIONS IN CONDENSED SYSTEMS

Determining the Structural Parameters of Fractal and Nonfractal Objects in Multiple Small-Angle Neutron Scattering Experiments

G. P. Kopitsa[a], S. V. Grigoriev[a], V. V. Runov[a], V. M. Garamus[b], and D. Bellmann[b]

[a]*Petersburg Nuclear Physics Institute, Russian Academy of Sciences, Gatchina, Leningradskaya oblast, 188300 Russia*
[b]*GKSS Research Centre, D-21502 Geesthacht, Germany*
e-mail: kopitsa@mail.pnpi.spb.ru
Received November 10, 2004

Abstract—An experimental procedure employing setups with standard resolution characteristics for multiple small-angle neutron scattering in fractal and nonfractal media is described. Specific features of the proposed method, which are related to a limited resolution of the spectrometer, are considered in the case of large-scale inhomogeneities with the characteristic size exceeding the inverse spatial resolution. A new approach to the extraction of information about the fractal dimension of the system studied is demonstrated, which takes into account the dependence of the attenuation and broadening of the transmitted neutron beam on the sample thickness. © *2005 Pleiades Publishing, Inc.*

1. INTRODUCTION

The method of small-angle neutron scattering (SANS) is widely used for the investigation of nuclear and magnetic inhomogeneities in various materials, including porous media, alloys, etc., which contain a high concentration of contrast inhomogeneities with sizes spread over the scale from tens of ångstöms to several hundred microns. The SANS experiments in such media usually reveal a power dependence of the scattering intensity I on the momentum transfer (scattering vector) q,

$$I(q) \propto q^{-\Delta}, \quad \Delta \le 4,$$

in a certain interval of $q > 1/R$, where R is the characteristic scale of the scattering system. There is a commonly accepted trend to perform SANS measurements in the regime of single scattering (that is, under the condition that $L < l$, where L is the sample thickness and l is the neutron mean free path in the medium) and treat the possible multiple scattering (multiple SANS, MSANS) as a factor complicating the interpretation of data. The value of Δ or its deviation from the Porod asymptotics ($\Delta = 4$) is used to judge on the fractal character (dimension) of the system and on the correlator of scattering inhomogeneities (for more detail, see [1–3]). However, an analysis of the SANS data in this limit hardly allows one to extract information concerning the characteristic scale of the scattering system (of course, except for the possibility of scale evaluation from the uncertainty relation). Information of this kind can be obtained in the case of $q < 1/R$ corresponding to the passage to the Guinier regime [4]. However, both the $q < 1/R$ asymptotics and the Guinier regime are difficult to access for the scattering in strongly dispersive media with high concentrations of inhomogeneities. Moreover the condition $L < l$ frequently cannot be satisfied because of the difficulties of preparing sufficiently thin samples; in such cases, the scattering unavoidably has a multiple character.

This paper considers the possibility of evaluating, in principle, the characteristic scale of a scattering system by measuring both the broadening w of a transmitted neutron beam and the neutron mean free path in the sample using the standard SANS setups in the regime of elastic multiple scattering ($L > l$). The mean free path can be estimated from data on the attenuation of the primary beam as a function of L due to the scattering by angles $\Omega > \Omega_{min}$, where Ω_{min} is determined by the resolution of the instrument. Methods for the estimation of characteristic size using the beam broadening in the neutron scattering experiments has been widely used and extensively developed in both experimental and theoretical aspects, beginning with the work of Weiss [5] (see, e.g., [6–8] and references therein). One aim of this paper is to draw the attention to the relative character of estimates obtained from simultaneous measurements of the beam broadening and the integral cross section of scattering for the angles $\Omega > \Omega_{min}$. In other words, the resolution of the SANS setup restricts the possibilities of studying the large-scale inhomogeneities both in the case of single scattering and in the multiple scattering regime. Despite this restriction, MSANS is a powerful tool for the investigation of various substances and the determination of structural parameters of fractal and nonfractal objects. However, it should be recognized

that the real task of such investigations is to experimentally evaluate the characteristic scale of inhomogeneities making the main contribution to the scattering measured in the resolution limits of a given instrument, rather than analyzing the spectrum of inhomogeneities that may spread up to sizes that go unrecorded because of the limited resolution. This paper presents an experimental realization of this approach and shows examples of the application of MSANS to determining the structural parameters of systems.

It should be emphasized that multiple scattering substantially differs from the single scattering event. Indeed, in the latter case, the information is obtained using the coherent properties of radiation: the incident and scattered neutron waves are considered as coherent. In contrast, multiple scattering is a diffusion process, and what we measure in experiment is the degree of coherence. In this context, it is interesting to consider MSANS using the concept of coherent or correlation volume of the neutron beam [9].

The correlation volume can be intuitively defined as a region where the coherent properties of neutrons are significant. These properties are described using the correlation function of a collimated beam, which, in turn, is a Fourier image of the instrument resolution function. It should be noted that the correlation length for such a volume in SANS experiments may reach 1000 Å.

When a neutron beam propagates in a medium and exhibits multiple scattering, the correlation length decreases, which reflects the loss of the beam coherence, which leads to broadening of the instrumental linewidth. Naturally, this loss of coherence depends only on the number of scattering events per unit range (scattering length) or, in other words, on the general integral cross section of neutron scattering. The attenuation of the neutron beam is related to decaying amplitude of the neutron wave inside the coherent volume. This amplitude consists of two components, the amplitudes of nonscattered and forward-scattered waves. Obviously, both the correlation length and the amplitude of the neutron wave within this length depend on the properties of a scattering medium.

For this reason, the second but no less important task of this study is to consider the possibility of extracting information about the fractal properties of the scattering medium from data on the broadening and attenuation of a neutron beam in the regime of multiple scattering. One difficulty in obtaining reliable information on the fractal dimension of the medium in the regime of single scattering is related to the need for studying the scattering intensity distribution $I(q)$ in a broad range of q (over more than three orders of magnitude), which is practically impossible for most existing SANS setups. The possibility of obtaining such estimates from data on multiple scattering was demonstrated by Maleyev [3].

The aforementioned problems will be considered based on the results of MSANS, SANS and ultra-small-angle neutron scattering (USANS) experiments described below. The measurements were performed for the model samples of YBCO ceramics, Al_2O_3 powder, limestone ($CaCO_3$) powder, and carbon (C) carbon black in a range of sample thicknesses $L/l < 5$.

The paper is organized as follows. Section 2 briefly summarizes the main stipulations of the MSANS theory developed in [3, 6, 10, 11], which are used below for the interpretation of experimental data. The experimental part is presented in Section 3. The results of experimental data processing are presented and discussed in Section 4, and Section 5 summarizes the main conclusions.

2. THEORY

Let us briefly consider the main stipulations of the theory developed in [3, 6, 10], which are used below for the interpretation of the results of MSANS measurements in various regimes. The aforementioned papers considered the regimes of diffraction [3] for $\alpha \ll 1$ and refraction [10] for $\alpha \gg 1$, where $\alpha = kR(U/E)$ is a change in the neutron wavefunction over an inhomogeneity scale R, $k = 2\pi/\lambda$, is the wavevector of neutrons with the energy E, $U = 2\pi\hbar^2\Delta(bN_0)/m_n$ is the potential energy of the inhomogeneity (optical potential), m_n is the neutron mass, $\Delta(bN_0)$ is the difference of the densities of the scattering lengths for the inhomogeneity and the medium, b is the coherent scattering amplitude, and N_0 is the number of formula units per unit volume (cm^3). The regime of refraction was analyzed in the limit of low concentrations of inhomogeneities in the sample, that is, under the condition that $\delta V/V \ll 1$, where V is the sample volume and δV is the volume fraction accounting for inhomogeneities of the characteristic scale R.

It was shown [3] that the characteristic momentum, which determines the beam broadening as a result of multiple scattering ($L > l$) from a fractal medium in the diffraction regime in the general case, can be written as

$$q_L^{(\Delta)} = \frac{1}{2R}\left(\frac{L}{g_\Delta l}\right)^\mu, \quad \alpha \ll 1, \tag{1}$$

where $\Delta = D_v$ ($D_v < 3$ is the dimension of a volume fractal) or $\Delta = 6 - D_s$ ($2 < D_s < 3$ is the dimension of a surface fractal); $\mu = f(\Delta)$; and $g_\Delta \approx 1$. Accordingly:

$$q_L^{(\Delta)} \propto L^{\mu_{v,s}}, \quad \mu_v = (D_v - 2)^{-1} > 1,$$

$$1/2 < \mu_s = (4 - D_s)^{-1} < 1.$$

In the particular case of $\Delta = 4$ (the Porod asymptotics), we have $\mu = 1/2$ and the scattering intensity $I(q)$ is

described by the diffusion formula:

$$I(q) \propto \exp\left(-\frac{q^2}{2q_L^2}\right), \quad q_L = \frac{1}{2gR}\sqrt{\frac{L}{l}}. \tag{2}$$

Taking into account corrections for the insufficiently rapid decrease in the single scattering cross section with increasing scattering angle [6], the characteristic momentum can be written as

$$q_L = \frac{1}{2R}\sqrt{\frac{L}{l}\ln\frac{L}{l}}, \tag{3}$$

where the mean free path length is given by the formula

$$l = \frac{k^2}{3\pi[\Delta(bN_0)]^2 R}\frac{V}{\delta V}. \tag{4}$$

According to [3], the scattering intensity distribution $I(q)$ in the regime of multiple scattering ($L > l$) is divided into two parts. The asymptotic part (for $q \gg q_L^{(\Delta)}$) is similar to the $I(q)$ distribution in the single scattering regime. In the central part (for $q \leq q_L^{(\Delta)}$), the distribution is close to that in the Guinier regime:

$$I(q) = I(0)\left[1 - \frac{q^2 R_g^2(L)}{3}\right]. \tag{5}$$

Here, $R_g(L)$ is the effective gyration radius defined as

$$R_g^2(L) = \frac{3\Gamma(4\mu)}{4\Gamma(2\mu)\left(q_L^{(\Delta)}\right)^2}, \tag{6}$$

where $\Gamma(x)$ is the gamma function.

The intensity $I(q = 0)$ of forward scattering (i.e., the attenuation) is expressed as [3]

$$I(q=0) = \frac{\mu\kappa^2\Gamma(2\mu)}{2\pi\left(q_L^{(\Delta)}\right)^2} = \frac{2\mu(\kappa R)^2}{\pi}\left(\frac{g_\Delta l}{L}\right)^{2\mu}\Gamma(2\mu), \tag{7}$$

where $2\mu = 2/(D_v - 2) > 2$ and $1 < 2\mu = 2/(4 - D_s) < 2$ for the volume and surface fractals, respectively, and κ is the neutron wavevector. In both cases, the intensity $I(q = 0)$ decreases with the sample thickness L faster than according to the L^{-1} law (characteristic of the diffusion model used for analysis of MSANS on inhomogeneities with sharp boundaries ($2\mu = 1$)). This behavior of $I(q = 0)$ (as well as of $q_L^{(\Delta)}$) in the case of MSANS in fractal media offers an example of the so-called anomalous diffusion (superdiffusion) [12].

In the regime of refraction [10] in a sample with a small concentration of spherical inhomogeneities and a not very large thickness ($l \ll L \ll L_0 = l\alpha^2\ln\alpha$), the intensity of multiple scattering is also described by a diffusion formula with the characteristic momentum

$$q_1 = \sqrt{\frac{L}{l}\ln\frac{\alpha^2 L}{2l}}\frac{kU}{2E}. \tag{8}$$

For $L \approx L_0$, the scattering intensity deviates from the behavior predicted by the diffusion model, and for $L \gg L_0$ it is described by the formula [10]

$$I(q) = \frac{k^2 q_2}{2\pi(q^2 + q_2^2)^{3/2}}, \quad q_2 = \frac{L}{2g_\Delta lR}. \tag{9}$$

In the asymptotic limit $q \gg q_2$, the intensity of multiple scattering coincides with that of a single scattering and decreases as q^{-3} [10].

To our knowledge, multiple scattering in the refraction regime—neither in the case of a high concentration of inhomogeneities (whereby $\delta V \sim V$ as in multidomain polycrystalline ferromagnets, granulated and ceramic materials, etc.), nor in fractal media—has not been considered in the literature.

3. EXPERIMENT

In our MSANS experiments, the attenuation $I(q = 0)/I_0$, the broadening w of the neutron beam, and the scattering intensity $I_s(q)$ (for 5×10^{-3} Å$^{-1} < q < 3.5 \times 10^{-2}$ Å^{-1}) were studied as functions of the sample thickness L for YBCO ceramics, Al_2O_3 powder, $CaCO_3$ powder, and carbon black. The sample parameters important from the standpoint of MSANS were as follows:

(i) $YBa_2Cu_3O_{7+\delta}$ (YBCO) ceramics: $bN_0 = 4.75 \times 10^{10}$ cm^{-2}; density, $\rho \approx 4.9$ g cm^{-3}; range of sample thicknesses, L is from 0.9 to 20 mm; $\delta L/L \leq 1.5\%$.

(ii) Al_2O_3 powder: $bN_0 = 5.38 \times 10^{10}$ cm^{-2}; average grain size, 18–20 μm; L is from 2 to 16 mm; $\delta L/L \leq 2.5\%$.

(iii) Limestone ($CaCO_3$) powder: $bN_0 = 5.11 \times 10^{10}$ cm^{-2}; $\rho \approx 2.93$ g cm^{-3}; L is from 0.1 to 8.9 mm; $\delta L/L \leq 1.5\%$.

(iv) Carbon black: $bN_0 = 6.5 \times 10^{10}$ cm^{-2}; L is from 0.2 to 9 mm; $\delta L/L \leq 1.5\%$.

The MSANS measurements were performed using the small-angle polarized neutron scattering facility Vector-20 (WWR-M reactor, Petersburg Nuclear Physics Institute, Russian Academy of Sciences, Gatchina), which operated in slit geometry with twenty ^{3}He detectors in the horizontal plane [6]. The scattering intensity could be scanned in a range of q up to 5×10^{-1} Å^{-1} by rotating the detector system. In this experiment, the polarization technique was used for monochromatization of the neutron beam monochromatic. The measurements were performed at a neutron wavelength of $\lambda = 8$ Å with $\Delta\lambda/\lambda = 9\%$, which excluded the Bragg scattering. The vertical and horizontal resolution calculated

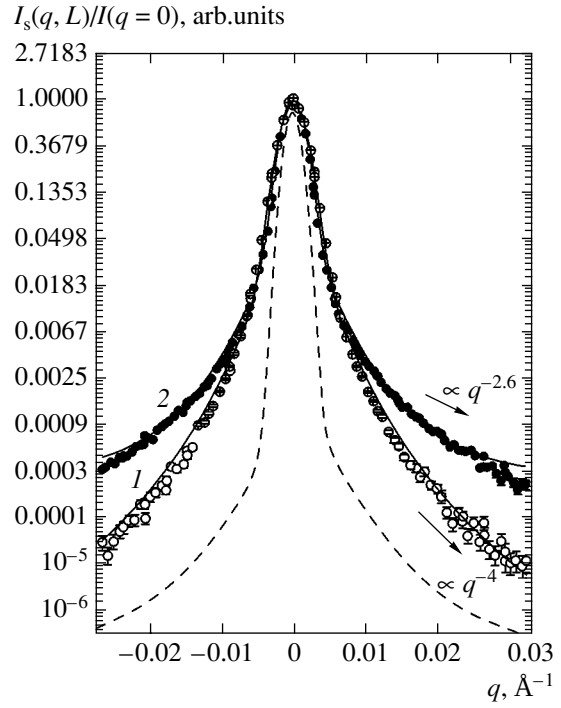

Fig. 1. The neutron beam shape measured in a regime of single scattering ($L < l$): (open circles) $CaCO_3$, $L = 0.67$ mm; (black circles) carbon black, $L = 0.83$ mm. Solid curves *1* and *2* show the results of calculations using formula (10); dashed curve represents the beam shape in the absence of a sample.

with allowance for the slit geometry [14] of the experimental setup was $\delta q_v = 3 \times 10^{-3}$ Å^{-1} and $\delta q_h = 8 \times 10^{-4}$ Å^{-1}, respectively.

In order to obtain independent data on the fractal dimension of carbon black and verify the MSANS results, we additionally studied this sample using the traditional SANS and USANS techniques in a broad range of momentum transfer ($1.5 \times 10^{-6} < q < 1.5 \times 10^{-1}$ Å^{-1}). The SANS measurements were performed using the SANS-1 facility (FRG1 reactor GKSS Research Centre, Geesthacht, Germany) [15], which operated in a geometry close to point geometry and was equipped with a two-dimensional (2D) position-sensitive ^{3}He detector. The working neutron wavelength was $\lambda = 8.1$ Å with $\Delta\lambda/\lambda = 10\%$. The experiments were performed for four distances between the sample and detector $R_{sd} = 0.7$, 1.8, 4.5, and 9.7 m, which allowed the momentum transfer to be varied within $3 \times 10^{-3} < q < 1.5 \times 10^{-1}$ Å^{-1}). The instrument resolution was approximated by the Gauss function and calculated separately for each R_{sd} value as described in [16].

The carbon black sample was placed in a 1-mm-thick quartz cell. The initial spectra measured in each q interval were corrected using standard procedures with allowance for scattering from the setup parts and the cell and for the room background [17]. The obtained 2D spectra were averaged with respect to azimuth and normalized to the cross section of noncoherent neutron scattering in a 1-mm-thick layer of water [17]. For $R_{sd} > 1.8$ m, the spectra were normalized to the cross section determined for $R_{sd} = 1.8$ m with additional allowance for the attenuation factor [17].

The USANS measurements were performed using a DCD double crystal diffractometer (at the same FRG1 reactor of the GKSS Research Center) at a working neutron wavelength of $\lambda = 4.43$ Å with $\Delta\lambda/\lambda = 1 \times 10^{-5}$ [18]. This instrument was equipped with a double monochromator unit based on perfect silicon crystals cut along the (1, 1, 1) plane. The first crystal was used to form the neutron beam and the second crystal performed the monochromator function. The angular distribution of neutrons in the beam past the sample (situated behind the double monochromator) was measured by rotating an analyzer crystal (identical to the monochromator crystal) at a minimum angular step of 2×10^{-7} deg. The FWHM of the instrument line was $w_0 = 2.6 \times 10^{-5}$ Å^{-1}. The momentum transfer was varied within $1.5 \times 10^{-6} < q < 5 \times 10^{-3}$ Å^{-1}.

Figures 1–3 show the pattern of typical changes in the shape of the neutron beam, $I_s(q)/I(0)$, and in the attenuation I/I_0 (where $I_0 = I(L = 0)$), measured by the central detector as $I(q = 0)$ as a function of the sample thickness.

The experimental beam attenuation profiles (Fig. 3) are normalized to the integral attenuation cased by neutron absorption in the samples.

4. RESULTS AND DISCUSSION

4.1 MSANS

4.1.1. Beam shape. It was found that the shape of the neutron beam upon scattering can be represented as a sum of two components: Gaussian, describing the beam width upon scattering, and Lorentzian of nth power ($n = f(\Delta)$), describing the dependence of the scattering intensity $I_s(q, L)$ on q at large momenta:

$$I(q) = A\exp\left[-\frac{(q - q_{01})^2}{2s^2}\right] + B\frac{sr^{2n}}{[(q - q_{02})^2 + sr^2]^n} + C, \quad (10)$$

where A, B, C, s, and n are free parameters and q_{01} and q_{02} are the centering parameters. The quantity $sr^2 = \delta q_v^2 + s_1^2$ is a sum of dispersions determining the momentum uncertainty in the beam (s_1 is the s value determined by fitting the experimental data to formula (10) for $sr^2 = \delta q_v^2$). The uncertainty δq_h related to the horizontal resolution (which is almost ten times as small as the verti-

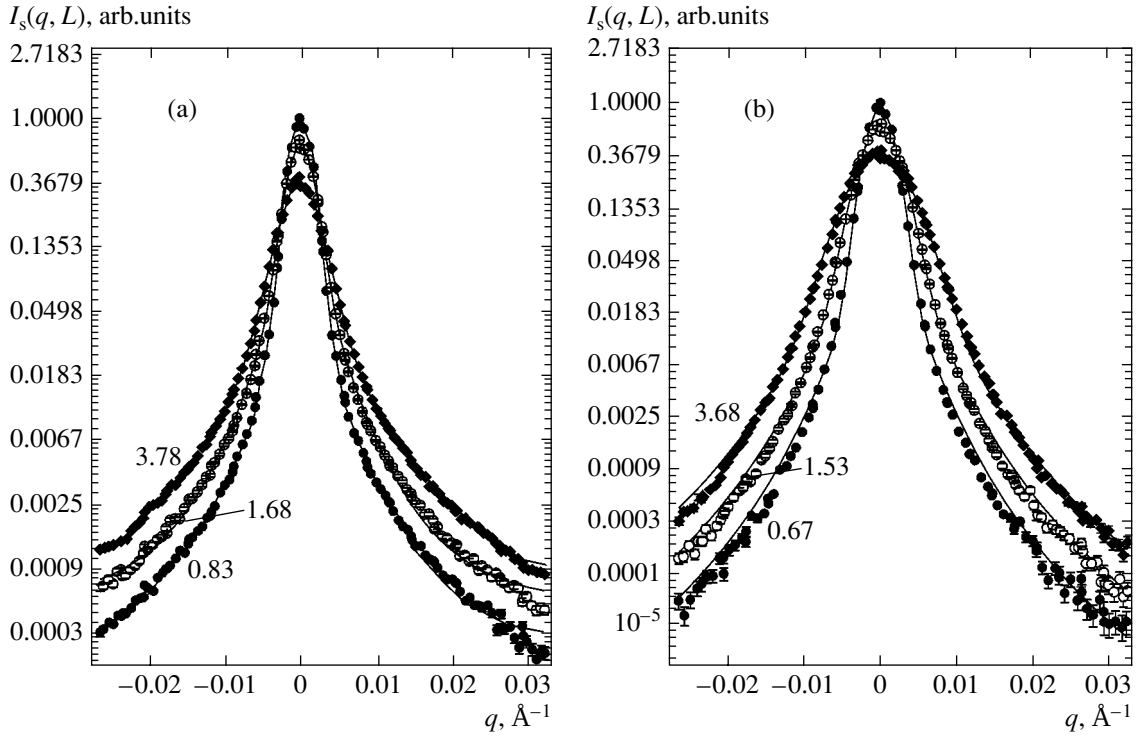

Fig. 2. Variation of the neutron beam shape for (a) carbon black and (b) $CaCO_3$ samples of different thickness L (indicated in millimeters at the curves). Points present the experimental data; solid curves show the results of calculations using formula (10).

cal resolution) is reflected predominantly by the s value, since

$$s^2 = \Delta w^2(L) + s_0^2, \tag{11}$$

where $\Delta w(L)$ is the beam broadening in a sample of thickness L and s_0 is the beam dispersion in the absence of the sample. In the course of fitting by least squares to formula (10), it was established that the dispersion s varies rather slightly and falls almost within the experimental error limits, irrespective of the fact whether this value is taken into account or not in the sr product (i.e., $s \approx s_1$). However, only allowance for the s value in the sr product provides a satisfactory description of scattering in the region of "tails". Substitution of a preset value of s_1 instead of the free parameter s into the sr product significantly simplifies the fitting procedure. Depending on the sample thickness, the sr product values fall within $sr = (5–6.5) \times 10^{-3}$ Å^{-1} (YBCO), $(5–8) \times 10^{-3}$ Å^{-1} ($CaCO_3$), $(5–8.5) \times 10^{-3}$ Å^{-1} (Al_2O_3), and $(5–7) \times 10^{-3}$ Å^{-1} (carbon black). The fitting by least squares gives the following values of exponent in formula (10): $n = 2$ ($CaCO_3$, Al_2O_3, YBCO) and $n = 1.3$ (carbon black). The dependences calculated using formula (10) with the parameters found through fitting by least squares are depicted by solid curves in Figs. 1 and 2.

4.1.2. Scattering intensity $I_s(q)$. Figure 4 shows the plots of $I_s(q)$ versus momentum q at $q > sr$ for $CaCO_3$ and carbon black (analogous curves were also obtained for Al_2O_3 and YBCO). It was found that these dependences could be satisfactorily described using the formula

$$I_s(q) = A_1/q^{\Delta}, \tag{12}$$

where $\Delta = 4 \pm 0.1$ (for $CaCO_3$, Al_2O_3, YBCO) or 2.6 ± 0.1 (for carbon black) and the parameter A_1 is virtually a linear function of L. The scattering data were processed by least squares (with corrections for the slit geometry) and analyzed in the range of momentum transfer 0.007 Å$^{-1} \le q \le 0.03$ Å^{-1}. A correction for the slit geometry is essential for $q < 10^{-2}$ Å^{-1}, where the experimental data (representing a convolution of the scattering intensity $I_s(q) \propto q^{-\Delta}$ with the instrument resolution function) deviate from the $q^{-\Delta}$ law (these deviations are not distinguished in Fig. 4). The power dependence of the scattering intensity on the momentum $I_s(q, L) \propto q^{-2.6}$, which is observed for carbon black, is similar to that for scattering on a volume fractal with the dimension $D_v = 2.6 \pm 0.1$.

4.1.3. Beam attenuation. For small sample thicknesses ($L < l$), the attenuation of the central beam as a function of L for all samples (Fig. 3) could be satisfactorily described using the formula

$$\frac{I(q = 0)}{I_0} = \exp\left(-\frac{L}{l_{\exp}}\right), \tag{13}$$

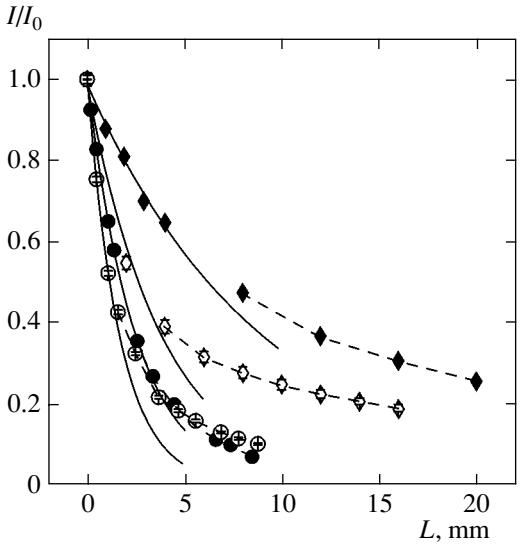

Fig. 3. Attenuation of the beam intensity measured using the central detector for neutrons scattered with a momentum transfer $q > q_{min}$ (q_{min} is determined by the instrument resolution) as a function of the sample thickness L: (●) carbon black; (○) $CACO_3$; (♦) YBCO; (◊) Al_2O_3. Solid curves show the results of fitting to the $\exp(-L/l_{exp})$ law; dashed curves show the results of calculations using formula (14).

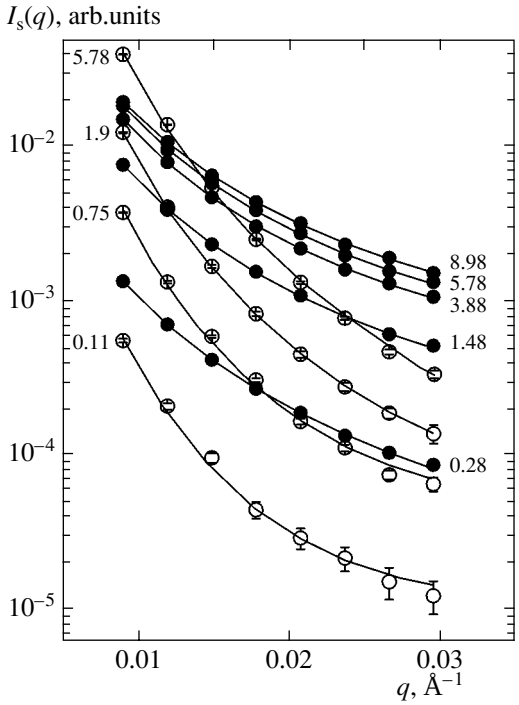

Fig. 4. Plots of the neutron scattering intensity $I_s(q)$ versus momentum transfer q ($q > sr$) for (●) $CaCO_3$ and (○) carbon black samples of various thicknesses L (indicated in millimeters at the curves). Solid and dashed curves show the results of fitting to the $I_s \propto q^{-\Delta}$ law. For all sample thicknesses, $\Delta = 4 \pm 0.6$ ($CaCO_3$) and 2.6 ± 0.01 (carbon black).

which was used for determining the neutron mean free path l_{exp}. The results of l_{exp} determination by this method are presented in Table 1. The calculated curves of I/I_0 versus L for the parameters determined by least squares are depicted by solid lines in Fig. 3.

As can be seen from Fig. 3, an increase in the sample thickness is accompanied by deviation of the experimental data from the exponential dependence, which is related to the multiple scattering. It was found that experimental data on the beam attenuation with increasing sample thickness for nonfractal objects are well described with allowance for multiple scattering in terms of expression (2) within the limits of the vertical and horizontal resolution of the central detector. The 2D convolution of the diffusion formula (2) at $q = 0$ with the instrument resolution functions in the two directions described by Gaussians with dispersions δq_h and δq_v, which was used for processing the data on the beam attenuation for $L > 0.5 l_{exp}$, is as follows:

$$\frac{I}{I_0} = \frac{2D\delta q_x \delta q_y}{\{[(2\delta q_x)^2 + FL][(2\delta q_y)^2 + FL]\}^{\mu}}, \qquad (14)$$

where D and F are free parameters and $\mu = 1/2$.

Table 1. The main parameters of samples determined from an analysis of the MSANS data (see the text for explanations)

Sample	l_{exp}, mm	Δ	μ	D	R, Å
Nonfractal					
Al_2O_3	3.9 ± 0.6	4 ± 0.6	0.5	3	203 ± 11
YBCO	9.4 ± 0.3	4 ± 0.6	0.5	3	171 ± 16
$CaCO_3$	1.7 ± 0.1	4 ± 0.1	0.5	3	216 ± 6
Fractal					
C (carbon black)	2.5 ± 0.1	2.6 ± 0.1	0.8 ± 0.1	$D_v = 2.6 \pm 0.1$*	
				$D_s = 2.75 \pm 0.15$**	351 ± 12

*From large-q asymptotics.

**From data on the neutron beam broadening and attenuation.

The results of least squares fitting to formula (14) for $CaCO_3$, Al_2O_3, and YBCO are depicted by dashed lines in Fig. 3. Expression (14) shows that, in the limit of $\delta q_x, \delta q_y \longrightarrow 0$, the attenuation asymptotically tends to $I/I_0 \propto 1/L$ in agreement with the theory [3]. The quantity F in formula (14) was treated as a free parameter, but, if the deviation of the beam attenuation from exponent is completely described by the diffusion formula (2) within the aperture of the central detector, we must have $FL = 2q_L^2$. Calculations showed that this relation is valid to within 3%, provided that the beam attenuation is measured in an optimized geometry ($\delta q_v = 1.8 \times 10^{-3}$ Å^{-1}), where q_L are taken from an analysis of data on the beam broadening (Fig. 5).

We have also used formula (14) in the analysis of data on the beam attenuation at $L > 0.5 l_{exp}$ for carbon black, but the exponent μ was treated as a free parameter. Then, the fitting by least squares gave $\mu = 0.8 \pm 0.1$. In the limit of $\delta q_x, \delta q_y \longrightarrow 0$, this yields the asymptotic behavior $I/I_0 \propto 1/L^{2\mu}$ with $2\mu = 1.6$. According to the theory [3], this behavior corresponds to the neutron beam attenuation upon multiple scattering on the surface fractal with the dimension $D_s = 4 - 1/\mu = 2.75$.

4.1.4. Beam broadening. Figure 5 presents our experimental data on the beam broadening as a function of the sample thickness, which was determined from relation (11) as

$$\Delta w^2 = s^2 - s_0^2. \quad (15)$$

As will be shown below, the characteristic scale of inhomogeneities determined in our experiments is on the order of several hundred ångströms. For this reason, the experimental data can be described in the diffraction approximation. Estimates show that the characteristic size R_0 (corresponding to $\alpha \approx 1$) at which the refraction regime also becomes significant is $R_0 \approx 2 \times 10^{-3}$ mm. The corresponding characteristic momentum according to Eq. (8) is $q_1 < 2 \times 10^{-4}$ Å^{-1}. Thus, the refraction scattering component corresponds to the range of momenta below the limiting resolution of the instrument and, hence, this component can be ignored in comparison to diffraction in the analysis of scattering. Analogous estimates were previously reported in [11] for SANS in YBCO ceramics.

As can be seen from Fig. 5, the beam broadening defined as $\Delta w = q_L$ (see Eqs. (1)–(3)) is satisfactorily

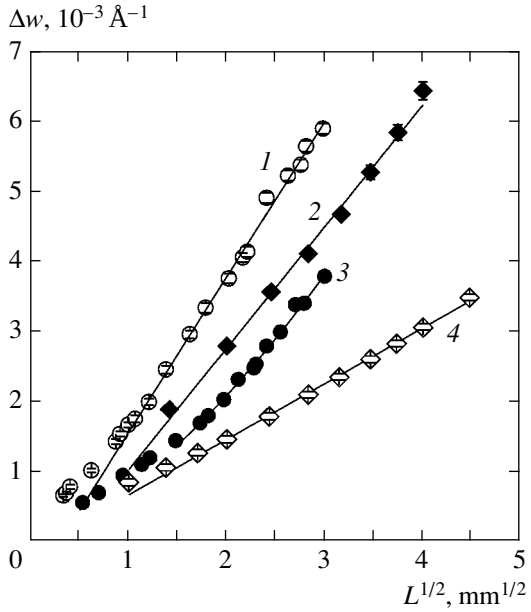

Fig. 5. Plots of the beam broadening $\Delta w = \sqrt{w^2 - w_0^2}$ versus sample thickness L for (*1*) $CACO_3$; (*2*) YBCO; (*3*) carbon black, and (*4*) Al_2O_3. Points present the experimental data; solid curves show the results of calculations using the formula $\Delta w = a + bL^{\mu}$.

described by the formula

$$\Delta w = a + bL^{\mu} \quad (16)$$

with a nonzero "cutoff" on the abscissa axis for $L \longrightarrow 0$. This relation was considered in much detail in [6–8]. An analysis of the data on $\Delta w(L)$ gave the following values of the exponent: $\mu = 0.5$ (for $CaCO_3$, Al_2O_3, YBCO) or ~0.8 (for carbon black), which is fully consistent with the values obtained above from the analysis of the central beam attenuation I/I_0 as a function of the sample thickness L.

Within the framework of the diffraction approximation, the characteristic size R of inhomogeneities making the main contribution to the scattering detected within the limits of resolution of a given instrument can be determined using formula (1) with the aforementioned parameters l_{exp} and q_L. These estimates of R in all samples under consideration for $L \geq l_{exp}$ are presented in Table 1 and plotted in Fig. 6, where solid and dashed curves show the data calculated using formula (16).

The scattering from inhomogeneities on this scale must lead to deviations from power dependences of the scattering intensity (Fig. 4) for $sr < q \leq 1/2R$. However,

Table 2. Fractal dimensions determined by analysis of the SANS data for carbon black

Interval of q, Å^{-1}	0.048–0.15	0.013–0.064	0.007–0.022	0.003–0.009
Fractal dimension D	2.54 ± 0.1	2.75 ± 0.05	2.56 ± 0.08	2.62 ± 0.02

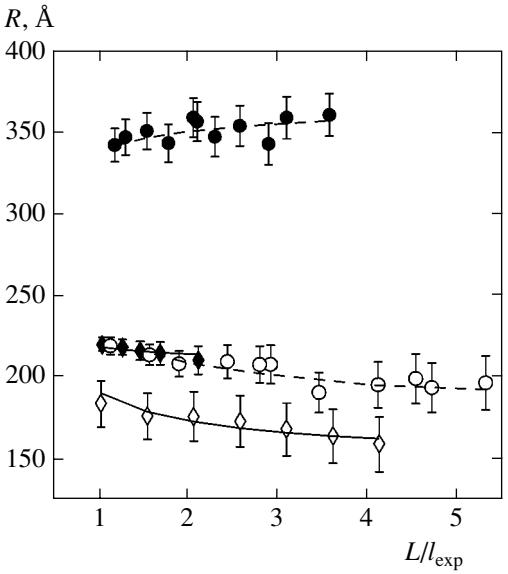

Fig. 6. Plots of the characteristic scale R of the scattering system versus L/l for (●) carbon black, (○) $CACO_3$; (♦) YBCO; and (◊) Al_2O_3. Points present the results of calculations using formula (5); solid and dashed curves show the results of fitting using formula (16).

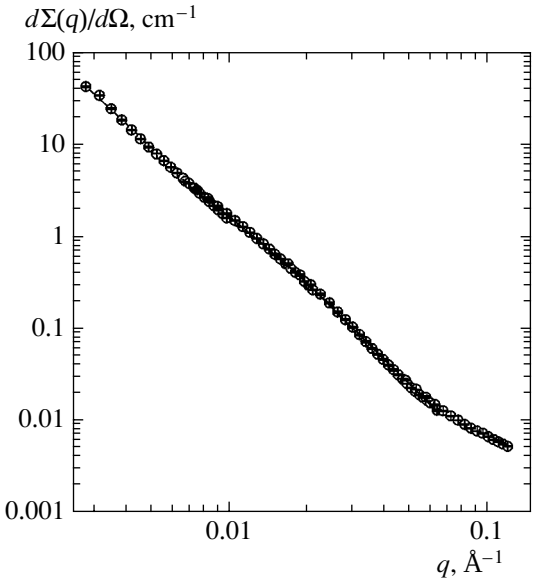

Fig. 7. A plot of the differential cross section of neutron scattering $d\Sigma(q)/d\Omega$ versus momentum transfer for a sample of carbon black with $L = 1.5$ mm. Points present the results of SANS measurements; solid curve shows the results of calculations using expression (17).

this condition was not met in our experiments, where the minimum sr value was $sr_{min} \approx 3 \times 10^{-3}$ Å^{-1}. In order to observe deviations from the power dependence of the scattering intensity at low q, the experiments have to be performed using thin samples and an experimental setup with sufficient resolution for a momentum transfer of $q < 10^{-3}$ Å^{-1}.

4.2. SANS and USANS

As can be seen from the MSANS data in Table 1, which were obtained using measurements of the neutron beam broadening and attenuation as dependent on the sample thickness L ($q \le q_L$), carbon black is a surface fractal with $D_s = 2.75 \pm 0.15$. At the same time, the exponent Δ determined from an analysis of the scattering intensity I_s as a function of the momentum q in the asymptotic limit for $q \gg q_L > 7 \times 10^{-3}$ Å^{-1} is 2.6 ± 0.1, which corresponds to the scattering on a volume fractal with $D_v = 2.6 \pm 0.1$. These results can be explained by assuming that (i) the samples of carbon black under study contain two (surface and volume) fractals and (ii) the main contributions of these fractals to the scattering intensity $I_s(q)$ are observed in different ranges of q. This implies that $I_s(q)$ plotted on the logarithmic scale must exhibit a bending point, which corresponds to the passage from one type of scattering to another. In order to check for this assumption, it was necessary to obtain independent estimates of the fractal dimension of carbon black. Such estimates can be obtained by measuring the neutron scattering intensity distribution $I_s(q)$ using the SANS and USANS techniques in a single scattering regime in the most broad range of the momentum transfer q.

Figure 7 shows a plot of the differential cross section of neutron scattering $d\Sigma(q)/d\Omega$ measured for a sample of carbon black with $L = 1.5$ mm using the SANS-1 setup in the momentum range 0.003 Å$^{-1} \le q \le 0.15$ Å^{-1}. The data were analyzed in terms of the formula

$$\frac{d\Sigma}{d\Omega}(q) = \frac{A^2}{q^D} + I_{inc}, \qquad (17)$$

where A_2 is a free parameter and I_{inc} is a constant quantity, which is independent of q and related to the scattering from inhomogeneities on the order of the wavelength λ (in this case, from one to several tens of ångströms). The final results were obtained by calculating a convolution of expression (17) with the instrument resolution function. The experimental curves of the differential cross section $d\Sigma(q)/d\Omega$ were processed by least squares for each of the four intervals of variation of the q value. The results of this analysis are summarized in Table 2.

As can be seen from the data in Table 2, the fractal dimensions fall within 2.54–2.75 depending on the interval of q values used for the analysis. At the same time, the fractal dimension ($D \approx 2.65$) obtained by averaging over all the q intervals under consideration is close to the estimate $D_v = 2.6 \pm 0.1$ obtained for the same sample of carbon black in our MSANS experiments.

Figure 8 shows the results of USANS measurements for the carbon black samples with $L = 0.2$ and 1.5 mm

measured using a double crystal diffractometer [18]. The attenuation of the neutron beam transmitted through the sample was very large: $1 - I(q = 0)/I_0 \approx 0.84$ and 0.97 for 0.2- and 1.5-mm-thick samples, respectively. This implies that the experimental data should be interpreted in terms of the MSANS theory [3]. In the standard analysis of USANS spectra for $L > l$, parameters characterizing the scattering system are usually determined from the $\Delta w(L)$ function [7, 8]. In the case under consideration, we are interested in determining the asymptotic behavior of $I(q)$ at large q. As was pointed out above (and demonstrated previously [3, 6, 9, 18]), the character of this behavior is similar to that in the case of single scattering.

We have analyzed the scattering intensity $I(q)$ at large q using a procedure described in [19]. According to this, the experimental data are approximated using a function of the type

$$I(q) = \frac{A_3}{q^2} + \frac{A_4}{q^\delta}, \qquad (18)$$

where the first term describes the scattering intensity variation on the wings of the instrument function and the second term reflects the asymptotic behavior of the scattering at large q in the sample studied. The values of the exponent δ determined by least squares fitting to formula (18) for $L = 0.2$ and 1.5 mm were $\delta = 2.35 \pm 0.03$ and 2.8 ± 0.03, respectively. According to [19], an increase in δ with the sample thickness is related to the pre-asymptotic terms of the expansion of $I(q)$ at large q. The $I(q)$ values calculated using formula (18) with the parameters determined by least squares are depicted by solid curves in Fig. 8.

For the correct comparison of USANS data to the results obtained in the conventional SANS experiments, it is necessary to take into account that the exponent in the dependence of the scattering intensity on the momentum transfer measured using the double-crystal technique is increased by unity [19]. Therefore, the asymptotic behavior of the scattering intensity $I(q)$ for carbon black in the interval 3×10^{-4} Å$^{-1} \le q \le 3 \times 10^{-3}$ Å^{-1} is satisfactorily described by the relation $I(q) \propto q^{-\Delta}$, where $\Delta = \delta + 1 = 3.35$–$3.38$, which is equivalent to the scattering on a surface fractal with the dimension $D_s = 6 - \Delta = 2.62$–2.65. This value is very close to the estimate ($D_s = 2.75 \pm 0.15$) obtained in our MSANS experiments.

Thus, we have measured the small-angle neutron scattering intensity $I_s(q)$ for carbon black in the range of momentum transfer 0.0003 Å$^{-1} \le q \le 0.15$ Å^{-1} using the SANS and USANS techniques. The obtained data unambiguously indicate that there are two intervals of q in which the scattering intensity $I_s(q)$ obeys the law $I_s(q) \propto q^{-\Delta}$ with different values of the exponent Δ. In the interval of $q \le q_c$ (where $q_c \approx 0.003$ Å^{-1} is the point of bending on the $I_s(q)$ curve), the exponent is close to 3.35, whereas at $q \ge q_c$, we have $\Delta \approx 2.65$. This asymptotic behavior of $I_s(q)$ shows the presence of two correlators, which characterize the system under consideration and predominate in the corresponding interval of q. The first correlator corresponds to a surface fractal with the dimension $D_s = 2.65$, while the second correlator corresponds to a volume fractal with the same dimension $D_v \approx 2.65$.

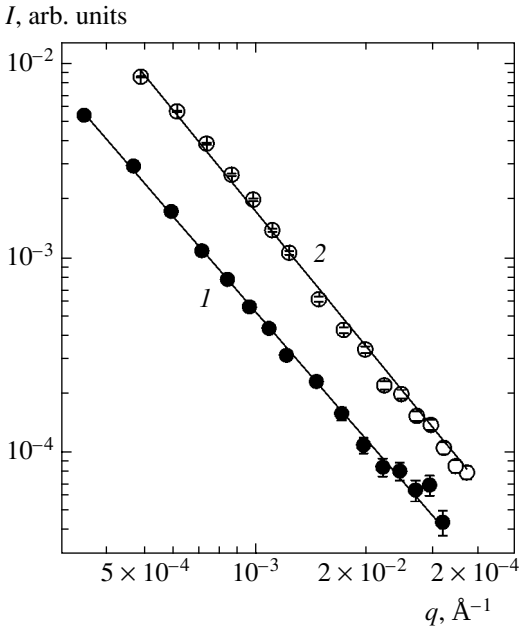

Fig. 8. Plots of the neutron scattering intensity versus momentum transfer for carbon black samples with L = 0.2 (*1*) and 1.5 mm (*2*). Points present the results of USANS measurements; solid curves show the results of calculations using expression (18) for $q \gg q_L$.

5. CONCLUSIONS

(i) We have experimentally demonstrated the possibility of using MSANS method [3, 6, 10] for evaluating the structural parameters (the characteristic scale R and the mean free path l) of a scattering system using the standard instruments where these values cannot be determined in the standard SANS regime.

(ii) A new method has been proposed for estimating the fractal system dimension using data on the attenuation and broadening of the transmitted neutron beam in the MSANS regime.

(iii) A comparison of the MSANS data to the values obtained by the classical SANS and USANS methods in the regime of single scattering showed a good coincidence of the results. In particular, a volume fractal with the dimension $D_v = 2.6 \pm 0.15$ in the asymptotic limit of large q and a surface fractal for carbon black with the dimension $D_v = 2.7 \pm 0.15$ for $q \le q_L$ were observed both in our MSANS experiments and in the SANS and USANS measurements.

ACKNOWLEDGMENTS

The authors are grateful to A.I. Okorokov for his constant attention and support; to S.V. Maleyev, B.P. Toperverg and D. N. Aristov for fruitful discussions and help in interpreting the results, to M.K. Runova for assistance in data processing; to S.A. Klimko for his help in experiments; and to A.I. Sibilev for his help in sample preparation.

This study was supported in part by the Russian Foundation for Basic Research (project no. 04-02-16342), the Federal Program "Investigations of the Basic Properties of Highly Correlated Systems by Neutron Scattering in Constant-Flux Reactors" (project no. 40.012.1.1.1149), and the Presidential Program of Support for Leading Scientific Schools in Russia (project no. NSh-1671-2003.2).

REFERENCES

1. J. K. Kjems, T. Freltoft, D. Richter, and S. K. Sinha, Physica B (Amsterdam) **136**, 285 (1986).
2. S. K. Sinha, Physica D (Amsterdam) **38**, 310 (1989).
3. S. V. Maleyev, Phys. Rev. B **52**, 13163 (1995).
4. A. Guinier and G. Fournet, *Small-angle Scattering of X-rays* (Wiley, New York, 1955).
5. R. J. Weiss, Phys. Rev. **83**, 379 (1951).
6. S. V. Maleev and B. P. Toperverg, Zh. Éksp. Teor. Fiz. **78**, 315 (1980) [Sov. Phys. JETP **51**, 158 (1980)].
7. S. Sh. Shil'shteĭn, V. A. Somenkov, M. Kalanov, and N. O. Elyutin, Fiz. Tverd. Tela (Leningrad) **18**, 3231 (1976) [Sov. Phys. Solid State **18**, 1886 (1976)].
8. Yu. G. Abov, Yu. I. Smirnov, D. S. Denisov, *et al.*, Fiz. Tverd. Tela (St. Petersburg) **34**, 1408 (1992) [Sov. Phys. Solid State **34**, 748 (1992)].
9. R. Gahler, J. Felber, F. Mezei, and R. Golub, Phys. Rev. A **58**, 280 (1998).
10. S. V. Maleyev, R. V. Pomoptsev, and Yu. N. Skryabin, Phys. Rev. B **50**, 7133 (1994).
11. A. I. Okorokov, V. V. Runov, A. D. Tret'yakov, *et al.*, Zh. Éksp. Teor. Fiz. **100**, 257 (1991) [Sov. Phys. JETP **73**, 143 (1991)].
12. J.-P. Bouchaud and A. Georges, Phys. Rep. **195**, 127 (1990).
13. S. V. Grigoriev, V. V. Runov, A. I. Okorokov, *et al.*, Nucl. Instrum. Methods Phys. Res. A **389**, 441 (1997); Preprint No. 2028, PIYaF RAN (Inst. of Nuclear Physics, Russian Academy of Sciences, Gatchina, 1995).
14. W. Schmatz, T. Springer, J. Schelten, and K. Ibel, J. Appl. Crystallogr. **7**, 96 (1974).
15. H. B. Shuhrmann, N. Burkhardt, G. Dietrich, *et al.*, Nucl. Instrum. Methods Phys. Res. A **356**, 133 (1995).
16. J. S. Pedersen, D. Posselt, and K. Mortensen, J. Appl. Crystallogr. **23**, 321 (1990).
17. G. D. Wignall and F. S. Bates, J. Appl. Crystallogr. **20**, 28 (1986).
18. D. Bellmann, M. Klatt, R. Kampmann, and R. Wagner, Physica B (Amsterdam) **241–243**, 71 (1998).
19. Yu. G. Abov, D. S. Denisov, F. S. Dzheparov, *et al.*, Zh. Éksp. Teor. Fiz. **114**, 2194 (1998) [JETP **87**, 1195 (1998)].

Translated by P. Pozdeev

Journal of Experimental and Theoretical Physics, Vol. 101, No. 3, 2005, pp. 437–451.
Translated from Zhurnal Éksperimental'noĭ i Teoreticheskoĭ Fiziki, Vol. 128, No. 3, 2005, pp. 508–524.

ORDER, DISORDER, AND PHASE TRANSITIONS IN CONDENSED SYSTEMS

New Types of Spatial Structures in Multisublattice Antiferromagnets

A. B. Borisov

Institute of Metal Physics, Ural Division, Russian Academy of Sciences, ul. S. Kovalevskoĭ 18, Yekaterinburg, 620219 Russia

e-mail: borisov@imp.uran.ru

Received February 10, 2005

Abstract—A broad class of three-dimensional space structures in multisublattice antiferromagnets was found in the isotropic approximation (the principal chiral field model on the SU(2) group). According to the Andreev–Marchenko theory, this approximation is applicable to spin glasses and provides qualitative understanding of structures in real multisublattice antiferromagnets. Special substitutions were used to reduce the equations of the model to new equations with simple geometric interpretation. A differential geometry method was applied to obtain various structure types (some of which were determined by arbitrary functions), including localized and nonlocalized textures, structures with the degree of mapping equal to one, antiferromagnetic "targets" and three-dimensional sources, and two- and three-dimensional vortex and spiral structures. Possibilities for experimentally checking the presence of localized, vortex, and spiral structures in antiferromagnets were demonstrated. © *2005 Pleiades Publishing, Inc.*

1. INTRODUCTION

In the usual phenomenological theory, complex magnetic structures are treated as sets of magnetic sublattices inserted into one other. According to a continual description, each magnetic sublattice is characterized by the mean magnetic moment density $\mathbf{M}_j$, where j is the number of the sublattice. This is not an effective approach to analyzing dynamics and magnetic spatial structures in the long-wave approximation. When the major role in a magnetic system is played by exchange interactions, we can obviate the necessity of using a large number of magnetic sublattices and find simpler and more effective dynamical equations [1–4]. The appearance of magnetically ordered states is always accompanied by spontaneous distortions of exchange interaction symmetry. Indeed, the Hamiltonian of exchange interactions is invariant with respect to arbitrary rotations of all spins through equal angles, but no magnetic structure is invariant with respect to all such rotations, because there are macroparameters (macroscopic multipole moments) that are not invariant with respect to rotations of all spins through equal angles. Local spin rotations that depend on the coordinates and time and change the equilibrium macroparameter values are elementary magnetic excitations of systems. Because of the short-range character of exchange forces, the energy of these elementary excitations (magnons) vanishes as the momentum tends to zero. Suppose that the ground state of a magnet is only invariant with respect to the SO(3) group identity transformation. According to the Andreev–Marchenko [1–3] and Volkov–Zheltukhin [4] theories, the most general equation for the long-wave phenomenological potential energy U density (in crystals without an inversion center at zero spontaneous magnetization) invariant with respect to the SO(3) group of spin rotations then has the form

$$U = \frac{1}{2}(c_{ik,lm}\omega_{i,l}\omega_{k,m}). \quad (1)$$

Here, $\omega_{i,l}$ are invariant with respect to spin rotations (generated by right shifts under the SU(2) group) and relate rotations of the spin rotation matrix ($G \in \mathrm{SU}(2)$), whose parameters depend on the coordinates, at the points x_i and $x_i + dx_i$ as follows:

$$\frac{\partial G}{\partial x_k} = i\sigma_p\omega_{p,k}G. \quad (2)$$

Finding two- and three-dimensional structures with an arbitrary invariant $c_{ik,lm}$ tensor, whose components play the role of elasticity moduli, is a difficult task that has not been solved completely. In this work, we find new types of spatial textures in multisublattice antiferromagnets in the isotropic approximation on the assumption that

$$c_{ik,lm} \propto \delta_{ik}\delta_{lm}. \quad (3)$$

Although this approximation is strictly applicable to spin glass only [2, 3], it allows the problem to be simplified and provides qualitative understanding of structures in real multisublattice antiferromagnets. A similar approximation is used in the continual theory of nematics (one-constant approximation) and elasticity theory when anisotropic crystals are approximated by isotropic media. Further, equivalent forms of the equations

that follow from (1) and (3) can conveniently be used. It immediately follows from (1), (2), and (3) that, to within scale transformations, U can be written as

$$\frac{1}{2}\mathrm{Sp}\left(\frac{\partial G^{-1}}{\partial x_i}\frac{\partial G}{\partial x^i}\right).$$

This equation describes the nonlinear model of the principal chiral field on the SU(2) group. Substituting the decomposition of the G matrix in terms of the Pauli matrices σ_j ($j = 1, 2, 3$) and unit matrix σ_0,

$$G = in_j\sigma_j + n_0\sigma_0, \tag{4}$$

into this equation yields the stationary n-field model ($n \in S^3$), $n_\mu = (n_0, \mathbf{n})$ with the constraint $\mathbf{n}^2 + n_0^2 = 1$, in the form

$$U = \frac{1}{2}\left(\frac{\partial \mathbf{n}}{\partial x_i}\frac{\partial \mathbf{n}}{\partial x_i} + \frac{\partial n_0}{\partial x_i}\frac{\partial n_0}{\partial x_i}\right). \tag{5}$$

Model (5) is universal and has many physical applications in field theory and physics of condensed media. It describes the low-energy dynamics of π-mesons [5] (field n is proportional to the triplet of pions) and pion condensate in the stationary case. Model (5) is conformally invariant [6] and integrable [7, 8] by the method of the inverse scattering problem in spaces (2, 0) and (1, 1). In the three-dimensional space, the appearance of spatial structures is strongly impeded because the equations with the field triplet are nonlinear. In this work, we find a broad class of solutions to model (1), (3) with the use of special substitutions, which reveal a strong relation between this model and classic differential geometry problems.

The paper is organized as follows. In Section 2, we use three substitutions that, although they do not completely cover the diversity of all solutions to (1), (3), increase the number of equations and reduce system (1), (3) to new systems with simple geometric interpretation. The first such system is a trigonal system for harmonic coordinates. It is solved in Section 3 by the differential geometry integration method. First, we perform the hodograph transformation, that is, change the roles played by dependent and independent variables. However, further, as distinct from the standard hodograph transformation, we do not replace field derivatives but define them as new variables related to the metric tensor components induced by such a transformation. The equation to be solved is then rewritten in terms of metric tensor components. Since the independent variables were originally Euclidean, the curvature tensor is zero in terms of the metric introduced. As a result, we obtain a self-consistent system of equations for the metric tensor components. The zero-curvature equation then proves to be the principal equation, and the sought system of equations, its reduction. Solving this system allows classic geometrical equations to be used to find a solution to the sought differential equation in the form of implicit functions. We show that, in spite of its somewhat limited character, this differential geometry approach based on embedding a nonlinear partial-derivative equation into a certain differential relation in the Euclidean space gives a broad class of spatial structures that are very difficult to obtain by other methods. As a result, we obtain seven spatial textures, including vortices, solitons, spatial sources, nonlocalized structures, and structures with the degree of mapping equal to one, which are similar in certain their properties to topological solitons. Many of these solutions are determined by arbitrary functions. In Section 3, we obtain structures related to the second and third substitutions. For the second substitution, the field θ locally depends on the auxiliary field a, $\theta = \theta(a)$. The fields a, b, and c are harmonic functions with gradients related in a certain way. Differential geometry is applied to find four spatial structures, including antiferromagnetic "targets" and spiral vortices, and their dipole configurations. Lastly, at the end of Section 3, we discuss spatial spiral structures related to the substitution that allows the solution to model (5) to be reduced to the R^3 solution to the same model, where the G matrix depends on two harmonic fields with constraints on their gradients. In the Conclusions, we discuss possibilities for experimentally observing the structures found in this work in antiferromagnets.

2. SUBSTITUTIONS AND THE DIFFERENTIAL GEOMETRY INTEGRATION METHOD

In this section, we suggest new substitution types that transform the equations of model (1), (3) into simpler equations and lead to new differential geometry problems in the stationary case. In the Euler parameterization of the G matrix, we have

$$G = \begin{pmatrix} \exp\left(\frac{(b+c)i}{2}\right)\cos\frac{\theta}{2} & \exp\left(-\frac{(-b+c)i}{2}\right)i\sin\frac{\theta}{2} \\ \exp\left(\frac{(-b+c)i}{2}\right)i\sin\frac{\theta}{2} & \exp\left(-\frac{(b+c)i}{2}\right)\cos\frac{\theta}{2} \end{pmatrix}, \tag{6}$$

with the angles θ ($0 \le \theta \le \pi$), b ($0 \le b \le 2\pi$), and c ($0 \le c \le 2\pi$) we obtain the equations

$$\begin{aligned} \Delta b + \cos\theta\Delta c - \sin\theta\nabla c\nabla\theta &= 0, \\ \Delta c + \cos\theta\Delta b - \sin\theta\nabla b\nabla\theta &= 0, \\ \Delta\theta + \sin\theta\nabla b\nabla c &= 0. \end{aligned} \tag{7}$$

Broad classes of solutions to model (7) can be found using the following substitutions:

(1) Equations (7) are satisfied if the fields (θ, b, c) obey the simple and compact system of equations

$$\Delta b = \Delta c = \Delta\theta = 0, \tag{8}$$

$$\nabla c\nabla\theta = \nabla b\nabla\theta = \nabla b\nabla c = 0, \tag{9}$$

which is invariant with respect to permutations of θ, b, c and the coordinates x, y, and z. The vector fields ∇c, ∇b, and $\nabla\theta$ are the normals to the surfaces b = const, c = const, and θ = const, which intersect each other at right angles. Geometrically, solving (8), (9) determines triorthogonal harmonic coordinate surfaces. Starting with fundamental monograph [9], the triorthogonal coordinate system has been discussed in many monographs on differential geometry. The problem of constructing all triorthogonal coordinate systems has a long history and has recently been solved by Zakharov [10] in terms of the inverse scattering problem. Harmonicity condition (8) is a nontrivial reduction of the Lame equations and the corresponding U–V pair.

(2) To perform the next substitution, we assume the θ field to be locally dependent on an auxiliary field $a(\mathbf{r})$, $\theta = \theta(a)$. Direct calculations then easily show that Eqs. (7) follow from the equations

$$\theta_{,aa} = \sin\theta(a), \tag{10}$$

$$\Delta b = \Delta a = \Delta c = 0, \tag{11}$$

$$\nabla c\nabla a = 0, \quad \nabla b\nabla a = 0, \quad (\nabla a)^2 = \nabla b\nabla c \tag{12}$$

for the fields $\theta(a)$, a, b, and c.

(3) Lastly, we use the ansatz generalization suggested in [11, 12] for the **n**-field model ($n \in S^2$). In the stationary case, the equations that follow from (5) have the simple form

$$\Delta n_\mu = 0 \quad (\mu = 0, 1, 2, 3). \tag{13}$$

Let the fields n_μ locally depend on auxiliary fields $\alpha(\mathbf{r})$ and $\beta(\mathbf{r})$, that is, $\alpha(\mathbf{r})$, $\beta(\mathbf{r})$: $n_\mu = n_\mu(\alpha, \beta)$. It is easy to see that the $n_\mu(\alpha, \beta)$ field also satisfies the n-field equation in the two-dimensional space (α, β),

$$n_{\mu,\alpha\alpha} + n_{\mu,\beta\beta} = 0, \tag{14}$$

if the fields (α, β) obey the equations

$$\Delta\beta = \Delta\alpha = 0, \tag{15}$$

$$\nabla\beta\nabla\alpha = 0, \quad (\nabla\alpha)^2 = (\nabla\beta)^2. \tag{16}$$

Equations (15), (16) are a direct generalization of the analyticity condition to the three-dimensional case, because they are equivalent to the analyticity condition for the $\alpha + i\beta$ function with respect to the $x + iy$ variable at $D = 2$. Geometrically, solving these equations determines two orthogonal harmonic coordinate surfaces with equal normal lengths. Systems of type (8), (9) were discussed in [13] for the introduction of conjugate harmonic functions in the three-dimensional space.

To summarize, the suggested substitutions lead to new differential geometry problems, those of the introduction of new coordinate systems that satisfy conditions (8), (9), (11), (12), (15), and (16). Although a general solution to (8), (11), and (15) is easy to write, the inclusion of conditions (9), (12), and (16) then encounters difficulties that can be removed by using the differential geometry integration method [11, 12], which reduces the problems to equations with smaller numbers of new independent variables.

3. SPATIAL STRUCTURES RELATED TO THE TRIORTHOGONAL COORDINATE SYSTEM AND THE DIFFERENTIAL GEOMETRY INTEGRATION METHOD

It is pertinent to first briefly discuss the direct method [14] for obtaining some solutions to (8), (9) with the use of the 11 popular orthogonal coordinate systems described in [15]. Let $u_i = u_i(x, y, z)$ (i = 1, 2, 3) be a curvilinear orthogonal coordinate system. The coordinate system obtained via the local substitutions $u_i \longrightarrow W_i(u_i(x, y, z))$ (i = 1, 2, 3) is then also orthogonal. The W_i (i = 1, 2, 3) harmonic functions can be found for seven orthogonal coordinate systems as follows. In these systems, the Laplace operator for an arbitrary $W(u_1, u_2, u_3)$ function is

$$\Delta W = \sum_{i=1}^{3} g_i(u_1, u_2, u_3)\frac{\partial}{\partial u_i}\left(f_i(u_i)\frac{\partial W}{\partial u_i}\right),$$

where the form of the $g_i(u_1, u_2, u_3)$ and $f_i(u_i)$ (i = 1, 2, 3) functions is known. The fields $w_i(x, y, z) = W_i(u_i)$ (i = 1, 2, 3) that satisfy the equations

$$f_i(u_i)\frac{\partial W_i(u_i(x, y, z))}{\partial u_i} = C_i$$

with constant C_i (i = 1, 2, 3) values are therefore harmonic and orthogonal.

Obtaining a general solution to (8), (9) requires the use of classic differential geometry methods. First, let us perform the hodograph transformation. Put $y_1 = x$, $y_2 = y$, and $y_3 = z$ and $x_1 = \theta$, $x_2 = b$, and $x_3 = c$, exchange the roles played by dependent and independent coordinates, and seek

$$y_i = y_i(x_1, x_2, x_3) \quad (i = 1, 2, 3)$$

as a function of x_1, x_2, and x_3. In terms of geometry, this dependence means the introduction of a curvilinear coordinate system with the length element

$$ds^2 = dy_i dy_i = g_{ik}dx_i dx_k$$

into the Euclidean space with the coordinates y_1, y_2, y_3 (here and throughout, the summation over repeating indices is implied). The g_{ik} metric tensor and the inverse tensor g_{ik} are

$$g_{ik} = \frac{\partial y_p}{\partial x_i}\frac{\partial y_p}{\partial x_k}, \quad g^{ik} = \frac{\partial x_i}{\partial y_p}\frac{\partial x_k}{\partial y_p}. \tag{17}$$

For convenience and completeness, we give the necessary differential geometry propositions. In a curvilinear coordinate system, at every point

$$\mathbf{r} = (y_1, y_2, y_3) = \mathbf{r}(x)$$

the local basis

$$\mathbf{e}_i = \mathbf{r}_{,i}\left(\mathbf{r}_{,i} = \frac{\partial \mathbf{r}}{\partial x_i}\right)$$

is defined. Its changes in space in the vector

$$\mathbf{e}_{i,j} = \Gamma_{ij}^k \mathbf{e}_k \tag{18}$$

and coordinate

$$y_{n,i,j} = \Gamma_{ij}^k y_{n,k} \tag{19}$$

forms are determined by the Christoffel symbols

$$\Gamma_{ij}^k = \frac{1}{2} g^{kn}(g_{in,j} + g_{jn,i} - g_{ij,n}). \tag{20}$$

The condition of system (18) integrability (the condition that the space is Euclidean) results in the vanishing,

$$R_{prsi} = 0, \tag{21}$$

of the Riemann tensor R_{prsi}

$$R_{prsi} = \frac{\partial \Gamma_{p,ri}}{\partial x_s} - \frac{\partial \Gamma_{p,rs}}{\partial x_i} + \Gamma_{rs}^m \Gamma_{m,pi} - \Gamma_{ri}^m \Gamma_{m,ps}. \tag{22}$$

Here, $\Gamma_{m,ps} = g_{mn}\Gamma_{ps}^n$. Lastly, note the important relation

$$\frac{\partial^2 x_p}{\partial y_i \partial y_j} = -\Gamma_{ks}^p \frac{\partial x_k}{\partial y_i}\frac{\partial x_s}{\partial y_j}, \tag{23}$$

which is easy to obtain by differentiating the identity

$$\frac{\partial y_p}{\partial x_i}\frac{\partial x_i}{\partial y_n} = \delta_{pn}$$

with respect to x_j and using (19).

Let us apply classical geometry methods to solve (8), (9). It follows from (9) that the twice contravariant metric tensor $g^{ik} = (g^{-1})_{ik}$, which depends on x_1, x_2, and x_3, has the diagonal form ($g^{12} = g^{13} = g^{23} = 0$),

$$g^{-1} = \begin{pmatrix} 1/H_1^2 & 0 & 0 \\ 0 & 1/H_2^2 & 0 \\ 0 & 0 & 1/H_3^2 \end{pmatrix}, \tag{24}$$

where H_i^2 ($i = 1, 2, 3$) are the diagonal components of the metric tensor g_{ik}. As distinct from the standard hodograph transformation, we treat H_i as new independent fields and write the corresponding equations for them. Condition (21) gives six Lame equations for determining the H_i functions. They can be written in a short form using the Darbu symbols

$$\beta_{ij} = \frac{1}{H_i}\frac{\partial H_j}{\partial x_i} \quad (i \neq j).$$

The Lame equations then become

$$\begin{gathered} \frac{\partial \beta_{ij}}{\partial x_i} + \frac{\partial \beta_{ij}}{\partial x_i} + \beta_{ik}\beta_{jk} = 0, \\ \frac{\partial \beta_{ij}}{\partial x_k} + \beta_{ik}\beta_{kj} = 0, \end{gathered} \tag{25}$$

where the i, j, and k indices are different and equal to one of the numbers 1, 2, and 3. These equations take into account orthogonality condition (9) and the Euclidean character of the independent variables x, y, and z of the fields θ, b, and c. The requirement of field harmonicity is a reduction of the Lame equations. It immediately follows from (23) that Eqs. (8) are written as the nonlinear first-order equations

$$g^{jk}\Gamma_{i,jk} = 0 \quad (i = 1, 2, 3) \tag{26}$$

for the fields H_i, where $\Gamma_{i,jk}$ stands for the Christoffel symbols for metric (24). It follows that solving (8), (9) reduces to the geometric problem of determining a system of coordinates with metric (24) in the Euclidean space with additional conditions, that is, to solving (25) for H_1, H_2, and H_3 with reductions (26). If the metric tensor is known, the dependence $y_i = y_i(x_1, x_2, x_3)$ ($i = 1, 2, 3$) and therefore the dependence of the fields θ, b, and c on x, y, and z can be found by the integration of the redefined but linear system (19).

It immediately follows from system (26) that the values

$$\frac{H_1 H_2 H_3}{H_i^2}$$

do not depend on the variable x_i ($i = 1, 2, 3$). Note that this condition is a particular case of the Robertson condition [16] for systems of curvilinear coordinates that admit the separation of variables in the three-dimensional Laplace equation. As a result, the diagonal metric tensor components are factored as

$$\begin{aligned} H_1 &= \frac{1}{\sqrt{F_2(x_1, x_3)}\sqrt{F_3(x_1, x_2)}}, \\ H_2 &= \frac{1}{\sqrt{F_1(x_2, x_3)}\sqrt{F_3(x_1, x_2)}}, \\ H_3 &= \frac{1}{\sqrt{F_1(x_2, x_3)}\sqrt{F_2(x_1, x_3)}} \end{aligned} \tag{27}$$

by the F_i functions ($i = 1, 2, 3$), now of two variables. Substituting these relations into Lame equations (25)

yields six equations for determining the F_i fields. The first three equations have the form

$$-F_1F_{2,x_1}F_{3,x_2} + F_{1,x_2}(F_3F_{2,x_1} - F_2F_{3,x_1}) = 0 \quad \text{(with cyclically permuted indices 1, 2, 3).} \tag{28}$$

The second group of equations contain second-order partial derivatives,

$$\begin{aligned} &-2(F_3F_{1,x_2}^2 + F_2F_{1,x_3}^2) + F_1(2F_3F_{1,x_2,x_2} \\ &\quad + 2F_2F_{1,x_3,x_3} + F_{1,x_3}F_{2,x_3} \\ &\quad - F_{2,x_1}F_{3,x_1} + F_{1,x_2}F_{3,x_2}) = 0 \end{aligned} \quad \text{(with cyclically permuted indices 1, 2, 3).} \tag{29}$$

Let us briefly discuss solution (28), (29). It follows from (28) that

$$\begin{aligned} F_{3,x_1} &= \frac{F_3F_{1,x_3}F_{2,x_1}}{F_2F_{1,x_3} - F_1F_{2,x_3}}, \\ F_{3,x_2} &= \frac{-F_3F_{1,x_2}F_{2,x_3}}{F_2F_{1,x_3} - F_1F_{2,x_3}}. \end{aligned} \tag{30}$$

First, consider the simple cases when either the numerator, denominator, or both of them simultaneously vanish in (30). Otherwise, the condition of their compatibility

$$\frac{F_1F_{1,x_2x_3}}{F_{1,x_3}F_{1,x_2}} = \frac{F_2F_{2,x_2x_3}}{F_{2,x_3}F_{2,x_1}} \tag{31}$$

leads to the simple equations

$$F_{1,x_3} = F_1^{g_3}g_2, \quad F_{2,x_3} = F_2^{g_3}g_1. \tag{32}$$

The form of the fields g_i (i = 1, 2, 3) that only depend on x_3 is determined by the substitution of (32) into system (29). We showed that, as a result, $g_3 = 2$ or $g_3 = 1/2$. With $g_3 = 2$, we obtain general ellipsoidal coordinates (see below). After the determination of F_i (i = 1, 2, 3), the dependences $x = x(\theta, b, c)$, $y = y(\theta, b, c)$, and $z = z(\theta, b, c)$ are found by solving linear system (19). Since the metrics that we obtained satisfied the Robertson condition, these dependences could be found in an explicit form. For brevity, we omit detailed calculations for all cases and only give the final results for the fields F_i (i = 1, 2, 3) and (θ, b, c) (in the cylindrical coordinate system (r, z, φ)),

(1)

$$\begin{aligned} F_1 &= \frac{1}{2\alpha}g\sinh^2\frac{x_2}{2g}, \quad F_2 = \frac{1}{2g\alpha}f^2\cosh^2\frac{x_1}{2f}, \\ F_3 &= \frac{2f^2g\cosh^2\dfrac{x_1}{2f}\sinh^2\dfrac{x_2}{2g}}{Q^2\alpha\cosh\dfrac{1}{2}\left(\dfrac{x_1}{f} - \dfrac{x_2}{g}\right)\cosh\dfrac{1}{2}\left(\dfrac{x_1}{f} + \dfrac{x_2}{g}\right)}, \end{aligned} \tag{33}$$

where f, g, Q, and α are the constant parameters and the (θ, b, c) fields are determined by the equations

$$\begin{aligned} \tanh\frac{\theta}{2f} &= \frac{-\sqrt{r^2 + (z-\alpha)^2} + \sqrt{r^2 + (z+\alpha)^2}}{2\alpha}, \\ \cosh\frac{bg}{2} &= \frac{\sqrt{r^2 + (z-\alpha)^2} + \sqrt{r^2 + (z+\alpha)^2}}{2\alpha}, \\ c &= Q\varphi. \end{aligned} \tag{34}$$

The vortex solution for the c field is characterized by index Q, which takes on integral values. At $Q = 1$, coordinate system (34) is related to the coordinates (u, v, φ) of a prolate ellipsoid of revolution [15] as $\sin u = \tanh(\theta/2f)$ and $\cosh v = \coth(bg/2)$. The θ and b fields determine nonlocalized textures, because we have $0 < \tanh(\theta/2f) < 1$ and $0 < \coth(bg/2) < \infty$ over the whole interval of x, y, and z variations. It follows that $0 < \theta < \infty$ and $0 < b < \infty$.

(2)

$$\begin{aligned} F_1 &= \frac{e^{-x_2/g}}{4}, \quad F_2 = \frac{e^{x_1/f}}{4}, \\ F_3 &= \frac{e^{x_1/f}f^2g^2}{(f^2 + e^{x_1/f + x_2/g}g^2)Q^2} \end{aligned} \tag{35}$$

(f, g = const). The c field has a vortex form, and the θ and b fields determine nonlocalized structures,

$$\begin{aligned} \theta &= -f\ln\left(\frac{g(-z + \sqrt{r^2 + z^2})}{2f^2}\right), \\ b &= g\ln\left(\frac{z + \sqrt{r^2 + z^2}}{2g}\right), \quad c = Q\varphi \ \ (Q \in Z). \end{aligned} \tag{36}$$

At $Q = 1$, this coordinate system is related to parabolic coordinates of revolution [15] by simple substitutions.

(3) The F_i (i = 1, 2, 3) and (θ, b, c) fields then have the form

$$\begin{aligned} F_3 &= \frac{4(1 + e^{x_2/g})^2f^2g^2\left(\cos\dfrac{x_1}{2f} + \sin\dfrac{x_1}{2f}\right)^2}{Q^2\left(1 + e^{2x_2/g} - 2e^{x_2/g}\sin\dfrac{x_1}{f}\right)}, \\ F_2 &= f^2\left(1 + \sin\frac{x_1}{f}\right), \quad F_1 = \frac{(1 + e^{x_2/g})^2g^2}{2e^{x_2/g}}, \end{aligned} \tag{37}$$

$$\theta = \frac{\pi}{2} - f\arcsin\frac{1}{8r^2}\left(-1-8z^2 + \sqrt{(1-8r^2)^2 + 16z^2(1+8r^2+4z^2)}\right),$$
$$\cosh\frac{b}{g} = \frac{1}{8r^2}\left(1+8z^2 + \sqrt{(1-8r^2)^2 + 16z^2(1+8r^2+4z^2)}\right), \quad (38)$$
$$c = Q\varphi \quad (Q \in Z)$$

(f, g = const). At $f = -1$, the θ field forms a soliton structure localized close to the origin (see Fig. 1). The field changes from zero to π and has the simple asymptotic behavior

$$\theta \longrightarrow 4\sqrt{2}\,z \quad (\sqrt{r^2+z^2} \longrightarrow 0),$$
$$\theta \longrightarrow z - \frac{1}{\sqrt{2}R} \quad (R = \sqrt{r^2+z^2} \longrightarrow \infty).$$

(4)

$$F_1 = \frac{1}{f}gQ\sinh^2\frac{x_2}{g}, \quad F_2 = \frac{1}{g}fQ\cosh^2\frac{x_1}{f},$$
$$F_3 = \frac{2fg\cosh^2\frac{x_1}{f}\sinh^2\frac{x_2}{g}}{Q\left(\cosh\frac{2x_1}{f} + \cosh\frac{2x_2}{g}\right)} \quad (39)$$

(f, g = const, $Q \in Z$). The c field has a vortex form, and the θ and b fields give the delocalized textures

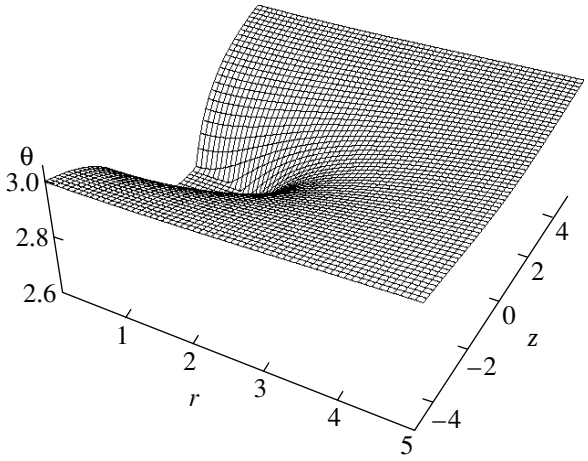

Fig. 1. Spatial distribution of the θ(r, z) field. The field tends to zero as $r^2 + z^2 \longrightarrow 0$.

$$\cosh\frac{\theta}{f} = \frac{1}{\sqrt{2}r}\{-1+r^2+z^2+[r^4+(-1+z^2)^2 + 2r^2(1+z^2)]^{1/2}\}^{1/2},$$
$$\cosh\frac{b}{g} = \frac{1}{\sqrt{2}r}\{1+r^2-z^2+[r^4+(-1+z^2)^2 + 2r^2(1+z^2)]^{1/2}\}^{1/2}, \quad (40)$$
$$c = Q\varphi.$$

(5) The fields F_i (i = 1, 2, 3) depend on the $P(x_2, x_3)$ function,

$$F_3 = 1, \quad F_2 = f^2, \quad F_1 = e^{P(x_2, x_3)}, \quad (41)$$

which satisfies the Laplace equation

$$P_{x_2, x_2} + f^2 P_{x_3, x_3} = 0 \quad (42)$$

(f = const). Selecting P as the real part of the complex function $F(x_2 + ix_3/f)$ yields a solution in the implicit form

$$\theta = fz, \quad x + iy = \int\exp\left(-\frac{F}{2}\left(b + \frac{ic}{f}\right)\right)db. \quad (43)$$

This quasi-two-dimensional structure is characterized by the simplest dependence of the θ field on the coordinates and the diversity of two-dimensional solutions for the b and c fields characteristic of velocity fields for two-dimensional incompressible liquids. For instance, if F depends linearly on $x_2 + ix_3/f$, we obtain the solutions

$$b = \varphi Q_1 + \frac{Q_2\ln r}{f},$$
$$c = f\left(-(Q_1\ln r) + \frac{\varphi Q_2}{f}\right) \quad (Q_1, Q_2 \in Z), \quad (44)$$

which include vortices (for the c field) and logarithmic sources (for the b field) at $Q = 0$ or logarithmic spirals if $Q_1 \neq 0$.

(6) The structure is determined by the P field,

$$F_1 = \frac{(kgQ)^2 x_2^2}{4}, \quad F_2 = \frac{(kgQ)^2}{2e^{P(x_1, x_3)}}, \quad F_3 = \frac{x_2^2}{4} \tag{45}$$

(g, k, Q = const), that satisfies the elliptic Liouville equation

$$e^P + P_{x_1, x_1} + g^2 k^2 Q^2 P_{x_3, x_3} = 0. \tag{46}$$

This equation has a general solution written in terms of the $F(x_1 + ix_3/gkQ)$ analytic function and its complex conjugate $\bar{F}(x_1 - ix_3/gkQ)$,

$$P(x_1, x_3) = \ln\left(\frac{-8F'\left(x_1 + \frac{ix_3}{gkQ}\right)\bar{F}'\left(x_1 - \frac{ix_3}{gkQ}\right)}{\left(F\left(x_1 + \frac{ix_3}{gkQ}\right) + \bar{F}\left(x_1 - \frac{ix_3}{gkQ}\right)\right)^2}\right).$$

Such solutions, however, give imaginary H_1 and H_3 values. Selecting a one-dimensional solution to (46) in the form

$$P = \ln\left(\frac{1}{2}k^2 \operatorname{sech}^2 \frac{kx_1}{2}\right)$$

yields the structure

$$\tanh(k\theta) = -\cos\Theta, \quad b = \frac{g}{R}, \quad c = Q\varphi \ \ (Q \in Z) \tag{47}$$

in the spherical system of coordinates R, Θ, φ ($r = R\sin\Theta$, $z = R\cos\Theta$). This structure has a nonlocal θ field distribution, the field of a three-dimensional point source for b, and a vortex for the c field.

(7) The F_i fields depend on the fields μ, ν, and λ,

$$\lambda = \frac{\operatorname{cn}^2\left(\frac{\theta}{c_1}, k\right)}{\operatorname{sn}^2\left(\frac{\theta}{c_1}, k\right)}, \quad \mu = -\left(\frac{\operatorname{cn}^2\left(\frac{b}{c_2}, k_1\right)k_1^2}{\operatorname{dn}^2\left(\frac{b}{c_2}, k_1\right)}\right), \quad \nu = -\operatorname{dn}^2\left(\frac{c}{c_3}, k\right) \tag{48}$$

as follows:

$$F_1 = \frac{c_2 c_3}{(\mu - \nu)c_1}, \quad F_2 = \frac{c_1 c_3}{(-\lambda + \nu)c_2}, \quad F_3 = \frac{c_1 c_2}{(-\lambda + \mu)c_3}. \tag{49}$$

Here, $k_1 = \sqrt{1 - k^2}$, k is the modulus of the Jacobi elliptic functions, and c_i (i = 1, 2, 3) are constants. Equations (49) yield a solution for θ, b, and c in the implicit form

$$x = \frac{k\operatorname{sn}\left(\frac{c}{c_3}, k\right)}{\operatorname{dn}\left(\frac{b}{c_2}, k_1\right)\operatorname{sn}\left(\frac{\theta}{c_1}, k\right)},$$

$$y = -\frac{k\operatorname{cn}\left(\frac{c}{c_3}, k\right)\operatorname{dn}\left(\frac{\theta}{c_1}, k\right)\operatorname{sn}\left(\frac{b}{c_2}, k_1\right)}{\operatorname{dn}\left(\frac{b}{c_2}, k_1\right)\operatorname{sn}\left(\frac{\theta}{c_1}, k\right)}, \tag{50}$$

$$z = \frac{\operatorname{cn}\left(\frac{\theta}{c_1}, k\right)\operatorname{cn}\left(\frac{b}{c_2}, k_1\right)\operatorname{dn}\left(\frac{c}{c_3}, k\right)}{\operatorname{dn}\left(\frac{b}{c_2}, k_1\right)\operatorname{sn}\left(\frac{\theta}{c_1}, k\right)}.$$

It follows that the fields μ, ν, and λ are the general ellipsoidal coordinates (elliptic coordinates in space) [15–17] if they change over the intervals

$$\{-1 < \nu < -1 + k^2 < \mu < 0 < \lambda < \infty\}. \tag{51}$$

Put

$$\left\{c_1 = \frac{\pi}{K(k)}, c_2 = \frac{\pi}{K(k_1)}, c_3 = \frac{\pi}{2K(k)}\right\}, \tag{52}$$

where $K(k)$ is the total elliptic integral of the first kind. Mapping (50), (52) of the group manifold SU(2) into R^3 is then mutually unambiguous and has a degree of mapping [18] equal to one. Although elliptic coordinates in space in various parameterizations have been described in several monographs (parameterization (50) coincides with that in [17] to within field shifts and scale transformations), their more detailed study is necessary for our purposes. Equation (50) yields the symmetry relations

$$b(x, y, z) = -b(x, y, -z) + 2\pi,$$
$$c(x, y, z) = -c(x, -y, z) + \pi = c(-x, -y, z) + \pi,$$

which immediately determine the regions of b and c field values and definition,

$$0 < b < \pi (z > 0), \quad \pi < b < 2\pi (z < 0),$$
$$0 < c < \pi/2 \quad (x > 0, y < 0),$$
$$\pi/2 < c < \pi \quad (x > 0, y > 0),$$
$$\pi < c < 3\pi/2 \quad (x < 0, y > 0),$$
$$3\pi/2 < c < 2\pi \quad (x < 0, y < 0).$$

It follows that $b = 0$ at $z = 0$, and the c field has a nontrivial structure of a vortex line directed along the z axis with a 2π field jump in the $x = 0$, $y < 0$ half-plane. Note

that the c field coincides with the $\varphi + \pi/2$ polar angle at $z = 0$ and $k = 0$, because we then have

$$x = \frac{\sin c}{\sin(\theta/2)}, \quad y = -\frac{\cos c}{\sin(\theta/2)}.$$

An explicit equation for complex three-dimensional structure (50), (52) can be obtained as follows. The equation

$$\frac{x^2}{1+t} + \frac{y^2}{1-k^2+t} + \frac{z^2}{t} = 1 \tag{53}$$

determines the second-order surface. The roots of this equation t_1, t_2, and t_3 selected in the intervals $-1 < t_1 < -1 + k^2 < t_2 < 0 < t_3 < \infty$ and known to coincide with ν, μ, and λ give expressions for the latter in terms of x, y, and z. The θ, b, and c fields are then found from (48) by numerical methods. The localized distributions of the θ field at various z values are shown in Fig. 2. Equations (48), (53) give

$$\theta \propto \frac{1}{x^2 + y^2 + z^2} \quad (x^2 + y^2 + z^2 \longrightarrow \infty)$$

for the asymptotic behavior of the θ field. The b field is localized at small z values and delocalized at large z (Fig. 3). The vortex character of the c field is shown in Fig. 4 for two z values; a field jump by 2π is clearly seen.

Structures (50) are not topological, because the absence of constant limits of the b and c fields (as $x^2 + y^2 + z^2 \longrightarrow \infty$), as with the spherical coordinates Θ and φ, prevents the compactification of the space R^3 into sphere S^3 and the introduction of a topological invariant from $\pi_3(SU(2))$ [18] that coincides with the degree of mapping.

4. SPATIAL STRUCTURES RELATED TO THE SECOND AND THIRD SUBSTITUTIONS

Let us discuss the solution to (11), (12) for the second substitution using the differential geometry integration method. We will use the notation $y_1 = x$, $y_2 = y$, $y_3 = z$ and $x_1 = a$, $x_2 = b$, $x_3 = c$ and seek $y_i = y_i(x_1, x_2, x_3)$ ($i = 1, 2, 3$) as a function of x_1, x_2, and x_3. It then follows from (12) and (17) that the metric tensor $g^{ik} = (g^{-1})_{ik}$ related to this transformation is not diagonal,

$$g^{-1} = \begin{pmatrix} h_1^2 & 0 & 0 \\ 0 & h_2^2 & h_1^2 \\ 0 & h_1^2 & h_3^2 \end{pmatrix}. \tag{54}$$

After the hodograph transformation, Eqs. (11) are written in form (26) with metric tensor (54). We showed that the solution to these equations had the form

$$h_1 = \frac{1}{(-U_{x_2x_3}^2 + U_{x_2x_2}U_{x_3x_3})^{1/2}},$$
$$h_2 = \frac{(U_{x_3x_3})^{1/2}}{(U_{x_2x_3})^{1/2}(U_{x_2x_3}^2 - U_{x_2x_2}U_{x_3x_3})^{1/2}}, \tag{55}$$
$$h_3 = \frac{U_{x_2x_2}^{1/2}}{U_{x_2x_3}^{1/2}(U_{x_2x_3}^2 - U_{x_2x_2}U_{x_3x_3})^{1/2}},$$

where the $U(x_1, x_2, x_3)$ field is the sum of three arbitrary fields that depend on two variables only,

$$U(x_1, x_2, x_3) = U_1(x_2, x_3) + U_2(x_1, x_3) + U_3(x_1, x_2). \tag{56}$$

The explicit form of the U_i field is determined by solv-

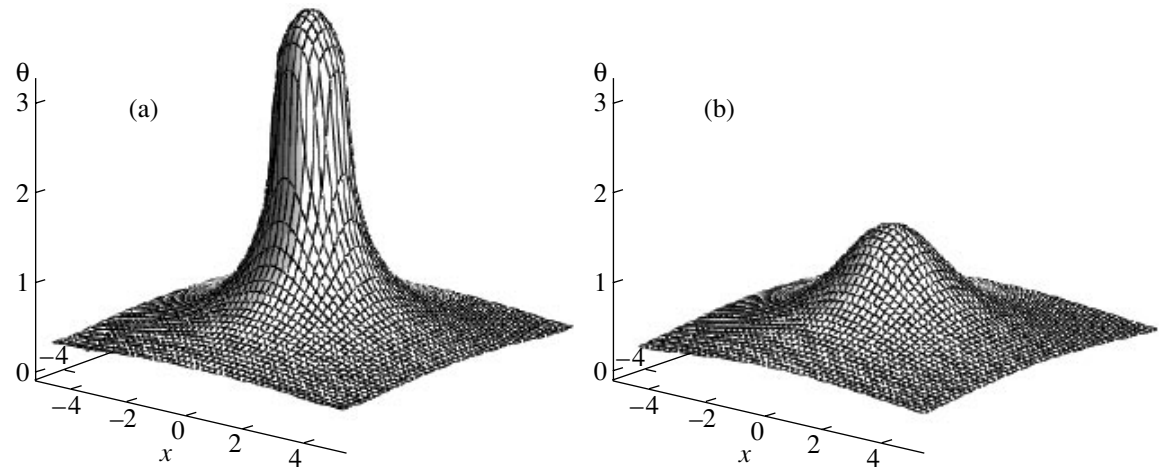

Fig. 2. Localized $\theta(x, y, z)$ field structure in a texture related to the triorthogonal harmonic coordinate system ($k = 0.3$). Solitons at (a) $z = 0$ and (b) $z = 1$ are shown.

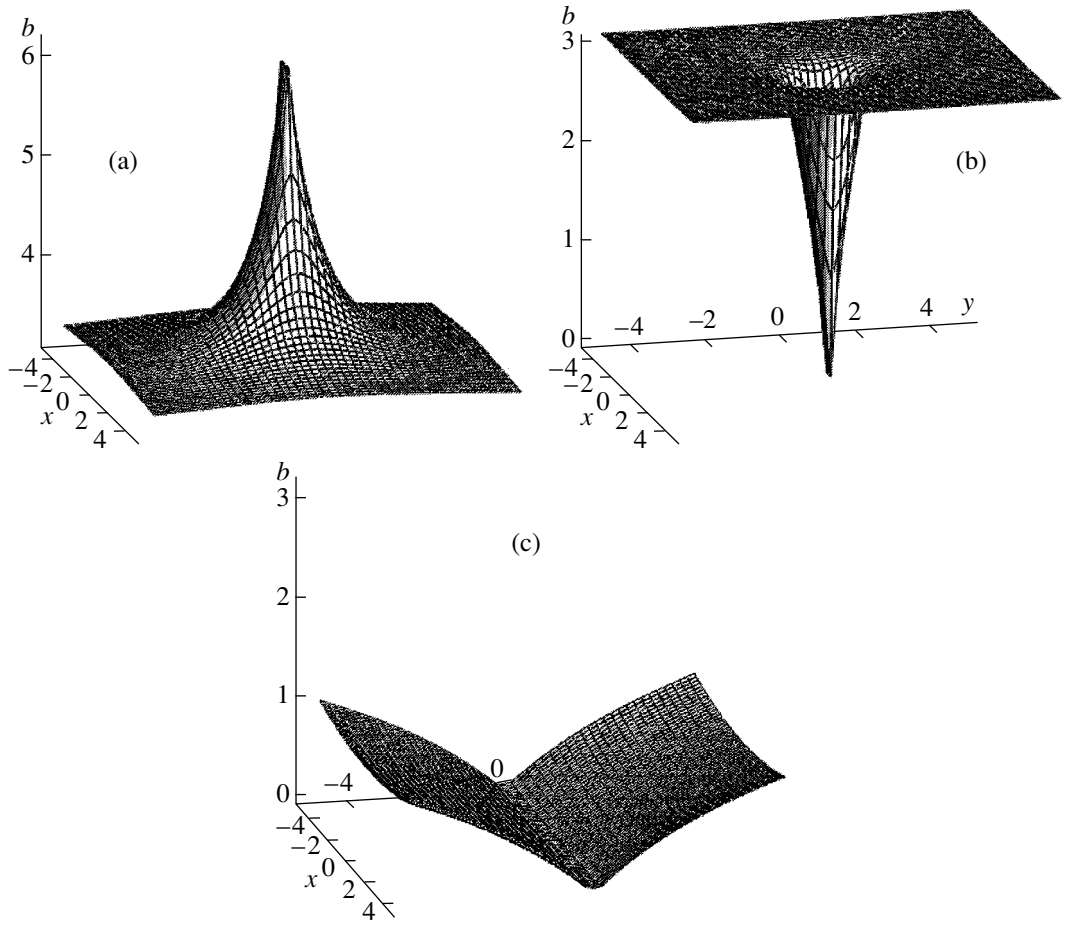

Fig. 3. Field $b(x, y, z)$ structure in a texture related to the triorthogonal harmonic coordinate system ($k = 0.3$). Field localization at (a) $z = -1$ and (b) $z = 0.1$ and (c) field diagonalization at $z = 100$ are shown.

ing (21) with metric tensor (55). These equations are cumbersome, and we give only one of them,

$$\det\begin{pmatrix} U_{x_2,x_2,x_2} & U_{x_2,x_2,x_3} & U_{x_2,x_3,x_3} \\ U_{x_2,x_2,x_3} & U_{x_2,x_3,x_3} & U_{x_3,x_3,x_3} \\ U_{x_2,x_2} & U_{x_2,x_3} & U_{x_3,x_3} \end{pmatrix} = 0 \qquad (57)$$

The first and second matrix rows in this equation are the derivatives of the third row with respect to x_2 and x_3, respectively. This equation has a solution provided the first or second row is zero or there is a linear dependence between matrix columns,

$$\begin{pmatrix} U_{x_2,x_2,x_2} \\ U_{x_2,x_2,x_3} \\ U_{x_2,x_2} \end{pmatrix} = f_1\begin{pmatrix} U_{x_2,x_2,x_3} \\ U_{x_2,x_3,x_3} \\ U_{x_2,x_3} \end{pmatrix} + f_2\begin{pmatrix} U_{x_2,x_3,x_3} \\ U_{x_3,x_3,x_3} \\ U_{x_3,x_3} \end{pmatrix}. \qquad (58)$$

The first two conditions are equivalent to one, because system (11), (12) is invariant with respect to b and c permutations. Combined with the solution to (21), these conditions give the results described below (items (8) and (9)). It can be shown that the other solution types compatible with (58) exist provided the f_1 and f_2 functions are constant or depend on x_1. After the determination of the U_i ($i = 1, 2, 3$) functions, the dependences $x = x(a, b, c)$, $y = y(a, b, c)$, and $z = z(a, b, c)$ are found by solving linear system (19). The θ, b, and c textures are analyzed using a soliton solution to (10),

$$\theta = 4\arctan e^a, \qquad (59)$$

or a soliton lattice solution,

$$\cos\frac{\theta}{2} = \mathrm{sn}\left(\frac{a}{k}, k\right). \qquad (60)$$

We omit the details of all calculations and only discuss the final results for the h_i ($i = 1, 2, 3$) and Q, b, and c

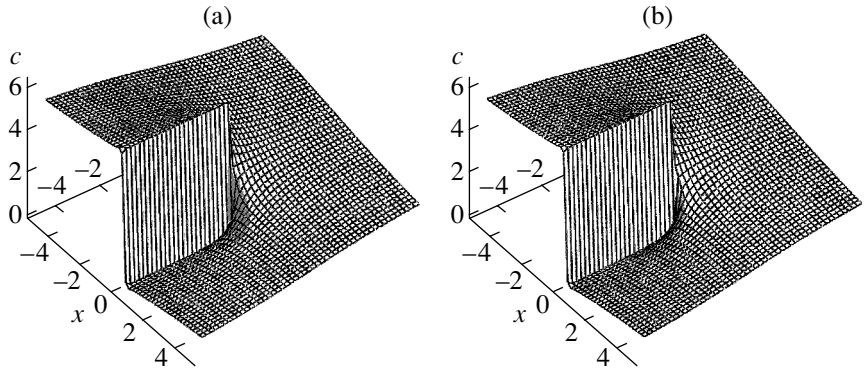

Fig. 4. Field $c(x, y, z)$ vortex structure in a texture related to the triorthogonal harmonic coordinate system ($k = 0.3$). Field distributions at (a) $z = -0.1$ and (b) $z = 1$ with a 2π jump in the $x = 0$, $y < 0$ half-plane are shown.

fields (in the cylindrical coordinate system (r, z, φ)).

(8)

$$h_1 = \exp\left(\frac{x_1}{\sqrt{Q_1Q_2}}\right), \tag{61}$$

$$h_2 = Q_2^{-1/2}\exp\left(\frac{x_1}{\sqrt{Q_1Q_2}}\right)p^2\sqrt{Q_1}\sqrt{\exp\left(\frac{-2x_1}{\sqrt{Q_1Q_2}}\right)+\frac{Q_2^2}{p^4Q_1^2}},$$

$$h_3 = Q_2^{-1/2}\exp\left(\frac{x_1}{\sqrt{Q_1Q_2}}\right)\sqrt{Q_1},\quad Q_1Q_2 > 0.$$

The b and c fields have a vortex form, and the a field is the logarithmic potential of a source,

$$a = -\sqrt{Q_1Q_2}\ln r,\quad b = gz + \varphi Q_2,\quad c = \varphi Q_1. \tag{62}$$

According to (59), this gives a localized distribution for θ,

$$\theta = 4\arctan\left(r^{-\sqrt{Q_1Q_2}}\right),$$

over the interval $[0, 2\pi]$.

(9) The h_i ($i = 1, 2, 3$) fields depend on the $R(x_1, x_2)$ function,

$$h_1 = g^2e^{-R/2},\quad h_2 = \frac{g^2e^{-R/2}}{f},$$
$$h_3 = \frac{\sqrt{e^R + f^4g^6}}{e^{R/2}fg}, \tag{63}$$

which satisfies the Laplace equation

$$P_{x_1, x_1} + Q^2P_{x_2, x_2} = 0. \tag{64}$$

Consider a solution to this equation in the form

$$R(x_1, x_2) = T(x_1 - ix_2/Q) + \text{c.c.}$$

The structure then has the simplest dependence on z, and the manifold of solutions is determined by the equations

$$c = \frac{b}{Q^2} + Gz,\quad x + iy = \int_{-\infty}^{a - ib/Q} e^{T(x)}dx \tag{65}$$

with constant C and Q values. It follows that $a - ib/Q$ is an arbitrary analytic function of $x + iy$. Let us discuss the simplest structure types with selecting θ in the form of soliton lattice (60) and the solution for $a - ib/Q$ in the form

$$a - i\frac{b}{Q} = \sum_{s=1}^{n}(f_s + ig_s)\ln(x + iy - c_s)$$
$$(f_s, g_s \in R) \tag{66}$$

with complex c_s constants. The constants f_s and g_s can be found from the condition of unambiguity of the matrix D (Eq. (5)). The change in the field a in going around the singularity line must be multiple to $2kK(k)$ (the period of the function $\text{sn}^2(a/k, k)$), and the change in the fields b and c must be multiple to 2π. We therefore obtain

$$\cos\theta = 2\text{sn}^2\left(\frac{a}{k}, k^2\right) - 1,\quad f_s = \frac{Q_s}{Q},$$
$$g_s = -\left(\frac{kKN_s}{\pi}\right)\left(N_s, Q_s, \frac{Q_s}{Q^2} \in Z\right) \tag{67}$$
$$(s = 1, 2, \ldots, n).$$

At $n = 1$, formulas (67) describe spiral vortices,

$$\cos\theta = -1 + 2\text{sn}^2\left(\frac{K\varphi N_1}{\pi} + \frac{Q_1\ln r}{kQ}, k\right), \tag{68}$$

$$b = \frac{kKQN_1\ln r}{\pi} - \varphi Q_1,$$
$$c = Gz + \frac{kKN_1\ln r}{\pi Q} - \frac{\varphi Q_1}{Q^2}. \tag{69}$$

The θ, b, and c fields at fixed z with discrete parameters

$N_1 \neq 0$, Q_1 take on constant values on curves in the (x, y) plane that are logarithmic spirals. At $N_1 = Q_1 = Q = 1$, the solution to (68) is two spiral domains (regions with opposite cosθ values) separated by two logarithmic spirals (see Fig. 5). At an N, expression (68) describes an |N|-turn logarithmic spiral whose chirality (the direction of spiral twisting) is determined by the sign of the product N_1Q_1Q. The k parameter determines the degree of spiral twisting, which increases as k decreases. The cosθ field graph and the configuration of domains for a two-turn spiral are shown in Fig. 6. The width of spiral solitons (domain boundaries) depends on k and increases as the distance from the vortex center grows. At $N = 0$, we have a system of concentric (with respect to the r variable) ring domains, that is, an antiferromagnetic target (Fig. 7), which is an infinite band domain structure with respect to the ln$r$ variable.

Since spiral structures are characterized by two integral numbers (N and Q), the structures of dipoles are more diversified than vortex structures. By way of example, let us consider several types of spiral dipoles for the θ field that consist of vortex spirals with the numbers (N_1, Q_1) and (N_2, Q_2). At large distances, such a dipole transforms into a concrete spiral configuration with the numbers $(N_1 + N_2, Q_1 + Q_2)$. A dipole consisting of two spiral structures with the numbers (–1, 1) forms a two-turn spiral at large distances (Fig. 8), a dipole with (–1, 1) and (–1, –1) forms a structure (2, 0) (Fig. 9) whose field at large distances depends only on the polar angle, and a dipole with (1, 1) and (–1, 1), an antiferromagnetic target structure (Fig. 10). The interaction of two vortices with the parameters (N, Q) and $(-N, -Q)$ is attractive in character. The corresponding solution has the lowest energy and localized character, $\theta \longrightarrow \pi$ as $r \longrightarrow \infty$ (Fig. 11).

(10) The structure is determined by the $P(x_1, x_3)$ field,

$$h_1 = \frac{1}{G}e^{P/2}(-x_2 + G^2x_3),$$

$$h_2 = \frac{1}{G^2}(x_2 - G^2x_3)\sqrt{G^2 + \frac{e^P G^4}{(x_2 - G^2x_3)^2}}, \qquad (70)$$

$$h_3 = \frac{1}{G^2}e^{P/2}(-x_2 + G^2x_3),$$

that satisfies the Liouville elliptic equation

$$2G^2e^P + P_{x_3,x_3} + G^2P_{x_1,x_1} = 0. \qquad (71)$$

In the spherical coordinate system, its one-dimensional solutions $P = -2\ln(C\,\mathrm{sech}(Cx_1))$ give the texture

$$c = \frac{\varphi}{CG}, \quad b = \frac{g}{R} + \frac{G\varphi}{C},$$
$$\tanh(aC) = \cos\theta, \quad \left(\frac{1}{CG} \in Z, \frac{G}{C} \in Z\right) \qquad (72)$$

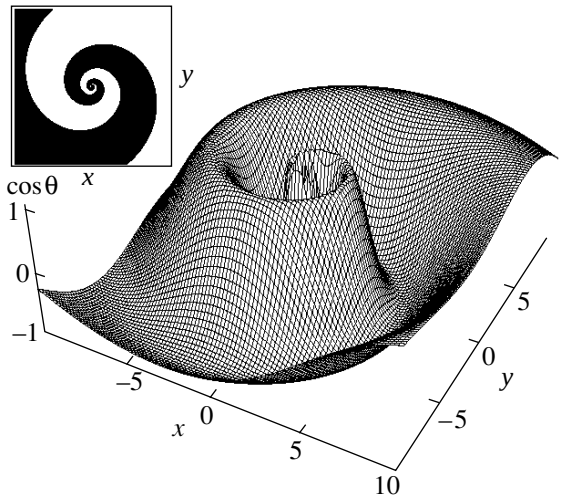

Fig. 5. Spatial distribution of cosθ in a one-turn spiral (k = 0.5, N_1 = 1, Q_1 = 1, and Q = 1). Domains with negative (dark regions) or positive (light regions) cosθ values are shown in the inset.

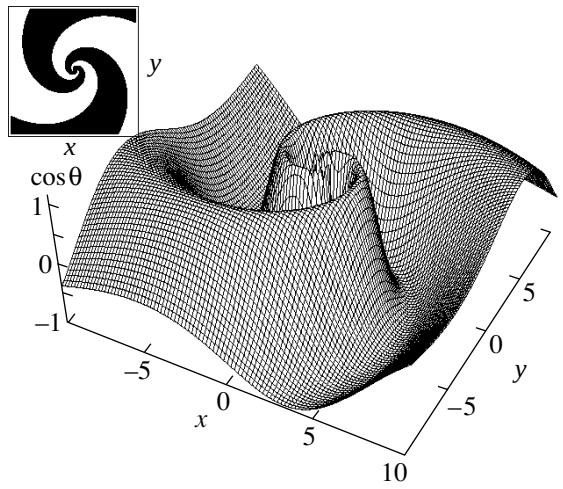

Fig. 6. Core structure for a two-turn spiral (k = 0.5, N_1 = 2, Q_1 = 1, and Q = 1).

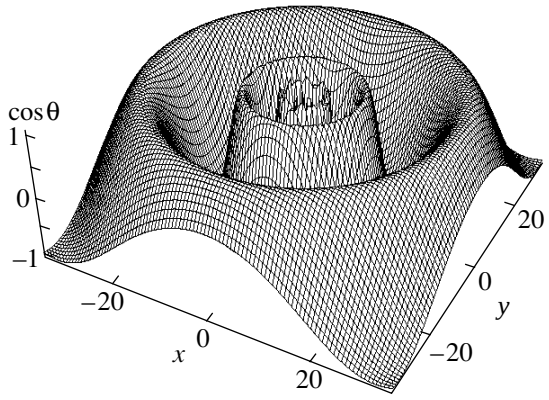

Fig. 7. Spatial distribution of cosθ in an antiferromagnetic target (k = 0.3, N_1 = 0, Q_1 = 1, and Q = 1).

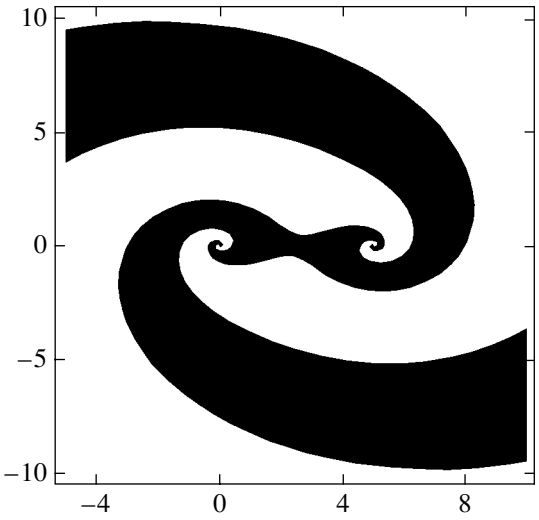

Fig. 8. Spiral dipole consisting of two one-turn spirals with the parameters $N_1 = -1$, $Q_1 = 1$ and $N_2 = -1$, $Q_2 = 1$ that forms a two-turn spiral at large distances. The distance in the pair $d = 5$, $Q = 1$, and $k = 0.7$.

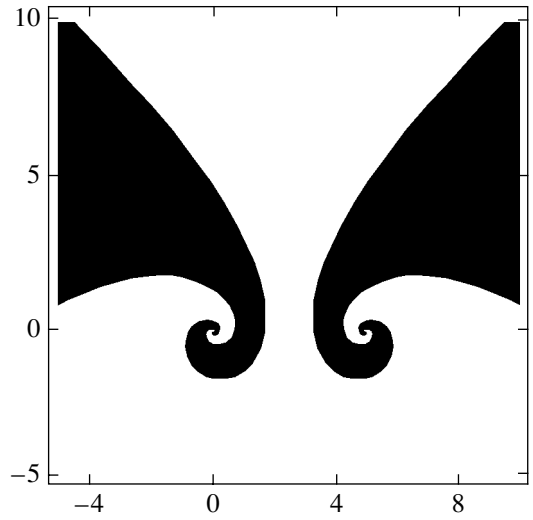

Fig. 9. Spiral dipole consisting of two one-turn spirals with the parameters $N_1 = -1$, $Q_1 = 1$ and $N_2 = -1$, $Q_2 = -1$. The distance in the pair $d = 5$, $Q = 1$, and $k = 0.7$.

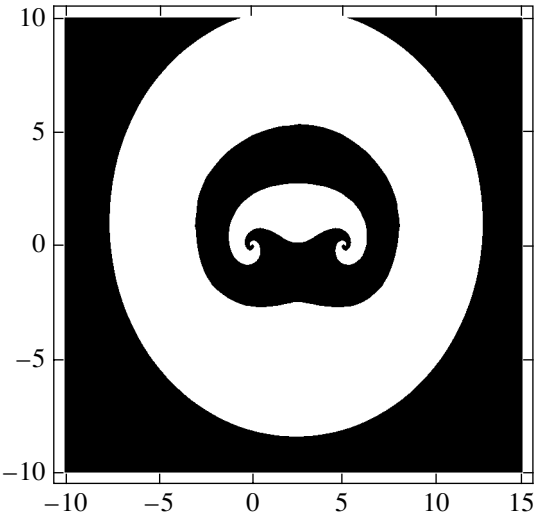

Fig. 10. Spiral dipole consisting of two one-turn spirals with the parameters $N_1 = 1$, $Q_1 = 1$ and $N_2 = -1$, $Q_2 = 1$ that forms an antiferromagnetic target at large distances. The distance in the pair $d = 5$, $Q = 1$, and $k = 0.7$.

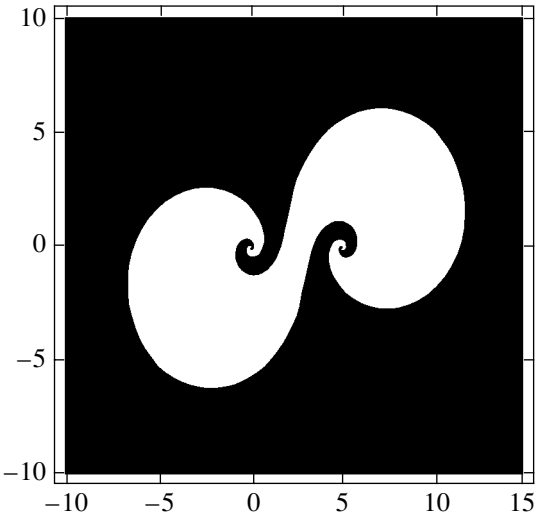

Fig. 11. Spiral dipole consisting of two one-turn spirals with the parameters $N_1 = -1$, $Q_1 = 1$ and $N_2 = 1$, $Q_2 = -1$ that forms a uniform state, $\theta = \pi$, at large distances. The distance in the pair $d = 5$, $Q = 1$, and $k = 0.7$.

of a vortex for the c field and the field of a vortex and spatial source for the b field. Although distribution (72) is similar to (47), Eq. (59) changes the θ field over the interval $[0, 2\pi]$.

(11) As with elliptic coordinates in space, the fields h_i ($i = 1, 2, 3$) are given by three elliptic functions $F_i(u_i)$ (there is no summation over repeating dummy indices) of the variables $u_1 = x_1$, $u_2 = \sqrt{c_1}\,(x_2 + c_2 x_3)/(c_1 - c_2)$, and $u_3 = \sqrt{c_2}\,(x_2 + c_1 x_3)/(c_1 - c_2)$ with constant c_i values,

$$h_1 = -\frac{\sqrt{c_1}\sqrt{c_2}}{\sqrt{F_1 - F_2}\sqrt{-F_1 + F_3}},$$

$$h_2 = \frac{\sqrt{c_1}\sqrt{c_2}\sqrt{(-c_1 + c_2)F_1 - c_2F_2 + c_1F_3}}{\sqrt{F_1 - F_2}\sqrt{F_2 - F_3}\sqrt{-F_1 + F_3}}, \quad (73)$$

$$h_3 = \frac{\sqrt{(-c_1 + c_2)F_1 + c_1F_2 - c_2F_3}}{\sqrt{F_1 - F_2}\sqrt{F_1 - F_3}\sqrt{F_2 - F_3}}.$$

The $F_i(u_i)$ functions satisfy the equation

$$F_{i,u_i}^2 = -a_0 - a_1F_i(u_i) - a_2F_i^2(u_i) - a_3F_i^3(u_i). \quad (74)$$

The corresponding structure will be described in detail elsewhere.

Let us discuss the textures related to substitution (14)–(16). A solution to the system of nonlinear equations (15), (16) was found in [19] in the implicit form

$$A(\omega) + yB(\omega) \pm z\sqrt{-1 - B^2(\omega)} = x \quad (75)$$

with arbitrary analytic functions $A(\omega)$ and $B(\omega)$ of $\omega = \alpha + i\beta$. Given the form of these functions, $\alpha(x, y, z)$ and $\beta(x, y, z)$ are found explicitly by solving complex equation (75). This equation is an analog of the Riemann wave for the Hopf equation and admits direct generalization to the N-dimensional space case. Generally, as in hydrodynamics, the solution to this equation is not unambiguous, and the determination of unambiguous spatial structures of the fields θ, b, and c requires invoking ambiguous solutions to (14). For this reason, we restrict ourselves to consideration of unambiguous solutions of the simplest form. Put $\theta = \theta(\alpha)$, $b = b(\beta)$, and $c = c(\beta)$. It then follows from Eq. (14) that

$$b = -\beta\frac{Q_1}{Q}, \quad c = \beta\frac{Q_2}{Q}. \quad (76)$$

The $\theta(\alpha)$ field satisfies the sine-Gordon equation ($-\sin\theta(\alpha)Q_1Q_2/Q^2 + \theta''(\alpha) = 0$), which, at $Q_1Q_2 > 0$, has the solution

$$\cos\frac{\theta}{2} = \mathrm{sn}\left(\frac{\alpha\sqrt{Q_1Q_2}}{kQ}, k\right) \quad (0 < k \le 1). \quad (77)$$

At $Q_1Q_2 < 0$, a solution for $\theta(\alpha)$ can be derived from (75), (76) by shifting θ by π. The simplest solution to (75) is obtained when $A(\omega)$ and $B(\omega)$ are selected as

$$A(\omega) = 0, \quad B(\omega) = \frac{i(-1 + F(\omega))}{1 + F(\omega)} \quad (78)$$

with an arbitrary F function. Then,

$$\omega = F(\Omega), \quad \Omega = \tan\frac{\Theta}{2}\exp i\varphi \quad (79)$$

or ω is the antianalytic function $\omega = F(\Omega^*)$ of the complex variable Ω, which is a stereographic projection of the sphere of a unit radius in the three-dimensional space ($x = \sin\Theta\cos\varphi$, $y = \sin\Theta\sin\varphi$, $z = \cos\Theta$. Let ω be given by the potential of a vortex source, $\omega = \alpha + i\beta = (Q + if)\ln\Omega$ ($Q, f \in R$). The solution to (79) is then a linear defect with singular field θ derivative values on the z axis ($\theta \longrightarrow 0$, $\theta \longrightarrow \pi$). In going around the singularity line, the change in the b and c fields should be multiple to 2π, and the change in the argument of the elliptic function in (77) should be multiple to 2K (the half-period of the $\mathrm{sn}(u, k)$ elliptic function), as follows from the requirement that $\cos\theta$, b, and c be unambiguous. The structure is then characterized by integral S, Q_1, and Q_2 values, and its general form is

$$\cos\frac{\theta}{2} = \mathrm{sn}\left(-\frac{KS\varphi}{\pi} + \frac{1}{k}\ln\left(\tan\frac{\Theta}{2}\right)\sqrt{Q_1Q_2}, k\right), \quad (80)$$

$$b = -\varphi Q_1 - \frac{1}{\pi}kSK\ln\left(\tan\frac{\Theta}{2}\right)\sqrt{\frac{Q_1}{Q_2}}, \quad (81)$$

$$c = \varphi Q_2 + \frac{1}{\pi}kKS\ln\left(\tan\frac{\Theta}{2}\right)\sqrt{\frac{Q_2}{Q_1}}. \quad (82)$$

At $S = 0$ and in the simplest (soliton) case ($k = 1$), we have

$$\cos\frac{\theta}{2} = \frac{-1 + \left(\tan^2\frac{\Theta}{2}\right)^{\sqrt{Q_1Q_2}}}{1 + \left(\tan^2\frac{\Theta}{2}\right)^{\sqrt{Q_1Q_2}}}, \quad (83)$$

$$\theta = 2\pi + 2\Theta, \quad c = -b = \varphi \quad (Q_1 = Q_2 = 1) \quad (84)$$

and structure (84) leads to the field $n_\mu = (-z/R, 0, -x/R, -y/R)$, whose components coincide with the hedgehog field components ($\mathbf{m} = -\mathbf{r}/|\mathbf{r}|$).

At $S \neq 0$, the θ field has a singular line ($z = 0$) and the field $\cos\theta$ assumes the constant value

$$\cos\frac{\theta}{2} = \mathrm{sn}\left(\frac{c_1\sqrt{Q_1Q_2}}{k}\right)$$

on the helicoidal surfaces

$$z = -R\tanh\left(c_1 + \frac{kS\varphi K(k)}{\pi\sqrt{Q_1Q_2}}\right)$$

that pass through the origin and, at a fixed $z = h$ value, on spirals of the form

$$r = \pm\frac{h}{\sinh\left(c_1 + \frac{kS\varphi K(k)}{\pi\sqrt{Q_1}Q_2}\right)}.$$

Figure 12 shows $\cos\theta$ and the field b plotted at $S = 1$ and a finite z.

The general unique solution for a system of interacting spatial spirals

$$\omega = \alpha + i\beta = \sum_{j=1}^{n}\left(\frac{2ikK}{\pi}S_j + Q_j\right) \times \ln\left(\tan\frac{\Theta}{2}e^{i\varphi} - \tan\frac{\Theta_j}{2}e^{i\varphi_j}\right) + w(\Omega) \quad (85)$$

is characterized by an arbitrary meromorphic function $w(\Omega)$, the k parameter, integral S_j and N_j values, and arbitrary real constants θ_j and φ_j; it contains a set of sin-

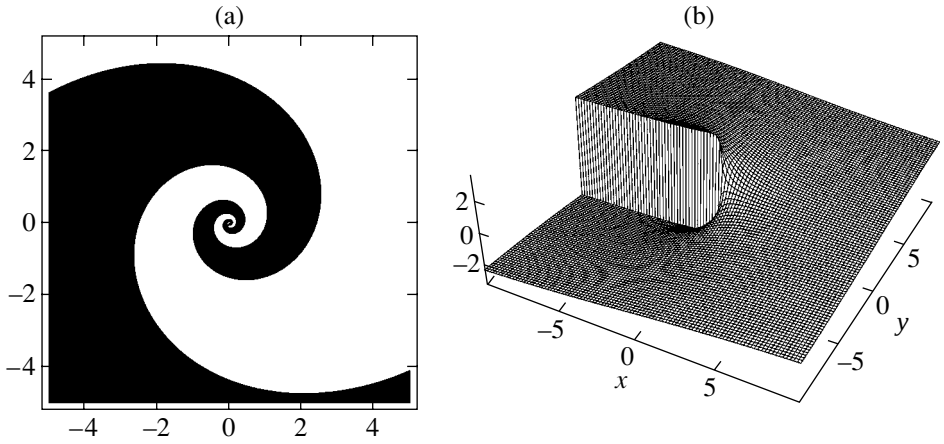

Fig. 12. Field $\cos\theta(x, y, z)$ and $b(x, y, z)$ distributions in the $z = 4$ plane in a three-dimensional spiral structure ($k = 1/3$, $S = 1$, $Q_1 = -1$, and $Q_2 = -1$). (a) Domains with negative (dark regions) and positive (light regions) $\cos\theta(x, y, z)$ values and (b) vortex $b(x, y, z = 4)$ field structure with a 2π jump in the $y = 0$, $x < 0$ half-plane are shown.

gular rays that issue from the origin at angles θ_j and φ_j ($j = 1, \ldots, n$). At $r \ll z$, the structure described by (77) and (85) is a set of $|S_j|$-turn logarithmic spirals.

5. CONCLUSIONS

To summarize, we found new types of three-dimensional textures in multisublattice antiferromagnets and showed that applying classic differential geometry methods is fruitful. Substitutions of type (14)–(16) (combined with the differential geometry method) can be generalized to the n-field model ($n \in S^N$), systems of orthogonal n-fields on Stiefel manifolds [7], etc., in spacetime of arbitrary dimensions.

Let us briefly discuss observing the textures found experimentally in antiferromagnets. Scale-invariant equations (7) are written in the exchange approximation only, without including magnetostatic fields, which are low in antiferromagnets, or anisotropy fields. The form of the textures found is therefore only valid at distances $r < l = \sqrt{\alpha/\beta}$ (α is the exchange interaction constant and β is the anisotropy constant). The influence of the anisotropy constant would change the structure at large distances from singular lines. Note that, in ferromagnets, quasi-stationary target- and spiral domain-type magnetic structures are observed in thin magnetic films with strong perpendicular anisotropy of the easy axis type after pumping with a harmonic or pulsed magnetic field [20, 21]. Recently, magnetic structures in nanomagnets (magnetic dots) have been the object of considerable attention. In these structures, various vortex-like states with possible magnetization displacement from the disk plane are observed [22]. The existence of two-dimensional vortex structures in magnetic dots was substantiated by electron and magnetic force microscopy [23]. Switching processes induced by planar or perpendicular pulsed magnetic fields excite skyrmion-type magnetic structures, theoretically predicted in [24], or spiral structures [25] in such systems. In antiferromagnetic nanosystems, vortex and spiral structures can be observed by spin-polarized scanning tunnel microscopy (SPSTM), especially considering prospects for creating SPSTM with atomic resolution. SPSTM operates on the principle of scanning the surface of a film with a thin magnetized point (scattering field on the order of 0.1 T) when recording magnetic signals. In multisublattice (as in one-sublattice [26]) antiferromagnets, local magnetization is proportional to the second derivatives of fields and sharply increases near vortex lines and singular structure centers.

ACKNOWLEDGMENTS

The author thanks V.E. Zakharov, V.V. Kiselev, E.A. Kuznetsov, A.V. Mikhailov, and A.B. Shabat for fruitful discussions and useful comments, the participants of the session of the Council on Nonlinear Dynamics of the Russian Academy of Sciences for their interest in this work, N.M. Zubarev for fruitful discussions of substitutions in the model of chiral fields, F.R. Rybakov for the calculations of solitons in the triorthogonal harmonic coordinate system, and D.V. Dolgikh for help with computer graphics.

This work was financially supported by the Russian Foundation for Basic Research (project no. 03-01-00100).

REFERENCES

1. A. F. Andreev and V. I. Marchenko, Zh. Éksp. Teor. Fiz. **70**, 1523 (1976) [Sov. Phys. JETP **43**, 794 (1976)].
2. A. F. Andreev, Zh. Éksp. Teor. Fiz. **74**, 786 (1978) [Sov. Phys. JETP **47**, 411 (1978)].
3. A. F. Andreev and V. I. Marchenko, Usp. Fiz. Nauk **130**, 39 (1980) [Sov. Phys. Usp. **23**, 21 (1980)].
4. D. V. Volkov and A. A. Zheltukhin, Zh. Éksp. Teor. Fiz. **78**, 1867 (1980) [Sov. Phys. JETP **51**, 937 (1980)].

5. M. K. Volkov and V. N. Pervushin, *Essentially Nonlinear Quantum Theories, Dynamical Symmetries and the Physics of Mesons* (Atomizdat, Moscow, 1979) [in Russian].
6. A. M. Pogorelov, Usp. Fiz. Nauk **134**, 575 (1981).
7. V. E. Zakharov, S. V. Manakov, S. P. Novikov, and L. P. Pitaevskiĭ, *Theory of Solitons: The Inverse Scattering Method* (Nauka, Moscow, 1980; Consultants Bureau, New York, 1984).
8. V. E. Zakharov and A. V. Mikhaĭlov, Zh. Éksp. Teor. Fiz. **74**, 1953 (1978) [Sov. Phys. JETP **47**, 1017 (1978)].
9. G. Darboux, *Lecons sur le systèmes orthogonaux et les coordonnées curvilignes* (Gauthier-Villars, Paris, 1910).
10. V. E. Zakharov, Duke Math. J. **94**, 103 (1998).
11. A. B. Borisov, Dokl. Akad. Nauk **389**, 603 (2003) [Dokl. Phys. **48**, 169 (2003)].
12. A. B. Borisov, Mat. Fiz. Anal. Geom. **10**, 326 (2004).
13. M. A. Lavrent'ev and B. V. Shabat, *Problems of Hydrodynamics and Their Mathematical Models* (Nauka, Moscow, 1973) [in Russian].
14. V. V. Dyakin, private communication (2003).
15. G. A. Korn and T. M. Korn, *Mathematical Handbook for Scientists and Engineers*, 2nd ed. (McGraw-Hill, New York, 1968; Nauka, Moscow, 1977).
16. P. M. Morse and H. Feshbach, *Methods of Theoretical Physics* (McGraw-Hill, New York, 1953; Inostrannaya Literatura, Moscow, 1958), Vol. 1.
17. *Higher Transcendental Functions (Bateman Manuscript Project)*, Ed. by A. Erdelyi (McGraw-Hill, New York, 1953; Nauka, Moscow, 1973), Vol. 1.
18. B. A. Dubrovin, S. P. Novikov, and A. T. Fomenko, *Modern Geometry* (Nauka, Moscow, 1979), p. 742 [in Russian].
19. A. B. Borisov, Pis'ma Zh. Éksp. Teor. Fiz. **76**, 95 (2002) [JETP Lett. **76**, 84 (2002)].
20. G. S. Kandaurova and A. É. Sviderskiĭ, Zh. Éksp. Teor. Fiz. **97**, 1218 (1990) [Sov. Phys. JETP **70**, 684 (1990)].
21. G. S. Kandaurova, Phys. Usp. **45**, 1051 (2002).
22. T. Shinjo, T. Okuno, R. Hassdorf, *et al.*, Science **289**, 930 (2000).
23. X. Zhu, P. Grütter, V. Metlushko, and B. Ilic, Phys. Rev. B **66**, 024423 (2002).
24. A. A. Belavin and A. M. Polyakov, JETP Lett. **22**, 245 (1975).
25. R. Höllinger, A. Killinger, and U. Krey, J. Magn. Magn. Mater. **261**, 178 (2003).
26. B. A. Ivanov and A. K. Kolezhuk, Fiz. Nizk. Temp. **21**, 355 (1995) [Low Temp. Phys. **21**, 275 (1995)].

Translated by V. Sipachev

Journal of Experimental and Theoretical Physics, Vol. 101, No. 3, 2005, pp. 452–467.
Translated from Zhurnal Éksperimental'noĭ i Teoreticheskoĭ Fiziki, Vol. 128, No. 3, 2005, pp. 525–543.

ORDER, DISORDER, AND PHASE TRANSITIONS IN CONDENSED SYSTEMS

Tetracritical Point and Staggered Vortex Currents in Superconducting State

V. I. Belyavsky*, Yu. V. Kopaev, and M. Yu. Smirnov**
Lebedev Institute of Physics, Russian Academy of Sciences, Moscow, 119991 Russia
*e-mail: *vib@box.vsi.ru; **kopaev@lebedev.sci.ru*
Received March 1, 2005

Abstract—A phase diagram reflecting the main features of the typical phase diagram of cuprate superconductors has been studied within the framework of the Ginzburg–Landau phenomenology in the vicinity of a tetracritical point, which appears as a result of the competition of the superconducting and insulating pairing channels. The superconducting pairing under repulsive interaction corresponds to a two-component order parameter, whose relative phase is related to the orbital antiferromagnetic insulating ordering. Under weak doping, the insulating order coexists with the superconductivity at temperatures below the superconducting phase transition temperature and is manifested as a weak pseudogap above this temperature. A part of the pseudogap region adjacent to the superconducting state corresponds to developed fluctuations of the order parameter in the form of quasi-stationary states of noncoherent superconducting pairs and can be interpreted as a strong pseudogap. As the doping level is increased, the system exhibits a phase transition from the region of coexistence of the superconductivity and the orbital antiferromagnetism to the usual superconducting state. In this state, a region of developed fluctuations of the order parameter in the form of quasi-stationary states of uncorrelated orbital circular currents exists near the phase transition line. © *2005 Pleiades Publishing, Inc.*

1. INTRODUCTION

The superconductivity in cuprates appears upon doping of the parent antiferromagnetic insulator and takes place in a certain dopant concentration interval limited both from below and from above: $x_* < x < x^*$. At the boundaries x_* and x^* of this interval, the superconducting phase transition temperature T_C is zero. Being a function of the dopant concentration, the superconducting transition temperature $T_C(x)$ reaches the maximum value at a certain optimum doping x_{opt}. The antiferromagnetic spin order inherent in the parent insulator (characterized by the Néel temperature $T_N(x)$) is effectively suppressed by doping, and the long-range antiferromagnetic order in the form of a spin density wave (SDW) disappears at a certain doping $x_N < x_*$. A short-range antiferromagnetic order (SDW fluctuations) is observed up to $x \approx x_{\text{opt}}$ [1].

As the temperature is increased, the superconducting phase transition in the region of overdoping ($x_{\text{opt}} \lesssim x < x^*$) in the phase diagram acquires, as is commonly accepted, the features of the superconducting transition in the usual superconductors [1]. This implies that the normal state existing at temperatures above $T_C(x)$ in the region of overdoping is a Fermi liquid, so that the phase transition from superconducting to normal phase in this region can be satisfactorily described within the framework of the standard Bartdeen–Cooper–Schrieffer (BCS) mean field theory.

In the region of underdoping ($x_* < x \lesssim x_{\text{opt}}$) in the phase diagram, the system exhibits a phase transition from the superconducting state to a phase where the one-particle density of states is strongly suppressed. This state is characterized by a pseudogap in the spectrum of one-particle excitations. Establishing the nature of this pseudogap is among the basic problems in the physics of cuprates. The region of the pseudogap state is manifested in various experiments, but the temperature interval of these manifestations at a given level of doping x from the interval $x_* < x \lesssim x_{\text{opt}}$ is expediently divided into two parts [1]. The low-temperature part (strong pseudogap region) at $T_C(x) < T < T^*_{\text{str}}$ is characterized by enhancement of the Nernst effect and can be related to the existence of noncoherent superconducting pairs. Then, T^*_{str} corresponds to the disappearance of such pairs, that is, to the rupture of bonds between particles forming these pairs. In the high-temperature part (weak pseudogap region) at $T^*_{\text{str}}(x) < T < T^*_w(x)$, anomalies in the physical properties related to suppression of the one-particle density of states survive until, at $T > T^*_w(x)$, the system occurs in a state corresponding to the Fermi liquid [1].

It would be quite natural to assume that the very existence of the pseudogap state is caused by a certain insulating ordering, which is related to the antiferromagnetic ground state of the parent insulator and survives at relatively small carrier densities introduced into the crystal by doping [2]. In experiment, the values

of T^*_{str} and T^*_w, at which the strong and weak pseudogaps appear with decreasing temperature, are manifested as the crossover temperatures in the course of continuous variation of the physical properties, rather than as the temperatures of phase transitions corresponding to anomalies in the thermodynamic quantities. The concept of crossover quite naturally agrees with the interpretation of a strong pseudogap, whereas the explanation of a weak pseudogap (implying insulating ordering) necessarily leads to the conclusion that T^*_w must correspond to a phase transition from the insulating state to the state of Fermi liquid. For this reason, it is assumed that the weak pseudogap is actually a true energy gap corresponding to this (hidden) insulating ordering, which is difficult to distinguish in experiment. For example, the absence of an anomaly in the heat capacity on the passage from the normal state to the pseudogap state can be related to the fact that this phase transition is of an infinite order [3].

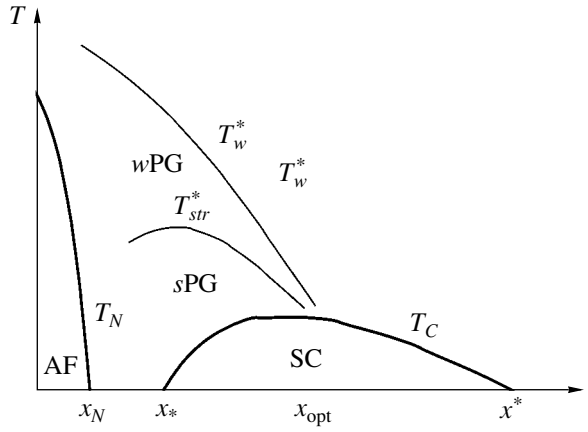

Fig. 1. The typical phase diagram of a hole-doped cuprate compound. AF is the region of long-range spin antiferromagnetic order, SC is the region of superconducting state, and *w*PG and *s*PG are the regions of weak and strong pseudogap, respectively.

An analysis of the available experimental data shows that the pseudogap and the superconducting gap possess the same symmetry. A singlet superconducting pairing corresponds to an orbital structure of the order parameter, which can be interpreted both in terms of the *d*-wave symmetry ($d_{x^2-y^2}$ pairing) and in terms of the "extended" *s*-wave symmetry (*s* + *g* pairing) [4, 5]. The identical distribution of zeros in the superconducting gap and in the pseudogap makes it highly probable that the insulating pairing channel (leading to the weak-pseudogap state) is related to the orbital antiferromagnetic ordering [6].

The features of the phase diagram of cuprates (Fig. 1) imply the need to consider the competition and coexistence of various channels of the insulating and superconducting pairing, which leads to a large variety of the ordered states. These states can be manifested by the corresponding phases formed in various regions of the phase diagram [7, 8]. The orbital antiferromagnetic order, manifested as a toroidal magnetic state [9] in three-dimensional (3D) systems, leads to a staggered flux state [10] in quasi-2D cuprate compounds. This state corresponds to a checkerboard-ordered distribution of circular orbital currents in cuprate planes. A microscopic analysis within the framework of the *t*–*J* model with allowance for the SU(2) equivalence of the *d*-wave pairing and the orbital antiferromagnetic (staggered) flux phase [11] shows that the checkerboard order in the distribution of current circulations survive in the superconducting state. Such current circulations can be interpreted either as fluctuations of the orbital antiferromagnetic order inside the conventional superconducting phase or as a special superconducting phase with the coexistence of two types of ordering (superconducting and orbital antiferromagnetic).

In the case when the orbital currents circulate via chemical bonds between atoms, the orbital antiferromagnetic ordering corresponds to a commensurate charge density wave [12]. Owing to the presence of zeros in the order parameter, this *d*-wave density wave (DWW) [2] must possess a higher stability with respect to doping than the SDW possessing the s-wave symmetry [13]. Moreover, in systems with strong electron–phonon interactions (including doped cuprates), the spin antiferromagnetic ordering in the form of SDWs (having no zeros in the order parameter) is additionally suppressed. On the contrary, in the case of orbital antiferromagnetic ordering, the electron–phonon interactions play the role of a stabilizing factor. Owing to this, the region of orbital antiferromagnetic long-range ordering (e.g., in the form of DDWs [2]) or short-range ordering (DDW fluctuations [14]) can be expanded to reach rather high doping levels and high temperatures.

One can suggest that the intervals of doping, in which the orbital antiferromagnetic ordering coexists with superconducting ordered states, overlap in cuprates. A competition between these states may account for certain features in the phase diagrams of cuprates, at least in the interval of doping where the superconductivity exists.

This paper is devoted to the phenomenology of competitive orbital-antiferromagnetic and superconducting ordered states, which provides for a qualitative interpretation of the features of the phase diagrams of cuprates. A macroscopic description [15] of the superconducting pairing with a large total momentum of the pair with repulsive interaction (this state can be considered as a remnant of the antiferromagnetic state with a close energy, from which the superconducting state arises upon doping) leads to a two-component order parameter possessing a zero line that crosses the Fermi contour in the kinematically allowed domain [16]. Under conditions of ideal mirror nesting of the Fermi contour [16, 17], an asymptotically exact (even at an arbitrarily weak repulsion) nontrivial solution of the self-consistency equation exists provided that a linear

operator with a kernel determined by the repulsive potential has at least one negative eigenvalue [16]. In addition, the repulsive potential possessing this property leads to the existence of quasi-stationary states of pairs with large momentum [17], which may exist in a certain region of temperatures (corresponding to the pseudogap state) above the superconducting transition temperature. The pairing with a large momentum under repulsive interaction admits a natural interpretation of the two-component order parameter, which allows the features of the phase diagrams of cuprates to be considered as resulting from the competition and coexistence of the superconducting and orbital-antiferromagnetic phases. Features of the Fermi contour shape and its evolution caused by doping, which are related to the appearance of an orbital-antiferromagnetic insulating state [18], ensure realization of the mirror nesting conditions necessary for the superconducting pairing.

2. PAIRNG WITH LARGE MOMENTUM

The insulating singlet orbital antiferromagnetic order is characterized by a certain vector **K** (dependent on the level of doping), which has a physical meaning of the momentum in the coupled state of an electron–hole pair. This vector determines the spatial periodicity of a magnetic structure formed in the cuprate plane. As a factor competitive with the orbital antiferromagnetic order, we will consider a superconducting singlet channel of pairing with a large momentum **K**. In this case, the orbital structure of the superconducting order parameter retains a memory of the antiferromagnetic state of the parent compound, from which both the orbital-antiferromagnetic insulating state and the superconducting state appear as a result of doping.

An analysis of the superconducting pairing within the framework of the Hubbard model (η-pairing) showed [19] that, at half-filling, there are numerous eigenstates of the Hubbard Hamiltonian, which correspond to singlet Cooper pairs with a zero total momentum (η_0-pairs) or to the pairs with (π, π) momentum on a 2D square lattice (η_π-pairs). As a result of doping, the total momentum of the pair deviates from (π, π) (the value at half-filling state) and in the general case becomes incommensurate [2] (for this reason, the corresponding superconducting channel is naturally referred to as η_K-pairing).

A superconducting pairing with a nonzero (but small) total momentum also follows from solving the problem of coexistence of the superconductivity and ferromagnetism [20, 21]. For $\mathbf{K} \neq 0$, there appears a kinematic constraint on the range of momentum **k** of the relative motion of the pair. This corresponds to a decrease in the number of one-particle states contributing to the wavefunction of the pair. It should be noted that, at a commensurate momentum $\mathbf{K} = (\pi, \pi)$ corresponding to the half-filled state, the kinematically allowed domain vanishes. If the momentum **K** of the pair is nonzero, the kinetic energy of the pair vanish only at certain points of the Fermi contour belonging to the kinematically allowed domain, rather than over the entire Fermi contour (as is for $\mathbf{K} = 0$ in the absence of a kinematic constraint). The density of states of the relative motion vanishes on the Fermi contour. This eliminates a logarithmic singularity in the self-consistency equation, so that the superconducting pairing becomes impossible at an arbitrarily small value of the effective coupling constant.

For a special shape of the Fermi contour, a situation is possible in which the energy of a quasi-particle becomes zero on finite segments of the Fermi contour within the kinematically allowed domain. This results in a finite density of states of the relative motion on the Fermi contour. To this end, it is necessary that, for a given momentum **K** of the pair, the electron energy dispersion $\varepsilon(\mathbf{k})$ would obey the mirror nesting condition [16]

$$\varepsilon\left(\frac{\mathbf{K}}{2} + \mathbf{k}\right) + \varepsilon\left(\frac{\mathbf{K}}{2} - \mathbf{k}\right) - 2\mu = 0, \qquad (1)$$

where μ is the chemical potential of electrons. Owing to the fact that the Fermi contour in cuprates occurs in an extended vicinity of the saddle point of the electron dispersion, condition (1) (restoring the logarithmic singularity in the self-consistency equation) can be satisfied at least approximately. This provides for the possibility of obtaining an asymptotically exact (even for an arbitrarily small coupling constant) solution for the superconducting gap [22].

In the case of pairing with a zero total momentum of the pair, the mirror nesting condition is trivially valid over the entire Fermi contour owing to the general feature of the electron dispersion: $\varepsilon(-\mathbf{k}) = \varepsilon(\mathbf{k})$. For an arbitrary $\mathbf{K} \neq 0$ and an arbitrary dispersion, condition (1) (considered as the equation for the momentum **k** of the relative motion) leads to a solution determining two points on the Fermi contour, which are symmetric relative to the **K** direction. However, there are several reasons [16] for which a 2D dispersion can lead to a special structure of energy isolines such that, for certain momenta of the pairs, condition (1) is satisfied on finite segments of these isolines or even on some closed isolines. As the doping level changes, the Fermi contour passes from one isoline to another and, in the general case, the momentum **K** providing the best mirror nesting condition changes as well.

A simple example of the mirror nesting of the Fermi contour is offered by the case (typical of cuprates) observed in angle-resolved photoemission spectroscopy (ARPES) experiments, whereby the Fermi contour has the shape of a square with rounded corners [16]. In this case, a change in the sign of the curvature of almost rectilinear segments of the Fermi contour (caused by their proximity to the saddle point of the dispersion function) leads to an increase in the length of segments

satisfying condition (1). In compounds with the double-band electron spectrum, condition (1) is quite naturally satisfied for finite segments of the Fermi contour, which belong to different energy bands [16]. The appearance of a quasi-one-dimensional spatially inhomogeneous stripe structure also leads to the deformation of energy isolines favoring the validity of condition (1) on finite segments of the Fermi contour.

According to the ARPES data, a simply connected Fermi contour is observed in overdoped cuprates. In contrast, the Fermi contour in underdoped compounds (where an insulating gap appears in the electron spectrum) acquires the shape of hole pockets symmetric relative to directions of the $[\pi, \pi]$ type. In each of these pockets, the mirror nesting condition is perfectly satisfied on the entire Fermi contour for the total pair momentum directed along this $[\pi, \pi]$ direction, provided that the magnitude of this momentum is two times the distance to the pocket center [16].

It should be noted that an perfect mirror nesting (in contrast to the perfect conventional nesting leading to an insulating instability) is characterized by coincidence of the occupied region of the momentum space with another occupied region, and of the vacant region with another vacant region, when the Fermi contour is shifted by the nesting vector. For the conventional nesting, such a shift leads to coincidence of the occupied and vacant regions. A Fermi contour having the shape of hole pockets also features the conventional nesting, with the nesting vector practically coinciding with the total momentum of the superconducting pair.

3. SUPERCONDUCTING PAIRING UNDER REPULSIVE INTERACTION

The question what is the predominating mechanism of pairing interactions in cuprates is still open and, along with the traditional pairing caused by the electron–phonon interaction [23–25], the interaction by exchange with antiferromagnetic magnons [26] and purely electron (Coulomb) pairing mechanisms have been also considered. Allowance for the Coulomb repulsion is of principal importance in cuprates, which belong to the systems with strong on-site electron correlations [27]. A qualitative analysis of the Coulomb repulsion, along with the attraction caused by the electron-phonon interaction, within the BCS scheme leads to the conclusion that the Cooper pairing appears when the effective coupling constant for the electron–phonon interaction exceeds an effective value of the Coulomb constant reduced by the Tolmachev logarithm [28] rather than the nonreduced constant.

The Coulomb repulsion can lead to superconducting pairing even in the absence of the attraction caused by electron–phonon interaction [29]. The corresponding superconducting order parameter cannot be a function of constant sign depending on the momentum of the relative motion of the pair. It exhibits a zero line crossing the Fermi contour at several points, which reflect the crystal symmetry [16]. The symmetry of the superconducting order parameter, as dependent on the number and arrangement of zeros on the Fermi contour, can be conditionally referred to as the *d*-wave (in the case of four zeros, whereby a $\pi/2$ rotation in the momentum space leads to a change in sign of the order parameter) or the expanded *s*-wave symmetry.

The superconducting order parameter as a function of the momentum $\mathbf{k}$ of the relative motion of the pair is conveniently represented an expansion in a complete orthonormal system of eigenfunctions $\varphi_s(\mathbf{k})$ of a linear operator with the kernel $U(\mathbf{k} - \mathbf{k}')$, which is equal to Fourier transform of the pairing screened Coulomb repulsion potential. Here, the index s runs over the numbers of eigenfunctions determined by solving the linear integral equation

$$\varphi_s(\mathbf{k}) = \lambda_s \int U(\mathbf{k} - \mathbf{k}')\varphi_s(\mathbf{k}')d^2k', \qquad (2)$$

where λ_s are the corresponding eigenvalues of the above operator and the integral is taken over the kinematically allowed domain.

The maximum area of the kinematically allowed domain for η_K-pairing corresponds to the momentum $\mathbf{K}$ of the pair along one of the symmetry directions in the momentum space. For large $\mathbf{K}$, such a domain amounts to only a small part of the 2D Brillouin zone. Therefore, the true kernel $U(\mathbf{k}–\mathbf{k}')$ can be replaced by a degenerate one, representing the first terms of the expansion into series in powers of the argument [16]:

$$U_d(k) = U_0 r_0^2\left(1 - \frac{k^2 r_0^2}{2}\right), \qquad (3)$$

where r_0 has the meaning of the effective screening radius and $U_0 \sim e^2/r_0$ is the characteristic interaction constant. This degenerate kernel has two even and two odd (with respect to the $\mathbf{k} \longrightarrow -\mathbf{k}$ transformation) eigenfunctions. The first two correspond to the case of eigenvalues with opposite signs [17].

The existence of at least one negative eigenvalue of the interaction operator ensures the existence of a nontrivial solution of the self-consistency equation [16]. Thus, the screened Coulomb repulsion between electrons may lead to superconducting ordering with an unconventional symmetry of the order parameter (different from the *s*-wave symmetry typical of the BCS model with attraction). It should be noted that, in the insulating (electron–hole) pairing channel, this interaction corresponds to the attraction between electron and hole, and it leads, in particular, to orbital antiferromagnetic ordering.

In the case of repulsion, the complete system of eigenfunctions of the operator of pairing interaction contains not less that two functions that are even with respect to the $\mathbf{k} \longrightarrow -\mathbf{k}$ transformation [16]. Therefore,

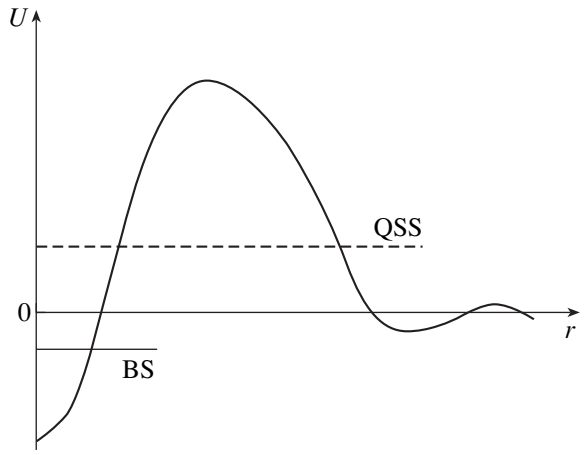

Fig. 2. Schematic pairing repulsive potential U as a function of the distance r between interacting particles. Solid and dashed lines show the energy levels of a bound state (BS) and a quasi-stationary state (QSS) of the pair.

the superconducting order parameter also has no less than two components (coefficients of expansion with respect to this system of functions). Note that, in the case of attractive pairing, it is sufficient to have only one eigenfunction (that corresponding to a single negative eigenvalue), as in the BCS model.

Figure 2 shows the shape of a repulsive potential U admitting the η_K-pairing, plotted as a function of the distance r between particles. Such a coordinate dependence takes place (owing to the Friedel oscillations) for a screened Coulomb potential in the degenerate electron system of a crystal. This potential also admits, in addition to a bound state of the η_K pair corresponding to the superconducting condensate, the appearance of quasi-stationary states of the η_K-pairs [17], which can exist (as noncoherent pair excitations) in a certain temperature interval above the superconducting transition temperature. Obviously, the attractive pairing does not admit such quasi-stationary states.

4. THE GINZBURG–LANDAU η_K FUNCTIONAL

The superconducting order parameter dependent on the momentum $\mathbf{k}$ of the relative motion of the pair can be conveniently expressed in a form explicitly reflecting the crystal symmetry. The kinematically allowed domain Ξ, in which the momentum $\mathbf{k}$ is defined, can be represented as a superposition of subdomains Ξ_j, each of these being the kinematically allowed domain for one of the crystallographically equivalent momenta $\mathbf{K}_j$ of the pair. In the case of a square lattice, where $\mathbf{K}_j$ is parallel to one of the symmetry axes, the index j runs from 1 to 4. For large $\mathbf{K}_j$, the subdomains Ξ_j are usually only slightly superimposed and their overlap can be ignored to the first approximation. In this approximation, solutions to the self-consistency equation can be independently obtained for each particular subdomain. These solutions $\Psi_j(\mathbf{k})$ are similar, differing only in the domains of variation of the momentum of relative motion.

The order parameter can be written in the form of a linear combination of $\Psi_j(\mathbf{k})$ functions:

$$\Psi(\mathbf{k}) = \sum_j \gamma_j \Psi_j(\mathbf{k}), \tag{4}$$

where the coefficients γ_j are normalized as $\sum_j |\gamma_j|^2 = 1$ and determined by the interaction mixing the momenta in various crystallographically equivalent kinematically allowed domains Ξ_j. Thus, these coefficients set a one-dimensional irreducible representation of the crystal symmetry group, according to which the order parameter is transformed.

For each momentum $\mathbf{K}_j$, we can determine a complete orthonormal system of eigenfunctions $\varphi_{sj}(\mathbf{k})$ of the operator of pairing interaction and expand the order parameter for the Ξ_j subdomain:

$$\Psi_j(\mathbf{k}) = \sum_s \Psi_s \varphi_{js}(\mathbf{k}). \tag{5}$$

The quantities Ψ_s are identical for all j and play the role of the order parameter components. The dependence of this parameter on the momentum of relative motion in Eq. (5) is fully described by the $\varphi_{js}(\mathbf{k})$ eigenfunctions, which are determined from Eq. (2) independently of the self-consistency equation. In the case of the simplest degenerate kernel $U_d(\mathbf{k} - \mathbf{k}')$ describing the screened Coulomb repulsion, there are two such components ($s = 1, 2$). It should be noted that the minimum number of the order parameter components necessary for the description of attractive pairing is one, whereas the description of repulsive pairing requires not less than two components.

The zero line of the order parameter separates the kinematically allowed domain into two parts, each part being a domain of constant sign for the $\Psi_j(\mathbf{k})$ function. The opposite signs of the order parameter in the regions on different sides from the zero line allow this parameter to be approximately described [30, 31] by setting the average values (with opposite signs) in the two parts of the kinematically allowed domain [16]. This approximate description formally corresponds to modification of the eigenfunctions used in expansion (5), whereby one of these functions (that with a positive eigenvalue) is set constant and the other (with a negative eigenvalue) is piecewise constant with a discontinuity on the zero line. Defined in this way, the eigenfunctions determine a new degenerate kernel, which approximately describes the screened Coulomb interaction [32]. The average values of the order parameter, which have different signs on the opposite sides of the zero line and represent real solutions of the self-consistency equa-

tion, turn out to be equivalent to two complex components, Ψ_1 and Ψ_2, provided that their relative phase is π.

Not restricting the consideration to this condition, that is, admitting complex solutions for the amplitudes $u_{\mathbf{k}}$ and $v_{\mathbf{k}}$ of the Bogoliubov transformation leading to the self-consistency equation, we can write the order parameter as

$$\Psi(\mathbf{k}) = \sum_s \Psi_s \varphi_s(\mathbf{k}), \tag{6}$$

where

$$\varphi_s(\mathbf{k}) = \sum_j \gamma_j \varphi_{js}(\mathbf{k}) \tag{7}$$

are the eigenfunctions of the operator of pairing interaction defined in the entire kinematically allowed domain Ξ. These functions reflect the full symmetry of the cuprate plane, and the coefficients γ_j determine an irreducible representation corresponding to the symmetry of the order parameter (6). Therefore, it is convenient to select the Bloch phase factor from these coefficients, such that $\gamma_j \longrightarrow \gamma_j \exp(-i\mathbf{K}_j \cdot \mathbf{R})$, where $\mathbf{R}$ is the radius vector of the center of mass of the pair and γ_j are numerical factors (independent of $\mathbf{R}$). Since the order parameter is a scalar function defined in the kinematically allowed domain Ξ of the Brillouin zone, its contravariant components with respect to $\varphi_s(\mathbf{k})$ must be written as

$$\Psi_s(\mathbf{R}) = \Psi_s^{(0)} \sum_j \gamma_j e^{i\mathbf{K}_j \cdot \mathbf{R}}. \tag{8}$$

In the case of a weak spatial inhomogeneity of the system, the quantities $\Psi_s^{(0)}$ determining the amplitude of the order parameter are slowly (on a unit cell scale) varying functions of $\mathbf{R}$. With respect to the symmetry properties, the order parameter written in the form (8) is analogous to that obtained in the Fulde–Ferrel–Larkin–Ovchinnikov generalized state.

The amplitudes $\Psi_1^{(0)}(\mathbf{R})$ and $\Psi_2^{(0)}(\mathbf{R})$ have the meaning of the components of a wavefunction describing the motion of the center of mass of the pair. These functions can be considered as components of the superconducting order parameter for the repulsive pairing in a system described within the framework of the macroscopic Ginzburg–Landau phenomenological scheme [15].

Both amplitudes, as functions of the temperature, simultaneously vanish at $T = T_s$, which is the temperature at which the superconducting order parameter (6) vanishes in the mean field approximation. In this context, it should be noted that the states of mixed symmetry such as $d_{x^2-y^2} + e^{i\theta}\chi$ (where χ is the contribution of states, e.g., with s-wave or d_{xy} symmetry, and θ is the relative phase of the order parameter components) correspond in the general case to different mean field temperatures for the phase transitions to the states with $d_{x^2-y^2}$ and χ symmetry. In particular, the phase transition can be absent for one of such states [33, 34].

In the case of attractive pairing, the superconducting phase transition in the BCS model corresponds to a single-component complex order parameter. The phase of this complex quantity reflects the establishment of phase coherence in the system of Cooper pairs upon spontaneous doubling of the charge of carriers, while the modulus is determined by the binding energy of the relative motion of the pair. Therefore, the second complex component of the order parameter in the case of repulsive pairing probably reflects the other degree of freedom related to the relative motion of the pair, for example, the appearance of a spontaneous orbital current. Then, the relative phase of the order parameter components determines the contribution of each degree of freedom (charge and current) to the superconducting order parameter.

The free energy density determining the Ginzburg–Landau functional can be represented as a sum of three components [15]:

$$f = f_0 + f_g + f_m. \tag{9}$$

The first term in the right-hand side is the expansion in powers of the order parameter, which can be written in the general case as

$$f_0 = \sum_{ss'} A_{ss'} \Psi_s^* \Psi_{s'} + \frac{1}{2} \sum_{ss'tt'} B_{ss'tt'} \Psi_s^* \Psi_{s'}^* \Psi_t \Psi_{t'}, \tag{10}$$

where matrices $A_{ss'}$ and $B_{ss'tt'}$ are functions of the temperature and the doping (which contain three and five independent components, respectively), and the indices numbering the order parameter components in the sums take the values 1 and 2. The second (gradient) term f_g in Eq. (9) can be written as [15]

$$f_g = \frac{\hbar^2}{4m} \sum_{ss'} [\hat{\mathbf{D}}\Psi_s]^\dagger M_{ss'} [\hat{\mathbf{D}}\Psi_{s'}], \tag{11}$$

where matrix $M_{ss'}$ is positive, depends on the temperature and doping, and has three independent components. The operator of covariant differentiation with respect to components of the radius vector $\mathbf{R}$ of the center of mass of the pair is as follows:

$$\hat{\mathbf{D}} = -i\nabla - \frac{2e}{\hbar c}\mathbf{A}, \tag{12}$$

where $\mathbf{A}$ is the vector potential determining the magnetic induction $\mathbf{B} = \operatorname{curl} \mathbf{A}$ averaged over the relative

motion of the pair. This term includes the contributions due to both an external field and the field related to the appearance of spontaneous currents. The third term f_m in Eq. (9) accounts for a change in the energy density of the medium upon the appearance of the magnetic field:

$$f_m = \mathbf{H} \cdot \mathbf{B}/8\pi, \quad (13)$$

where $\mathbf{H} = \mathbf{B}/\mu$ is the magnetic field strength and $\mu \approx 1$ is the magnetic permeability of the nonsuperconducting phase. Upon η_K-pairing, the matrices averaged over the relative motion of the pair, which determine contributions (10) and (11) to the free energy, are represented by integrals over the kinematically allowed domain corresponding to momenta $\mathbf{K}_j$ of the crystallographically equivalent pairs of the superconducting condensate [15].

The free energy is invariant with respect to the unitary transformation of the order parameter components, which is performed using 2×2 matrices of the SU(2) group. By specially selecting such a transformation, it is possible to diagonalize $A_{ss'}$ and $M_{ss'}$ matrices. Once this diagonalization is performed, the matrices in relations (10) and (11) can be expressed as $A_{ss'} = A_s\delta_{ss'}$ and $M_{ss'} = M_s\delta_{ss'}$, where A_s and M_s are functions of the temperature and the doping level.

The superconducting phase transition temperature $T_s(x)$ corresponding to the mean field approximation is determined from the condition $\det A_{ss'}(T, x) = 0$. After diagonalization of the $A_{ss'}$ matrix, this condition takes the form $A_1(T, x)A_2(T, x) = 0$. As was noted above, both components of the order parameter vanish at the same temperature. Therefore, it is necessary to provide that two conditions are simultaneously satisfied, $A_1(T, x) = 0$ and $A_2(T, x) = 0$, and this is precisely what takes place in the case of η_K-pairing under repulsive interaction condition [15]. Thus, we may assume that, near the phase transition line, $A_s(T, x) = -\tau_1 A_s^{(0)}(x)$, where $A_s^{(0)}(x)$ are positive functions of the doping level, $\tau_1 = (T_s - T)/T_s$, and it is assumed that $|\tau_1| \ll 1$. The $B_{ss'tt'}$ and $M_{ss'}$ matrices do not vanish at $T = T_s$. For this reason, it is possible to replace the argument T near the phase transition line by T_s and consider these matrices as functions of only the doping x. It should be emphasized that this approximation is acceptable only in cases when the superconducting transition temperature $T_C(x)$ coincides with the value $T_s(x)$ according to the mean field approximation. According to the existing notions, this coincidence takes place only in the overdoped region [1].

5. SPATIALLY HOMOGENEOUS η_K-STATES

In the absence of an external magnetic field and structural inhomogeneities, the state of the system with a long-range superconducting order is determined from the condition of minimum of the free energy density f_0. Complex components of the order parameter are characterized by their moduli (ψ_1, ψ_2), the relative phase β, and the phase Φ corresponding to the superconducting condensate, which is not included in expansion (10). Thus, we can write

$$\Psi_1 \equiv \psi_1 e^{i\Phi}, \quad \Psi_2 \equiv \psi_2 e^{i\beta} e^{i\Phi}. \quad (14)$$

A minimum of the free energy at $\tau_1 < 0$ corresponds to the obvious trivial solution $\psi_1 = \psi_2 = 0$ with indeterminate relative phase. At $\tau_1 > 0$, the problem has nontrivial solutions for which the thermal equilibrium values of parameters ψ_1, ψ_2, and β are determined by the elements of matrices $A_{ss'}$ and $B_{ss'tt'}$ (which depend on the doping) and, hence, are also the functions of x.

The ratio ψ_1/ψ_2 determining the degree of asymmetry of the order parameter is a continuous function of x. For this reason, in the qualitative investigation of the superconducting ordering, we may assume without loss of generality that $\psi_1 = \psi_2 \equiv \psi$. Thus, the problem of the free energy minimization is reduced to a variational problem with two unknowns (ψ and β). The free energy density (10) takes the form

$$f_0 = a_1\psi^2 + \frac{1}{2}(B + 2C\cos\beta + D\cos^2\beta)\psi^4, \quad (15)$$

where $a_1 = A_1 + A_2 \equiv -a\tau_1$, $B \equiv B_{1111} + 2B_{1122} + B_{2222}$, $C = 2(B_{1112} + B_{1222})$, and $D = 4B_{1122}$. Here, the coefficients $a \equiv A_1^{(0)} + A_2^{(0)}$, B_{1111}, B_{1122}, and B_{2222} are definitely positive, while B_{1112} and B_{1222} may have any sign. For certainty, we assume $C > 0$ (this choice does not influence the qualitative conclusions concerning the character of superconducting states admitted for the free energy (15).

Investigation of the extrema of function (15) showed that a minimum of the free energy for $\tau_1 < 0$ (i.e., for $T > T_s$) corresponds to the solution $\psi = 0$ at an arbitrary relative phase. For $\tau_1 > 0$ ($T < T_s$), the minimum is attained at $\beta = \pi$ and $\psi \neq 0$ provided that $C \geq D$. In the opposite case ($C \leq D$), a nontrivial solution $\psi \neq 0$ corresponds to the relative phase $\beta \leq \pi$ determined from the relation $\cos\beta = -C/D$.

Since the coefficients C and D are functions of the doping x, the equality $C(x) = D(x)$ can be considered as the equation determining the doping $x = x_0$ at which the system exhibits a qualitative change in the superconducting order. Let us denote $C/D = c(x)$ and expand this function in a small vicinity of the point $x = x_0$ as

$$c(x) = 1 + c'(x_0)(x - x_0). \quad (16)$$

Assuming that a superconducting state with the relative phase $\beta = \pi$ corresponds to $x > x_0$, we obtain $c'(x_0) > 0$. Then, for $x < x_0$, the relative phase is $\beta(x) < \pi$ and β is

a continuous function $\beta(x)$, such that $\beta(x) \longrightarrow \pi$ for $x \longrightarrow x_0$.

The order parameter, which can be used to distinguish the thermal equilibrium superconducting phases with $\beta < \pi$ (β phase) and $\beta = \pi$ (π phase), is naturally defined as $\alpha = \pi - \beta$. Then, for $x > x_0$ we have $\alpha = 0$, while for $x < x_0$ we have $\alpha \neq 0$ (under the above assumption that $C > 0$ the order parameter falls within $0 < \alpha < \pi/2$). In the vicinity of the transition ($x = x_0$), the order parameter α is small and the free energy density can expanded in even powers of α as

$$f_0 = f_\pi + \frac{1}{2}Dc'(x_0)(x - x_0)\psi^4\alpha^2 + \frac{1}{8}D\psi^4\alpha^4. \quad (17)$$

Here, $f_\pi = -a\tau_1\psi^2 + (B - D)\psi^4/2$ is the free energy density of the π phase.

A minimum of the free energy is reached for $\alpha = 0$, provided that $c'(x_0)(x - x_0) > 0$ (which corresponds to the π phase, $x > x_0$), and for

$$\alpha^2 = 2c'(x_0)(x_0 - x), \quad (18)$$

provided that $c'(x_0)(x - x_0) < 0$ (which corresponds to the β phase, $x < x_0$). The square modulus of the equilibrium order parameter in a small vicinity of the phase transition point ($x = x_0$) is $\psi^2 = a\tau_1/(B - D)$. Then expression (17) for the free energy density of the β phase can be written as

$$f_0 \equiv f_\beta = f_\pi - \nu\tau_1^2(x - x_0)^2, \quad (19)$$

where $\nu = a^2D/(B - D)^2 > 0$.

6. THE η_K-PAIRING AND SPONTANEOUS CURRENTS

Real components of the order parameter with different signs (corresponding to the relative phase $\beta = \pi$) necessarily appear in the case of superconducting pairing under repulsive interaction [16]. Deviation of the relative phase from π corresponds to a solution of the self-consistency equation with complex coherence factors and admits a quite clear interpretation. Indeed, a change in the phase of the operator of annihilation of an electron with spin $\sigma = \uparrow, \downarrow$ at a lattice site with the radius vector $\mathbf{n}$ can be related [35] to the vector potential of a certain magnetic field $\mathbf{A}(\mathbf{n})$:

$$\hat{c}_{\mathbf{n}\sigma} \longrightarrow \hat{c}_{\mathbf{n}\sigma}\exp\left[i\frac{e}{\hbar c}\mathbf{A}(\mathbf{n})\cdot\mathbf{n}\right]. \quad (20)$$

Then, the phase $\beta(\mathbf{n}, \mathbf{n}')$ of the anomalous average $\langle\hat{c}_{\mathbf{n}\uparrow}\hat{c}_{\mathbf{n}'\downarrow}\rangle$ (determining the superconducting order parameter) in the lattice site representation can be written as

$$\beta(\mathbf{n}, \mathbf{n}') = \pi - \frac{e}{\hbar c}[\mathbf{A}(\mathbf{n})\cdot\mathbf{n} + \mathbf{A}(\mathbf{n}')\cdot\mathbf{n}']. \quad (21)$$

Expressing $\mathbf{n}$ and $\mathbf{n}'$ via the radius vector of the center of mass $\mathbf{R} = (\mathbf{n} + \mathbf{n}')/2$ and the radius vector of relative motion $\mathbf{r} = \mathbf{n} - \mathbf{n}'$ and substituting the obtained expressions into formula (21), it is possible to separate a contribution to the phase of the superconducting condensate that depends only on $\mathbf{R}$: $\Phi(\mathbf{R}) = (2e/\hbar c)\mathbf{A}(\mathbf{R})\cdot\mathbf{R}$. This contribution does not influence the free energy density expansion (10).

The additive to $\Phi(\mathbf{R})$ in Eq. (21), which depends only on the radius vector of relative motion, determines the relative phase α of the order parameter components. Near the phase transition point ($x = x_0$), where $\alpha \ll 1$, we obtain an estimate

$$\alpha \approx -\frac{e}{2\hbar c}\frac{\partial A_k}{\partial x_l}x_k x_l, \quad (22)$$

where repeated indices of the 2D coordinates x_k of the radius vector $\mathbf{r}$ of relative motion imply summation and take the values 1 and 2.

We may suggest that deviation of the phase of the superconducting order parameter from π, which is a natural consequence of η_K-pairing, is related to orbital antiferromagnetic ordering. This ordering is manifested in the superconducting state by antiferromagnetically correlated orbital current circulations [11] and can survive at temperatures above the superconducting transition temperature in the form of a long-range [2] or short-range [14] orbital antiferromagnetic order. In this case, a real magnetic field in (22), which is related to the orbital currents, can be considered as a gauge field establishing correlation between superconducting and orbital antiferromagnetic degrees of freedom (ψ and α, respectively). This field is analogous to the gauge field introduced into the Ginzburg–Landau functional, for example, in a boson variant of the scheme of charge and spin separation [36].

The order parameter (6) has a spatial structure corresponding to a separation of the cuprate plane into cells with a period of $2\pi/\mathbf{K}_j$ (in the general case, incommensurate). The directions of orbital current circulations in the neighboring cells must be opposite. In the Ginzburg–Landau phenomenology, it is implied that the order parameter is averaged over the relative motion of the pair. Therefore, taking into account the checkerboard order in the distribution of orbital currents, the mean square (within the cell) value of the orbital antiferromagnetic order parameter can be estimated as

$$\alpha^2 \simeq \frac{\pi^2}{2}\left(\frac{e}{2\hbar c}\right)^2\frac{B^2}{K_j^2}, \quad (23)$$

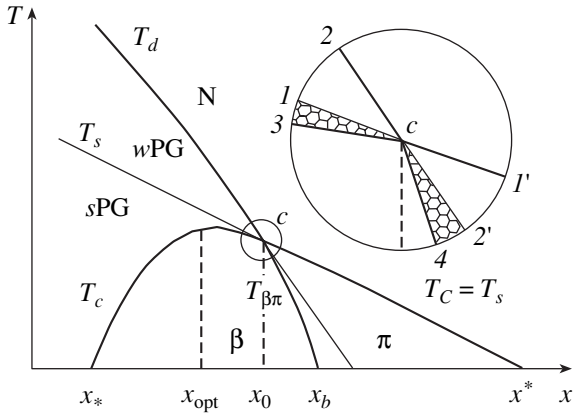

Fig. 3. The region of the phase diagram corresponding to the existence of an orbital antiferromagnetic and superconducting phases in the vicinity of the tetracritical point *c*. Thick solid curves show the lines of phase transitions. The inset shows the vicinity of the tetracritical point on a greater scale: sectors *1c3* and *4c2'* corresponds to the region of developed fluctuations of superconducting pairs and the region of orbital currents, respectively.

where B is the cell-average magnetic induction of the field of orbital currents.

The appearance of orbital currents in the superconducting state implies that the Ginzburg–Landau functional must take into account the contribution due to the energy of the magnetic field of these currents. In expression (13), which describes the magnetic field effect on the free energy density, this contribution $f_m(\alpha)$ (which is external with respect to the charge degree of freedom ψ) is formally taken into account provided that **B** denotes the magnetic induction due to the field of orbital currents.

One can readily check that simple addition of a term of the $f_m(\alpha) = \kappa\alpha^2$ type with a positive coefficient κ to f_0 excludes the possibility of the appearance of a minimum in the free energy density $f_0 + f_m(\alpha)$ for $\alpha \neq 0$. This fact naturally implies the necessity of considering a competition between the two channels of pairing: superconducting η_K-pairing versus insulating orbital-antiferromagnetic pairing with the order parameter α. In the Ginzburg–Landau η_K functional (9), this order parameter is manifested by a current degree of freedom in the two-component order parameter.

7. COMPETITION OF THE SUPERCONDUCTING AND ORBITAL-ANTIFERROMAGNETIC CHANNELS OF PAIRING

Spontaneous orbital currents can also arise in the absence of a superconducting order. The corresponding insulating orbital antiferromagnetic order in a 2D system is characterized by a single parameter, which has the meaning of a modulus of the difference of magnetizations of two sublattices of an orbital antiferromagnet. This difference is proportional to α. In the absence of superconductivity, the free energy density in the vicinity of the orbital antiferromagnetic phase transition can be represented as the expansion in even powers of α:

$$f_d = a_2\alpha^2 + \frac{1}{2}b_2\alpha^4, \tag{24}$$

where b_2 is a positive function of the doping x and a_2 is a coefficient (also dependent on the doping x), which vanishes at the insulating phase transition temperature $T_d(x)$ corresponding to the mean field approximation. In the vicinity of the phase transition, the latter coefficient can be expressed as $a_2 = -a'\tau_2$, where a' is a positive function of x and $\tau_2 = (T_d - T)/T_d$ (it is assumed that $|\tau_2| \ll 1$). Note that the energy of the magnetic field of spontaneous currents $f_m(\alpha)$ proportional to α^2, which enters into the Ginzburg–Landau η_K functional, is naturally included into the first term in expression (24) thus simply redefining the temperature $T_d(x)$ of the insulating phase transition.

A relationship between the two types of ordering is established in the same natural manner. Still restricting the consideration to a spatially homogeneous case in the absence of external magnetic fields (whereby both ψ and α are independent of the radius vector **R** of the center of mass), we must retain only the contribution due to the field of spontaneous orbital currents in the gradient term (11) in the Ginzburg–Landau η_K functional. The vector potential **A** of this field is proportional to α. In the spatially inhomogeneous system under consideration, the gradient component f_g contains only the vector potential related to the field of spontaneous orbital currents. Then, as can be seen from Eq. (11), the gradient term averaged over the relative motion of the pair can be expressed as $f_{12} = b_{12}\psi^2\alpha^2$, where b_{12} is a phenomenological parameter dependent on the doping x. Under the assumption that $\psi \ll 1$ and $\alpha \ll 1$, the contribution of f_{12} to the free energy density is of the fourth order of smallness.

Thus, an expression for the free energy density, which describes the competition of the superconducting and orbital-antiferromagnetic ordered states has (to within fourth-order terms) the following form:

$$f = a_1\psi^2 + a_2\alpha^2 + \frac{1}{2}b_1\psi^4 + b_{12}\psi^2\alpha^2 + \frac{1}{2}b_2\alpha^4. \tag{25}$$

The free energy density expansion (25) is valid in a small vicinity of both phase transitions, that is, in a relatively small region of the phase diagram where the curves $T_s(x)$ and $T_d(x)$ either intersect or pass very closely to each other.

The doping leads to suppression of both the orbital antiferromagnetism and the superconductivity. The

temperatures of the corresponding phase transitions, $T_d(x)$ and $T_s(x)$, determined in the mean field approximation in the absence of coupling between the orbital-antiferromagnetic and superconducting ordered states (i.e., for $b_{12} = 0$ in expansion (25)) are naturally considered as monotonically decreasing functions of x. Taking into account the features of the typical phase diagram of cuprates (Fig. 1), we may suggest that the orbital antiferromagnetic state, which dominates for small x, in weakly doped cuprates is suppressed with increasing x more rapidly than the superconducting order, which makes possible the intersection of $T_s(x)$ and $T_d(x)$ curves at a certain point. According to formula (19), this point corresponds to $x = x_0$ (Fig. 3, point c). It should be noted that we might also assume that, in the case of weak doping, $T_s > T_d$, but this assumption leads to a phase diagram that is qualitatively different from that depicted in Fig. 1. Since the expansion of the free energy density (25) is valid only in a small vicinity of the point c of intersection of these curves (circled and presented on a greater scale in the inset in Fig. 3), the continuation of lines beyond this small region is rather conditional.

For $T > \max(T_d, T_s)$, the free energy minimum is attained at $\psi = 0$ and $\alpha = 0$ (sector *2c1'* in Fig. 3), which corresponds to the normal phase. The *2c* segment of the boundary of this sector is the line of a phase transition from the normal to orbital antiferromagnetic phase (α phase). In the latter phase, $\psi = 0$ and $\alpha = -a_2/b_2$. The insulating α phase exists inside sector *2c3*, a part (*1c3*) of which occurs in the region of temperatures below $T_s(x)$. The lower boundary (segment *c3*) of sector *2c3* is determined by the condition $b_2a_1 - b_{12}a_2 = 0$, The *c1'* segment of the boundary of the normal phase is the line of a phase transition from the normal to superconducting π phase corresponding to sector *1'c4*. A part (*2'c4*) of this sector occurs in the region of temperatures below $T_d(x)$. The *3c4* sector, where

$$\psi^2 = -\frac{b_2a_1 - b_{12}a_2}{b_1b_2 - b_{12}^2}, \quad \alpha^2 = -\frac{b_1a_2 - b_{12}a_1}{b_1b_2 - b_{12}^2}, \qquad (26)$$

corresponds to the superconducting β phase, where the superconductivity coexists with the spontaneous orbital antiferromagnetism. It should be noted that, for $b_{12} = 0$, the dielectric α phase, superconducting π phase, and superconducting β phase would correspond to sectors *2c1*, *1'c2'*, and *1c2'*, respectively.

The superconducting transition temperature $T_C(x)$ is represented by line *3c1'*, in which segment *c1'* corresponds to a transition from the normal to superconducting (π) phase at temperature $T_C(x) \equiv T_s(x)$, and segment *3c*, to a transition from the orbital antiferromagnetic to superconducting (β) phase at a temperature

$$T_C = T_s\frac{1-\lambda}{1-\lambda T_s/T_d}, \qquad (27)$$

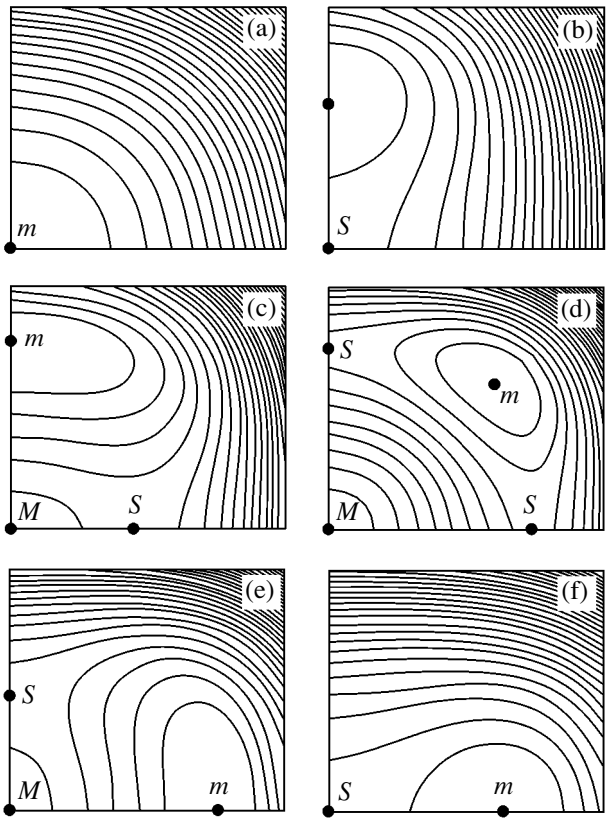

Fig. 4. The topology of free energy isolines in the coordinates of ψ (horizontal axis) versus α (vertical axis) showing sectors of the phase diagram in the vicinity of the tetracritical point c (Fig,. 1): (a) *2c1'*; (b) *2c1*; (c) *1c3*; (d) *3c4*; (e) *4c2'*; (f) *2'c1'*. Black points indicate maxima (*M*), minima (*m*), and saddle points (*S*) of the free energy.

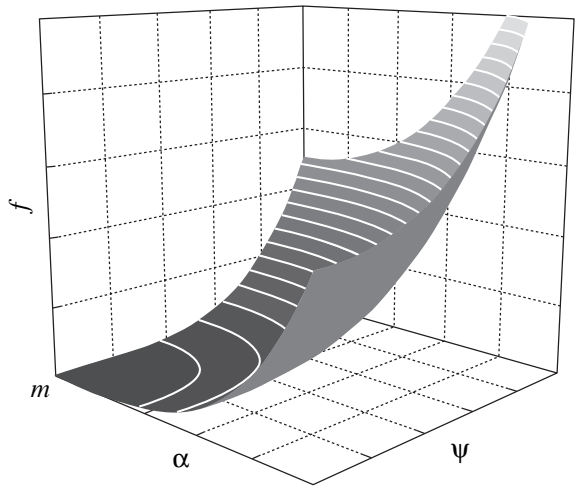

Fig. 5. Free energy density of the normal phase with the minimum (*m*) corresponding to $\psi = \alpha = 0$.

where $\lambda = b_{12}a'/b_2a$. This temperature is lower than $T_s(x)$ and (since we have $T_s > T_d$ for $x > x_0$) the $T_C(x)$ function exhibits bending at point c, which implies that there is a tendency of the transition temperature to

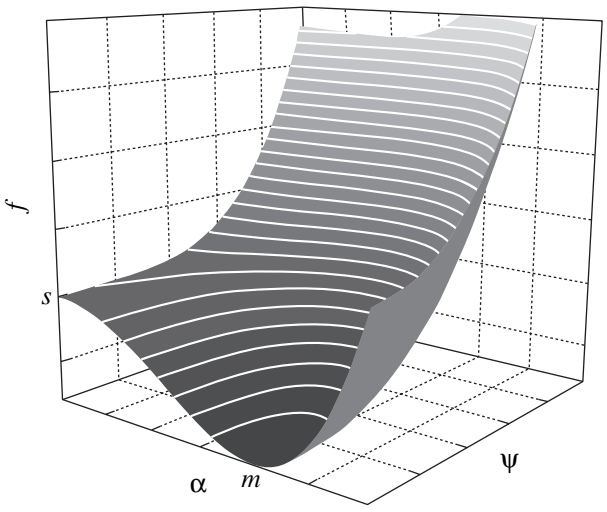

Fig. 6. Free energy density of the α phase with the minimum (*m*) shifted from the origin along the α axis and a saddle point (*s*) nucleating at the origin.

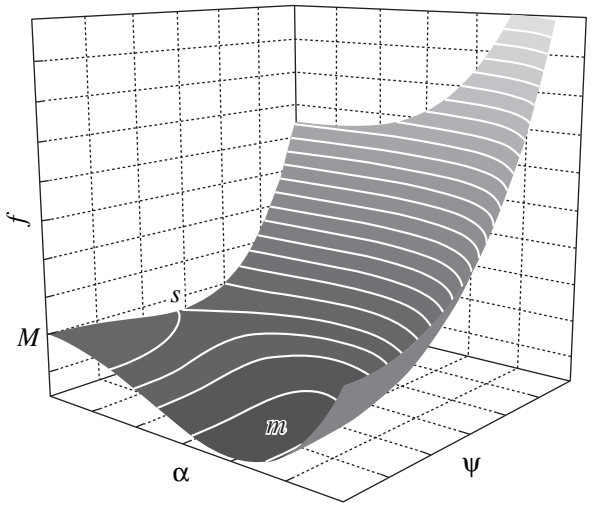

Fig. 7. Free energy density in the region of developed fluctuations in the α phase with a saddle point (*s*) shifted from the origin along the ψ axis.

decrease as compared to the mean field temperature $T_s(x)$.

Line *c4* corresponding to a phase transition between the two superconducting states, $\pi \longleftrightarrow \beta$, determines the temperature

$$T_{\beta\pi} = T_d \frac{1-\lambda'}{1-\lambda' T_d/T_s}, \qquad (28)$$

where $\lambda' = b_{12}a/b_1a'$. The $T_{\beta\pi}(x)$ function of doping *x*, corresponds to a line originating from point *c* and terminating at a certain point $x = x_b$ on the *x* axis. Thus, point *c* in Fig. 3 is a tetracritical point at which four lines of phase transitions intersect [37].

Figure 4 shows the topology of the free energy isolines $f(\psi, \alpha) = \text{const}$. In sector *2c1'* corresponding to the normal phase, the free energy density has a minimum at $\psi = 0$ and $\alpha = 0$ (Fig. 5). Upon crossing line *2c* and passage to the α phase, this minimum shifts along the α axis to the point ($\psi = 0$, $\alpha = \sqrt{-a_2/b_2}$) (Fig. 6). However, this minimum is a single special point on the free energy surface only in the upper part (sector *2c1*) of the domain of existence of the insulating α phase (sector *2c3*), rather than in the entire domain. Indeed, on crossing line *1c* and passing to the minimum determining a thermal stable insulating state, there appears a saddle point at ($\psi = \sqrt{-a_1/b_1}$, $\alpha = 0$), where the free energy has a minimum with respect to variable ψ at $\alpha = 0$ (Fig. 7). Sector *3c4* (β phase) corresponds to the region of existence of the orbital antiferromagnetism and superconductivity. The free energy density (Fig. 8) has an absolute minimum at a certain point ($\alpha \neq 0$, $\psi \neq 0$) and two saddle points (one on each axis). On line *c4* of the phase transition $\beta \longrightarrow \pi$, the minimum coincides with one of the saddle points (that occurring on the ψ axis), while on crossing line *c2'*, the other saddle point (on the α axis) shifts to the origin (see Figs. 7 and 6, where the coordinate axes should be interchanged $\psi \longleftrightarrow \alpha$).

In the vicinity of the tetracritical point, the states in sector *1c3* (see the inset to Fig. 3) corresponding to the absolute minimum and the saddle point have close values of the free energy. For this reason, there is a rather large probability of the fluctuational appearance of noncoherent, long-lived quasi-stationary states of superconducting pairs with a relative phase of π. These states correspond to the saddle point at ($\psi = \sqrt{-a_1/b_1}$, $\alpha = 0$) in the temperature interval $T_C(x) < T < T_s(x)$. The decay of such a quasi-stationary state, which is accompanied

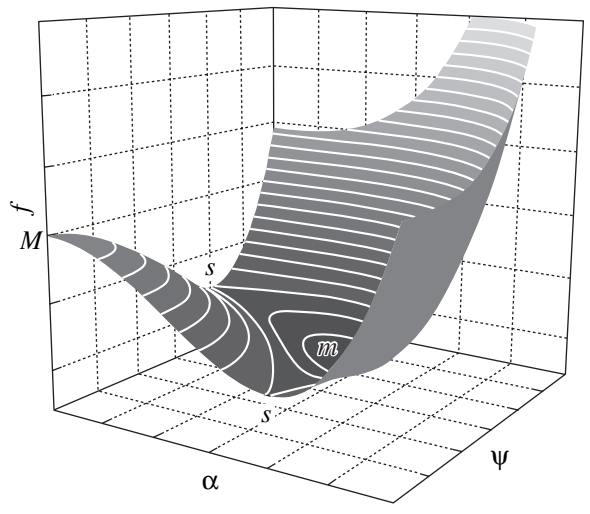

Fig. 8. Free energy density of the β phase with the minimum (*m*) at $\alpha \neq 0$, $\psi \neq 0$ and the saddle points (*s*) on both axes. The appearance of a local maximum at the origin is related to the nucleation of the second saddle point.

by a decrease in the modulus of the superconducting order parameter from $\psi = \sqrt{-a_1/b_1}$ to $\psi = 0$ while the relative phase increases from zero to an equilibrium value of $\alpha = \sqrt{-a_2/b_2}$, can be considered equivalent to the appearance of uncorrelated pairs of the oppositely oriented circular currents or the vortex–antivortex pairs [38]. Intermediate states in the process of decay of the aforementioned quasi-stationary states are fluctuational states of the β phase belonging to the same (or close) isolines passing from the vicinity of a saddle point to the vicinity of the absolute minimum of the free energy.

Thus, the temperature $T_s(x)$ for $x < x_0$ (Fig. 3, line *1c*) bounding from above the region of developed fluctuations of the modulus of the superconducting order parameter is not related to any phase transition. This line can be considered as the upper boundary of a region in the phase diagram, where the appearance and decay of the quasi-stationary superconducting pairs with a relative phase of π lead to the existence of orbital vortex currents. Such currents may lead to a significant enhancement of the Nernst effect observed in cuprates in the region of a strong pseudogap [39]. For this reason, the temperature $T_s(x)$ for $x < x_0$ can be interpreted as a crossover bounding this region from above: $T_s(x) \approx T^*_{str}(x)$. It should be noted that a strong pseudogap can extend to the region of ultimately weak doping ($x < x_*$).

For $x_* < x < x_0$, a phase transition from the insulating α phase to a superconducting phase can be formally described using a single order parameter ψ, provided that $\tau = (T_C - T)/T_C$ is small ($|\tau| \ll 1$). Substituting an equilibrium value of the relative phase α given by formula (26) into Eq. (25) yields an expansion of the free energy density in powers of ψ:

$$f_s = -\frac{1}{2}\frac{a_2^2}{b_2} + \left(a_1 - \frac{b_{12}a_2}{b_2}\right)\psi^2 + \frac{1}{2}b_1\psi^4. \qquad (29)$$

In the vicinity of the $\alpha \longleftrightarrow \beta$ phase transition line, we can assume that $(a_1 - b_{12}a_2/b_2) = -\tilde{a}\tau$, where $\tilde{a} = a - b_{12}a'/b_2$ is a positive function of x. The coefficient at ψ^2 in the expansion of the free energy density (29) is determined by the value of $\tilde{a} < a$, because the phase transition temperature T_C for $x_* < x < x_0$ is lower than the temperature T_s corresponding to the mean field approximation (T_s coincides with T_C only in the region of overdoping, $x_0 < x < x^*$). Since it is the coefficient at ψ^2 that determines the slope of the free energy surface in the vicinity of the minimum, we may conclude that, on going from the tetracritical point to the region of weak doping via sector *3c4* (corresponding to the β phase), there is a tendency toward an increase in fluctuations of the superconducting order parameter ψ. This conclusion can be considered as evidence for the fact that the mean field approximation with a single-component order parameter does not provide an adequate description of the superconducting phase transition in the region of underdoping on the phase diagram. On the contrary, a two-component order parameter, which naturally follows from the concept of η_K-pairing and takes into account both the charge and current degrees of freedom, unavoidably leads to the pattern of developed fluctuations of the order parameter.

On going from the normal phase (Fig. 3, sector *2c1'*) to the π phase (sector *1'c4*) across line *c1'*, the free energy minimum shifts from the point ($\psi = 0$, $\alpha = 0$) to the point ($\psi = \sqrt{-a_1/b_1}$, $\alpha = 0$). This minimum is the absolute one in the entire domain of existence of the π phase (sector *1'c4*), but an additional special point—a saddle point with the coordinates $\psi = 0$, $\alpha = \sqrt{-a_2/b_2}$ appears in sector *2'c4* (see the inset to Fig. 3). In the vicinity of the tetracritical point, the free energy at the absolute minimum and at the saddle point in this sector has close values and, hence, there is a rather large probability of the fluctuational appearance of quasi-stationary orbital vortex currents. The decay of such quasi-stationary states, whereby the relative phase of the order parameter decreases from $\alpha = \sqrt{-a_2/b_2}$ at the saddle point to $\alpha = 0$ while the modulus of the order parameter increases from zero to an equilibrium value of $\psi = \sqrt{-a_1/b_1}$, proceeds via states with $\alpha \neq 0$ and $\psi \neq 0$, that is, via nonequilibrium states of the β phase. For $x_0 < x < x^*$, the temperature $T_s(x)$ corresponding to the mean field approximation is the temperature of the phase transition from the normal phase to the superconducting π phase, so that $T_s(x) = T_C(x)$. For this reason, the superconducting phase transition from the normal phase to the π phase in the region of overdoping on the phase diagram can be satisfactorily described within the framework of the Landau theory of phase transitions with a single-component order parameter and, hence, this transition exhibits features of the phase transitions according to the BCS theory.

It should be noted that the level of optimum doping formally determined from the position of maximum of the $T_C(x)$ curve is definitely lower than the doping corresponding to the tetracritical point: $x_{opt} < x_0$. For this reason, line *c4* (corresponding to the lower boundary of the π phase) that continues to the region of low temperatures terminates at a certain point with $x = x_b$, where $x_0 < x_b < x^*$. For this reason, the further decrease in the temperature upon the phase transition from the normal phase to the π phase in the doping interval $x_0 < x < x_b$ results in the system falling into the region of developed fluctuations manifested by quasi-stationary orbital vortex currents, after which the system exhibits a phase transitions at $T = T_{\beta\pi}(x)$ between the two superconducting states: the π phase and the β phase, where the superconductivity coexists with the orbital antiferromagnetism. This phase transition in the superconducting state can be detected, for example, as an anomaly in the

temperature dependence of the heat capacity. At the phase transition temperature $T_{\beta\pi}(x)$, the modulus of the order parameter ψ remains continuous, while the relative phase α changes between zero in the π phase and a nonzero value at $T < T_{\beta\pi}(x)$.

In concluding this section, we will outline in accordance with [40] the hierarchy of the symmetry groups of various phases in the vicinity of the tetracritical point. If the cuprate plane has a square lattice with a 2D crystal class $G = C_{4v}$, then the extended point symmetry group of the most symmetric normal phase is given by the direct product $G_N = G \times R \times U(1)$, where R is the group comprising the identical transformation and the transformation of time reversal (changing the directions of currents to the opposite) and $U(1)$ is the group of gauge transformations.

A transition from the normal to the insulating π phase corresponds to the loss of the gauge symmetry, so that a point symmetry group of the π phase corresponds to the nonmagnetic crystal class $G_\pi = G \times R$.

A transition from the normal to the insulating α phase, which is accompanied by the development of spontaneous orbit vortex currents, leads to the loss of some crystal symmetry. The new symmetry corresponds to group H, which is an index 2 subgroup of group G. The point symmetry group of the α phase corresponds to the superconducting magnetic crystal class with a variety of elements $G_\alpha = (H + RgH) \times U(1)$, where g is an element of G not belonging to H.

The loss of the gauge symmetry upon the transition from the α phase to the β phase results in that the new point symmetry group of the β phase corresponds to the magnetic class $G_\beta = H + RgH$. Group G_β is simultaneously a subgroup of G_α and G_π, which, in turn, are the subgroups of G_N.

Group $G = C_{4v}$ has two index 2 subgroups: $H = C_4$ and $H = C_{2v}$. However, the first of these possibilities corresponds to the ferromagnetic crystal class $C_{4v}(C_4)$, while the second variant corresponds to the antiferromagnetic class $C_{4v}(C_{2v})$ exactly reflecting the current distribution in a 2D flux phase.

8. AN η_K SUPERCONDUCTOR IN A MAGNETIC FIELD

An external magnetic field with the induction $\mathbf{B} = \mathrm{curl}\,\mathbf{A}$ is, like the vector potential $\mathbf{A}$ of this field, a slowly varying (on the scale of interatomic distances) function of the spatial coordinates and can be readily included into the general definition (9) of the Ginzburg–Landau functional. In addition, the free energy density (24) of the orbital antiferromagnet must be supplemented by a term dependent on $\mathbf{B}$ (besides a change in the free energy density related to the external magnetic field, $f_m(\alpha)$, already entering into this functional). Separating a contribution due to the spontaneous orbital currents from the vector potential, the magnetic field energy density f'_m can be expressed as

$$f'_m = \kappa\alpha^2 + \mathbf{H}\cdot\mathbf{B}/8\pi. \tag{30}$$

Here and below, the notation $\mathbf{A}$, $\mathbf{B} = \mathrm{curl}\,\mathbf{A}$, and $\mathbf{H}$ refers to the external magnetic field. The first term in formula (30) is related to the spontaneous currents and has to be combined with the first term in the free energy density (24) of the orbital antiferromagnet. The terms linear in $\mathbf{B}$ (as well as in $\mathbf{A}$) are eliminated because determination of the order parameter in the Ginzburg–Landau phenomenology implies averaging over the relative motion of η_K-pair.

In a similar manner, we can transform the gradient term (1) to $f_g = b_{12}\psi^2\alpha^2 + f'_g$, where

$$f'_g = \frac{\hbar^2}{4m}\sum_s M_s\left|\hat{\mathbf{D}}\Psi_s\right|^2. \tag{31}$$

It is assumed that matrix $M_{ss'}$ entering into the definition of (11) is diagonalized together with $A_{ss'}$ in (10); in defining the operator of covariant differentiation (12), we take into account only the vector potential of the external magnetic field.

In supplementing the free energy of the orbital antiferromagnet with a term dependent on the external magnetic field, note that the orbital antiferromagnetic order parameter in the case of two antiferromagnetic sublattices (to which the consideration here is restricted) has the form of $\mathbf{L} = \mathbf{M}_1 - \mathbf{M}_2$, where $\mathbf{M}_1$ and $\mathbf{M}_2$ are the magnetizations of sublattices (with equal moduli in the absence of an external field [41]). Since these magnetizations are related to the orbital currents circulating in the cuprate plane, both $\mathbf{M}_1$ and $\mathbf{M}_2$ (and, hence $\mathbf{L}$) are perpendicular to this plane. Therefore, in 2D systems such as cuprate compounds, the orbital antiferromagnetic order parameter can be determined by setting a single quantity (i.e., $L = |\mathbf{L}|$) which, in accordance with the adopted interpretation of the relative phase of the superconducting order parameter, must be proportional to α ($L \propto \alpha$). The angle θ between $\mathbf{L}$ and $\mathbf{B}$ is not a variable parameter, since it is simply determined by the orientation of the external magnetic field with respect to the cuprate plane normal. Thus, we obtain two scalar combinations of the $\mathbf{L}$ and $\mathbf{B}$ vectors—L^2B^2 and $(\mathbf{L}\cdot\mathbf{B})^2$, which are of the fourth order of smallness—entering into the free energy of the antiferromagnet, which can be written as

$$f_d = d\alpha^2 B^2. \tag{32}$$

Here, $d = d_1 + d_2\cos^2\theta$ is a phenomenological parameter determined by the two positive functions of the doping, $d_1(x)$ and $d_2(x)$.

The free energy acquires the following form:

$$F = \int d^3R\left[\sum_s \frac{\hbar^2 M_s}{4m}\left|\hat{\mathbf{D}}\Psi_s\right|^2 + f + p(\alpha)B^2\right], \quad (33)$$

where $p(\alpha) = (\mu^{-1} + 8\pi d\alpha^2)/8\pi$ and f is given by relation (25). In this equation, the vector potential of the external field and the parameters ψ and α are variable functions of the radius vector $\mathbf{R}$ of the center of mass of the pair, which are slowly varying on the scale of the unit cell.

Variation of the free energy functional with respect to the vector potential leads to the following equation:

$$\frac{2e^2 M}{mc^2}\psi^2\mathbf{A}' + 2p(\alpha)\mathrm{curl}\,\mathrm{curl}\mathbf{A}' + 4d\alpha[\nabla\alpha\times\mathrm{curl}\mathbf{A}'] = 0, \quad (34)$$

where $M = M_1 + M_2$ is the trace of the matrix, the vector potential is determined to within a gauge transformation, $\mathbf{A}' = \mathbf{A} - (\hbar c/2e)\nabla\Phi$, and Φ is the phase of the superconducting condensate.

Variation of the functional (33) with respect to ψ and α yields two additional equations:

$$\frac{\hbar^2}{4m}M\left(i\nabla + \frac{2e}{\hbar c}\mathbf{A}'\right)^2\psi + a_1\psi + b_1\psi^3 + b_{12}\alpha^2\psi + \frac{\hbar^2}{4m}M_2(\nabla\alpha)^2\psi = 0, \quad (35)$$

$$-\frac{\hbar^2}{4m}M_2(\psi^2\nabla^2\alpha + 2\psi\nabla\psi\nabla\alpha) + a_2\alpha + b_2\alpha^3 + b_{12}\psi^2\alpha + d\alpha(\mathrm{curl}\mathbf{A}')^2 = 0. \quad (36)$$

Equations (34)–(36) constitute a complete system of the Ginzburg–Landau equations describing the competition and coexistence of the η_K and orbital-antiferromagnetic ordered states in the vicinity of the tetracritical point.

Even under the aforementioned simplifying assumptions, the system of equations (34)–(36) is much more complicated than a system of two equations describing a conventional superconductor in an external magnetic field. For this reason, consideration will be restricted to some simplest consequences of Eqs. (34)–(36).

In the absence of ordering ($\psi = 0$, $\alpha = 0$), Eq. (34) shows that μ has a meaning of the magnetic permeability of the normal phase: $\mu = \mu_N = 1 + 4\pi\chi_N$, where χ_N is the magnetic susceptibility of the normal phase.

A homogeneous state of the α phase in a magnetic field corresponds to an order parameter defined as

$$\alpha^2 = -(a_2 + dB^2)/b_2. \quad (37)$$

Then, the magnetic susceptibility of the α phase in a magnetic field can be expressed as

$$\chi_\parallel^{(\alpha)} \approx \chi_N + \frac{2(d_1 + d_2)}{b_2}a_2, \qquad \chi_\perp^{(\alpha)} \approx \chi_N + \frac{2d_1}{b_2}a_2, \quad (38)$$

where $\chi_\parallel^{(\alpha)}$ ($\chi_\perp^{(\alpha)}$) is the longitudinal (transverse) magnetic susceptibility of the α phase relative to the applied magnetic field. Note that, in writing relations (37), we took into account that the magnetic permeabilities of the normal and α phases only slightly differ from unity in the vicinity of the tetracritical point (where $a_2 = -a'\tau^2 < 0$ and $\tau_2 \ll 1$): $\mu_N \approx \mu_\alpha \approx 1$. Since $|\chi_N| \ll 1$, the transition from a paramagnetic normal phase to a state of the α phase with giant diamagnetism (observed in the region of a strong pseudogap in the magnetic field [42]) takes place at the temperature

$$\tilde{T}_d = T_d(1 - b_2\chi_N/2\tilde{d}a'), \quad (39)$$

where $\tilde{d} = d_1 + d_2$ for the magnetic field oriented across the cuprate plane and $\tilde{d} = d_1$ for the field parallel to this plane.

For the superconducting π phase ($\psi \neq 0$, $\alpha = 0$), Eqs. (34) and (35) lead to the usual Meissner effect. The depth of the magnetic field penetration into the π phase is defined as

$$\lambda_\pi = \sqrt{\frac{mc^2 b_1}{8\pi M e^2 |a_1|}}. \quad (40)$$

In the case of the superconducting β phase, which corresponds to the coexistence of superconductivity and orbital antiferromagnetism, the coordinate dependences of both the magnetic field and the parameters ψ and α can be rather complicated. In particular, the spatial inhomogeneity of one of these parameters leads to the inhomogeneous distribution of the other parameter.

9. CONCLUSIONS

The question of what is the microscopic mechanism of superconductivity in cuprate compounds is of principal importance. Taking into account that the Coulomb repulsion in cuprates is among the most significant factors determining their special properties, it would be natural to assume that this very interaction underlies the mechanism of superconductivity in cuprates.

If the formation of a superconducting state is caused by the singlet pairing at a large total momentum $\mathbf{K}$ of the pair, the symmetry of the energy gap $\Delta(\mathbf{k})$ is naturally determined by the crystal symmetry of the cuprate plane. An asymptotically exact (even at an arbitrarily small intensity of the interaction) nontrivial solution of the self-consistency equation for η_K-pairing exists in

the case of the perfect mirror nesting of the Fermi contour. A small deviation from the perfect mirror nesting results in that a superconducting solution appears for a finite (albeit rather small) effective coupling constant. The shape of the Fermi contour in doped cuprates in a rather broad range of dopant concentrations corresponds to perfect nesting for some large (in the general case, incommensurate) values of the momentum **K**.

The formation of the imaginary part of the order parameter with a relative phase different from π can be interpreted as the appearance of a contribution of the current density wave related to the relative motion of the pair. We can suggest that this ordering is related to the formation of an insulating antiferromagnetic structure of orbital currents, while a deviation of the relative phase from π plays the role of the order parameter. It should be noted that this parameter of the insulating ordering naturally appears in the scheme with η_K-pairing under repulsive interaction.

Thus, the region of the phase diagram corresponding to the superconductivity is divided into two parts reflecting two phases. One of these phases (π phase) exists in overdoped compounds, wile the other (β phase) is found in underdoped compositions. The $T_{\beta\pi}$ line of the transition between these phases originates from the tetracritical point ($x = x_0$) and terminates at a certain point with $x = x_b > x_0$ on the $T = 0$ axis. Upon the phase transition from the normal phase to the π phase in the doping interval $x_0 < x < x_b$, the further decrease in the temperature leads to the second phase transition: from the π phase to the β phase. The region of this transition, as well as the $\alpha \longrightarrow \beta$ transition in underdoped compounds, is preceded by a region of the developed fluctuations of the order parameter, which are related to the appearance of a saddle point in the family of free energy isolines (Fig. 4) in addition to the absolute minimum corresponding to the π phase. The saddle point can be related to certain quasi-stationary states involving the orbital vortex currents. Thus the phase diagram exhibits a certain symmetry with respect to the transformation of parameter $\psi \longleftrightarrow \alpha$.

In concluding, it should be noted that a thermodynamic analysis of the phase diagram in the vicinity of the tetracritical point with allowance for the competition between the superconducting and orbital-antiferromagnetic states (which is a natural consequence of the η_K-pairing under repulsive interaction) lead to definite conclusions concerning the main features of the whole phase diagram in the regions of temperature and doping corresponding to superconducting region. These conclusions do not contradict the well-known experimental facts concerning the behavior of cuprates in the corresponding temperature and doping intervals. In particular, a qualitative interpretation is obtained for enhancement of the Nernst effect in the region of a strong pseudogap (crossover from strong to weak pseudogap, related to the disappearance of the saddle point on the ψ axis, is naturally explained [17] by smearing of the level of the quasi-stationary state on approaching a maximum of the potential barrier depicted in Fig. 2) and a decrease in the superfluid density [1] and an increase in the $2\Delta/T_C$ ratio in underdoped composition (relative to the universal value of 3.52 according to the Bartdeen–Cooper–Schrieffer (BCS) theory [43]). It should be noted that an analysis of the superconducting phase transition within the framework of the BCS theory is effective only for overdoped compounds, since the description of the phase transition to the superconducting β phase using a single-component order parameter is inadequate.

A $\beta \longleftrightarrow \pi$ transition between the two superconducting states, which is a second-order phase transition and takes place in a relatively narrow doping interval ($x_0 < x < x_b$) can be detected, for example, by measuring a jump in the temperature dependence of the heat capacity. It should also be noted that, in the general case, the maximum of the superconducting transition temperature $T_C(x)$, which corresponds to $x = x_{opt}$, does not coincide with the position $x = x_0$ of the tetracritical pint: $x_{opt} < x_0$ (Fig. 3). This conclusion is confirmed by experimental data [44]. Therefore, if the region of overdoping is defined, as usual, by the condition $x_{opt} < x < x^*$, it is quite natural to assume that strong fluctuations of the order parameter may arise in this region. Fluctuations, such as the vortex excitations in the form of quasi-stationary staggered orbital vortex currents, can be also detected using tunneling microscopy.

ACKNOWLEDGMENTS

This study was supported in part by the Russian Foundation for Basic Research (project no. 02-02-17133).

REFERENCES

1. P. A. Lee, N. Nagaosa, and X.-G. Wen, cond-mat/0410445.
2. S. Chakravarty, R. B. Laughlin, D. K. Morr, and C. Nayak, Phys. Rev. B **63**, 094503 (2001).
3. S. Chakravarty, Phys. Rev. B **66**, 224505 (2002).
4. G. Zhao, Phys. Rev. B **64**, 024503 (2001).
5. B. H. Brandow, Phys. Rev. B **65**, 054503 (2002).
6. B. I. Halperin and T. M. Rice, Solid State Phys. **21**, 115 (1968).
7. S. Sachdev, Science **288**, 475 (2000).
8. M. Guidry, L.-A. Wu, Y. Sun, and C.-L. Wu, Phys. Rev. B **63**, 134516 (2001).
9. B. A. Volkov, A. A. Gorbatsevich, Yu. V. Kopaev, and V. V. Tugushev, Zh. Éksp. Teor. Fiz. **81**, 729 (1981) [Sov. Phys. JETP **54**, 391 (1981)].
10. J. B. Marston and I. Affleck, Phys. Rev. B **39**, 11538 (1989).
11. D. A. Ivanov, P. A. Lee, and X.-G. Wen, Phys. Rev. Lett. **84**, 3958 (2000).
12. C. Nayak, Phys. Rev. B **62**, 4880 (2000).

13. V. A. Volkov and O. A. Pankratov, Zh. Éksp. Teor. Fiz. **75**, 1362 (1978) [Sov. Phys. JETP **48**, 687 (1978)].
14. P. A. Lee, N. Nagaosa, T.-K. Ng, and X.-G. Wen, Phys. Rev. B **57**, 6003 (1998); P. A. Lee, cond-mat/0201052.
15. V. I. Belyavskiĭ and Yu. V. Kopaev, Zh. Éksp. Teor. Fiz. **127**, 45 (2005) [JETP **100**, 39 (2005)].
16. V. I. Belyavskiĭ, Yu. V. Kopaev, V. M. Sofronov, and S. V. Shevtsov, Zh. Éksp. Teor. Fiz. **124**, 1149 (2003) [JETP **97**, 1032 (2003)].
17. V. I. Belyavskiĭ, Yu. V. Kopaev, Yu. N. Togushova, and S. V. Shevtsov, Zh. Éksp. Teor. Fiz. **126**, 672 (2004) [JETP **99**, 585 (2004)].
18. V. I. Belyavskiĭ, V. V. Kapaev, and Yu. V. Kopaev, Pis'ma Zh. Éksp. Teor. Fiz. **81**, 650 (2005) [JETP Lett. **81**, 527 (2005)].
19. C. N. Yang, Phys. Rev. Lett. **63**, 2144 (1989).
20. P. Fulde and R. A. Ferrel, Phys. Rev. **135**, A550 (1964).
21. A. I. Larkin and Yu. N. Ovchinnikov, Zh. Éksp. Teor. Fiz. **47**, 1136 (1964) [Sov. Phys. JETP **20**, 762 (1965)].
22. V. I. Belyavskiĭ, V. V. Kapaev, and Yu. V. Kopaev, Pis'ma Zh. Éksp. Teor. Fiz. **76**, 51 (2002) [JETP Lett. **76**, 44 (2002)].
23. A. A. Abrikosov, Physica C (Amsterdam) **341–348**, 97 (2000).
24. E. G. Maksimov, Usp. Fiz. Nauk **170**, 1033 (2000) [Phys. Usp. **43**, 965 (2000)].
25. A. S. Alexandrov and P. E. Kornilovitch, J. Phys.: Condens. Matter **14**, 5337 (2002).
26. A. V. Chubukov, D. Pines, and J. Schmalian, in *The Physics of Conventional and Unconventional Superconductors*, Ed. by K. H. Bennemann and J. B. Ketterson (Springer, Berlin, 2002).
27. P. W. Anderson, Science **237**, 1196 (1987).
28. N. N. Bogolyubov, V. V. Tolmachev, and D. V. Shirkov, *A New Method in the Theory of Superconductivity* (Akad. Nauk SSSR, Moscow, 1958; Consultants Bureau, New York, 1959).
29. W. Kohn and J. M. Luttinger, Phys. Rev. Lett. **15**, 524 (1965).
30. V. I. Belyavsky and Yu. V. Kopaev, Phys. Rev. B **67**, 024513 (2003).
31. V. I. Belyavsky and Yu. V. Kopaev, Phys. Lett. A **322**, 244 (2004).
32. V. I. Belyavsky, Yu. V. Kopaev, and Yu. N. Togushova, Phys. Lett. A **338**, 69 (2005).
33. Y. Ren, J.-H. Xu, and C. S. Ting, Phys. Rev. Lett. **74**, 3680 (1995).
34. A. Ghosh and S. K. Adhikari, Phys. Rev. B **60**, 10401 (1999).
35. E. M. Lifshitz and L. P. Pitaevskiĭ, *Course of Theoretical Physics*, Vol. 5: *Statistical Physics*, 2nd ed. (Nauka, Moscow, 2001; Pergamon, New York, 1980), Part 2.
36. V. N. Muthukumar and Z. Y. Weng, Phys. Rev. B **65**, 174511 (2002).
37. L. D. Landau and E. M. Lifshitz, *Course of Theoretical Physics*, Vol. 5: *Statistical Physics*, 4th ed. (Nauka, Moscow, 1995; Butterworth, London, 1999), Part 1.
38. M. Franz, Z. Tešanović, and O. Vafek, Phys. Rev. B **66**, 054535 (2002).
39. Z. A. Xu, N. P. Ong, Y. Wang, *et al.*, Nature **406**, 486 (2000).
40. G. E. Volovik and L. P. Gor'kov, Zh. Éksp. Teor. Fiz. **88**, 1412 (1985) [Sov. Phys. JETP **61**, 843 (1985)].
41. L. D. Landau and E. M. Lifshitz, *Electrodynamics of Continuous Media* (Nauka, Moscow, 1982; Pergamon, Oxford, 1984).
42. Y. Wang, L. Li, M. J. Naughton, *et al.*, cond-mat/0503190.
43. M. Oda, T. Matsuzaki, N. Momono, and M. Ido, Physica C (Amsterdam) **341–348**, 847 (2000).
44. G. Zheng, P. L. Kuhns, A. P. Reyes, *et al.*, cond-mat/0502117.

Translated by P. Pozdeev

Journal of Experimental and Theoretical Physics, Vol. 101, No. 3, 2005, pp. 468–471.
Translated from Zhurnal Éksperimental'noĭ i Teoreticheskoĭ Fiziki, Vol. 128, No. 3, 2005, pp. 544–548.

ORDER, DISORDER, AND PHASE TRANSITIONS IN CONDENSED SYSTEMS

Self-Similar Evolution of the Surface Morphology of a Stressed Amorphous Alloy Foil

N. N. Gorobei, A. S. Luk'yanenko, and A. E. Chmel

Ioffe Physicotechnical Institute, Russian Academy of Sciences, St. Petersburg, 194021 Russia
e-mail: chmel@mail.ioffe.ru

Received November 19, 2004

Abstract—A time-ordered sequence of topographic images of a stressed amorphous $Fe_{70}Cr_{15}B_{15}$ ribbon is presented. It is shown that the surface of this material (unlike polycrystalline metal foil) has a fractal structure due to the nonequilibrium conditions of its formation. As a tensile stress of about 500 MPa is applied to the surface, the fractal dimension of the surface increases from 1.21 ± 0.02 to 1.34 ± 0.03, then drops to 1.12 ± 0.03, and finally increases to 1.22 ± 0.02. In about 1.5 hours, a complex surface morphology characterized by a roughness amplitude of several tens of nanometers evolves into a regular pattern of shear bands with amplitude of about 300 nm. Self-affine changes in surface morphology are explained by competition between several processes, including crack propagation, surface smoothing, and self-diffusion. © *2005 Pleiades Publishing, Inc.*

1. INTRODUCTION

Spatiotemporal self-similarity is a well-known property of fracture processes demonstrated experimentally on nanoscopic [1], microscopic [2], laboratory [3], and geophysical [4] scales. The energy redistribution due to microfracturing and deformation by external forces gives rise to long-range dynamic interactions (with a characteristic radius much greater than the size of structural units on the scale level in question). As a result, an open, dynamically coupled system develops fractal properties in quantitative distributions of its components (such as products of fracture) [5, 6], their geometry [7, 8], and time-ordered sequences of fracture events on all scale levels [9, 10]. The common physical mechanism responsible for the fractal behavior remains unclear. The available specific models (e.g., scaling of microstructural parameters in stressed metal as an analog of self-similar aggregation [11], scale-invariant dislocation dynamics in a crystal [12, 13], or atomic rearrangements in glasses [14]) rely on properties of particular materials or fracture conditions and cannot be applied to processes controlled by different mechanisms. Accordingly, the self-similarity of a fracture is generally considered as a common, but insignificant, property of the critical state of a multicomponent system. This interpretation ignores the fact that a sequence of fracture events occurring on various structural levels brings an initially disordered system into a regular state characterized by a self-similar structure. This is particularly clear with regard to fracture of amorphous alloys, where fractal structure evolves in highly uniform materials containing no structural units. Structural order in the first coordination shells in metallic glasses (e.g., capped trigonal prisms [15]) reflects the most probable atomic configurations in clusters rather than exactly reproduced basic structural units, such as tetrahedra in oxide glasses.

However, available experimental data (see review in [7]) and some analytical studies [4, 14, 16, 17] suggest that fractal structure is not just a concomitant of a fracture, but its necessary condition. In other words, a fracture can nucleate and develop on any structural level only under conditions favoring the formation of self-similar structure. This process is examined in the present study of the evolution of the surface morphology of a stressed amorphous alloy foil. In previous experiments on normal metals (such as gold, copper, and molybdenum) [18–20], the evolution of the surface of a stressed sample was interpreted in terms of changes in dislocation structure. In a methodologically related study of an amorphous alloy [21], the evolution of the strained surface was not examined.

2. EXPERIMENT

We used a scanning tunneling microscope (STM) to investigate the nanoscopic surface structure with a resolution of 300 data points per 6-micrometer scan. A 0.03 mm thick amorphous $Fe_{70}Cr_{15}B_{15}$ ribbon produced by using the single-roller melt-spinning technique was bent and attached to a cylinder of diameter 15 mm. Its outer surface was subjected to a tensile stress of about 500 MPa, which corresponds to approximately one-tenth of the tensile strength of the foil. The surface was stressed nonuniformly because of the varying thickness of foil produced under dynamic conditions. However, the nonuniformity length scale was much greater than the scanning area (approximately 20 μm^2). Therefore, the macroscopic stress nonuniformity could not cause any qualitative change in the microscopic process

under study. The longitudinal scan time was 30 s per scan. After scanning a 3×6 μm^2 area, the probe was returned to its starting position and a new topographic image was recorded. The first topographic image was recorded a few minutes after stress had been applied. The scanning was continued until regular transverse groovelike bands appeared (in about 1.5 h under the stress conditions indicated above). The band pattern persisted for several hours. We studied the transient process that preceded the formation of the persistent pattern, which was interpreted as shear banding in [22, 23].

3. RESULTS

Figure 1 shows examples of topographic images obtained before stressing and at certain instants after stress had been applied. It is clear that the tensile stress caused a rapid increase in roughness amplitude and a gradual increase in surface complexity via the disappearance of relatively flat regions characteristic of the unstressed sample. To perform a statistical analysis, i.e., to quantify the roughness of the initial and stretched surfaces, we examined the profiles measured at successive stages of stressing. To determine the fractal dimension D as a universal characteristic of self-similar objects, we measured the changes in surface height associated with small increments Δ of the coordinate r along the path of the scanning probe. A self-affine (anisotropic) structure must satisfy the power law

$$\langle |h(r+\Delta) - h(r)| \rangle \propto \Delta^H, \quad (1)$$

where h is surface height, H is the Hurst (roughness) exponent, $\Delta \longrightarrow 0$, and the angle brackets denote an average over all pairs of points in the measured profile. For a two-dimensional profile,

$$D = 2 - H. \quad (2)$$

The values of H were determined as the slopes of log–log plots of $|h(r + \Delta) - h(r)|$ versus the absolute value of Δ averaged over h_i (i = 1, 2, …, 300) (Fig. 2). The deviations of the plots from straight lines at small and large Δ are explained by the limitations due, respectively, to STM resolution and lack of representative data on deep valleys in surface profiles.

Power-law scaling implies that the measured profile is self-affine (has no characteristic roughness amplitude) [7]. A varying H reflects a gradual change in self-affine structure. For the initial (unstressed) sample, the fractal dimension determined by using formula (4) is $D = 1.21 \pm 0.02$.

This is an unexpected result. In the limit of a flat surface, $D = 1$. A fractal dimension higher than unity is characteristic of a self-similar surface profile, which can hardly be expected to develop as a result of a natural solidification process (as distinct from a fracture surface produced under nonequilibrium conditions [7–9, 17]). For example, $D_{Cu} = 1.00 \pm 0.05$ was obtained for the fractal surface of polycrystalline copper in [20].

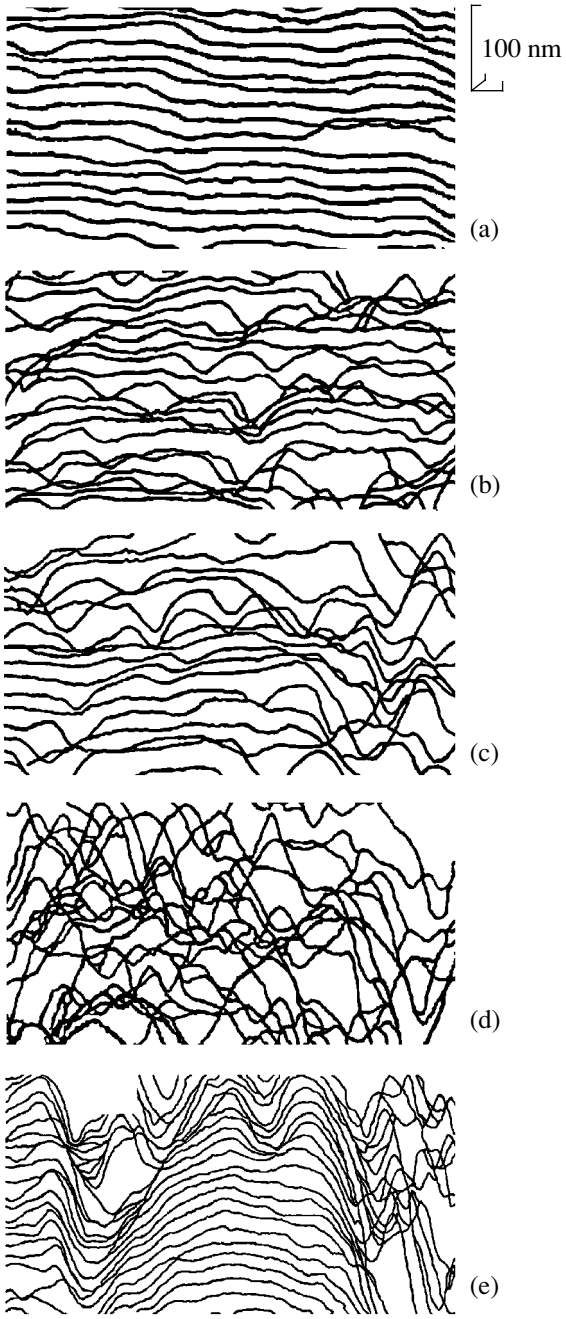

Fig. 1. Surface profiles recorded (a) before stressing and (b) 9, (c) 31, (d) 79, and (e) 150 min after stress had been applied.

The deviation of the surface fractal dimension of an amorphous alloy from unity (Fig. 2a) should be attributed to the solidification conditions on a surface produced by rapid quenching from a melt: the nonequilibrium state of the surface is reflected in its geometry.

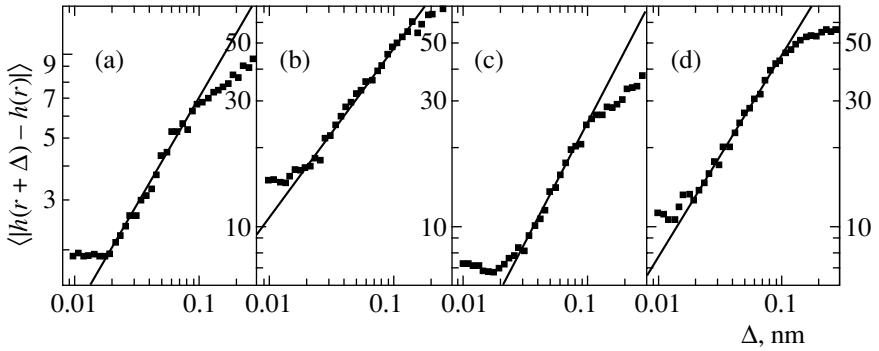

Fig. 2. Height difference averaged over all points in a measured profile vs. horizontal distance Δ for a $Fe_{70}Cr_{15}B_{15}$ ribbon (a) before stressing and (b) 15, (c) 31, and (d) 89 min after stress has been applied. Lines correspond to (1) with $H = 0.79$ (a), 0.66 (b), 0.88 (c), and 0.78 (d).

Figure 3 illustrates the evolution of the surface fractal dimension for $Fe_{70}Cr_{15}B_{15}$ ribbons under isometric stress. It is clear that D increases from 1.21 to 1.34 during the first 15 min, drops to 1.12 in the next 10 min, and then gradually increases to 1.22. The three-stage surface evolution is explained by the competition between several processes having different effects on the surface geometry. Note that "nonmonotonic" behavior of amorphous alloys under stress was observed in [23].

The initial increase in fractal dimension occurs as a result of fast propagation of defects from the surface into the bulk (stage I), which is easy to notice by simply comparing the roughness amplitudes measured before and during stressing (see Figs. 1a and 1b). The subsequent drop in D (stage II) was also observed in [21] for the amorphous alloy $Fe_{77}Ni_1Si_9B_{13}$, where it was attributed to an effect analogous to the smoothing of a crumpled sheet of paper under tensile stress. However, the initial value of D was not specified. The increase in D at the stage of initial crack propagation may have been overlooked in [21], because only the states of the surface before and after stressing were compared, whereas the evolution of surface morphology was not analyzed.

In our experiments, the decrease in D due to smoothing must have been overcome immediately by the increase in D due to crack propagation. After the cracks have stopped growing, the smoothing effect prevails (stage II).

Further evolution (stage III) obviously leads to an increasingly complex surface structure (Fig. 1d) characterized by monotonic increase in fractal dimension. We believe that the final stage of surface evolution is dominated by self-diffusion.

Stage III comes to an end when a steady, transversely oriented texture rapidly develops as $D = 1.22$ is reached, which corresponds to $H = 0.78$ according to (2). It should be recalled here that $H = 0.78$–0.80 has been interpreted as a universal (material-independent) indicator of "fast" surface fracture in several studies [7, 20, 24]. Since a similar Hurst exponent of 0.79 was measured here for a rapidly quenched amorphous alloy, we can now ascertain that this value may be characteristic of any surface produced under nonequilibrium (dynamic) conditions.

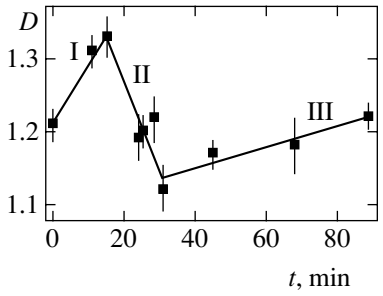

Fig. 3. Fractal dimension of surface profile for a $Fe_{70}Cr_{15}B_{15}$ ribbon at successive stages of stressing represented by line segments.

ACKNOWLEDGMENTS

We thank A.M. Leksovskiĭ for reading the manuscript and discussing the results.

REFERENCES

1. A. Chmel and V. S. Shashkin, Europhys. Lett. **55**, 235 (2001).
2. J. J. Mecholsky, D. E. Passoja, and K. S. Feinberg-Ringel, J. Am. Ceram. Soc. **72**, 60 (1989).
3. A. Zang, F. C. Wagner, S. Stanchits, *et al.*, Geophys. J. Int. **135**, 1113 (1998).
4. D. Sornette and C. G. Sammis, J. Phys. I **5**, 607 (1995).
5. A. Petri, G. Paparo, A. Vespignani, *et al.*, Phys. Rev. Lett. **73**, 3423 (1994).
6. A. Carpinteri, G. Lacidogna, and N. Pugno, Int. J. Fract. **129**, 131 (2004).
7. E. Bouchaud, J. Phys.: Condens. Matter **9**, 4319 (1997).
8. A. Chmel, G. T. Petrovsky, V. S. Shashkin, and A. N. Smirnov, Int. J. Fract. **101**, L41 (2000).

9. G. Caldarelli, C. Castellano, and A. Petri, Philos. Mag. B **79**, 1939 (1999).

10. R. Korsnes, S. R. Souza, R. Donangelo, *et al.*, Physica A (Amsterdam) **331**, 291 (2004).

11. D. A. Hughes, Q. Liu, D. C. Chrzan, and N. Hansen, Acta Mater. **45**, 105 (1997).

12. J. Weiss, J. R. Grasso, M.-C. Miguel, *et al.*, Mater. Sci. Eng. A **309–310**, 360 (2001).

13. M.-C. Miguel, A. Vespignani, S. Zapperi, *et al.*, Nature **410**, 667 (2001).

14. J. K. West, J. J. Mecholsky, and L. L. Hench, J. Non-Cryst. Solids **260**, 99 (1999).

15. D. B. Miracle, J. Non-Cryst. Solids **317**, 40 (2003).

16. Ya. L. Kobelev, L. Ya. Kobelev, and E. P. Romanova, Dokl. Akad. Nauk **370**, 757 (2000) [Dokl. Phys. **45**, 194 (2000)].

17. P. G. Kapiris, G. T. Balasis, J. A. Kopanas, *et al.*, Nonlinear Proc. Geophys. **11**, 137 (2004).

18. V. I. Vettegren', S. Sh. Rakhimov, and V. N. Svetlov, Fiz. Tverd. Tela (St. Petersburg) **40**, 2180 (1998) [Phys. Solid State **40**, 1977 (1998)].

19. A. Ya. Bashkarev, V. I. Vettegren', and V. N. Svetlov, Fiz. Tverd. Tela (St. Petersburg) **44**, 1260 (2002) [Phys. Solid State **44**, 1316 (2002)].

20. M. Zaiser, F. Madani, V. Koutsos, and E. Aifantis, cond-mat/0405069.

21. V. L. Gilyarov, V. E. Korsukov, P. N. Butenko, and V. N. Svetlov, Fiz. Tverd. Tela (St. Petersburg) **46**, 1806 (2004) [Phys. Solid State **46**, 1868 (2004)].

22. A. M. Braginskiĭ, A. Yu. Vinogradov, A. M. Leksovskiĭ, and B. M. Medvedev, Pis'ma Zh. Tekh. Fiz. **12**, 1111 (1986) [Sov. Tech. Phys. Lett. **12**, 459 (1986)].

23. A. Yu. Vinogradov, A. M. Leksovskiĭ, V. A. Bershteĭn, *et al.*, Fiz. Tverd. Tela (Leningrad) **30**, 550 (1988) [Sov. Phys. Solid State **30**, 314 (1988)].

24. A. Hansen, E. L. Hinrichsen, K. J. Maloy, and S. Roux, Phys. Rev. Lett. **71**, 205 (1993).

Translated by A. Betev

Journal of Experimental and Theoretical Physics, Vol. 101, No. 3, 2005, pp. 472–480.
Translated from Zhurnal Éksperimental'noĭ i Teoreticheskoĭ Fiziki, Vol. 128, No. 3, 2005, pp. 549–558.

ORDER, DISORDER, AND PHASE TRANSITIONS IN CONDENSED SYSTEMS

A Two-Dimensional Heisenberg $S = 1$ Antiferromagnet with Exchange Interactions of Two Types on a Hexagonal Lattice: RSRG and DMRG Analyses

V. E. Sinitsyn, A. S. Boyarchenkov, A. S. Ovchinnikov, and I. G. Bostrem

Ural State University, pr. Lenina 51, Yekaterinburg, 620053 Russia
e-mail: alexander.ovchinnikov@usu.ru

Received December 14, 2004

Abstract—An anisotropic Heisenberg spin $S = 1$ model on a two-dimensional hexagonal lattice (formed from interacting chains) with antiferromagnetic nearest-neighbor interactions of two types is analyzed by the real space renormalization group method. The problem of the influence of interchain pairing on the critical properties of the model is studied, and the phase diagram of the model is constructed. The two-dimensional density matrix renormalization group algorithm is used to calculate the ground state energy for the isotropic case as a function of the ratio between interchain and intrachain interactions. © *2005 Pleiades Publishing, Inc.*

1. INTRODUCTION

In the past decade, magnetic systems with structures formed from interacting spin systems have been the object of extensive studies. If the interchain exchange value is much smaller than intrachain interaction, these systems possess properties of one-dimensional magnets at fairly high temperatures. Interchain magnetic interactions, however, begin to play an important role and determine the magnetic behavior of the system as the temperature lowers.

In this work, we apply the real space and density matrix renormalization group methods (RSRG and DMRG) to study a two-dimensional magnetic system with a hexagonal lattice formed by antiferromagnetically interacting spin $S = 1$ chains with intrachain antiferromagnetic interaction, when the model is equivalent to a two-dimensional spin $S = 1$ antiferromagnet with nearest-neighbor interactions of two types. For this purpose, we use the Heisenberg Hamiltonian with Ising-type exchange anisotropy in the RSRG method and the isotropic version of the model in DMRG calculations. Our main goal was to find out how interchain pairing influenced the critical properties and energy of the system in its ground state.

Our interest in this problem largely stems from the preparation of a new class of organic magnets PNNNO and F_2PNNNO. Each of these compounds contains spin $S = 1/2$ pairs coupled by the ferromagnetic interaction J_F. The antiferromagnetic interaction between these pairs forms the corresponding spatial crystal structure. Because of the strong ferromagnetic interaction J_F (on the order of 600 K), the PNNNO and F_2PNNNO compounds can be treated as systems of antiferromagnetic spin $S = 1$ chains (see Fig. 2a type I in [1]).

It was found experimentally that interchain interaction was three-dimensional in character in PNNNO and two-dimensional ($2D$) in F_2PNNNO. As a consequence, the properties of PNNNO can be explained using the model of one-dimensional antiferromagnetic chains that experience Néel ordering in the three-dimensional space at a temperature of about 1 K thanks to weak interchain interaction, whereas the F_2PNNNO compound with comparable antiferromagnetic

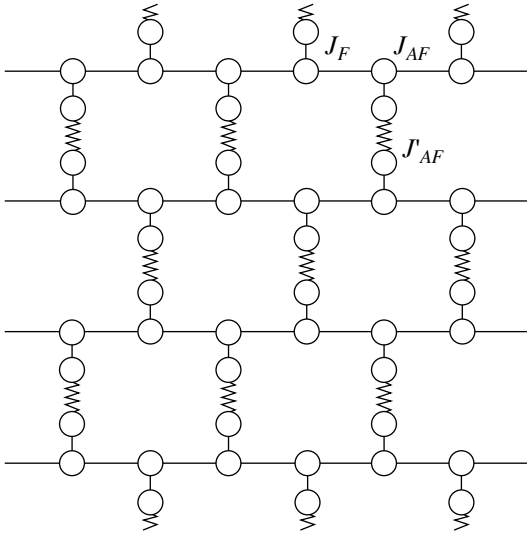

Fig. 1. Magnetic model of the F_2PNNNO compound: uniform chains with intramolecular ferromagnetic pairing (J_F) and intrachain antiferromagnetic exchange (J_{AF}). The chains interact antiferromagnetically (J'_{AF}). The limiting variant of the model ($J_F \longrightarrow \infty$) is the antiferromagnetic hexagonal spin $S = 1$ lattice.

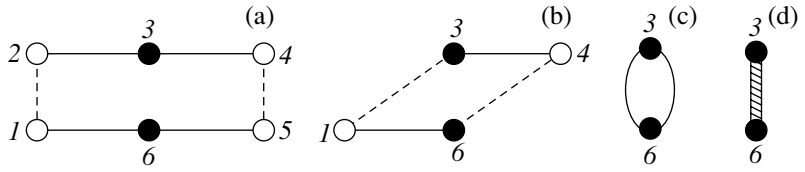

Fig. 2. Graph used in the renormalization group procedure.

exchange interaction values J_{AF} and J'_{AF} is a two-dimensional spin S = 1 system on a hexagonal lattice (Fig. 1).

At the same time, interest in antiferromagnetic spin S = 1 systems increased after the discovery that the interaction of ^{23}Na pseudospins related to their fine structure was antiferromagnetic [2]. A description of the properties of spin 1 bosons, whose role is played by ultracold ^{23}Na atoms on an optical lattice under the conditions of one particle per node [3, 4], generally requires taking into account not only spin (dimeric and chiral) correlations, which arise in considering magnetic spin = 1/2 systems, but also "new" nematic correlations [5].

Lastly, a hexagonal lattice with frustrated interaction between the next-to-nearest neighbors has been extensively studied within the framework of the quantum dimeric model [6], where singlet phases with crystal-like ordering are formed in the ground state [7, 8] (a review of the earlier studies of magnetic models on hexagonal lattices can be found in [9]). This was substantiated numerically for the Heisenberg spin s = 1/2 ($J_1 - J_2 - J_3$) model, in which the phase of singlet valence bonds was formed [10]. Note that measurements of the magnetic properties of F_2PNNNO give direct evidence of the singlet character of its ground state with a gap in the excitation spectrum. This conclusion is substantiated by magnetization measurements in high fields (by the presence of an $M_z = 0$ magnetization curve plateau). All these observations do not rule out the formation of a state of the spin liquid type. Note from the outset that the results obtained for the spin S = 1 model should be used with caution when the F_2PNNNO system is considered, because, generally speaking, the structure of the real compound is formed by spins 1/2.

Lastly, a consideration of the Heisenberg Hamiltonian with exchange anisotropy of the Ising type for spin S = 1 systems by the real space renormalization group method is of theoretical interest on its own in view of a recent study of the behavior of a weakly anisotropic Heisenberg spin S = 1/2 antiferromagnet on a square lattice at finite temperatures using the Monte Carlo quantum method [11]. The Ising universality class was shown to appear already at low anisotropy values (on the order of $10^{-2} \sim 10^{-3}$ in exchange integral units), which, according to the authors of [11], virtually ruled out the possibility of the destruction of long-range order by quantum fluctuations under these conditions. These results are quantitatively at variance with RSRG calculations, which predict a substantially larger critical anisotropy value (~0.2) for this model.

We shall solve the principal problem using a generalization of the well-known RSRG method, which was for the first time suggested by Mariz *et al*. for the quantum anisotropic Heisenberg spin S = 1/2 model [12]. Generalizing this method to spins $S > 1/2$ is a nontrivial problem, although here we also encounter usual difficulties related to the necessity of expanding exponential operators and the "multiplication" of exchange interactions because of the vector character of spin operators.

The paper is organized as follows. In Section 2, we develop the real space renormalization group method for spin S = 1 and apply it to the quantum anisotropic Heisenberg model on a hexagonal lattice with exchange interactions of two types. Section 3 presents the results of DMRG calculations of the ground state energy for the isotropic case at various ratios between these exchange interactions.

2. RSRG ANALYSIS

After the real space renormalization group method was successfully applied to study two-dimensional Ising systems [13, 14], a large number of works in which this approach was used to analyze phase transitions in quantum systems have been published [15–17]. In the past decade, the RSRG method was employed to calculate the phase diagram of the anisotropic Heisenberg spin S = 1/2 antiferromagnet on a square lattice [18, 19]. In these works, a special hierarchical lattice was used to approximate the initial square lattice, and the renormalization group procedure itself (cluster enlargement) was performed with summing over the internal spin states.

Recently, the linear perturbation renormalization group method (LPRG) has been suggested to study weakly interacting classical and quantum spin chains [20]. This method uses the natural small parameter of the system, namely, the ratio between interchain and intrachain pairing. It also uses the renormalization group transformation, which is the standard decimation procedure for Ising spins and a generalization of the Suzuki–Takano approximate decimation procedure [21] for quantum spins. Unfortunately, the LPRG method based on perturbation theory can only be used when the

ratio between interchain pairing and intrachain exchange interaction is small.

2.1. Model

Let us consider a system with anisotropic Heisenberg interaction described by the dimensionless Hamiltonian

$$-\beta H = \sum_{\langle i,j\rangle} K_{ij}[(1-\Delta_{ij})(S_i^x S_j^x + S_i^y S_j^y) + S_i^z S_j^z], \quad (1)$$

where $\beta = 1/k_B T$, $K_{ij} \equiv J_{ij}/k_B T$, J_{ij} is the exchange interaction value, $\langle ij\rangle$ denotes pairs of the interacting nearest neighbors, Δ_{ij} is the anisotropy parameter, and S_i^α $\{\alpha = x, y, z\}$ are the components of spin $S = 1$ on node i. Hamiltonian (1) corresponds to the Ising ($\Delta_{ij} = 1$), isotropic Heisenberg ($\Delta_{ij} = 0$), and XY ($\Delta_{ij} = -\infty$) models.

We shall briefly describe the main elementary operations central to the renormalization group procedure suggested in [12]. A pair of bonds placed in parallel and characterized by the parameters (K_1, Δ_1) and (K_2, Δ_2) is equivalent to one bond with the parameters (K_p, Δ_p) defined as

$$K_p = K_1 + K_2,$$

$$K_p\Delta_p = K_1\Delta_1 + K_2\Delta_2.$$

This rule, which corresponds to the usual Migdal–Kadanoff procedure [22, 23], can trivially be generalized to n parallel bonds.

Combining two series-connected bonds with the parameters (K_1, Δ_1) and (K_2, Δ_2) is not so simple because the spin operators do not commute with each other. After applying the renormalization group procedure, scaling, and removing intermediate spins ("decimation"), the Hamiltonian changes its form, and its new exchange parameters are some functions of the initial exchange interactions. The initial Hamiltonian has the form

$$H_{123} = K_1[(1-\Delta_1)(S_1^x S_3^x + S_1^y S_3^y) + S_1^z S_3^z] + K_2[(1-\Delta_2)(S_3^x S_2^x + S_3^y S_2^y) + S_3^z S_2^z].$$

We must replace two series-connected bonds by one bond with the interaction Hamiltonian

$$H'_{12} = K_s[(1-\Delta_s)(S_1^x S_2^x + S_1^y S_2^y) + S_1^z S_2^z] + K'_0. \quad (2)$$

This is achieved by imposing the requirement that the contribution of the interaction of two terminal atoms 1 and 2 to the partition function be invariant; that is,

$$\exp H'_{12} = \mathrm{Tr}_3 \exp H_{132}, \quad (3)$$

where Tr_3 denotes the trace over the states of intermediate spin 3 and K'_0 is some additional constant necessary for (3) to have a solution. Equation (3) relates the exchange parameters of the bonds to be combined (K_1, Δ_1) and (K_2, Δ_2) to the renormalized parameters (K_s, Δ_s, K'_0). Note that the corresponding relations can be written explicitly for the anisotropic Heisenberg spin $S = 1/2$ model [12, 18].

To construct the recursive equations for renormalization group transformations (3) in the spin $S = 1$ model, let us expand both sides of the equality using a certain matrix basis and equate the corresponding coefficients of this expansion. The problem of the "multiplication of constants" that then arises will be solved by retaining only those exchange constants that are present in initial Hamiltonian (1).

Note that, because of the properties of the Pauli matrices, the matrix representations of H and $\exp H$ have the same structure for spin 1/2; that is, the nonzero matrix elements of H and $\exp H$ are positioned identically. This rule does not hold for spin $S = 1$, which considerably complicates calculations.

Following [12], let us write $\exp H'_{12}$ in the form

$$\exp H'_{12} = \sum_{n_1=0}^{\infty}\sum_{n_2=0}^{\infty} K_{n_1 n_2} A_1^{n_1} \otimes A_2^{n_2},$$

where $\otimes$ is the exterior product and $A_{1,2}$ stands for the usual powers of the spin operators $S_{1,2}^{x,y,z}$. The $K_{n_1 n_2}$ coefficients depend on K_s, Δ_s, and K'_0. Since $A_{1,2}^n$ are 3×3 matrices, they can be expanded using the basis set of polarization matrices T_q^k ($k = 0, 1, 2$ and $q = -k, -k+1, \ldots, k$ (see Appendix),

$$A_i^n = aT_0^0(i) + \sum_{M=\pm 1,0} b^M T_M^1(i) + \sum_{M=\pm 2,\pm 1,0} c^M T_M^2(i), \quad i = 1, 2.$$

The T_q^k matrices can in turn be written explicitly in terms of the spin operators [24]

$$T_0^0 = \frac{1}{\sqrt{3}} I, \quad T_{\pm 1}^1 = \mp\frac{1}{2}(S^x \pm iS^y),$$

$$T_0^2 = \sqrt{\frac{3}{2}}\left((S^z)^2 - \frac{2}{3}I\right),$$

$$T_{\pm 1}^2 = \mp\frac{1}{2}[(S^x S^z + S^z S^x) \pm i(S^y S^z + S^z S^y)],$$

$$T_{\pm 2}^2 = \frac{1}{2}[(S^x)^2 - (S^y)^2 \pm i(S^x S^y + S^y S^x)].$$

The $\exp(H)$ operation should not change Hamiltonian H symmetry. The requirement of invariance then gives

the most general decomposition form,

$$\begin{aligned}\exp H'_{12} &= \alpha_1(T^0_0(1)\otimes T^0_0(2)) + \alpha_2(T^1_0(1)\otimes T^1_0(2))\\ &+ \alpha_3(T^2_0(1)\otimes T^2_0(2)) + \beta(T^1_1(1)\otimes T^1_{-1}(2)\\ &+ T^1_{-1}(1)\otimes T^1_1(2)) \\ &+ \gamma(T^2_2(1)\otimes T^2_{-2}(2) + T^2_{-2}(1)\otimes T^2_2(2))\\ &+ \sigma(T^2_1(1)\otimes T^2_{-1}(2) + T^2_{-1}(1)\otimes T^2_1(2)),\end{aligned} \quad (4)$$

with a new set of interaction constants α_1, α_2, α_3, β, γ, and σ (the indices in parentheses are the node numbers). Applying (4) yields

$$\exp H'_{12} = \begin{pmatrix} A_{12} & 0 & 0 & 0 & 0 & 0 & 0 & 0 & 0\\ 0 & B_{12} & 0 & C_{12} & 0 & 0 & 0 & 0 & 0\\ 0 & 0 & D_{12} & 0 & F_{12} & 0 & G_{12} & 0 & 0\\ 0 & C_{12} & 0 & B_{12} & 0 & 0 & 0 & 0 & 0\\ 0 & 0 & F_{12} & 0 & E_{12} & 0 & F_{12} & 0 & 0\\ 0 & 0 & 0 & 0 & 0 & B_{12} & 0 & C_{12} & 0\\ 0 & 0 & G_{12} & 0 & F_{12} & 0 & D_{12} & 0 & 0\\ 0 & 0 & 0 & 0 & 0 & C_{12} & 0 & B_{12} & 0\\ 0 & 0 & 0 & 0 & 0 & 0 & 0 & 0 & A_{12}\end{pmatrix}, \quad (5)$$

where the matrix elements $A_{12} \equiv \alpha_1/3 + \alpha_2/2 + \alpha_3/6$, $B_{12} \equiv \alpha_1/3 - \alpha_3/3$, $C_{12} \equiv -\beta/2 - \sigma/2$, $D_{12} \equiv \alpha_1/3 - \alpha_2/2 + \alpha_3/6$, $E_{12} \equiv \alpha_1/3 + 2\alpha_3/3$, $F_{12} \equiv -\beta/2 + \sigma/2$, and $G_{12} \equiv \gamma$ are introduced.

We can similarly obtain a closed equation for the expansion of $\mathrm{Tr}_3\exp H_{123}$ whose structure is similar to that for $\exp H'_{12}$; the coefficients of (4) are then functions of the parameters present in H_{123}.

Calculating exponential functions of matrices requires the numerical diagonalization of 9×9 and 27×27 matrices related to H'_{12} and H_{123}, respectively, to be performed. The equations

$$\exp H'_{12} = U_{12}\exp(H^D_{12})U^\dagger_{12},$$

$$\exp H_{123} = U_{123}\exp(H^D_{123})U^\dagger_{123},$$

where U_{12} and U_{123} are the unitary matrices that diagonalize H'_{12} and H_{123} into H^D_{12} and H^D_{123}, can be used to numerically find $\exp H'_{12}$ and $\exp H_{123}$ as functions of the corresponding sets of exchange parameters. Direct numerical calculations show that $\exp H'_{12}$ and $\mathrm{Tr}_3\exp H_{123}$ have identical matrix structures (5). The calculations give the sets of parameters $\{\alpha_1, \alpha_2, \alpha_3, \beta, \gamma, \sigma\}$ for $\exp H_{12}$ and $\{\bar\alpha_1, \bar\alpha_2, \bar\alpha_3, \bar\beta, \bar\gamma, \bar\sigma\}$ for $\mathrm{Tr}_3\exp H_{123}$. The required renormalization group equations are obtained by imposing the conditions

$$\alpha_1 = A_{12} + B_{12} + D_{12} = \bar A_{12} + \bar B_{12} + \bar D_{12} = \bar\alpha_1, \quad (6)$$

$$\alpha_2 = A_{12} - D_{12} = \bar A_{12} - \bar D_{12} = \bar\alpha_2, \quad (7)$$

$$\beta = -C_{12} - F_{12} = -\bar C_{12} - \bar F_{12} = \bar\beta \quad (8)$$

and

$$\begin{aligned}\alpha_3 &= E_{12} - B_{12} = \bar E_{12} - \bar B_{12} = \bar\alpha_3,\\ \gamma &= G_{12} = \bar G_{12} = \bar\gamma,\\ \sigma &= F_{12} - C_{12} = \bar F_{12} - \bar C_{12} = \bar\sigma.\end{aligned} \quad (9)$$

Clearly, the number of these equations exceeds the number of interactions in initial Hamiltonian (2) because all possible bilinear interactions between terminal spins are generated. To perform decimation, we retain three equations (6), (7), and (8) corresponding to Heisenberg interactions in initial Hamiltonian (1), which implicitly determine K_s, Δ_s, and K'_0 as functions of (K_1, Δ_1) and (K_2, Δ_2). This system of equations is a direct analog of the renormalization group equations for spin $S = 1/2$ (see Eqs. (12) in [12]).

The next important step of the renormalization group procedure is the selection of the hierarchical lattice. We will use the simplest lattice variant with 6 nodes and 6 bonds shown in Fig. 2, whose point symmetry coincides with that of the initial lattice. Next, we impose the condition that the initial and renormalized graphs should be characterized by equal contributions of the interaction of terminal spins 3 and 6 to the partition function. At the first stage, we apply decimation R_S, when the spins 1 and 3 (or 4 and 6) are retained, whereas the spins 2 and 5 are removed. At the second stage, the decimation procedure is repeated to remove the spins 1 and 4. Lastly, we apply the Migdal–Kadanoff "bond shift" to combine the remaining bonds placed in parallel and eventually determine the renormalized parameters. As a result, we obtain the recursive equations

$$\begin{aligned}(K_S, \Delta_S) &= R_S(K_2, \Delta_2; K_1, \Delta_1),\\ (K'_S, \Delta'_S) &= R_S(K_S, \Delta_S; K_1, \Delta_1),\\ (K_p, \Delta_p) &= 2(K'_S, \Delta'_S).\end{aligned} \quad (10)$$

The critical points of the system are defined as the nontrivial fixed points of these equations, which can conveniently be rewritten as the complex function

$$(K_p, \Delta_p) = 2R_S(R_S(K_1, \Delta_1; K_2, \Delta_2); K_1, \Delta_1). \quad (11)$$

Unfortunately, as distinct from the $S = 1/2$ problem, explicit renormalization group equations cannot be

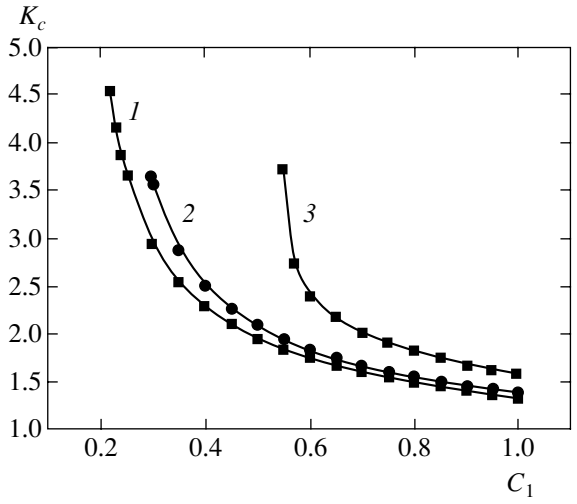

Fig. 3. Reciprocal critical temperature (K_c) as a function of the $C_1 = J'_{AF}/J_{AF}$ ratio calculated using renormalization group recursive equations for various anisotropy values: Δ = (*1*) 1.0, (*2*) 0.8, and (*3*) 0.6.

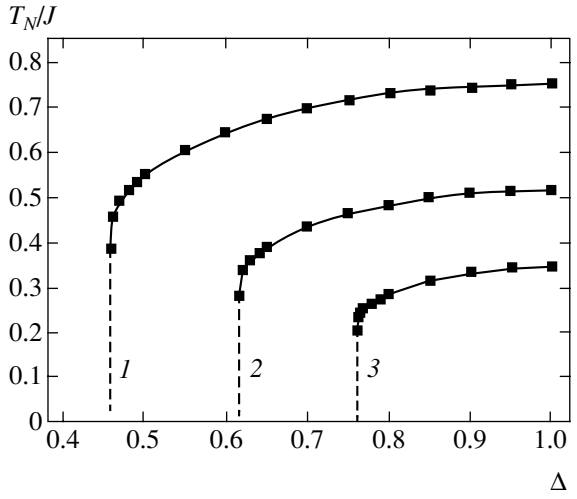

Fig. 4. (T_N, Δ) phase diagram for various $C_1 = J'_{AF}/J_{AF}$ ratio values: (*1*) 1.0, (*2*) 0.5, and (*3*) 0.3. The regions above (below) the critical lines correspond to disordered (ordered) phases. The dashed lines were drawn by eye.

obtained; we therefore briefly describe the numerical procedure that we used. The initial parameters were the ratio between the interchain and intrachain pairings $C_1 = J'_{AF}/J_{AF}$ and the anisotropy parameter $\Delta = \Delta_1$. In addition, we assumed that $\Delta_2 = C_1\Delta$, that is, the form of anisotropy was the same for intrachain and interchain interactions. Setting an arbitrary starting intrachain pairing value $K_1^{(i)}$ (the intrachain interaction constant is then $K_2^{(i)} = C_1 K_1^{(i)}$), we performed two sequential decimation steps to obtain the renormalized pairing constant K'_S. At each step, system (6), (7), (8) was solved. (This can be done using the standard procedure for solving nonlinear systems of equations [25].) Next, we doubled the result obtained in these transformations to find the eventual $K^{(f)}$ value as a function of the starting value $K_1^{(i)}$. At the final stage, we determined the fixed point K_c of the equation $K_1^{(i)} = K^{(f)}(K_1^{(i)})$, for instance, using the dichotomy method.

2.2. Results

The reciprocal critical temperature $K_c = 1/T_c$ is shown in Fig. 3 as a function of the C_1 parameter for several anisotropy parameter Δ values. According to this figure, the critical temperature rapidly decreases as interchain interaction weakens. The dependences of the critical temperature on the exchange anisotropy parameter Δ are presented in Fig. 4; all of them correspond to the Ising universality class. As distinct from several real space renormalization group studies for spin $S = 1/2$, the phase diagrams for the ferromagnetic and antiferromagnetic models are identical; that is, the critical temperature decreases to zero at some nonzero critical Δ_c value. A weakening of interchain pairing strengthens quantum fluctuations, which results in an increase in Δ_c as C_1 decreases.

Note that we did not observe a reentrant behavior of the (T, Δ) critical line in the temperature range of our simulations such as was reported in some RSRG studies of spin $s = 1/2$ models [18, 19]. The results obtained in [18, 19] imply the presence of an ordered phase at relatively high temperatures and its disappearance when the system is cooled. In this connection, it is pertinent to mention work [26]: according to its authors, these results are an artifact of the method; that is, reentrant behavior is observed because of the finite size of the cluster used in the renormalization group procedure. The effect must disappear as the size of the cluster increases.

Close to the critical anisotropy value $\Delta = \Delta_c$, the Néel temperature obeys the law

$$T_N \propto \frac{1}{\ln(\Delta - \Delta_c)} \tag{12}$$

(see Fig. 5), which is in qualitative agreement with the result obtained for the spin $S = 1/2$ model. Unfortunately, numerical calculation results cannot be extrapolated to $T = 0$. For this reason, we cannot draw any definite conclusions about the character of the ground state of the model. Scaling equation (12) remains valid at various ratios between interchain and intrachain pairings. The logarithmic dependence of T_N and T_c on the difference $\Delta - \Delta_c$ was obtained for an anisotropic spin $s = 1/2$ antiferromagnet [27, 28] using scaling theory and the quantum Monte Carlo method, but with the $\Delta_c = 0$ critical value.

Lastly, let us consider the equivalence (isomorphism) of the critical properties of the ferromagnetic and antiferromagnetic models. It is well known that, in classical spin models such as the Ising and classical Heisenberg models, the critical temperature (if any) is the same for the ferromagnetic (Curie temperature) and antiferromagnetic (Néel temperature) exchange interactions between the nearest neighbors. This is a direct consequence of free energy being an even function of the exchange parameter. Studies of the quantum Heisenberg spin 1/2 model for the primitive and body-centered cubic lattices, however, showed that the Néel temperature was higher than the Curie temperature by approximately 10%, although this difference rapidly decreased as S increased [29]. Recently, this problem was again studied for three-dimensional spin $S = 1/2$, 1, and 3/2 models using the method of high-temperature expansions [30]. For some quantum systems such as the transverse Ising model and the XY model with quantum spin 1/2, there is isomorphism of the critical properties of the ferromagnetic and antiferromagnetic systems [31]. Note that studies of the critical properties of the Heisenberg spin 1/2 model with anisotropic exchange on a square lattice by approximate methods, for instance, by the method of Green functions, give $T_c = T_N$ at all anisotropy parameter values [32, 33]. The real space renormalization group method used in [18, 19] gave $T_N < T_c$ for $0 \le \Delta < 1$. The authors used a special selection of the hierarchical lattice approximating the square lattice. The Curie temperature T_c for ferromagnetic interaction continuously decreases to zero as the anisotropy parameter Δ becomes smaller, which gives $T_c = 0$ in the isotropic limit ($\Delta = 0$), in complete agreement with the Mermin–Wagner theorem [34]. On the other hand, the results obtained for antiferromagnetic interaction were similar to those presented in this work; namely, Néel ordering was absent below some critical $\Delta < \Delta_c$ value. Clearly, this problem requires additional studies.

One of the main qualitative results of our RSRG analysis is the absence of long-range order in the isotropic limit $\Delta = 0$. In Section 3, we describe DMRG calculations of the ground state energy of the model. We show that this value is substantially lower than that predicted for classical Néel ordering, which is evidence of the existence of fairly strong quantum fluctuations in the system.

3. DMRG ANALYSIS

The density matrix renormalization group (DMRG) algorithm is one of the most powerful methods for studying the properties of low-dimensional systems. This approach allows us to obtain very accurate results for the wavefunction of the sought state (the ground or one of the low-lying excited states) and observables (energy, correlation functions, etc.) using a basis set of comparatively small dimension m (usually, $m \sim 50$–150).

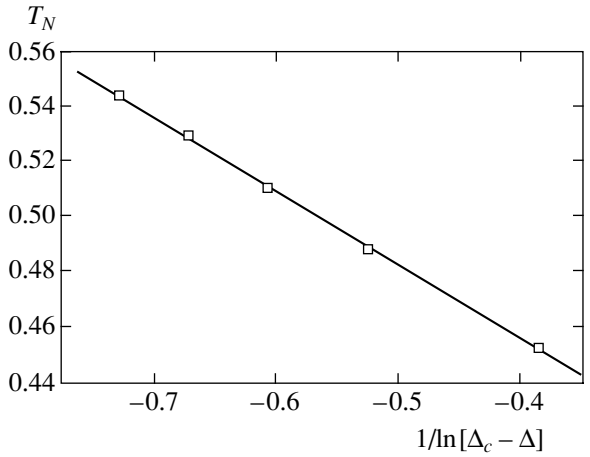

Fig. 5. (T_N, Δ) phase diagram for small T_N values close to Δ_c; $\Delta_c \approx 0.46$ for $C_1 = 1.0$.

The key problem of the DMRG algorithm is the selection of these m basis functions that should minimize the difference between the true wavefunction ψ and its DMRG approximation $\tilde{\psi}$.

An original one-dimensional DMRG algorithm was suggested by White [35, 36] in the early 1990s. The method gives very accurate values for the ground state energy of Heisenberg spin $S = 1/2$ and 1 chains and several other models [37]. Extending the DMRG algorithm to two-dimensional systems, however, proved to be a nontrivial task that has not been formulated uniquely by now.

The DMRG method was for the first time applied to the two-dimensional frustrated quantum spin model of the CaV_4O_9 compound [38]. More recently, the method was used to study the two-dimensional t–J model [39–41] and quantum Hall systems [42, 43]. Various applications of the DMRG algorithm to two-dimensional systems are reviewed in [44].

The principal difference between the variants suggested by various authors lies in the method for "increasing" the system. For instance, one of the simplest extensions to two-dimensional systems is as follows. Whereas separate nodes are as a rule added to the system in the one-dimensional DMRG algorithm, we can add whole columns of spins to the lattice in the two-dimensional version [45]. The lattice size then remains constant along the y axis and increases along the x axis during calculations. Although this approach is fairly easy to implement, it has an important shortcoming, an undesirable increase in the amount of computations because a description of the interaction of two "columns" of spins of height M requires including M additional bonds into the Hamiltonian at every step. In other approaches, a system is increased by blocks of an even more complex shape [46–48], which allows the topological characteristics of two-dimensional lattices to remain unchanged but, as previously, which requires

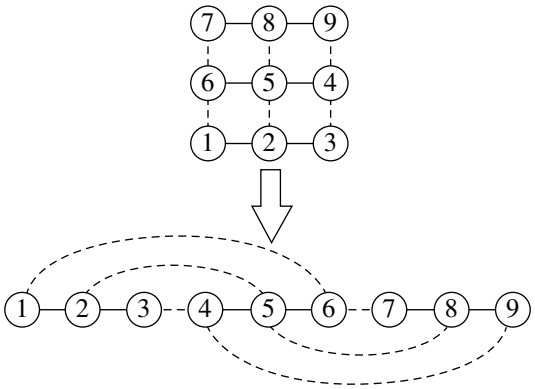

Fig. 6. Map of two-dimensional lattice to spin chain.

including a large number of new bonds and imposes expensive computation time.

From the point of view of computations proper, the simplest are "linear growth" methods, when one node is added at each step of increasing the system. One of such DMRG algorithm variants was suggested in [49] to study the two-dimensional Hubbard model. The algorithm is based on mapping the two-dimensional spin lattice onto a one-dimensional spin chain (see Fig. 6). Initially, nearest-neighbor interactions are taken into account in the two-dimensional system. However, when this system is appropriately mapped onto the one-dimensional chain, there appear interactions between nodes situated fairly far from each other. The traditional DMRG algorithm can be applied to a one-dimensional chain constructed this way (we used the variant for finite lattices). We employed this method to study the properties of the ground state of the isotropic Heisenberg spin $S = 1$ antiferromagnet on a hexagonal lattice with exchange interactions of two types, $J_1 = J_{AF}$ and $J_2 = J'_{AF}$.

The ground state energy E_0 was calculated for the 6×3 cluster. The J_2/J_1 parameter was varied from 2 to 0.01. In all the calculations, a basis set of dimension $m = 50$ was used. The E_0 values obtained are listed in the table in exchange integral J_1 units. The same table contains the energy per bond E_0/N. For the 6×3 lattice, the number of bonds is $N = 21$ (15 horizontal and 6 vertical bonds). According to [35], the ground state energy of noninteracting isotropic Heisenberg $S = 1$ chains should be $-1.401 \times 15 = -21.0125$, which is the sum over three independent chains each containing five bonds. It follows from the table that E_0 tends to that value as $J_2/J_1 \longrightarrow 0$, which is evidence that the results obtained are acceptable.

Table

J_2/J_1	E_0	E_0/N	E_N
2.0	–35.1	–1.67	–27.0
1.0	–27.21	–1.296	–21.0
0.5	–23.95	–1.141	–18.0
0.333	–23.08	–1.099	–17.0
0.1	–22.218	–1.0580	–15.6
0.01	–22.1119	–1.0529	–15.06

The ground state energy reaches its limiting value fairly rapidly, in approximately 50 steps. Note that the dependence of the ground state energy E_0 on the step number n of the DMRG algorithm is a step function. A similar behavior of the ground state energy as the number of iterations increases was reported in recent work [46], where a spin $S = 1/2$ antiferromagnet on a square lattice was studied.

The last column of the table contains the ground state energy E_N for classical Néel ordering. (For the cluster studied in this work, $E_N = J_1[-15 - 6J_1/J_2]$.) The substantial difference between these values and the values obtained in the DMRG calculations is evidence of strong quantum fluctuations in the ground state of the system.

Note in conclusion that the renormalization group analysis results, which predict the existence of critical anisotropy, are in qualitative agreement with studies of the ground state properties of two-dimensional quantum spin systems whose ground states can be ordered valence bond states (VBS). The model of vertex states [50] and the variational method of tensor products (one of the density matrix renormalization group variants) [51] were applied to study spin 3/2 models on a hexagonal lattice and spin 2 models on a square lattice. These VBS models contain the so-called "deformation" parameter (a controlled variational parameter that changes the weight of maximally polarized states largely present in the Néel phase), which corresponds to the *xxz* type of Hamiltonian anisotropy. It was shown that, in the isotropic case, VBS models described a disordered phase different from the Néel phase. The main result of these studies was the existence of a second-order phase transition from disordered phases with exponentially damped spin–spin correlation functions into phases with Néel ordering and long-range correlations as the deformation (anisotropy) parameter increased. This phase transition has the universality class of the two-dimensional Ising model.

An analysis of two-dimensional quantum spin 1 systems by variational renormalization group methods encounters objective difficulties. For instance, the method of matrix products [52, 53] allows VBS states in one-dimensional spin 1 chains to be successfully included, but this approach cannot be extended to two-dimensional systems in the form of the method of tensor products, because such systems do not have the ground state of ordered valence bonds (the spin S value is inconsistent with the number of nearest neighbors; that is, $2S \neq z$). The problem is still open, although the results that we present lead us to suggest that critical

anisotropy and the related phase transition also exist in the two-dimensional quantum spin $S = 1$ systems.

ACKNOWLEDGMENTS

The authors thank M.V. Sadovkii and N.V. Baranov for discussions. This work was financially supported by the Civil Research and Development Foundation, USA (grant REC-005).

APPENDIX

Spin $S = 1$ polarization matrices have the form

$$T_0^0 = \frac{1}{3}\begin{pmatrix} 1 & 0 & 0 \\ 0 & 1 & 0 \\ 0 & 0 & 1 \end{pmatrix}, \quad T_1^1 = -\frac{1}{\sqrt{2}}\begin{pmatrix} 0 & 1 & 0 \\ 0 & 0 & 1 \\ 0 & 0 & 0 \end{pmatrix},$$

$$T_{-1}^1 = \frac{1}{\sqrt{2}}\begin{pmatrix} 0 & 0 & 0 \\ 1 & 0 & 0 \\ 0 & 1 & 0 \end{pmatrix}, \quad T_0^1 = \frac{1}{\sqrt{2}}\begin{pmatrix} 1 & 0 & 0 \\ 0 & 0 & 0 \\ 0 & 0 & -1 \end{pmatrix},$$

$$T_0^2 = \frac{1}{\sqrt{6}}\begin{pmatrix} 1 & 0 & 0 \\ 0 & -2 & 0 \\ 0 & 0 & 1 \end{pmatrix}, \quad T_1^2 = \frac{1}{\sqrt{2}}\begin{pmatrix} 0 & -1 & 0 \\ 0 & 0 & 1 \\ 0 & 0 & 0 \end{pmatrix},$$

$$T_{-1}^2 = \frac{1}{\sqrt{2}}\begin{pmatrix} 0 & 0 & 0 \\ 1 & 0 & 0 \\ 0 & -1 & 0 \end{pmatrix}, \quad T_2^2 = \begin{pmatrix} 0 & 0 & 1 \\ 0 & 0 & 0 \\ 0 & 0 & 0 \end{pmatrix},$$

$$T_{-2}^2 = \begin{pmatrix} 0 & 0 & 0 \\ 0 & 0 & 0 \\ 1 & 0 & 0 \end{pmatrix}.$$

REFERENCES

1. Y. Hosokoshi, Y. Nakazawa, K. Inoue, *et al.*, Phys. Rev. B **60**, 12924 (1999).
2. J. Stenger, S. Inoue, D. M. Stamper-Kurn, *et al.*, Nature **396**, 345 (1999).
3. T. L. Ho and S. K. Yip, Phys. Rev. Lett. **84**, 4031 (2000).
4. S. Yip, J. Phys.: Condens. Matter **15**, 4583 (2003).
5. S. Yip, Phys. Rev. Lett. **90**, 250402 (2003).
6. D. S. Rokhsar and S. A. Kivelson, Phys. Rev. Lett. **61**, 2376 (1988).
7. R. Moessner, S. L. Sondhi, and P. Chandra, Phys. Rev. B **64**, 144416 (2001).
8. E. Fradkin, D. A. Huse, R. Moessner, *et al.*, Phys. Rev. B **69**, 224415 (2004).
9. A. Mattsson, P. Frojdh, and T. Einarsson, Phys. Rev. B **49**, 3997 (1994).
10. J. B. Fouet, P. Sindzingre, and C. Lhuillier, Eur. Phys. J. B **20**, 241 (2001).
11. A. Cuccoli, T. Roscilde, V. Tognetti, *et al.*, Phys. Rev. B **67**, 104414 (2003).
12. A. M. Mariz, C. Tsallis, and A. O. Caride, J. Phys. C: Solid State Phys. **18**, 4189 (1985).
13. Th. Niemeijer and J. M. J. van Leeuwen, Phys. Rev. Lett. **31**, 1411 (1973).
14. L. P. Kadanoff and A. Houghton, Phys. Rev. B **11**, 377 (1975).
15. J. Rogiers and R. Dekeyser, Phys. Rev. B **13**, 4886 (1976).
16. A. L. Stella and F. Toigo, Phys. Rev. B **17**, 2343 (1978).
17. R. C. Brower, F. Kuttner, M. Nauenberg, and K. Subbarao, Phys. Rev. Lett. **38**, 1231 (1977).
18. A. M. C. de Souza, Phys. Rev. B **48**, 3744 (1993).
19. N. S. Branco and J. R. de Sousa, Phys. Rev. B **62**, 5742 (2000).
20. J. Sznajd, Phys. Rev. B **63**, 184404 (2001).
21. M. Suzuki and H. Takano, Phys. Lett. A **69A**, 426 (1979); H. Takano and M. Suzuki, J. Stat. Phys. **26**, 635 (1981).
22. A. B. Migdal, Zh. Éksp. Teor. Fiz. **69**, 810 (1975) [Sov. Phys. JETP **42**, 413 (1975)]; Zh. Éksp. Teor. Fiz. **69**, 1457 (1975) [Sov. Phys. JETP **42**, 743 (1975)].
23. L. P. Kadanoff, Ann. Phys. (N.Y.) **100**, 359 (1976).
24. D. A. Varshalovich, A. N. Moskalev, and V. K. Khersonskii, *Quantum Theory of Angular Momentum* (Nauka, Leningrad, 1975; World Sci., Singapore, 1988).
25. W. H. Press, B. P. Flannery, S. A. Teukolsky, and W. T. Vetterling, *Numerical Recipes in C: The Art of Scientific Computing* (Cambridge Univ. Press, Cambridge, 1992).
26. J. R. de Souza and I. G. Araujo, Phys. Lett. A **272**, 333 (2000).
27. H.-Q. Ding, J. Phys.: Condens. Matter **2**, 7979 (1990).
28. S. S. Aplesnin, Phys. Status Solidi B **207**, 491 (1998).
29. G. S. Rushbrooke and P. J. Wood, Mol. Phys. **6**, 409 (1963).
30. J. Oitmaa and W. Zheng, J. Phys.: Condens. Matter **16**, 8653 (2004).
31. J. R. de Souza and I. G. Araujo, J. Magn. Magn. Mater. **202**, 231 (1999).
32. R. P. Singh, Z. C. Tao, and M. Singh, Phys. Rev. B **46**, 1244 (1992).
33. B. G. Liu, Phys. Rev. B **41**, 9563 (1990).
34. N. D. Mermin and H. Wagner, Phys. Rev. Lett. **17**, 1133 (1966).
35. S. R. White, Phys. Rev. Lett. **69**, 2863 (1992).
36. S. R. White, Phys. Rev. B **48**, 10345 (1993).

37. *Density-Matrix Renormalization*, Ed. by I. Peschel, X. Wang, M. Kaulke, and K. Hallberg (Springer, Heidelberg, 1998).
38. S. R. White, Phys. Rev. Lett. **77**, 3633 (1996).
39. S. R. White and D. J. Scalapino, Phys. Rev. Lett. **80**, 1272 (1998).
40. S. R. White and D. J. Scalapino, Phys. Rev. B **60**, R753 (1999).
41. S. R. White and D. J. Scalapino, Phys. Rev. B **61**, 6320 (2000).
42. N. Shibata and D. Yoshioka, Phys. Rev. Lett. **86**, 5755 (2001).
43. D. Yoshioka and N. Shibata, Physica E (Amsterdam) **12**, 43 (2002).
44. N. Shibata, J. Phys. A: Math. Gen. **36**, R381 (2003).
45. M. S. L. du Croo de Jongh, J. M. J. van Leeuwen, and W. van Saarloos, Phys. Rev. B **62**, 14844 (2000).
46. D. J. J. Farnell, Phys. Rev. B **68**, 134419 (2003).
47. P. Henelius, Phys. Rev. B **60**, 9561 (1999).
48. T. Xiang, J. Lou, and Z. Su, Phys. Rev. B **64**, 104414 (2001).
49. S. Liang and H. Pang, Phys. Rev. B **49**, 9214 (1994).
50. H. Niggemann, A. Klümper, and J. Zittartz, Z. Phys. B **104**, 103 (1997).
51. Y. Hieida, K. Okunishi, and Y. Akutsu, New J. Phys. **1**, 7 (1999).
52. A. Klümper, A. Schadschneider, and J. Zittartz, Z. Phys. B **87**, 281 (1992).
53. A. Klümper, A. Schadschneider, and J. Zittartz, J. Phys. A **24**, L955 (1991).

Translated by V. Sipachev

Journal of Experimental and Theoretical Physics, Vol. 101, No. 3, 2005, pp. 481–486.
Translated from Zhurnal Éksperimental'noĭ i Teoreticheskoĭ Fiziki, Vol. 128, No. 3, 2005, pp. 559–566.

ORDER, DISORDER, AND PHASE TRANSITIONS IN CONDENSED SYSTEMS

Magnetic Relaxation in Rare-Earth Oxide Pyrochlores

I. A. Ryzhkin

Institute of Solid-State Physics, Russian Academy of Sciences, Chernogolovka, Moscow oblast, 142432 Russia
e-mail: ryzhkin@issp.ac.ru

Received December 16, 2004

Abstract—A theory of magnetic relaxation is developed for geometrically frustrated three-dimensional magnets that can be described by an antiferromagnetic Ising model. These magnetic materials are exemplified by some of the recently synthesized rare-earth oxide pyrochlores, such as $Dy_2Ti_2O_7$, $Ho_2Ti_2O_7$, or $Yb_2Ti_2O_7$. A model based on an analogy between the spin ordering in Ising magnets and proton ordering in ice is proposed. In this model, magnetic point defects treated as noninteracting quasiparticles characterized by well-defined energies, mobilities, and effective magnetic charges play a fundamental role analogous to that of ion defects in the physics of ice or by electrons and holes in semiconductors. The proposed model is used to derive expressions for magnetic susceptibility as a function of frequency and temperature. © *2005 Pleiades Publishing, Inc.*

1. INTRODUCTION

Some of the recently synthesized rare-earth oxide pyrochlores, such as $Dy_2Ti_2O_7$, $Ho_2Ti_2O_7$, or $Yb_2Ti_2O_7$, belong to the class of geometrically frustrated magnets (GFMs) [1], in which magnetic lattices cannot satisfy all of the conditions for local magnetic order simultaneously. Originally, a physical model of this kind was considered in a study of the triangular lattice Ising antiferromagnet [2], where spins cannot be antiparallel in all nearest neighbor pairs simultaneously, because closed loops of bonds contain an odd number of vertices. In rare-earth oxide pyrochlores, rare-earth magnetic ions reside at the vertices of linked regular tetrahedra (see Fig. 1). The impossibility of simultaneous fulfillment of ordering conditions for all spins (frustration) entails ground-state degeneracy and very special temperature behavior. At extremely high temperatures ($kT \gg J$, where k is Boltzmann's constant and J is the coupling constant), magnetic coupling is negligible and the spin system is obviously in a paramagnetic state. At lower temperatures ($kT \sim J$), magnetic coupling cannot be neglected and spins are correlated. However, it was shown experimentally that spins still exhibit paramagnetic behavior in the sense that magnetic susceptibility follows the Curie law, $\chi \propto 1/T$ [1, 3, 4]. The persistence of this behavior of a spin system at extremely low temperatures ($kT \ll J$) has generated the term *cooperative paramagnetism*.

What is the mechanism of transition between paramagnetic and cooperative paramagnetic states? Does any magnetically ordered state exist at extremely low temperatures? What is the nature of the cooperative paramagnetic state? What are its properties? These are the key questions arising in studies of GFMs. In this paper, magnetic relaxation in geometrically frustrated three-dimensional magnets is analyzed in the theoretical framework of an Ising model. The analysis is focused on the class of models with magnetic lattice consisting of corner-sharing tetrahedra (see Fig. 1), as in oxide pyrochlores. It is shown here that the magnetic behavior exhibited by these systems can be described by the "magnetic variant" of the theory of proton ordering in ice [5, 6]. The present treatment relies on a formal analogy (originally put forward in [7]) between spin ordering in certain ferromagnets and the proton ordering governed by the ice rules. Trying to find an explanation for the ice rules, I proposed a Hamiltonian for the Coulomb interaction between protons in ice, which turned out to be formally identical to an antiferromagnetic Ising Hamiltonian [8, 9], and derived the ice rules as an obvious consequence of the short-range part of the Coulomb interaction. The similarity of the Hamiltonians suggests that there is a fundamental analogy in both static ordering and dynamic behavior. In this study, the analogy is used to describe magnetic

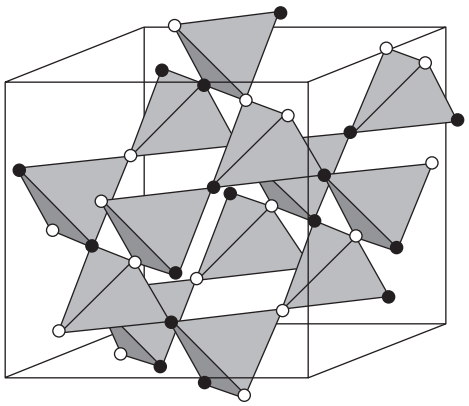

Fig. 1. Magnetic lattice of a rare-earth oxide pyrochlore schematically represented as a network of regular tetrahedra with magnetic ions at their vertices. Open and closed circles are "up" and "down" spins.

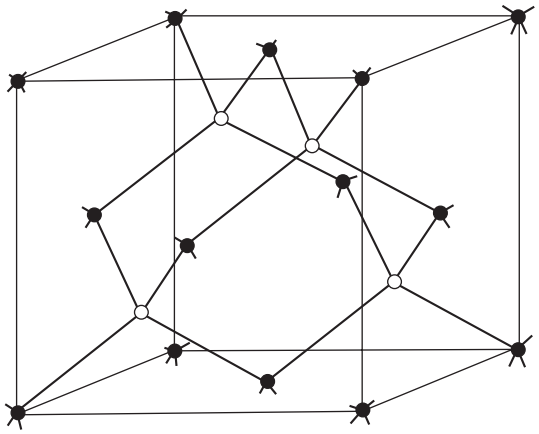

Fig. 2. Diamond lattice dual to the lattice shown in Fig. 1, with vertices at the centers of the tetrahedra. Open and closed circles constitute face-centered cubic sublattices. Each vertex is the junction point of four bonds with the nearest neighbors. Magnetic ions reside at the midpoints of bonds, and magnetic anisotropy axes are parallel to bonds.

relaxation in the system under analysis, i.e., its response to applied magnetic field characterized by arbitrary time dependence.

The presentation below is organized as follows. First, the Hamiltonian of the system is presented, and both ground and excited states are described. Next, a proportional to local magnetization is introduced to characterize spin ordering, and the relationship between the dynamics of defects and the configuration vector is analyzed. Finally, an expression is derived for frequency-dependent magnetic susceptibility.

2. GROUND STATES AND DEFECTS

Since the present approach substantially relies on the aforementioned analogy between spin ordering in rare-earth oxide pyrochlores and proton ordering in ordinary ice, it should be emphasized that the mechanism of magnetic relaxation considered here is completely analogous to electrical relaxation in ice as described by the theory developed mainly in [5, 10–12]. The most elegant formulation of the theory, based on thermodynamics of irreversible processes, was given in [5]. A detailed discussion of its applications and comparison with experimental results were presented in [6]. Since these publications may not be readily available, a self-contained analysis including a detailed derivation of the equations of the Jaccard theory is presented here instead of simply referring to [5].

It should also be mentioned that some rare-earth oxide pyrochlores are inherently frustrated Heisenberg antiferromagnets. These materials are not analyzed in this paper.

It is most surprising that behavior characteristic of frustrated magnets is also exhibited by other oxide pyrochlores ($Dy_2Ti_2O_7$, $Ho_2Ti_2O_7$, and $Yb_2Ti_2O_7$), in which spin–spin interaction per se is described by the ferromagnetic Heisenberg model (i.e., the corresponding energy proportional to $-\boldsymbol{\sigma}_{i\alpha} \cdot \boldsymbol{\sigma}_{j\beta}$. However, these materials are characterized by strong uniaxial magnetic anisotropy, with axes pointing from the centers of tetrahedra to their vertices. Since the cosine of the tetrahedral angle is –1/3, the effective coupling corresponds to an antiferromagnetic Ising model [8, 9]:

$$H = \frac{J}{2}\sum_{nn}\sigma_{i\alpha}\sigma_{j\beta}, \qquad (1)$$

where $J > 0$, the subscript i refers to shaded tetrahedra in Fig. 1, the subscript α labels the spins in each tetrahedron, and the sum runs over all nearest neighbor pairs (see Fig. 1). The Ising spin $\sigma_{i\alpha}$ can be either +1 or –1. For convenience, the dual lattice consisting of the tetrahedron centers (see Fig. 2) is considered in conjunction with the magnetic lattice (Fig. 1). For rare-earth oxide pyrochlores, it is a diamond lattice consisting of two interpenetrating face-centered cubic sublattices. If one of these is treated as a basic one, then subscripts i and α refer to vertices and midpoints of nearest neighbor bonds in this sublattice, respectively. By convention, $\sigma_{i\alpha} = 1$ and –1 for spins that are, respectively, parallel and antiparallel to the unit vector $\mathbf{e}_{i\alpha}$ of a magnetic anisotropy axis pointing toward the tetrahedron center (or a unit bond vector in the dual lattice).

The ground state of the four spins at the vertices of a pyrochlore-lattice tetrahedron corresponds to any configuration with two spins up and two down. There exist six distinct configurations of this kind, and the corresponding energy is $-J$ per spin. The crystal consisting of N tetrahedra is in the lowest energy state when each tetrahedron is in the ground state, since the Hamiltonian for the crystal can be represented as a sum over all constituent tetrahedra. Therefore, the energy of the ground state of the crystal is $-J$ per spin. The number of such states can be calculated by following the approximation proposed by Pauling [13]. There are 16 distinct configurations of a pyrochlore-lattice tetrahedron; i.e., the relative number of distinct ground-state configurations is 6/16. If the spins are uncorrelated, then the number of ground states of the crystal is $(3/8)^N$ times the total number 2^{2N} of distinct spin configurations: $w = (3/2)^N$.

No spin can be flipped without increasing the energy of the system in any ground state at zero temperature, whereas flipping a spin at a finite temperature increases its energy by $\epsilon_\pm = 4J$ and creates two defect states schematized in Fig. 3. The positive magnetic defect defined as the tetrahedral four-spin configuration with three spins up and one down is a magnetic analog of an ionic defect in ice. Accordingly, the negative magnetic defect (with three spins down and one up) is analogous to a negative ionic defect. Any spin configuration containing magnetic defects admits spin flips without any

increase in energy. Indeed, flipping one of the three identical spins in a magnetic defect is equivalent to moving the defect to another site without creating a new defect (see Fig. 3). A sequence of spin flips makes up the path of a defect considered as a moving quasiparticle. This explains the fundamental role played by defects in magnetic relaxation.

Note that the use of the nearest neighbor model with Hamiltonian (1) implies that the coupling between defects drops to zero even across the lattice spacing. This approximation is obviously valid for exchange (short-range) interaction, whereas the slowly decreasing magnetic dipole–dipole interaction characteristic of the materials in question may be expected to lift the degeneracy inherent in the nearest neighbor model. However, experiments have shown that measured residual entropy is close to that predicted by Pauling's model, no ordered structures have been found, and computations predict that the relative number of nondegenerate states is small. Analogously (and even more surprisingly), the long-range part of the Coulomb interaction does not lift the ground-state degeneracy in the physics of ice, while the ice rules stem from its short-range part. Even though this problem has been addressed in a vast literature, its complete solution is not known to this day (see [14] for the latest results).

A relatively long-range interaction between defects can be neglected when the concentration of defects is low, which is normally the case. However, even in the absence of direct interaction, frustrated systems are characterized by a specific interaction due to the dependence of entropy on the average distance between defects. This dependence is determined by the spin–spin correlation function, which has actually been calculated in [15]. The calculated results suggest that this interaction decays with increasing distance faster than the direct Coulomb interaction and can therefore be neglected. Thus, defects can be treated as noninteracting particles analogous to ions in the lattice gas models of superionic conductors, mainly because their concentration is low and the ensuing results agree with experiment.

To calculate the equilibrium defect concentration, note that each vertex of the dual lattice can be in one of 14 states: six defect-free states, four orientations of a positive defect, and four orientations of a negative defect. The two states with all spins up or down are ignored since the corresponding energies are too high. If the corresponding numbers N_i of vertices in these states ($i = 1, \ldots, 14$) are treated as independent, then the total number of distinct configurations is $N!/\Pi N_i$, including those with correlated and anticorrelated nearest neighbor vertices (with parallel and antiparallel spins at the midpoints of nearest neighbor bonds). It is obvious that configurations of the latter type must be not be counted. If the probability of a correlated configuration is 1/2 (as in Pauling's model), then the number of correlated configurations is $w_\pm = (1/2)^{2N}N!/\Pi N_i$,

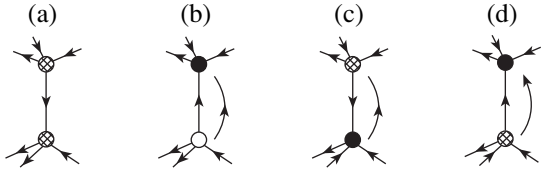

Fig. 3. Fragments of magnetic lattices with (a) no defects, (b) a pair of magnetic defects created by flipping a spin on the vertical bond, and (c, d) displacement of a magnetic defect downwards by a lattice spacing caused by a spin flip on the vertical bond. Hatched, closed, and open circles represent defect-free vertices and positive and negative magnetic defects, respectively.

where 2^N is the number of bonds in the crystal. If defects are created in pairs and all defect orientations are equally probable ($N_1 = \ldots = N_6$, $N_7 = \ldots = N_{14}$), the entropy per spin is $-k\{2x\ln x + (1-2x)\ln(2(1-2x)/3)\}$, where $x = N_\pm/N$ is the concentration of defects per vertex. Hence, the Helmholtz free energy per vertex is

$$f(x) = \epsilon_\pm x + kT \times\left\{2x\ln x + (1-2x)\ln\left(\frac{2}{3}(1-2x)\right)\right\}, \quad (2)$$

and the equilibrium defect concentration is

$$x_\pm = \frac{\frac{2}{3}\exp\left(-\frac{\epsilon_\pm}{2kT}\right)}{1+\frac{4}{3}\exp\left(-\frac{\epsilon_\pm}{2kT}\right)}. \quad (3)$$

At the relatively low temperatures typical for most experiments, the concentration of defects is exponentially small:

$$x_\pm \approx \frac{2}{3}\exp\left(-\frac{\epsilon_\pm}{2kT}\right).$$

With increasing temperature the concentration tends to the finite limit $x_\pm \approx 2/7$.

3. MAGNETIC CHARGES AND GOVERNING EQUATIONS

Magnetic defects can carry effective magnetic charges. To demonstrate this possibility, an arbitrary spin configuration is represented as a superposition of intersecting polygonal strings of dual-lattice bonds whose magnetic moments are ordered along the corresponding strings. In defect-free configurations (with two nearest spins up and two down for each dual-lattice vertex), each string either closes on itself or terminates on the crystal surface. In a configuration with defects, a string may terminate on a defect, i.e., inside the crystal.

The magnetic field generated by each string of magnetic dipoles is equivalent to the superposition of the fields of magnetic charges placed at its ends. Even though this can be demonstrated by straightforward calculation, a much simpler proof relies on analogy with macroscopic electrostatics. Indeed, the macroscopic magnetic field can be calculated by adding the applied magnetic field to the field generated by all magnetic dipoles. By analogy with macroscopic electrostatics, the latter field is equal to that generated by space charge with density $-\mathrm{div}\mathbf{M}$, where $\mathbf{M}$ is magnetic moment density. Since the divergence does not vanish only for defects of the type illustrated by Fig. 3, it is clear that positive and negative defects can be associated with positive and negative magnetic charges, respectively.

The absolute value of the magnetic charge carried by a defect can be expressed in terms of spin magnetic moment as follows. Since the displacement of a positive defect to the nearest neighbor dual-lattice vertex in an applied magnetic field corresponds to flipping one of its nearest spins, the resulting change in energy is $\delta E = 2\mu H$, where H is the strength of magnetic field parallel to the spin's magnetic moment. On the other hand, if the same displacement is treated the motion of a magnetic defect with charge m driven by the force $F = mH$, then the energy increment is $\delta E = mHa$, where a is the dual-lattice spacing. Comparing the two expressions, we obtain $m = 2\mu/a$. To avoid confusion, the ratio of the force to the magnetic field strength is treated as the key parameter. Accordingly, the dimension of magnetic charge is Hm/A, and the corresponding dimension Hm^2/A of μ is that of Coulomb's magnetic moment, which is related to Ampére's magnetic moment μ_a as $\mu = \mu_a\mu_0$, where μ_0 is the free-space permeability. Note that the magnetic field generated by spins cannot be treated as the field of effective magnetic charges. For example, the demagnetizing field generated by spins in a uniformly polarized sample does not vanish even in the absence of defects. However, this demagnetizing field can be taken into account in a standard manner by introducing a surface polarization charge density.

The analysis above is part of a theory in which magnetic defects are interpreted as quasiparticles. Accordingly, a correlated spin system should be treated as a system of defects, while the spins of all ground-state sites are not taken into account. However, a model of this kind differs from conventional quasiparticle theories in that both ground and excited states are infinitely degenerate. These states are completely characterized by specifying not only the number and location of magnetic defects, but also the spin configuration of the entire crystal. However, this information is redundant for many purposes. In particular, it is shown below that magnetic phenomena can be described in terms of a single vector variable: a configuration vector proportional to local magnetization. Configurations with distinct spin orderings characterized by equal magnetizations are equivalent in terms of their magnetic properties. In view of this fact and the analogy with the physics of ice, the configuration vector is defined as follows [5, 16]:

$$\mathbf{\Omega}(\mathbf{r}) = \frac{a}{2}\sum_{i\alpha}\sigma_{i\alpha}\frac{\mathbf{e}_{i\alpha}}{V}, \tag{4}$$

where the sum runs over all spins inside a macroscopically small volume V around the point $\mathbf{r}$. It is clear that the configuration vector is proportional to the local magnetization $\mathbf{\Omega} = \mathbf{M}/m$.

Another, probably more important, role played by the configuration vector stems from its relationship to defect fluxes. Suppose that N_s spins initially parallel to a unit vector $\mathbf{e}$ in a macroscopically small volume V have flipped. The ensuing change in the configuration vector is $\delta\mathbf{\Omega} = -a\mathbf{e}N_s/V$. Since each spin flip is equivalent to the displacement of a positive defect by $d\mathbf{r}_+ = -a\mathbf{e}$ or of a negative defect by $d\mathbf{r}_- = a\mathbf{e}$, the change in the configuration vector can be represented as $\delta\mathbf{\Omega} = d\mathbf{r}_+N_+ - d\mathbf{r}_-N_-$, where N_+ and N_- denote, respectively, the number of displacements of positive and negative defects caused by spin flips ($N_s = N_+ + N_-$). Accordingly, $\partial\mathbf{\Omega}/\partial t = \mathbf{j}_1 - \mathbf{j}_2$, where $\mathbf{j}_{1,2} = \mathbf{v}_\pm N_\pm/V$ denotes the positive- or negative-defect flux. This relation can be rewritten in integral form:

$$\mathbf{\Omega}(t) - \mathbf{\Omega}(0) = \int_0^t (\mathbf{j}_1 - \mathbf{j}_2)dt'. \tag{5}$$

Note also that the residual entropy of the system is slightly reduced by specifying the configuration vector, i.e., by more detailed characterization of spin ordering. It was shown in [16] that this reduction can be represented as

$$S_c(\mathbf{\Omega}) - S_c(0) = -\frac{4}{\sqrt{3}}ak|\mathbf{\Omega}|^2. \tag{6}$$

Equations (5) and (6) can be used to express the defect fluxes in terms of applied magnetic field and configuration vector. This can be done in a standard manner by invoking the expression for local entropy production density used in thermodynamics of irreversible processes [5]. In the present context, it can be written as follows:

$$T\dot{S} = \sum_{i=1}^{2}\mathbf{j}_i\cdot m_i\mathbf{H} + T\dot{S}_c, \tag{7}$$

where $i = 1$ and 2 correspond, respectively, to positive and negative defects and $m_{1,2} = \pm 2\mu/a$ denote their respective magnetic charges. The first term in (7) is the work done by the applied magnetic field per unit time. The second term related to the aforementioned ordering

caused by defect fluxes. Substituting (5) and (6) into (7) yields

$$T\dot{S} = \sum_{i=1}^{2} \mathbf{j}_i \cdot (m_i \mathbf{H} - \eta_i \Phi \boldsymbol{\Omega}), \quad (8)$$

where $\eta_{1,2} = \pm 1$ and $\Phi = (8/\sqrt{3})akT$. Alternatively, the same quantity can be represented in terms of generalized driving forces $\mathbf{f}_i$ as $\sum \mathbf{j}_i \cdot \mathbf{f}_i$. Comparing the two representations, we obtain an expression for the driving forces:

$$\mathbf{f}_i = m_i \mathbf{H} - \eta_i \Phi \boldsymbol{\Omega}. \quad (9)$$

Here, the second term reflects spin ordering: when the spins are partially ordered, there exists a nonzero defect flux even in the absence of applied magnetic field. This contribution to the generalized force is due to entropy, but not to any effect of applied field. By using the expression for the generalized forces and introducing mobilities μ_i and defect concentrations $n_i = x_i N$, the fluxes can be written as

$$\mathbf{j}_i = \mu_i n_i (m_i \mathbf{H} - \eta_i \Phi \boldsymbol{\Omega}). \quad (10)$$

Here, the off-diagonal elements of the transport coefficient matrix (cross-field transport coefficients) are neglected in the linear approximation as quantities of second order in density.

4. MAGNETIC SUSCEPTIBILITY

Equations (5) and (10) constitute a closed system, which can be solved to find $\boldsymbol{\Omega}$ and $\mathbf{j}_i$ for an arbitrary time-dependent applied magnetic field. These simple equations are remarkable in that each instantaneous flux density in (10) depends on its previous values by virtue of (5).

These equations can be used to find the frequency dependence of magnetic susceptibility as follows. When a uniform magnetic field with strength $\sim\exp(-i\omega t)$ is applied to the system, the distribution of magnetic defects (magnetic charge carriers) remains uniform. Since all relations in the present theory are linear, all variables are characterized by harmonic time dependence. Therefore, the Fourier transform of Eq. (5) yields

$$\boldsymbol{\Omega}_\omega = (\mathbf{j}_{1\omega} - \mathbf{j}_{2\omega})/(-i\omega).$$

By substituting the Fourier transform of (10) for $\mathbf{j}_{1\omega}$ and $\mathbf{j}_{2\omega}$, magnetization is expressed in terms of the configuration vector as

$$\mathbf{M}_\omega = \chi(\omega)\mathbf{H}_\omega, \quad \chi(\omega) = \frac{m^2/\Phi}{1 - i\omega\tau}, \quad (11)$$

where the relaxation time τ is defined by the relation $\tau^{-1} = (\mu_1 n_1 + \mu_2 n_2)\Phi$ and the low-frequency magnetic susceptibility is $\chi(0) = (\sqrt{3}/2)(\mu^2/a^3)/kT$. The absolute value of this susceptibility is twice as large as the susceptibility of normal paramagnet at similar density and temperature. However, the result obtained for a cooperative paramagnet holds at an arbitrarily low temperature; i.e., the former susceptibility can be much higher than the latter. An estimate for the static susceptibility of a rare-earth oxide pyrochlore at $T = 10$ K is obtained by using $g \approx 9$ in $\mu = g\mu_B$ and $a = 2 \times 10^{-10}$: $\chi_a = \chi/\mu_0 \approx 7.5$, where the dimensionless susceptibility is defined in terms of the Ampére's magnetic moment as $\chi_a = M_a/H$.

5. CONCLUSIONS

It is shown that magnetic processes in geometrically frustrated magnets can be described in terms of defect concentrations, defect flux densities, and a configuration vector (Eqs. (3), (10), and (5), respectively). The model yields expressions for frequency-dependent magnetic susceptibility and static magnetic susceptibility (Eq. (11)). Note also that the "magnetic variant" of the Jaccard theory developed here provides a basis for direct treatment of a variety of unusual magnetic phenomena analogous to certain electrical phenomena in ice: magnetic charge transport, magnetic field screening, and other physical processes due to the existence of magnetic charge associated with defects.

Finally, some comments are in order concerning the scope of the theory and possible lines of further development. For simplicity, it is assumed in the present analysis that the defects are uniformly distributed and their concentration is given by (3). Since magnetic defects are created in pairs, this implies that the macroscopic density of magnetic charge is zero, i.e., magnetic field can only be generated externally. In a nonuniform state, the defect concentrations are functions of coordinates, and two additional equations are required to find them. As in the theory of electrical properties of ice, these equations can be derived from the continuity equation for the fluxes, relation (6), and the magnetic analog of Poisson's equation [17].

ACKNOWLEDGMENTS

This work was supported by the Russian Foundation for Basic Research, project no. 01-02-16459.

REFERENCES

1. A. P. Ramirez, Annu. Rev. Mater. Sci. **24**, 453 (1994).
2. G. N. Wannier, Phys. Rev. **79**, 357 (1950).
3. M. J. Harris, S. T. Bramwell, D. F. McMorrow, *et al.*, Phys. Rev. Lett. **79**, 2554 (1997).

4. A. P. Ramirez, A. Hayashi, R. J. Cava, *et al.*, Nature **399**, 333 (1999).
5. C. Jaccard, J. Phys.: Condens. Matter **3**, 99 (1964).
6. V. F. Petrenko and R. W. Whitworth, *Physics of Ice* (Oxford Univ. Press, Oxford, 1999).
7. P. W. Anderson, Phys. Rev. **102**, 1008 (1956).
8. I. A. Ryzhkin, Solid State Commun. **52**, 49 (1984).
9. I. A. Ryzhkin, in *Physics and Chemistry of Ice*, Ed. by N. Maeno and T. Hondoh (Hokkaido Univ. Press, Sapporo, 1992), p. 141.
10. N. Bjerrum, K. Dan. Vidensk. Selsk. Mat. Fys. Medd. **27**, 1 (1951).
11. H. Granicher, C. Jaccard, P. Sherrer, and A. Steinemann, Discuss. Faraday Soc. **23**, 50 (1957).
12. L. Onsager and M. Dupuis, in *Termodinamica dei processi irreversibili, Rendiconti della Scuola Internazionale di Fisica "Enrico Fermi"* (Varenna, 1959), Corso X, p. 294.
13. L. Pauling, J. Am. Chem. Soc. **57**, 2680 (1935).
14. S. V. Isakov, R. Moessner, and S. L. Sondhi, cond-mat/0502137.
15. J. F. Nagle, Chem. Phys. **43**, 317 (1979).
16. I. A. Ryzhkin and R. W. Whitworth, J. Phys.: Condens. Matter **9**, 395 (1997).
17. V. F. Petrenko and I. A. Ryzhkin, Zh. Éksp. Teor. Fiz. **87**, 558 (1984) [Sov. Phys. JETP **60**, 320 (1984)].

Translated by A. Betev

Journal of Experimental and Theoretical Physics, Vol. 101, No. 3, 2005, pp. 487–493.
Translated from Zhurnal Éksperimental'noĭ i Teoreticheskoĭ Fiziki, Vol. 128, No. 3, 2005, pp. 567–574.

ORDER, DISORDER, AND PHASE TRANSITIONS IN CONDENSED SYSTEMS

Electromagnetic Field Penetration through Lanthanum Manganites

V. V. Ustinov[a], A. P. Nossov[a,*], A. B. Rinkevich[a,], and V. G. Vasil'ev[b]**

[a]*Institute of Metal Physics, Ural Division, Russian Academy of Sciences, Yekaterinburg, 620219 Russia*
[b]*Institute of Solid State Chemistry, Ural Division, Russian Academy of Sciences, Yekaterinburg, 620129 Russia*
**e-mail: nossov@imp.uran.ru*
***e-mail: rin@imp.uran.ru*
Received February 21, 2005

Abstract—The process of electromagnetic field penetration through lead-doped lanthanum manganites exhibiting colossal magnetoresistance has been studied. The measurements have been performed in a range of radio frequencies from 20 kHz to 10 MHz in the temperature interval containing a magnetic phase transition. Application of a constant external magnetic field leads to an increase in the transmission coefficient. Relative variations of the electromagnetic field transmission coefficient are several times as large as the relative change in the dc magnetoresistance. The temperature dependence of the relative change in the transmission coefficient has been studied. Variations of the transmission coefficient sharply decrease in the vicinity of the phase transition temperature, but they still remain rather large at temperatures above the Curie point. *© 2005 Pleiades Publishing, Inc.*

1. INTRODUCTION

The discovery of the phenomenon of colossal magnetoresistance (CMR) in the vicinity of a magnetic phase transition temperature in lanthanum manganites has stimulated an enduring activity in investigations of the physical properties of a broad class of strongly correlated oxide-based materials with perovskite structures and related mesoscopic systems. It was found that the physical properties of these materials are determined by the strong relationship between their structure and the magnetic and charge subsystems. At present, the static electrical and magnetic properties of doped manganites near the magnetic phase transition temperature have been studied in sufficient detail [1, 2].

A special position in the arsenal of methods used for the investigation of such systems is occupied by the dynamic electromagnetic techniques, which provide diagnostics of the response of the spin subsystem to external action in a broad frequency range. In application to manganites, most extensively developed are the methods based on the ferromagnetic resonance and antiresonance in the microwave frequency range. At the same time, the study of manganites by radio frequency (rf) techniques has received much less attention. However, the rf range is of considerable importance because the effects observed at these frequencies have mach greater magnitudes than those detected by the dc measurements. By varying the probing signal frequency, it is possible to control the skin depth and make it comparable to the sample size, thus providing a smooth transition between various mechanisms involved in the interaction of the probing electromagnetic field with the spin subsystem of the probed material.

The skin effect in manganites in the rf range has been studied in [3], where it was pointed out that the method of electromagnetic field penetration is an effective tool for the investigation of dynamic properties of these materials. A detailed study of the magnetoimpedance effect was performed in [4, 5], where the data obtained in a broad frequency range were compared to the results of CMR measurements in the dc regime. The magnetic state of manganites in these experimenters was studied in the region of the magnetic phase transition temperature T_C.

The magnetic susceptibility measured in manganites at low frequencies and in a constant magnetic field significantly decreases at $T > T_C$, and the temperature dependence of the susceptibility frequently deviates from that according to the Curie law [6, 7]. Data on the absorption of electromagnetic waves obtained in the microwave range [7] and from the surface impedance measurements [8] showed that the effects related to the magnetic antiresonance exist above the Curie temperature (T_C). These results can probably be interpreted in terms of conservation of the local magnetic order in manganites in a certain temperature interval extending well above T_C.

The measurements of the electromagnetic characteristics of manganites in the rf range at temperatures near the magnetic phase transition and the elucidation of physical mechanisms responsible for the variation of these characteristics are very important and interesting problems. These were the main goals of the present

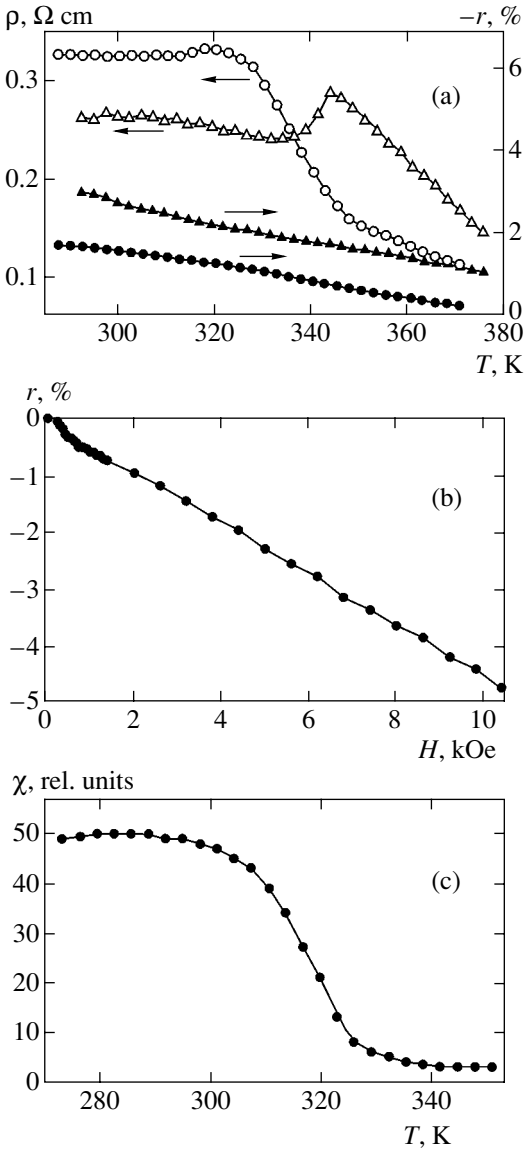

Fig. 1. The results of the resistivity (ρ), magnetoresistance (*r*) and magnetic susceptibility (χ) measurements for lead-doped lanthanum manganites: (a) the temperature dependence of resistivity and MR for compositions 1 (circles) and 2 (triangles); (b) the field dependence of the relative MR of composition 2 at $T = 291$ K; (c) the temperature dependence of the magnetic susceptibility of composition 1.

study, in which the experiments were performed using the method of electromagnetic field penetration. This method has been developed in detail previously and successfully applied to the investigation of manganites and some other low-conductivity media [9, 10]. Under conditions where the thickness of a sample plate through which the probing field penetrates is smaller than the skin depth, variations of the electromagnetic wave transmission coefficient in the applied magnetic field are determined by changes in the sample impedance. These changes of the impedance are related to variations of the electric resistance and the dynamic magnetic permeability. Therefore, by studying rf electromagnetic field penetration in a sample in the vicinity of the magnetic phase transition temperature, it is possible to obtain information concerning the state of the magnetic subsystem of the sample material.

In our experiments, the electromagnetic field penetration through lead-doped lanthanum manganites has been studied in a range of radio frequencies from 20 kHz to 10 MHz. Such manganites, exhibiting a magnetic phase transition above room temperature, are model magnetic systems whose static properties are determined by the double exchange in the presence of strong spin-lattice interactions. We have studied electromagnetic field penetration through a manganite plate at temperatures both below and above the magnetic phase transition temperature. The results of our investigation of the rf characteristics will be compared to the results of measurements of the static magnetic and magnetotransport properties in order to reveal differences between the static and dynamic properties of manganites in the vicinity of the magnetic phase transition.

2. EXPERIMENTAL METHOD

Samples of lead-doped lanthanum manganites $La_{0.85}Pb_{0.15}MnO_3$ and $La_{0.75}Pb_{0.25}MnO_3$ (below, compositions 1 and 2, respectively) were synthesized via thermal treatment of preliminarily prepared precursors—lead and manganese oxalates. The precursors were annealed for 12 h in air at 800°C and pressed, after which the blanks were additionally annealed for 12 h in oxygen flow at 950°C. The content of lead and manganese and the Mn^{3+}/Mn^{4+} ratio in the pressings were determined by means potentiometric titration. The electromagnetic field penetration experiments were performed on 1.2-mm-thick plates cut from the massive blanks. The results of our measurements of the magnetoresistance (MR) and the magnetic susceptibility (χ) are presented in Fig. 1.

The temperature dependences of the resistivity $\rho(T)$ and the relative MR defined as

$$r = \frac{\rho(H) - \rho(0)}{\rho(0)} \times 100\%$$

(where H is the magnetic field strength) presented in Fig. 1a are typical of the doped manganites. The data on the MR presented in Fig. 1 were obtained for $H = 10$ kOe. At room temperature ($T = 291$ K) and $H = 0$, the resistivity was 0.134 Ω cm for composition 1 and 0.185 Ω cm for composition 2. In both manganites, the MR is negative and its temperature dependence exhibits a maximum (which is more pronounced for composition 2) near the magnetic phase transition temperature. As the temperature is increased further, the MR decreases. The maximum relative MR measured at $H = 10$ kOe did not exceed –6.3 and –5.4% for composi-

tions 1 and 2, respectively. The field dependence of the relative MR measured at room temperature can be divided into two parts (Fig. 1b). The first part extends over field strengths below 600 Oe. In this region, the MR exhibits a nonlinear dependence on the applied field strength. In the second region covering the fields above 600 Oe, the MR exhibits approximately linear growth with the field strength.

Figure 1c shows the temperature dependence of the magnetic susceptibility measured for composition 1 at a frequency of 80 Hz. As can be seen, χ exhibits a sharp decrease in the region of the magnetic phase transition. The curves measured in the sample heating and cooling mode were practically identical. Using the temperature dependence of χ, we determined the magnetic phase transition temperature as $T_{C1} = 322$ K for composition 1 and $T_{C2} = 341$ K for composition 2.

The absolute value of the electromagnetic field transmission coefficient D was measured in the range of frequencies from 20 kHz to 10 MHz at various temperatures and applied constant magnetic field strengths. Figure 2 shows a schematic diagram of the experimental arrangement. The probing alternating (rf) magnetic field H_{in} was generated by a coil situated on one side of the sample plate. The transmitted field H_{out} on the other side of the plate was detected using another coil. The manganite plate served as a screen. The absolute value of the transmission coefficient was calculated using the formula $|D| = |H_{out}/H_{in}|$. The constant magnetic field was always applied in the plane of the sample and was parallel to the probing alternating field. The absolute value of D was studied as a function of the applied constant field strength and/or the temperature in a range from 273 to 365 K.

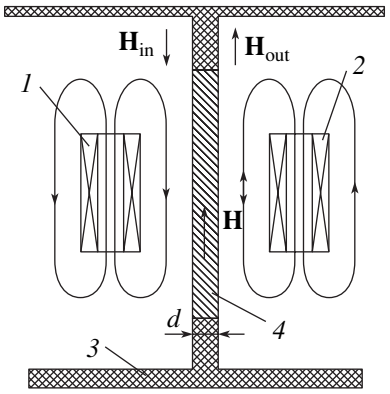

Fig. 2. A schematic diagram of the experimental arrangement: (*1*) probing coil; (*2*) detecting coil; (*3*) shield; (*4*) sample plate.

3. EXPERIMENTAL RESULTS

The rf electromagnetic field transmission coefficient D strongly depends on the applied constant magnetic field strength. The fact that the relative change in the transmission coefficient may exceed the corresponding value (r) of the static MR was reported previously [9]. The field dependence of the relative change in the transmission coefficient was determined as

$$r_m = \frac{D(H) - D(0)}{D(0)} \times 100\%.$$

Figure 3a shows the plots of r_m versus magnetic field strength for composition 2 measured at room temperature and various frequencies. As can be seen, the relative variations of this value reach 85%. As the probing field frequency is increased, the r_m value also grows and the curve exhibits a maximum. At high frequencies, the relative variations of the transmission coefficient tend to decrease.

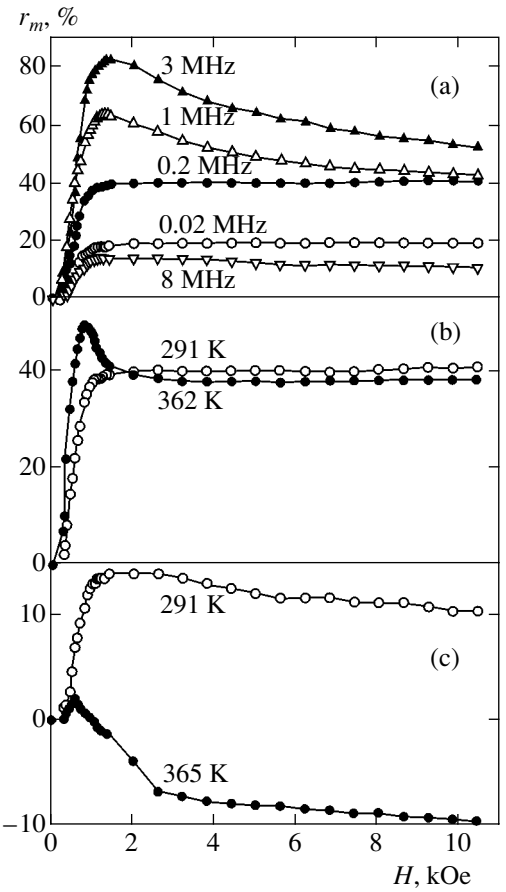

Fig. 3. Plots of the relative change r_m in the transmission coefficient versus magnetic field strength for composition 2 measured (a) at room temperature ($T = 291$ K) and various frequencies and (b, c) at different temperatures (below and above T_C) at $f = 0.2$ (b) and 8 MHz (c).

Figures 3b and 3c show the field dependences of r_m measured at different temperatures: below and above the temperature of the magnetic phase transition. The data presented in Fig. 3b were obtained at a frequency of $f = 200$ kHz, while the curves in Fig. 3c were measured at $f = 8$ MHz. As can be seen, heating a sample

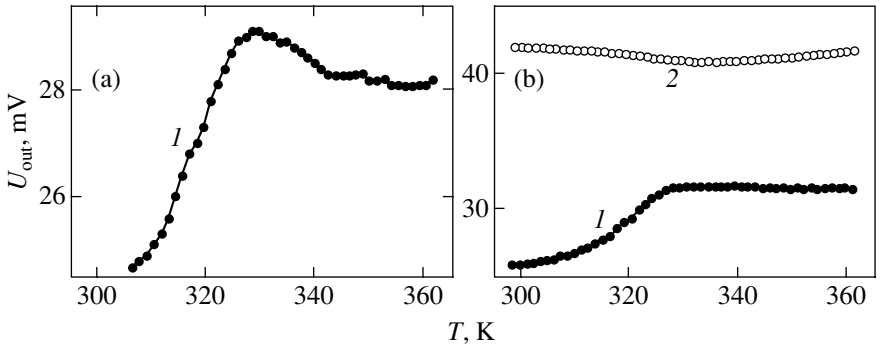

Fig. 4. The temperature dependences of the rf signal amplitude U_{out} transmitted through a plate of composition 1 measured at f = 0.2 (a) and 8 MHz (b) in a zero field (*1*) and in a field of H = 8 kOe (*2*).

above the phase transition temperature dramatically changes the field dependence of the transmission coefficient.

Figure 4 shows the temperature dependence of the amplitude U_{out} of a signal transmitted through the sample plate. The U_{out} value is proportional to the transmission coefficient D. All these measurements were performed in the sample cooling mode. Figure 4a presents a curve obtained at f = 200 kHz in the absence of an applied constant magnetic field. As can be seen the amplitude of the transmitted signal significantly decreases at temperatures below the phase transition temperature. Figure 4b compares the $U_{out}(T)$ curves measured at f = 8 MHz before and after application of a constant field with a strength of 8 kOe. As can be seen from curve *1* measured for H = 0, the transmitted signal amplitude also decreases at temperatures below the phase transition temperature. Curve *2* shows that the application of an external field sufficient to saturate the sample removes pronounced features in the region of the phase transition.

Let us consider the temperature dependences of the relative change r_m in the transmission coefficient measured for the same sample in the nonmagnetized (H = 0) and saturation-magnetized (H = 8 kOe) states. Figure 5 shows the results of such comparative measurements at a frequency of 8 MHz. The data presented in Figs. 4b and 5 are well consistent with each other. As the temperature increases to approach T_C, the efficiency of action of the applied constant field decreases.

4. THEORY OF THE rf ELECTROMAGNETIC FIELD PENETRATION THROUGH A CONDUCTING FERROMAGNETIC PLATE

This section briefly considers the theory of the electromagnetic field penetration through a conducting ferromagnetic plate. At a sufficiently high (microwave) frequency on the order of several gigahertz, the transmission coefficient is significantly influenced by the ferromagnetic resonance and antiresonance effects [11, 12]. Let us restrict the consideration to much lower frequencies in the rf range. The problem of description of the rf electromagnetic field penetration through a medium has been extensively studied. For a theoretical description of the observed phenomena, we will use an approximation ignoring the resonance and antiresonance effects, but admitting broad variation of the following parameters: frequency, skin depth, and magnetic permeability.

A formula for the coefficient of radiation transmission through a conducting plate under normal skin effect conditions [13] is as follows:

$$D = \frac{2Z_m}{2Z_m\cosh(k_m d) + Z\sinh(k_m d)}, \qquad (1)$$

where $k_m = (1 + i)/\delta$ is the wavenumber in the conducting medium, $\delta = \sqrt{2\rho/\omega\mu\mu_0}$ is the skin depth, $\mu = 1 +$

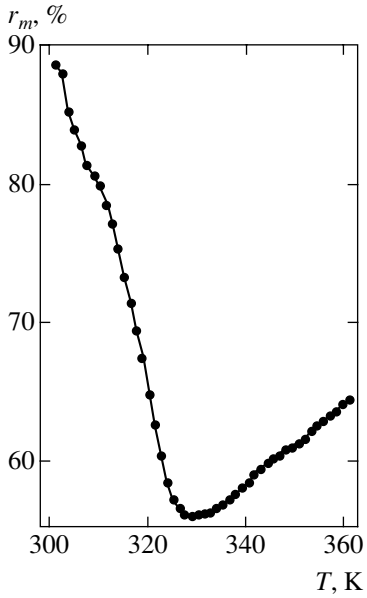

Fig. 5. The temperature dependence of the relative change r_m in the transmission coefficient measured for composition 1 at f = 8 MHz and H = 8 kOe.

χ is the relative dynamic differential permeability, and $\omega = 2\pi f$.

As can be seen, the transmission coefficient D depends on the relations (i) between impedances of the sample (Z_m) and the surrounding space ($Z = \sqrt{\mu_0/\varepsilon_0}$) and (ii) between the plate thickness d and the skin depth δ. The impedance of the sample plate is given by the formula

$$Z_m = \frac{1+i}{\delta}\rho. \tag{2}$$

For a well conducting medium, this value is always smaller than Z ($|Z_m| \ll Z$).

There are two possible situations in which one of the two terms in the denominator of expression (1) predominate. The case of low frequencies and thin plates corresponds to the condition

$$2Z_m\cosh(k_m d) \gg Z\sinh(k_m d).$$

This condition is satisfied provided that

$$k_m d \ll 1, \quad d \ll 2\rho/Z. \tag{3}$$

In this case, the transmission coefficient is determined by the formula

$$D = 1/\cosh(k_m d),$$

which further simplifies for $d \ll \delta$ to yield

$$|D| \approx 1 - \frac{1}{3}\left(\frac{d}{\delta}\right)^4. \tag{4}$$

The corresponding relative change in the transmission coefficient in this case can be calculated using the formula

$$r_m = -\frac{1}{12}d^4\omega^2\mu_0^2\left(\frac{\mu^2(H)}{\rho^2(H)} - \frac{\mu^2(0)}{\rho^2(0)}\right). \tag{5}$$

Since $d \ll \delta$, we may assume that r_m is small. If the MR is small—that is, $\rho(H) \approx \rho(0)$—and the initial permeability is large ($\mu(0) \gg 1$ in a saturating field, where $\mu(H) \approx 1 \ll \mu(0)$), a change in the absolute value of the transmission coefficient is given by the formula

$$r_m \approx \frac{d^4\mu^2(0)\mu_0^2}{12\rho^2(0)}\omega^2 \quad (\text{for } H \longrightarrow \infty). \tag{6}$$

Thus, a change in the transmission coefficient for the rf field penetrating through a very thin plate at low frequencies for $\mu(0) \gg 1$ are related predominantly to variations in the magnetic permeability. The change is small ($r_m \ll 1$), has a positive sign, and (in the absence of frequency dispersion of the material constants) is proportional to the frequency squared ($r_m \sim \omega^2$).

In the other limiting case in which $2Z_m\cosh(k_m d) \ll Z\sinh(k_m d)$ in the denominator of expression (1), the transmission coefficient is given by the formula

$$D = \frac{2Z_m}{Z\sinh(k_m d)} = \frac{2(1+i)\rho}{Z\delta} \times \frac{1}{\sinh(d/\delta)\cos(d/\delta) + i\cosh(d/\delta)\sin(d/\delta)}, \tag{7}$$

which yields for a thin screen ($d \ll \delta$)

$$D = \frac{2\rho}{Z\mu d}. \tag{8}$$

In this limiting case, the transmission coefficient is real provided that the material constants are real. Expression (8) gives the following formula for the relative variations in the absolute value of the transmission coefficient:

$$\frac{\Delta D(H)}{D(0)} = \frac{\Delta\rho(H)/\rho - \Delta\mu(H)/\mu}{1 + \Delta\mu(H)/\mu}, \tag{9}$$

where $\Delta\rho(H)/\rho$ is the relative change of the resistivity in the constant magnetic field H and $\Delta\mu(H)/\mu$ is the relative change of the magnetic permeability. For $|\Delta\rho/\rho| \ll 1$ and $\mu(H \longrightarrow \infty) \longrightarrow 1$, we obtain [9]

$$\frac{\Delta D(H \longrightarrow \infty)}{D(0)} \approx \mu(0) - 1. \tag{10}$$

Using formula (10), it is possible to evaluate the initial dynamic magnetic permeability from the corresponding relative change of the electromagnetic field transmission coefficient. In this limiting case, we can also use relation (8) to derive the following formula taking into account the MR of the plate:

$$\left|\frac{D(H \longrightarrow \infty)}{D(0)}\right| = \mu(0)\left(1 + \frac{\Delta\rho}{\rho}\right). \tag{11}$$

Finally, let us consider the case of a thick conducting plate, which corresponds to $d \gg \delta$. In this case, formula (7) yields

$$|D| = \frac{2\rho}{Z\delta\sinh^2(d/\delta)} = \frac{8\rho}{Z\delta}\exp\left(-\frac{d}{\delta}\right). \tag{12}$$

Obviously, a decisive factor influencing the transmission coefficient in this case is the skin effect. If the applied constant field exceeds the saturation level, relation (12) reduces to

$$\frac{D(H \longrightarrow \infty)}{D(0)} = \frac{\rho(H)\delta(0)}{\rho(0)\delta(H)}\exp\left[-d\left(\frac{1}{\delta(H)} - \frac{1}{\delta(0)}\right)\right].$$

Substituting explicit expressions for the skin depth $\delta = \sqrt{2\rho/\omega\mu\mu_0}$ for the normal skin affect and assuming

that $\mu(0) \gg 1$, we eventually obtain

$$\left|\frac{D(H \longrightarrow \infty)}{D(0)}\right| = \sqrt{\frac{\rho(H)}{\rho(0)\mu(0)}}\exp\left[\frac{d}{\delta(0)}\right]. \quad (13)$$

It should be noted that the above description of the electromagnetic field penetration through a ferromagnetic conducting plate has (in addition to the explicitly formulated assumptions) the following limitations. It was also assumed that the plate not limited in the *xy* plane, while the real experiments are performed with a plate of finite dimensions. In addition, the theoretical analysis assumes that the probing rf field is homogeneous, whereas in the experiments this field represents a stray field of the coil. These circumstances affect the absolute values of the transmission coefficient. However, from the standpoint of the analysis of the field and temperature dependences of the transmission coefficient, the influence of these additional factors on the r_m value is not as significant. Therefore, application of the proposed simplified approach to the interpretation of qualitative features of the experimental results is quite justified.

5. DISCUSSION OF EXPERIMENTAL RESULTS

In order to compare the experimental results to the theoretical formulas obtained for the relative variations of the transmission coefficient, it is necessary to determine the region of parameters in which the measurements were performed. Using the values of the sample resistivity, it is easy to estimate the skin depth at a relative permittivity equal to unity: $\delta_1 = \sqrt{2\rho/\omega\mu_0}$. For a frequency of 1 MHz, this formula yields $\delta_1 = 18.2$ and 21.4 mm for compositions 1 and 2, respectively. As can be readily seen, this implies that the condition $\delta_1 \gg d$ is satisfied in the entire range of frequencies used in our experiments.

First, let us consider the results of measurements of the coefficient D as a function of the magnetic field strength. The data presented in Fig. 3a were obtained at room temperature, that is, for the sample occurring in a ferromagnetic state. As the field magnetic strength grows, the transmission coefficient increases and, when the measurements are performed at a frequency of 0.2 MHz, reaches a maximum and saturates in stringer fields. A difference between the D values at $H = 8$ kOe and $H = 0$ at all frequencies exceeds 10%, while the relative MR measured in the dc regime at $H = 8$ kOe is significantly lower. Therefore, we may conclude that variations of the rf electromagnetic field transmission coefficient under these conditions are caused predominantly by changes in the magnetic permeability.

The growth of the r_m value with increasing frequency for $f \leq 3$ MHz can be related to the passage from a low-frequency range (where the changes in D are small and can be described using formula (5)) to the range where the transmission coefficient obeys formula (9) and exhibits much greater variations. Numerical estimates showed that condition (3) is never realized in our experiments and, hence, even at the lowest frequencies the system occurs in the state of passage to the condition $2Z_m\cosh(k_m d) \ll Z\sinh(k_m d)$. Then, a drop in the relative variations of the transmission coefficient at the frequencies above 3 MHz can be related to the decrease in the dynamic magnetic permeability caused by the frequency dispersion.

The results of measurements of the field dependence of D at a frequency of 0.2 MHz for two temperatures (Fig. 3b) revealed the appearance of a maximum at a field of about 0.8 kOe on the curve corresponding to $T > T_C$. It should be noted that the magnitude of r_m in the region of strong fields is practically the same for both temperatures. The large value of relative changes in the transmission coefficient suggests that the observed effect cannot be related to the MR. Then, we have only to assume that the manganite sample under study at $T = 362$ K (i.e., above T_C) retains a local ferromagnetic order and has a rather large dynamic magnetic permeability. An estimate obtained using formula (10) for the experimental conditions corresponding to Fig. 3b yields the initial relative magnetic permeability $\mu(0) \approx 1.4$. Analogous field dependences measured at 8 MHz are depicted in Fig. 3c. As can be seen, a change in the transmission coefficient measured at $T = 291$ K (i.e., below T_C) is always positive and, hence we may suggest that it is caused by variations of the permeability μ. Above T_C, the character of the observed field dependence has changed and the transmission coefficient variations are negative. This sign of r_m can be expected when the MR is a key factor. Note that, at the higher frequency, the effect of the magnetic permeability at temperature above T_C is significantly less pronounced.

The results of measurements presented in Fig. 4 also generally correspond to the above interpretation. Indeed, as can be seen from Fig. 4a, the amplitude of the signal transmitted through the plate significantly increases at $T > T_C$, which is related to a decrease in the magnetic permeability. The signal amplitude transmitted in a strong field is significantly higher than that observed in a zero field (Fig. 4b). An anomaly observed near the Curie temperature is more pronounced in the zero field than in a saturating field. The values of r_m reflect differences in the level of signals transmitted in a zero field and in the saturating field.

The data in Fig. 5 show that, as the temperature increases and approaches T_C, the relative change in the absolute value of the transmission coefficient sharply decreases. This is caused by decrease in the initial magnetic permeability $\mu(0)$. However, significant (about 60%) variations in the transmission coefficient are still retained near and above T_C. These variations cannot be related to the MR, since the observed changes have

opposite sign and a magnitude several times that of the MR. Therefore, we must suggest that these changes even at $T > T_C$ are related predominantly to variations of the magnetic permeability.

Naturally, the results of magnetic susceptibility measurements presented in Fig. 1c show that the long-range magnetic order is not retained at $T > T_C$ in the whole sample. These results can be explained if we assume that a short-range local magnetic order may exist in a certain temperature interval above T_C. The obtained data do not allow us to estimate the dimensions of such ordered local regions, but they give the value of the dynamic initial magnetic permeability $\mu(0)$ for a thick sample. According to this, lead-doped manganites are characterized by $\mu(0) \approx 1.4$–1.6 at frequencies up to several hundred kilohertz. Finally, it should be noted that the results of experiments [4, 6, 7] performed at higher frequencies (several gigahertz) and the phenomena observed in [5, 14] can also be related to the presence of a local magnetic ordering above the Curie temperature.

6. CONCLUSIONS

Electromagnetic field penetration through lead-doped lanthanum manganites was studied in a range of radio frequencies from tens of kilohertz to tens of megahertz and it was established that the absolute value of the transmission coefficient sharply increases at temperatures above T_C. Application of a constant magnetic field significantly decreased the relative variations of the transmission coefficient near and above the Curie temperature. The data on the electromagnetic field transmission coefficient were compared to the results of static measurements of the CMR and the magnetic permeability. The results were convincingly interpreted using the theory of the electromagnetic field penetration under conditions of the normal skin effect. Using the obtained expressions for a change in the transmission coefficient in the applied magnetic field, it is possible to obtain estimates of the dynamic magnetic permeability from the results of experiments on the field penetration.

The obtained experimental data show evidence that significant (on the order of 60%) changes in the transmission coefficient in the presence of an applied magnetic field take place in the temperature interval $T_C < T < T_C + 20$ K. These changes are probably related to a local magnetic order retained in doped manganites in the vicinity of the Curie temperature.

ACKNOWLEDGMENTS

This study was supported in part by the Program "Quantum Macrophysics" of the Presidium of the Russian Academy of Sciences, the Presidential Program of Support for Leading Scientific Schools (project no. NSh-1380-2003.2), and the Russian Foundation for Basic Research (project no. 04-02-16191).

REFERENCES

1. É. L. Nagaev, Usp. Fiz. Nauk **166**, 833 (1996) [Phys. Usp. **39**, 781 (1996)].
2. J. Coey, M. Viret, and S. von Molnar, Adv. Phys. **48**, 167 (1999).
3. F. Owens, J. Appl. Phys. **82**, 3054 (1997).
4. M. Dominguez, S. M. Bhagat, S. E. Lofland, *et al.*, Europhys. Lett. **32**, 349 (1995).
5. S. E. Lofland, P. H. Kim, P. Dahiroc, *et al.*, J. Phys.: Condens. Matter **9**, 6697 (1997).
6. J. Fontcuberta, B. Martinez, J. L. Garsia-Munos, *et al.*, Solid State Commun. **97**, 1033 (1996).
7. S. E. Lofland, V. Ray, P. H. Kim, *et al.*, Phys. Rev. B **55**, 2749 (1997).
8. A. Schwartz, M. Scheffer, and S. M. Anlage, Phys. Rev. B **61**, R870 (2000).
9. A. Rinkevich, A. Nossov, M. Rigniant, *et al.*, IEEE Trans. Magn. **38**, 257 (2002).
10. V. V. Ustinov, A. P. Nosov, A. B. Rinkevich, *et al.*, Dokl. Akad. Nauk **380**, 179 (2001) [Dokl. Phys. **46**, 615 (2001)].
11. B. Heinrich and V. F. Meshcheryakov, Pis'ma Zh. Éksp. Teor. Fiz. **9**, 618 (1969) [JETP Lett. **9**, 378 (1969)].
12. Z. Celinski, K. B. Urquhart, and B. Heinrich, J. Magn. Magn. Mater. **166**, 6 (1997).
13. R. A. Semenov, *Technical Electrodynamics* (Svyaz', Moscow, 1972) [in Russian].
14. T. Saitoh, D. S. Dessau, Y. Moritomo, *et al.*, Phys. Rev. B **62**, 1039 (2000).

Translated by P. Pozdeev

Journal of Experimental and Theoretical Physics, Vol. 101, No. 3, 2005, pp. 494–503.
Translated from Zhurnal Éksperimental'noĭ i Teoreticheskoĭ Fiziki, Vol. 128, No. 3, 2005, pp. 575–585.

ORDER, DISORDER, AND PHASE TRANSITIONS IN CONDENSED SYSTEMS

Superconducting Current in Hybrid Heterojunctions of Metal-Oxide Superconductors: Size and Frequency Dependences

Yu. V. Kislinskii[a], P. V. Komissinski[a, b], K. Y. Constantinian[a,*], G. A. Ovsyannikov[a], T. Yu. Karminskaya[c], I. I. Soloviev[c], and V. K. Kornev[c]

[a]*Institute of Radio-Engineering and Electronics, Russian Academy of Sciences, Moscow, 125009 Russia*

[b]*Chalmers University of Technology, SE-41296, Göteborg, Sweden*

[c]*Moscow State University, Moscow, 119992 Russia*

**e-mail: karen@hitech.cplire.ru*

Received March 2, 2005

Abstract—We have detected experimentally considerable deviations of the frequency dependences of the Shapiro step amplitudes and the critical current of Nb/Au/$YBa_2Cu_3O_x$ thin-film hybrid Josephson heterojunctions prepared on $YBa_2Cu_3O_x$ metal-oxide superconductor films with a tilted *c* axis from the regularities inherent in Josephson junctions of traditional superconductors with an *s*-symmetry of the order parameter. It is shown that possible formation of "splintered" fluxons with a size $\lambda_s < \lambda_J$ due to faceting of the interface and formation of a chain of nanosize 0 and π junctions must be taken into account in describing processes in lumped heterojunctions (whose size L is smaller than the Josephson penetration depth λ_J determined from the averaged value of the critical current density). For heterojunctions with a size $\lambda_s < L < \lambda_J$, a substantial decrease in the maximal amplitude of the first Shapiro step with increasing voltage (Josephson oscillation frequency) is observed at voltages much smaller than the energy gap in niobium ($V \ll \Delta_{Nb}/e$); this effect is manifested most strongly when the size L is greater than λ_s. A fractional Shapiro step and a subharmonic detector response have been observed in the current–voltage characteristics of heterojunctions; the dynamic processes responsible for their emergence and indicating the presence of the second harmonic in the current–phase relation are studied. It is shown that the effect of interface faceting on the current–phase relation increases with a heterojunction size $L > \lambda_s$. © *2005 Pleiades Publishing, Inc.*

1. INTRODUCTION

In most metal-oxide superconductors with a high superconducting transition temperature, the $d_{x^2-y^2}$ symmetry type of the superconducting order parameter dominates (D superconductors) [1, 2]. In Josephson junctions of D superconductors misoriented in the *ab* plane relative to one another, π junctions are formed under certain conditions; for such junctions, the ground state with a phase difference equal to π in the superconducting order parameter is stable [2–9]. In the case of faceting of the interface in Josephson junctions of D superconductors, alternation of 0 and π junctions leads to alternating modulation of the critical current density $j_c(x)$ along the interface on the nanoscale; as a result, pairs of "splintered" fluxons [10] containing a magnetic flux $\Phi_1 < \Phi_0/2$ and $\Phi_2 > \Phi_0/2$, $\Phi_1 + \Phi_2 = \Phi_0$ are formed (Φ_0 is the magnetic flux quantum). Such fluxes were detected experimentally in [11] in bicrystal Josephson junctions D_0/D_{45}.[1] For a large amplitude of spatial variation of the critical current, the size of the splintered fluxon is smaller than the Josephson penetration depth λ_J [10], which provides a new scale of the size dependence of static and dynamic processes in junctions. Fluxons with a fractional magnetic flux quantum were observed in junctions (including those formed by ordinary S superconductors) with inhomogeneities on the order of λ_J [12]. Judging from our earlier preliminary results [4], it cannot be ruled out that such fluxon formations may substantially affect the frequency dependence of dynamic parameters of junctions containing a D superconductor. Theoretical calculations [13] for junctions of D superconductors predict singularities in

[1] In the D_0 superconductor, one of the axes (*a* or *b*) in the basal *ab* plane is directed along the normal to the bicrystal interface (for bicrystal Josephson junctions) or to the plane of the junction (for planar Josephson junctions), while in the D_{45} superconductor, it is turned through an angle of $\theta = 45°$ relative to these axes.

the amplitude of the superconducting current component for gap voltages $V \approx \Delta_D/e$ (Δ_D is the energy gap in a D superconductor) analogous to the Riedel singularity observed in junctions of S superconductors. However, no information is available at present on the frequency dependence of the superconducting current in junctions of D superconductors under voltages much smaller than the superconducting gap.

In Josephson junctions of D superconductors, low-energy bound Andreev states are formed on the (110) plane [2]; these states are clearly manifested in the form of a singularity in the conductivity of junctions at low voltages [2–7, 14] and strongly affect the superconducting current I_s of the junctions. In particular, such states lead to a deviation of the $I_s(\varphi)$ dependence (φ is the phase difference between the wavefunctions of the electrodes of the Josephson junction) from the sinusoidal shape [2–7, 15]. According to the results of theoretical calculations [10, 11], Josephson junctions with an alternating critical current density j_c contain, along with the first harmonic ($\sin\varphi$), the second harmonic ($\sin 2\varphi$). A nonsinusoidal current–phase relation was observed in asymmetric bicrystal Josephson junctions D_0/D_{45} in [8, 16]; we also observed earlier an analogous dependence in hybrid heterojunctions $Nb/Au/YBa_2Cu_3O_x$ prepared on $YBa_2Cu_3O_x$ (YBCO) films with a tilted crystallographic axis *c* [3]. Note that the second harmonic ($\sin 2\varphi$) was observed in small-size heterojunctions (on the order of tens of micrometers) [3, 17], while deviations from the sinusoidal dependence in larger heterojunctions (on the order of tenths of a millimeter) were not detected [18].[2] It should be noted that the specific growth of a YBCO film tilted at an angle specified by a specially oriented (in the (7 10 2) plane) $NdGaO_3$ substrate is such that facets whose faces are oriented either along the *c* axis (001) or in the *ab* plane (110) are formed in the junction region of the heterojunction [4, 19]. Accordingly, it follows from the results of theoretical calculations [2, 5–7] that the transport properties of junctions between such faces and an S superconductor (Nb in our case) must differ substantially, forming alternating nanojunctions of various types (S/D_C and S/D_{45}) in heterojunctions in view of the *d* symmetry of the order parameter.

Here, we report on the results of experimental investigations of the magnetic field dependences of the superconducting critical current as well as the frequency dependence of the superconducting current and Shapiro steps in Nb/Au/YBCO hybrid heterojunctions on films with a tilted *c* axis. Assuming the possible formation of fractional fluxons in such heterojunctions and taking into account size limitations [10], we performed experiments on samples with a size *L* ranging from 10 to 50 μm. The second harmonic amplitude in the current–phase relation is estimated quantitatively and physical mechanisms explaining the experimental data are discussed.

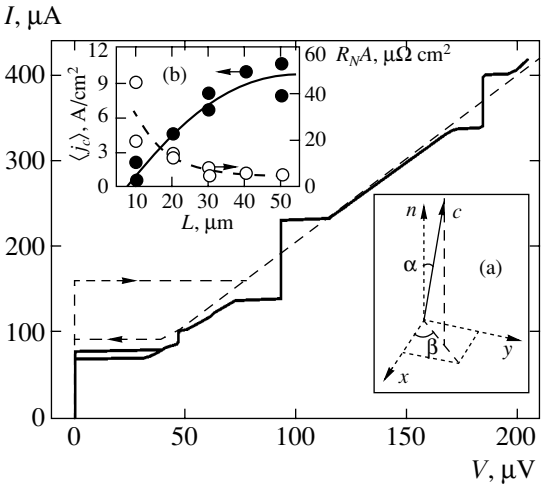

Fig. 1. IV curve of a $Nb/Au/YBa_2Cu_3O_x$ heterojunction with $L = 40$ μm at $T = 4.2$ K: autonomous IV characteristic (dashed curve) and IV characteristic recorded under the action of electromagnetic radiation of frequency $f_e = 43.45$ GHz (solid curve). The direction of the bias current is shown by arrows. Inset (a) is schematic representation of an inclined YBCO film with the (1 1 20) orientation, $\alpha \approx 11°$ and $\beta \approx 45°$. Inset (b) is the dependence of the critical current density $\langle j_c \rangle$ and the characteristic resistance R_NA of the junction on its linear size *L* (dashed and solid curves are functional dependences providing the best approximation of experimental data).

2. EXPERIMENTAL TECHNIQUE

YBCO epitaxial films with a thickness of 150 nm were deposited by laser sputtering at a temperature of 770–790°C in oxygen under a pressure of 0.6 mbar. For growing YBCO films, we chose $NdGaO_3$ substrates with the (7 10 2) orientation. Detailed studies using X-ray diffractometry revealed that YBCO films formed on the (7 10 2) plane of the $NdGaO_3$ substrate as a result of epitaxial growth have the (1 1 20) orientation, so that the crystallographic *c* axis is deflected from the normal to the substrate plane through an angle $\alpha \approx 11°$, remaining in the (110) plane of the YBCO film (see inset (a) to Fig. 1). Preliminary investigations proved that a film inclination by 10°–14° is optimal for the electron transport along the *ab* plane, preserving the monodomain nature of the film [19] and ensuring the formation of the crystallographic structure of Nb/Au/YBCO heterojunctions with alternating transitions of the S/D_C and S/D_{45} type. Obtained YBCO films had a superconducting transition temperature $T_c = 87$–90 K and a critical current density of 10^4–10^5 A/cm² at $T = 77$ K [3, 4, 17]. The Au films were deposited in two stages: first by laser sputtering in situ in the same vacuum chamber at

[2] In view of the smallness of the superconducting current density in all hybrid heterojunctions studied, the condition for a lumped Josephson junctions was satisfied: the junction size *L* was smaller than the Josephson penetration depth λ_J for a magnetic field.

Sizes and electrophysical parameters of heterojunctions at $T = 4.2$ K

No.	L, μm	I_c, μA	R_N, Ω	V_c, μV	β_c	λ_j, μm
1	50	198	0.44	87	3	117
2	50	267	0.2	53	4	101
3	40	160	0.36	58	6	104
4	30	60	0.93	55	3	127
5	30	74	0.56	41	5	115
6	20	18	3.6	65	4	156
7	20	8.5	3.1	26	–	227
8	10	0.7	45.3	32	–	390
9	10	2.0	19.8	40	–	233

100°C, which minimized the decrease in the oxygen content and ruled out the effect of various impurities in the formation of the YBCO/Au two-layer structure. A test measurement of the superconducting transition temperature of the YBCO film after the formation of the YBCO/Au structure resulted in the value of $T_c = 89$ K for a superconducting transition width of $\Delta T < 0.5$ K. The formation of heterojunctions was completed by radiofrequency magnetron sputtering of an additional Au layer with a thickness on the order of 10 nm and a 200-nm-thick Nb film. Photolithography and ion-beam etching in argon were used for the formation of the geometry of square planar heterojunctions with an area $A = L^2$, where $L = 10$–50 μm [3, 4, 17]. In our opinion, the superconducting transition temperature of the YBCO film in completely prepared heterojunctions decreased to $T_c \approx 84$ K during the bombardment of the film by argon ions in the course of formation of the structure geometry. The superconducting transition temperature of Nb films was $T_c = 9.1$–9.2 K.

Electrophysical parameters of the films and heterojunctions were measured using a four-point scheme with a bias current in a temperature range of $T = 4.2$–300 K in magnetic fields $H < 50$ Oe under the action of electromagnetic radiation at frequencies $f_e = 36$–120 GHz.

3. ELECTROPHYSICAL CHARACTERISTICS OF HETEROJUNCTIONS

The Josephson effect was observed in all heterojunctions studied by us; the current–voltage (IV) characteristics of these heterojunctions did not display an excess current (Fig. 1). This circumstance indicates the absence of microshorts with direct conductivity, i.e., direct "short-circuits" between YBCO and Nb films, which usually lead to the emergence of excess current. In view of the small thickness of the Au interlayer, mutual diffusion of Nb and YBCO is possible. However, Nb/YBCO junctions have a very high characteristic resistance due to the formation of oxide layers of niobium. Additional measurements revealed that the characteristic resistance of Nb/YBCO junctions is $R_NA = 0.1$–1 Ω cm^2, which is several orders of magnitude higher than the characteristic resistance $R_NA = 10^{-6}$–10^{-5} Ω cm^2 of Au/YBCO junctions (R_N is the normal resistance). Using the values of R_NA, we estimated the transparency of the potential barrier at the Au/YBCO interface averaged over the area of the junction and over the directions of quasiparticles momenta; the resulting values of $\bar{D} = 10^{-5}$–10^{-4} are typical of superconducting tunnel junctions. It should be noted here that the resistance of the Nb/Au interface is substantially lower (by several orders of magnitude) than that of the Au/YBCO interface due to better matching of the Fermi velocity and the absence of chemical interaction of the materials [20].

The superconducting critical current density averaged over the area of the heterojunctions at $T = 4.2$ K is given by

$$\langle j_c \rangle = I_c/A = 1\text{–}10 \text{ A/cm}^2,$$

where I_c is the critical current. The values of the Josephson penetration depth λ_J for a magnetic field, which are calculated by the formula

$$\lambda_J^2 = \frac{\Phi_0}{2\pi\mu_0\lambda\langle j_c\rangle}, \quad (1)$$

where μ_0 is the permeability of vacuum, lie in the interval 100–400 μm and are much higher than the maximal linear size of the junctions studied here (see table). The quantity $\lambda \approx 220$ nm in formula (1) is the sum of the London penetration depths for YBCO and Nb. For the Nb/Au/YBCO heterojunctions studied here, the condition

$$L < 4\lambda_J \quad (2)$$

is satisfied; this condition implies that such heterojunctions must possess the properties of lumped Josephson junctions and the values of $\langle j_c \rangle$ and R_NA must be independent of the junction size L [21, 22].[3] However, the experimentally observed values of $\langle j_c \rangle$ and R_NA depend on the size of the heterojunctions (see inset b to Fig. 1). The increase in the values of R_NA observed upon a decrease in size $L \leq 20$ μm indicates a decrease in the barrier transparency D, which may be due to an oxygen-depleted YBCO layer formed in regions near the

[3] For $L > 4\lambda_J$, a Josephson junction should be treated as a distributed structure in which dynamic processes are determined by the motion of Josephson fluxons.

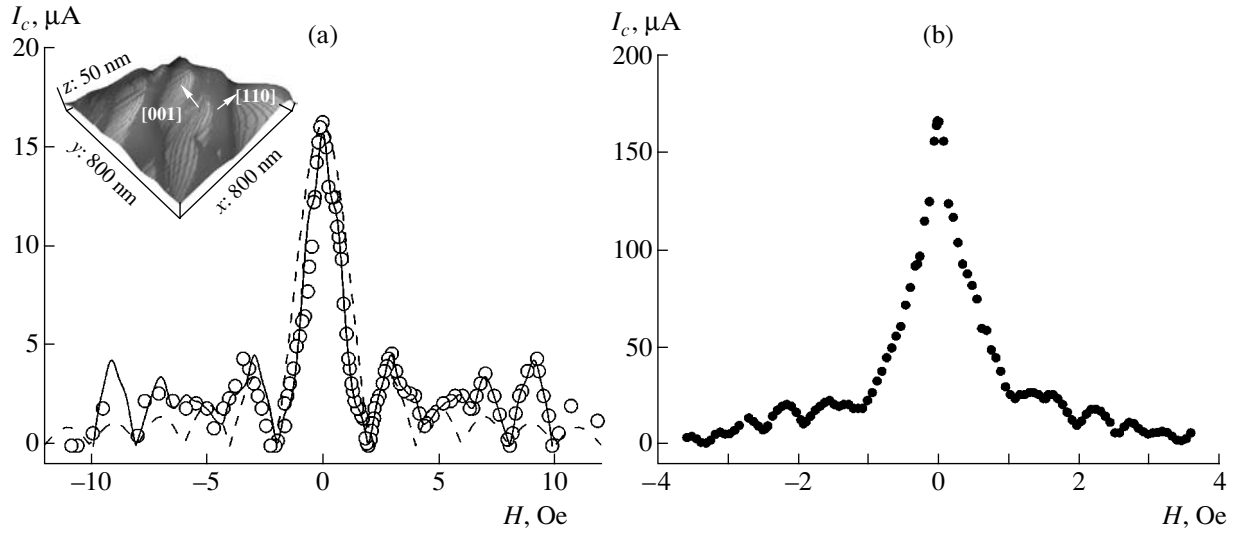

Fig. 2. Experimental magnetic field dependences of the critical current at $T = 4.2$ K for heterojunctions with sizes $L = 20$ μm (a) and 50 μm (b). The Fraunhofer dependence $|\sin H|/H$ is shown by the dashed curve. The solid curve is the calculated $I_c(H)$ dependence in the model of alternating density of the superconducting critical current. The inset shows the image of the (1 1 20) surface of the YBCO film, obtained using an atomic force microscope. The crystallographic orientations of the growth steps of the YBCO film are shown by arrows.

edges of the heterojunctions during sample preparation [20]. For junctions with a size $L < 40$ μm, the value of $\langle j_c \rangle$ increases in proportion to L and attains saturation for $L > 40$ μm. With increasing L, the contribution from the edge regions with a reduced value of $\langle j_c \rangle$ to the total superconducting current through the heterojunction decreases, and the edge effects can be disregarded even for $L = 30$ μm (see inset b to Fig. 1). It should be noted that the characteristic voltage $V_c = I_c R_N$ remains virtually unchanged upon a change in L, which is typical of tunnel junctions of S superconductors. For Josephson junctions based on high-T_c superconductors of metal-oxide materials, the value of V_c depends on $\langle j_c \rangle$ as a rule. For example, the value of V_c for bicrystal YBCO junctions is proportional to $V_c \propto \sqrt{\langle j_c \rangle}$ [2, 8], which is usually explained in the literature by the existence of different transport mechanisms for the superconducting and normal components of the current [9, 18].

4. MAGNETIC-FIELD DEPENDENCES OF THE CRITICAL CURRENT OF HETEROJUNCTIONS AND THEIR STRUCTURE

For heterojunctions with $L = 20$ μm, the experimental $I_c(H)$ dependence of the critical current on the magnetic field in the region of the first peak (Fig. 2a) is close to the "Fraunhofer" dependence $|\sin H|/H$ typical of lumped Josephson junctions with $L \approx 2\lambda_J$ [22]. It can be seen from Fig. 2a that as the magnetic field increases to $|H| > 5$ Oe, the deviation of the $I_c(H)$ dependence from $|\sin H|/H$ increases, indicating that the distribution of the superconducting current can be treated as quasi-uniform [8, 18]. A more accurate approximation of the experimental $I_c(H)$ dependences in the range of high fields $H \geq 5$ Oe can be obtained using a theoretical model in which the absolute value, as well as the sign of j_c, varies over the length of the junction [8, 10, 11, 23, 24]. It is impossible to unambiguously determine the distribution of the superconducting current density j_c in a junction from the experimental dependence $I_c(H)$. The evaluation of j_c gives at least several solutions that describe the $I_c(H)$ dependence in the region of peripheral peaks more exactly than $|\sin H|/H$. The experimentally measured $I_c(H)$ dependences can be approximated much better on the basis of alternating rather than unipolar distributions $j_c(x)$. The accuracy of calculations of $j_c(x)$ increases with expansion of the range of the experimental magnetic field, which was limited in our case by the trapping of magnetic flux quanta for $H \approx 10$ Oe. In stronger fields, a hysteresis loop was observed in the magnetic-field dependences and the dependences were poorly reproduced. In Fig. 2, we represent only reproducible unambiguous $I_c(H)$ dependences.

For junctions of larger size ($L > 30$ μm), the $I_c(H)$ dependence strongly differs from $|\sin H|/H$; in the region of the first peak, it resembles the dependences observed in distributed junctions, although condition (2) for lumped junctions is still observed (see Fig. 2b and table). It was shown theoretically in [10, 11] that the presence of a faceted interface in a Josephson junction, for which the conditions $\lambda \ll b \ll \lambda_J$ holds (b is the characteristic size of the facet), leads to the formation of "splintered" Josephson fluxons with a fractional magnetic flux quantum. The characteristic size λ_s of such a splintered Josephson fluxon for a one-dimen-

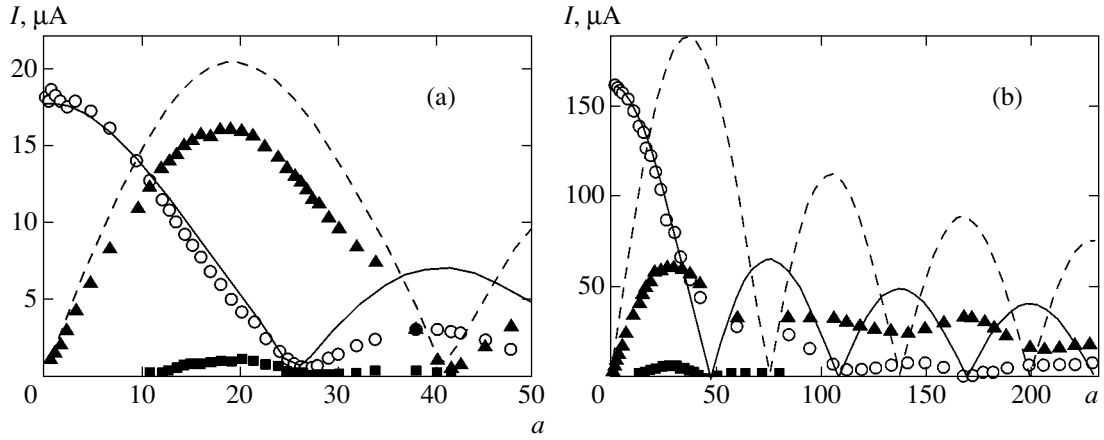

Fig. 3. Experimental dependence of critical current I_c (○), first I_1 (▲) and fractional $I_{1/2}$ (■) Shapiro steps on the dimensionless amplitude a of the high-frequency current $I_\sim$ for two heterojunctions at $T = 4.2$ K: (a) $L = 20$ μm, $f_e = 51.42$ GHz; (b) $L = 40$ μm, $f_e = 50.61$ GHz. The theoretical $I_c(a)$ and $I_1(a)$ dependences are shown by the solid and dashed curves, respectively. Calculations were made taking into account the second harmonic in the current–phase relation and the capacitance of the heterojunction (a) and in the framework of the RSJ (b).

sional dependence $j_c(x)$, which can be modeled by the expression

$$j_c(x) = \langle j_c \rangle + j_1 \sin(2\pi x/b),$$

can be estimated as

$$\lambda_s \approx \sqrt{2}\frac{\lambda_J^2 \langle j_c \rangle}{b j_1}, \qquad (3)$$

where j_1 is the amplitude of alternating modulation of the critical current density in the junction. For $j_1 \gg \langle j_c \rangle$, the fluxon size is small ($\lambda_s \ll \lambda_J$).

In our case, in view of the specific nature of deposition of YBCO films on inclined $NdGaO_3$ substrates with the (7 10 2) orientation, growth steps with a height of about 20 nm and a characteristic length of 200–300 nm in the plane of the substrate are present on the (1 1 20) surface of the YBCO films (see the inset to Fig. 2a and the results of atomic-force microscope measurements presented in [3, 4]). Such growth steps are mainly oriented along the (001) and (110) crystallographic planes of the YBCO film. According to the results of theoretical calculations [2, 5–7], the junctions with the (001) and (110) planes give different types of junctions (S/D_c and S/D_{45}, respectively) in view of the *d* symmetry of the order parameter in the YBCO film. It was shown earlier in experimental studies [17, 18] that the S/D_c junctions at $T = 4.2$ K can be treated as Josephson 0 junctions with a nonsinusoidal current–phase relation; in this case, the second harmonic amplitude amounts to about 10% of the critical current. As regards the S/D_{45} junctions, Andreev states with energies $\varepsilon \ll \Delta_D$ are formed in them in addition to Andreev states with $\varepsilon \approx \Delta_D$ on the order of the superconducting gap in a D superconductor like in S/D_c junctions [2, 8]. It was proved theoretically in [2, 5, 6, 8] that the stable state in the S/D_{45} Josephson junctions at helium temperatures is a state with a phase shift equal to π, with the characteristic voltage

$$V_c \approx \frac{\Delta_D^2 \overline{D}}{ekT}$$

and with a large second harmonic amplitude in the current–phase relation. Thus, due to the presence of alternating S/D_c and S/D_{45} junctions, the structure of the heterojunctions studied here has the form of a chain of parallel-connected 0 and π Josephson junctions.

In the heterojunctions studied so far, faceting predominantly occurs in only one direction [3, 5]; consequently, we can also use one-dimensional expressions in our case [10]. For example, using our estimates for j_1 and $\langle j_c \rangle$ we obtain from expression (3) $\lambda_s \approx 10$ μm for heterojunction no. 3 with $\lambda_J = 104$ μm, $\lambda = 0.22$ μm and $b = 0.2$ μm. It should be noted that the condition $\lambda \ll b$ which is used in calculations [10] does not hold exactly in our experiments; for this reason, the estimates of the value of λ_s based on formula (3) are correct only in order of magnitude. However, the other necessary condition for the existence of splintered fluxons [10, 11],

$$b \ll \lambda_J \sqrt{\frac{\langle j_c \rangle}{j_1}} \approx 1 \text{ μm},$$

is satisfied to a high degree of accuracy.

Experiments [11] show that splintered fluxons are unstable formations. In all probability, the instabilities on the IV curves and magnetic-field dependences of the critical current in large-size heterojunctions ($L > 40$ μm),

which were observed in our experiments, are precisely due to instability of such fluxon formations.

As a result, despite the strict fulfillment of condition (2), the magnetic-field dependences observed for the heterojunctions studied here are typical rather for distributed Josephson structures with an alternating distribution of the superconducting current density and a fluxon penetration size $\lambda_s < \lambda_J$.

5. DYNAMIC PROPERTIES OF HETEROJUNCTIONS

The IV curve presented in Fig. 1 was measured under the action of external monochromatic electromagnetic radiation with a frequency $f_e = 43.45$ GHz for $L = 40$ μm. It should be noted that the IV curve exhibits the first (I_1), second (I_2), and even fractional ($I_{1/2}$) Shapiro steps. An analogous form of the IV curve is also observed for heterojunctions with a size $L \geq 20$ μm. Figure 3 shows the dependences of the critical current amplitudes I_c and first Shapiro step I_1 on amplitude a of the high-frequency current $I_\sim$ normalized to the critical current ($a = I_\sim/I_c$). According to the results of calculations based on the resistive model of Josephson junctions (RSJ) [21, 22], the $I_c(a)$ and $I_1(a)$ dependences shown in Fig. 3a proved to be proportional to Bessel functions $J_n(a)$ for small-size heterojunctions with $L \leq 20$ μm. With increasing L, a considerable deviation of the experimental $I_c(a)$ and $I_1(a)$ dependences from those calculated in the RSJ is observed. For example, the difference between the first peak $I_{1\max}$ in the $I_1(a)$ dependence from the theoretical value calculated in the RSJ amounts to 25% for heterojunctions with $L = 20$ μm (Fig. 3a), while the deviation from the theory for heterojunctions with $L = 40$ μm is 70% (Fig. 3b). Figure 3b shows that the shape of the $I_c(a)$ and $I_1(a)$ dependences also changes as the size of junctions increases to $L > 20$ μm; this may be due to the enhanced effect of the second harmonic in the current–phase relation for large heterojunctions (with $L > \lambda_s$) [10, 11, 21, 22]. It should be noted that the amplitude of fractional Shapiro steps increases with junction size L and with the critical current.

Let us consider the frequency dependences of the maximal values of the amplitudes of the first harmonic Shapiro step $I_{1\max}(f_e)$ shown in Fig. 4 for junctions with $L = 20$ and 40 μm. For lumped Josephson junctions, the value of $I_{1\max}(f_e)$ is determined by the amplitude of the first harmonic of Josephson oscillation, which increases with frequency and attains saturation for $hf_e > 2eI_cR_N$ in accordance with the resistive model (solid curve in Fig. 4) [21, 22].

For junctions of S superconductors, the RSJ approximation disregarding the presence of a Riedel singularity for $V \approx \Delta_D/e$, which follows from the results of microscopic theory, correctly describes the available experimental data up to voltages (Josephson oscillation frequencies) corresponding to the superconducting gap $2\Delta/e$ (e.g., $\Delta_{Nb}/h \approx 700$ GHz for Nb) [22]. However, as can be seen from Fig. 4, the normalized value of $I_{1\max}/I_c$ in our experiment noticeably decreases even at a frequency $f_e > 40$ GHz, which is much lower than frequency Δ_{Nb}/h. It should be noted that the effect of the Riedel singularity in tunnel junctions of S superconductors is manifested in the increase in the ratio $I_{1\max}/I_c$ [25]. For large heterojunctions ($L = 40$ μm) the observed decrease in the ratio $I_{1\max}/I_c$ was stronger than for small heterojunctions ($L = 20$ μm).[4] The theoretical calculations performed in [13] for Josephson junctions of D superconductors reveal a weak frequency dependence of the superconducting current component up to frequencies Δ_D/h corresponding to the gap voltage and exceeding 1 THz. Consequently, in the framework of existing theories, the change in the value of $I_{1\max}/I_c$ must be small in the frequency range $f_e = 35$–80 GHz. A possible reason for the noticeable decrease in the values of $I_{1\max}/I_c$ with frequency may be energy pumping from the first harmonic of the current–phase relation, which determines the value of $I_{1\max}$, to the second harmonic for $L \geq \lambda_s$ [10, 11]. The effect of the nonuniform distribution of the external microwave current at natural resonance of heterojunctions on the dynamics of formation of the Shapiro step (and the value of $I_{1\max}$), which we observed earlier in distributed heterojunctions of S superconductors [26], cannot not be ruled out either. The resonance frequency of natural electromag-

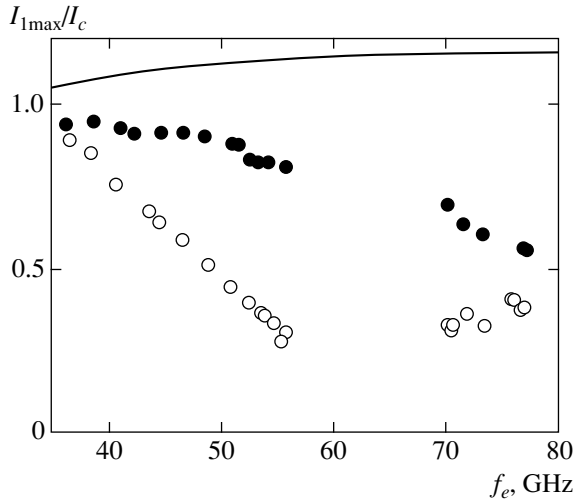

Fig. 4. Dependences of the normalized maximal amplitude of the first Shapiro step on the frequency of the external electromagnetic action for heterojunctions with $L = 20$ μm (dark circles) and 40 μm (light circles). The solid curve shows the frequency dependence of $I_{1\max}/I_c(0)$ calculate in the RSJ.

[4] Since the maximal value $I_{1\max}$ of the Shapiro step is measured, the frequency dependence of the heterojunction impedance, which affects the matching with the external system, can be ignored.

netic oscillations in the structures under study with a strongly nonuniform critical current density distribution may be close to the frequency of formation of standing waves. This effect is analogous to the Fiske resonance with the effective velocity of wave propagation on the order of $c_s = \omega_p \lambda_s$, where $\omega_p = \sqrt{2\pi I_c/\Phi_0 C}$ is the plasma frequency. As a result, the resonance frequency $f_s = c_s/2L$ turns out to belong, in order of magnitude, to the frequency range represented in Fig. 4. It should be noted that the IV curves did not display singularities corresponding to Fiske resonances.

6. SUPERCONDUCTING CURRENT–PHASE RELATION

It follows from Figs. 1 and 3 that the application of external monochromatic electromagnetic radiation to heterojunctions with $L = 20$–50 μm leads to the emergence of fractional Shapiro steps $I_{1/2}(a)$ in addition to harmonic steps on the IV curves at $V = (1/2)(hf_e/2e)$. For small-size heterojunctions ($L = 10$ μm), no fractional steps were detected; this is apparently due to the fact that the expected values of $I_{1/2\max}(a)/I_c(0) \le 0.1$ for these junctions were found to be smaller than the limiting current resolution of the measuring system (0.2 μA). A possible reason for the emergence of $I_{1/2}(a)$ steps on the IV curves of the heterojunctions is the deviation of the current–phase relation from the sinusoidal shape [3, 16]:

$$I_s(\varphi) = I_{c1}\sin\varphi + I_{c2}\sin 2\varphi.$$

It should be noted that the IV curves of the heterojunctions (both autonomous and those obtained under the action of an external electromagnetic field including those on which fractional Shapiro steps were observed) were symmetric about $V = 0$ in contrast to the IV curves for distributed Josephson junctions for $L > 4\lambda_J$ [27].

Higher harmonics in the current–phase relation ($\sin 2\varphi$, $\sin 3\varphi$, etc.) can be observed at low temperatures in Josephson junctions of the superconductor-normal metal-superconductor (SNS) type [21, 22]. Typical values of transparency for SNS junctions are $\overline{D} \sim 1$. However, the transparency values typical of our heterojunctions are $\overline{D} = 10^{-5}$–$10^{-4} \ll 1$, which enables us to treat them, rather, as tunnel Josephson junctions [3]; however, in contrast to the latter junctions, their current–phase relation is not necessarily sinusoidal.

Under the action of large-amplitude electromagnetic radiation (with $a \ge 1$), the quasiparticles energy distribution function may change, leading to the emergence of fractional Shapiro steps [28]. For this reason, we also measured the selective detector response of heterojunctions at frequencies $f_e = 35$–120 GHz at a small amplitude of electromagnetic radiation. Under these conditions, the detector response at voltages $V \approx (1/2)(hf_e/2e)$ corresponding to the emergence of the fractional Shapiro step $I_{1/2}(a)$ was observed for all junctions in which a step was detected. Thus, the emergence of the second harmonic in the current–phase relation in the form of fractional Shapiro steps was found to be independent of the amplitude of the external radiation. Indeed, the characteristic relaxation times for excited quasiparticles in superconducting metal-oxide materials are on the order of 10^{-13}–10^{-12} s [29], which is an order of magnitude smaller than the period of oscillations of external electromagnetic radiation in our experiments (10^{-11} s). Consequently, the quasiparticle energy distribution function remains close to equilibrium under the action of electromagnetic radiation with a frequency up to 100 GHz.

Deviations of the current–phase relation from sinusoidal shape (and, hence, fractional Shapiro steps) can be observed on the IV curves of distributed Josephson junctions in view of a nonuniform distribution of the superconducting current over the area of the junction (e.g., when condition (2) of a lumped junction is violated) [21, 22]. It was noted in Section 3 during the discussion of size effects that condition (2) holds for all heterojunctions studied by us. To find the effect of a nonuniform distribution of the superconducting current in a heterojunction on the current–phase relation, let us first consider heterojunctions for which a more stringent criterion for a lumped junction as compared to (2) is satisfied, i.e., $L < \lambda_s, \lambda_J$.

It was shown in Section 4 that the heterojunctions under consideration can be treated as a chain of Josephson 0 and π nanojunctions S/D_c and S/D_{45} in view of the (7 10 2) crystallographic orientation of the YBCO film and the morphology of its surface. It was noted above that the YBCO order parameter contains both *d*-symmetric and *s*-symmetric components, which are responsible for the emergence of current–phase relations of S/D_c and S/D_{45} nanojunctions of the first (I_{c1}) and second (I_{c2}) harmonics, respectively [17]:

$$I_{c1}R_N \approx \Delta_s\Delta_{\mathrm{Nb}}/e\Delta_D, \quad (4)$$

$$I_{c2}R_N \approx \overline{D}\Delta_{\mathrm{Nb}}/e. \quad (5)$$

In these expressions, we assume that the order parameter in YBCO is described by the expression

$$\Delta(\theta) = \Delta_D\cos 2\theta + \Delta_s,$$

where θ is the angle between the electron momentum and the direction of the *a* axis, and Δ_s is the *s* component of the order parameter. Taking into account the experimental transparency values $\overline{D} \approx 10^{-4}$, we obtain from expressions (4) and (5) the ratio of the amplitudes

of the harmonics in the current phase dependence,

$$q = \frac{I_{c2}}{I_{c1}} \approx \overline{D}\frac{\Delta_D}{\Delta_s} \approx 10^{-3},$$

for values of $\Delta_s/e \approx 1$ mV and $\Delta_D/e \approx 20$ mV typical of heterojunctions [3]. Such a level of deviation of the shape of the current–phase relation from sinusoidal cannot be detected at $T = 4.2$ K because of thermal fluctuations. At the same time, the contribution from Andreev levels to the superconducting current of S/D_{45} junctions leads to substantial increase in the second harmonic amplitude in the current–phase relation [2, 5]:

$$q \approx \frac{\Delta_D^3 \overline{D}}{kT\Delta_S\Delta_{Nb}kT} \approx 0.8.$$

A quantitative estimate of the contribution of the second harmonic in the current–phase relation to the height of the harmonic Shapiro step was obtained using the fact that the height of the nth harmonic step in the high-frequency RSJ approximation ($hf_e > 2eI_cR_N$) for $q \neq 0$ varies as the sum of Bessel functions J_n with different phases,

$$I_n/I_c = 2\max_{\Theta}[J_n(x)\sin\Theta + qJ_{2n}(2x)\sin 2\Theta], \quad (6)$$

where $x = a/\omega(\omega^2\beta_c^2 + 1)^{1/2}$; $\omega = hf_e/2eI_cR_N$ is the normalized frequency of the varying electromagnetic field; $\beta_c = 4\pi eI_cR_N^2C/h$ is the MacCumber parameter, which is determined by the capacitance C of the Josephson junction. The maximum of the expression in the brackets is taken for the phase shift Θ between Josephson oscillation and external radiation [21, 22, 30]. The values of the MacCumber parameter were obtained from the hysteresis on the IV curves for the heterojunctions under investigation and are given in the table; it can be seen that the value of $\beta_c = 3$–6 weakly depends on the size of the junctions. Expression (6) implies that the value of q at a frequency $hf_e > 2eI_cR_N$ can be calculated from the minima of the experimental dependence $I_c(a)/I_c(0)$. For example, at the first minimum, we have

$$q = \frac{I_c(a)}{I_c(0)J_0(2x)},$$

which gives $q = 0.14$ for the experimental dependence shown in Fig. 3a. It should be noted that this method of estimating q rules out the effect of the capacitance of the junction, but does not allow us to determine the sign of the second harmonic amplitude in the current–phase relation.

The finite capacitance of the junction and the second harmonic in the current phase dependence lead to the formation of fractional Shapiro steps on the IV curves with a height

$$\frac{I_{1/2}}{I_c} = 2\max_{\Theta}\left\{\sin\Theta\left[qJ_1(2x) + \beta_c\frac{J_1(x)J_0(x)}{(\beta_c\omega)^2/4 + 1}\right.\right.$$
$$\left.\left. + 4q^2\beta_c\frac{J_2(2x)J_0(2x)}{(\beta_c\omega)^2 + 1}\cos\Theta\right]\right\}. \quad (7)$$

The expression in the brackets is sign-alternating; consequently, the $I_{1/2}(a)$ dependence differs from that obtained earlier for bicrystal junctions with a low capacitance [15]: $I_{1/2}(a) \propto J_1(2x)$, $x = a/\omega$. Values of $q < 0$ provide good agreement with experiment (Fig. 5). For $q > 0$, the calculated values of $I_{1/2}(a)$ substantially exceed the measured values and do not lead to the experimentally observed minimum between $a = 0$ and the first minimum of the $I_c(a)$ function. Negative values of q follow from theoretical calculations for S/D_{45} junctions [2, 5–7] and were observed earlier in experimental investigations of bicrystal Josephson junctions [9].

Pay attention to the fact that a slight change in the normalized frequency ω of the external radiation noticeably changes the shape of the $I_{1/2}(a)$ dependence. This is due to the simultaneous effect of the capacity of the junction and the nonsinusoidal current–phase relation on the process of formation of a fractional Shapiro step (the first two terms in expression (7) have opposite signs). The same behavior of the $I_{1/2}(a)$ dependence is also observed in our case (see Fig. 5), although the maximal value of $I_{1/2}(a)$ differs from the theoretical estimate by a factor of several units. It should be noted that we did not use any fitting parameters for comparing

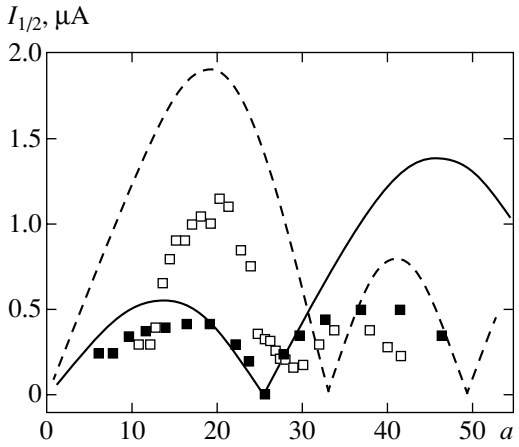

Fig. 5. Heights of fractional Shapiro steps $I_{1/2}$ for heterojunctions with $q = -0.14$ and $\beta_c = 4$ as functions of the normalized amplitude a of the external high-frequency current for frequencies $f_e = 51.42$ GHz (light squares) and 70.2 GHz (dark squares). The dashed and solid curves correspond to the $I_{1/2}(a)$ dependences calculated by formula (7) for normalized frequencies $\omega = 1.62$ and 2.2, respectively.

the experimental and theoretical results in Fig. 5. The second harmonic amplitude in the current–phase relation and the amplitude scale of external electromagnetic radiation were determined from comparing the results of calculation based on formula (6) with the experimental $I_c(a)$ dependence (see Fig. 3a).

According to [10, 11], the second harmonic amplitude $q \sim L^2/\lambda_s^2$ in the current–phase relation must increase with increasing size of heterojunctions ($L > \lambda_s$) due to the presence of parallel-connected 0 and π constants in the junctions. Indeed, the second harmonic amplitude $q = -0.4$ determined by formula (6) from the data presented in Fig. 3b for $L = 30$ μm increases to a value of $q = -0.9$ upon an increase in the junction size to $L = 40$ μm; in accordance with the results of calculations [11], all values of $q < 0$.

7. CONCLUSIONS

It was found from electrophysical and microwave properties of Nb/Au/YBCO thin-film hybrid heterojunctions that the critical current density in the junction is nonuniformly distributed over the junction length even for lumped junctions (which are smaller than the Josephson penetration depth, $L < \lambda_J$). Owing to faceting of the interface in Au/YBCO films and the effect of *d* symmetry of the superconducting order parameter in YBCO, the heterojunctions studied here are correctly described by the model of a chain of 0 and π junctions. In such chains, "splintered" Josephson fluxons can be formed with fractional values of the magnetic flux quantum and with values of λ_s several times smaller than the Josephson penetration depth for a magnetic field.

It was found experimentally that the maximal value of the first Shapiro step decreases with increasing frequency of external electromagnetic radiation. Such a behavior of high-frequency dynamic processes occurring at frequencies $f_e \ll \Delta_{Nb}/h$ may be due to the emergence of splintered fluxons leading to a nonuniform distribution of the magnetic and microwave fields in heterojunctions. This effect was enhanced with increasing junction size ($L > \lambda_s$); the departure of the magnetic-field dependence of the critical current from the Fraunhofer dependence also increased.

The fractional Shapiro step and the subharmonic selective detector response, which were experimentally observed in the heterojunctions studied here, are associated with the presence of the second harmonic in the current–phase relation. The second harmonic amplitude in the current–phase relation and its sign (the second harmonic amplitude is negative for heterojunctions under investigation) were estimated using experimental methods.

ACKNOWLEDGMENTS

The authors are grateful to I.V. Borisenko and I.K. Bdikin for their assistance in experiments, to Yu.S. Barash, V.V. Ryazanov, J. Mygind, T. Claeson, and F. Lombardi for fruitful discussions, and to É.B. Goldobin for a careful reading of the manuscript before publication and for helpful remarks.

This study was partly supported by the Russian Foundation for Basic Research (project no. 04-02-16818a), INTAS (grant nos. 2001-0809 and 2001-0249), OXIDE Program of the Swedish Foundation for Strategic Research (SSF, ISTC) (grant no. 2369), ESF Program "Pi-Shift," and the grant from the President of the Russian Federation supporting leading Science Schools (no. NSh-1344.2003.2).

REFERENCES

1. C. C. Tsuei and J. R. Kirtley, Rev. Mod. Phys. **72**, 969 (2000).
2. T. Lofwander, V. S. Shumeiko, and G. Wendin, Supercond. Sci. Technol. **14**, R53 (2001).
3. F. V. Komissinski, K. I. Constantinian, Yu. V. Kislinskiĭ, and G. A. Ovsyannikov, Fiz. Nizk. Temp. **30**, 795 (2004) [Low Temp. Phys. **30**, 599 (2004)].
4. F. V. Komissinski, G. A. Ovsyannikov, Yu. V. Kislinskiĭ, *et al.*, Zh. Éksp. Teor. Fiz. **122**, 1247 (2002) [JETP **95**, 1074 (2002)].
5. R. A. Riedel and P. F. Bagwell, Phys. Rev. B **57**, 6084 (1998).
6. Y. Tanaka and S. Kashiwaya, Phys. Rev. B **53**, R11957 (1996).
7. Yu. S. Barash, Phys. Rev. B **61**, 678 (2000).
8. H. H. Hilgenkamp and J. Mannhart, Rev. Mod. Phys. **74**, 485 (2002).
9. E. Il'ichev, M. Grajcar, R. Hlubina, *et al.*, Phys. Rev. Lett. **86**, 5369 (2001).
10. R. G. Mints, Phys. Rev. B **57**, R3221 (1998).
11. R. G. Mints, I. Papiashvilli, J. R. Kirtley, *et al.*, Phys. Rev. Lett. **89**, 067004 (2002).
12. E. Goldobin, D. Koelle, and R. Kleiner, Phys. Rev. B **67**, 224515 (2003).
13. Yu. S. Barash and A. A. Svidzinskiĭ, Zh. Éksp. Teor. Fiz. **111**, 1120 (1997) [JETP **84**, 619 (1997)].
14. L. H. Greene, P. Hentges, H. Aubin, *et al.*, Physica C (Amsterdam) **387**, 162 (2003).
15. G. A. Ovsyannikov, I. V. Borisenko, and K. Y. Constantinian, Vacuum **58**, 149 (2000).
16. E. Il'ichev, V. Zakozarenko, R. Ijsselsteijn, *et al.*, Phys. Rev. Lett. **81**, 894 (1998).
17. P. V. Komissinskiĭ, G. A. Ovsyannikov, E. Il'ichev, and Z. G. Ivanov, Pis'ma Zh. Éksp. Teor. Fiz. **73**, 405 (2001) [JETP Lett. **73**, 361 (2001)]; P. V. Komissinski, E. Il'ichev, G. A. Ovsyannikov, *et al.*, Europhys. Lett. **57**, 585 (2002).

18. R. Kleiner, A. S. Katz, A. G. Sun, *et al.*, Phys. Rev. Lett. **76**, 2161 (1996).

19. I. K. Bdikin, P. B. Mozhaev, G. A. Ovsyannikov, *et al.*, Fiz. Tverd. Tela (St. Petersburg) **43**, 1548 (2001) [Phys. Solid State **43**, 1611 (2001)].

20. F. V. Komissinskiĭ, G. A. Ovsyannikov, and Z. G. Ivanov, Fiz. Tverd. Tela (St. Petersburg) **43**, 769 (2001) [Phys. Solid State **43**, 801 (2001)].

21. K. K. Likharev and B. T. Ul'rikh, *Systems with Josephson Contacts: Foundations of Theory* (Mosk. Gos. Univ., Moscow, 1978) [in Russian].

22. A. Barone and G. Paterno, *Physics and Applications of the Josephson Effect* (Wiley–Interscience, New-York, 1982; Mir, Moscow, 1984).

23. N. V. Klenov, V. K. Kornev, I. I. Solov'ev, *et al.*, Nelin. Mir **3**, 75 (2005).

24. O. Nesher and E. N. Ribak, Appl. Phys. Lett. **71**, 1249 (1997).

25. D. A. Weitz, W. J. Skocpol, and M. N. Tinkham, Phys. Rev. B **18**, 3282 (1978).

26. B. Mayer, T. Doderer, R. P. Huebener, and A. V. Ustinov, Phys. Rev. B **44**, 12463 (1991).

27. A. V. Ustinov, J. Mygind, and V. A. Oboznov, J. Appl. Phys. **72**, 1203 (1992).

28. K. W. Lehnert, N. Argaman, H.-R. Blank, *et al.*, Phys. Rev. Lett. **82**, 1265 (1999).

29. J. Mannhart, Supercond. Sci. Technol. **9**, 49 (1996).

30. T. Y. Karminskaya and V. K. Kornev, in *Proceedings of International Students' Workshop on Microwave Applications of New Physical Phenomena* (St. Petersburg, Russia, 2004), p. 238.

Translated by N. Wadhwa

Journal of Experimental and Theoretical Physics, Vol. 101, No. 3, 2005, pp. 504–512.
Translated from Zhurnal Éksperimental'noĭ i Teoreticheskoĭ Fiziki, Vol. 128, No. 3, 2005, pp. 586–596.

ORDER, DISORDER, AND PHASE TRANSITIONS IN CONDENSED SYSTEMS

Features of the Effect of the Josephson Medium Parameters on Vortex Formation and Critical Current

L. V. Belevtsov[a,*] and A. A. Kostikov[b]

[a] *Galkin Physicotechnical Institute, National Academy of Sciences of Ukraine, Donetsk, 83114 Ukraine*
[b] *Donbass State Machine Building Academy, Kramatorsk, Donetsk oblast, 84313 Ukraine*
**e-mail: apmath@dgma.donetsk.ua*

Received March 4, 2005

Abstract—The response of an intergranular Josephson junction to displacements of an Abrikosov vortex in a superconducting polycrystal is studied theoretically. The vortex filament in the vicinity of the junction excites a tunnel current in the junction and also generates a Josephson vortex with which it merges upon emergence at the surface of the junction. It is shown that the process of the Josephson vortex formation passes through a stage of overcoming a potential barrier, whose height depends on the distance between the Abrikosov vortex and the junction, as well as on the effective thickness of the junction, which is determined by the characteristic grain size, grain anisotropy, and the intensity of the intergranular coupling. The magnetic field dependence of the critical current of the intergranular Josephson junction is determined for various grain and intergranular parameters, as well as for the triangular and square configurations of the Abrikosov vortex lattice. The results indicate that a high degree of texturing in the grain size, anisotropy, and intensity of intergranular coupling is very important for obtaining high critical currents in pure polycrystalline materials. *© 2005 Pleiades Publishing, Inc.*

1. INTRODUCTION

Penetration of magnetic field into a type II superconductor begins with the formation of vortex filaments at the superconductor surface, followed by their diffusion to the bulk of the sample [1]. Accordingly, when the external field decreases to values lower than the critical field H_{c1}, the vortex filaments move towards the surface and are expelled from the superconductor. It was shown in [2] that an Abrikosov vortex (AV) in the vicinity of a Josephson junction excites tunnel currents in it. When the AV is expelled to the contact region, it is transformed into a Josephson vortex, although the geometrical and energy parameters of these two vortices are different.

Interesting properties of high-T_c polycrystals, which are important for applications, stimulated the study of granular superconductors with Josephson junctions between the grains. New surface barriers for penetration of an AV into a grain were predicted theoretically by one of the authors in [3]. In this case, the vortex dynamics was controlled by the grain characteristics and properties of intergranular Josephson SIS junctions, which is caused by structural distortions of the AV and its interaction with the surface and grain boundaries. In light of these concepts, it is natural to expect that the characteristics of the Josephson medium and the AV will influence the Josephson effects in the intergranular junction and, as a consequence, the magnetic field dependence of the intergranular critical current.

In analyzing transport phenomena in type II superconductors, it is important that the maximal undamped current I_c is determined by the interaction of Abrikosov vortices with crystal defects. Contacts between individual superconducting grains in ceramic or polycrystalline HTSC materials are often treated as defects [4]. In many cases, the current density in Josephson junctions or the Josephson phase difference exhibit an ambiguous dependence on magnetic field H; the form of the field dependence $I_c(H)$ may strongly differ for different crystals depending on the quality of the material [5, 6].

This study is devoted to analyzing how the vortex dynamics affects the process of vortex formation in an intergranular junction of a grained superconducting structure, as well as how the grain parameters and properties of the intergranular medium affect the magnetic field dependence $I_c(H)$ of the critical current. We will consider a vortex-laminar model of an SIS junction, presented schematically in Fig. 1. The coordinate system is chosen so that the plane of a Josephson intergranular junction coincides with the xy plane and the magnetic field is directed along the y axis parallel to the grain surface, $H_y^{\rm app} = (0, H, 0)$. The field penetrates the contact, a grain from the side of the surface and from the side of the SIS junction to a depth of λ_J, λ_{ab}, and λ_c, respectively. The currents induced by the external field flow in the xy plane. The x axis passes through the junction and the gain under investigation is bounded on the z axis by straight lines $z = 0$ and $z = a$. Superconducting

laminas are separated from one another by an insulating layer of thickness t.

The structure of the article is as follows. In Section 2 gives the main equations describing the behavior of the phase difference φ for the order parameters of adjacent grains separated by a Josephson junction. The solution to the equation for the additional gradient of phase φ is obtained. In Section 3, the effect of characteristics of the Josephson medium on the energy of a weak coupling between two grains is considered. The magnetic field dependence of the critical current in the intergranular junction is determined in Section 4 for various parameters of the medium, as well as in the cases when triangular and square configurations of the vortex lattices are formed in the grain by the external magnetic field. Experimental evidence supporting the results is analyzed.

2. INTERACTION OF A VORTEX FILAMENT WITH AN INTERGRANULAR JOSEPHSON JUNCTION

2.1. Basic Equations

Let us consider a vortex filament whose currents reach the surface and banks of a junction. The position of the vortex corresponds to coordinates (x_0, y_0). We assume that $\kappa \gg 1$ and the vortex axis coincides with the y axis and is parallel to the sample surface and to the inner walls of the grains. The magnetic field added by the vortex is distorted by the surfaces so that, first, no additional field is produced either on the surface or in Josephson junctions (since the field is preset and is equal to H_y^{app} at the surface and to $H_y^{\text{app}} \exp(z/\lambda_J)$ in the junctions), and second, the current normal to the surfaces vanishes. This can be done by supplementing the vortex with its mirror image relative to surfaces with opposite directions of the field and current (Fig. 1). The energy of the vortex is mainly concentrated in the region $\xi_{ab} \ll x \ll \lambda_{ab}$ and $\xi_c \ll z \ll \lambda_c$. To analyze the problem, the structure of the vortex core is immaterial. It is only important that the order parameter and the current associated with it decrease as we approach the center of the core and vanish at the core center. The field of the vortex satisfies the anisotropic London equation with $2(2L + 1)$ sources:

$$\nabla \times [\lambda^2] J + H = \Phi_0 \mathbf{e}_y \sum_{n=-L}^{L} \{(-1)^n \delta(\rho - \rho_n^{(+)}) + (-1)^{n+1} \delta(\rho - \rho_n^{(-)})\}. \quad (1)$$

Here, L is the number of coordination zones counted from the vortex to its image and images of the images. Figure 1 shows three superconducting laminas, {–1}, {0}, and {1}, corresponding to a single coordination zone $L = 1$ (in the general case, $L \longrightarrow \infty$); $\mathbf{e}_y$ is the unit vector directed along the y axis; $\Phi_0 = h/2e$ is the magnetic flux quantum; $\delta(\rho - \rho_n)$ is the 2D Dirac delta function in the xz plane; $\rho_{\pm n}^{(+)} = [x_0, (-1)^n(z_0 - a/2) \pm na]$ is the position of the vortex ($n = 0$) and its images ($n \neq 0$) in the region of superconducting grains (along the z axis), where indices $+n$ and $-n$ correspond to counts to the right and left from the vortex, respectively; $\rho_{\pm n}^{(-)} = [-x_0, (-1)^n(z_0 - a/2) \pm na]$ is the position of images located outside the superconducting region ($x < 0$); and $[\lambda^2]$ is a tensor describing anisotropy of the material, which will be treated as a diagonal tensor. We also assume that $a \gg \xi_{ab}, \xi_c$; in this way, we can ignore the effect of grain boundaries on the order parameter in the grains. Using the Maxwell equation $\nabla \times H = J$ for the geometry depicted in Fig. 1, we obtain the following equation for field distribution in a grain:

$$\lambda_c^2 \frac{\partial^2 H_y}{\partial z^2} + \lambda_{ab}^2 \frac{\partial^2 H_y}{\partial x^2} - H_y = -\Phi_0 \sum_{n=-L}^{L} (-1)^n \delta(x - x_0) \times \delta\left[z - \frac{a}{2} - (-1)^n\left(z_0 - \frac{a}{2}\right) - na\right] + (-1)^n \delta(x + x_0) \delta\left[z - \frac{a}{2} - (-1)^n\left(z_0 - \frac{a}{2}\right) - na\right]. \quad (2)$$

This equation differs substantially from the anisotropic London equation in the presence of sources for a vortex carrying a magnetic flux quantum Φ_0 and its mirror images.

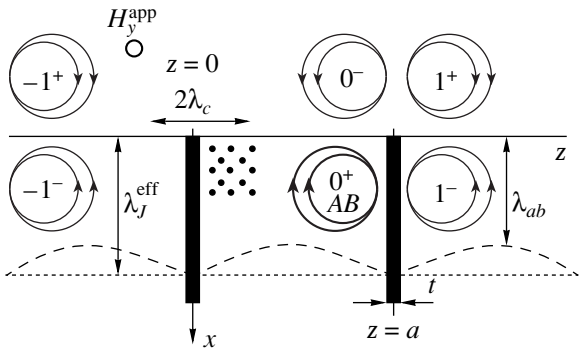

Fig. 1. Abrikosov vortex 0^+ in a type II superconductor in an external magnetic field $H \sim H_{c1}$ and the set of image vortices with positive and negative vorticity in the limit when the characteristic grain size $a/2\lambda_c \gg 1$. The magnetic field is applied parallel to the surface and grain boundaries and penetrates a grain to depth of λ_{ab} from the side of the surface and λ_c from the side of Josephson junctions, while the penetration depth in the junction is λ_J.

Steady-state effects of weak superconductivity can be described using the Ferrell–Prange equation [7]. In the subsequent analysis, it is necessary to describe the behavior of phase difference φ of the order parameters of superconducting grains separated by intergranular SIS junctions in the case when an AV is located in the vicinity of one of the grains. The effect of this filament is that it produces a nonzero current at one of the surfaces forming the Josephson junction. The presence of the surface current leads to the emergence of an additional gradient of phase φ, which in turn induces an additional Josephson tunnel current through the junction. In this case, the relation between the phase gradient and magnetic field H is described by the formula [2]

$$\frac{d\varphi}{dx} = \frac{2e\Lambda_0}{\hbar c}H - \frac{2m}{n_s e\hbar}J_v(x). \tag{3}$$

Here, $\Lambda_0 = 2\lambda_c$, n_s is the number of superconducting electrons, and $J_v(x)$ is the current produced by the vortex filament at the surface of the Josephson junction. To find this current, we will use the solution to Eq. (2) for the magnetic field distribution of the vortex filament with the coordinates $x = x_0$ and $z = z_0$ of the center, which takes into account the interaction of the filament with the grain surface and with the intergranular junction in an anisotropic material [8]:

$$H_v(x, x_0, z, z_0) = \frac{\Phi_0}{2\pi\Lambda^2}$$

$$\times \sum_{n=-\infty}^{\infty} \{(-1)^n K_0[D_n(z, z_0, x - x_0)] \tag{4}$$

$$+ (-1)^{n+1} K_0[D_n(z, z_0, x + x_0)]\},$$

where

$$D_n(z, z_0, x \pm x_0) = \sqrt{A^2(x \pm x_0) + B_n^2(z, z_0)},$$

$$A(x \pm x_0) = \frac{x \pm x_0}{\lambda_{ab}},$$

$$B_n(z, z_0) = \frac{z - a/2 - (-1)^n(z_0 - a/2) - na}{\lambda_c}.$$

Here, $\Lambda = \sqrt{\lambda_{ab}\lambda_c}$ and K_0 is the Macdonald function. Using Eq. (4), we can find the current at the surface of an intergranular junction in accordance with the Maxwell equation

$$J_v(x) = -\frac{c}{4\pi}\left.\frac{\partial H}{\partial z}\right|_{z=0},$$

which is produced by the vortex filament passing through point (x_0, z_0):

$$J_v = \frac{c}{8\pi^2}\frac{\Phi_0}{\Lambda^3}\sum_{n=-\infty}^{\infty} B_n(0, z_0)$$

$$\times\left\{\frac{(-1)^{n+1}}{D_n(0, z_0, x - x_0)}K_1[D_n(0, z_0, x - x_0)]\right. \tag{5}$$

$$\left. + \frac{(-1)^{n+2}}{D_n(0, z_0, x + x_0)}K_1[D_n(0, z_0, x + x_0)]\right\}.$$

Taking into account relation (3), we obtain the following equation instead of the Ferrell–Prange equation:

$$\lambda_J^2\frac{\partial^2\varphi}{\partial x^2} + \frac{\Lambda}{2J_{c0}}\frac{dJ_v}{dx} = \sin\varphi. \tag{6}$$

Here, the increment ΔJ_v of the surface current is determined by relation (5) and J_{c0} is the Josephson current amplitude. The boundary conditions to Eq. (6) can be written in the form

$$d\varphi/dx \longrightarrow 0 \text{ for } x \longrightarrow \pm\infty. \tag{7}$$

These conditions are satisfied under the assumption that $\varphi \longrightarrow 0$ for $x \longrightarrow -\infty$ and $\varphi \longrightarrow 2\pi$ for $x \longrightarrow \infty$.

In deriving Eq. (6), we disregarded the reciprocal effect of the intergranular junction on the structure of the vortex filament. Such an approach is justified since surface current (5) is much larger than the maximal Josephson tunnel current J_{c0}. Consequently, we can disregard branching of the vortex current associated with the tunnel junction and assume that the junction itself is a free surface.

The problem can be formulated as follows. Let the initial magnetic field $H > H_{c1}^G$ (H_{c1}^G is the lower critical field in the grain) decrease to values $H < H_{c1}^G$. This causes the expulsion of vortex filaments to the grain surface or to the intergranular Josephson junction. Let an AV be located at point $(0, z_0(t))$. We assume that the field and current distributions at instant t are described by expressions (4) and (5), into which we must substitute the coordinate $z_0(t)$ of the center of the filament, taken at the same instant. The use of static formulas is justified by the fact that the velocity of the AV is much smaller than the characteristic velocity of electrons in the vortex (velocities at distances on the order of Λ from the center of the vortex).

2.2. Weak Intergranular Coupling

Let us find the solution to Eq. (6) for the case when the coupling intensity between grains is quite low. In this case, Eq. (6) contains a small parameter facilitating the construction of the solution. This parameter is the ratio of λ_{ab} to the longitudinal size λ_J of the Josephson

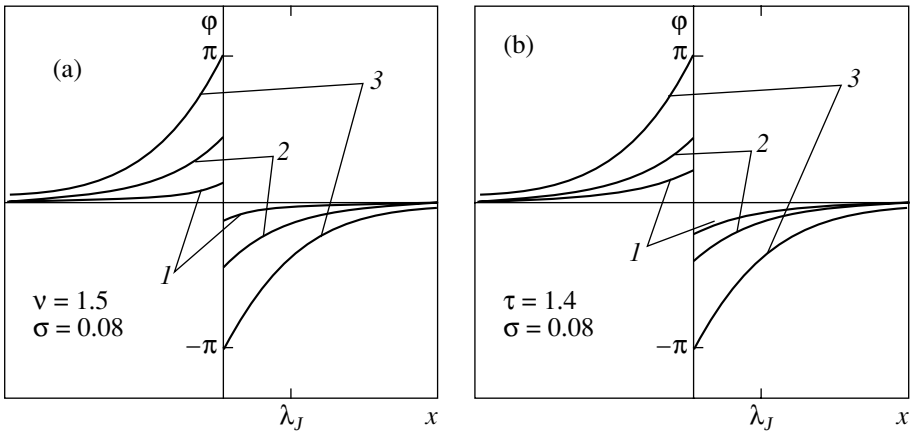

Fig. 2. Dependence of the intergrain phase difference φ on the x coordinate: (a) the characteristic grain size $\tau = 0.2$ (*1*) and 1.4 (*2*); (b) anisotropy parameter $\nu = 0.8$ (*1*) and 2 (*2*) when the AV is at point $z_0 = 0.7\lambda_c$. Curve *3* corresponds to distance $z_0 = 0$ between the AV and the junction.

vortex: $\sigma = \lambda_{ab}/\lambda_J \sim 10^{-4}$–$10^{-2}$. In view of the smallness of σ, it is sufficient to find the solution to Eq. (6) in the zeroth approximation, which can be done as follows.

In the region determined by the inequality $|x - x_0| < \lambda_{ab}$, the second term on the left-hand side of Eq. (6), which is associated with the surface current, is much larger than the Josephson tunnel current. Consequently, we assume that the right-hand side of this equation is equal to zero in this region. This gives the solution in the form

$$\varphi(x) = -\frac{2}{\Lambda}\int_{-\infty}^{x}\sum_{n=-\infty}^{\infty} B_n(0, z_0)$$

$$\times\left\{\frac{(-1)^{n+1}}{D_n(0, z_0, x - x_0)}K_1[D_n(0, z_0, x - x_0)]\right. \qquad (8)$$

$$\left. + \frac{(-1)^{n+2}}{D_n(x, z_0, x + x_0)}K_1[D_n(0, z_0, x + x_0)]\right\}dx.$$

Here, integration is formally extended to values of x since the integrand decreases exponentially outside this region. Outside the region $|x - x_0| < \lambda_{ab}$, surface current can be ignored in comparison to the Josephson current. Consequently, the behavior of the solution in this region is described by the conventional Ferrell–Prange equation.

The obtained solutions should be joined in intermediate regions as follows. In the region $-\infty < x < x_0 - \lambda_{ab}$, phase $\varphi(x)$ satisfies the Ferrell–Prange equation

$$\lambda_J^2\frac{d^2\varphi}{dx^2} = \sin\varphi$$

and the following boundary conditions: $\varphi(-\infty) = 0$ and

$$\varphi|_{x = x_0 - \lambda_{ab}} = \varphi(x_0 - \lambda_{ab})$$

at the boundary $x = x_0 - \lambda_{ab}$, where $\varphi(x_0 - \lambda_{ab})$ is defined by formula (8). In the region $|x - x_0| < \lambda_{ab}$, the solution is defined by formula (3). In the region $x_0 + \lambda_{ab} < x < \infty$, phase $\varphi(x)$ satisfies the Ferrell–Prange equation and the following boundary conditions:

$$\varphi|_{x = x_0 + \lambda_{ab}} = \varphi(x_0 + \lambda_{ab})$$

at the boundary $x = x_0 + \lambda_{ab}$ and $\varphi(\infty) = 0$ at infinity. Here, $\varphi(x_0 + \lambda_{ab})$ is also defined by formula (8).

Solution (8) exhibits an explicit dependence on the characteristic grain size $\tau = a/2\lambda_c$ and granular anisotropy $\nu = \lambda_c/\lambda_{ab}$. Figure 2 shows the solutions to Eq. (6) for various values of τ (Fig. 2a) and ν (Fig. 2b). Curves *1* and *2* correspond to an AV localized at point $z_0 = 0.7\lambda_c$, while curve *3* corresponds to $z_0 = 0$. It can be seen from the figure that the phase jump Δφ increases upon a decrease in coordinate z_0, i.e., as the AV approaches the intergranular junction. This phase jump generates phase perturbation along the junction, which corresponds to known results [2]. At the same time, it can be seen from Fig. 2 (curves *1* and *2*) that an increase in the values of τ and ν also leads to an increase in the phase jump Δφ. Thus, phase jump $\Delta\varphi \longrightarrow 2\pi$ even for $z_0 \neq 0$. Such a behavior precisely indicates [2] the generation of "half" of the Josephson vortex.

Equation (6) is invariant to the substitution of $2\pi n$ for φ, where n is an integer. If we add 2π to $\varphi(x)$ for $x > 0$, we obtain a continuous function $\varphi = \varphi(x)$. In our case, the phase of only a part of the system (for $x > 0$) is transformed, which can be explained as follows. As an AV moves to the intergranular Josephson junction or upon an increase in the granular characteristics τ or ν, it induces in the junction the perturbation $\varphi(x)$, which becomes more and more similar to a Josephson vortex. For $z_0 = 0$ or $z_0 \neq 0$, when the values of τ and ν are such that they bring the phase jump to $\Delta\varphi = 2\pi$, a Josephson vortex is formed all over the intergranular junction

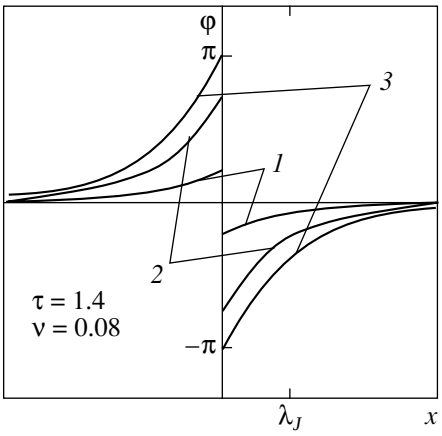

Fig. 3. Dependence of the intergrain phase difference φ on the *x* coordinate; the intergranular coupling intensity σ = 0.07 (*1*), 0.125 (*2*), and 0.15 (*3*). The distance between the AV and the junction is $z_0 = 0.7\lambda_c$.

except the central region near λ_c. The existence of this region indicates that the AV has not yet decayed. The decay of the filament begins when its normal core comes in contact with the junction. The size of the normal core along the *z* axis is approximately equal to ξ_c (ξ_c is the correlation length along the *c* axis, i.e., in a direction perpendicular to the (001) planes). In this sense, the increase in τ and ν accelerates the "contact" with the AV since it effectively increases the thickness of the Josephson junction and leads to "elimination" of this part of the junction (it conditionally splits into two independent parts, each of which can be separately subjected to phase transformation. After the complete disintegration of the AV, only the Josephson vortex is left in the intergranular junction.

2.3. Strong Intergranular Coupling

When the intergranular coupling intensity σ is high, expression (8) is inapplicable. To find phase φ, Eq. (6) was solved numerically. Figure 3 shows the dependence of phase φ on coordinate *x* for various values of intensity σ of coupling between grains. Curves *1*, *2*, and *3* correspond to the case when the AV is far from the junction at a distance $z_0 = 0.7\lambda_c$. It can easily be seen that the phase jump $\Delta\varphi \longrightarrow 2\pi$ with increasing σ. Thus, an increase in the intergranular coupling intensity increases the effective thickness of the Josephson junction, i.e., accelerating the generation of a Josephson vortex by an Abrikosov vortex.

3. ENERGY OF INTERGRANULAR COUPLING

In accordance with prevailing concepts [9], a high-T_c superconductor consists of superconducting grains whose size is small as compared to the London penetration depth, and the state of the superconductor is described by the complex order parameter with phase φ_i for each grain *i*. Grains *i* and *j* are coupled in energy in accordance with the Hamiltonian

$$\mathcal{H} = -\sum_{\langle i,j\rangle} J_{ij}\cos(\varphi_i - \varphi_j - A_{ij}), \qquad (9)$$

which includes the magnetic field effect, viz., the phase vector potential

$$A_{ij} = \frac{2\pi}{\Phi_0}\int_i^j A dl. \qquad (10)$$

It was noted by Deutscher and Müller [10] that expression (9) describes the intrinsic behavior of weak bonds in high-T_c superconductors. Each phase φ_i in the superconducting banks couples neighboring banks via the Josephson interaction parameter J_{ij}. The question arises: how do intergranular parameters τ and ν, as well as the parameter σ describing the intensity of coupling between the grains, affect the energy E_J of intergranular Josephson coupling? To answer this question, let us consider the expression for E_J in the form

$$E_J = \frac{hJ_{c0}}{2e}\int_0^L (1-\cos x)dx, \qquad (11)$$

where L_x is the linear size of the junction along the *x* axis ($\sim\lambda_J$).

Expression (11) does not take into account the terms proportional to J_{c0}^2 and corresponding to the energy of the magnetic field of the current of weak couplings and the kinetic energy of electrons. We will consider an intergranular junction whose size $L_x \geq \lambda_J$. The dependence of phase φ on *x* in such a junction in the presence of an AV is described by Eq. (6). The results of calculation of the dependence of E_J on the distance z_0 from the AV to the intergranular junction are shown in Fig. 4. It should be noted above all that the behavior of the $E_J(z_0)$ curves has the form of potential barriers for generation of a Josephson vortex. The energy barrier $E_J(z_0)$ is represented, first, by the height $E_J^{\max}$ of the potential barrier and, second, by the effective intergranular junction width $t_{\text{eff}} \approx 2z_0^c$ (z_0^c is the distance between the AV and the junction, for which $E_J(z_0^c) = E_J^{\max}$). It can easily be seen from the difference of the curves in Fig. 4 that the barrier height $E_J(z_0)$ depends on parameters τ, ν, and σ. The larger the value of z_0 for which E_J starts decreasing, the sooner the generation of a Josephson vortex by an Abrikosov vortex moving towards the contact. Let us consider the effect of variation of the parameters of the Josephson medium on vortex formation in the junction.

(a) The characteristic size of a grain. A variation of τ barely changes the potential barrier height E_J, while the effective thickness t_{eff} of the barrier increases with τ.

(b) Anisotropy. A change in ν barely changes the barrier height E_J, while the value of t_{eff} increases with ν.

(c) Intensity of intergranular coupling. It can be seen from Fig. 4c that the barrier height E_J is proportional to σ^{-1}, while $t_{\text{eff}} \propto \sigma$.

The expulsion of the AV to the junction nullifies the correction to energy associated with superconductivity. The equilibrium state for generation of a Josephson vortex sets in when the Josephson coupling energy E_J assumes the extremal (minimal) energy (point $z_0 = 0$). In other words, at the instant when the AV comes in contact with the junction, it completely decays and a Josephson vortex is formed.

The density $n(H)$ of the field distribution of the AV plays the role of external magnetic field in the formation of a Josephson vortex. The process of generation has the form of energy "pumping." The potential barrier E_J formed in this case hampers the formation of a Josephson vortex as well as its decay in a manner analogous to the situation at the edge of a superconductor with an AV entering and leaving it. An increase in the density $n(H)$ of the AV field suppresses the energy barrier at a certain distance z_0^c, which depends on the intergranular parameters τ and ν as well as the intergranular coupling intensity σ. It can be concluded that the potential barrier height E_J in super-small-grain materials also depends of the "reflectivity" of the material, viz., the number of "mirror" images of the AV [8], as well as on the degree of purity of a polycrystalline superconductor.

4. EFFECT OF CHARACTERISTICS OF THE JOSEPHSON MEDIUM ON THE CRITICAL CURRENT OF A SIS JUNCTION

Type II superconductors in an external magnetic field H acquire AV configurations forming vortex lattices. In view of the AV magnetic field nonuniformity, the dependence of the critical current in an intergranular junction on the external field may considerably differ from the conventional "Fraunhofer" dependence for homogeneous Josephson junctions [11]. In this section, we consider the results of analysis of the effect of granular characteristics τ and ν as well as the intergranular coupling intensity σ on the $I_c(H)$ dependence. The presence of singularities associated with the type of the crystal lattice (with triangular and square symmetry) on the $I_c(H)$ curves is also discussed.

For the vortex-laminar model under investigation, the critical current of a SIS junction is defined by the formula [12]

$$I_c^2 = I_{c0}^2 \left| \int_0^L \exp(i\theta(x))dx \right|^2. \qquad (12)$$

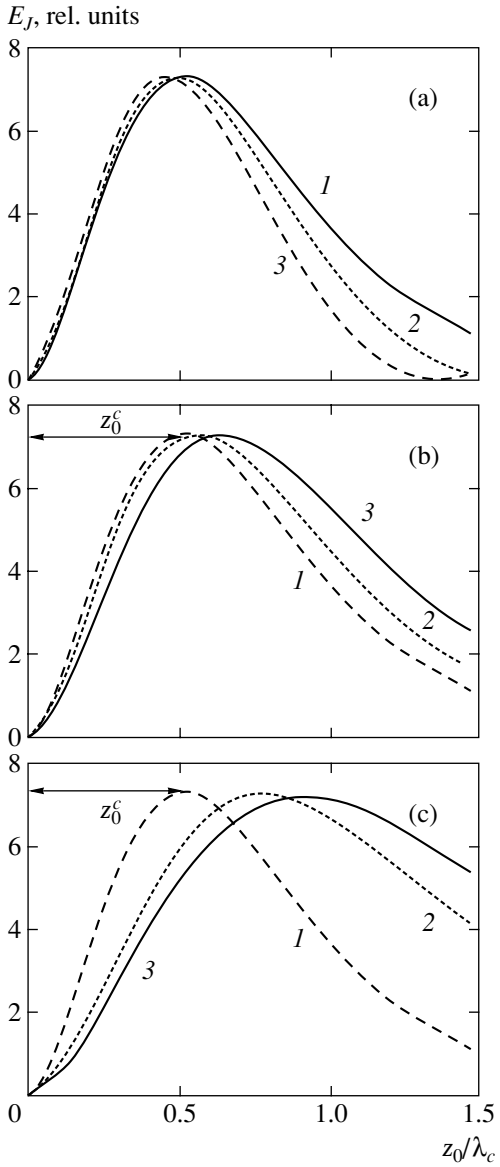

Fig. 4. Potential barrier E_J preventing generation of a Josephson vortex in the intergranular junction by an Abrikosov vortex expelled towards the junction as a function of reduced distance z_0/λ_c: (a) $\nu = 1.5$, $\sigma = 0.075$, and $\tau = 1.4$ (*1*), 0.7 (*2*), and 0.5 (*3*); (b) $\tau = 1.4$, $\sigma = 0.075$, and $\nu = 1.5$ (*1*), 2 (*2*), and 3 (*3*); and (c) $\tau = 1.4$, $\nu = 1.5$, and $\sigma = 0.075$ (*1*), 0.15 (*2*), and 0.225 (*3*).

The phase difference θ depends on the external field H and AV coordinates (x_i, z_i) in a grain, as well as on parameters τ, σ, and ν,

$$\theta = \sum_{i=1}^{N} -\frac{2}{\Lambda}\int_0^x \varphi(x \pm x_i, z_i)dx + \frac{2\pi\Phi x}{\Phi_0 L_x}, \qquad (13)$$

where N is the number of vortex filaments in the grain. Solution $\varphi(x)$ for each AV is defined by Eq. (6). For a low intensity of the coupling between the grains, when $\sigma \sim 0.01$, function $\varphi(x)$ has the form (8).

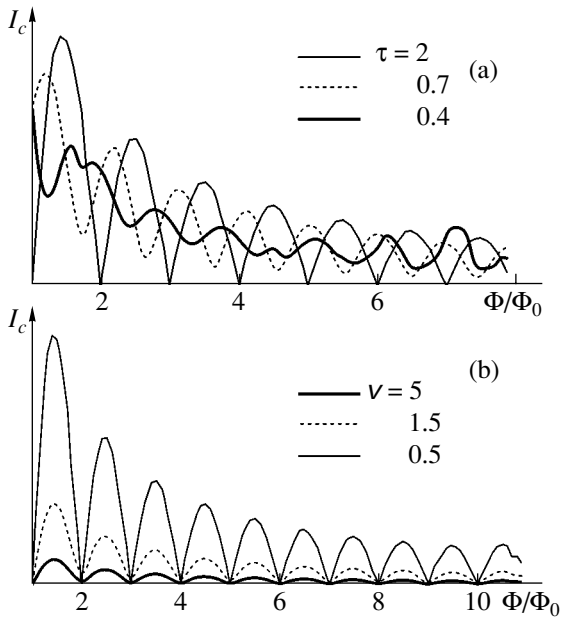

Fig. 5. Dependence of $I_c(\Phi)$ for intergranular coupling intensity $\sigma = 0.07$ for various values of characteristic grain size τ and anisotropy parameter ν: (a) $\tau = 0.4$, 0.7, and 2; $\nu = 1.5$; (b) $\nu = 0.5$, 1.5, and 5; $\tau = 1.5$.

It should be noted that the structural pattern in a real superconducting system is undoubtedly more complicated. The angle ϑ of disorientation of neighboring grains [13], the contact area S [14, 15], the orientation of the intergranular boundary plane relative to the (001) and (100) planes in which the anisotropic correlation length assumes extremal values [16], and other factors noticeably affect the value of current I_c. However, for the results obtained in this section, the very fact of the influence of boundaries on the AV and its effect on phase φ and current I_c of the intergranular SIS junction is significant; therefore, we believe that our model can be used for analyzing transport properties of superconducting polycrystals.

4.1. Role of Granular Characteristics on $I_c(H)$ in the Field Range $H \geq H_{c1}^G$

In the range of fields slightly stronger than the lower critical field H_{c1}^G in a grain, the equilibrium density n_L of the filaments is low and the distance d between neighboring AV is large ($d > \lambda_{ab}, \lambda_c$). In this case, distance d is connected with the granular induction via the relation

$$B \equiv n_L = q\frac{\Phi_0}{d^2}, \qquad (14)$$

where $q = 2/\sqrt{3}$ for the triangular configuration of the vortex lattice and $q = 1$ for the square lattice. In gains with a size $a > \lambda_c$, the number of emerging vortex filaments can be quite large since the repulsion of filaments in fields $H > H_{c1}^G$ is exponential, ~exp(–d/Λ) (i.e., having a finite range on the order of Λ), and this almost does not increase the energy of interaction.

In fields $H > H_{c1}^G$, the coordinates of the rows in the vortex lattice, which are closest to the surface and of the intergranular junction are $x \approx d/2$ and $z \approx d/2(a - d/2)$, respectively. Since the vortex lattice lies in the region $x \in [0, \lambda_J]$ and $z \in [0, a]$, equilibrium values of d for the given field H_y^{app} can be represented as

$$d = (a\lambda_{ab})^{1/2}\left(q\frac{\Phi}{\Phi_0}\right)^{-1/2}.$$

Thus, Eq. (6) was solved numerically for various values of the external field. The resultant contribution from all AVs to the current-phase behavior was calculated by formula (12).

4.1.1. Effect of characteristic grain size. Figure 5 shows the dependence of the critical current I_c on the magnetic field of a grain for various values of characteristic grain size τ and anisotropy parameter ν. It can be seen in Fig. 5a that the behavior of the function with increasing τ resembles the familiar Fraunhofer dependence. The maximal intergranular current corresponds to large values of τ. Such a behavior can be a consequence of a weak dynamic interaction between neighboring intergranular junctions, which emerges due to nonequilibrium effects [17]. In the model considered here, the smaller the value of τ, the stronger the interaction and the smaller the value of the order parameter $\Psi_{GB}(\Phi, T)$ at the grain boundary. Thus, the $I_c(\varphi)$ dependence is similar to the results obtained in [18] for various values of temperature T.

4.1.2. Effect of grain anisotropy on $I_c(\varphi)$. The following effects, which are of interest for technology of obtaining new materials with a high current-carrying capacity, are associated with grain anisotropy. Grain boundaries facilitate the formation of currents flowing at right angles to the current existing in homogeneous materials. As a result, the boundaries enhance the manifestation of anisotropy in the penetration of a field in a granular material. Figure 5b shows the $I_c(\varphi)$ dependence for various values of anisotropy parameter ν. It can be seen that the behavior of $I_c(\varphi)$ upon a change in ν resembles the conventional Fraunhofer dependence. However, the maximal intergranular current I_c is the smaller, the larger the value of ν. This effect can be explained from simple considerations. With increasing anisotropy $\nu = \lambda_c/\lambda_{ab}$, the depth of magnetic field penetration in a grain from the side of the Josephson junction increases. As a result, the effective thickness of the contact increases, while the order parameter $\Psi_{GB}(\Phi, T)$ at the grain boundary decreases.

4.2. Effect of the Intensity on Intergranular Coupling on $I_c(\varphi)$

Important effects of the granular structure of HTSC materials appear due to the presence of a broad spectrum of intergranular coupling intensity σ. The most convincing proof of the fact that intergranular space is of Josephson nature and, hence can be defined by the coupling intensity σ, follows from experiments under high pressures [19, 20]. The fundamental difference between the responses of the critical current I_c of an intergranular Josephson junction and the conventional pair-breaking current J_{cg} to pressure is the presence of the exponential factor $I_c \sim \exp(-d_N U^{1/2})$ for SIS junctions and $I_c \sim \exp(-2d_N/\xi_N)$ for SNS junctions. For this reason, experiments in high-pressure physics are based on a change in the parameters of intergranular junctions, viz., their thickness d_N and the barrier height U (insulator and/or normal layer), which directly change the intergranular coupling intensity (i.e., $I_c \propto P \propto \sigma(\propto \lambda_J^{-1})$).

Figure 6 shows the field dependence of the Josephson current $I_c(\Phi)$ for various parameters σ of the intergranular coupling intensity. It can be immediately seen that strictly sinusoidal behavior of $I_c(\Phi)$ corresponds only to 10–11 periods. In this region, function $I_c(\Phi)$ has the following singularities. First, the maximal current corresponds to smaller values of σ; second, the larger the value of σ, the more exactly the given dependence corresponds to the well-known Fraunhofer dependence in a small Josephson junction (this dependence has the form of $1/B$ with intense oscillations). However, several qualitative differences exist. The most important is that the period of oscillations is proportional to σ so that the frequency of function $I_c(\Phi)$ increases by a factor of k as soon as the value of σ increases k-fold. In other words, oscillations correspond to the presence of additional flux quanta passing through a grain. Such a form of oscillations was observed in experiments with BSCCO samples, in which the field dependence of stress was measured [21]. In strong fields, function $I_c(\Phi)$ is transformed into a peculiar sinusoidal dependence. This transition was observed in the $I_c(\Phi)$ dependence in a Josephson junction corresponding to a large-angle grain boundary in a polycrystalline $YBa_2Cu_3O_\delta$ film [22]. In addition, $I_c \propto \sigma$ in this field region. Such a transport behavior matches the experimental results [23] in which a noticeable increase in the value of I_c was observed ($d\ln I_c/dP = 0.2 \pm 0.02$ kbar^{-1}), indicating that application of pressure (increase in σ) improves the quality of intergranular Josephson coupling.

It should be noted that, first, the structure of grains and intergranular junctions in real superconducting polycrystals is highly disordered, which leads to size- and orientation distributions. This may weaken or even suppress some of the predicted effects. Second, allowance for symmetry in the order parameter in HTSC materials might be important since it leads to the growth of π contacts.

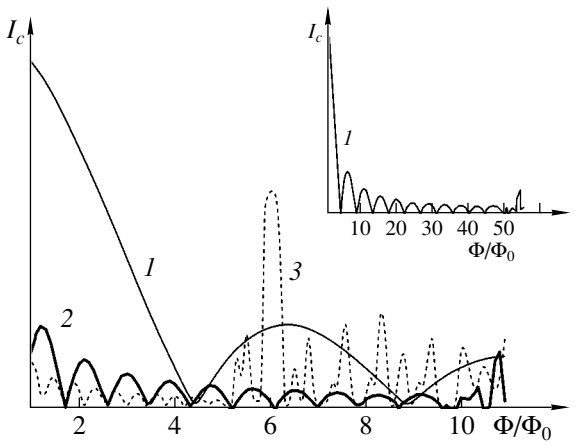

Fig. 6. Magnetic field dependence of the intergranular critical current $I_c(\Phi)$ for $\sigma = 0.07$ (*1*), 0.7 (*2*), and 0.35 (*3*); $\tau = 1.5$, and $\nu = 1.5$.

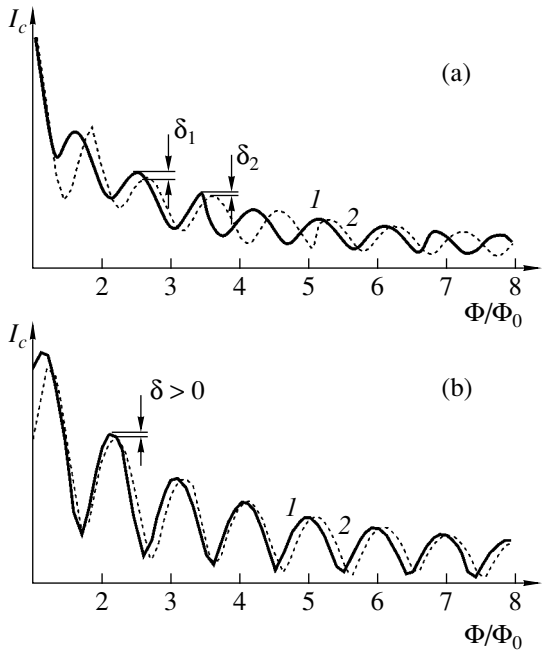

Fig. 7. Field dependence of the intergranular critical current I_c for triangular (*1*) and square (*2*) configurations of the vortex lattice for $\tau = 0.4$ (a), 0.6 (b), $\sigma = 0.07$, and $\nu = 1.5$.

4.3. Effect of the Vortex Lattice Symmetry Type on $I_c(\Phi)$

In a mixed state, the transport current through the intergranular junctions depends on the phase distribution $\theta(x)$. This dependence is interesting since a well-ordered vortex lattice was observed in recent experiments on bulk $La_{1.83}Sr_{0.17}CuO_{4+\delta}$ samples [24]. In addition, a transition from the triangular to the square

lattice configuration upon an increase in the field. Figure 7 shows the oscillating dependence $I_c(\Phi)$ in the case of formation of a triangular (curve *1*) and square (curve *2*) vortex lattice in a grain for $\tau = 0.4$ (Fig. 7a) and 0.6 (Fig. 7b), when $\sigma = 0.07$ and $\nu = 1.5$. The peak of the sinusoid is high for the triangular lattice. However, this tendency is not observed for large values of Φ. In addition, the phase difference in an anomalous Fraunhofer-like $I_c(\Phi)$ dependence is the larger, the smaller the value of τ (Fig. 7a). It should be noted that the latter results correspond only to super-small-grain structures with a grain size on the order of 1 μm.

5. CONCLUSIONS

A method for investigating phase dynamics in an intergranular Josephson junction with expulsion of Abrikosov vortices from grains and the presence of vortex lattices is developed on the basis of the vortex-laminar model. The results correspond to a number of the most important and fundamental experimental facts in transport phenomena in grained HTSC materials.

In particular, this approach clarifies the physical meaning of the main singularities on the magnetic field dependences $I_c(\Phi)$. The characteristic grain size τ, grain anisotropy ν, and the intergranular coupling intensity σ directly affect the intergrain critical current and determine the nature of the transformation of the AV into a Josephson vortex near the banks of the contact on a scale on the order of ξ_c.

In addition, the period of oscillations of critical current $I_c(\Phi)$ may acquire an addition flux quantum Φ_0 per grain upon a change in the intergrain coupling intensity σ. Our results are in accordance with the experimental data on the effect of high pressures on the $I_c(\Phi)$ dependence obtained for HgBaCaCuO polycrystals. It is shown qualitatively how the technological parameters of HTSC materials should be varied to increase their current-carrying capacity.

It is shown that generation of a Josephson vortex by an Abrikosov vortex passes though a stage of overcoming the energy barrier E_J in the intergranular junction; the barrier height depends on the Josephson medium parameters τ, ν, and σ, as well as on the distance z_0 between the Abrikosov vortex and the junction.

The role of the vortex lattice symmetry in the Josephson critical current is clarified. It is shown that the type of the vortex lattice may determine the transport properties of the system only in super-small-grained structures with $a \sim 1$ μm in fields $H \sim H_{c1}^G$.

Our results can be used in the physics of processes with dynamics described by Eq. (6) as well as in practical development of Josephson technologies in micro- and nanoelectronics.

ACKNOWLEDGMENTS

The authors are grateful to A.I. D'yachenko and Yu.A. Genenko for discussion of the results.

REFERENCES

1. C. P. Bean and J. D. Livingston, Phys. Rev. Lett. **12**, 14 (1964).
2. S. I. Denisov, Fiz. Tverd. Tela (Leningrad) **18**, 119 (1976) [Sov. Phys. Solid State **18**, 66 (1976)].
3. L. V. Belevtsov, Europhys. Lett. **59**, 768 (2002); J. Low Temp. Phys. **131**, 37 (2003); Phys. Status Solidi B **237**, 523 (2003).
4. B. A. Glowacki, M. Majoros, M. Vickers, *et al.*, Supercond. Sci. Technol. **14**, 193 (2001).
5. A. J. Panson, G. R. Wagner, A. I. Braginski, *et al.*, Appl. Phys. Lett. **50**, 1104 (1987).
6. M. V. Fistul', Zh. Éksp. Teor. Fiz. **96**, 369 (1989) [Sov. Phys. JETP **69**, 209 (1989)].
7. R. A. Ferrell and R. E. Prange, Phys. Rev. Lett. **10**, 479 (1963).
8. L. V. Belevtsov, Fiz. Nizk. Temp. **31**, 155 (2005) [Low Temp. Phys. **31**, 116 (2005)].
9. C. Ebner and D. Stroud, Phys. Rev. B **31**, 165 (1985).
10. G. Deutscher and K. A. Müller, Phys. Rev. Lett. **59**, 1745 (1987).
11. H. Hilgenkamp, J. Mannhart, and B. Mayer, Phys. Rev. B **53**, 14586 (1996).
12. M. V. Fistul', Pis'ma Zh. Éksp. Teor. Fiz. **49**, 95 (1989) [JETP Lett. **49**, 113 (1989)].
13. D. Dimos, P. Chaudhari, J. Mannhart, and F. K. LeGoues, Phys. Rev. Lett. **61**, 219 (1988).
14. H. Dersch and G. Blatter, Phys. Rev. B **38**, 11391 (1988).
15. L. V. Belevtsov and V. N. Pervukhin, Europhys. Lett. **67**, 648 (2004).
16. S. E. Babcock and D. C. Larbalestier, J. Mater. Res. **5**, 919 (1990).
17. S. N. Artemenko and A. G. Kobel'kov, Phys. Rev. Lett. **78**, 3551 (1997).
18. V. V. Dorin and M. V. Fistul', Zh. Éksp. Teor. Fiz. **101**, 1275 (1992) [Sov. Phys. JETP **74**, 683 (1992)].
19. V. M. Svistunov, A. I. D'yachenko, and V. Yu. Tarenkov, Int. J. Mod. Phys. B **25**, 3255 (1991).
20. V. M. Svistunov, A. I. D'yachenko, and V. Yu. Tarenkov, Physica C (Amsterdam) **185–189**, 2429 (1991).
21. S. Ooi, T. Mochiku, and K. Hirata, cond-mat/0112209.
22. D. K. Lathrop, B. H. Moeckly, S. E. Russek, and R. A. Buhrman, Appl. Phys. Lett. **58**, 1095 (1991).
23. A. I. D'yachenko, V. Yu. Tarenkov, A. V. Abalioshev, *et al.*, Physica C (Amsterdam) **251**, 207 (1995).
24. R. G. Gilardi, J. Mesot, A. Drew, *et al.*, Phys. Rev. Lett. **88**, 217003 (2002).

Translated by N. Wadhwa

Journal of Experimental and Theoretical Physics, Vol. 101, No. 3, 2005, pp. 513–520.
Translated from Zhurnal Éksperimental'noĭ i Teoreticheskoĭ Fiziki, Vol. 128, No. 3, 2005, pp. 597–606.

ORDER, DISORDER, AND PHASE TRANSITIONS IN CONDENSED SYSTEMS

Investigation of Stability of Ordered Manganites

S. V. Trukhanov

State Research Institute of Solid-State and Semiconductor Physics, National Academy of Sciences of Belarus, Minsk, 220072 Republic of Belarus
e-mail: truhanov@ifttp.bas-net.by

Received April 4, 2005

Abstract—Cation-ordered manganites of the $PrBaMn_2O_6$ system have been obtained using a two-stage synthesis and characterized with respect to the chemical composition, crystal structure, magnetic and magnetotransport properties, and the stability of the ordered state on heating. The physical properties of the cation-ordered $PrBaMn_2O_6$ manganites obtained using this method significantly differ from the properties of cation-disordered $Pr_{0.50}Ba_{0.50}MnO_3$ synthesized by means of the conventional ceramic technology and depend on the degree of ordering of the Pr^{3+} and Ba^{2+} cations. In particular, the cation-disordered $Pr_{0.50}Ba_{0.50}MnO_3$ has a cubic perovskitelike unit cell (SG = $Pm\bar{3}m$, $Z = 1$), while cation-ordered $PrBaMn_2O_6$ has a tetragonal unit cell (SG = $P4/mmm$, $Z = 2$). Cation states in the system under study are reversible. The cation-ordered $PrBaMn_2O_6$ state remains stable upon heating in an oxidizing medium ($P[O_2] = 1$ bar) up to 1300°C. The ordering of the Pr^{3+} and Ba^{2+} cations leads to a significant increase in the critical temperatures of phase transitions. In particular, $PrBaMn_2O_6$ with the maximum degree of ordering is a metallic ferromagnet with the Curie temperature $T_C \sim 320$ K, whereas T_C of a fully disordered sample is on the order of 140 K. The samples with intermediate degrees of ordering contain two magnetic phases. Slightly below T_C, all such samples exhibit a metal–insulator transition and a peak of the magnetoresistance, which amounts to approximately 10 and 65% in a magnetic field of 9 kOe for the fully ordered $PrBaMn_2O_6$ and disordered $Pr_{0.50}Ba_{0.50}MnO_3$, respectively. The results are interpreted in terms of the Goodenough–Kanamori empirical rules for indirect exchange interactions with allowance for the degree of ordering of the Pr^{3+} and Ba^{2+} cations. © *2005 Pleiades Publishing, Inc.*

1. INTRODUCTION

Rare earth manganites with a perovskite structure and the general formula $Ln_{1-x}A_xMnO_3$ (Ln = La, Nd, Pr; A = Ca, Sr, Ba) have been extensively studied for more than half a century [1, 2]. The interest in these compounds is still high [3], which is related, in particular, to the need for elucidating the nature of the phenomenon of colossal magnetoresistance.

The action of a magnetic field on classical metals containing free charge carriers leads to an increase in the resistivity. For this reason, such metals exhibit a positive anisotropic magnetoresistance (MR), which depends on the mutual orientation of the current direction and the magnetic induction vector [4].

Ferromagnetic superconductors, in which fully or partly localized charge carriers are present at temperatures below T_C (the Curie temperature), exhibit a negative isotropic MR, which is related to the fact that the mobility of partly localized charge carriers is higher in a ferromagnetic medium than in a paramagnetic one. The MR of this type reaches maximum in the region of T_C, which is explained by a shift of the ferromagnetic ordering toward higher temperature under the action of the external magnetic field [5]. Such a behavior is typical of the homogeneous media, while polycrystalline substances exhibit the so-called giant MR, which is related to the tunneling of charge carriers via a real physical barrier—the boundary between ceramic grains [6]. As a rule, the MR of this type is maximum at liquid helium temperature, which corresponds to the maximum degree of polarization of local spins.

In the beginning of the 1990s, it was established that systems such as $Pr(Nd)_{1-x}Ca_xMnO_3$ exhibit a metamagnetic transition from an antiferromagnetic charge-ordered state to ferromagnetic charge-disordered state in the external field. Upon this transition, the resistivity drops by several orders of magnitude. This phenomenon was termed colossal MR [7].

Subsequent investigations of the properties of manganites showed that the proper understanding of this phenomenon requires taking into account the presence and interplay of several degrees of freedom in the system under consideration, including the lattice, orbital, charge, and spin ones [8]. The properties of manganites depend on a large number of factors such as the chemical composition, stoichiometry, type of unit cell distortion, Mn–O bond length, Mn–O–Mn bond angle, etc. However, the main factor determining the properties of manganites is the Mn^{3+}/Mn^{4+} ratio between the numbers of differently charged manganese ions: this ratio being close to unity is a necessary condition both for

the realization of exchange interactions of the "double exchange" type and for the establishment of a charge order in the system [9]. The magnitude of Mn^{3+}/Mn^{4+} can be changed by introducing substitutional defects into three sublattices of the perovskite structure through (i) Ca^{2+}, Sr^{2+}, and Ba^{2+} substitution in sublattice A [10]; (ii) Mg^{2+}, Ga^{3+}, Ti^{4+}, and Nb^{5+} substitution in sublattice B [11]; and (iii) variation of the oxygen content [12]. Among various substituted manganites, most thoroughly studied in recent years are Ba-substituted ones.

In recent years, manganites of the $LnBaMn_2O_6$ system (Ln = Y and rare earth ions) have been found to possess unique physical properties, which is related to the ordering of cations in sublattice A of the perovskite structure [13–41]. The main structural feature of these cation-ordered compounds consists in the alternation of MnO_2 planes with two other planes—LnO and BaO, each containing cations of one type—which results in a periodic distortion of MnO_6 octahedra. The physical properties of such cation-ordered $LnBaMn_2O_6$ manganites cannot be explained taking into account the tolerance factor alone, as in the case of a statistical distribution of substituent cations in manganites of the $Ln_{0.50}Ba_{0.50}MnO_3$ type.

Previously, it was demonstrated that cation-ordered compounds can be obtained using the method of reversible topotaxic redox reactions. $LnBaMn_2O_6$ manganites with stoichiometric oxygen content synthesized in air by means of the conventional ceramic technology possess a cubic structure with a statistical distribution of Ln^{3+} and Ba^{2+} cations, whereas anion-deficient $LnBaMn_2O_5$ compounds have a tetragonal unit cell with an ordered distribution of Ln^{3+} and Ba^{2+}. The basal planes of the perovskite cubooctahedron are fully occupied by ions of the same type and alternate in the [001] direction. This crystal structure is similar to that of $YBaCuFeO_5$ [42]. Oxidation of the anion-deficient $LnBaMn_2O_5$ compounds leads to the formation of a stoichiometric cation-ordered $LnBaMn_2O_6$ also possessing a tetragonal structure. This type of cation ordering increases the temperature of the phase transition from a metallic ferromagnetic state to a dielectric paramagnetic state, for example, from $T \approx 140$ K to 320 K in the case of Pr^{3+}. In both cases, the MR effect is observed at temperatures slightly below T_C [22]. Good prospects for the practical use of such materials are related to the fact that the phase transitions take place at room temperature.

In cation-ordered $PrBaMn_2O_6$ and $NdBaMn_2O_6$, the main magnetic state is the A-type antiferromagnet [40]. In cation-ordered $LaBaMn_2O_6$, an antiferromagnetic phase of the CE type coexist with the ferromagnetic phase, which implies that the electron phase separation in manganites is not only related to a statistical occupation of sublattice A, but that it also depends on the competition between superexchange interactions and charge ordering. The latter factor is also significantly influenced by even slight changes in local structure on the level of the first coordination sphere [43].

In this context, it was of interest to study in more detail the physicochemical properties of cation-ordered Ba-substituted manganites. This investigation was devoted to the $PrBaMn_2O_6$ system, which was characterized with respect to the chemical composition, crystal structure, magnetic and magnetotransport properties, and the stability of the ordered state on heating.

2. EXPERIMENTAL METHODS

The initial cation-ordered compound with the formula $PrBaMn_2O_6$ was obtained by means of a two-stage synthesis. In the first stage, cation-disordered $Pr_{0.50}Ba_{0.50}MnO_3$ was synthesized using the conventional ceramic technology in air at 1550°C and then reduced by heating in vacuum at 800°C for 24 h to obtain the $O_{2.50}$ phase:

$$Pr_{0.5}Ba_{0.5}MnO_3 + 0.2Ta \longrightarrow Pr_{0.5}Ba_{0.5}MnO_{2.50} + 0.1Ta_2O_5. \quad (1)$$

As will be shown below, the $O_{2.50}$ phase is characterized by the ordered arrangement of the Pr^{3+} and Ba^{2+} cations in the (001) planes alternating in the [001] direction. As a result, the unit cell of this phase is doubled, and the phase with double unit cell will be denoted below "O_5." At the second stage, the anion-deficient $PrBaMn_2O_5$ was oxidized in air at 800°C for 5 h to obtain a stoichiometric O_6 phase. Then, the stoichiometric cation-ordered $PrBaMn_2O_6$ manganite was subjected to isochronous step annealing in air for 10 h at 1100, 1200, and 1300°C.

The chemical composition of samples was studied by Auger electron spectroscopy (AES) on a PHI Model 660 scanning Auger microprobe. The measurements were performed in high vacuum before and after cleaning the sample surface with an Ar^+ ion beam. The microstructure of all samples was studied on a NANOLAB-7 scanning electron microscope. The quantitative content of chemical elements was determined and their homogeneous distribution was checked using two complementary X-ray microprobes: MS-46 (wavelength-dispersive X-ray spectrometer) and system 860-500 (energy-dispersive X-ray spectrometer). Prior to measurements, the samples were degreased by ultrasonic rinsing in ethanol for 5 min. The oxygen content was determined by thermogravimetric analysis (TGA). Thus, the chemical formula of the synthesized compounds could be written as $Pr_{0.50}Ba_{0.50}MnO_{3\pm0.01}$ and $PrBaMn_2O_{6\pm0.02}$ for the O_3 and O_6 phases, respectively.

The structure of samples was studied by X-ray diffraction at room temperature on a DRON-3 diffractometer using CrK_α radiation filtered by a graphite monochromator. The measurements were performed in the angle interval $10° \le 2\theta \le 100°$ at a step of $\Delta\theta = 0.03$.

The degree of ordering A for the Pr^{3+} and Ba^{2+} cations for all compounds $[Pr_gBa_{1-g}]_P[Pr_{1-g}Ba_g]_BMn_2O_6$ was determined from an analysis of the intensity of superstructural (0 0 1/2) reflection and calculated as

$$A = (2g - 1) \times 100\%, \quad (2)$$

where $[]_P$ and $[]_B$ are the crystallographic positions of Pr and Ba, respectively, and g is a quantity varying from 0.5 for fully disordered (A = 0%) to 1 for completely ordered (A = 100%) samples.

The dynamic magnetic susceptibility χ was measured in a temperature interval from 77 to 350 K using a mutual induction bridge at an alternating magnetic field frequency of 1200 Hz. The Curie temperature T_C was determined at a minimum of the derivative of χ with respect to the temperature ($d\chi/dT$). The resistivity was studied in a temperature interval from 77 to 350 K using the standard four-point-probe technique and the samples with ultrasonically applied indium eutectic contacts. The negative isotropic MR was determined as

$$MR = \left(\frac{\rho(H) - \rho(0)}{\rho(0)}\right) \times 100\%, \quad (3)$$

where $\rho(H)$ and $\rho(0)$ are the resistivities measured in a magnetic field of H = 9 kOe and in the absence of an applied magnetic field.

3. EXPERIMENTAL RESULTS AND DISCUSSION

The oxygen content in all samples was determined by TGA. It was established that the anion-deficient cation-ordered O_5 annealed in air at 300–800°C converts into a stoichiometric O_6 phase with retained ordered arrangement of the Pr^{3+} and Ba^{2+} cations in the (001) planes. The subsequent step annealing in air at 900–1300°C did not change the oxygen content in the O_6 phase (Fig. 1). According to the TGA data, the annealing of a cation-ordered $PrBaMn_2O_6$ (A = 100%), in air for 3 h at 900°C changed the sample mass by less than 0.06%.

Analysis of all samples by AES did not reveal any elements other than the main components Pr, Ba, Mn, and O. Figure 2 shows the typical AES spectrum of a sample of cation-ordered $PrBaMn_2O_6$ (A = 100%). The ratio between cations in all cases was 1 : 1 : 2 (to within the measurement accuracy). The AES measurements were performed in high vacuum before and after cleaning of the sample surface with a beam of high-energy Ar^+ ions. The presence of a peak of carbon (C) in the differential spectrum of the initial sample (Fig. 2a) is explained by the adsorption of CO_2 from air on the manganite surface. This impurity peak disappears upon the Ar^+ ion bombardment of the sample surface (Fig. 2b).

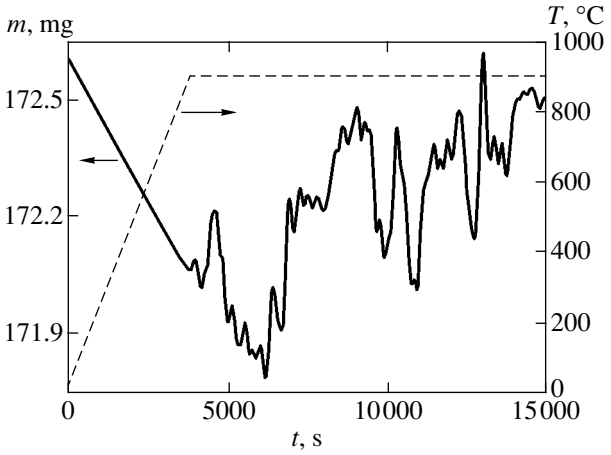

Fig. 1. TGA data for a cation-ordered $PrBaMn_2O_6$ sample (A = 100%).

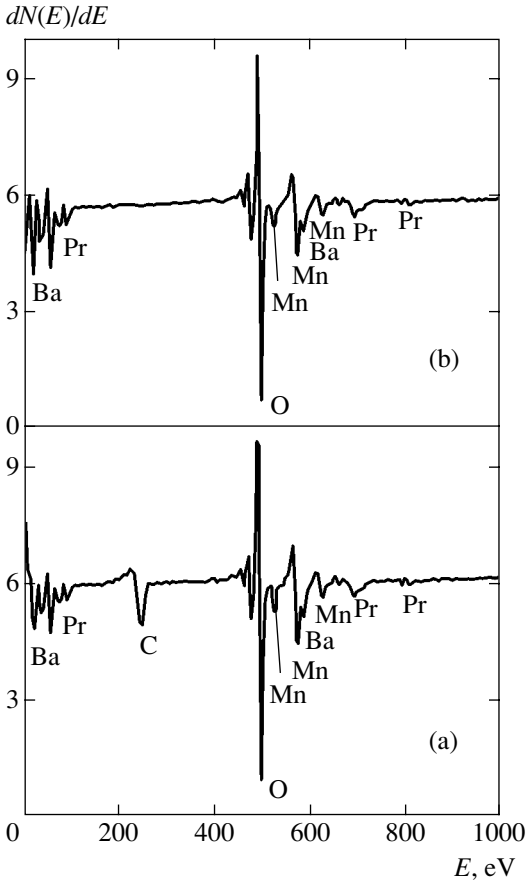

Fig. 2. Differential AES spectra of a cation-ordered $PrBaMn_2O_6$ sample (A = 100%) measured (a) before and (b) after cleaning of the sample surface with a beam of high-energy Ar^+ ions.

The sample morphology and the homogeneity of distribution of the component elements were studied by scanning electron microscopy (SEM). A typical SEM micrograph of a cation-ordered $PrBaMn_2O_6$ (A =

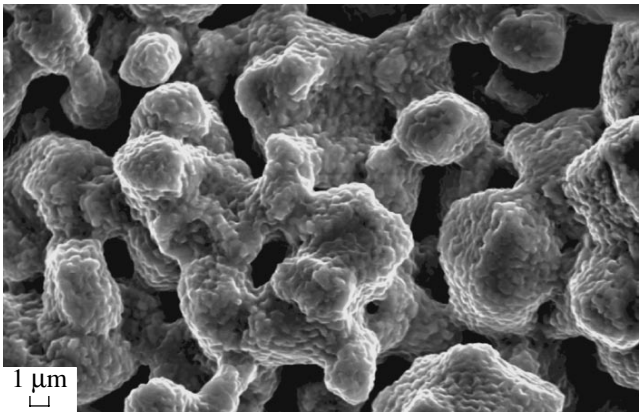

Fig. 3. Typical SEM micrograph of a cation-ordered $PrBaMn_2O_6$ sample (A = 100%).

100%) sample is presented in Fig. 3. The results of SEM measurements showed that the initial stoichiometric cation-disordered $Pr_{0.50}Ba_{0.50}MnO_3$ sample is characterized by the average grain size ($\langle D\rangle \approx 5$ μm), while all cation-ordered $PrBaMn_2O_6$ samples (irrespective of the degree of ordering A contained nanodimensional grains ($\langle D\rangle \approx 300$ nm). By "grains" we imply the homogeneous regions separated from each other by continuous boundary surfaces. The nanograins combine to form a certain mosaic structure, which is common for the entire polycrystalline sample. As can be seen from Fig. 3, the grains exhibit a certain size distribution. It was also established that all samples are characterized by a homogeneous distribution of chemical elements corresponding to the nominal chemical formula $PrBaMn_2O_6$. The grain size determines, to a certain extent, the properties of the crystal structure. A decrease in the grain size to the nanodimensional level is accompanied by a certain decrease in the unit cell volume, which is explained by an increase in the forces of surface tension relative to the bulk elastic forces. It was also concluded that the sequential "deep" redox reactions are capable of significantly modifying the solid surface morphology [44].

Most substituted manganites possess a distorted unit cell, which is a result of decreasing symmetry relative to the initial cubic. There are two commonly accepted factors responsible for the distortion of the oxygen octahedron in MnO_6: (i) a mismatch between the effective ion radius and the cavity size (size effect) and (ii) the Jahn–Teller effect inherent in Mn^{3+} ions in a high-spin state (S = 2). In the former case, a minimum free energy of the crystal structure is achieved via rotation of the MnO_6 octahedron about the unit cell axes, while in the second case the energy is minimized at the expense of deformation of the MnO_6 octahedron. A rotation around the [100], [110], and [111] axes leads to tetragonal, orthorhombic, and rhombohedral distortion, respectively. The two factors may superimpose and act simultaneously [45].

According to the X-ray diffraction data, the initial cation-disordered $Pr_{0.50}Ba_{0.50}MnO_3$ manganite at room temperature is a cubic perovskite (SG = $Pm\bar{3}m$, Z = 1) with the unit cell parameters a = 3.901 Å (V = 59.37 Å^3). The X-ray diffractograms revealed no impurity or superstructural reflections. The presence of a cubic symmetry was indicative of a statistical distribution of cations in the crystals structure. All the cation-ordered $PrBaMn_2O_6$ samples exhibited a tetragonal distortion (SG = $P4/mmm$, Z = 2), which was related to the ordering of the Pr^{3+} and Ba^{2+} cations in the (001) planes and doubling of the cell in the [001] direction. The unit cell parameters of a cation-ordered $PrBaMn_2O_6$ sample annealed in air for 5 h at 800°C are as follows: a = 3.900 Å, c = 7.775 Å (V = 118.26 Å^3). Direct evidence for the ordering of cations in this compound was the presence of superstructural reflections in the X-ray diffractograms. Additional evidence was provided by the results of previous experiments using the methods of electron diffraction and high-resolution electron microscopy [22]. The appearance of ordering of the Pr^{3+} and Ba^{2+} cations leads to a decrease (by one formula unit) in the unit cell volume. The cation-ordered $PrBaMn_2O_6$ samples possess a smaller comparable unit cell volume than the cation-disordered $Pr_{0.50}Ba_{0.50}MnO_3$, and this volume depends on the degree of ordering in sublattice A. The main structural feature of these cation-ordered compounds is the alternation of MnO_2 planes with PrO and BaO planes.

The degree of ordering of the Pr^{3+} and Ba^{2+} cations was determined using data on the intensity of the superstructural (0 0 1/2) reflection relative to that for the initial cubic cell. For CrK_α radiation, this reflection is situated at $2\theta \approx 17°$ (Fig. 4). The intensity of this reflection for the initial cation-disordered $Pr_{0.50}Ba_{0.50}MnO_3$ compound synthesized using the conventional ceramic technology and for the cation-ordered $PrBaMn_2O_6$ sample annealed in air for 10 h at 1300°C was zero. Therefore, the degree of ordering in these samples was also A = 0%. The cation-ordered $PrBaMn_2O_6$ sample annealed in air for 5 h at 800°C exhibited the maximum degree of ordering: A = 100%. For the cation-ordered $PrBaMn_2O_6$ samples annealed in air for 10 h at 1100 and 1200°C, the degree of ordering had intermediate values of A = 70 and 50%, respectively. Thus, an increase in the temperature of annealing leads to degradation of the ordered state up to the complete disordering in the limit at 1300°C. As can be seen from Fig. 4, a decrease in the degree of ordering is accompanied by an increase in the unit cell volume, which is manifested by the shift of the Bragg reflection toward smaller 2θ angles. It should be noted that the cation states in the system under consideration are reversible.

Figure 5 shows the temperature variation of the dynamic magnetic susceptibility χ and its derivative with respect to temperature ($d\chi/dT$) for the cation-ordered $PrBaMn_2O_6$ samples with various degrees of ordering.

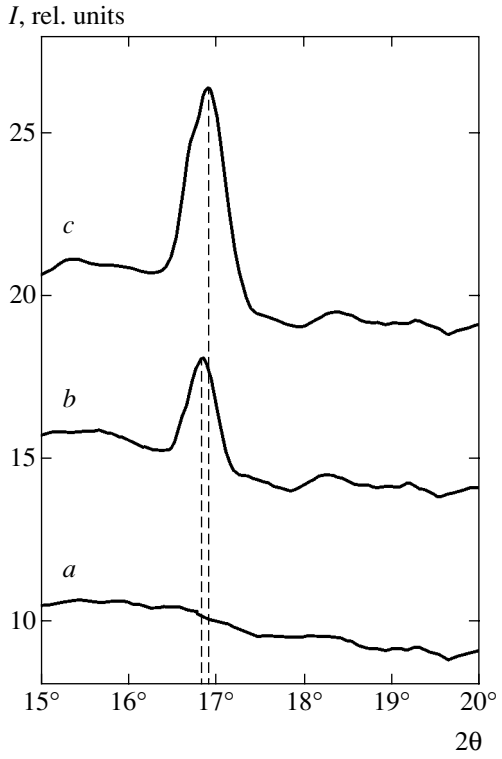

Fig. 4. Room-temperature X-ray diffractograms showing superstructural (0 0 1/2) reflections for the cation-ordered $PrBaMn_2O_6$ samples with $A = 0$ (*a*), 70% (*b*), and 100% (*c*).

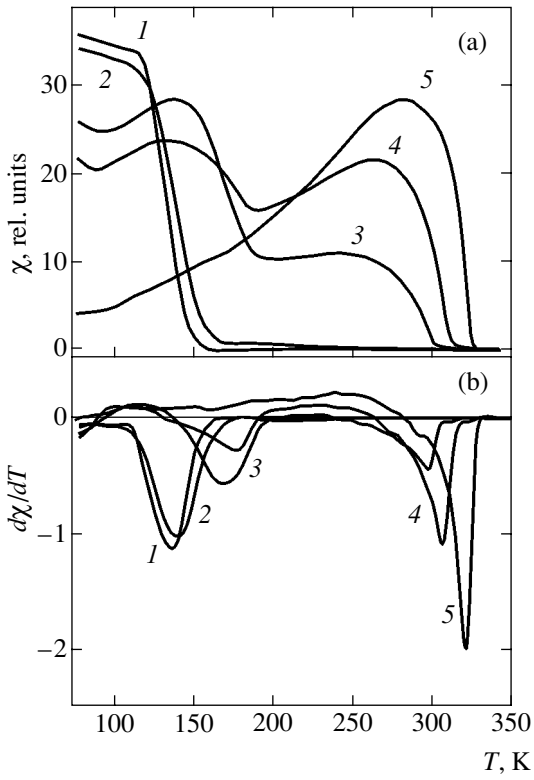

Fig. 5. Plots of the (a) dynamic magnetic susceptibility χ and (b) its derivative $d\chi/dT$ versus temperature for (*1*) the initial cation-disordered $Pr_{0.50}Ba_{0.50}MnO_3$ and (*2*–*5*) cation-ordered $PrBaMn_2O_6$ samples with $A = 0$ (*2*), 50% (*3*), 70% (*4*), and 100% (*5*).

The initial cation-disordered $Pr_{0.50}Ba_{0.50}MnO_3$ is a ferromagnet with $T_C \approx 140$ K. The ordering of cations leads to a sharp increase in T_C, which reaches $T_C \approx 320$ K for cation-ordered $PrBaMn_2O_6$ with $A = 100\%$. The samples with $A = 50$ and 70% are characterized by $T_C \approx 166$ and 306 K, respectively. In addition, the latter partly ordered samples exhibit anomalies in the region of 180 K, which are related to the low-temperature ferromagnetic phase. Thus, the step annealing of cation-ordered $PrBaMn_2O_6$ samples leads to degradation of the high-temperature ferromagnetic phase and a decrease in the degree of ordering, which corresponds to restoration of the initial magnetic properties.

Figure 6 shows the temperature dependence of the resistivity and MR (measured at $H = 9$ kOe) for cation-ordered $PrBaMn_2O_6$ samples with various degrees of ordering. All sample exhibit the metal–dielectric transition and MR peaks slightly below T_C. A decrease in the degree of ordering is accompanied by depression of the transition temperature and leads to the growth of both resistivity and MR. For the completely cation-ordered $PrBaMn_2O_6$ sample ($A = 100\%$), the MR peak at $T_C \approx 311$ K amounts to approximately 10%, whereas the completely cation-disordered sample ($A = 0$) as MR ≈ 66% at $T_C \approx 137$ K. This property (MR peak observed above room temperature) makes cation-ordered $PrBaMn_2O_6$ manganites promising materials for practical applications.

There is a certain correlation between the degree of ordering of the Pr^{3+} and Ba^{2+} cations, the unit cell volume, and the Curie temperature. As can be seen from Fig. 7, an increase in the degree of ordering is accompanied by a correlated decrease in the unit cell volume and an increase in the Curie temperature.

In order to explain the existence of a metallic ferromagnetic state in substituted manganites, Zener [46] and De Gennes [47] developed the so-called double exchange model. The main function in this mechanism is performed by partly collectivized (itinerant) e_g electrons, which pass (without their changing spin orientation) from Mn^{3+} ($t_{2g}^3 e_g^1$, $S = 2$) to Mn^{4+} (t_{2g}^3, $S = 3/2$) via O^{2-} anions. The total spins of fully localized t_{2g}^3 electrons are polarized by the jumps of collectivized e_g electrons and the material becomes ferromagnetic below T_C. In addition to the Mn^{3+}/Mn^{4+} ratio, the magnetic properties of manganites are determined to a considerable extent by the following parameters: (i) the average ion radius $\langle r_A \rangle$ of the perovskite sublattice A [48], (ii) the variance σ^2 of the radii of chemical elements occupying sublattice A [49], and (iii) average Mn–O

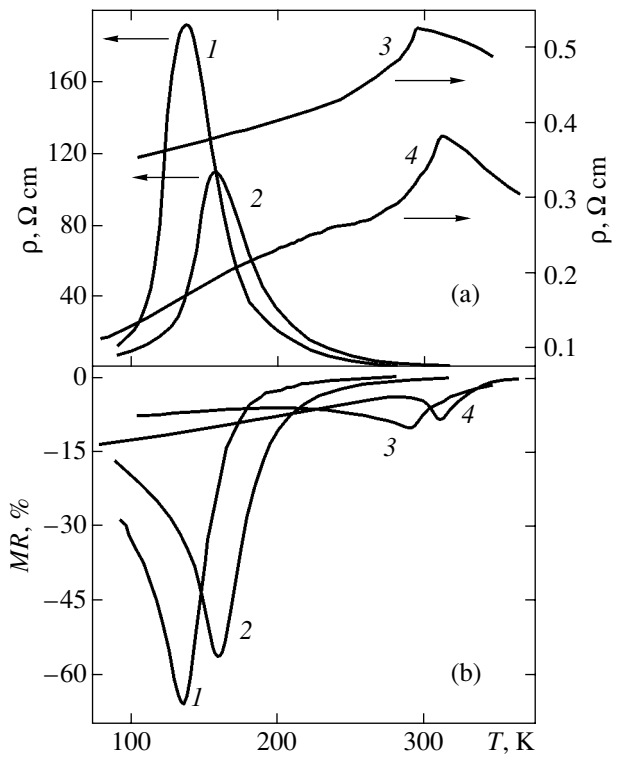

Fig. 6. Plots of the (a) resistivity and (b) magnetoresistance (measured at H = 9 kOe) versus temperature for cation-ordered $PrBaMn_2O_6$ samples with A = 0 (*1*), 50% (*2*), 70% (*3*), and 100% (*4*).

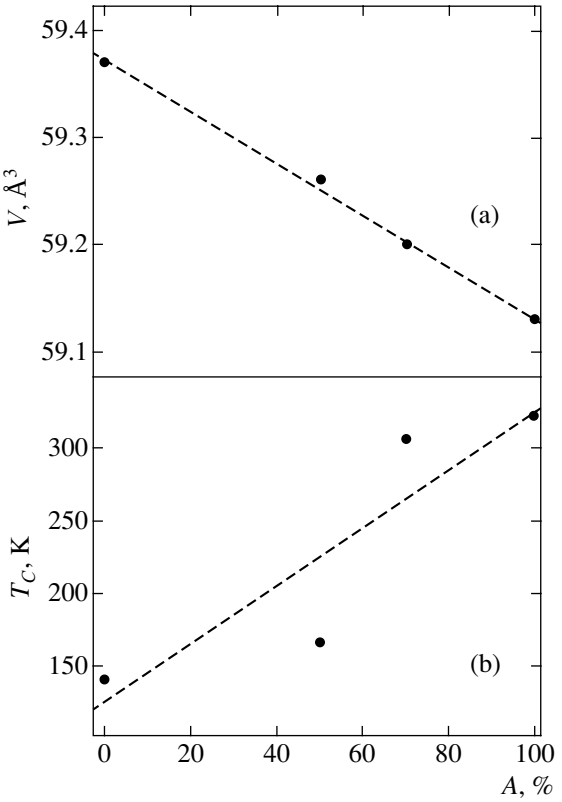

Fig. 7. Plots of the (a) unit cell volume V and (b) Curie temperature T_C versus degree of ordering for cation-ordered $PrBaMn_2O_6$.

bond length [50]. As a rule, a decrease in the average radius $\langle r_A \rangle$ and an increase in the variance σ^2 and the Mn–O bond length lead to a decrease in T_C.

The condition that the ratio Mn^{3+}/Mn^{4+} is close to unity determines the concentration boundary of the transition from ferromagnetic to antiferromagnetic state [51]. For this reason, the spontaneous magnetic moment and the Curie temperature for such compounds are somewhat lower than the possible theoretical values. As the relative content of Mn^{4+} ions increases, the manganite state changes from ferromagnetic to antiferromagnetic and dielectric. According to the Goodenough–Kanamori empirical rules [52], the closer the average Mn–O–Mn bond angle to 180°, the higher the intensity of exchange interactions. The local distribution of the Mn–O–Mn bond angles is determined to a considerable extent by the character of cation arrangement in sublattice A. A statistical distribution of cation leads to strong local distortions in the distribution of Mn–O–Mn bond angles, which leads to a decrease in the intensity of exchange interactions. For this reason, a low Curie temperature ($T_C \approx 140$ K) is observed for the cation-disordered sample.

The ordering of the Pr^{3+} and Ba^{2+} cations in sublattice A leads to two consequences: (i) an increase in periodicity of distribution of the Mn–O–Mn bond angles (and, probably, an increase in the average value of this angle) and (ii) a decrease in the average Mn–O bond length (as a result of decreasing unit cell volume). These changes lead to a significant increase in the Curie temperature (according to the experimental data, up to $T_C \approx 320$ K). Intermediate ordered states are characterized by intermediate T_C values, a decrease in the degree of ordering leading to a depression of the Curie temperature. The increase in the average value and the periodicity of distribution of the Mn–O–Mn bond angle and in the average length of the Mn–O bond leads to an increase in the integral of e_g electron transfer and, hence, favors the charge carrier transport. As a result, the critical temperature of the metal–dielectric transition also increases with the degree of ordering. The peak of MR also exhibits a shift. Thus, there is a certain correlation between the spin and charge states.

It should be noted that the nature of the cation-ordered state formation in Ba-substituted manganites is by no means completely clear, since no such ordering has been observed for the other substituents such as Ca and Sr. At present, we may only ascertain that there are two factors favoring this ordering: (i) the appearance of a large number of oxygen vacancies in the initially disordered $Pr_{0.50}Ba_{0.50}MnO_3$ compound and (ii) a decrease in the average size of ceramic grains down to the nano-

dimensional level. This decrease in the grain size leads to an increase in the forces of surface tension relative to the bulk elastic forces, which produces an additional compression equivalent to external pressure.

4. CONCLUSIONS

This paper presents the results of an experimental investigation of the chemical composition, crystal structure, magnetic and magnetotransport properties of cation-ordered manganites of the $PrBaMn_2O_6$ system.

Using a two-stage synthesis, a series of $PrBaMn_2O_6$ manganites with an ordered arrangement of the Pr^{3+} and Ba^{2+} cations were obtained. The stability of this ordered state was studied on heating to elevated temperatures.

The physical properties of the cation-ordered $PrBaMn_2O_6$ manganites obtained using the two-stage synthesis significantly differ from the properties of cation-disordered $Pr_{0.50}Ba_{0.50}MnO_3$ synthesized by means of the conventional ceramic technology and depend on the degree of ordering of the Pr^{3+} and Ba^{2+} cations.

In particular, the cation-disordered $Pr_{0.50}Ba_{0.50}MnO_3$ has a cubic perovskitelike unit cell (SG = $Pm\bar{3}m$, $Z = 1$), while cation-ordered $PrBaMn_2O_6$ has a tetragonal unit cell (SG = $P4/mmm$, $Z = 2$). The average grain size in this cation-ordered compound is about 300 nm. Cation states in the system under study are reversible. The cation-ordered $PrBaMn_2O_6$ state remains stable upon heating in an oxidizing medium ($P[O_2] = 1$ bar) up to 1300°C. As the degree of ordering of the Pr^{3+} and Ba^{2+} cations decreases, the corresponding unit cell volume grows.

The ordering of the Pr^{3+} and Ba^{2+} cations leads to a significant increase in the critical temperatures of phase transitions. In particular, $PrBaMn_2O_6$ with the maximum degree of ordering ($A = 100\%$) is a metallic ferromagnet with the Curie temperature $T_C \approx 320$ K, whereas T_C of a fully disordered sample is on the order of 140 K. The samples with intermediate degrees of ordering contain two magnetic phases. Slightly below T_C, all such samples exhibit a metal–insulator transition and show a peak of the magnetoresistance, which amounts to approximately 10 and 65% in a magnetic field of 9 kOe for the fully ordered $PrBaMn_2O_6$ and disordered $Pr_{0.50}Ba_{0.50}MnO_3$, respectively. The results can be interpreted in terms of the Goodenough–Kanamori empirical rules for indirect exchange interactions with allowance for the degree of ordering of Pr^{3+} and Ba^{2+} cations. It is suggested that such indirect exchange interactions Mn^{4+}–O–Mn^{3+} are positive in the orbital-disordered phase in the case of octahedral coordination of manganese ions.

ACKNOWLEDGMENTS

This study was supported in part by the State Program of Targeted Basic Research “Nanomaterials and Nanotechnologies” (Project 3.3) and the Basic Research Foundation of the Republic of Belarus (project no. F04R-076).

REFERENCES

1. G. H. Jonker and J. H. Van Santen, Physica (Utrecht) **16**, 337 (1950).
2. J. H. Van Santen and G. H. Jonker, Physica (Utrecht) **16**, 599 (1950).
3. S. M. Dunaevskiĭ, Fiz. Tverd. Tela (St. Petersburg) **46**, 193 (2004) [Phys. Solid State **46**, 193 (2004)].
4. C. Kittel, *Introduction to Solid State Physics*, 4th ed. (Wiley, New York, 1971; Nauka, Moscow, 1962).
5. S. V. Trukhanov, I. O. Troyanchuk, N. V. Pushkarev, and H. Szymczak, Zh. Éksp. Teor. Fiz. **122**, 356 (2002) [JETP **95**, 308 (2002)].
6. N. Zhang, S. Zhang, W. P. Ding, *et al.*, Solid State Commun. **107**, 417 (1998).
7. Y. Tokura and Y. Tomioka, J. Magn. Magn. Mater. **200**, 1 (1999).
8. J. M. D. Coey, M. Viret, and S. von Molnár, Adv. Phys. **48**, 167 (1999).
9. S. V. Trukhanov, J. Mater. Chem. **13**, 347 (2003).
10. E. L. Nagaev, Phys. Rep. **346**, 387 (2001).
11. I. O. Troyanchuk, M. V. Bushinsky, H. Szymczak, *et al.*, Eur. Phys. J. B **28**, 75 (2002).
12. I. O. Troyanchuk, S. V. Trukhanov, H. Szymczak, *et al.*, Zh. Éksp. Teor. Fiz. **120**, 183 (2001) [JETP **93**, 161 (2001)].
13. T. P. Beales, M. Molgg, J. Jutson, and C. M. Friend, Phys. Status Solidi A **161**, 271 (1997).
14. F. Millange, V. Caignaert, B. Domenges, *et al.*, Chem. Mater. **10**, 1974 (1998).
15. A. Barnabé, F. Millange, A. Maignan, *et al.*, Chem. Mater. **10**, 252 (1998).
16. J. A. McAllister and J. P. Attfield, J. Mater. Chem. **8**, 1291 (1998).
17. F. Millange, E. Suard, V. Caignaert, and B. Raveaul, Mater. Res. Bull. **34**, 1 (1999).
18. V. Caignaert, F. Millange, B. Domengès, *et al.*, Chem. Mater. **11**, 930 (1999).
19. I. O. Troyanchuk, S. V. Trukhanov, H. Szymczak, and K. Baerner, J. Phys.: Condens. Matter **12**, L155 (2000).
20. S. V. Trukhanov, I. O. Troyanchuk, I. M. Fita, *et al.*, J. Magn. Magn. Mater. **237**, 276 (2001).
21. T. Nakajima, H. Kageyama, and Y. Ueda, J. Phys. Chem. Solids **63**, 913 (2002).
22. S. V. Trukhanov, I. O. Troyanchuk, M. Hervieu, *et al.*, Phys. Rev. B **66**, 184424 (2002).
23. T. Nakajima, H. Kageyama, H. Yoshizawa, and Y. Ueda, J. Phys. Soc. Jpn. **71**, 2843 (2002).
24. T. Arima, D. Akahoshi, K. Oikawa, *et al.*, Phys. Rev. B **66**, 140408(R) (2002).

25. S. V. Trukhanov, I. O. Troyanchuk, D. D. Khalyavin, *et al.*, Zh. Éksp. Teor. Fiz. **121**, 388 (2002) [JETP **94**, 329 (2002)].
26. M. Uchida, D. Akahoshi, R. Kumai, *et al.*, J. Phys. Soc. Jpn. **71**, 2605 (2002).
27. R. Vidya, P. Ravindran, A. Kjekshus, and H. Fjellvag, Phys. Rev. B **65**, 144422 (2002).
28. J. Wang, W. Zhang, and D. Y. Xing, Phys. Rev. B **66**, 052410 (2002).
29. A. J. Williams and J. P. Attfield, Phys. Rev. B **66**, 220405(R) (2002).
30. C. Autret, A. Maignan, C. Martin, *et al.*, Appl. Phys. Lett. **82**, 4746 (2003).
31. P. Ravindran, R. Vidya, P. Vajeeston, *et al.*, J. Solid State Chem. **176**, 338 (2003).
32. H. Kageyama, T. Nakajima, M. Ichihara, *et al.*, J. Phys. Soc. Jpn. **72**, 241 (2003).
33. J. Spooren, A. Rumplecker, F. Millange, and R. I. Walton, Chem. Mater. **15**, 1401 (2003).
34. T. Nakajima, H. Kageyama, H. Yoshizawa, *et al.*, J. Phys. Soc. Jpn. **72**, 3237 (2003).
35. T. Nakajiama, H. Kageyama, and Y. Ueda, Physica B (Amsterdam) **329**, 844 (2003).
36. H. Aliaga, D. Magnoux, A. Moreo, *et al.*, Phys. Rev. B **68**, 104405 (2003).
37. Y. Ueda and T. Nakajima, J. Phys.: Condens. Matter **16**, S573 (2004).
38. N. Takeshita, C. Terakura, D. Akahoshi, *et al.*, Phys. Rev. B **69**, 180405(R) (2004).
39. D. Akahoshi, Y. Okimoto, M. Kubota, *et al.*, Phys. Rev. B **70**, 064418 (2004).
40. T. Nakajima, H. Yoshizawa, and Y. Ueda, J. Phys. Soc. Jpn. **73**, 2283 (2004).
41. J. Spooren, R. I. Walton, and F. Millange, J. Mater. Chem. **15**, 1542 (2005).
42. V. Caignaert, I. Mirebeau, F. Bouree, *et al.*, J. Solid State Chem. **114**, 24 (1995).
43. D. Akahoshi, M. Uchida, Y. Tomioka, *et al.*, Phys. Rev. Lett. **90**, 177203 (2003).
44. S. V. Trukhanov, Zh. Éksp. Teor. Fiz. **127**, 107 (2005) [JETP **100**, 95 (2005)].
45. S. V. Trukhanov, L. S. Lobanovski, M. V. Bushinsky, *et al.*, J. Phys.: Condens. Matter **15**, 1783 (2003).
46. C. Zener, Phys. Rev. **82**, 403 (1951).
47. P.-G. De Gennes, Phys. Rev. **118**, 141 (1960).
48. L. M. Rodriguez-Martinez and J. P. Attfield, Phys. Rev. B **58**, 2426 (1998).
49. R. Mahesh and M. Itoh, Phys. Rev. B **60**, 2994 (1999).
50. E. O. Wollan and W. C. Koehler, Phys. Rev. **100**, 545 (1955).
51. H. Fujishiro, M. Ikebe, and Y. Konno, J. Phys. Soc. Jpn. **67**, 1799 (1998).
52. J. B. Goodenough, A. Wold, R. J. Arnot, and N. Menyuk, Phys. Rev. **124**, 373 (1961).

Translated by P. Pozdeev

Journal of Experimental and Theoretical Physics, Vol. 101, No. 3, 2005, pp. 521–527.
Translated from Zhurnal Éksperimental'noĭ i Teoreticheskoĭ Fiziki, Vol. 128, No. 3, 2005, pp. 607–614.

ORDER, DISORDER, AND PHASE TRANSITIONS IN CONDENSED SYSTEMS

The Influence of the Icosahedral Percolation Transition in Supercooled Liquid Iron on the Diffusion Mobility of Atoms

A. V. Evteev, A. T. Kosilov, E. V. Levchenko, and O. B. Logachev
Voronezh State Technical University, Moskovskiĭ pr. 14, Voronezh, 394026 Russia
e-mail: evteev@vmail.ru
Received April 8, 2005

Abstract—The paper develops concepts of the structure of pure amorphous metals and atomic mechanisms of its formation. It is shown that a stable percolation cluster of interpenetrating and contacting icosahedra whose vertices and centers are occupied by atoms is formed under the conditions of isothermal annealing of instantaneously supercooled iron melt only below the critical temperature ~1180 K identified with the glass transition temperature. The duration of isothermal annealing up to the formation of the icosahedral percolation cluster does not exceed $\sim 1.5 \times 10^{-11}$ s at 900–1180 K. The time of the beginning of homogeneous nucleation was found to be minimum at the critical temperature above which stable icosahedral percolation cluster did not form. Arguments are provided in favor of the assumption that the formation of icosahedral percolation cluster interferes with the beginning of crystallization. A quantitative model is suggested to describe the diffusion mobility of atoms in metallic glasses. In this model, the mean-square displacement of atoms is represented as the sum of the contributions of the linear (Einstein) and logarithmic components. The latter appears because of irreversible structural relaxation. The icosahedral percolation transition was shown to change the activation parameters of the model jumpwise. © *2005 Pleiades Publishing, Inc.*

1. INTRODUCTION

In recent years, more and more data have been collected in favor of the concept first formulated in [1] in terms of the free volume model. According to this concept, percolation transitions play a fundamental role in structural self-organization of amorphous materials close to the glass transition temperature T_g. A fractal percolation cluster is formed in a disordered system (melt or glass) from local atomic configurations of the same type (Delaunay simplexes with an increased or decreased density of filling the space with atoms [2], icosahedra interpenetrating and contacting with each other [3, 4], and defects in the network of covalent bonds [5]). The formation of a percolation cluster is evidence of system transition into a new structural state (from liquid to vitreous or vice versa, from vitreous to liquid) and, as a consequence, a change in atomic dynamics. Recently, it was shown theoretically on the basis of a thermodynamic description of structural defects [5] that glass transition in amorphous SiO_2 could be treated as a percolation transition in the system of network defects presumably consisting of defect SiO molecules, which substantially influence diffusion and viscous flow [6]. The suggested approach can in principle be extended to glass formation in other materials. Its development, however, requires identifying the structural elements of percolation clusters for every type of amorphous materials and studying their thermodynamic parameters. In the majority of cases, this is a difficult problem that cannot be solved analytically. For instance, as distinct from the structure of amorphous SiO_2, which, by virtue of the special features of local bonds in it, can be treated as a topologically disordered three-dimensional network comprising SiO_4 tetrahedra connected by bridge oxygen atoms, the structure of amorphous metals cannot be given such an unambiguous description and represents a complex mosaic of a fairly large set of coordination polyhedra of different types [4].

Currently, one of the most effective approaches to studying the principles of the structural organization of disordered systems is computer simulation, which opens up possibilities for analyzing the atomic structure and dynamics and the mechanisms governing the space-time evolution of all system particles [7–11]. This approach inspires certain hopes for constructing a complete theory of metallic glass structure formation from melts and their rearrangement during structural relaxation. For instance, studies of the glass transition of iron melt by molecular dynamics simulation with the Johnson pair interatomic interaction potential [12] at a constant volume [13] and, more recently, at a constant pressure [14] showed that a correlation of local atomic stresses appeared below ~1400–1600 K. This was evidence of atomic ordering in the liquid phase followed by glass transition. These spatial correlations of local atomic stresses were accompanied by substantial changes in the dynamic properties of the model. At

the same time, no significant structural reorganization was observed; the authors only mentioned an important phenomenon, namely, a transition between bond orientation ordering types in the supercooled liquid phase [13].

A structural model of the glass transition of pure metals was suggested in [3, 4]. According to this model, the atomic structures of metallic melts and glasses are fundamentally different. It was shown in [4] by molecular dynamics simulations with the Pak–Doyama pair interatomic interaction potential [15] that a central role in the structural organization of the amorphous phase of pure iron is played by the formation (at the glass transition temperature, $T_g \sim 1180$ K) and growth of a percolation cluster of interpenetrating and contacting icosahedra whose vertices and centers are occupied by atoms. Interpenetrating icosahedra are those sharing seven atoms, and contacting ones share three (face contact), two (edge contact), or one (vertex contact) atoms. The mechanisms that were shown to govern the self-organization of the icosahedral structure during glass transition well correlated with the temperature dependences of the main thermodynamic characteristics of the model [4]; certain features of these dependences were characteristic of a second-order phase transition [16]. These mechanisms also explained the behavior of thermodynamic characteristics at the microscopic level. The results made it possible to suggest [4] that a fractal cluster that consists of icosahedra incompatible with translational symmetry and comprises more than half of all the atoms plays the role of a binding framework that hinders crystallization. It is the basic element of the structural organization of the solid amorphous state of pure metals that radically distinguishes it from melts. Because of the closeness of the Johnson and Pak–Doyama pair potentials, it is also important that a temperature of 1460 K, below which size fluctuations of small-sized clusters comprising icosahedra interpenetrating and contacting with each other increase sharply [4], is fairly close to the temperature at which local atomic stresses begin to correlate [13, 14].

A more detailed quantitative analysis of structural rearrangements and the influence of the icosahedral percolation transition on the diffusion mobility of atoms and nucleation with subsequent crystallization can be performed by conducting isothermal annealings of an instantaneously supercooled melt close to the glass transition temperature.

In this work, we use the results of a series of computer molecular dynamics experiments to study the influence of the isothermal annealing temperature on the kinetics of the icosahedral percolation transition (which we identify with glass transition) and the beginning of homogeneous nucleation in a supercooled iron melt. We also consider the influence of the icosahedral percolation transition on the activation parameters that determine the diffusion mobility of atoms.

2. DESCRIPTION OF THE MODEL

The initial molecular dynamics model of liquid iron was constructed at $T = 2300$ K and had a density of 7800 kg/m^3 (the density was set in conformity with the data on α-Fe [17] with about a 1% correction for the amorphous state). The initial structure was a random close packing of atoms. The interaction between the atoms was described using the Pak–Doyama empirical pair potential [15]

$$\begin{aligned}\phi(r) &= -0.188917(r - 1.82709)^4 \\ &+ 1.70192(r - 2.50849)^2 - 0.198294 \text{ eV},\end{aligned} \quad (1)$$

where r is in angstroms. The potential cutoff radius (the distance at which the potential and its first derivative smoothly vanished) was taken to be $r_c = 3.44$ Å. The potential parameters were determined from the data on the elastic properties of α-Fe. The use of this potential for modeling liquid and amorphous iron [18–20] and iron–metalloid alloys [21, 22] provided close agreement between calculation results and experimental structural characteristics. The model contained 100000 atoms in a basic cube with periodic boundary conditions. The velocities of atoms at the initial time were set according to the Maxwell distribution. Molecular dynamics simulations were performed by numerically integrating equations of motion in time steps of $\Delta t = 1.523 \times 10^{-15}$ s using the Verlet algorithm [23]. The system was maintained at a fixed temperature for 3000 time steps (isothermal conditions). The temperature was then allowed to change, and thermal equilibrium at a constant internal energy (adiabatic conditions) was attained during the 3000 time steps.

Next, the system was studied under isochoric conditions over the temperature range 1240–900 K in steps of 20 K. The procedure for modeling involved an instantaneous drop in melt temperature to the required value followed by isothermal annealing until a crystalline nucleus of a critical size began to grow rapidly. The structural characteristics of the system were measured cyclically every $5000\Delta t$, or 0.7615×10^{-11} s. Each annealing cycle at the required temperature took a time of $1000\Delta t$ under isothermal and $4000\Delta t$ under adiabatic conditions. The thermodynamic characteristics of the system were averaged over a time period of $2000\Delta t$ at the end of each cycle. Note that the temperature T of the system under adiabatic conditions and the required temperature of measurements (the temperature of the "environment") did not coincide exactly. After every cycle, the system was driven to the state with $T = 0$ K by the method of static relaxation. The atoms then occupied equilibrium positions in local potential wells, and their mean-square displacements were calculated.

The instant of the formation of a crystalline nucleus of a critical size that began to grow rapidly and of an icosahedral percolation cluster was identified by two methods, namely, using statistical geometric analysis

based on Voronoi polyhedra and cluster analysis based on percolation theory; these methods are described in detail in [3, 4, 24, 25].

3. RESULTS AND DISCUSSION

We found that, in the model of an instantaneously supercooled iron melt, the formation and subsequent growth of a percolation cluster built of icosahedra interpenetrating and contacting with each other whose vertices and centers are occupied by atoms occurred only below the critical temperature $T_g \sim 1180$ K under isothermal conditions (Fig. 1). Note that this temperature coincided with the temperature of the formation of icosahedral percolation cluster during glass transition of iron melt in the molecular dynamics model under the conditions of linear cooling at a rate of 4.4×10^{12} K/s [4]. In addition, the glass transition temperature coincided with the temperature at which the time of annealing up to the beginning of homogeneous nucleation was minimum.

This time sharply increases and the number of icosahedra in the system decreases as the temperature grows ($T > T_g$). No stable percolation cluster of interpenetrating and contacting icosahedra does not form then.

The beginning of homogeneous nucleation at temperatures below the glass transition temperature ($T < T_g$) is always preceded by the formation and growth of an icosahedral percolation cluster. Importantly, the duration of annealing before the formation of an icosahedral percolation cluster did not exceed 1.5×10^{-11} s in the temperature range studied, 900–1180 K. The formation of an icosahedral percolation cluster was observed either at the first ($t = 0.7615 \times 10^{-11}$ s) or at the second ($t = 1.523 \times 10^{-11}$ s) cycle of measurements counting from the instant of the beginning of isothermal annealing.

The time up to the beginning of homogeneous nucleation, the size to which the icosahedral percolation cluster manages to grow, and the total number of icosahedra in the system increase as the temperature decreases. We found that the fractal icosahedral cluster and the total number of icosahedra continued to grow for some time after the beginning of homogeneous nucleation. This is evidence that the formation of crystalline nuclei and their growth at early stages occur by addition of atoms situated in "pores" of fractal icosahedral cluster rather than by absorption of icosahedra. The presence of a fractal cluster stable toward decomposition limits the mobility of atoms that do not participate in constructing it. This restrains homogeneous nucleation.

In order to determine the character and strength of the influence of icosahedral percolation transition on the diffusion mobility of atoms, we constructed the kinetic curves for the mean-square displacements of atoms close to the T_g temperature. It follows from an analysis of the data obtained in computer experiments and shown in Fig. 2 that the time dependence of the mean-square displacement of atoms at temperatures higher than T_g is linear in conformity with the Einstein equation $\langle \Delta r^2(t) \rangle = 6Dt$, where D is the self-diffusion coefficient. Below T_g, this dependence acquires an essentially nonlinear transition character at the initial

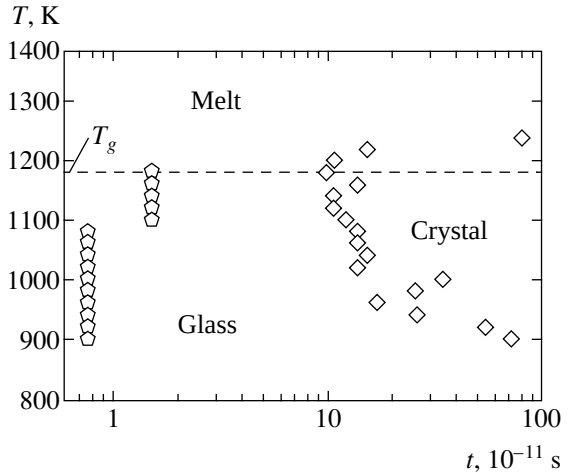

Fig. 1. Isothermal kinetic diagram of the beginning of homogeneous nucleation in the molecular dynamics model of an instantaneously supercooled iron melt (rhombuses). Pentagons correspond to the formation of a stable icosahedral percolation cluster. No stable icosahedral percolation cluster is formed at temperatures above $T_g \sim 1180$ K (dashed horizontal line).

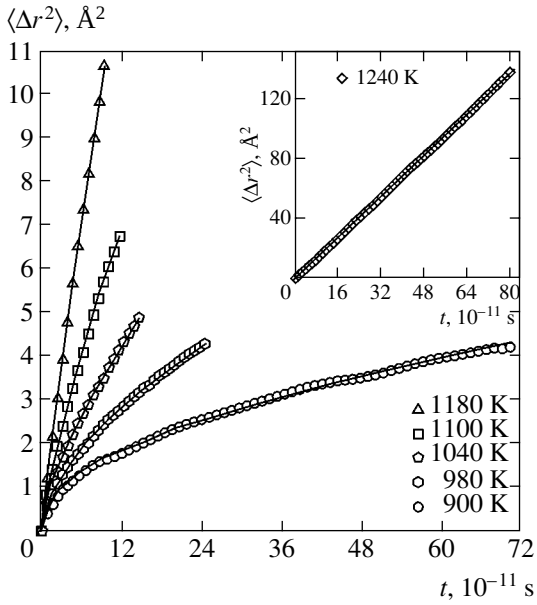

Fig. 2. Kinetics of mean-square displacements of atoms in the molecular dynamics models of liquid and amorphous iron (from $\tau = 0.7615 \times 10^{-11}$ s to the beginning of crystallization) at various temperatures (symbols) and approximating curves obtained using the model that takes into account the kinetics of irreversible structural relaxation (solid lines).

annealing stages, which is especially noticeable when the temperature decreases, and gradually becomes steady-state and linear. The appearance of the nonstationary stage in the kinetics of the mean-square displacement of atoms at $T < T_g$ can only be related to the formation of icosahedral percolation cluster, that is, to the transition of a supercooled melt into the metallic glass state and subsequent structural relaxation.

An analysis of the kinetics of transition processes and related mean-square displacements of atoms at temperatures below the glass transition temperature was performed using the activation energy spectrum model [26] for irreversible structural relaxation [27]. According to [27], structural relaxation can be treated as a sequence of spatially isolated irreversible elementary thermally activated rearrangements in certain structure regions, which are relaxation centers with distributed activation energies. The relaxation centers are physically distinguished structure regions with excess free volume. There are stoppers that restrain local rearrangements of atomic configurations in adjacent structure regions [27]. Of all the coordination polyhedra that we encounter in closely packed structures (both ordered and disordered), the icosahedron is the most compact and energetically stable. Relaxation centers should therefore be situated outside both fractal and smaller icosahedral clusters, that is, in their pores. Thermally activated stopper removal results in free volume redistribution in volume Ω adjacent to a relaxation center, which increases the mobility of neighboring atoms and thereby activates the second stage of the process. This is the cooperative displacement of atoms in the surrounding region, which can be treated as local viscous flow [27]. No matter what the character of the activation energy spectrum, structural relaxation continues up to the beginning of crystallization, which results in the cutoff of the spectrum near the activation energy E_c. This energy is some effective parameter of the model that we use.

The kinetic equation for the spectral density (distribution function) of relaxation centers $n(E, t)$ has the form

$$\frac{dn}{dt} = -n\nu_0 \exp\left(-\frac{E}{k_B T}\right), \tag{2}$$

where ν_0 is the characteristic frequency on the order of the Debye frequency. Equation (2) is central to the activation energy spectrum model [26]. The integration of this equation under isothermal annealing conditions allows us to track changes in the spectral density of relaxation centers with time. After annealing at temperature T for time τ, the spectral density of relaxation centers takes the form

$$n(E, \tau) = n_0(E)\Theta(E, \tau), \tag{3}$$

where $n_0(E)$ is the initial spectral density of relaxation centers and

$$\Theta(E, \tau) = \exp\left[-\nu_0 \tau \exp\left(-\frac{E}{k_B T}\right)\right], \tag{4}$$

is the characteristic function of isothermal annealing. The time of preannealing in our computer experiment was $\tau = 0.7615 \times 10^{-11}$ s.

If the $n_0(E)$ function is fairly flat, that is, if it changes much more slowly than the exponential function $\Theta(E, t)$ varies, annealing development is largely determined by the exponential term. During annealing, the $\Theta(E, t)$ curve shifts along the E axis but virtually does not change its shape of a step function, which sharply increases from zero to one near the characteristic energy $E_0 = k_B T \ln(\nu_0 t)$ [26] corresponding to the inflection point. It follows from the definition of E_0 that virtually all the relaxation centers with activation energies $E \le E_0$ come into action by the time t. As a first approximation, the $\Theta(E, t)$ dependence can be described by the Heavyside step function [28] $\Theta(E - E_0)$. Importantly, using this approximation does not cause a loss in the accuracy of structural relaxation kinetics calculations. To show this, let us consider the exact solution to the problem.

Time t will be counted from the moment when preannealing during time τ ends. The time t dependence of the spectral density of relaxation centers then takes the form

$$\begin{aligned} n(E, t) &= n(E, \tau)\Theta(E, t) \\ &= n_0(E)\exp\left[-\nu_0(\tau + t)\exp\left(-\frac{E}{k_B T}\right)\right]. \end{aligned} \tag{5}$$

According to the superposition principle, the total density of relaxation centers that remain intact by the time t is given by the equation

$$\begin{aligned} N_{RC}(t) &= \int_0^\infty n_0(E) \\ &\times \exp\left[-\nu_0(\tau + t)\exp\left(-\frac{E}{k_B T}\right)\right] dE. \end{aligned} \tag{6}$$

It follows that the mean-square displacement of atoms under the conditions of irreversible structural relaxation can be written as

$$\langle \Delta r^2(t) \rangle = \delta r^2 \Omega (N_{RC}(0) - N_{RC}(t)) + 6Dt, \tag{7}$$

where δr^2 is the mean-square displacement of atoms that accompanies the thermally activated removal of one relaxation center.

According to the popular hypothesis about the activation energy spectrum of irreversible structural relaxation in metallic glasses, this spectrum is generally uniform and has no significant singularities [27]. We can therefore assume that $n_0(E) = n_0 = \text{const}$ to check (7) (Fig. 3). The upper limit of the integral in (6) can conveniently be replaced by $E_{\max} \longrightarrow \infty$; (6) then takes the form

$$N_{RC}(t) = n_0 k_B T \int_{(\tau+t)/t_{\max}}^{\nu_0(\tau+t)} \frac{\exp(-x)}{x} dx = n_0 k_B T \left[\mathrm{Ei}(-\nu_0(\tau+t)) - \mathrm{Ei}\left(-\frac{\tau+t}{t_{\max}}\right)\right], \quad (8)$$

where the notation

$$t_{\max} = \nu_0^{-1} \exp(E_{\max}/k_B T)$$

is used and

$$-\mathrm{Ei}(-x) = \int_x^\infty \frac{\exp(-x)}{x} dx \quad (9)$$

is the integral exponential function [28]. Under the conditions of the problem under consideration ($\nu_0 \sim 10^{13}$ s^{-1}, and $\tau = 0.7615 \times 10^{-11}$ s), we have $-\mathrm{Ei}(-\nu_0(\tau + t)) < 10^{-34}$. The first term in (8) can therefore be ignored and the second term can be written using the known expansion of the integral exponential function into a series [28],

$$N_{RC}(t) = -n_0 k_B T \times \left[C + \ln\left(\frac{\tau+t}{t_{\max}}\right) + \sum_{i=1}^{\infty} \frac{(-1)^i}{i!\,i} \left(\frac{\tau+t}{t_{\max}}\right)^i \right], \quad (10)$$

where $C = 0.5772$ is the Euler constant. As $E_c \ll E_{\max}$, the argument under the sum sign in (10) can be estimated as a value much smaller than one. It follows that, at an arbitrary time moment preceding crystallization, we have

$$N_{RC}(0) - N_{RC}(t) = n_0 k_B T \ln\left(\frac{t}{\tau} + 1\right). \quad (11)$$

This allows Eq. (7) for the mean-square displacement of atoms to be rewritten as

$$\langle \Delta r^2(t) \rangle = \delta r^2 n_0 \Omega k_B T \ln\left(\frac{t}{\tau} + 1\right) + 6Dt. \quad (12)$$

In Fig. 2, the time dependences of the mean-square displacement of atoms before the beginning of crystallization at several temperatures after preannealing for $\tau = 0.7615 \times 10^{-11}$ s are shown by symbols and their approximations according to (12), by solid lines. We see that the model is in close agreement with the computer experiment results. Similar calculations were performed for other temperatures between 1240 and 900 K (the interval studied in this work) and for 1260 K (the instant of the beginning of crystallization at this temperature was not determined because of enormous real time expenditures of molecular dynamics computations). Our analysis allowed us to obtain the temperature dependence of the product $\delta r^2 n_0 \Omega$ (Fig. 4) and the self-diffusion coefficient D (Fig. 5).

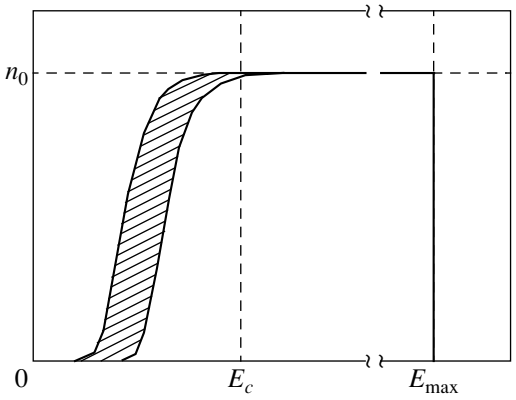

Fig. 3. Schematic drawing of changes in the spectral density of relaxation centers during isothermal annealing (the plane spectrum approximation).

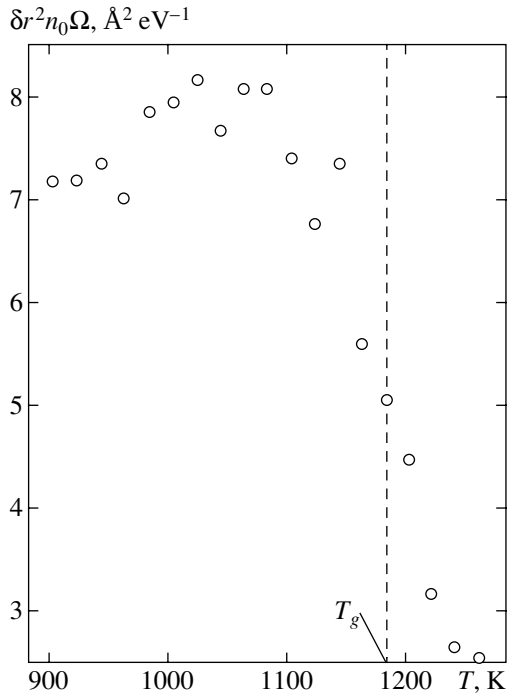

Fig. 4. Temperature dependence of the $\delta r^2 n_0 \Omega$ product.

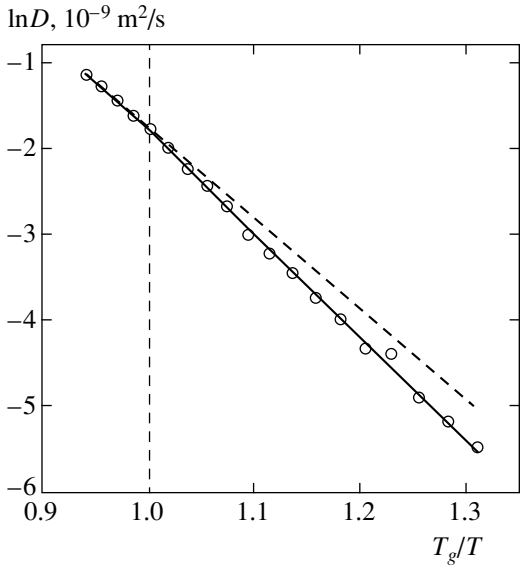

Fig. 5. Temperature dependence of the self-diffusion coefficient.

Changes in the spectral density of relaxation centers as the temperature increases are shown in Fig. 4 within a factor of $\delta r^2\Omega$. Since $\delta r^2\Omega$ weakly depends on temperature, it follows from Fig. 4 that a sharp decrease in the spectral density of relaxation centers occurs near T_g as the temperature increases. This is evidence of the transition of the structure of the model system from the glassy state to a supercooled melt.

Figure 5 shows that the temperature dependence of the self-diffusion coefficient both above and below T_g is well described by the Arrhenius equation $D = D_0\exp(-E_s/k_BT)$. The self-diffusion activation energy E_s and the preexponential factor D_0, however, change jumpwise at $T = T_g$ because of the transition of a supercooled melt into the metallic glass state. The activation parameters for the supercooled melt and metallic glass are $E_s^{(m)} = 1.05$ eV, $D_0^{(m)} = 5.25 \times 10^{-6}$ m^2/s and $E_s^{(g)} = 1.2$ eV, $D_0^{(g)} = 2.05 \times 10^{-5}$ m^2/s, respectively.

4. CONCLUSIONS

A stable percolation cluster of interpenetrating and coming into contact icosahedra whose vertices and centers are occupied by atoms is formed under isothermal conditions in the molecular dynamics model of an instantaneously cooled iron melt only at a temperature below critical (~1180 K). We identify this temperature with the glass transition temperature. The formation of an icosahedral percolation cluster below this temperature occurs at the initial stages of isothermal annealing, and the expectation time for the process does not exceed 1.5×10^{-11} s. The critical temperature above which no stable icosahedral percolation cluster is formed coincides with the temperature at which the time of the beginning of homogeneous nucleation is minimum. The time of the beginning of homogeneous nucleation and the size of the cluster increase as the temperature decreases. This substantiates the suggestion that a fractal cluster comprising icosahedra that are incompatible with translational symmetry and are built of more than half of all the atoms plays the role of a binding framework that restrains crystallization and is the basic element of the structural organization of the solid amorphous state of pure metals that radically distinguishes it from melts.

We obtained an equation that correctly describes the influence of irreversible structural relaxation on the kinetics of the mean-square displacements of atoms in metallic glasses. The icosahedral percolation transition in supercooled liquid iron was shown to cause a sharp change in the activation parameters that determined the diffusion mobility of atoms.

REFERENCES

1. M. H. Cohen and G. S. Grest, Phys. Rev. B **20**, 1077 (1979).
2. N. N. Medvedev, A. Geiger, and W. Brostow, J. Chem. Phys. **93**, 8337 (1990).
3. A. V. Evteev, A. T. Kosilov, and E. V. Levchenko, Pis'ma Zh. Éksp. Teor. Fiz. **76**, 115 (2002) [JETP Lett. **76**, 104 (2002)].
4. A. V. Evteev, A. T. Kosilov, and E. V. Levchenko, Zh. Éksp. Teor. Fiz. **126**, 600 (2004) [JETP **99**, 522 (2004)].
5. M. I. Ojovan, Pis'ma Zh. Éksp. Teor. Fiz. **79**, 769 (2004) [JETP Lett. **79**, 632 (2004)].
6. R. H. Doremus, J. Appl. Phys. **92**, 7619 (2002).
7. J. M. Ziman, *Models of Disorder: The Theoretical Physics of Homogeneously Disordered Systems* (Cambridge Univ. Press, Cambridge, 1979; Mir, Moscow, 1982).
8. R. Zallen, *The Physics of Amorphous Solids* (Wiley, New York, 1983).
9. V. A. Polukhin and N. A. Vatolin, *Modeling of Amorphous Metals* (Nauka, Moscow, 1985) [in Russian].
10. P. H. Gaskell, in *Materials Science and Technology*, Ed. by J. Zarzycki (VCH, Cambridge, 1991), Vol. 9, p. 175.
11. V. A. Likhachev and V. E. Shudegov, *Organization Principles of Amorphous Structures* (S.-Peterb. Gos. Univ., St. Petersburg, 1999) [in Russian].
12. R. A. Johnson, Phys. Rev. **134**, A1329 (1964).
13. S.-P. Chen, T. Egami, and V. Vitek, Phys. Rev. B **37**, 2440 (1988).
14. L. J. Lewis, Phys. Rev. B **39**, 12954 (1989).
15. H. M. Pak and M. Doyama, J. Fac. Sci., Univ. Tokyo, Ser. B **30**, 111 (1969).
16. L. D. Landau and E. M. Lifshitz, *Course of Theoretical Physics*, Vol. 5: *Statistical Physics*, Part 1, 4th ed. (Nauka, Moscow, 1995; Butterworths, London, 1999).

17. C. J. Smithells, *Metals Reference Book*, 5th ed. (Butterworths, London, 1976; Metallurgiya, Moscow, 1980).

18. R. Yamamoto, H. Matsuoka, and M. Doyama, Phys. Status Solidi A **45**, 305 (1978).

19. D. K. Belashchenko, Fiz. Met. Metalloved. **60**, 1076 (1985).

20. A. V. Evteev and A. T. Kosilov, Rasplavy **1**, 55 (1998).

21. A. V. Evteev and A. T. Kosilov, Rasplavy **4**, 82 (2001).

22. A. V. Evteev, A. T. Kosilov, and E. V. Levtchenko, Acta Mater. **51**, 2665 (2003).

23. L. Verlet, Phys. Rev. **159**, 98 (1967).

24. A. V. Evteev, A. T. Kosilov, and A. V. Milenin, Pis'ma Zh. Éksp. Teor. Fiz. **71**, 294 (2000) [JETP Lett. **71**, 201 (2000)].

25. A. V. Evteev, A. T. Kosilov, and A. V. Milenin, Fiz. Tverd. Tela (St. Petersburg) **43**, 2187 (2001) [Phys. Solid State **43**, 2284 (2001)].

26. W. Primak, Phys. Rev. **100**, 1677 (1955).

27. V. A. Khonik, A. T. Kosilov, V. A. Mikhailov, and V. V. Sviridov, Acta Mater. **46**, 3399 (1998).

28. G. A. Korn and T. M. Korn, *Mathematical Handbook for Scientists and Engineers*, 2nd ed. (McGraw-Hill, New York, 1968; Nauka, Moscow, 1977).

Translated by V. Sipachev

Journal of Experimental and Theoretical Physics, Vol. 101, No. 3, 2005, pp. 528–534.
Translated from Zhurnal Éksperimental'noĭ i Teoreticheskoĭ Fiziki, Vol. 128, No. 3, 2005, pp. 615–622.

ORDER, DISORDER, AND PHASE TRANSITIONS IN CONDENSED SYSTEMS

Ferromagnetism in a New Dilute Magnetic Semiconductor $Sb_{2-x}Cr_xTe_3$

V. A. Kulbachinskiĭ[a], P. M. Tarasov[a], and E. Brück[b]

[a] *Low Temperature Physics Department, Moscow State University, Vorob'evy gory, Moscow, 119992 Russia*

[b] *Van der Waals–Zeeman Instituut, Universiteit van Amsterdam, Valckenierstraat 65, 1018 XE Amsterdam, The Netherlands*

e-mail: kulb@mig.phys.msu.ru

Received April 21, 2005

Abstract—Magnetic and galvanomagnetic properties of single crystals of a new dilute magnetic semiconductor *p*-$Sb_{2-x}Cr_xTe_3$ ($x = 0$, 0.0115, 0.0215) are investigated in a temperature range of 1.7–300 K. A ferromagnetic phase with a Curie temperature of $T_C \approx 5.8$ ($x = 0.0215$) and 2.0 K ($x = 0.0115$) is detected. The easy magnetization axis is parallel to the C_3 crystallographic axis. Analysis of the Shubnikov–de Haas effect observed in these crystals in strong magnetic fields leads to the conclusion that the hole concentration decreases as a result of doping with Cr. Negative magnetoresistance and the anomalous Hall effect are observed in Cr-doped samples at liquid helium temperature. © *2005 Pleiades Publishing, Inc.*

1. INTRODUCTION

Layered semiconductors of the Sb_2Te_3 type have a rhombohedral structure (space symmetry group $R\bar{3}m$–D_{3d}^5) with dyad axis C_2 and triad axis C_3. Five-layered packets of atomic layers Te^1–Sb–Te^2–Sb–Te^1 (Te^1 and Te^2 denote two possible positions of atoms in the lattice) with a covalent-ionic bond form the antimony telluride lattice. A weak Van der Waals interaction is observed between the five-layered packets (between layers Te^1–Te^1). Atoms of the each subsequent layer are located above the centers of the triangles formed by the atoms of the preceding layer (i.e., the Te^1 and Sb atoms occupy the octahedral positions in the structure).

Crystals of Sb_2Te_3 always exhibit *p*-type conductivity due to the high concentration of charged point defects of predominantly antistructural type (i.e., Sb atoms occupy the positions of Te atoms). The formation of such defects is due to weak polarity of Sb–Te bonds.

A change in the bond polarity upon doping changes the concentration of point defects and, hence, the hole concentration. Consequently, doping by an element of a certain group of the Periodic Table may lead to either a donor or acceptor effect irrespective of the number of the group, since doping affects the polarity of the bond. By way of example, we can mention In, which belongs to group III and acts as a donor in Sb_2Te_3 [1, 2].

Compound Sb_2Te_3 is a narrow-gap semiconductor with an indirect forbidden bandgap $E_g = 0.25$ eV (at 295 K) and $E_g = 0.26$ eV (at 4.2 K) [3]. The valence band consists of the upper band of light holes, and the lower band, of heavy holes, each of which is sixfold degenerate. The Fermi surface for both bands is a six-ellipsoidal surface [1, 4]. Anisotropy of the cross sections of the ellipsoids of the light hole band is $\eta = S_{max}/S_{min} \approx 3.8$, where S_{max} and S_{min} are the areas of the maximal and minimal cross sections of an ellipsoid. The angle of inclination of the ellipsoids to the basal plane in Sb_2Te_3 is $\theta \approx 52.5°$.

In dilute magnetic semiconductors, a small number of magnetic ions (e.g., of transition metals or rare-earth elements) are in a nonmagnetic matrix. The indirect

Frequency F of Shubnikov–de Haas oscillations, concentration P of light holes at $T = 4.2$ K, resistivities $\rho_{4.2}$ at $T = 4.2$ K and ρ_{300} at $T = 300$ K, Hall mobility μ, Hall concentration $1/eR_H$ of holes at $T = 4.2$ K, and experimentally determined chromium concentration in $Sb_{2-x}Cr_xTe_3$

Sample	F, T	P, 10^{19} cm^{-3}	$\rho_{4.2}$, μΩ cm	ρ_{300}, μΩ cm	μ, m^2/V s	$1/eR_H$, 10^{19} cm^{-3}	Cr, at %
Sb_2Te_3	54.7	3.4	38.8	260	0.103	12.5	0
$Sb_{2-x}Cr_xTe_3$ ($x = 0.0115$)	43.4	2.3	142	437	0.029	8.3	0.23
$Sb_{2-x}Cr_xTe_3$ ($x = 0.0215$)	46.2	2.6	106	314	0.066	9.9	0.43

1063-7761/05/10103-0528$26.00

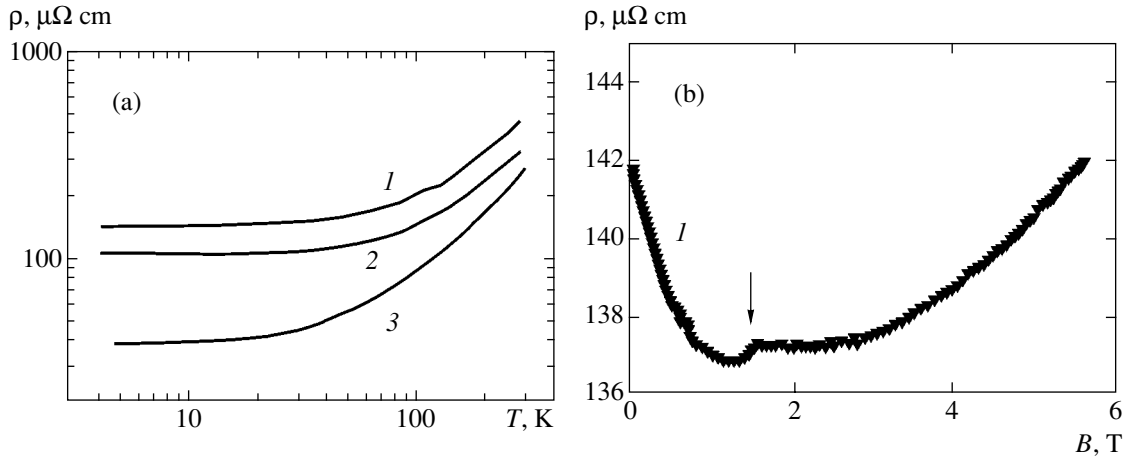

Fig. 1. (a) Temperature dependences of resistivity along the C_2 axis and (b) negative magnetoresistance for $Sb_{2-x}Cr_xTe_3$ single crystals studied with different concentrations of chromium: 0.23 at % (*1*); 0.43 at % (*2*), and Sb_2Te_3 (*3*).

exchange interaction of magnetic moments of the impurity changes the optical, galvanomagnetic, and magnetic properties of the original semiconductor [5, 6]. An interesting manifestation of such an interaction is ferromagnetism observed in dilute magnetic *p*-type semiconductors. Hole-induced ferromagnetism was observed for the first time in bulk crystals of PbSnMnTe [7], i.e., in a semiconductor consisting of IV–VI–group elements (IV–VI semiconductor). Subsequently, manganese-doped epitaxial III–V semiconductor films (In, Mn)As on a GaAs substrate, as well as ferromagnetic films (Ga, Mn)As (see reviews [8, 9]).

Apart from academic interest in hole-induced ferromagnetism in dilute magnetic semiconductors, bright prospects exist for application of this phenomenon in spintronics (design of devices with controllable spin transport). Bismuth and antimony tellurides are of special interest since these compounds exhibit the highest thermoelectric efficiency Z [10]. It has been discovered recently that doping of Bi_2Te_3 with iron increases the Seebeck coefficient of this material [11, 12]. In addition, *p*-Bi_2Te_3(Fe) exhibits ferromagnetism at low temperatures [11–14]. Subsequently, ferromagnetism was also detected in $Sb_{2-x}V_xTe_3$ [15], $Bi_{2-x}Mn_xTe_3$ [16], and $Sb_{2-x}Cr_xTe_3$ [17]. It should be noted that ferromagnetism was not observed in $Bi_{2-x}Gd_xTe_3$ [18] or $Sb_{2-x}Mn_xTe_3$ [19]. Here, we study the magnetic and galvanomagnetic properties of single crystals of the dilute magnetic semiconductor *p*-$Sb_{2-x}Cr_xTe_3$. For a better understanding of the effect of chromium on the properties of original *p*-Sb_2Te_3 crystals, the Shubnikov–de Haas effect was investigated.

2. MEASURING TECHNIQUE AND SAMPLES

Single crystals were grown by the Bridgman technique from the components taken in the stoichiometric ratio corresponding to the required composition $Sb_{2-x}Cr_xTe_3$. The ingots can easily be cleaved along cleavage planes perpendicular to the C_3 axis, i.e., along the (0001) planes, which are usually parallel to the ampoule axis. Samples with a characteristic size of $1 \times 0.5 \times 4$ mm used for measurements were cut using the electroerosion technique. Electric contacts were soldered using the BiSb alloy.

The Cr concentration in specific samples was determined using a JEOL 8621 electronic microanalyzer following magnetic and electric measurements on a given sample. The measurements also revealed that chromium is distributed uniformly over the sample. It was found that the Cr concentration amounts to 0.23 and 0.43 at % in two doped samples, which corresponds to $x = 0.0115$ and $x = 0.0215$ in the formula $Sb_{2-x}Cr_xTe_3$.

The temperature dependences of the resistance, magnetoresistance, and Hall effect were measured by the standard four-probe technique; the current was directed along the C_2 axis. To separate the signals associated with the Hall effect and magnetoresistance, measurements were made for two directions of the magnetic field. The magnetic field up to 6 T was produced by a superconducting solenoid and was directed at right angles to the layers along the C_3 axis. The Shubnikov–de Haas effect was measured in pulsed magnetic fields up to 54 T with a pulse duration of 10 ms. Magnetic measurements in the temperature range 1.7–300 K in magnetic fields up to 5 T were carried out using a SQUID MPMS-5S magnetometer (Quantum Design Co., Ltd). Some parameters of the studied samples are given in table.

3. RESULTS OF MEASUREMENTS

3.1. Galvanomagnetic Properties

Resistivity ρ of all samples decreases upon cooling and attains saturation at low temperatures (Fig. 1a). In the temperature range 150–300 K, the $\rho(T) \propto T^m$

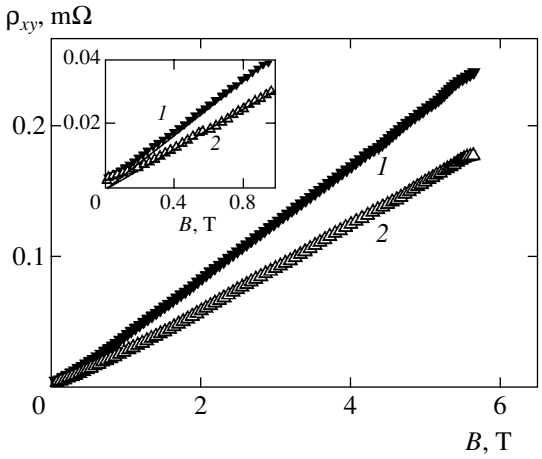

Fig. 2. Hall resistance ρ_{xy} of $Sb_{2-x}Cr_xTe_3$ samples with a chromium concentration of 0.23 at % (*1*) and 0.43 at % (*2*) at $T = 4.2$ K. The inset shows the deviation (anomalous Hall effect) of the $\rho_{xy}(B)$ dependence (symbols) in weak magnetic fields from the linear dependence (solid lines).

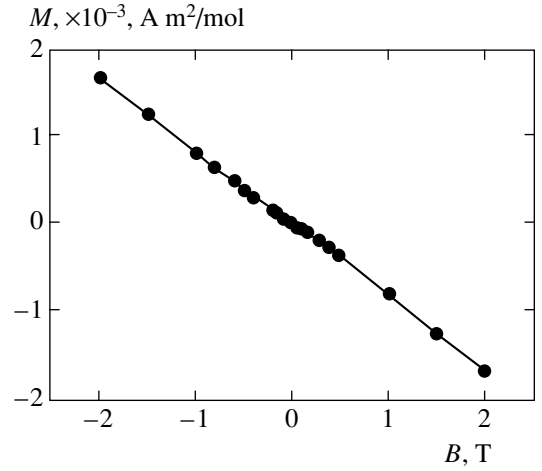

Fig. 3. Magnetic field dependence of the magnetization of a pure Sb_2Te_3 sample at $T = 5$ K.

dependence with exponent $m \approx 1.2$ is observed. Deviation from $m = 1.5$, which is typical of phonon scattering, is apparently due to additional scattering of holes from ionized impurities and with the temperature dependence of the effective mass in this temperature range. Doping with chrome reduces the mobility (see table), although the decrease is nonmonotonic. The mobility for a Cr concentration of 0.43 at % in the sample is higher than for a concentration of 0.23 at %. The latter circumstance is, in all probability, due to different amounts of uncontrollable defects in the samples, which appear during their growth. The resistance in Cr-doped samples increases, although it is slightly lower in samples with a higher Cr concentration. The resistance in doped samples also increases due to additional scattering of holes from localized magnetic moments of chromium ions. The latter circumstance is confirmed by the existence of a negative magnetoresistance in weak magnetic fields. By way of example, Fig. 1b shows the magnetoresistance of a sample with a chromium concentration of 0.23 at % at $T = 4.2$ K. In a magnetic field of $B \approx 1.5$ T, the $\rho(B)$ dependence exhibits an anomaly shown by the arrow.

The Hall coefficient R_H is positive in all samples and increases with chromium concentration, which points toward a decrease in the hole concentration. However, it cannot be used for calculating the hole concentration since bismuth and antimony tellurides contain two groups of holes with different concentrations and mobilities, which are unknown. For this reason, the Hall coefficient in these semiconductors exhibits a complex dependence on temperature and magnetic field even in the absence of magnetic impurity [2, 20]. Thus, we used the Shubnikov–de Haas effect for estimating the change in the light hole concentration upon doping of Sb_2Te_3 with chromium (see below). To compare different samples, the table contains the values of $1/eR_H$ obtained at $B = 0.2$ T, which can conditionally be referred to the "Hall concentrations" of holes. The presence of a magnetic impurity of Cr led to the anomalous Hall effect in the samples (see, for example, [21]). The anomalous Hall effect can be written in the form

$$\rho_{xy} = R_H B + R_a \mu_0 M, \qquad (1)$$

where R_H is the ordinary Hall coefficient, R_a is the anomalous Hall coefficient, and M is the magnetization. Hall resistivity ρ_{xy} as a function of the magnetic field is shown in Fig. 2. The inset to Fig. 2 shows the deviation of the $\rho_{xy}(B)$ dependence from the linear law (straight lines) in weak magnetic fields due to the presence of the anomalous Hall effect. The deviation is small since the observed ferromagnetism is quite weak.

3.2. Magnetic Properties

Magnetic susceptibility χ of the initial Sb_2Te_3 single crystal is diamagnetic, virtually independent of temperature, and amounts to -8×10^{-10} m^3/mole in the principal crystallographic directions. The magnetic field dependences of magnetization for Sb_2Te_3 at $T = 5$ K are shown in Fig. 3. The slight deviation from the ideal diamagnetic behavior for $B = 0$ may be due to the presence of impurities in the crystal. For chromium, its concentration would not exceed 1.4 ppm. Such an amount of impurity may be contained in components from which single crystals were grown.

Figure 4 shows the temperature dependence of the magnetic susceptibility of two $Sb_{2-x}Cr_xTe_3$ samples per chromium ion minus the diamagnetic background of the matrix in the direction of the C_3 axis in a magnetic field of $B = 10$ mT. It can be seen that the Curie temperature is $T_C \approx 5.8$ and 2.0 K for Cr concentrations of 0.43 and 0.23 at %, respectively. The absolute value of χ

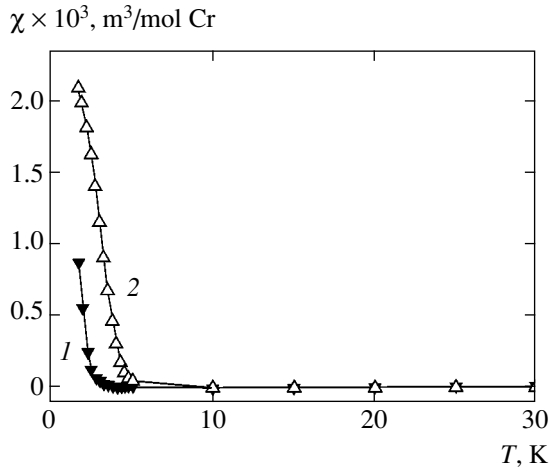

Fig. 4. Temperature dependence of susceptibility χ in a magnetic field B = 10 mT for two $Sb_{2-x}Cr_xTe_3$ samples with different Cr concentrations: 0.23 at % (*1*) and 0.43 at % (*2*).

increases with the chromium concentration in the sample. Figure 5a shows the dependence of magnetization on the magnetic field of the sample with a chromium concentration of 0.43 at % at T = 1.7 K for orientations of magnetic field B parallel to the C_3 and C_2 axes. Hysteresis loops are shown in Fig. 5b. For $B \parallel C_3$, the loops are narrow with a coercive force of approximately 15 mT; the saturation magnetization corresponds to $3.8\mu_B$ per Cr ion. These data indicate the existence of ferromagnetism in Cr-containing samples and are in accordance with the temperature dependence of the magnetic susceptibility obeying the Curie–Weiss law with a positive paramagnetic Curie temperature. The data presented in Fig. 5 also show that the C_3 axis is an easy magnetization axis. When the magnetization is measured along the axis $B \parallel C_2$, the width of the hysteresis loop increases to 70 mT, but field B = 2.5 T turns out to be insufficient for saturation of magnetization. Similar results can also be obtained for a sample with a Cr concentration of 0.23 at %; hysteresis loops show that C_3 is an easy magnetization axis (Fig. 6).

3.3. Shubnikov–de Haas Effect

The Shubnikov–de Haas effect was studied at T = 4.2 K in a magnetic field parallel to the C_3 axis (Fig. 7a). For such an orientation, the cross sections of all six ellipsoids of the upper valance band of light holes coincide and a single frequency of oscillations is observed (this can be seen from the Fourier spectra; Fig. 7b). The amplitude of oscillations in doped samples noticeably decreases. The oscillation frequencies are presented in the table. Using these frequencies, we can calculate the concentration of light holes (see table). The computational technique is described in [22, 23]. The light hole concentration is smaller than the total concentration of holes in the sample; however, its variation reflects the variation of the total hole concentration. It follows from the above data that doping with chromium reduces the hole concentration, although this effect is not monotonic: in the sample with a higher Cr concentration (0.43 at %) the hole concentration is slightly higher than in the sample with a Cr concentration of 0.23 at %. It was noted above that this might be due to different defect concentrations of the samples.

The donor action of chromium in the range of low concentrations is associated with its effect on the polarity of bonds. The weak polarity of the Sb–Te bonds leads to the presence of a large number of antistructural defects in the lattice (antimony atoms replace tellurium atoms). Doping with chromium changes the polarity of bonds, which leads to a change in the concentration of charged point defects and, hence, changes the hole concentration.

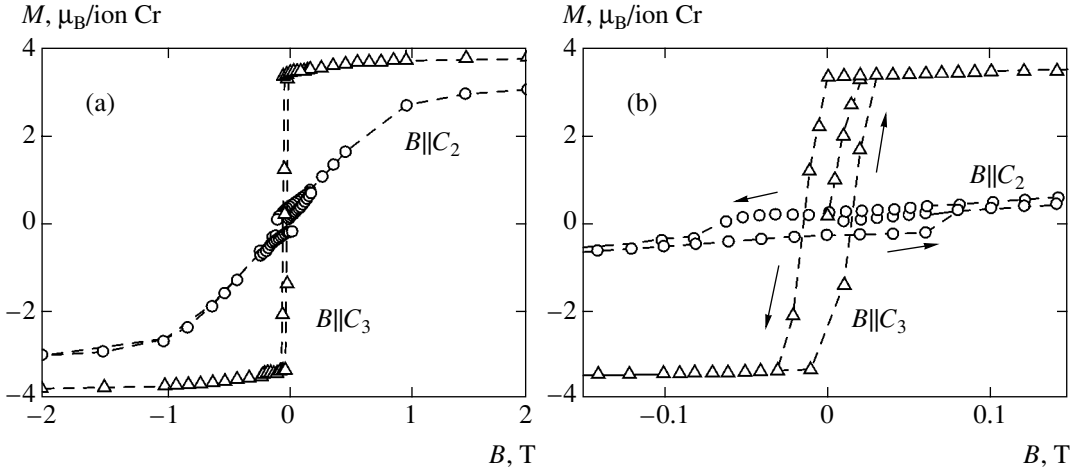

Fig. 5. (a) Dependence of magnetization at T = 1.7 K on magnetic field B for two magnetic field orientations $B \parallel C_3$ and $B \parallel C_2$ for a $Sb_{2-x}Cr_xTe_3$ sample with a Cr concentration of 0.43 at % and (b) hysteresis loops in a weak magnetic field.

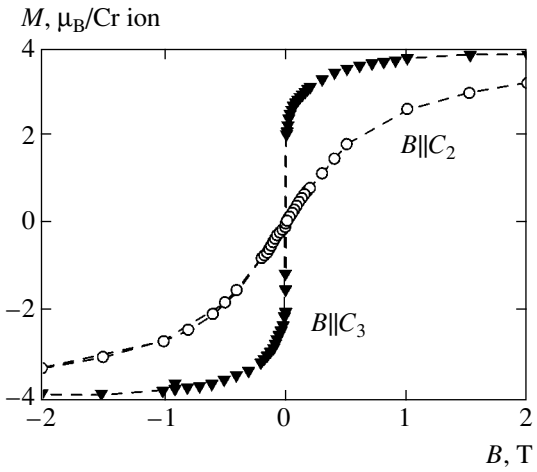

Fig. 6. Dependence of magnetization at $T = 1.7$ K on magnetic field B for two magnetic field orientations $B \parallel C_3$ and $B \parallel C_2$ for a $Sb_{2-x}Cr_xTe_3$ sample with a Cr concentration of 0.23 at %.

Chromium atoms mainly substitute antimony atoms in the lattice; the tellurium concentration remains at a level of 60%; in this way a solid solution of $Sb_{2-x}Cr_xTe_3$ is formed. This assumption is confirmed by a decrease in the unit cell volume since the covalent radius of chromium, $r_{Cr} = 0.127$ nm, is slightly smaller than that of antimony, $r_{Sb} = 0.138$ nm [24]. According to the results of X-ray diffraction measurements, the lattice parameters in a Sb_2Te_3 sample are $a = 0.42643(5)$ nm and $c = 3.0427(4)$ nm, while in a sample with 0.43 at % Cr, these parameters are $a = 0.402602(4)$ nm and $c = 3.0431(3)$ nm. An increase in the polarity of the bond upon the substitution of chromium for antimony leads to a decrease in the probability of formation of antistructural defects. In the case of $Sb_{2-x}Cr_xTe_3$, Sb atoms with electronegativity $X_{Sb} = 1.9$ are replaced by Cr atoms with electronegativity $X_{Cr} = 1.5$, which increases the polarity of the bond.

4. DISCUSSION

Direct interaction between magnetic ions in dilute magnetic semiconductors p-$Sb_{2-x}Cr_xTe_3$ studied here is ruled out in view of their low concentration. Consequently, only the long-range oscillating RKKY interaction executed by holes can be responsible for the ferromagnetic transition. The sign of the RKKY interaction corresponds to a ferromagnetic interaction since the first zero of the interaction, after which the interaction reverses its sign and becomes antiferromagnetic, lies at distances considerably longer (in view of the low hole concentration) than the length at which the interaction is truncated. Obviously, ferromagnetism is not observed for the n-type conductivity since small effective masses and a small exchange integral for electrons hamper the ferromagnetic interaction. The theory of exchange interaction is sufficiently developed for type III–V semiconductors [9, 25]. For a new family of dilute magnetic semiconductors of the type of the new semiconductor $Sb_{2-x}Cr_xTe_3$ studied here, such a theory has not been developed. For this reason, to estimate the magnetic interaction, we can use the results of publications [26–28], in which the theory was developed for homogeneous systems with a random distribution of localized spins. According to this theory, the Curie temperature T_C can be determined from the formula

$$k_B T_C = \frac{cS(S+1)}{3}\frac{J_{pd}^2}{(g^*\mu_B)^2}\chi_f(p, T), \qquad (2)$$

where c is the magnetic impurity concentration and S is the spin of the chromium ion determined from the magnetization measurements, J_{pd} is the constant of

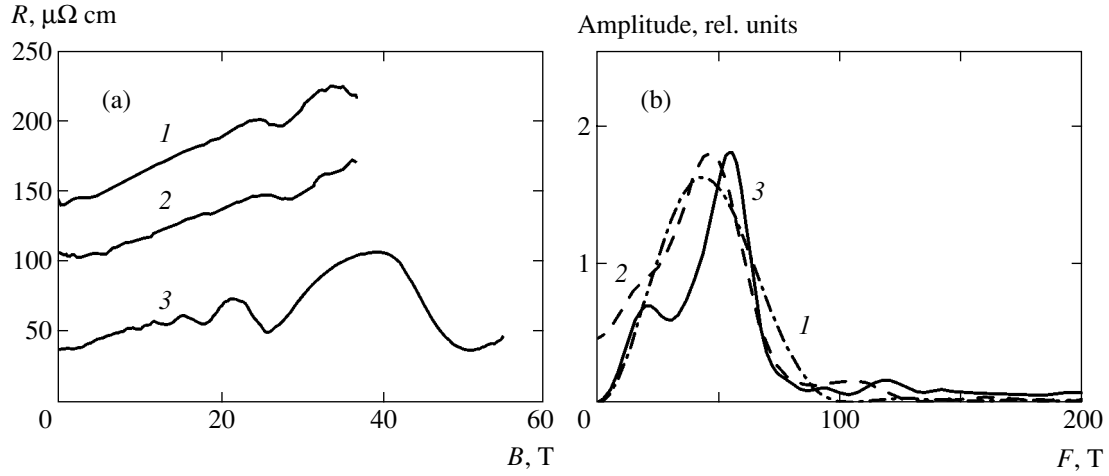

Fig. 7. (a) Shubnikov–de Haas oscillations for $B \parallel C_3$ at $T = 4.2$ K and (b) Fourier spectrum for $Sb_{2-x}Cr_xTe_3$ samples with different Cr concentrations: 0.23 at % (*1*), 0.43 at % (*2*), and Sb_2Te_3 (*3*).

exchange interaction between localized magnetic moments of the chromium ion and the spins of charge carriers, g^* is the effective Lande factor, $\mu_B$is the Bohr magneton, and χ is the magnetic susceptibility, which is a function of hole concentration p and temperature T. It should be recalled that formula (2) for dilute magnetic system was derived by Abrikosov and Gor'kov [29] (see also discussion in [9]). Disregarding the correlation effects, we can use the Pauli expression for estimating susceptibility,

$$\chi = \frac{(g\mu_B)^2 p}{E_F} = \frac{8}{3}\frac{(g\mu_B)^2 m^* k_F}{h^2},$$

where E_F and k_F are the Fermi energy and momentum, h is the Planck constant, and m^* is the effective mass of holes. Jungwirth *et al*. [26–28] proposed that an additional contribution from the exchange interaction be taken into account,

$$\chi = \frac{(g\mu_B)^2 e^2 m^{*2}}{\varepsilon h^4}$$

(ε is the dielectric constant). For a high hole concentration, as in the case of Sb_2Te_3, the Pauli contribution dominates. According to the results of experiments, chromium ions are in the Cr^{3+} state with a magnetic moment

$$\mu = g\mu_B\sqrt{S(S+1)} \approx 3.8\mu_B$$

(see Figs. 5 and 6) with a spin $S = 3/2$. If we take the mass of a free electron for the effective mass m^* of holes [1], $g = 2$, $S = 3/2$, the experimentally determined temperature T_C of transition to the ferromagnetic state, and the experimental value of the chrome concentration in the sample, the exchange interaction constants can be estimated on the basis of formula (2) as $J_{pd} = 0.3$ and 0.2 eV nm^3 for samples with a chromium concentration of 0.43 and 0.23 at %, respectively. These values are of the same order of magnitude as those used for $Mn_xGa_{1-x}As$ [26]. The exchange energy can be estimated by multiplying the obtained values by the concentration of p holes. Using the values from the table, we obtain a value smaller than 10 meV, which is smaller than the values for dilute magnetic III–V semiconductors [30].

It should be noted in conclusion that dilute magnetic semiconductors $R_{2-x}M_xQ_3$, where R and Q are elements of groups V and VI, respectively, and M is a magnetic impurity, form a new class of dilute magnetic semiconductors exhibiting ferromagnetism at low temperatures. As in III–V semiconductors, ferromagnetism is induced by holes since it is not observed in n-type samples [31]. Here, we have studied a new dilute semiconductor $Sb_{2-x}Cr_xTe_3$ with the p-type conductivity, in which hole-induced ferromagnetism is observed with a Curie temperature $T_C \approx 5.8$ K with a chrome concentration of 0.43 at %. The easy magnetization axis is parallel to the C_3 crystallographic axis. Magnetic measurements show that chromium is in the Cr^{3+} state. The most probable mechanism of exchange interaction responsible for ferromagnetism is the RKKY interaction in $Sb_{2-x}Cr_xTe_3$. Doping with chromium reduces the hole concentration in the investigated concentration range. The presence of a magnetic impurity leads to a negative magnetoresistance and an anomalous Hall effect.

ACKNOWLEDGMENTS

The authors are grateful to T. Gortenmulder, who analyzed the chromium content in the samples.

REFERENCES

1. V. A. Kulbachinskiĭ, Z. M. Dashevskii, M. Inoue, *et al.*, Phys. Rev. B **52**, 10915 (1995).
2. N. B. Brandt and V. A. Kulbachinskii, Semicond. Sci. Technol. **7**, 907 (1992).
3. V. A. Kul'bachinskiĭ, H. Ozaki, Y. Miyahara, and K. Funagai, Zh. Éksp. Teor. Fiz. **124**, 1358 (2003) [JETP **97**, 1212 (2003)].
4. V. A. Kul'bachinskiĭ, A. Yu. Kaminskiĭ, V. G. Kytin, *et al.*, Zh. Éksp. Teor. Fiz. **117**, 1242 (2000) [JETP **90**, 1081 (2000)].
5. *Semiconductors and Semimetals*, Vol. 25: *Diluted Magnetic Semiconductors*, Ed. by J. K. Furdyna and J. Kossut (Academic, Boston, 1986).
6. N. Samarth, Solid State Phys., Adv. Res. Appl. **58**, 1 (2004).
7. T. Story, R. R. Galazka, R. B. Frankel, and P. A. Wolff, Phys. Rev. Lett. **56**, 777 (1986).
8. H. Ohno, J. Magn. Magn. Mater. **200**, 110 (1999).
9. V. A. Ivanov, T. G. Aminov, V. M. Novotvortsev, and V. T. Kalannikov, Izv. Ross. Akad. Nauk, Ser. Khim., No. 11, 2255 (2004).
10. *Thermoelectric Materials—The Next Generation Materials for Small-Scale Refrigeration and Power Generation Applications*, Ed. by T. M. Tritt, M. G. Kanatzidis, G. D. Mahan, and H. B. Lion, Jr. (Materials Research Society, Pittsburgh, 1999), MRS Symp. Proc., No. 545.
11. V. A. Kul'bachinskiĭ, A. Yu. Kaminskiĭ, K. Kindo, *et al.*, Pis'ma Zh. Éksp. Teor. Fiz. **73**, 396 (2001) [JETP Lett. **73**, 352 (2001)].
12. V. A. Kulbachinskii, A. Yu. Kaminskii, V. G. Kytin, and A. de Visser, J. Magn. Magn. Mater. **272–276**, 1991 (2004).
13. V. A. Kulbachinskii, A. Yu. Kaminsky, K. Kindo, *et al.*, Phys. Lett. A **285**, 173 (2001).
14. V. A. Kulbachinskii, A. Yu. Kaminsky, K. Kindo, *et al.*, Physica B (Amsterdam) **311**, 292 (2002).
15. J. S. Dyck, W. Chen, P. Hajek, *et al.*, Physica B (Amsterdam) **312–313**, 820 (2002).

16. J. Choi, S. Choi, Jiyoun Choi, *et al.*, Phys. Status Solidi B **241**, 1541 (2004).
17. V. A. Kul'bachinskiĭ, P. M. Tarasov, and E. Brük, Pis'ma Zh. Éksp. Teor. Fiz. **81**, 426 (2005) [JETP Lett. **81**, 342 (2005)].
18. M. El Kholdi, M. Averous, S. Charar, *et al.*, Phys. Rev. B **49**, 1711 (1994).
19. J. S. Dyck, P. Svanda, P. Lostak, *et al.*, J. Appl. Phys. **94**, 7631 (2003).
20. V. A. Kulbachinskii, A. Yu. Kaminskii, K. Kindo, *et al.*, Phys. Status Solidi B **229**, 1467 (2002).
21. *The Hall Effect and Its Applications*, Ed. by C. L. Chien and C. R. Westgate (Plenum, New York, 1980).
22. V. A. Kulbachinskii, A. Yu. Kaminskii, R. A. Lunin, *et al.*, Semicond. Sci. Technol. **17**, 1133 (2002).
23. V. A. Kul'bachinskiĭ, G. V. Zemitan, C. Drasar, and P. Lostak, Fiz. Tverd. Tela (St. Petersburg) **40**, 441 (1998) [Phys. Solid State **40**, 404 (1998)].
24. P. Lostak, C. Drasar, J. Navratil, and L. Benes, Cryst. Res. Technol. **31**, 403 (1996).
25. P. M. Krstajic, F. M. Peeters, V. A. Ivanov, *et al.*, Phys. Rev. B **70**, 195215 (2004).
26. T. Jungwirth, W. A. Atkinson, B. H. Lee, and A. H. MacDonald, Phys. Rev. B **59**, 9818 (1999).
27. T. Jungwirth, J. König, J. Sinova, *et al.*, Phys. Rev. B **66**, 012402 (2002).
28. T. Jungwirth, J. Mašek, J. Sinova, and A. H. MacDonald, Phys. Rev. B **68**, 161202(R) (2003).
29. A. A. Abrikosov and L. P. Gor'kov, Zh. Éksp. Teor. Fiz. **43**, 2230 (1962) [Sov. Phys. JETP **16**, 1575 (1963)].
30. T. Dietl, H. Ohno, and F. Matsukura, Phys. Rev. B **63**, 195205 (2001).
31. Y. Sugama, T. Hayashi, H. Nakagawa, *et al.*, Physica B (Amsterdam) **298**, 531 (2001).

Translated by N. Wadhwa

Journal of Experimental and Theoretical Physics, Vol. 101, No. 3, 2005, pp. 535–546.
Translated from Zhurnal Éksperimental'noĭ i Teoreticheskoĭ Fiziki, Vol. 128, No. 3, 2005, pp. 623–635.

ORDER, DISORDER, AND PHASE TRANSITIONS IN CONDENSED SYSTEMS

Room-Temperature Phase Separation in Weakly Doped Lanthanum Manganites

N. I. Solin

Institute of Metal Physics, Ural Division, Russian Academy of Sciences, Yekaterinburg, 620219 Russia
e-mail: solin@imp.uran.ru

Received April 29, 2005

Abstract—The properties of single crystals of weakly doped lanthanum manganites $La_{1-x}A_xMnO_3$ (A = Ca, Ce, Sr; x = 0, 0.07–0.1) have been studied in the temperature range from 77 to 400 K. It is established that these lanthanum manganites exhibit (in addition to the well-known characteristic features observed in the region of the temperature of magnetic ordering) changes in the electrical and magnetic properties in the region of room temperature ($T \approx 270$–300 K), which is about two times the Curie temperature ($T_C \approx 120$–140 K) and is far from the temperature of structural transitions in the samples studied. The results are explained in terms of phase separation related to the formation of magnetic clusters in the nonconducting medium. The phase separation is caused by a gain in the exchange energy and by the development of elastic stresses in the crystal lattice and proceeds via combination of small-radius magnetic polarons into a large-size magnetic cluster containing several charge carriers. The short-range order in the cluster appears and the phase separation begins at a temperature T_{ps}, which is close to $T_C \approx 300$ K, typical of doped conducting manganites. The results of magnetic measurements show that, as the temperature decreases from 300 to 190 K, the size of superparamagnetic droplets increases from about 8 to 15 Å. © *2005 Pleiades Publishing, Inc.*

1. INTRODUCTION

Despite many years of research, there is no commonly accepted opinion concerning the mechanism of electric conductivity in lanthanum manganites. The existing double exchange model alone cannot explain experimental data reported for the semiconductor–metal transition and the colossal magnetoresistance observed in $La_{1-x}Sr_xMnO_3$ with x = 0.2–0.3 in the region of the Curie temperature ($T_C \approx 300$ K). It was suggested [1] that the electrical properties of these compounds are determined by the polaronic mechanism, related to a strong electron–phonon coupling and the Jahn–Teller splitting of levels in Mn^{3+} ions. Evidence in favor of the polaronic mechanism is provided by a large difference between the activation energies determined from the temperature dependence of the electric resistance and thermopower [2]. The magnetic and electrical properties of manganites were also considered within the framework of the double exchange model assuming that the charge carriers exhibit localization caused by spin disorder and random distribution of magnetic inhomogeneities [3, 4]. Calculations [4] showed that, in the presence of a certain nonmagnetic disorder, a spin disorder in the paramagnetic region may cause the localization of charge carriers at the Fermi level and the appearance of the Anderson semiconductor–metal transition near the Curie temperature for x = 0.2–0.3. It was suggested [5] that, in doped manganites with a strong electron–phonon coupling, two polarons might combine so as to form an immobile bipolaron in the paramagnetic region with a narrow polaron band. In the ferromagnetic region, the exchange interaction of polaron carriers with localized spins breaks bipolarons and increases the electric conductivity because of a sharp growth in the carrier density while retaining the polaronic character of conductivity below T_C.

Recent investigations [6–8] showed that the properties of manganites could be also explained [9–11] within the framework of a phase separation model [12, 13]. According to this model [13], a gain in the exchange energy makes it favorable for electrons to create conducting ferromagnetic clusters in a nonconducting antiferromagnetic matrix. Such magnetic droplets in antiferromagnetic matrices were detected by neutron scattering techniques [8, 14–16] in single crystals of $La_{1-x}A_xMnO_3$ (A = Ca, Sr) with x = 0.05–0.08). At liquid helium temperatures, the droplets are anisotropic and acquire the shape of oblate ellipsoids with dimensions from 8 to 17 Å. No such droplets have been found in undoped $LaMnO_3$. In $La_{1-x}Ca_xMnO_3$ with $x \geq$ 0.1–0.2, magnetic clusters with a size of 14–17 Å have not been observed either [15]. The authors believe that magnetic clusters merge together (coalesce) in compounds with $x \geq 0.1$. The results of recent neutron scattering investigations [17] showed that an increase in the level of doping from x = 0.06 to 0.07 led in $La_{0.93}Sr_{0.07}MnO_3$ to a transition from small-scale ($2R_{cl} \approx$ 17 Å) to large-scale phase separation, and the average

linear size of magnetic clusters at 4.2 K amounted to $2R_{cl} \approx 200$ Å.

Hennion *et al.* [8] showed that the magnetic droplets exist in the temperature interval from 2 K up to temperatures in the vicinity of the Curie temperature $T_C \approx$ 120–140 K of these manganites. In usual magnetic materials, the magnetic polarons break near the Curie temperature T_C [11]. It was suggested [18] that the phase separation in lanthanum manganites may proceed even at higher temperatures. In order to check for this assumption, it is necessary to study the behavior of linear expansion coefficients and the electrical, magnetic, and other properties of manganites up to high (about 1000 K) temperatures [18]. Indeed, if the magnetic clusters are formed due to the phase separation [15, 17], they probably possess the saturation magnetization and the Curie temperature $T_C \approx 300$ K characteristic of continuous strongly doped lanthanum manganites and, hence, they must not necessarily break near the Curie temperature $T_C \approx$ 120–140 K characteristic of weakly doped lanthanum manganites.

Some experimental data for manganites can be interpreted as manifestations of the onset of phase separation in a far paramagnetic region [19–21]. The room-temperature features in the resistance and magnetoresistance, thermopower, and magnetic susceptibility of $La_{0.92}Ca_{0.08}MnO_3$ single crystals [19] and in the linear and volume expansion coefficients of $La_{0.93}Sr_{0.07}MnO_3$ single crystals [21] were attributed to the formation of magnetic clusters near the room temperature. Recently, Kugel' *et al.* [22] described the electrical and magnetic properties of various manganites ($Pr_{0.71}Ca_{0.29}MnO_3$, $(La_{1-y}Pr_y)_{0.3}Ca_{0.3}MnO_3$, $La_{0.8}Mg_{0.2}MnO_3$) in a broad temperature interval in the paramagnetic region using the model of inhomogeneous state and explained the obtained results by the presence of magnetic droplets with an average size of about 30 Å.

The phenomenon of phase separation can be most clearly manifested in the properties of weakly doped manganites. Unfortunately, the electrical properties of such manganites are still insufficiently studied and no qualitative theory (capable of tracing a relation of these properties to the phase separation) is available for the electric conductivity in phase-separated media [18]. The qualitative relationship between the magnetoresistance and the magnetic clusters formed at temperatures near T_C in conducting ferromagnetic manganites is known [6, 7]. However, only elucidation of the mechanisms responsible for the resistance and magnetoresistance of manganites, determination of the dependence of these properties on the level of doping, and comparison of the experimental data to predictions of the magnetic cluster model will apparently provide for real progress in understanding of the effect of phase separation on the electrical phenomena and the colossal magnetoresistance in manganites. This paper presents the results of investigation of the problems outlined above.

In this study, the dc and ac resistance and magnetoresistance, thermopower, and magnetic properties of a series of single crystals of weakly doped lanthanum manganites $La_{1-x}A_xMnO_3$ (A = Ca, Ce, Sr; $x = 0.07$–0.1) have been measured in a broad range of temperatures and magnetic fields. It is established that these manganites exhibit changes in the electrical and magnetic properties in the region of room temperature (T = 270–300 K), which is about two times the Curie and Néel temperatures ($T_C \approx T_N \approx$ 120–140 K)) and is significantly lower than the temperature of structural transitions in the samples studied. The observed effects include changes in the activation energy of the resistivity (ΔE_ρ) and thermopower (ΔE_s), the preexponential factor (σ^0) of the electric conductivity, and the kinetic coefficient (S_0) of thermopower, the appearance of magnetoresistance, and the spontaneous magnetization. The observed behavior is characteristic of a paramagnetic medium with dispersed magnetic nanoparticles [23]. The single crystals of $La_{0.92}Ca_{0.08}MnO_3$ and $La_{0.93}Sr_{0.07}MnO_3$, which are characterized by significantly different (according to the neutron scattering data [8, 17]) dimensions of magnetic clusters, have been studied in more detail.

The results of this comparative study will be interpreted in terms of the phase separation model [9–13, 18], which implies the appearance of an inhomogeneous magnetic state (cluster) and its variation with temperature. At high temperatures ($T > 300$ K) in the paramagnetic region, small-radius polarons can form as a result of strong electron–phonon coupling [1, 5] and localize on the Jahn–Teller lattice distortions. The interaction of charge carriers with magnetic moments decreases the system energy for the parallel orientation of these moments, thus creating a "ferromagnetic" region—a magnetic polaron—surrounding a charge carrier. In the usual magnetic materials, these "thermal" polarons appear near T_C [11]. In the case of low doping (below percolation threshold: $x \le 0.1 < x_{per} = 1/3$), a state of minimum energy can be achieved due to phase separation (with the formation of magnetic droplets [12]) even at temperatures much higher than the Curie temperature $T_C \approx 125$ K for weakly doped lanthanum manganites. A gain in the exchange energy and the development of elastic stresses in the crystal lattice allow small-radius magnetic polarons to combine into a large-size magnetic cluster containing several electrons (their number is equal to that of combined polarons). For this reason, the short-range order in the cluster appears at a temperature of $T_{ps} \approx$ 250–300 K, which is close to T_C of doped conducting manganites with $x \approx 0.2$–0.3. The magnetic cluster has a magnetic moment of about 10–$12\mu_B$ (μ_B is the Bohr magneton) [19] and a radius $R_{pol} = R_{Mn-Mn} = 1a \approx 4$ Å (a is the lattice parameter), which accounts for a change in the linear expansion coefficient [21]. As the temperature decreases, the cluster size monotonically increases. The theoretical predictions agree with the results of magnetic measure-

The properties of single crystals of weakly doped lanthanum manganites

	T, K	ΔE_ρ, meV	σ^0, Ω^{-1} cm^{-1}	ΔE_s, meV	S_0	W_1, meV	T_C, K	T_N, K	$T_{OO'}$, K
$LaMnO_3$[1]	$400 > T > 300$	330	2300	100	1.1	230	142	140	750
	T < 270	250	120					[16]	[16]
$La_{0.93}Ce_{0.07}MnO_3$[1]	$400 > T > 300$	390	2700				138		≈750
Ar	T < 270	310	120				–		?
$La_{0.92}Ca_{0.08}MnO$[2]	$400 > T > 300$	220	1350	160	–2.4	60	128	122	580
	$270 > T > 90$	170	200	115	–0.4	55	–	[16]	[15]
$La_{0.9}Ca_{0.1}MnO_3$[2]	$370 > T > 300$	325	2×10^4	180	–4.5	145	138	112	510
	$270 > T > 170$	145	300	70	≈0	75	[15]	[15]	[15]
	$170 > T > 80$	93	8	–	–	–	–	–	–
$La_{0.875}Ca_{0.125}MnO_3$[2]	$400 > T > 300$	145	1600	60	–1.3	85	158	–	340
	T < 270	130	600	45	0	85	[15]	–	[15]
$La_{0.93}Sr_{0.07}MnO_3$[1]	$400 > T > 300$	280	2100	120	–2.1	160	132	121	≈490
	$270 > T > 170$	145	160	65	≈0	80	–	[17]	[26]

Note: ΔE_ρ is the resistivity activation energy; ΔE_s is the thermopower activation energy; W_1 is the hopping conductivity activation energy; σ^0 is the preexponential factor of the electric conductivity, S_0 is the kinetic coefficient (slope) of thermopower; T_C is the Curie temperature; T_N is the Néel temperature of the noncollinear ferromagnet; and $T_{OO'}$ is the structural phase transition temperature.

[1] The crystal was grown by A.M. Balbashov *et al.* [24] in the Moscow State Power Engineering University (Moscow).

[2] The crystal was grown by L. Pinsard *et al.* [25] in the Laboratoire de Chimic des Solides, Universite Paris–Sud (France).

ments. For example, the magnetic susceptibility measurements for $La_{0.9}Ca_{0.1}MnO_3$ in a magnetic field of up to 45 kOe showed that superparamagnetic clusters appear at $T \approx 300$ K and their dimensions increase with decreasing temperature.

2. SAMPLES AND TECHNIQUES

The single crystal sample of $La_{0.92}Ca_{0.08}MnO_3$ represented a distorted antiferromagnet with a slanting angle of $\theta \approx 13°$, $T_C = 126$ K, $T_N = 122$ K, in-plane ferromagnetic exchange energy $J_1 = 1$ meV, interlayer antiferromagnetic exchange energy $J_2 = -0.28$ meV, and a structural transition temperature of $T_{OO'} = 580$ K [15, 16]. The single crystal of $La_{0.93}Sr_{0.07}MnO_3$ represented a distorted antiferromagnet with a slanting angle of $\theta \approx 25°$, $T_C = 128$ K, $T_N = 121$ K [17], and a structural transition temperature of $T_{OO'} = 490$ K. Some parameters of the other samples are presented in the table.

The dc resistance measurements were performed using the conventional four-point-probe technique with a digital voltmeter possessing the input impedance above 10^9 Ω. The microwave conductivity and the permittivity ε' were measured using the resonator technique at 9.2 GHz [27]. The thermopower was measured in vacuum using the four-point-probe scheme at a temperature difference of 4–8 K between temperature sensors. The magnetic measurements were performed on a SQUID magnetometer of the MPMS-5XL type (Quantum Design Co.) at the Center for Magnetometry of the Institute of Metal Physics (Yekaterinburg).

3. RESULTS

According to the results of thermopower measurements, the single crystals under study are semiconductors of the *p*-type. As can be seen from the experimental data presented in Fig. 1, the thermopower S at a fixed temperature decreases with increasing degree of calcium or strontium substitution. The temperature dependence of S exhibits qualitatively the same behavior in all samples. In the temperature interval from 400 to 300 K (Fig. 1), this dependence obeys an activation relation characteristic of semiconductors [28]:

$$S = \frac{k}{e}\left(\frac{\Delta E_s}{kT} + S_0\right), \quad (1)$$

where ΔE_s is the thermopower activation energy, e is the electron charge, and k is the Boltzmann constant. As the temperature decreases further, the thermopower keeps increasing, but the slope of the S versus $1/T$ curve exhibits a step at $T \approx 270$ K and S remains constant in a certain temperature interval. This behavior of the ther-

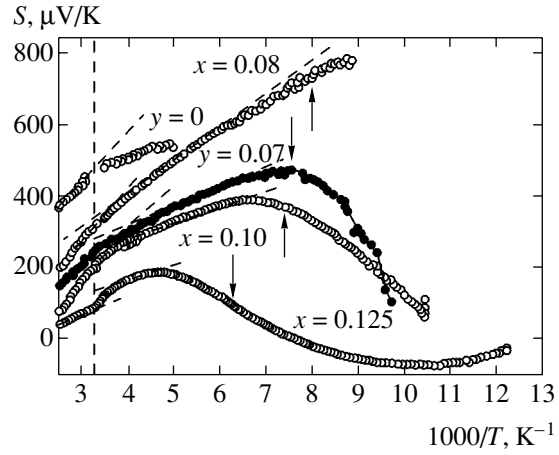

Fig. 1. Temperature dependences of the thermopower slope in $La_{1-x}Ca_xMnO_3$ (x = 0.08, 0.10, 0.125) and $La_{1-y}Sr_yMnO_3$ (y = 0.07) single crystals. Arrows indicate the Curie temperatures T_C.

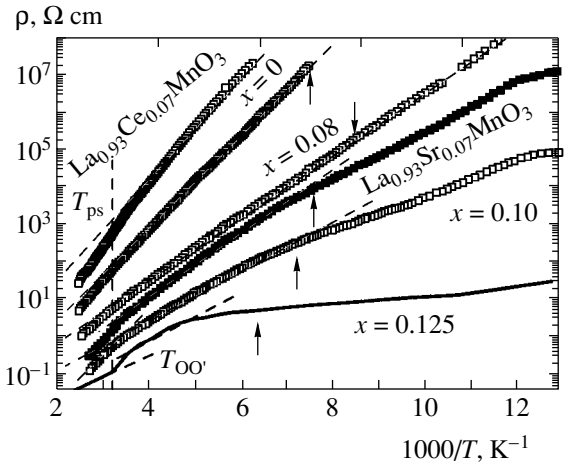

Fig. 2. Temperature dependences of the dc resistivity of $La_{1-x}Ca_xMnO_3$ (x = 0, 0.08, 0.10, 0.125) and $La_{0.93}Sr_{0.07}MnO_3$ (dark symbols), and $La_{0.93}Ce_{0.07}MnO_3$ single crystals. Arrows indicate the Curie temperatures T_C.

mopower can be described in terms of temperature-dependent ΔE_s and S_0 (see table).

On approaching T_C in $La_{0.92}Ca_{0.08}MnO_3$, the slope of the S versus $1/T$ curve exhibits slight variations, while in the other samples the thermopower at this point sharply decreases. The thermopower slope of $La_{0.875}Ca_{0.125}MnO_3$ (as well as the resistivity of this crystal, see Fig. 2) exhibits a jump in the vicinity of the structural phase transition ($T_{OO'}$ = 340 [15]), changes sign to negative on approaching T_C, passes through a minimum, and then increases with further decrease in temperature. It should be noted that a similar change in the sign of thermopower near T_C was observed in $La_{0.9}Sr_{0.1}MnO_3$ [29].

The kinetic coefficient S_0 in expression (1) for Ca- and Sr-doped samples is negative and varies from –4.5 to –1.3 (in contrast to semiconductors, where this coefficient is usually positive and characterizes dissipation processes). In undoped $LaMnO_3$, the value of this coefficient ($S_0 \approx 1.1$) is close to that in disordered media [28]. Negative values of S_0 (about –0.5) were previously reported in [2, 30] and discussed in [19].

The temperature dependence of the resistivity of $La_{1-x}A_xMnO_3$ (A = Ca, Ce, Sr) single crystals above $T \approx 300$ K (see Fig. 2) is described by the activation relation

$$\rho_0(T) \equiv \frac{1}{\sigma_0} = \frac{1}{\sigma^0}\exp\frac{\Delta E_\rho}{kT} = \frac{1}{\sigma_0}\exp\left(\frac{\Delta E_s + W_1}{kT}\right). \quad (2)$$

At lower temperatures, the resistivity can also be described by expression (2) with temperature-dependent parameters σ^0 (preexponential coefficient of conductivity) and ΔE_ρ (resistivity activation energy). The ΔE_ρ and σ^0 values exhibit a decrease on approaching to the ferromagnetic region, which is typical of manganites.

In addition, as the temperature decreases below 400 K, the σ^0 and ΔE_ρ values of doped manganites exhibit a decrease in the region of room temperature ($T \approx 300$–320 K), which is about two times the temperature of magnetic ordering (T_C = 125–140 K) and is far from the temperature of structural transitions in the samples studied (see table). In this region, the ΔE_ρ value decreases by approximately 150 meV, while σ^0 drops by at least a factor of ten (see table). The resistivities of undoped and cerium-doped lanthanum manganites rapidly increase with decreasing temperature and become unmeasurable ($\rho_0 > 10^8$ Ω cm) at $T < T_C$. At $T <$ 300 K, the $\rho_0(1/T)$ curves for these compounds exhibit a nearly activation character in a broad range of resistivities. In $La_{0.92}Ca_{0.08}MnO_3$, the ΔE_ρ value remains unchanged in a broad range of resistivity variation (within seven orders of magnitude) at temperatures below 300 K. In cerium-doped samples, the ΔE_ρ value exhibits an increase. We can suggest that the increase in this activation energy observed upon doping with Ce^{4+} is related to the compensation of holes (Mn^{4+} ions), which are probably present in undoped $LaMnO_3$ containing lanthanum and oxygen vacancies. As the degree of doping with Ca and Sr increases, the ΔE_ρ and σ^0 values tend to decrease.

In the region of room temperature, the manganite samples under study also exhibited a change in magnetoresistance. Figures 3 and 4 show the temperature dependences of the resistivity ρ, magnetoresistance $MR_H \equiv [\rho(H) - \rho(H = 0)]/\rho(H)$ and thermopower S_k in the single crystals of $La_{0.92}Ca_{0.08}MnO_3$ and $La_{0.93}Sr_{0.07}MnO_3$. At room temperature (297 K), the dc magnetoresistance is small and behaves like

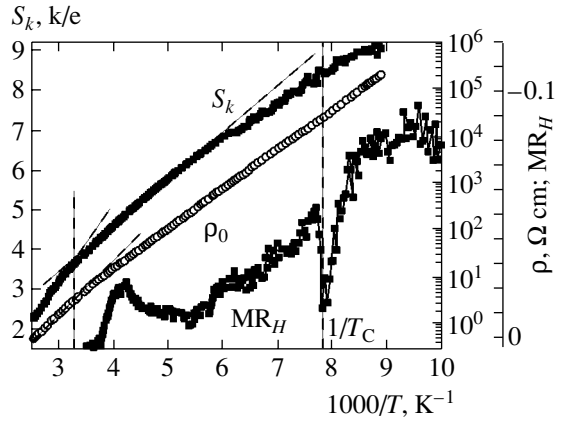

Fig. 3. The temperature dependences of the thermopower $S_k \equiv S/(k/e)$, the dc resistivity ρ_0, and the dc magnetoresistance MR_H at H = 17 kOe in the single crystal of $La_{0.92}Ca_{0.08}MnO_3$.

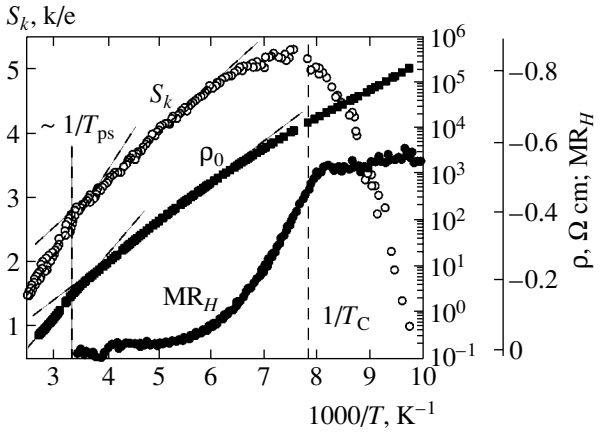

Fig. 4. The temperature dependences of the thermopower $S_k \equiv S/(k/e)$, the dc resistivity ρ_0, and the dc magnetoresistance MR_H at H = 17 kOe in the single crystal of $La_{0.93}Sr_{0.07}MnO_3$.

$MR_H \sim H^2$. For example, at H = 17 kOe, we have $MR_H = -10^{-3}$ and -2×10^{-3} for $La_{0.92}Ca_{0.08}MnO_3$ and $La_{0.93}Sr_{0.07}MnO_3$, respectively. In both samples, the magnetoresistance exhibited a sharp increase in the region of $T \approx 260$–280 K (Figs. 3 and 4) to reach a level of $MR_H \approx -(2–3)\%$ and then exhibited a slower growth as the temperature increased up to T_C. In addition, the MR_H of the single crystal of $La_{0.92}Ca_{0.08}MnO_3$ exhibited an abrupt drop in a narrow (±5 K) temperature interval at $T \approx T_C = 128$ K. In the vicinity of 100 K, the magnetoresistance of $La_{0.93}Sr_{0.07}MnO_3$ is almost ten times that of $La_{0.92}Ca_{0.08}MnO_3$. As can be seen from Figs. 3 and 4, the MR_H value increases at T = 260–280 K, which is slightly lower than the temperatures corresponding to changes in ΔE_s and ΔE_ρ.

As can be seen from Figs. 3 and 4, the resistivity activation energy ΔE_ρ exhibits consistent changes in the entire temperature interval where the thermopower activation energy ΔE_s varies. As the temperature decreases below T = 300 K and approaches T_C, the character of the temperature dependences of S and ρ_0 of $La_{0.92}Ca_{0.08}MnO_3$ vary rather slightly, while the analogous quantities in $La_{0.93}Sr_{0.07}MnO_3$ change significantly and the ΔE_ρ and ΔE_s values decrease with temperature. The deviations of $S(1/T)$ and $\rho_0(1/T)$ from the linear dependence and a sharp growth in the magnetoresistance take place at approximately the same temperature ($T \approx 160$ K). Similar consistent variation of the thermopower and resistivity is observed (see Figs. 1 and 2) in the other weakly doped manganites studied.

The plots of magnetoresistance versus magnetic field strength at T = 77 K for $La_{0.93}Sr_{0.07}MnO_3$ and $La_{0.9}Ca_{0.1}MnO_3$ exhibit a similar behavior: in both cases MR_H monotonically increases to approximately the same level with increasing field strength. Below T_C, the MR_H value depends on the magnetic field orientation relative to the crystallographic axes: the anisotropy δMR_H is about 10% for H = 17 kOe (T = 77 K) [21]. Figure 5 shows the field dependence of the magnetoresistance for $La_{0.93}Sr_{0.07}MnO_3$ at temperatures above and below T_C. As can be seen, $MR_H \propto H$ at $T > T_C$ and $MR_H \propto H^2$ at 77 K ($T < T_C$).

The temperature dependences of the ac (microwave) resistivity ρ_{mw} at a frequency of 9.2 GHz in $La_{0.92}Ca_{0.08}MnO_3$ and $La_{0.93}Sr_{0.07}MnO_3$ far of T_C exhibited approximately the same character (Fig. 6). In both samples, ρ_{mw} above $T \approx 275$ K are determined by the dc conductivity: $\rho_{mw} = \rho_0$. As the temperature decreases, the dc conductivity contribution drops rapidly and becomes insignificant at T = 150–160 K as compared to the high-frequency component: $\rho_{mw} \ll \rho_0$. As the tem-

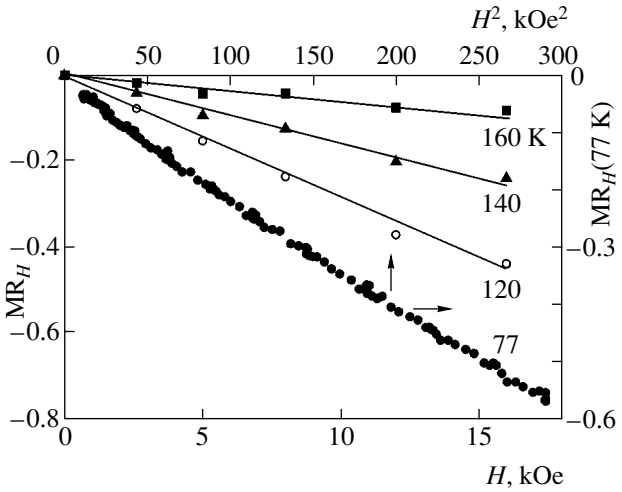

Fig. 5. Plots of the magnetoresistance versus magnetic field strength for the $La_{0.93}Sr_{0.07}MnO_3$ single crystal at T = 120, 140, 160 K (left and bottom coordinate axes) and 77 K (right and top coordinate axes).

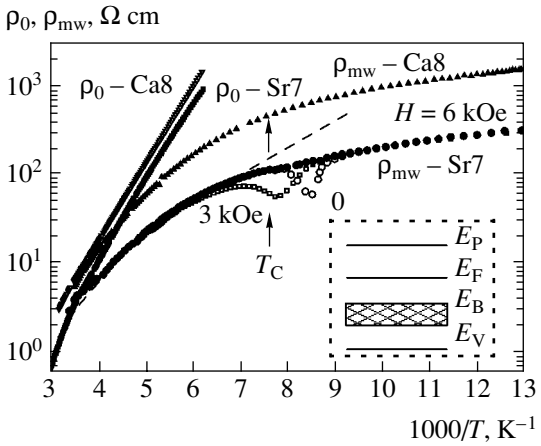

Fig. 6. The temperature dependences of the dc (ρ_0) and microwave (ρ_{mw}) resistivities of $La_{0.93}Sr_{0.07}MnO_3$ (Sr7) and $La_{0.92}Ca_{0.08}MnO_3$ (Ca8) single crystals. Points present the experimental data; dashed line shows the results of calculations ρ_{mw} (see the text). The inset is a schematic diagram of the proposed band structure of weakly doped lanthanum manganites in the paramagnetic region (E_P is the polaron band; E_B is the band of localized states).

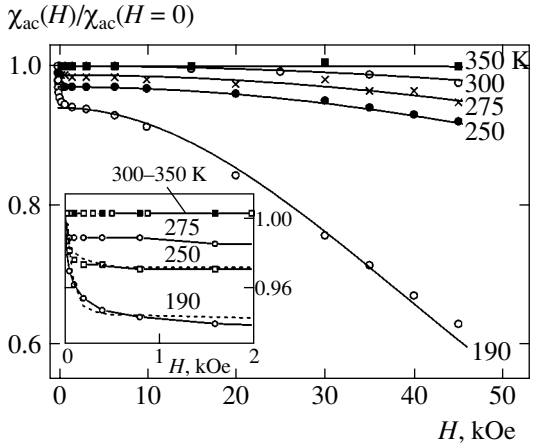

Fig. 7. The field dependences of the differential magnetic susceptibility χ_{ac} of $La_{0.9}Ca_{0.1}MnO_3$ measured at 80 GHz and various temperatures (the inset shows data for weak fields on a grater scale). Points present the experimental data; solid and dashed curves show the results of calculations (see the text).

perature decreases further, ρ_{mw} in $La_{0.93}Sr_{0.07}MnO_3$ exhibits minima in a narrow temperature interval near T_C ($T = 115 \pm 15$ K) on the background of approximately exponential growth of $\rho_{mw}(1/T)$ with $\Delta E_{mw} \approx 80$ meV. In the applied magnetic field, the anomalies of ρ_{mw} shift by $\Delta T \approx 20$–25 K toward higher temperatures and practically vanish in the fields above 6–7 kOe. The anomalous behavior of ρ_{mw} is accompanied by an increase in the permittivity ε' from 19.5 to 21 with decreasing temperature; the anomaly in ε' is also suppressed by the applied magnetic field [31]. This temperature dependence of the complex permittivity $\varepsilon^* = \varepsilon' + i\varepsilon''$ of $La_{0.93}Sr_{0.07}MnO_3$ is characteristic of the polaronic conductivity and corresponds to relaxation losses of the Debye type [32, 33]. No such anomalies in ρ_{mw} and ε' at 9.2 GHz near T_C are observed in $La_{0.92}Ca_{0.08}MnO_3$. At the same time, variations of the ε' and ε'' values near the Curie temperature were also reported for some other weakly doped manganites [26, 34].

Variations have been also observed in the magnetic properties of weakly doped lanthanum manganites measured in the region of room temperature. The temperature dependences of the magnetic susceptibility χ_0 of undoped samples and those weakly doped with Sr, Ce, and Ca in the paramagnetic region ($T = 200$–300 K) can be approximately described using the Curie–Weiss law with the effective moments μ_{eff}, which are greater than the theoretical values by (1–2)μ_B [35]. A characteristic feature of weakly doped lanthanum manganites is the dependence of their magnetic susceptibility on the magnetic field strength at temperatures below $T \approx 270$ K [19, 21]. For example, the differential magnetic susceptibility χ_{ac} measured at 80 GHz at temperatures above $T_{ps} \approx 270$ K is independent of the applied constant magnetic field, while below T_{ps} this susceptibility becomes field-dependent (see the inset to Fig. 7). Indeed, χ_{ac} exhibits a sharp drop in the fields below $H_N \leq 500$ Oe and weakly depends on the field above H_N. The H_N value grows with decreasing temperature. Similar field dependences of χ_{ac} with the same characteristic temperature $T_{ps} \approx 270$–300 K were observed for $La_{0.92}Ca_{0.08}MnO_3$ [19] and $La_{0.93}Sr_{0.07}MnO_3$ [21] in weak magnetic fields ($H \leq 1$ kOe). It might seem that χ_{ac} could stabilize in stronger fields. However, the measurements of χ_{ac} in $La_{0.90}Ca_{0.10}MnO_3$ in the fields up to 45 kOe showed (Fig. 7) that $\chi_{ac}(H)$ exhibited no saturation upon an increase in the magnetic field. At $T = 350$ K, no influence of the applied magnetic field (up to 45 kOe) on χ_{ac} was observed to within the experimental accuracy. However, at lower temperatures ($T = 300$–190 K), χ_{ac} decreases with increasing magnetic field strength and this dependence becomes stronger with decreasing temperature. Such magnetic behavior is usually observed in paramagnetic media with dispersed nanoparticles and in superparamagnets [23].

4. DISCUSSION

The observed temperature dependences of the resistivity and thermopower with the temperature-dependent activation energies ΔE_ρ and ΔE_s (Figs. 1–4) are typical of disordered semiconductors. For a simple energy band structure (see the inset to Fig. 6), taking into account nonlocalized (valence) and localized (near the valence band) charge carriers, the dc and ac conductivities are probably determined by the following mechanisms [28].

(a) Transfer of nonlocalized charge carriers. The temperature dependences of the dc conductivity (for

holes) and thermopower can be expressed as

$$\sigma_0 = \sigma_{min}\exp\left(-\frac{E_F + E_V}{kT}\right) = \sigma_{min}\exp\left(-\frac{\Delta E_\rho}{kT}\right), \quad (3)$$

$$S = \frac{k}{e}\left(\frac{E_F - E_V}{kT} + S_0\right) = \frac{k}{e}\left(\frac{\Delta E_s}{kT} + S_0\right), \quad (4)$$

where E_F is the Fermi level, E_V is the top of the valence band (mobility edge) separating the nonlocalized and localized states, and $\sigma_{min} \approx 300$–$1000\ \Omega^{-1}\ cm^{-1}$ is the minimum metallic conductivity. This mechanism does not contribute to the ac conductivity at frequencies below 10^{15} Hz. As can be seen, the activation energies for the thermopower and resistivity in this mechanism coincide: $\Delta E_s = \Delta E_\rho$.

(b) Hopping of carriers localized in the tail of the valence band. For this process, the dc conductivity and thermopower are expressed as

$$\sigma_0 = \sigma_2\exp\left(-\frac{E_F - E_B + W_1}{kT}\right) = \sigma_2\exp\left(-\frac{\Delta E_\rho}{kT}\right), \quad (5)$$

$$\sigma_\omega \sim \sigma(\omega)\exp\left(-\frac{E_F - E_B}{kT}\right) = \sigma(\omega)\exp\left(-\frac{E_{mw}}{kT}\right), \quad (6)$$

$$S = \frac{k}{e}\left(\frac{E_F - E_B}{kT} + S_0\right) = \frac{k}{e}\left(\frac{\Delta E_s}{kT} + S_0\right), \quad (7)$$

where W_1 is the jump activation energy, $E_B - E_V$ is the tail of the localized states, $\sigma(\omega) \sim \omega^s$, and $s = 0.8$–1 [28, 33]. As can be seen, $\Delta E_\rho = \Delta E_s + W_1$ and $\Delta E_{mw} = \Delta E_s$, that is, the activation energies for the thermopower and resistivity in this case are different in the dc mode and coincide in the ac mode. As a rule, $\sigma_2 \approx 1$–$10\ \Omega^{-1}\ cm^{-1}$, which is about two orders of magnitude smaller than σ_{min} [28].

(c) Hopping of carriers localized at the Fermi level. In this case, the conductivity is expressed as

$$\sigma_0 = \sigma_3\exp\left(-\frac{W_2}{kT}\right) = \sigma_3\exp\left(-\frac{E_3}{kT}\right), \quad (8)$$

where $\sigma_3 \le \sigma_2$ and W_2 is the hoping activation energy. The ac conductivity by this mechanism is either proportional to the temperature or independent of the temperature, and $\sigma(\omega) \sim \omega^s$, where $s = 0.8$–1. This mechanism, which is usually manifested at rather low temperatures, where $\sigma_0 \sim \exp(-B/T^{1/4})$, was not observed for the samples under consideration in the entire temperature range studied.

The high values of σ_0 (10^3–$2 \times 10^4\ \Omega^{-1}\ cm^{-1}$) observed in weakly doped manganites at high temperatures (see table) can be explained by the contribution of nonlocalized charge carriers. The temperature dependences of the dc and ac (microwave) conductivities in $La_{0.93}Sr_{0.07}MnO_3$ single crystals below $T = 300$ K (see the dashed ρ_{mw} line in Fig. 6) were explained [31] as being determined by the contributions of nonlocalized charge carriers and those localized in the tail of the valence band (expressions (3) and (6)). However, the difference between the ΔE_ρ and ΔE_s values and a nonzero jump activation energy W_1 are indicative of the absence of a contribution due to the nonlocalized carriers. A small conductivity at a relatively large acceptor concentration ($x \le 0.1$) can be explained by the fact that the charge carriers can be localized (in addition to the tail of the valence band) at Mn^{4+} ions with the formation of a polaron band E_P in the bandgap (see the inset to Fig. 6). Then, the dc resistivity and thermopower are described [28, 32] by the expressions of type (5) and (7), where $E_F - E_B$ should be replaced by $E_F - E_P$ and $\sigma_2 \longrightarrow \sigma_P$ weakly depends on the temperature and can be greater than σ_{min} (being dependent on the polaron density and mobility) [28].

One characteristic feature of the polaronic mechanism is the frequency dependence of the permittivity $\varepsilon^* = \varepsilon' + \varepsilon''$ and the ac conductivity $\sigma_\omega^{pol} \sim \omega\varepsilon''$ [32, 33]:

$$\sigma_\omega^{pol} \sim \frac{\omega^2\tau}{1 + \omega^2\tau^2}, \quad \varepsilon' \sim \frac{1}{1 + \omega^2\tau^2}, \quad (9)$$

where $\tau = \tau_0\exp(E_D/kT)$ is the characteristic hopping time, E_D is the Debye energy, and $1/\tau_0 \sim \omega_{ph}$ is a constant on the order of the optical phonon frequency. For the charge carriers localized in the tail of the valence band, the conductivity increases in proportion to the frequency, while for polarons, the conductivity exhibits nonmonotonic variation: it shows a Debye character with a maximum at $\omega\tau = 1$, and ε' monotonically varies depending on the temperature and frequency.

The anomalies observed in the temperature dependences of ε' and ρ_{mw} of $La_{0.93}Sr_{0.07}MnO_3$ near T_C (Fig. 6) are characteristic of the polaronic conductivity and can be explained by electron hopping between the two nearest neighbor localized states (e.g., between Mn^{3+} and Mn^{+4} ions) spaced by the distance R and the potential barrier E_D. The narrow temperature interval of the anomaly in ρ_{mw} implies that the Debye energy (i.e., the polaron localization energy) is temperature dependent (a possible reason will be considered below). It should be noted that the frequency and temperature dependences of $\varepsilon^* = \varepsilon' + i\varepsilon''$ observed for weakly doped single crystals of $La_{1-x}Sr_xMnO_3$ of a close composition with $x = 0.075$ [36] also revealed relaxation losses of the Debye type, and it was also concluded that the frequency and temperature dependences of σ_ω were indicative of the contribution due to tunneling between large-radius polarons.

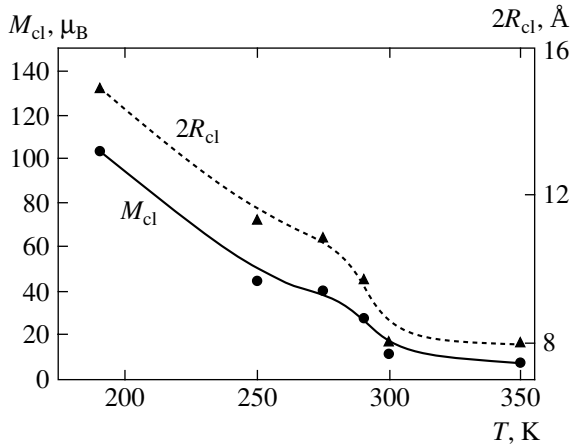

Fig. 8. The temperature dependence of the magnetic moment (M_{cl}) and radius (R_{cl}) of superparamagnetic clusters in $La_{0.9}Ca_{0.1}MnO_3$.

Thus, the high values of the preexponential factor σ^0 (see table), the presence of relaxation losses of the Debye type (Fig. 6), and the results of investigation of the frequency and temperature dependences $\sigma(\omega, T)$ [36], allow us to conclude that the conductivity of weakly doped lanthanum manganites contains a contribution due to the polaronic mechanism. We might also attempt to explain variations in the character of conductivity below $T \approx 300$ K by assuming that the contribution from carriers localized in the tail of the valence band increases with decreasing temperature. However, the relatively large values of σ^0 ($>10^2$ Ω^{-1} cm^{-1}, see table) and the appearance of anomalies at the same temperatures in the region of $T \approx 300$ K in the magnetic and electrical properties of samples with different levels of doping allow us to suggest that this phenomenon is related to a change in the character of the polaronic conductivity. Previously [19, 21], it was suggested that such features could be explained by the formation of magnetic nanoclusters.

The formation of magnetic nanoclusters may also explain the anomalies in magnetic properties (Fig. 7); moreover the size of such nanoclusters can be in some cases evaluated using the results of magnetic measurements. In sufficiently large monodomain particles, anisotropic forces hold the magnetization vector aligned in a direction corresponding to the minimum energy. When the size of droplets approaches the interatomic distances, the particle energy $K_{eff}V_{cl}$ (K_{eff} is the effective energy of the magnetic anisotropy and V_{cl} is the cluster volume) decreases below the thermal level, the magnetization vector loses stability and starts performing thermal motions of the Brownian type (although the saturation magnetization and the Curie temperature may still retain the values characteristic of the continuous solid) [23]. The dependence of the magnetization of such a (superparamagnetic) cluster on the temperature and the magnetic field is described (for $K_{eff}V_{cl} < k_BT$) by the Langevin formula [37]:

$$I_{cl} = NM_{cl}\left(\coth x - \frac{1}{x}\right), \qquad (10)$$

where $x = M_{cl}H/k_BT$, $M_{cl} = n_{cl}S$ is the magnetic moment of the cluster, S is the molecular magnetic moment, n_{cl} is the number of molecules in the cluster, and N is the number of superparamagnetic particles per unit volume of the sample.

The contribution of the superparamagnetic particle to the low-frequency differential magnetic susceptibility can be expressed as

$$\chi_{ac}^{cl} = \frac{dI_{cl}}{dH} = C\left(-\frac{1}{\sinh^2 x} + x^{-2}\right), \qquad (11)$$

where $C = NM_{cl}^2/k_BT$ is a field-independent coefficient. At large values of M_{cl}, all the variations of $I_{cl}(H)$ and $\chi_{ac}(H)$ in superparamagnetic particles may take place (even at high temperatures) in readily accessible field on the order of 10^4 Oe [37].

The variations of $\chi_{ac}(H)$ in $La_{0.9}Ca_{0.1}MnO_3$ observed in fields up to 2 kOe can be roughly described in terms of expression (11) with $M_{cl} = (8–12) \times 10^4\mu_B$ (see the dashed lines in the inset to Fig. 7). This case corresponds (in a spherical model) to a cluster with a diameter of about 150 Å or $V_{cl} = 3 \times 10^{-18}$ cm^3, $S = 2$, and a distance of $R_{Mn–Mn} = 4$ Å between the neighboring manganese ions. Taking into account that the value of the magnetic anisotropy in perovskites is on the order of $H_{eff} \approx 1$ kOe [38], we obtain an estimate of $K_{eff} \approx 10^6$ erg/cm^3. From this we infer that the droplets are probably not superparamagnetic. The observed growth in the saturation field for χ_{ac} with decreasing temperature (see the inset to Fig. 7) can be explained by an increase in the demagnetizing field $H_N = N_{dem}M$ accompanying the increase in the magnetization with the temperature (N_{dem} is the demagnetizing factor of the droplet). Assuming that the increase in the effective moment μ_{eff} in $La_{0.9}Ca_{0.1}MnO_3$ approximately by $1\mu_B$ above the theoretical value is entirely due to these clusters, and using the expression for the magnetic susceptibility $\chi(T)$ of magnetic clusters [22], we can estimate the density of large clusters as $n \approx 10^{13}$–10^{14} cm^{-3}. This value corresponds to spacing between clusters exceeding 10^3 Å. Apparently, this cluster density is very small and the distances between them are too large to account for the observed variations in the electrical properties near $T = 300$ K. In order to explain the behavior of χ_{ac} in strong magnetic fields, it is necessary to assume that the system contains small clusters in addition to the large (≥150 Å) ones. The changes in $\chi_{ac}(H)$ of $La_{0.9}Ca_{0.1}MnO_3$ observed in strong fields at a fixed temperature can be described (see the solid curves in Fig. 7) using expression (11). The magnetic moment of

the cluster increases from $\leq 8\mu_B$ at 350 K to $100\mu_B$ at 190 K (Fig. 8). In the spherical model, such effective magnetic moments correspond to particles with diameters $2R_{cl}$ ranging from 8 to about 15 Å.

Figure 9 shows the temperature dependences of the activation energies ΔE_s, ΔE_ρ, and W_1 for three manganites, which were calculated using Eqs. (1) and (2). In determining ΔE_ρ, it was assumed that σ^0 in relation (2) is independent of temperature (in the relatively small temperature interval under consideration, this assumption insignificantly influences the value of ΔE_ρ). As can be seen, the values of ΔE_ρ, ΔE_s, and W_1 are almost constant at $T \approx 270$–400 K for all three samples. Note that the behavior of these quantities in $La_{0.93}Sr_{0.07}MnO_3$ and $La_{0.90}Ca_{0.10}MnO_3$ is much alike, while differing from how they behave in $La_{0.92}Ca_{0.08}MnO_3$. Below $T \approx 270$ K, the values of ΔE_ρ and ΔE_s monotonically decrease with decreasing temperature. In $La_{0.93}Sr_{0.07}MnO_3$ and $La_{0.9}Ca_{0.1}MnO_3$, the values of ΔE_s exhibit a sharp decrease near the corresponding values of T_C, whereas no such significant variations of ΔE_s at T_C is observed for $La_{0.92}Ca_{0.08}MnO_3$. Below $T \approx 270$ K, the values of W_1 in $La_{0.93}Sr_{0.07}MnO_3$ and $La_{0.9}Ca_{0.1}MnO_3$ decrease with temperature and exhibit a sharp increase at T_C. Unlike this, W_1 in $La_{0.92}Ca_{0.08}MnO_3$ weakly varies (remains practically constant) in the entire temperature range under consideration.

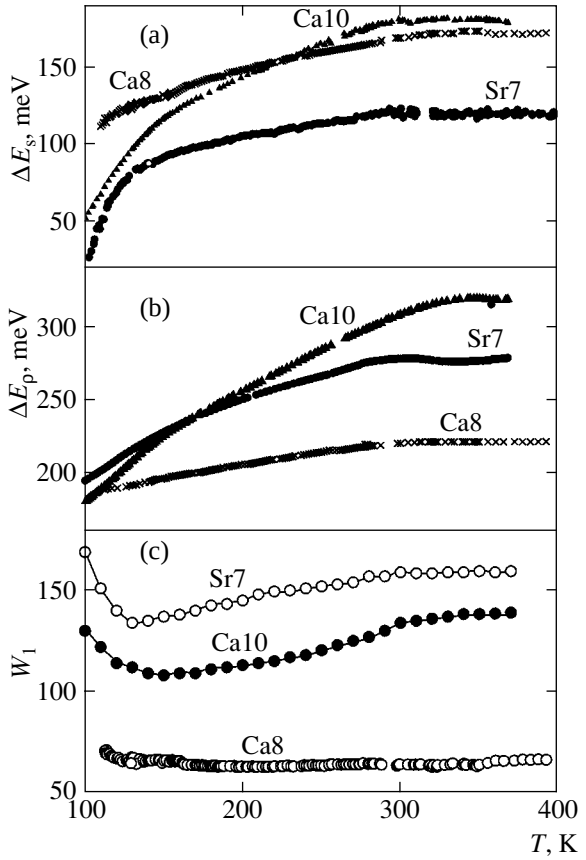

Fig. 9. Temperature dependences of the activation energies of (a) thermopower (ΔE_s), (b) resistivity (ΔE_ρ), and (c) hopping conductivity (W_1) for $La_{0.93}Sr_{0.07}MnO_3$ (Sr7), $La_{0.92}Ca_{0.08}MnO_3$ (Ca8), and $La_{0.90}Ca_{0.10}MnO_3$ (Ca10) single crystals.

At present, no simple formulas are known that would adequately describe the properties of phase-separated materials [18]. The results presented above can be qualitatively rationalized using the following assumptions.

(a) At high temperatures ($T > 300$ K), the charge carriers in manganites exhibit localization (pinning) with the formation of polarons [1] or bound (immobile) bipolarons [5], which is caused by a strong electron–phonon coupling, a spin disorder and random distribution of magnetic inhomogeneities [3], or the Jahn–Teller lattice distortion. As a result, the carriers form a localized impurity band with a gap of $\Delta/2$ in the forbidden band [5]. For this reason, the density of charge carriers involved in the conduction becomes much smaller than the number of acceptors and obeys the law $n \sim \exp(-\Delta E_s/kT)$. In this temperature range, the values of ΔE_ρ, ΔE_s, and W_1 are practically independent of the temperature.

(b) An electron trapped by a Mn^{3+} ion is in fact bound to six Mn^{3+} ions in the nearest environment of the acceptor, thus forming a polaron with the radius $R_{pol} = R_{Mn–Mn} = 1a \approx 4$ Å (a is the crystal lattice parameter). Interaction of the charge carrier with magnetic moments decreases the system energy in the case of a parallel orientation of spins and create a "ferromagnetic" region (paramagnetic polaron) around the trapped charge carrier [39]. In the usual magnetic semiconductors, the magnetic polarons can appear only in the immediate vicinity of the Curie temperature [11]. Using the concept of "thermal ferrons," it is impossible to explain the formation of ferromagnetic clusters at temperatures 2–2.5 times greater than the Curie temperature T_C and the rapid growth of their dimensions with decreasing temperature (Fig. 8), at weak temperature dependence of the polaron size ($R_{pol} \propto T^{-1/5}$) [3, 11]. Weakly doped lanthanum manganites offer a unique possibility of obtaining such clusters at temperatures significantly higher than their T_C values. At a degree of doping below the percolation threshold ($x \leq 0.1 < x_{per} \approx 0.2$–$0.3$), the density of carriers is small and the crystals have $T_C \approx 120$–140 K. However, taking into account statistical distribution of impurities, this doping admits the formation of clusters—in the form of nanoislands of various sizes containing several acceptors—in which the number of carriers is sufficient to give rise to a ferromagnetic order with $T_C \approx 300$ K in conducting manganites. Sufficiently large droplets contribute to χ_{ac} only in weak fields (see the inset to Fig. 7).

However, there are many more clusters in which the number of carriers is insufficient to establish a magnetic order in conducting manganites at $T_C \approx 300$. For $x = 0.07$–0.1, the average spacing of acceptors (about 9 Å) is close to the size (8 Å) of a polaron in which the electron is localized and the electron wavefunctions of the nearest neighbor polarons can overlap. This overlapping may render the polarons anisotropic [21] and favor the interaction of clusters with the formation of bound polarons. A gain in the exchange energy and the development of elastic stresses in the crystal lattice allow several (two, three, etc.) small-radius magnetic polarons to combine into a large-size magnetic cluster (droplet) containing several electrons. For this reason, the short-range order in the cluster appears and the phase separation begins at a temperature of $T_{ps} \approx$ 250–300 K, which is close to T_C of doped conducting manganites with $x \approx 0.2$–0.3. Sufficiently small droplets exhibit superparamagnetic properties.

(c) The exchange interaction between localized (p) and delocalized (d) charge carriers makes the gap $\Delta/2$ of the aforementioned impurity band dependent on the magnetization [5]. Calculations showed that, provided the exchange interaction is sufficiently strong ($J_{pd}S > \Delta$, where J_{pd} is the pd exchange energy), the gap in strongly doped lanthanum manganites with $x = 0.25$ in the ferromagnetic region vanishes, the density of charge carriers increases, and the resistivity sharply decreases. Upon passage to the ferromagnetic region in weakly doped manganites possessing low magnetization, the gap probably only decreases (rather than vanishing completely), which is confirmed by the temperature dependence of ΔE_s (Fig. 9). This assumption agrees with the results of magnetic measurements for $La_{0.92}Ca_{0.08}MnO_3$, where the magnetization at 100 K is almost three times as small as that in $La_{0.9}Ca_{0.1}MnO_3$. Accordingly, the thermopower activation energy (ΔE_s) in the former manganite remains virtually unchanged, while that in the latter sharply decreases near T_C. The appearance of magnetic clusters below $T \approx 300$ K and the related growth of magnetization well explain the decrease in ΔE_s in the paramagnetic region, which can be seen in Fig. 9.

(d) The theory of the transport properties of phase-separated manganites [11] assumes that the jump activation energy W_1 (characterizing the mobility of charge carriers as $\mu \propto \exp(-W_1/kT)$) is determined by the Coulomb energy (dependent on the cluster size) [32]:

$$W_1 \approx \frac{e^2}{2\varepsilon_p R_{cl}}, \tag{12}$$

where $1/\varepsilon_p = 1/\varepsilon_\infty - 1/\varepsilon_0$, ε_∞ and ε_0 being the high- and low-frequency values of the permittivity [32]. The estimate $W_1 \approx 0.2$ eV obtained using formula (12) for $\varepsilon_p = 10$ and $R_{cl} = 4$ Å agrees with the experimental values of W_1 (see table and Fig. 9) at high temperatures. A somewhat lower value of W_1 in $La_{0.92}Ca_{0.08}MnO_3$ is probably related to the anisotropy of the properties (mobility) of charge carriers, which was reported for $La_{0.93}Sr_{0.07}MnO_3$ [21].

The observed decrease in W_1 for $La_{0.9}Ca_{0.1}MnO_3$ at temperatures below $T = 300$ K (Fig. 9) qualitatively agrees with the increasing size of clusters (Fig. 8). However, a sharp growth in the W_1 value in the vicinity of T_C observed for $La_{0.93}Sr_{0.07}MnO_3$ is at variance with the neutron scattering data, according to which R_{cl} in this crystal increases up to 100 Å below T_C [17]. The carrier mobility (characterized by the jump activation energy W_1) not only depends on R_{cl}, but is also determined by the distance between clusters L_{cl} (which influences the overlap of the wavefunctions of their potential wells [32]. The conversion of polarons into clusters leads to an increase in their spacing and to a change in W_1. Upon coalescence of N_{pol} small-radius polarons into N_{cl} clusters of radius R_{cl}, the distance between these clusters increases as $L_{cl} = (4\pi/3x)^{1/3}R_{cl}$ in proportion to R_{cl} (as in the case of formation of dew drops from mist) and $L_{cl} \gg a$, where $N_{pol} = xa^{-3}$, $N_{cl} = N_{pol}/n_{pol}^{cl}$, and $n_{pol}^{cl} = 4\pi(R_{cl}/a)^3/3$ is the number of polarons in the cluster. For example, $L_{cl} \approx 4R_{cl}$ for $x = 0.05$–0.08, in agreement with the neutron data for $La_{1-x}A_xMnO_3$ (A = Ca, Sr) [8, 15, 17]. The probability of jumps between clusters is given by the formula [28, 32],

$$W \sim \exp\left(-\frac{W_1}{kT}\right)\exp(-\alpha_0 L_{cl}), \tag{13}$$

where $\alpha_0 \approx a^{-1}$ characterizes the overlap of wavefunctions of the neighboring clusters. The first term in formula (13), which is related to the Coulomb blockade, vanishes or is significantly simplified upon a large-scale phase separation. For example, W_1 decreases from about 200 to 10 meV when R_{cl} increases to $\sim 10^2$ Å. The second term in formula (13), which is related to the tunneling length, may lead to a strong decrease in mobility at $\alpha_0 L_{cl} \gg 1$. This can even overwhelm the disappearance of the Coulomb blockade, switch off the cluster conductivity, and make certain other mechanisms important (e.g., related to carrier hopping in the tail of the mobility edge). The increase in W_1 for $La_{0.93}Sr_{0.07}MnO_3$ and $La_{0.9}Ca_{0.1}MnO_3$ near T_C (Fig. 9) probably merely reflects a decrease in the drift mobility of carriers as a result of the increase in the tunneling length.

The results of magnetoresistance measurements also confirm the cluster nature of the resistivity in the samples studied. The origin of the magnetoresistance in phase-separated manganites is the variation of R_{pol} and, hence, of the Coulomb energy W_p in the magnetic field [11]. At temperatures $T > 270$ K, the magnetization of polarons proceeds via rotation of the magnetic moments of Mn^{3+}

and, hence, the polaron size is independent of the magnetic field up to very high strengths: $R_{pol}(H) = 1a$ and $MR_{pol} \approx 0$. The magnetoresistance $MR \propto H^2 \approx 10^{-3}$ observed at 297 K and 17 kOe is related to a decrease in scattering on the magnetic inhomogeneities.

In order to estimate the magnetoresistance in the paramagnetic region, it is possible to use the expression $MR_H = 1 - \exp(W_1 bH/2kT)$ for the paramagnetic state, where $b \equiv b^{PM} = gS\mu_B/5kT\ln(2S + 1)$, where g is the gyromagnetic ratio [11, 40]. In the paramagnetic region, $MR_H^{PM} \sim b^{PM}H/T^2$. As can be seen (Fig. 4), $MR_H^{PM} \sim H$ and increases with decreasing temperature for $T < T_C$, while the estimate of $MR_H^{PM} = 3$–5% agrees with the values of magnetoresistance for $La_{0.92}Ca_{0.08}MnO_3$ and $La_{0.93}Sr_{0.07}MnO_3$.

In order to analyze the behavior of magnetoresistance at temperatures below T_C, it is probably necessary to take into account variations not only in the mobility of charge carriers, but in their density as well, which may account for the higher values of $MR_H \sim H^2$. At present, the nature of the phase separation in doped manganites is incompletely clear. It is usually believed that the phase separation has a purely magnetic nature and is caused by a gain in the exchange energy. However, this assumption does not take into account the Jahn–Teller character of Mn^{3+} ions and a strong interaction between the electron and ion (lattice) subsystems in manganites [1]. Non-Jahn–Teller Mn^{4+} ions produce elastic deformation of the lattice, which is evidenced by sharp changes in the coefficients of volume and linear expansion observed in manganites in the vicinity of T_C [7, 21]. For a correct analysis of the influence of phase separation, especially large-scale one, on the electrical properties of manganites, it is necessary to take into account the elastic energy related to lattice distortions upon the formation of an inhomogeneous state [11].

The difference in the size of clusters revealed by the neutron scattering data [8, 17] may account for the minima of ρ_{mw} (Fig. 6) and their strong dependence on the temperature and applied magnetic field in $La_{0.93}Sr_{0.07}MnO_3$ with large clusters and for the absence of such features in $La_{0.92}Ca_{0.08}MnO_3$ with small clusters. The time of tunneling between clusters, which is determined by the formula $\tau = \tau_0\exp(E_D/kT)$ for Eqs. (9), varies in $La_{0.93}Sr_{0.07}MnO_3$ (Fig. 9) within broad limits because of strong and sudden changes of W_1 and ΔE_s depending on the temperature. In this case, the condition of Debye relaxation $\omega\tau = 1$ is satisfied in a narrow temperature interval. Considerable variation in the position of the ρ_{mw} minimum as a function of the magnetic field (Fig. 6) is also indicative of a strong dependence of W_1 and, hence of the cluster size, on the magnetic field. In $La_{0.92}Ca_{0.08}MnO_3$, where the values of W_1 and ΔE_s weakly vary with the temperature (Fig. 9) and the condition of Debye relaxation it 9.2 GHz is not satisfied, anomalies in ρ_{mw} and ε' are absent.

5. CONCLUSIONS

The properties of single crystals of weakly doped lanthanum manganites $La_{1-x}A_xMnO_3$ (A = Ca, Ce, Sr; x = 0, 0.07–0.1), including electric dc and ac (microwave) resistivity and magnetoresistance, thermopower, and magnetic properties, have been studied in the temperature range from 77 to 400 K. At high temperatures ($T > 300$ K), the conductivity can be interpreted within the framework of the polaronic mechanism. In the paramagnetic region, polarons are formed as a result of strong electron–phonon coupling and are probably polarized. It is established that the lanthanum manganites studied exhibit variations in the electrical properties (manifested by changes in the activation energies of the resistivity, thermopower, jumps, magnetoresistance, etc.) and magnetic properties (the development of spontaneous magnetization and field-dependent differential magnetic susceptibility) in the range below room temperature ($T \approx 270$–300 K), which is about two times the Curie temperature of manganites and is far from the temperature of structural transitions in the samples studied.

It is suggested that the observed changes, as well as the anomalies in the coefficients of linear expansion [21], are related to the appearance of a short-range magnetic order and to an increase in the size of polarons. The results of magnetic measurements showed the presence of relatively large (above 100 Å) and small (8–15 Å) magnetic clusters. The concentration of large clusters is small (10^{13}–10^{14} cm^{-3}), so that the conductivity in the paramagnetic region is mostly determined by the small clusters, judging by the estimates of the polaron jump activation energy. The appearance of large clusters (islands with T_C equal to that of the conducting manganites with x = 0.2–0.3) can be related (in addition to technological artifacts) to the statistical character of acceptor impurity distribution in the single crystal matrix. Small clusters can form because of a gain in the exchange energy and the development of elastic stresses in the crystal lattice, via combination of small-radius magnetic polarons (with two, three, or more acceptors) into large-size magnetic cluster containing several charge carriers. The short-range order in the cluster appears and the phase separation begins at a temperature ($T_{ps} \approx 250$–300 K) close to T_C of doped conducting manganites with x = 0.2–0.3. The results of this study and the estimates obtained agree with the phase separation model.

ACKNOWLEDGMENTS

The author is grateful to A.V. Korolev for conducting magnetic measurements and for discussions; to M. Hennion, L. Pinsard, and A.M. Balbashov for

kindly providing the samples for investigation; and to N.N Loshkareva for discussions.

This study was supported in part by the Russian Foundation for Basic Research (project nos. 05-02-16303 and 05-03-34971) and the program "Novel Materials and Structures" of the Department of Physics of the Russian Academy of Sciences.

REFERENCES

1. A. J. Millis, P. B. Littlewood, and B. I. Shraiman, Phys. Rev. Lett. **74**, 5144 (1995).
2. M. Jaime, M. B. Salamon, M. Rubinstein, *et al.*, Phys. Rev. B **54**, 11914 (1996).
3. C. M. Varma, Phys. Rev. B **54**, 7328 (1996).
4. L. Sheng, D. Y. Xing, D. N. Sheng, and C. S. Ting, Phys. Rev. Lett. **79**, 1710 (1997).
5. A. S. Alexandrov and A. M. Bratkovssky, Phys. Rev. Lett. **82**, 141 (1999); J. Phys.: Condens. Matter **11**, 1989 (1999).
6. R. M. Kusters, J. Singleton, D. A. Keen, *et al.*, Physica B (Amsterdam) **155**, 362 (1989).
7. J. M. De Teresa, M. R. Ibarra, P. A. Algarabel, *et al.*, Nature **386**, 256 (1997).
8. M. Hennion, F. Mussa, G. Biotteau, *et al.*, Phys. Rev. Lett. **81**, 1957 (1998).
9. A. Moreo, S. Yunoki, and E. Dagotto, Science **283**, 2034 (1999).
10. Yu. A. Izyumov and Yu. I. Skryabin, Usp. Fiz. Nauk **171**, 121 (2001) [Phys. Usp. **44**, 109 (2001)].
11. M. Yu. Kagan and K. I. Kugel', Usp. Fiz. Nauk **171**, 577 (2001) [Phys. Usp. **44**, 553 (2001)].
12. É. L. Nagaev, Usp. Fiz. Nauk **166**, 833 (1996) [Phys. Usp. **39**, 781 (1996)].
13. É. L. Nagaev, Pis'ma Zh. Éksp. Teor. Fiz. **6**, 484 (1967) [JETP Lett. **6**, 18 (1967)].
14. M. Hennion, F. Mussa, G. Biotteau, *et al.*, Phys. Rev. B **61**, 9513 (2000).
15. G. Biotteau, M. Hennion, F. Mussa, *et al.*, Phys. Rev. B **64**, 104421 (2001).
16. F. Mussa, M. Hennion, G. Biotteau, *et al.*, Phys. Rev. B **60**, 12299 (1999).
17. S. F. Dubinin, V. E. Arkhipov, S. G. Teploukhov, *et al.*, Fiz. Tverd. Tela (St. Petersburg) **43**, 2192 (2003) [Phys. Solid State **45**, 2297 (2003)].
18. E. Dagotto, New J. Phys. **7**, 67 (2005).
19. N. I. Solin, V. V. Mashkautsan, A. V. Korolev, *et al.*, Pis'ma Zh. Éksp. Teor. Fiz. **77**, 275 (2003) [JETP Lett. **77**, 230 (2003)].
20. N. A. Babushkina, E. A. Chistotina, K. I. Kugel', *et al.*, Fiz. Tverd. Tela (St. Petersburg) **45**, 480 (2003) [Phys. Solid State **45**, 508 (2003)].
21. N. I. Solin, V. A. Kazantsev, L. D. Fal'kovskaya, and S. V. Naumov, Fiz. Tverd. Tela (St. Petersburg) **47**, 1826 (2005) [Phys. Solid State **47**, 1900 (2005)].
22. K. I. Kugel', A. L. Rakhmanov, A. O. Sboĭchakov, *et al.*, Zh. Éksp. Teor. Fiz. **125**, 648 (2004) [JETP **98**, 572 (2004)].
23. C. P. Bean and J. D. Livingston, J. Appl. Phys. **30** (Suppl.) 1205 (1959).
24. A. M. Balbashov, S. G. Karabashev, Ya. M. Mukovskii, *et al.*, J. Cryst. Growth **167**, 365 (1996).
25. F. Mussa, M. Hennion, J. Rodriguez-Carvajal, *et al.*, Phys. Rev. B **54**, 15149 (1996).
26. A. A. Mukhin, V. Yu. Ivanov, V. D. Travkin, *et al.*, Pis'ma Zh. Éksp. Teor. Fiz. **68**, 331 (1998) [JETP Lett. **68**, 356 (1998)].
27. L. I. Buravov and I. F. Shchegolev, Prib. Tekh. Éksp. **2**, 171 (1971); N. I. Solin, S. V. Naumov, and A. A. Samokhvalov, Fiz. Tverd. Tela (St. Petersburg) **42**, 899 (2000) [Phys. Solid State **42**, 925 (2000)].
28. N. F. Mott and E. A. Davis, *Electronic Processes in Non-Crystalline Materials* (Clarendon, Oxford, 1979; Mir, Moscow, 1982), Chaps. 2–4, 6.
29. N. N. Loshkareva, Yu. P. Sukhorukov, and É. A. Neĭfel'd, Zh. Éksp. Teor. Fiz. **117**, 440 (2000) [JETP **90**, 389 (2000)].
30. G. Zhao, Y. S. Wang, D. J. Kang, *et al.*, Phys. Rev. B **62**, R11949 (2000).
31. N. I. Solin and S. V. Naumov, Fiz. Tverd. Tela (St. Petersburg) **45**, 460 (2003) [Phys. Solid State **45**, 486 (2003)].
32. I. G. Austin and N. F. Mott, Adv. Phys. **18**, 41 (1969).
33. A. R. Long, Adv. Phys. **31**, 553 (1982); S. R. Elliott, Adv. Phys. **36**, 135 (1987).
34. V. Yu. Ivanov, V. D. Travkin, A. A. Mukhin, *et al.*, J. Appl. Phys. **83**, 7180 (1998); A. Pimenov, Ch. Hartinger, A. Loidl, *et al.*, Phys. Rev. B **59**, 12419 (1999).
35. N. N. Loshkareva, A. V. Korolev, T. I. Arbuzova, *et al.*, Fiz. Tverd. Tela (St. Petersburg) **44**, 1827 (2002) [Phys. Solid State **44**, 1916 (2002)].
36. A. Seeger, P. Lunkenheimer, J. Hemberger, *et al.*, J. Phys.: Condens. Matter **11**, 3273 (1999).
37. S. V. Vonsovskiĭ, *Magnetism* (Nauka, Moscow, 1971; Wiley, New York, 1974), Chap. 23.
38. A. V. Korolyov, V. Ye. Arkhipov, and V. S. Gaviko, J. Magn. Magn. Mater. **213**, 63 (2000); S. E. Loffland, V. Ray, P. H. Kim, *et al.*, J. Phys.: Condens. Matter **9**, L633 (1997).
39. T. Kasuya and A. Yanase, Solid State Commun. **8**, 1543 (1970).
40. A. O. Sboĭchakov, A. L. Rakhmanov, K. I. Kugel', *et al.*, Zh. Éksp. Teor. Fiz. **122**, 869 (2002) [JETP **95**, 753 (2002)].

Translated by P. Pozdeev

Journal of Experimental and Theoretical Physics, Vol. 101, No. 3, 2005, pp. 547–553.
Translated from Zhurnal Éksperimental'noĭ i Teoreticheskoĭ Fiziki, Vol. 128, No. 3, 2005, pp. 636–644.

ELECTRONIC PROPERTIES OF SOLIDS

Magnetostatic Spin Waves in Two-Dimensional Periodic Structures (Magnetophoton Crystals)

S. L. Vysotskiĭ, S. A. Nikitov, and Yu. A. Filimonov

Institute of Radio-Engineering and Electronics, Russian Academy of Sciences, Moscow, 125009 Russia
e-mail: nikitov@cplire.ru

Received March 2, 2005

Abstract—Series of experiments are carried out to study the propagation of magnetostatic spin waves in ferromagnetic films containing 2D periodic structures formed by etched apertures. For spin waves, such films are analogous to photon crystals (namely, magnetophoton or magnon crystals). The spectra of waves transmitted through the structure display features associated with a change in the spin homogeneity due to etching or radiation loss, as well as with Bragg reflection effect or the emergence of forbidden gaps in the spectrum of propagating waves. © *2005 Pleiades Publishing, Inc.*

1. INTRODUCTION

A large number of research groups and individual scientists have been engaged in recent years in investigating the physics and technology of photon crystals (see, for example, monographs [1–4] and the literature cited therein). Photon crystals are essentially one-, two-, or three-dimensional periodic structures, in which the dielectric properties (refractive index) vary periodically; when an electromagnetic wave (light) propagates in such a crystal, forbidden gaps are formed in its spectrum. The effects characteristic of photon crystals are manifested when the length of the propagating wave is of the same order of magnitude as the period of the structure forming the photon crystal. Along with photon crystals in the optical range (which have a photon bandgap in the visible range), crystals with a photon bandgap in the microwave frequency range are of considerable interest. However, the size of a photon crystal in the range of centimeter or millimeter electromagnetic waves will be quite large, so that practical applications of such crystals are of no interest. An alternative to a photon crystal in the microwave range might be ferromagnetic media (magnetophoton or magnon crystals) [5–15], in which propagating waves are magnons (spin waves). Obtaining crystals analogous to photon crystals and based on magnetic materials (namely, magnon crystals), in which spin waves can propagate, has a number of advantages over photon crystals. First, the wavelength of a spin wave and, hence, the properties of such crystals depend on the external magnetic field and can be controlled by this field. Second, the wavelength of propagating spin waves for a wide class of ferromagnetic materials in the microwave range is on the order of tens or even hundreds of micrometers. The phase and group velocities of spin waves are also functions of the sample size and the applied external field and may vary over a wide range. As a rule, the velocity of spin waves is several orders of magnitude smaller than the velocity of electromagnetic waves in a given medium. Thus, it is possible to obtain crystals with a photon (or magnon) bandgap whose width is on the order of several millimeters. Such crystals may have a planar geometry, which can be extremely important for designing integrated devices such as narrow-frequency optical or microwave filters and high-speed switches. In the cited literature, a theory of microwave properties of magnetophoton and magnon crystals was worked out; in particular, the spectra of electromagnetic and spin waves in multilayer magnetic structures and 2D periodic structures was investigated, as well as nonreciprocal and other properties of magnetophoton crystals. A number of publications are devoted to optical properties of magnetophoton crystals [16–21] (see also the recent review [22]). We proposed [23] a realization of a 2D magnon crystal based on yttrium iron garnet (YIG) films and carried out preliminary measurements of the spectra of magnetostatic spin waves propagating in such crystals.

In this study, we continue the research aimed at obtaining 2D magnon crystals and analysis of their microwave properties; in particular, the propagation of magnetostatic spin waves in such crystals is studied and analyzed in detail.

2. SAMPLES AND EXPERIMENTAL TECHNIQUE

Experiments were made on structures based on a YIG epitaxial film with the following parameters: saturation magnetization $4\pi M_0$ = 1750 G, thickness $d \approx$ 16.1 μm, and the ferromagnetic resonance linewidth $2\Delta H \approx 0.6$ Oe. The film was grown on a gallium gadolinium garnet (GGG) substrate with the (100) crystallographic orientation. A 2D periodic structure with a size of 6×8 mm was etched in the central part of the film of

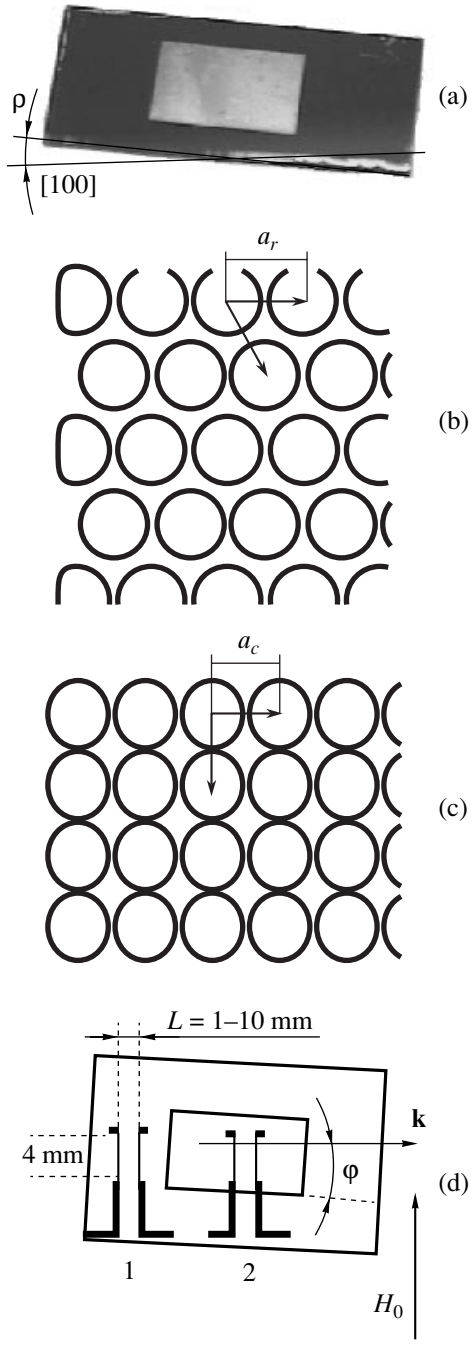

Fig. 1. (a) General view of a ferromagnetic film with an etched structure; (b, c) microphotographs of the surfaces of magnon crystals; (d) model of a delay line based on a YIG film. Angle ρ in (a) characterizes the rotation of the crystallographic ⟨100⟩ direction relative to the film edge. Angle φ in (d), defines the direction of propagation of surface magnetostatic spin wave relative to the longer edge of the film.

size 10 × 20 mm in the form of a system of pits with a diameter of $D \approx 32$ μm (Fig. 1a). We studied films with two types of 2D lattices. The first lattice had a nearly rhombic symmetry with a unit cell edge of $a_r \approx$ 37–40 μm (Fig. 1b). The second structure had the form of a square lattice with an edge length of $a_c \approx 37$ μm (Fig. 1c). For the rhombic lattice, structures with an etch depth t of pits $t_1 \approx 1$ μm and $t_2 \approx 2$ μm were investigated. The pit depth in the square lattice was $t_1 \approx 1$ μm. Measurements were made using a model surface magnetostatic spin wave delay line. The YIG films were fixed to 4-mm-long microstrip transducers with a width of 30 μm, prepared photolithographically on a polycore board. The distance L between the transducers could be varied in the limits L = 1–10 mm. The model of the delay line (Fig. 1d) was placed in the gap of an electromagnet so that the magnetic field $\mathbf{H}_0$ was directed along the transducer. Such a geometry corresponds to the excitation in an isotropic magnetic film of a surface dipole Damon-Eshbach magnetostatic spin wave with the dispersion relation [24]

$$f^2 = f_0^2 + \frac{f_m^2}{4}(1 - \exp(-2kd)), \qquad (1)$$

where f is the frequency of the surface magnetostatic spin wave, k is the wavenumber of the surface magnetostatic spin wave, $f_0^2 = f_H^2 + f_H f_m$ is the threshold frequency ($k \longrightarrow 0$) of the spectrum of the surface magnetostatic spin waves, $f_H = gH_0$, $f_m = g4\pi M_0$, and g = 2.8 MHz/Oe being the gyromagnetic ratio.

We studied the amplitude A and phase θ of the signal transmitted through the model, as well as the level of power P_R reflected from the input transducer for various orientations of the wavevector **k** of the surface magnetostatic spin wave relative to the axes of 2D lattice, which are characterized by angle φ (see Fig. 1d), as functions of frequency f for a fixed value of magnetic field H_0 ($A(f)$, $\theta(f)$, and $P_R(f)$) or of field H_0 for a fixed frequency ($A(H_0)$, $\theta(H_0)$, and $P_R(H_0)$). These dependences were compared for the cases when magnetostatic spin waves propagated outside the region containing a 2D lattice (curves *1* in Figs. 3, 5, and 6) or when at least one of microstrip transducers was in the region of the film occupied by a 2D lattice (curves *2* in Figs. 3, 5, and 6). The reflected signal was measured using a VSWR panoramic gauge and an attenuator R2-67. The amplitude-frequency and phase-frequency characteristics were obtained using an FK2-18 phase-difference and attenuation meter according to the standard scheme of connection of the delay line model in the break of the measuring loop. The phase-frequency characteristics were used for plotting the dispersion relation $f = f(k)$ by the standard technique [25] assuming that the phase incursion $\theta(f)$ of the surface magnetostatic spin wave is connected with its wavenumber by the relation $k(f) = \theta(f)/L$.

It should be noted that film etching to a depth $t \leq$ 2 μm did not lead to the emergence of strong additional anisotropy fields. This follows from a comparison of the dispersion relations $f = f(k)$ (see Fig. 2a), as well as orientation dependences of threshold frequencies $f_0(\varphi)$ (see Fig. 2b) corresponding to the etched and unetched

regions of the film. It can also be seen that the experimental dispersion dependences for spin waves in the wavenumber range $k \leq 400$ cm^{-1} were correctly described by the dispersion relations for such waves in a tangentially magnetized (100) YIG film with a normal uniaxial anisotropy of the easy plane type [26] for values of cubic ($K_1 = H_k M_0$) and uniaxial anisotropy ($K_u = H_u M_0/2$) constants $K_1 \approx 6.2 \times 10^3$ erg/cm^3 and $K_u \approx -10^4$ erg/cm^3 and a thickness of the unetched film region $d^* = d - t \approx 14$ μm (see Figs. 2a and 2b); here, H_k and H_u are the cubic and planar uniaxial anisotropy fields, respectively. We took into account the fact that the edges of the film form angles $\rho \approx 15°$ with the ⟨100⟩ crystallographic directions (see Fig. 1a). However, for $k > 400$ cm^{-1}, the uniaxial anisotropy constant was assumed to be $K_u \approx -1.15 \times 10^4$ erg/cm^3 for better coincidence of the results of calculations with the measuring data. Such a behavior of the dispersion of surface magnetostatic spin waves can be explained, for example, by nonuniformity of the uniaxial anisotropy constant distribution over the thickness due to elastic stresses in the film associated with mismatch between the YIG film and the GGG substrate lattice parameters.

3. EXPERIMENTAL RESULTS AND DISCUSSION

Before analyzing the results of measurements, note that, in accordance with the data in Fig. 2, the region of the film containing a 2D structure can be represented in the form of two contacting layers. The thickness of the upper layer is determined by the etch pit depth $t \leq 2$ μm, while the thickness of the second layer is $d^* \approx 14$ μm. Since surface magnetostatic spin waves with wavenumbers $k \leq 1200$ cm^{-1} were excited in our experiments, which correspond to wavelengths $\lambda \geq 52$ μm (see Fig. 2 and Fig. 4 below), the condition

$$\lambda > d^* \gg t \tag{2}$$

is found to be satisfied. This enables us to treat the film region with the 2D structure as a waveguide of thickness d^* with periodically varying electrodynamic boundary conditions due to the effect of demagnetizing fields of the pits. In this case, we can expect that a spin wave will experience scattering from the periodic structure. Such a mechanism might be manifested most effectively under the conditions of Bragg's diffraction from the periodic structure [27], when wavenumber k satisfies the condition

$$k \approx k_B \approx \pi/\Lambda, \tag{3}$$

where Λ is the period of the 2D lattice in the direction of wave propagation. In this case, a bandgap is formed in the spin wave spectrum [27].

We can also expect that the effect of the 2D lattice is reduced to a periodic change of not only electrodynamic, but also exchange boundary conditions for dynamic magnetization **m** due to a change in the spin mobility at excitation frequencies (1) both in the lattice itself and in a certain transition region at the boundary between the 2D lattice and unetched volume of the film. As a consequence, the dynamic spin pinning [28] takes place in the surface layer; in turn, this effect can be accompanied by a substantial increase in the efficiency of dipole wave hybridization with bulk exchange spin waves [29]. Obviously, in view of lateral inhomogeneity of the structure, we cannot expect in our case the emergence of resonant interaction of spin waves with bulk exchange modes as is the case in regular film-type YIG waveguides with pinned surface spins [30]. However, it can be expected that hybridization of a dipole spin wave with exchange waves will be manifested in the form of radiation loss [31].

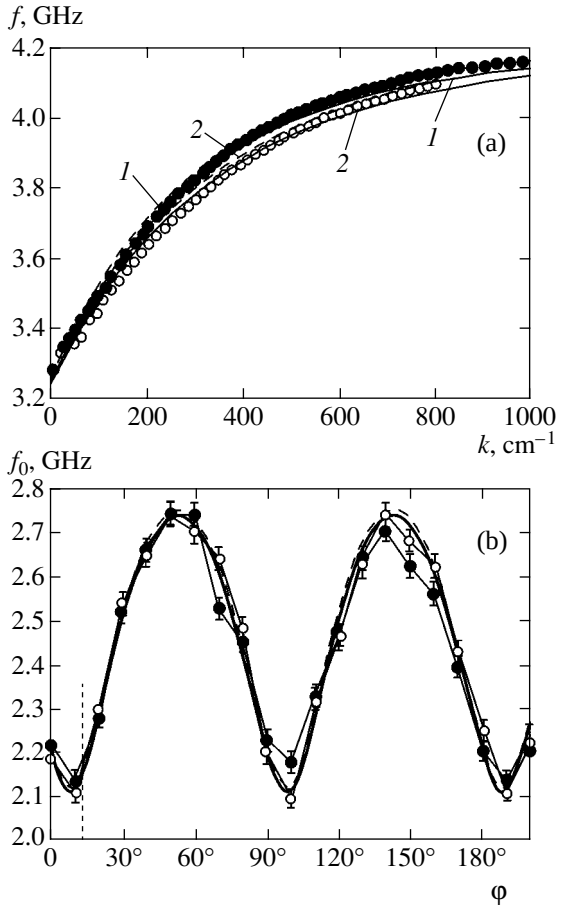

Fig. 2. (a) Measured and calculated dependences $f = f(k)$ for a magnetizing field $H_0 = 625$ Oe. Curves *1* and *2* correspond to the results of calculations for films of thicknesses $d \approx 16.1$ μm and $d^* \approx 14.1$ μm. (b) Measured and calculated dependences $f_0 = f_0(\varphi)$ for a magnetizing field $H_0 = 325$ Oe. Solid and dashed curves in (a) and (b) correspond to calculations for the uniaxial anisotropy field parameters $H_u = -70$ Oe and –80 Oe, respectively. Dark circles show the results of measurements on free regions of the film, while light circles correspond to the presence of a 2D structure.

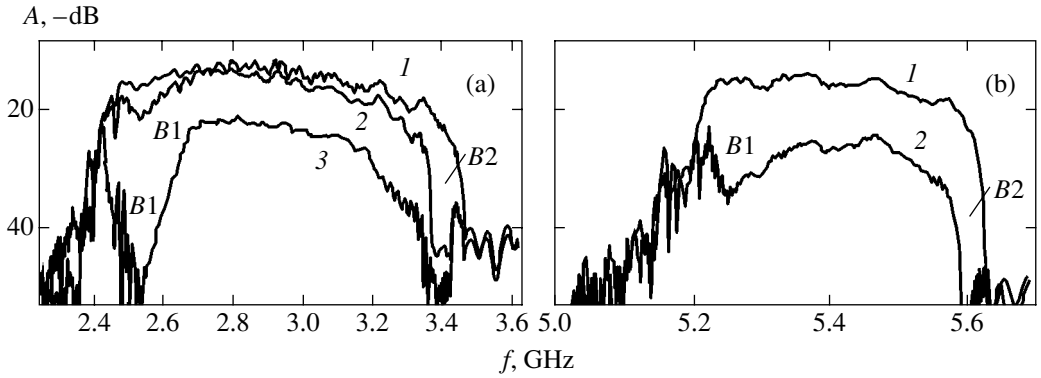

Fig. 3. Amplitude-frequency characteristic of the model for the spacing between aerials $L \approx 1.5$ mm in the case when they are arranged in the film regions without (*1*) and with (*2*) a square lattice for the magnetizing field $H_0 = 398$ (a) and 1190 Oe (b). Curve *3* is the amplitude-frequency characteristic with aerials arranged on the segment with a square lattice at a distance $L \approx 3$ mm. Spin waves propagate along the lattice axis ($\varphi = 0$).

It should be noted that the effect of surface spin pinning in approximation (2) with allowance for the symmetry of 2D structures can be associated with the existence of a uniaxial surface anisotropy with the axis normal to the film surface. In the case of a tangentially magnetized structure [32], such a surface anisotropy does not limit the mobility of the m_y component tangential to the film surface,

$$\frac{\partial m_y}{\partial z} = 0, \tag{4}$$

while the m_z component normal to the surface is found to be pinned,

$$\frac{\partial m_z}{\partial z} - h m_z = 0, \tag{5}$$

where parameter h characterizes the degree of spin pinning and has dimensions of cm^{-1}. In this case, the interaction between the dipole surface magnetostatic spin wave with exchange waves can be described by the effective pinning parameter [32]:

$$h^{\text{eff}} = \frac{h}{2}\left\{1 - \left[1 + \frac{4f^2}{f_m^2}\right]^{-1/2}\right\}. \tag{6}$$

The dependence of the effective pinning parameter on frequency (6) reflects the variation of ellipticity of magnetization precession in the film with frequency f,

$$\frac{m_z}{m_y} = \frac{if}{f_m + f_H + gM_0\alpha k^2}, \tag{7}$$

where $\alpha = 3 \times 10^{-12}$ cm^2 is the nonuniform exchange constant. It can be see from formula (7) that the magnetization precession ellipse for $f \ll f_m$ is extended along the film surface ($m_z \ll m_y$) and the effect of pinning on the motion of magnetization is weak. For this reason, the value of the effective pinning parameter h^{eff} (6) will also be small.

3.1. Square Lattice

Figure 3 shows the amplitude-frequency dependences of the model with a spacing L between the aerials of approximately 1.5 mm for two values of the magnetic field in the case when spin waves propagate along the axis of a 2D square lattice ($\varphi = 0$). Comparison of curves *1* and *2* shows that the lattice noticeably changes the conditions of spin wave propagation. In the magnetic field range $H_0 \le 500$ Oe (Fig. 3a), such variations are manifested in the form of two absorption bands ($B1$ and $B2$) of the signal. One of these bands ($B1$) is observed near the threshold frequency f_0 of the spectrum. To make the existence of the $B1$ band more visual, Fig. 3a shows the amplitude-frequency characteristic for a distance $L \approx 3$ mm between the transducers (see curve *3*). Band $B2$ is formed in the upper (short-wave) part of the excitation frequency band for spin waves. It should be noted that losses change insignificantly at frequencies that do not fall in absorption bands $B1$ and $B2$. At the same time, the lattice losses for $H_0 > 500$ Oe noticeably increase in the entire frequency band corresponding to the existence of spin waves as compared to losses in a free film (Fig. 3b). The nature of variations of the amplitude-frequency characteristic is such that an increase in the loss can mainly be attributed to the expansion of absorption band $B1$.

Curve *1* in Fig. 4 shows the dispersion relation of spin waves in a structure with a square lattice for parameters corresponding to Fig. 3a, which is plotted using the phase-frequency characteristic. It can be seen that a "gap" is formed in the dispersion relation in the range of wavenumber $k^*_{\text{cub}} \approx 950$ cm^{-1} at frequencies $f_B = 3390$ MHz, which belong to absorption band $B2$. In this case, no noticeable changes were observed in the dispersion relation at frequencies corresponding to the $B1$ absorption band.

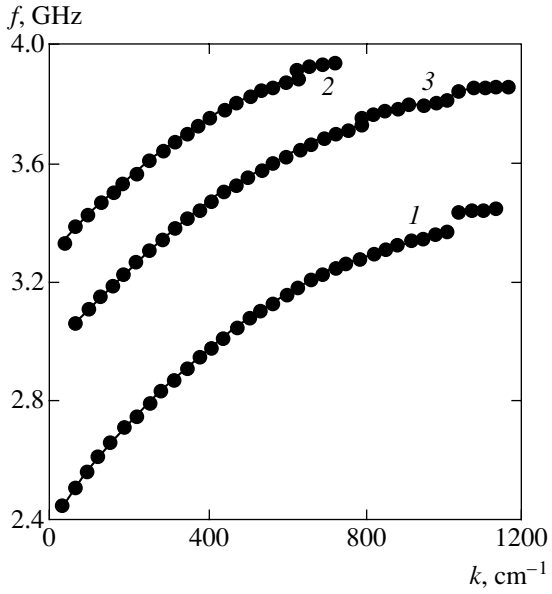

Fig. 4. Dispersion relations for spin waves in 2D structures with a square lattice for $\varphi = 0$, $H_0 \approx 398$ Oe (curve *1*); $\varphi = 45°$, $H_0 \approx 525$ Oe (curve *2*), and with a rhombic lattice for $\varphi = 15°$ (the direction of the wavevector of the spin wave is close to the direction of the lattice axis), $H_0 \approx 560$ Oe (curve *3*).

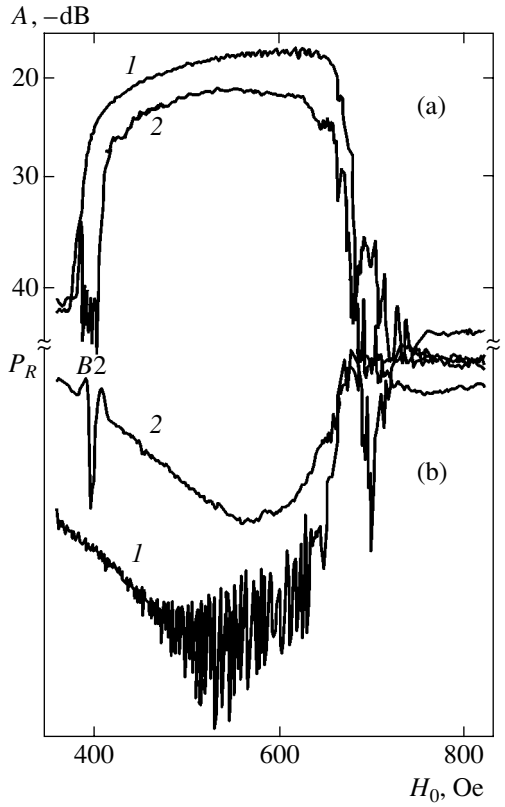

Fig. 5. Dependence of the levels of signal $A(H_0)$ transmitted through the model of the delay line (a) and reflected from the input transducer of microwave power $P_R(H_0)$ (b) on the magnetic field H_0 for the arrangement of the aerials in unetched region of the film (curves *1*) and in the region containing a square lattice (curves *2*). The frequency f = 3390 MHz of the microwave signal corresponds to the position of the *B2* gap in the amplitude-frequency characteristic of the model for experimental parameters corresponding to Fig. 3a.

Let us consider dependences $A(H_0)$ and $P_R(H_0)$ for a signal frequency of $f_B = 3390$ MHz for the same lattice (Fig. 5). Comparison of curves *1* and *2* shows that the level of reflected power oscillates in a field $H_0 \approx$ 400 Oe, while the $A(H_0)$ dependence acquires a region with strong attenuation, which corresponds to the *B*2 band on the amplitude-frequency dependence shown in Fig. 3a. On the contrary, for values of $H_0 \approx 500$–680 Oe for which the chosen frequency $f_B = 3390$ MHz is close to the threshold frequency f_0 of the spin wave spectrum and absorption band *B*1 is formed on the amplitude-frequency characteristic, no singularities were observed in the $P_R(H_0)$ dependence.

It follows from Figs. 3–5 that absorption band *B*2 is associated with the gap in the spectrum, within which the level of reflected power increases. Such a behavior of dispersion and reflected power indicates that the emergence of absorption band *B*2 is associated with "nontransmission" of the signal through the structure; the most probable reason for its emergence is Bragg scattering of spin waves from the periodic structure. This also follows from the close values of the wavenumbers corresponding, on the one hand, to the gap region in the dispersion relation for spin waves in Fig. 4 and, on the other hand, to the fulfillment of the Bragg resonance condition (3). Indeed, in the case when these waves propagate along the axes of the square lattice, the period Λ of the 2D structure coincides with the length a_c of the unit cell edge ($\Lambda = a_c \approx 37$ μm). Using Bragg resonance condition (3), we obtain $k_B \approx 850$ cm^{-1}, which is in good agreement with the values of wavenumbers in the gap region in Fig. 4 ($k_B \approx 850$ cm$^{-1} \approx k_c^* \approx 950$ cm^{-1}). The behavior of the *B*2 band upon a change in the orientation of wavevector **k** relative to the axes of the lattice indicates that its emergence on the amplitude-frequency characteristic in Fig. 3 is associated with Bragg resonance on a 2D square lattice. When the lattice rotates through an angle $|\varphi| > 15°$, the *B*2 band on the amplitude-frequency characteristic of the model vanished and emerged only for values of $\varphi \approx 45°$. In this case, the $A(H_0)$ dependence shows a dip, while the $P_R(H_0)$ dependence oscillates analogously to the case of $\varphi = 0$ depicted in Fig. 5. At the same time, the period of the 2D lattice for $\varphi \approx 45°$ is $\Lambda_c^{45°} \approx 37\sqrt{2} \approx$ 52 μm. In this case, the Bragg resonance should be manifested for a wavenumber $k_B \approx 600$ cm^{-1}. Indeed, the dispersion curve plotted for this case (curve *2* in Fig. 4) shows a gap in the spin wave spectrum for $k_c^{45°} \approx 630$ cm^{-1}.

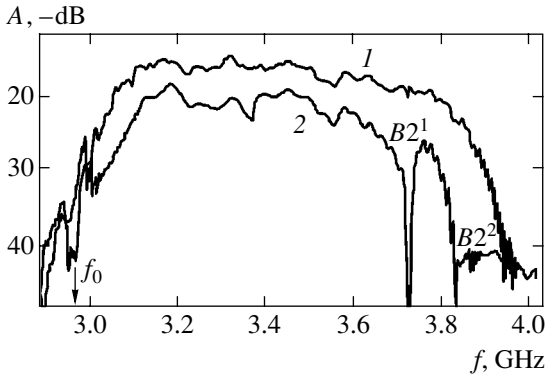

Fig. 6. Amplitude-frequency characteristic of the model with a rhombic lattice for spin waves propagating at an angle $\varphi \approx 15°$ (the direction of the wavevector is close to the direction of the lattice axis) for $H_0 \approx 560$ Oe.

Let us now consider the reason for the emergence of absorption band $B1$ and loss escalation in an increasing magnetic field. It follows from Figs. 4 and 5 that no noticeable deviations from the case of a free film are observed at frequencies corresponding to the $B1$ band either in the dispersion relation $f(k)$, or in the form of the $P_R(H_0)$ dependence. Consequently, emergence of losses in the $B1$ band and their growth with field H_0 should be attributed to the effects accompanying the wave propagation. It should be noted that an appreciable increase in losses in the film with a 2D structure occurs in fields $H_0 \geq 500$ Oe, when the condition $f \gg f_m/2 \approx 2.5$ GHz holds for the spin wave excitation frequency and, in accordance with relation (6), the effective pinning parameter for surface spins increases. These arguments allow us to attribute the emergence of the $B1$ absorption band and increase in losses with H_0 to the mechanism of radiation losses due to emission of bulk exchange spin waves from the film surface [31, 33].

However, we should note a number of substantial differences in the behavior of radiation loss in our case and also in YIG films with a spin pinning constant that does not vary over the film surface, in which the coupling between dipole and exchange waves is proportional to wavenumber k. For a fixed value of field H_0, this leads to an increase in radiation loss with k. On the contrary, in the case under investigation, radiation losses attain the highest values and are manifested primarily in the range of small wavenumbers. This difference can be explained by the following two circumstances. First, not only the magnetization components m_z normal to the surface, but also tangential components m_y will be pinned at spin wave frequencies due to the effect of the demagnetization fields of the pits in the surface layer of thickness t. Such a pinning mechanism will clearly be effective in the region of small magnetizing fields also. Second, in the range of small wavenumbers k, the lattice can be treated (relative to the surface magnetostatic spin wave) as a homogeneous layer with parameters differing from those in the bulk of the film since the wavelength is considerably larger than the lattice period,

$$\lambda \gg \Lambda. \tag{8}$$

The coupling of a spin wave with exchange waves over a wavelength is virtually constant, which ensures the effectiveness of the radiation loss mechanism. As the values of k increase, condition (8) becomes invalid and the concept of exchange waves propagating from the surface in the form of plane waves is violated. As a result, the overlap integral of the fields of the dipole spin wave and exchange waves decreases, which in turn reduces radiation loss upon an increase in wavenumber k.

3.2. Rhombic Lattice

We will consider the effect of a rhombic lattice on the propagation of a surface magnetostatic spin wave for pits with an etching depth $t_2 \approx 2$ μm, for which the effect is manifested more clearly than for $t_1 \approx 1$ μm. The emergence of the $B2$ absorption band associated with the Bragg diffraction for orientations of wavevector k close to the directions $\mathbf{a}_r$ of the lattice axes was a consequence of the rhombic lattice symmetry. In the lattice considered here, such situations could correspond to values of angles $\varphi_B^r \approx 25$, 90, 155, 210, 270, and 330° (see Fig. 1d). The experimental values of the angles were quite close to these values, but could differ by $\delta\varphi \approx \pm(5\ldots10)°$. The effect of angle φ of radiation exchange losses and on the $B1$ band could not be separated.

The behavior of the amplitude-frequency characteristic of a surface magnetostatic spin wave in a rhombic lattice upon an increase in the field was on the whole analogous to that in a square lattice, depicted in Fig. 3. However, in the range of not very strong fields H_0 in the shortwave part of the amplitude-frequency characteristic, two $B2$ absorption bands were observed instead of one band. Figures 6 and 4 (curve *3*) show the amplitude-frequency characteristic and the dispersion relation, respectively, for $\varphi \approx 20°$ and $H_0 \approx 560$ Oe. It can be seen that interference fading bands $B2$, corresponding to the emergence of a "gap" in the dispersion relation, are observed in the amplitude-frequency characteristic at frequencies $f_{B2}^1 \approx 3730$ MHz and $f_{B2}^2 \approx 3830$ MHz. The $P_R(H_0)$ dependences measured at the signal frequencies f_{B2} demonstrated, analogously to Fig. 5, oscillations of reflected power, which indicated deterioration of matching between the microstrip transducer and the film. It can be seen from Fig. 4 that the positions of the gaps in the dispersion relation correspond to wavenumbers $k_r^1 \approx 780$ cm^{-1} for the first gap $B2^1$ and $k_r^2 \approx 1050$ cm^{-1} for the second gap $B2^2$. If we take into account the fact that the lattice period $\Lambda \approx a_{\text{rom}} \approx$

40 μm, relation (3) gives $k_B \approx 785$ cm^{-1}, which correspond in order of magnitude to values of $k_r^1 \approx 780$ cm^{-1}.

If we also attribute the "second" absorption band $B2^2$ to Bragg diffraction from the 2D lattice, relation (3) implies that the period of the structure must be on the order of the pit diameter, $\Lambda \approx \pi/k_r^2 \approx 30$ μm $\approx D \approx$ 32 μm for the wavenumber $k_r^2 \approx 1050$ cm^{-1} corresponding to this absorption band. It should be noted that the effect of exchange radiation losses on the propagation of spin waves in the rhombic structure studied here is not as noticeable as in the case of a square lattice. This can be explained by the lower number density of pits per unit surface area of the film for the rhombic lattice (see Figs. 1b and 1c).

4. CONCLUSIONS

Thus, we have studied the propagation of surface magnetostatic waves in 2D magnon crystals. These crystals were obtained on the basis of thin ferromagnetic YIG films with structures formed by etch pits. When magnetostatic waves propagate in such crystals, their properties change substantially. The effectiveness of such a change is determined by the parameters of magnon crystals and the external magnetic field. In particular, the spectra of propagating waves display bandgaps at a frequency determined by the period of the structure formed by etch pits and the structure symmetry. Changes in the spectra of waves due to radiation losses during scattering of waves from surface inhomogeneities of the ferromagnetic film are also detected.

ACKNOWLEDGMENTS

This study was financed by the Russian Foundation for Basic Research (project nos. 04-02-17537 and 05-02-17361).

REFERENCES

1. J. D. Joannopoulos, R. D. Meade, and J. N. Winn, *Photonic Crystals: Molding the Flow of Light* (Princeton Univ. Press, Princeton, 1995).
2. *Photonic Bandgap Materials*, Ed. by C. M. Soukoulis (Kluwer Academic, The Netherlands, 1996).
3. K. Sakoda, *Optical Properties of Photonic Crystals* (Springer, Berlin, 2001), Springer Ser. Opt. Sci., Vol. 80.
4. S. G. Johnson and J. D. Joannopoulos, *Photonic Crystals: The Road from Theory to Practice* (Kluwer, Boston, 2002).
5. J. O. Vasseur, L. Dobrzynski, B. Dijafari-Rouhani, and H. Puszkarski, Phys. Rev. B **54**, 1043 (1996).
6. H. Al-Wahsh, A. Akjouj, B. Dijafari-Rouhani, *et al.*, Phys. Rev. B **59**, 8709 (1999).
7. C. S. Kee, J. E. Kim, H. Y. Park, *et al.*, Phys. Rev. B **61**, 15523 (2000).
8. M. Krawszyk, J. C. Levy, D. Mercier, and H. Puszkarski, Phys. Lett. A **282**, 186 (2001).
9. H. Al-Wahsh, A. Mir, A. Akjouj, *et al.*, Phys. Lett. A **291**, 333 (2001).
10. A. Mir, H. Al-Wahsh, A. Akjouj, *et al.*, Phys. Rev. B **64**, 224403 (2001).
11. A. Mir, H. Al-Wahsh, A. Akjouj, *et al.*, J. Phys.: Condens. Matter **14**, 637 (2002).
12. A. Akjouj, A. Mir, B. Djafari-Rouhani, *et al.*, Surf. Sci. **482–485**, 1062 (2002).
13. A. Figotin and I. Vitebsky, Phys. Rev. E **63**, 066609 (2001).
14. S. A. Nikitov, Ph. Tailhades, and C. S. Tsai, J. Magn. Magn. Mater. **236**, 320 (2001).
15. Yu. V. Gulyaev and S. A. Nikitov, Dokl. Akad. Nauk **380**, 469 (2001) [Dokl. Phys. **46**, 687 (2001)].
16. M. Inoue and T. Fujii, J. Appl. Phys. **81**, 5659 (1997).
17. M. Inoue, K. I. Arai, T. Fujii, and M. Abe, J. Appl. Phys. **83**, 6768 (1998).
18. S. Sakaguchi and N. Sugimoto, Opt. Commun. **162**, 64 (1999).
19. S. Sakaguchi and N. Sugimoto, J. Opt. Soc. Am. A **16**, 2045 (1999).
20. M. Inoue, K. I. Arai, M. Afujii, *et al.*, J. Magn. Soc. Jpn. **23**, 1861 (1999).
21. S. A. Nikitov and Ph. Tailhades, Opt. Commun. **190**, 389 (2001).
22. I. L. Lyubchanskii, N. N. Dadoenkova, M. I. Lyubchanskii, *et al.*, J. Phys. D: Appl. Phys. **36**, R277 (2003).
23. Yu. V. Gulyaev, S. A. Nikitov, L. V. Zhivotovskiĭ, *et al.*, Pis'ma Zh. Éksp. Teor. Fiz. **77**, 670 (2003) [JETP Lett. **77**, 567 (2003)].
24. R. W. Damon and J. R. Eshbach, J. Phys. Chem. Solids **19**, 308 (1961).
25. V. V. Medvedev and Yu. K. Fetisov, *Problems in Cybernetics. Devices and Systems* (Mosk. Inst. Radiotekh. Élektron. Avtomat., Moscow, 1983), p. 171 [in Russian].
26. R. A. Lemons and D. A. Auld, J. Appl. Phys. **52**, 7360 (1981).
27. Yu. V. Gulyaev, S. A. Nikitov, and V. P. Plesskiĭ, Radiotekh. Élektron. (Moscow) **23**, 2282 (1981).
28. P. E. Wigen, C. F. Kooi, and M. R. Shanabarger, Phys. Rev. Lett. **9**, 206 (1962).
29. Yu. I. Bespyatykh, V. I. Zubkov, and V. V. Tarasenko, Fiz. Tverd. Tela (Leningrad) **19**, 3409 (1977) [Sov. Phys. Solid State **19**, 1991 (1977)].
30. Yu. V. Gulyaev, A. S. Bugaev, P. E. Zil'berman, *et al.*, Pis'ma Zh. Éksp. Teor. Fiz. **30**, 600 (1979) [JETP Lett. **30**, 565 (1979)].
31. G. T. Kazakov, A. G. Sukharev, and Yu. A. Filimonov, Fiz. Tverd. Tela (Leningrad) **32**, 3571 (1990) [Sov. Phys. Solid State **32**, 2071 (1990)].
32. N. M. Salanskiĭ and M. Sh. Erukhimov, *Physical Properties and Application of Magnetic Films* (Nauka, Novosibirsk, 1975) [in Russian].
33. T. Wolfram and R. E. De Wames, Phys. Rev. B **1**, 4358 (1970).

Translated by N. Wadhwa

Journal of Experimental and Theoretical Physics, Vol. 101, No. 3, 2005, pp. 554–561.
Translated from Zhurnal Éksperimental'noĭ i Teoreticheskoĭ Fiziki, Vol. 128, No. 3, 2005, pp. 645–654.

ELECTRONIC PROPERTIES OF SOLIDS

Interface Phonons in Semiconductor Nanostructures with Quantum Dots

M. Yu. Ladanov[a], A. G. Milekhin[a], A. I. Toropov[a], A. K. Bakarov[a], A. K. Gutakovskii[a], D. A. Tenne[b], S. Schulze[c], and D. R. T. Zahn[c]

[a]*Institute of Semiconductor Physics, Siberian Division, Russian Academy of Sciences, pr. Akademika Lavrent'eva 13, Novosibirsk, 630090 Russia*
e-mail: milekhin@thermo.isp.nsc.ru
[b]*Department of Physics, Pennsylvania State University, 104 Davey Lab., University Park, PA 16802, USA*
[c]*Institut für Physik, Technische Universität Chemnitz, D-09107, Chemnitz, Germany*
Received April 21, 2005

Abstract—The vibrational spectra of structures with InAs quantum dots in an AlGaAs matrix and AlAs quantum dots in an InAs matrix are investigated experimentally and theoretically. The Raman spectra exhibit features that correspond to transverse-optical (TO), longitudinal-optical (LO), and interface phonons. The frequencies of interface phonons in InAs and AlAs quantum dots and in an AlGaAs matrix with various concentrations of aluminum are calculated with the use of experimental values of transverse- and longitudinal-optical phonons in the approximation of a dielectric continuum. It is shown that the model of a dielectric continuum adequately describes the behavior of interface phonons in structures with quantum dots under the assumption that the quantum dots are spheroidal. © *2005 Pleiades Publishing, Inc.*

1. INTRODUCTION

Periodic semiconductor structures with self-organized quantum dots, which are characterized by unique electronic and optical properties, are one of the most challenging objects of research in semiconductor physics. These objects attract interest in view of the possibility to design, on the basis of these objects, new devices such as quantum transistors, high-speed memory elements, narrowband light-emitting diodes, heterojunction lasers, and infrared (IR) photodetectors [1–3].

Progress in the epitaxial growth technology has made it possible to produce quantum-dot structures with controllable properties on the basis of a series of materials (InAs/Ga(Al)As, In(Ga)As/InP [4, 5], Ge/Si, GaSb/InP, GaN/AlN) [6–9]. The most thoroughly investigated system is InAs/Ga(Al)As; a large number of papers have been devoted to the study of its optical and electronic properties [2]. However, despite the fact that the vibrational spectrum contains information about the structural properties (the size, dispersion of size, and the shape) of quantum dots [10, 11] and mechanical stress in nanostructures [12, 13], the vibrational properties have been poorly studied even in this system. The most widespread methods for studying vibrational spectra are the Raman spectroscopy and the infrared (IR) spectroscopy. These methods are complementary because they use different selection rules; therefore, they allow one to study vibrational excitations of different types of symmetry. The Raman and IR spectroscopy have been applied to study optical phonons in stressed [13, 14] and relaxed [12, 15] quantum dots, in quantum dots of InGaAs solid solutions [16], and in a wetting layer [17, 18].

Earlier, a theoretical analysis of the spectrum of optical phonons in quantum dots was carried out within the model of valence-force fields [19, 20] and in the approximation of a dielectric continuum [15]. The model of valence-force fields is an empirical atomistic model and allows one to calculate the phonon frequencies in quantum dots consisting of a few thousand atoms. Calculations with the use of this model involve large arrays of data; this makes these calculations rather tedious. The approximation of a dielectric continuum is a macroscopic model and can rather easily be applied to the calculation of the frequencies of interface phonons localized near the interface between the materials of the quantum dots and the matrix [21].

The simplest model of a dielectric continuum deals with spherical quantum dots of one material embedded into the matrix of another material [22, 23]. In this case, the eigenfrequencies are determined from the condition

$$\frac{\epsilon_1(\omega_{lm})}{\epsilon_2(\omega_{lm})} = -1 - \frac{1}{l}, \qquad (1)$$

where ϵ_1 and ϵ_2 are the dielectric functions of the quantum dots and the matrix, respectively; ω_{lm} are the eigenfrequencies of interface phonons; and l is a quantum number of a phonon ($l = 1, 2, \ldots$).

As a rule, the shape of a real quantum dot is different from a sphere [24, 25] (a truncated pyramid for a system of InAs quantum dots in a GaAs matrix [26], a

hemisphere for Ge quantum dots in a Si matrix [27], and an ellipsoid for AlAs quantum dots in an InAs matrix [28]). Therefore, the model of a dielectric continuum was further developed in [29, 30], where it was assumed that quantum dots are spheroidal. The reduction of the symmetry of quantum dots from spherical to spheroidal complicates the condition for the eigenfrequencies of interface phonons: these frequencies will now depend on two quantum numbers, *l* and *m*.

In [30], the dielectric function of a matrix is considered that does not depend on frequency; this provides a unique set of interface modes whose frequencies lie between the frequencies of TO and LO phonons in quantum dots. Such an approach is justified if a model deals with quantum dots in a vitreous or an organic matrix.

In [29], it was assumed that the dielectric functions of both the quantum dots and the material of the matrix depend on frequency; unlike the dielectric-continuum model considered in [30], this yields two sets of interface modes. The first set, which refers to quantum dots, lies in the spectral range between TO and LO phonons in the material of quantum dots. The other set lies in the frequency range between the corresponding values of bulk phonons in the matrix material.

Despite the progress made in the theoretical description of interface phonons in spheroidal quantum dots, there is a lack of experimental research in interface phonons in structures with self-organized quantum dots [11, 13].

In this paper, we present the results of investigating interface phonons in structures with InAs and AlAs quantum dots by the methods of Raman spectroscopy and compare them with the data obtained by calculating the interface phonons in the approximation of a dielectric continuum.

2. THEORY

Let us write out the basic equations necessary for the analysis of the dielectric-continuum approximation in polar materials [30, 31]. The Born–Huang equation of motion can be represented as follows:

$$\ddot{w} = -\omega_{TO}^2 w + \sqrt{\frac{\epsilon_0 - \epsilon_\infty}{4\pi}\omega_{TO}^2}E, \tag{2}$$

where the polarization *P* can be expressed as

$$P = \sqrt{\frac{\epsilon_0 - \epsilon_\infty}{4\pi}\omega_{TO}^2}w + \frac{\epsilon_\infty - 1}{4\pi}E. \tag{3}$$

Here, $w = \sqrt{N\mu}\,u$, where *u* is a relative displacement between a pair of ions with reduced mass μ in a crystal with concentration *N*, *E* is the electric field, ω_{TO} and ω_{LO} are the frequencies of transverse- and longitudinal-optical phonons, and ϵ_0 (ϵ_∞) is the static (high-frequency) dielectric constant of a polar material. In addition, we assume that the Lidden–Sacks–Teller relation $\omega_{LO}^2/\omega_{TO}^2 = \epsilon_0/\epsilon_\infty$ holds.

For the electric field to satisfy the Maxwell equations, it is necessary that the electric induction

$$\mathbf{D} = \epsilon(\omega)\mathbf{E} = \mathbf{E} + 4\pi\mathbf{P}$$

should satisfy the Gauss equation

$$\nabla \cdot \mathbf{D} = 0.$$

Using the relation

$$\mathbf{E} = -\nabla\varphi,$$

we can write out the basic equation of dielectric approximation:

$$\epsilon(\omega)\nabla^2\varphi = 0. \tag{4}$$

It is assumed that the time dependence of all the quantities introduced above is harmonic: $f(t) \propto \exp(-i\omega t)$. In the absence of damping, the frequency-dependent dielectric function $\varepsilon(\omega)$ of a polar material is defined by

$$\epsilon(\omega) = \epsilon_\infty\frac{\omega_{LO}^2 - \omega^2}{\omega_{TO}^2 - \omega^2}. \tag{5}$$

Interface phonons are directly related to the electric potential, which must satisfy the Laplace equation $\nabla^2\varphi = 0$. Therefore, one of the possible solutions to Eq. (4) is $\epsilon(\omega) \neq 0$ for $\omega \neq \omega_{LO}$. The boundary condition at the interface *S* between two media, the continuity of the normal components of **D**, is expressed as

$$\epsilon_1\left[\frac{\partial\varphi_1}{\partial n}\right]_S = \epsilon_2\left[\frac{\partial\varphi_2}{\partial n}\right]_S. \tag{6}$$

Since the object of our study are interface phonons in spheroidal quantum dots, it is convenient to pass from Cartesian coordinates to spheroidal (prolate and oblate) coordinate systems [30].

The prolate system of coordinates ξ, η, ϕ is used for calculating the frequencies of interface phonons for prolate quantum dots and is expressed in terms of Cartesian coordinates as follows:

$$\begin{aligned} x &= b\sqrt{(\xi^2 - 1)(1 - \eta^2)}\cos\phi, \\ y &= b\sqrt{(\zeta^2 - 1)(1 - \eta^2)}\sin\phi, \\ z &= b\xi\eta, \end{aligned} \tag{7}$$

whereas the oblate system of coordinates is convenient for determining the frequencies of interface phonons in oblate quantum dots:

$$\begin{aligned} x &= b\sqrt{(\xi^2 + 1)(1 - \eta^2)}\cos\phi, \\ y &= b\sqrt{(\xi^2 + 1)(1 - \eta^2)}\sin\phi, \\ z &= b\xi\eta, \end{aligned} \tag{8}$$

where $\xi \geq 1$ for the prolate system, $\xi \geq 0$ for the oblate system, and $-1 \leq \eta \leq 1$ and $0 \leq \phi \leq 2\pi$ for both systems. The expression $\xi = \text{const}$ describes an ellipsoid of rotation with the rotation axis (z axis) directed along the principal axes of the ellipsoid; $2b$ is the interfocal distance.

Consider an elliptic surface defined by the formula $\xi = \xi_0 = \text{const}$. In our model, the interior domain defined by $1 \leq \xi \leq \xi_0$ for prolate and oblate systems of coordinates is one of the polar semiconductors with the dielectric function $\epsilon(\omega)$ given by (5), where ω is an eigenfrequency corresponding to interface vibrations of a spheroidal quantum dot. The exterior, with respect to the elliptic surface, domain defined by the relation $\xi \geq \xi_0$ is an infinite medium with the dielectric function given by (5).

The Laplace equation can be separated in prolate spheroidal coordinates; a solution to the above-described model can be sought for in the form

$$\begin{aligned}\varphi^{<} &= A_{lm} R_l^m(\xi) Y_{lm}(\eta, \phi), \quad \xi \leq \xi_0, \\ \varphi^{>} &= A_{lm} \frac{R_l^m(\xi_0)}{Q_l^m(\xi_0)} Q_l^m(\xi) Y_{lm}(\eta, \phi), \quad \xi \geq \xi_0,\end{aligned} \tag{9}$$

where A_{lm} are Fourier coefficients and $Y_{lm}(\eta, \phi)$ are ordinary harmonic spherical functions. The same expression applies to the oblate system of coordinates after certain transformations and the replacement $\xi \longrightarrow i\xi$.

The functions $R_l^m(\xi)$ and $Q_l^m(\xi)$ in Eq. (9) are expressed in terms of hypergeometric function F:

$$\begin{aligned}R_l^m(\xi) &= \frac{(2l)!(\xi^2 - 1)^{m/2} \xi^{l-m}}{2^l l!(l-m)!} \\ &\times F\left[\frac{m-l}{2}, \frac{m-l+1}{2}, \frac{1}{2} - l, \frac{1}{\xi^2}\right], \\ Q_l^m(\xi) &= \frac{2^m (l-m)! \Gamma(1/2)(\xi^2 - 1)^{m/2}}{\Gamma(l + 3/2)(2\xi)^{l+m+1}} \\ &\times F\left[\frac{l+m+1}{2}, \frac{l+m+2}{2}, l + \frac{3}{2}, \frac{1}{\xi^2}\right],\end{aligned} \tag{10}$$

where $\Gamma(x)$ is the gamma function. For the oblate system of coordinates, these functions are expressed in similar terms; however, after the replacement $\xi \longrightarrow i\xi$ and certain algebraic transformations, they can be represented as the following functions of $i\xi$:

$$\begin{aligned}R_l^m(i\xi) &= \frac{(2l)!(\xi^2 + 1)^{m/2} \xi^{l-m}}{2^l l!(l-m)!} \\ &\times F\left[\frac{m-l}{2}, \frac{m-l+1}{2}, \frac{1}{2} - l, -\frac{1}{\xi^2}\right], \\ Q_l^m(i\xi) &= \frac{2^l l!(l+m)!(\xi^2 + 1)^{m/2} \xi^{-l-m-1}}{(2l+1)!} \\ &\times F\left[\frac{l+m+1}{2}, \frac{l+m+2}{2}, l + \frac{3}{2}, -\frac{1}{\xi^2}\right].\end{aligned} \tag{11}$$

Here, the angular moments of the harmonic functions take the values $l = 1, 2, 3, \ldots$ and $|m| \leq l$.

For $\xi = \xi_0$, the boundary condition (6) defines the relations

$$\begin{aligned}f_{lm}^P(\xi_0) &= \frac{\epsilon(\omega)}{\epsilon_D(\omega)} \equiv \left(\frac{d}{d\xi} \ln Q_l^m(\xi)\Big|_{\xi_0}\right)\left(\frac{d}{d\xi} \ln R_l^m(\xi)\Big|_{\xi_0}\right)^{-1}, \\ f_{lm}^O(\xi_0) &= \frac{\epsilon(\omega)}{\epsilon_D(\omega)} \equiv \left(\frac{d}{d\xi} \ln Q_l^m(i\xi)\Big|_{\xi_0}\right) \\ &\times \left(\frac{d}{d\xi} \ln R_l^m(i\xi)\Big|_{\xi_0}\right)^{-1}\end{aligned} \tag{12}$$

for the prolate and oblate coordinate systems, respectively. The universal parameters f_{lm}^P and f_{lm}^O do not depend on the nature of the material or on the normalization of the functions R_l^m and Q_l^m; however, what is especially important, they depend on the geometry of quantum dots. The conditions

$$\begin{aligned}\frac{\omega_{lm}^2}{\omega_{\text{LO}}^2} &= \frac{\epsilon_0 - \epsilon_D f_{lm}^P(\xi_0)}{\epsilon_\infty - \epsilon_D f_{lm}^P(\xi_0)}, \\ \frac{\omega_{lm}^2}{\omega_{\text{TO}}^2} &= \frac{\epsilon_0 - \epsilon_D f_{lm}^O(\xi_0)}{\epsilon_\infty - \epsilon_D f_{lm}^O(\xi_0)}\end{aligned} \tag{13}$$

for the eigenfrequencies of interface phonons in prolate and oblate coordinate systems, respectively, allow one to calculate the frequencies of interface phonons.

Note that, in contrast to the case of spherical quantum dots, the eigenfrequencies of interface phonons depend on two quantum numbers, l and m, and on the parameter ξ_0. It can be shown that, for $\xi_0 \longrightarrow 0$, Eq. (13) yields the following relation for the eigenfrequencies in spherical quantum dots [31]:

$$\frac{\omega_l^2}{\omega_{\text{TO}}^2} = \frac{\epsilon_0 l + \epsilon_D(l+1)}{\epsilon_\infty l + \epsilon_D(l+1)}, \tag{14}$$

which is identical to formula (1).

For InAs quantum dots in the form of oblate spheroids in an AlAs matrix, the frequencies of interface modes as a function of the quantum number m for the semiaxis ratio $R_p/R_e = 1/2$ are shown in Fig. 1a. The semiaxis R_p lies in the plane of the layers of the structure, while R_e is perpendicular to the surface. Figure 1a shows that the calculated values of the frequencies of interface phonons in InAs quantum dots and in the AlAs matrix range within the limits of 230–236 cm^{-1} and 382–392 cm^{-1}, respectively, and lie between the frequencies of TO and LO phonons. As the quantum numbers of the calculated modes increase, the frequencies of these modes tend to the frequencies of interface phonons that propagate along plane heterojunction boundaries. For AlAs-like phonons, this value is equal to 383 cm^{-1}, whereas, for InAs-like phonons, it is equal to 235 cm^{-1}. Note that these values differ by several inverse centimeters from the frequencies of modes with small l and large m.

The set of frequencies of interface phonons for prolate quantum dots significantly differs form the relevant set for oblate quantum dots (Fig. 1b). This difference is especially significant for the frequencies of modes with small quantum numbers l and m.

In the model considered, the parameter that defines the shape of a quantum dot is the ratio R_e/R_p of large and small semiaxes.

Figure 2 shows the frequencies of interface phonons in quantum dots with the quantum numbers (1, 0) and (1, 1) as a function of the ratio R_e/R_p. It is especially important to determine the frequencies of these modes, because it is the phonons with small quantum numbers (l, m) equal to (1, 0) and (1, 1) that should make the main contribution to the Raman scattering of light [29].

For the ratio R_e/R_p ranging from 1/10 to 1 (prolate quantum dots), the frequencies of the first modes of interface phonons are shown in the left-hand part of the diagram, whereas the appropriate frequencies for R_e/R_p ranging from 1 to 10 are shown in the right-hand part. One can see that the frequencies of interface phonons exhibit the greatest variation in those quantum dots whose shape is close to a sphere.

Consider the case when the material of either the matrix or the quantum dots is a ternary solution $A_xB_{1-x}C$. This case is of definite interest because structures with InGaAs/AlGaAs quantum dots are already available. Since the dielectric function of a solid solution (in the absence of damping) is given by

$$\epsilon_a(\omega) = \epsilon_\infty^a \frac{(\omega_{\mathrm{LO},1}^2 - \omega^2)(\omega_{\mathrm{LO},2}^2 - \omega^2)}{(\omega_{\mathrm{TO},1}^2 - \omega^2)(\omega_{\mathrm{TO},2}^2 - \omega^2)}, \qquad (15)$$

where $\epsilon_\infty^a = \epsilon_{\infty,1}x + \epsilon_{\infty,2}(1-x)$, the solution to Eq. (13) represents three sets of interface phonons one of which corresponds to the material of a binary compound and the two other sets correspond to the material of a solid solution. For example, for InAs/AlGaAs quantum dots, these sets represent interface phonons in InAs quantum dots and AlAs- and GaAs-like interface phonons in the matrix. Note that, for structures in which both the

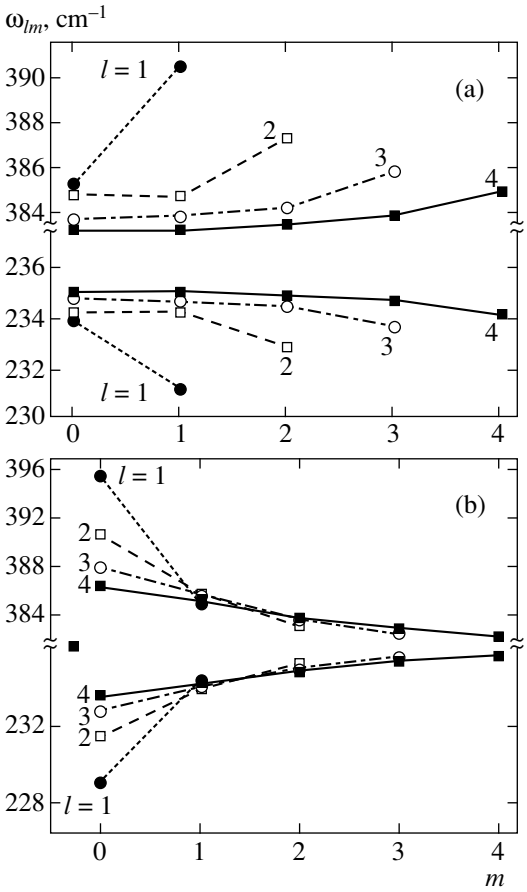

Fig. 1. Frequencies of interface modes in (a) oblate quantum dots for $R_p/R_e = 1/2$ and (b) prolate quantum dots for $R_p/R_e = 2$ as a function of the quantum numbers m and l. The frequencies of phonons with equal quantum numbers l and different numbers m are connected by lines.

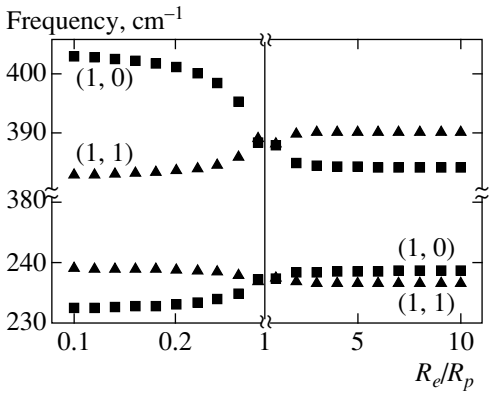

Fig. 2. Frequencies of interface phonons with quantum numbers (1, 0) and (1, 1) as a function of the ratio R_e/R_p for oblate (R_e/R_p = 1–10) and prolate (R_e/R_p = 0.1–1) quantum dots.

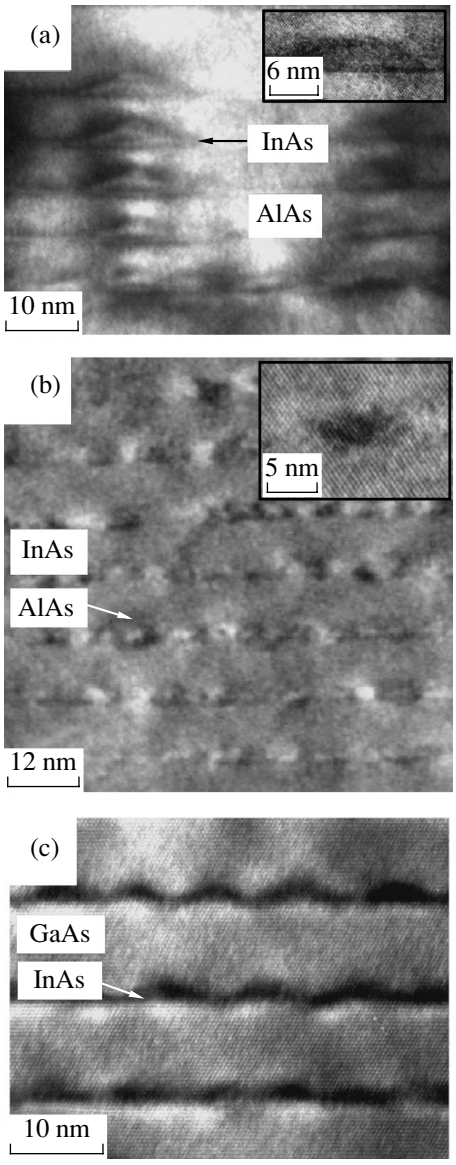

Fig. 3. Cross-sectional electron-microscope pictures of structures with InAs quantum dots in AlAs and GaAs matrices (samples A (a) and C (c), respectively) and AlAs quantum dots in an InAs matrix (sample B (b)). The insets represent detailed views of the quantum dots obtained at high resolution.

matrix material and the quantum dots represent solid solutions, one may expect that four sets of interface phonons exist.

3. EXPERIMENTAL

The structures studied were grown on GaAs substrates in the Stranski–Krastanov growth mode by molecular beam epitaxy on a Riber 32P equipment. Sample A consisted of ten periods each of which contained a layer with InAs quantum dots with a nominal thickness of 2.25 monolayers and an AlAs layer with a thickness of 25 nm. Sample B, consisting of 50 periods of AlAs quantum dots embedded into an InAs matrix, was grown on a silicon-doped ($N_{Si} = 2 \times 10^{18}$ cm^{-3}) InAs buffer layer of thickness 1.5 μm at a substrate temperature of 420°C. Each period contained a layer with AlAs quantum dots with a nominal thickness of 2.4 monolayers and a 12-nm-thick layer of InAs. Sample C consisted of 20 layers with InAs quantum dots with a nominal thickness of 2.5 monolayers coated by a 6-nm-thick GaAs layer.

The samples in which the matrix material was a solid solution $Al_xGa_{1-x}As$ consisted of five periods, each of which contained an 8-nm-thick layer of $Al_xGa_{1-x}As$ and a layer with InAs quantum dots. The content of aluminum was 0, 0.15, 0.25, 0.5, and 0.75. The structures were coated by a 20-nm-thick layer of GaAs.

The growth process was controlled by the reflection high-energy electron diffraction technique. According to the diffraction data, in all the samples, the transition from two-dimensional to three-dimensional growth mode (the onset of the formation of quantum dots) occurs after deposition of 1.9 monolayers of the quantum-dot material. After the formation of quantum dots, the first 8 nm of the AlAs layer was grown at the same temperature as the quantum dots (500°C). Then, the temperature was raised to 600°C and the remaining part of the AlAs layer was deposited.

The Raman spectra were recorded at a temperature of 80 K by a Dilor XY800 spectrometer. Ar^+- and Kr^+-lasers with wavelengths of 514.5 and 647.1 nm were used for the excitation. The spectra were measured in the geometry of backward scattering from a plane surface and from the cleaved edges of the samples oriented in the (110) plane. The following scattering geometries were used: $z(xx)\bar{z}$, $z(yx)\bar{z}$, $y'(zx')\bar{y}'$, and $y'(x'x')\bar{y}'$, where the axes x, y, z, x', and y' were parallel to the [100], [010], [001], [1$\bar{1}$0], and [110] directions, respectively. In the experiments with the geometry of backward scattering from a butt end, we used a microscope that allowed us to focus a laser beam to a spot 1 μm in diameter. The spectral resolution was 2 cm^{-1} throughout the spectral range.

4. RESULTS AND DISCUSSION

To control the quality of the samples and to determine their structural parameters, we used high-resolution transmission electron microscopy. The cross sections of the samples shown in Fig. 3 indicate that InAs quantum dots are lens-shaped (samples A and C) and AlAs quantum dots are spheroidal (sample B). InAs quantum dots have a base of about 10 nm and a height of about 1.5 nm. According to the images obtained by an electron microscope, the average size of AlAs quantum dots is 4–5 nm at the base and 2–4 nm in height.

Figure 4 presents the Raman spectra of the structures A, B, and C measured in different scattering

geometries that allow one to observe localized TO, LO, and/or interface phonons. According to the selection rules for plane superlattices, only LO phonons manifest themselves in the $z(yx)\bar{z}$ and $y'(x'x')\bar{y}'$ scattering geometries and only TO phonons, in the $y'(zx')\bar{y}'$ geometry. In the $z(yx)\bar{z}$ and $z(xx)\bar{z}$ scattering geometries, interface phonons may appear in the resonance conditions. The figure shows that these selection rules also hold for the investigated structures with quantum dots.

For example, TO and LO phonons in the matrix materials of the samples A, B, and C are observed in allowed scattering geometries at the frequencies 359 and 402 cm^{-1} (AlAs), 216 and 235 cm^{-1} (InAs), and 267 and 291 cm^{-1} (GaAs), respectively. The frequencies of the observed TO and LO phonons are close to the values of frequencies in bulk materials. Note that the Raman spectra of all samples exhibit features corresponding to the TO and LO phonons in the GaAs substrate (267 and 291 cm^{-1}).

Figure 4 shows that, at frequencies of 386, 228, and 277 cm^{-1}, which lie approximately at the midpoint between the frequencies of the TO and LO phonons, the spectra exhibit features associated with the interface phonons in AlAs, InAs, and GaAs matrices, respectively. These features will be discussed below.

The frequencies of optical phonons localized in quantum dots differ from the frequencies in bulk materials. For example, in samples A and C, the frequencies of TO and LO phonons in InAs quantum dots are shifted by 10–15 cm^{-1} to higher frequencies with respect to the frequencies of bulk phonons in InAs due to mechanical stresses in quantum dots. The lattice constant of InAs (0.60583 nm) is greater than that of GaAs (0.565325 nm) and AlAs (0.56622 nm); hence, mechanical stresses in InAs quantum dots in AlAs and GaAs matrices have the same sign: quantum dots experience contraction along the layers in which they are situated and expansion in the direction of growth of the structure [13].

The signs of mechanical stresses in sample B are reversed, which gives rise to a low-frequency shift (30–40 cm^{-1}) of the optical phonons localized in AlAs quantum dots of sample C [13].

Just as in the case of interface phonons in a matrix, the frequencies of interface phonons in quantum dots lie between the frequencies of TO and LO phonons localized in quantum dots. The frequency of an interface phonon in InAs quantum dots in sample A can be determined from the decomposition of the spectrum in the frequency region of optical phonons in InAs into two Lorentz curves that correspond to the lines of interface and LO phonons, as is shown in Fig. 4 by dashed lines, and is equal to 242 cm^{-1}. The line of interface phonons in AlAs quantum dots in sample B is observed at a frequency of 348 cm^{-1}, whereas sample C does not exhibit features corresponding to the interface phonons in InAs.

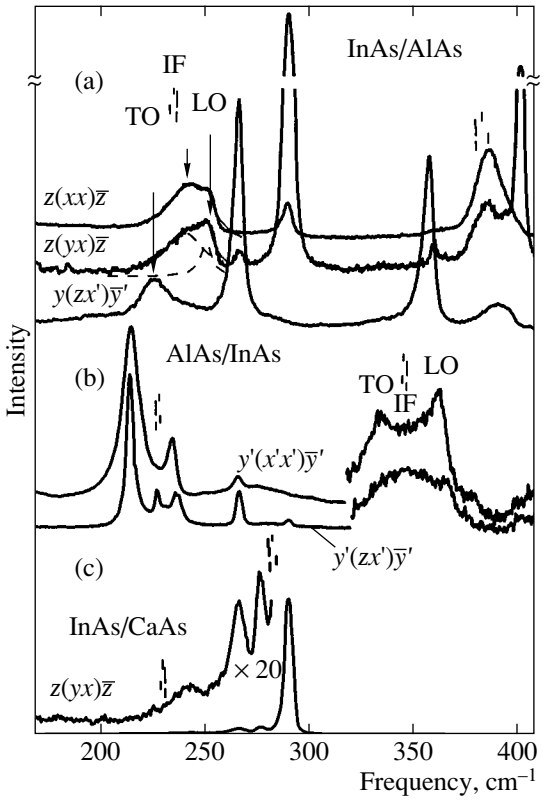

Fig. 4. Experimental Raman spectra of (a) InAs/AlAs, (b) AlAs/InAs, and (c) InAs/GaAs quantum-dot structures. Vertical bars over the graphs indicate the calculated frequencies of interface modes (IF), and vertical arrows indicate the features corresponding to TO and LO phonons in InAs/AlAs. The excitation energy of a laser is equal to 2.41 eV (514.5 nm) (spectra (a) and (b)) and 1.91 eV (647.1 nm) (spectrum (c)).

Now, let us consider a system in which the matrix material is a ternary solid solution $Al_xGa_{1-x}As$.

Figure 5 represents the experimental Raman spectra of $InAs/Al_xGa_{1-x}As$ structures with InAs quantum dots for various values of x recorded in the $z(xx)\bar{z}$ and $z(xy)\bar{z}$ scattering geometries in the spectral bands of optical phonons in InAs, GaAs, and AlAs. According to the selection rules for the Raman scattering, $InAs/Al_xGa_{1-x}As$ planar structures should exhibit LO phonons in the $z(xy)\bar{z}$ scattering geometry and interface phonons in the $z(xx)\bar{z}$ scattering geometry under resonance conditions. Figure 5 shows that these selection rules are also valid for structures with quantum dots. The Raman spectra recorded in the $z(xy)\bar{z}$ geometry predominantly exhibit LO phonons of InAs quantum dots and GaAs-like and AlAs-like LO phonons of the solid solution. In the $z(xx)\bar{z}$ geometry, one can observe additional features associated with interface phonons in the frequency range between TO and LO phonons in GaAs and AlAs.

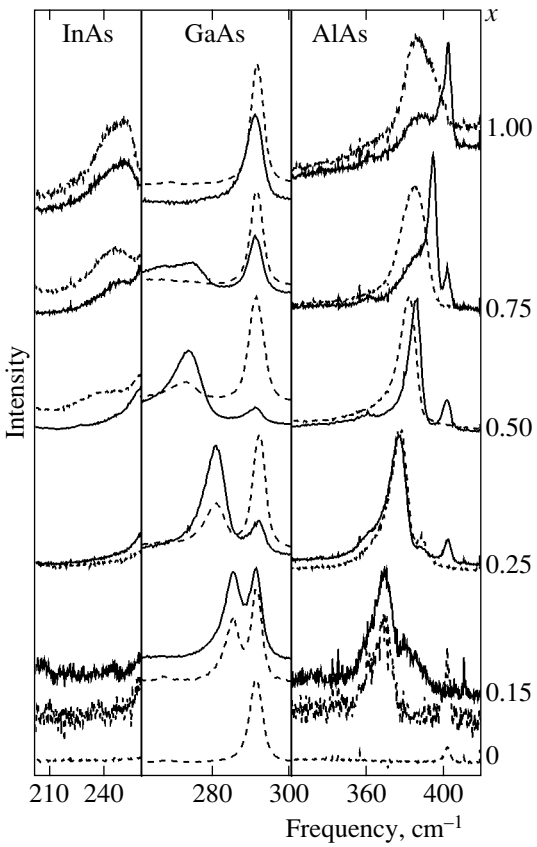

Fig. 5. Experimental Raman spectra of an InAs/$Al_xGa_{1-x}As$ structure for different values of x. Dashed lines show the spectra measured in the $z(xx)\bar{z}$ scattering geometry, and solid lines indicate the spectra measured in the $z(xy)\bar{z}$ scattering geometry. The excitation energy of a laser is equal to 1.91 eV (647.1 nm). The intensity scales of Raman scattering are different in the three parts of the spectrum.

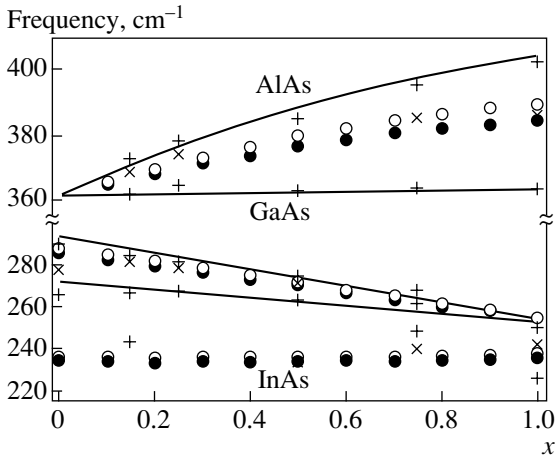

Fig. 6. Frequencies of interface phonons as a function of the composition of the $Al_xGa_{1-x}As$ matrix. The experimental values of AlAs- and GaAs-like optical (+) and interface (×) phonons are obtained from the analysis of Raman spectra. Solid lines correspond to the values of AlAs- and GaAs-like phonons in bulk AlGaAs versus the concentration of Al [14]. Calculated values of the frequencies of interface phonons in the (1, 0) and (1, 1) modes are shown by the symbols (●) and (○).

In the frequency range corresponding to optical phonons, InAs exhibits wideband features associated with the contribution of both interface and LO phonons in InAs quantum dots to the Raman scattering. The frequencies of these features virtually do not depend on the composition of the solid solution of the matrix. As the concentration of aluminum increases, the intensity of Raman scattering by the phonons of InAs quantum dots decreases, which may be attributed to the decrease in the energy of interband transitions in InAs quantum dots from 1.9 to 1.1 eV (the excitation energy is equal to 1.91 eV). As pointed out above, the vibrational spectrum of a AlGaAs matrix has a two-mode character. As the concentration of aluminum decreases, the frequency of an AlAs-like LO phonon decreases from 403 cm^{-1} (for $x = 1$) to 386 cm^{-1} (for $x = 0.5$). In the $z(xx)\bar{z}$ geometry, this spectrum exhibits a feature that corresponds to a line of interface phonons whose frequencies decrease from 386 cm^{-1} (for $x = 1$) to 381 cm^{-1} (for $x = 0.5$). Because of the small LO–TO splitting of AlAs-like phonons in AlGaAs with small values of x, the lines of interface phonons and LO phonons in the Raman spectra are not resolved. In the range of frequencies of optical phonons in GaAs, one can observe an intense peak associated with an LO phonon in the GaAs substrate (291 cm^{-1}) and an asymmetric feature associated with the contribution of interface and GaAs-like LO phonons, whose frequency increases, as x increases, from 273 cm^{-1} (for $x = 0.75$) to 285 cm^{-1} (for $x = 0.15$). Fitting by Lorentz curves allows one to separate the contributions of interface and LO phonons. The results of the fitting and the experimental results obtained from the Raman spectra are shown in Fig. 6.

Selection rules for the Raman scattering do not allow one to observe TO phonons in the $z(xx)\bar{z}$ and $z(yx)\bar{z}$ geometries for crystals with the symmetry of zinc blende. However, the feature at a frequency of 360 cm^{-1}, which weakly depends on the concentration of aluminum, is likely to correspond to an AlAs-like TO phonon and manifests itself due to the violation of the selection rules for structures with quantum dots.

The weak peak at a frequency of 402 cm^{-1} is observed in the spectra of all the samples investigated and corresponds to an LO phonon in thin spacer layers of AlAs.

Figure 6 shows that the two-mode behavior of optical phonons in the AlGaAs matrix agrees with the experimental data of [32] that were obtained for a bulk solid solution of $Al_xGa_{1-x}As$. The frequencies of interface phonons determined from the experiments are indicated by crosses.

Within the model of a dielectric continuum, we have calculated the frequencies of interface phonons in an

InAs/Al_xGa_{1-x}As quantum-dot structure in the approximation of spheroidal quantum dots with the parameters close to the experimental values (R_p/R_e = 1/2). The form of the dielectric function of the Al_xGa_{1-x}As matrix that was used in the calculation corresponds to formula (15). The circles in Fig. 6 represent the calculated InAs-, GaAs-, and AlAs-like interface modes with the quantum parameters $l = 1$ and $m = 0, 1$, because the main contribution to the Raman scattering should be made by modes with small quantum numbers [29]. One can see that the frequencies of calculated modes are in good agreement with the experimental data.

5. CONCLUSIONS

The Raman scattering of light by InAs/Al(Ga)As and AlAs/InAs periodic structures with self-organized quantum dots has been investigated. The Raman spectra measured in different scattering geometries exhibit features that correspond to optical TO and LO phonons and interface phonons. The frequencies of TO and LO phonons are displaced with respect to the corresponding values in bulk materials in view of mechanical stresses. The lines of Raman scattering by interface phonons are observed under conditions close to the resonance conditions. The frequencies of interface phonons lie in the spectral range between the frequencies of TO and LO phonons. The experimental frequencies of optical phonons have been used for calculating the frequencies of interface phonons in structures with quantum dots of different shapes in the approximation of a dielectric continuum. The frequencies of interface phonons obtained within this model depend on the shape of the quantum dots. It has been shown that the dielectric-continuum approximation is an adequate model for calculating the frequencies of interface phonons in InAs/Al_xGa_{1-x}As quantum-dot structures with any value of x. In this case, it is assumed that the shape of quantum dots is close to that observed in the spectra obtained by high-resolution electron microscopy. Thus, it has been shown that the Raman spectroscopy is sensitive to the shape of quantum dots.

REFERENCES

1. D. Bimberg, M. Grundmann, F. Heinrichsdorff, *et al.*, Thin Solid Films **367**, 235 (2000).
2. D. Bimberg, M. Grundmann, and N. N. Ledentsov, *Quantum Dot Heterostructures* (Wiley, Chichester, 1999).
3. N. N. Ledentsov, V. M. Ustinov, V. A. Shchukin, *et al.*, Fiz. Tekh. Poluprovodn. (St. Petersburg) **32**, 385 (1998) [Semiconductors **32**, 343 (1998)].
4. J. Groenen, C. Priester, and R. Carles, Phys. Rev. B **60**, 16013 (1999).
5. H. K. Shin, D. J. Lockwood, C. Lacelle, and P. J. Poole, J. Appl. Phys. **88**, 6423 (2000).
6. E. Martinez-Guerrero, C. Adelmann, F. Chabuel, *et al.*, Appl. Phys. Lett. **77**, 809 (2000).
7. G. Armelles, T. Utzmeier, P. A. Postigo, *et al.*, J. Appl. Phys. **81**, 6339 (1997).
8. Q. Xie, A. Madhukar, P. Chen, and N. Kobayashi, Phys. Rev. Lett. **75**, 2542 (1995).
9. Z. R. Wasilewski, S. Fafard, and J. P. McCarey, J. Cryst. Growth **201–202**, 1131 (1999).
10. D. A. Tenne, V. A. Haisler, A. K. Bakarov, *et al.*, Phys. Status Solidi B **224**, 25 (2001).
11. A. Milekhin, D. A. Tenne, and D. R. T. Zahn, in *Quantum Dots and Nanowires*, Ed. by S. Bandyopadhyay and H. S. Nalwa (Am. Sci., California, 2003), p. 375.
12. A. G. Milekhin, A. I. Nikiforov, O. P. Pchelyakov, *et al.*, Pis'ma Zh. Éksp. Teor. Fiz. **81**, 33 (2005) [JETP Lett. **81**, 30 (2005)].
13. D. A. Tenne, V. A. Haisler, A. I. Toropov, *et al.*, Phys. Rev. B **61**, 13785 (2000).
14. Z. C. Feng, A. A. Allerman, P. A. Barnes, and S. Perkowitz, Appl. Phys. Lett. **60**, 1848 (1992).
15. M. I. Vasilevskiy, Phys. Rev. B **66**, 195326 (2002).
16. A. G. Milekhin, D. A. Tenne, A. I. Toropov, *et al.*, Phys. Status Solidi C **1**, 2629 (2004).
17. J. Groenen, A. Mlayah, R. Carles, *et al.*, Appl. Phys. Lett. **69**, 943 (1996).
18. A. G. Milekhin, A. I. Toropov, A. K. Bakarov, *et al.*, Phys. Rev. B **70**, 085314 (2004).
19. S.-Fen. Ren, Z.-Q. Gua, and D. Lub, Solid State Commun. **113**, 273 (2000).
20. H. Fu, V. Ozolins, and A. Zunger, Phys. Rev. B **59**, 2881 (1999).
21. Yu. A. Pusep, G. Zanelatto, S. W. da Silva, *et al.*, Phys. Rev. B **58**, R1770 (1998).
22. R. Ruppin and R. Englman, Rep. Prog. Phys. **33**, 149 (1970).
23. E. Menendez, C. Trallero-Giner, and M. Cardona, Phys. Status Solidi B **199**, 81 (1997).
24. N. Liu, H. K. Lyeo, C. K. Shih, *et al.*, Appl. Phys. Lett. **80**, 4345 (2002).
25. J. Marquez, L. Geelhaar, and K. Jacobi, Appl. Phys. Lett. **78**, 2309 (2001).
26. D. M. Bruls, J. W. A. M. Vugs, P. M. Koenraad, *et al.*, Appl. Phys. Lett. **81**, 1708 (2002).
27. A. I. Yakimov, A. V. Dvurechenskii, A. I. Nikiforov, *et al.*, Phys. Rev. B **67**, 125318 (2003).
28. A. G. Milekhin, A. I. Toropov, A. K. Bakarov, *et al.*, Physica E (Amsterdam) **21**, 241 (2004).
29. P. A. Knipp and T. L. Reinecke, Phys. Rev. B **46**, 10310 (1992).
30. F. Comas, C. Trallero-Giner, N. Studart, and G. E. Marques, J. Phys.: Condens. Matter **14**, 6469 (2002).
31. M. C. Klein, F. Hache, D. Ricard, and C. Flytzanis, Phys. Rev. B **42**, 11123 (1990).
32. Z. C. Feng, S. Perkowitz, D. K. Kinell, *et al.*, Phys. Rev. B **47**, 13466 (1993).

Translated by I. Nikitin

Journal of Experimental and Theoretical Physics, Vol. 101, No. 3, 2005, pp. 562–567.
Translated from Zhurnal Éksperimental'noĭ i Teoreticheskoĭ Fiziki, Vol. 128, No. 3, 2005, pp. 655–661.

STATISTICAL, NONLINEAR, AND SOFT MATTER PHYSICS

A Model of Anomalous Transport

V. P. Shkilev

Institute of Surface Chemistry, National Academy of Sciences of Ukraine, Kiev, 03164 Ukraine
e-mail: shkilevv@ukr.net

Received February 25, 2005

Abstract—A lattice model is used to derive a system of equations describing anomalous transport in the case of low tracer concentration. In the adopted model, anomalous transport is due to nonequilibrium distribution of tracer particles over sites in an inhomogeneous lattice. It is shown that a well-known time-fractional differential equation can be derived from the lattice equations under certain additional assumptions. *© 2005 Pleiades Publishing, Inc.*

1. INTRODUCTION

Anomalous transport properties are exhibited by many physical systems [1–3]. Even though various theoretical approaches have been proposed to deal with transport in these systems, no satisfactory solution has been found to this day [4–7]. In the new approach proposed in this paper, a macroscopic transport equation is derived from a master equation without assuming local equilibrium distributions of particles over sites of different types.

Systems of equations analogous to the one proposed here were considered in [8–11]. However, since previous studies relied on a phenomenological approach, the parameters of the equations have never been related to microscopic quantities. Moreover, an important distinction of the system of equations proposed here is its symmetry with respect to type of lattice sites, which makes the system more amenable to analytical methods.

2. SYSTEM OF EQUATIONS

In this section, a lattice model is used to derive a system of differential equations for the partial concentrations of molecules occupying sites of several distinct types. The derivation is based on the following assumptions: the medium is macroscopically homogeneous and isotropic; there are a finite number of types of sites randomly distributed in space; macroscopic transport is due to thermally activated hopping of tracer particles between nearest neighbors; the hopping rate can be represented as the product of two functions depending only on the types of the sites occupied by the particle before and after a jump, respectively. The last assumption holds, for example, in the simple model of random traps, as well as in the more complicated model taking into account the varying height of the potential barrier separating sites [12].

In a lattice model, the tracer flux density across a plane surface element can be written as

$$q = \frac{1}{S}\sum_n\sum_m (W_{nm}P_m - W_{mn}P_n), \qquad (1)$$

where S is the surface area. The summation in (1) is performed over the pairs of sites that can be successively occupied by a tracer particle before and after a jump and can be connected by a straight line intersecting the surface element. Since only low tracer concentrations are considered, the hopping rate W_{nm} is independent of the site occupation probability P_n.

By treating the probabilities corresponding to sites of each type as differentiable functions, assuming that particles can hop only to short lengths, and considering a small surface element, the probabilities can be expressed approximately as

$$P_k \approx P_i + \mathbf{r}_{ok}\cdot\nabla P_i, \qquad (2)$$

where P_k is the occupation probability for the kth site of ith type lying in the neighborhood of the surface element, P_i is the occupation probability for a site of the ith type located at the center of the surface element, and $\mathbf{r}_{ok}$ is the radius vector from the center of the surface element to the kth site.

When the surface element is sufficiently large, correlation between the site locations involved in a jump across the surface can be neglected, and (2) can be substituted into (1) to derive the following expression for the flux vector:

$$\mathbf{J} = -\sum_{i=1}^{N}(-\mathbf{F}B_i\rho_i + D_i\nabla\rho_i). \qquad (3)$$

Here, N is the number of types of sites;

$$D_i = \frac{2h_i}{N_i}\sum_n \sum_{m \in i} h_{om} W_{nm},$$
$$B_i = \frac{2h_i}{N_i}\sum_n \sum_{m \in i} \alpha_{nm} h_{nm} W_{nm} \quad (4)$$

are the diffusivity and mobility associated with sites of the ith type, respectively; h_{om} and h_{nm} are the projections of $\mathbf{r}_{om}$ and $\mathbf{r}_{nm}$ on the normal to the surface element; $\rho_i = P_i/V_i$ is the concentration of particles occupying sites of the ith type; V_i is the average volume per site of the ith type; h_i is the largest hopping length for particles occupying sites of the ith type; N_i is the number of sites of the ith type contained in a parallelepiped with base S and height h_i; and $\mathbf{F}$ is the force driving the particles. When the force is weak, the probabilities W_{nm} are assumed to change by small increments:

$$W_{nm}^F = W_{nm}[1 - \alpha_{nm}(\mathbf{F} \cdot \mathbf{r}_{nm})], \quad (5)$$

where the positive coefficient α_{nm} depends on the potential energy profile in the neighborhoods of the nth and mth sites.

In the case of equilibrium distribution of particles over sites of different types, expression (3) reduces to the standard expression for the flux vector. However, essentially different results are obtained in the general case. In particular, convective flux is not proportional to the total particle concentration, and diffusive flux is not parallel to the gradient of the total concentration. An analogous phenomenological expression for the flux vector was proposed in [10], but the summation was performed over some loosely defined "diffusion paths" rather than types of sites.

The expression for the flux vector can be used to write the continuity equation as follows:

$$\frac{\partial \rho(r,t)}{\partial t} = \sum_{i=1}^{N} [-B_i(\mathbf{F} \cdot \nabla \rho_i(r,t)) + D_i \nabla^2 \rho_i(r,t)], \quad (6)$$

where

$$\rho = \sum_{i=1}^{N} \rho_i$$

is the total particle concentration.

To obtain a closed system of equations, Eq. (6) must be supplemented with equations describing the evolution of partial concentrations. To derive the required equations, consider the master equation

$$\frac{\partial P_n}{\partial t} = \sum_m (W_{nm} P_m - W_{mn} P_n). \quad (7)$$

Suppose that the hopping rate can be represented as the product of functions depending only on the type of site occupied before and after a jump, respectively: $W_{nm} = U_i V_j$, where i and j denote the types of the mth and nth sites, respectively. Let α_i be the relative number of sites of the ith type in a macroscopic volume. Consider a cell that is small in the macroscopic sense, but sufficiently large in the sense that the lattice-site distribution inside it is similar to that in the entire volume; i.e., the relative number of sites of the ith type contained in the cell is α_i. The sum of Eqs. (7) for all sites of a particular type in the cell divided by the cell volume is

$$\frac{\partial \rho_i}{\partial t} = -\rho_i V_i \sum_{j=1}^{N} \alpha_j U_j + \frac{1}{V}\sum_{n \in i} \sum_m W_{nm} P_m, \quad i = 1, 2, \ldots, N. \quad (8)$$

The product $\alpha_j U_j$ characterizes the partitioning of hopping particles between sites of different types. When the sites are randomly distributed in space, this distribution is independent of the type of site occupied before a jump. Therefore, the second term in (8) can be rewritten as a constant quantity independent of the site type i times $\alpha_i U_i$. This constant quantity can be found by adding up Eqs. (8) and comparing the result with the continuity equation. This leads to the equation

$$\frac{\partial \rho_i(r,t)}{\partial t} = -\nu_i \rho_i(r,t) + \gamma_i G(r,t), \quad i = 1, 2, \ldots, N, \quad (9)$$

where

$$G(r,t) = \sum_{j=1}^{N} \nu_j \rho_j(r,t) + \sum_{i=1}^{N} \{-B_i(\mathbf{F} \cdot \nabla \rho_i(r,t)) + D_i \nabla^2 \rho_i(r,t)\}, \quad (10)$$

$$\gamma_i = \frac{\alpha_i U_i}{\sum_{j=1}^{N} \alpha_j U_j}, \quad \nu_i = V_i \sum_{j=1}^{N} \alpha_j U_j. \quad (11)$$

The parameter γ_i is the relative number of particles jumping to sites of the ith type, and ν_i is the frequency of jumps from sites of the ith type.

An analogous system of equations was derived in [12], but the derivation presented therein is not physically correct. In particular, the meaning of the function representing the transition probability remains unclear.

Initially, it was defined as the rate of particle exchange between macroscopically small volumes containing large number of sites. Subsequently, it was found that the same function characterizes the rate of relaxation to an equilibrium distribution of particles over sites of different types in a macroscopically small volume. This finding can be explained only by analyzing the mechanism of transport on a microscopic level.

3. EINSTEIN RELATIONS

This section presents the derivation of the Einstein relations between the mobilities and diffusivities corresponding to particular types of sites. In a lattice model, these relations can be established only by assuming that the sites occupied before and after each jump are separated by a narrow potential barrier located exactly in the middle between the sites. Since this assumption is unrealistic for a disordered medium, the relations are derived here without using any lattice model. As a first step, the Green–Kubo formula is derived that relates the average displacement of a tracer particle driven by an external force to the root-mean-square particle displacement in the absence of forcing. Since standard assumptions are not valid in the present model, weaker assumptions are used. First, only particle velocities are characterized by an equilibrium distribution in unforced motion. Second, the velocity of an individual particle is not assumed to be a stationary random process.

Consider the spread of a cloud of particles initially concentrated at the origin. The particle motion is assumed to be governed by the laws of classical mechanics. The particle velocity distribution is assumed to quickly approach an equilibrium distribution. Then, the closed system consisting of the hopping particles and the medium is characterized by the product of a time-dependent distribution over generalized coordinates with an equilibrium distribution over generalized momenta:

$$f_0(q, p, t) = f_1(q, t) f_e(p). \tag{12}$$

Suppose that the velocity distribution quickly approaches a time-independent distribution close to the equilibrium distribution. Then, the distribution function for particles driven by a force can be written as

$$f(q, p, t) = f_2(q, t)(f_e(p) + \delta f(p)), \tag{13}$$

where δf is a small perturbation and the function $f_2(q, t)$ may substantially differ from $f_1(q, t)$. Even though the spatial distributions of tracer particles executing forced and unforced motion are substantially different, the corresponding distributions of particles over sites of particular type are similar by virtue of the homogeneity and isotropy of the medium and the random spatial distribution of lattice sites. Since the forcing is assumed to be weak, it does not modify the hopping frequency and the probabilities of hopping to sites of particular type, merely displacing the particles in a certain direction.

A standard method [13] is then applied to obtain the following expression for the mean increment of an arbitrary dynamical variable $B(q, p)$ characterizing the forced motion:

$$\langle \Delta B \rangle(t) = \int_0^t \int \{\Delta H, f_2(q, t') f_e(p)\} \times B(q_t(q, p), p_t(q, p)) dt' d\Gamma. \tag{14}$$

Here, $\{\ldots, \ldots\}$ denotes the Poisson bracket, $d\Gamma$ is a volume element in the phase space, $q_t(q, p)$ and $p_t(q, p)$ are the phase coordinates at the instant t for the unperturbed system with the Hamiltonian H starting from the point with phase coordinates q and p at the instant t', and ΔH is the Hamiltonian of the perturbation applied to the system.

If the x axis is parallel to the applied force, then the perturbation Hamiltonian and dynamical variable can be expressed as

$$\Delta H = \sum_i F x_i, \quad B = \sum_i V_{xi}, \tag{15}$$

where x_i is the x coordinate of the ith tracer particle, F is the magnitude of the applied force, and V_{xi} is the x component of the velocity of the ith tracer particle.

Since the velocities of individual particles are uncorrelated and $f_e(p)$ is a Maxwellian distribution when the tracer concentration is low, expression (15) can be substituted into (14) to obtain

$$\langle V_x \rangle^F(t) = \frac{F}{kT} \int_0^t \langle V_x(t) V_x(t') \rangle^0 dt'. \tag{16}$$

where the angle brackets labeled by superscripts F and 0 denote the averages corresponding to forced and unforced motion, respectively. The correlation function in the integrand corresponds to the unforced motion characterized by distribution function (12). Indeed, the velocities $V_x(t')$ and $V_x(t)$ are correlated via the phase flow of the unperturbed Hamiltonian H. Moreover, $V_x(t)$ depends only on $V_x(t')$ and on the type of the site occupied by the particle at the instant t', being independent of the exact spatial location of the particle. Therefore, since $f_1(q, t)$ and $f_2(q, t)$ describe similar distributions of particles over sites of different types, the function $f_2(q, t)$ in (14) can be replaced with $f_1(q, t)$.

The integral of (16) yields the Green–Kubo formula

$$\langle \Delta x \rangle^F = \frac{F}{6kT} \langle \Delta r^2 \rangle^0, \tag{17}$$

which can be used to derive the Einstein relations

$$B_i = \frac{D_i}{kT}, \quad i = 1, 2, \ldots, N. \tag{18}$$

This is done by calculating the averages $\langle \Delta x \rangle^F$ and $\langle \Delta r^2 \rangle^0$, using Eqs. (9) and (10), and requiring that (17) hold for arbitrary distributions of particles over sites of different types.

4. EVOLUTION EQUATION FOR TRACER CONCENTRATION

For simplicity, we henceforth assume that the hopping length is equal for tracer particles occupying sites of any type. Then, the corresponding diffusivity is

$$D_i = c\nu_i, \quad i = 1, 2, \ldots, N, \tag{19}$$

where the constant c is on the order of the mean square hopping length. This assumption is justified by the fact that the variation of diffusivity is primarily determined by the frequency ν_i.

After substituting (18) and (19) into Eqs. (9) and (10), the system is reduced to a single equation in the Laplace variable u:

$$\begin{aligned} &u\rho(r, u) - \rho^0(r) \\ &= \frac{u\psi}{1-\psi} cO\rho(r, u) + \frac{\varphi - \psi}{1-\psi} cO\rho^0(r), \end{aligned} \tag{20}$$

where

$$O = \nabla^2 - \frac{\mathbf{F} \cdot \nabla}{kT}$$

is the Fokker–Planck operator and

$$\psi(u) = \sum_{i=1}^{N} \frac{\gamma_i \nu_i}{\nu_i + u}, \quad \varphi(u) = \sum_{i=1}^{N} \frac{\beta_i \nu_i}{\nu_i + u}, \tag{21}$$

with $\beta_i = \rho_i^0(r)/\rho^0(r)$ denoting the relative number of particles occupying sites of the ith type located at a point r at $t = 0$.

To change from the Laplace variable back to physical time, the functions $u\psi/(1-\psi)$ and $(\varphi - \psi)/(1-\psi)$ are expanded in terms of simple fractions. The resulting integrodifferential equation describes the evolution of the total particle concentration as a function of r and t:

$$\begin{aligned} \frac{\partial \rho(r, t)}{\partial t} &= a_0 cO\rho(r, t) + \int_0^t \sum_{i=1}^{N-1} a_i \exp[-\lambda_i(t - t')] \\ &\times cO\rho(r, t')dt' + \sum_{i=1}^{N-1} b_i \exp(-\lambda_i t) cO\rho^0(r), \end{aligned} \tag{22}$$

where $-\lambda_i$ ($i = 1, 2, \ldots, N-1$) denotes the nonzero roots of the equation $\psi(u) = 1$, and the coefficients a_i and b_i are expressed in terms of the parameters of the functions $\psi(u)$ and $\varphi(u)$.

The solution to Eq. (22) can be represented as a series expansion in the eigenfunctions $X_n(r)$ of the operator cO:

$$\rho(r, t) = X_0(r) + \sum_{n=1}^{\infty} T_n(t) X_n(r). \tag{23}$$

The functions $T_n(t)$ characterizing the decay of the corresponding eigenfunctions are linear combinations of exponentials.

5. LATTICE WITH SITES OF TWO TYPES

In this section, a lattice with sites of two types is considered as an example to demonstrate that Eq. (22) can be used to describe anomalous transport. Anomalous transport is interpreted here as a regime in which either mean particle displacement under forcing or mean square displacement in the absence of forcing is a nonlinear function of time on a macroscopic scale. A random trap model, with γ_i equal to α_i is considered here to simplify physical interpretation of results.

According to Eq. (22), if the lattice consists of sites of only two types, then the mean square displacement in the absence of forcing is

$$\langle r^2 \rangle^0 = 6D\left\{ t + (b-1)\tau\left[1 - \exp\left(-\frac{t}{\tau}\right)\right]\right\}, \tag{24}$$

where

$$\tau = \frac{\tau_1 \tau_2}{\xi}, \quad a = \xi\left(\frac{\alpha_1}{\tau_1} + \frac{\alpha_2}{\tau_2}\right), \quad b = \xi\left(\frac{\beta_1}{\tau_1} + \frac{\beta_2}{\tau_2}\right),$$

$$\xi = \alpha_1\tau_1 + \alpha_2\tau_2, \quad \tau_i = \frac{1}{\nu_i}, \quad i = 1, 2,$$

and $D = c/\xi$ is the equilibrium value of diffusivity.

The parameters ξ and τ can be treated as mutually independent and may vary from zero to infinity, whereas b varies between ξ/τ_2 and ξ/τ_1.

It follows from (24) that the time derivative of the mean square displacement is $6Db$ at $t = 0$ and approaches $6D$ with increasing t. The physical meaning of the corresponding time scale is τ can be elucidated by analyzing system (9), (10) with zero spatial gradients. For a lattice with sites of only two types, the system reduces to the equation

$$\frac{\partial \rho_1}{\partial t} = -\frac{1}{\tau}\left(\rho_1 - \frac{\alpha_1 \tau_1 \rho^0}{\xi}\right), \tag{25}$$

which demonstrates that τ is the time of relaxation to a local equilibrium distribution.

The behavior of $\langle \mathbf{r}^2 \rangle^0(t)$ depends on the initial distribution of particles over sites of different types, i.e., on

the parameter b. When $b > 1$, the particles are more likely to be initially distributed over sites characterized by the shorter waiting time. Since the mobility of the particles that start moving from these sites is higher, the initial time derivative of the mean square displacement exceeds its equilibrium value. As the equilibrium particle distribution is approached, the time derivative of the mean square displacement gradually decreases to its equilibrium value. When $b < 1$, most particles initially occupy sites characterized by the lower mobility. Accordingly, the time derivative of mean square displacement increases with time, approaching its equilibrium value. At times longer than τ, every curve (24) is asymptotically close to the linear function with equilibrium slope.

According to (24), the mean square displacement at $t = \tau$ is

$$6[b - (b-1)\exp(-1)]\frac{c\tau}{\xi}.$$

Its numerical value may vary within a wide interval, depending on τ and ξ. If τ and ξ are comparable in order of magnitude, then the mean square displacement is a microscopic quantity at $t = \tau$, and its significant increase begins at $t \gg \tau$, which corresponds to a linear function $\langle \mathbf{r}^2 \rangle$ of t; i.e., no deviation from classical diffusion is observed. If τ is greater than ξ by orders of magnitude, then the mean square displacement can reach a macroscopic value at $t = \tau$. In this case, $\langle \mathbf{r}^2 \rangle$ is a nonlinear function of t, i.e., anomalous diffusion is observed.

Thus, the model considered here demonstrates that anomalous diffusion is due to an order-of-magnitude difference between the time τ of relaxation to a local equilibrium distribution of tracer particles over sites of different types and the mean waiting time ξ. According to the formulas relating τ and ξ to α_i and τ_i, the condition $\tau \gg \xi$ holds if both $\tau_2 \gg \tau_1$ and $\alpha_2 \ll 1$, i.e., if the sites characterized by the longer mean waiting time are relatively scarce.

6. FRACTIONAL DIFFERENTIAL EQUATION

It is well known [6, 14] that a time-fractional differential equation can be derived from Eq. (20) by setting $\varphi(u)$ equal to $\psi(u)$ and defining $\psi(u)$ as

$$\psi(u) = \frac{1}{1 + (Au)^n}, \tag{26}$$

where $A > 0$ and $0 < n < 1$.

The condition $\varphi(u) = \psi(u)$ is physically plausible if all potential barriers have equal heights, i.e., if $\gamma_i = \alpha_i$. Then, $\beta_i = \alpha_i$; i.e., particles are randomly distributed over sites of different types at $t = 0$.

Expression (26) can be used to determine the probability distribution of frequency by solving the integral equation

$$\int_0^\infty \frac{\nu}{u+\nu}\gamma(\nu)d\nu = \frac{1}{1 + (Au)^n}. \tag{27}$$

Its solution found by using methods of complex analysis is

$$\gamma(\nu) = \frac{\sin(n\pi)}{\pi\nu[(A\nu)^n + (A\nu)^{-n} + 2\cos(n\pi)]}. \tag{28}$$

It is a continuous function having a finite value at every frequency between zero and infinity. Since this result is inconsistent with the physics of the model considered here, the fractional differential equation can be used only as an approximation describing real processes within a finite time interval. At longer times, this equation is inapplicable, because it yields a nonlinearly increasing mean square displacement, whereas a linear increase is predicted by Eq. (22).

It is generally assumed that

$$\nu = \nu_0 \exp\left(-\frac{E}{RT}\right),$$

where ν_0 is a constant factor and E is an activation energy. In this case, (28) can be rewritten as a distribution over activation energies:

$$\gamma(E) = \frac{\sin(n\pi)}{\pi RT[(z)^n + (z)^{-n} + 2\cos(n\pi)]}, \tag{29}$$

where

$$z = \frac{1}{\nu_0}\exp\frac{\xi_E - E}{RT}.$$

The mean activation energy ξ_E is related to the parameter A as follows:

$$A = \frac{1}{\nu_0}\exp\frac{\xi_E}{RT}. \tag{30}$$

Since physically meaningful distribution (29) must be independent of temperature, the fractional differential equation cannot describe any process involving temperature variation. If it is still used as an approximation, then temperature-dependent A and n can be expressed in terms of the expected value and variance corresponding to distribution (29): A is given by (30), and

$$n = \left[1 + \frac{3\sigma^2}{(\pi RT)^2}\right]^{-1/2}, \tag{31}$$

where σ^2 is the variance of (29). The parameters ξ_E and σ^2 should be treated as temperature-independent constants.

7. CONCLUSIONS

Since the model of anomalous transport proposed in this paper contains many parameters, it can describe a diversity of processes. In this respect, it is more versatile than fractional differential equations, which are applicable only to a relatively narrow class of anomalous transport processes. Since all of these parameters characterize physical properties of the medium, they can be used not only to fit experimental data into the theoretical framework, but also to extract information about the microscopic structure of the medium. Even though practical determination of many parameters is a difficult problem, its analysis is a necessity because anomalous transport processes generally occur in media with complex structure that cannot be characterized by just a few parameters.

REFERENCES

1. W. D. Luedtke and U. Landmann, Phys. Rev. Lett. **82**, 3835 (1999).
2. J.-P. Bouchaud and A. Georges, Phys. Rep. **195**, 127 (1990).
3. M. B. Isichenko, Rev. Mod. Phys. **64**, 961 (1992).
4. R. Metzler and J. Klafter, Phys. Rep. **339**, 16 (2000).
5. V. Yu. Zaburdaev and K. V. Chukbar, Zh. Éksp. Teor. Fiz. **121**, 299 (2002) [JETP **94**, 252 (2002)].
6. A. I. Saichev and S. G. Utkin, Zh. Éksp. Teor. Fiz. **126**, 502 (2004) [JETP **99**, 443 (2004)].
7. I. A. Dranikov, P. S. Kondratenko, and A. V. Matveev, Zh. Éksp. Teor. Fiz. **125**, 1085 (2004) [JETP **98**, 945 (2004)].
8. P. W. Shmidlin, Phys. Rev. B **16**, 2362 (1977).
9. J. Noolandi, Phys. Rev. B **16**, 4474 (1977).
10. E. C. Aifantis, Acta Metall. **27**, 683 (1979).
11. J. B. Leblond and D. Dubois, Acta Metall. **31**, 1459 (1983).
12. V. Pereyra, G. Zgrablich, and V. P. Zhdanov, Langmuir **6**, 691 (1990).
13. P. Resibois and M. De Leener, *Classical Kinetical Theory of Fluids* (Wiley, New York, 1977; Mir, Moscow, 1980).
14. A. I. Saichev and G. M. Zaslavsky, Chaos **7**, 753 (1997).

Translated by A. Betev

Journal of Experimental and Theoretical Physics, Vol. 101, No. 3, 2005, pp. 568–574.
Translated from Zhurnal Éksperimental'noĭ i Teoreticheskoĭ Fiziki, Vol. 128, No. 3, 2005, pp. 662–672.

STATISTICAL, NONLINEAR, AND SOFT MATTER PHYSICS

Thermal 1/ω Fluctuations of a Quantum Oscillator under a Parametric Effect of a Random Field

B. A. Veklenko

Institute of High Temperatures, Russian Academy of Sciences, ul. Izhorskaya 13/19, Moscow, 127412 Russia
e-mail: VeklenkoBA@yandex.ru

Received November 3, 2004

Abstract—It is shown that the effect of a time-correlated Gaussian random field of sufficiently high intensity on the elasticity coefficient of a quantum oscillator manifests itself in the generation of thermal fluctuations with a 1/ω spectrum in the oscillator. It is also shown that, in any physical system described by the equation of an anharmonic oscillator, fluctuations with a 1/ω spectrum arise at an above-critical temperature. *© 2005 Pleiades Publishing, Inc.*

1. INTRODUCTION

So-called 1/ω noise, or flicker noise, is a quite common phenomenon [1, 2]. It was discovered in 1925 in electrical circuits [3]; however, its physical nature is still a subject of lively discussions [4–8]. It is believed that there exists a set of microscopic mechanisms of the generation of this type of noise [9]; however, none of these mechanisms is universally recognized. The most common mathematical model of 1/ω noise is based on the summation of the Lorentzians [7, 8]

$$\langle \mathscr{E}^2 \rangle_\omega = \int_0^\infty \frac{g(\tau)\tau d\tau}{1+\tau^2\omega^2} \propto \frac{1}{\omega}, \qquad (1)$$

which is equivalent to the assumption that there exists a spectrum of Gaussian distributions with the weight function $g(\tau)$ in the system. The left-hand side of Eq. (1) represents a noise emf in the electric circuit. The problem consists in that the required asymptotic behavior of the weight function $g(\tau) \propto \tau^{-1}$ as $\tau \longrightarrow \infty$ is difficult to implement [1, 7]. Therefore, it is unlikely that such a theory can describe a phenomenon that is so widespread in nature.

There have been attempts to study the nature of 1/ω noise by analyzing nonlinear differential equations by numerical methods [10].

The analysis of a series of experiments (see, for example, [11, 12]) provides evidence for the thermal nature of the 1/ω noise. Below, we will show one of the sources of this noise. Namely, we will show that such noise arises in a quantum oscillator under the parametric effect of a time-correlated random field of sufficiently high intensity. The proof of this does not require any conjectures. It is based on the fundamental equations of dynamics and on the Gibbs distribution. The assertion proved implies that the 1/ω noise may arise in any classical anharmonic oscillator placed in a thermostat with sufficiently high temperature.

Consider a quantum harmonic oscillator that interacts with a certain external field $\hat{\varphi}$; the system as a whole is in a thermodynamic equilibrium state. Assume that the Schrödinger equation is expressed as

$$i\frac{\partial \Psi}{\partial t} = \hat{H}\psi, \quad \hat{H} = \hat{H}^0 + \hat{H}',$$

$$\hat{H}^0 = \hbar\omega_0\left(\hat{\alpha}^\dagger\hat{\alpha} + \frac{1}{2}\right), \quad \omega_0^2 = \frac{\kappa}{m},$$

where ω_0 is the oscillator frequency, κ and m are certain positive constants, the creation $\hat{\alpha}^\dagger$ and annihilation $\hat{\alpha}$ operators satisfy the Bose–Einstein permutation relations, $\hat{H}'$ is the interaction Hamiltonian of the oscillator with an external field $\hat{\varphi}$, and $\hat{H}_\varphi$ is the Hamiltonian of a free external field.

Suppose for a while that $\hat{H}' = 0$. Introduce the coordinate operator

$$\breve{x}(t) = \sqrt{\frac{\hbar\omega_0}{2\kappa}}[\hat{\alpha}\exp(-i\omega_0 t) + \hat{\alpha}^\dagger(i\omega_0 t)] \qquad (2)$$

in the Heisenberg representation such that

$$\hat{H}^0 = \frac{m}{2}\left(\frac{d\breve{x}(t)}{dt}\right)^2 + \frac{\kappa}{2}x^2(\breve{t}),$$

$$m\frac{d^2\breve{x}(t)}{dt^2} + \kappa\breve{x}(t) = 0.$$

We will need the fluctuation–dissipation theorem [13]; as is known, the mathematical form of this theorem does not depend on the specific form of the interaction Hamiltonian. Therefore, it is convenient to obtain an

explicit form of this theorem by an example of the free ($\hat{H}' = 0$) field (2). Consider a correlator $\langle \check{x}(t)\check{x}(0)\rangle$, where the angular brackets denote the averaging of the operators both over the quantum states and in the statistical sense according to the Gibbs distribution.

One can easily verify by direct calculations that the Fourier transform of the required correlator has the form

$$\begin{aligned}\langle \check{x}\check{x}\rangle_\omega &= \int_{-\infty}^{\infty} e^{i\omega t}\langle \check{x}(t)\check{x}(0)\rangle dt \\ &= 2\pi\{\delta(\omega-\omega_0)N(\omega_0) + \delta(\omega+\omega_0)[1+N(\omega_0)]\} \\ &\times \frac{\hbar\omega_0}{2\kappa},\end{aligned} \tag{3}$$

where

$$N(\omega) = \langle \check{\alpha}^\dagger\check{\alpha}\rangle = \left(\exp\frac{\hbar\omega}{T} - 1\right)^{-1},$$
$$1 + N(\omega) = -N(-\omega),$$

and T is the temperature of the system. Let us introduce the retarded G_r and advanced G_a Green functions,

$$G(r,a)(t) = \pm\frac{i}{\hbar}\langle[\check{x}(t), \check{x}(0)]\rangle\theta(\pm t). \tag{4}$$

Here, $\theta(t)$ is the Heaviside step function. The direct calculation of the difference of the Fourier transforms yields

$$\begin{aligned}\langle \check{x}\check{x}\rangle_\omega &= -i\hbar[1+N(\omega)][G_r(\omega) - G_a(\omega)], \\ G_r(-\omega) &= G_r^*(\omega) = G_a(\omega).\end{aligned} \tag{5}$$

For the Green functions $G_{r,a}$ defined in terms of commutators (4), the form of this relation does not depend on the interaction Hamiltonian. Therefore, the first expression in (5) is in fact an identity whose validity is determined by the Gibbs distribution and by the fact that the system in question and its interaction with the environment can be described within the Hamiltonian formalism. Restricting the analysis to the range of classical frequencies, $\hbar\omega \ll T$, we have

$$\begin{aligned}\langle \check{x}\check{x}\rangle_\omega &= -\frac{iT}{\omega}[G_r(\omega) - G_a(\omega)], \\ \langle \check{x}\check{x}\rangle_\omega &= \langle \check{x}\check{x}\rangle_{-\omega}.\end{aligned} \tag{6}$$

A further objective of this paper is to find an explicit expression for the Green function $G_{r,a}$ in the presence of the interaction Hamiltonian $\hat{H}'$.

Suppose that the full Hamiltonian of the system has the form

$$\hat{H}_f = \hat{H}^0 + \hat{H}' - f(t)\hat{x}, \quad \hat{H}' = \frac{g}{2}\hat{\varphi}\hat{x}^2 + \hat{H}_\varphi,$$

$$\hat{x} = \sqrt{\frac{\hbar\omega_0}{2\kappa}}(\hat{\alpha} + \hat{\alpha}^\dagger),$$

where g is the parameter of interaction of the oscillator with the external field $\hat{\varphi}$ and $f(t)$ is a certain auxiliary regular classical function, which is assumed to be zero at the end of calculations. In the Heisenberg representation, we have

$$m\frac{d^2\check{x}_f(t)}{dt^2} + \kappa\check{x}_f(t) + g\check{\varphi}(t)\check{x}_f(t) = f(t), \tag{7}$$

where $\check{x}_f(t) = \check{x}(t)$ for $f = 0$. The solution to Eq. (7) can be represented as

$$\check{x}_f(t) = \check{x}(t) + \int \check{G}_r(t,t_1)f(t_1)dt_1, \tag{8}$$

where the operator Green function $\check{G}_r(t,t')$ satisfies the equation

$$m\frac{d^2\check{G}_r(t,t')}{dt^2} + \kappa\check{G}_r(t,t') + g\check{\varphi}(t)\check{G}_r(t,t') = \delta(t-t'). \tag{9}$$

After averaging in the aforementioned sense both sides of solution (8) and juxtaposing the equality obtained with the Kubo formula [14], we obtain

$$\langle \check{G}_r(t-t')\rangle = G_r(t-t').$$

In this manner, we will calculate the function G_r that enters formula (6). Now, let us average Eq. (9) over a statistical ensemble of systems,

$$\begin{aligned}m\frac{d^2\langle \check{G}_r(t,t')\rangle}{dt^2} + \kappa\langle \check{G}_r(t,t')\rangle + g\langle \check{\varphi}(t)G_r(t,t')\rangle \\ = \delta(t-t'),\end{aligned} \tag{10}$$

and determine $\langle \check{G}_r\rangle$ with the use of this equation. For simplicity, we will restrict the analysis to the case of classical frequencies ($\hbar\omega \ll T$), which is quite admissible when investigating the domain of $\omega \longrightarrow 0$. To solve Eq. (10), we introduce an auxiliary functional

$$\check{S} = \exp\left(-i\int_{-\infty}^{\infty}\rho(t)\check{\varphi}(t)dt\right),$$

where $\rho(t)$ is a certain smooth classical function. Let us multiply Eq. (9) by $\check{S}$ on the right and sum the result

over an ensemble of systems. For the auxiliary function

$$G_r(t, t'|\rho) = \frac{\langle \breve{G}_r(t, t')\breve{S}\rangle}{\langle \breve{S}\rangle},$$

we have

$$m\frac{d^2G_r(t, t'|\rho)}{dt^2} = \kappa G_r(t, t'|\rho) + ig\frac{\delta G_r(t, t'|\rho)}{\delta\rho(t)} + g\frac{\langle \breve{\varphi}(t)\breve{S}\rangle}{\langle \breve{S}\rangle}G_r(t, t'|\rho) = \delta(t-t'). \quad (11)$$

In the limit of classical frequencies, we may ignore the commutation relations of fields. It is obvious that

$$G_r(t, t'|\rho) = \langle \breve{G}(t-t')\rangle$$

for $\rho = 0$. Assuming that $\delta G_r(t, t'|\rho)/\delta\rho(z)$ is an unknown function, we obtain the following equation for it by varying expression (11) with respect to $\rho(z)$:

$$m\frac{d^2}{dt^2}\frac{\delta G_r(t, t'|\rho)}{\delta\rho(z)} + \kappa\frac{\delta G_r(t, t'|\rho)}{\delta\rho(z)} + ig\frac{\delta^2 G_r(t, t'|\rho)}{\delta\rho(t)\delta\rho(z)} + g\frac{\langle \breve{\varphi}(t)\rangle}{\langle \breve{S}\rangle}\frac{\delta G_r(t, t'|\rho)}{\delta\rho(z)} + g\left[-i\frac{\langle \breve{\varphi}(t)\breve{\varphi}(z)\breve{S}\rangle}{\langle \breve{S}\rangle} + i\frac{\langle \breve{\varphi}(t)\breve{S}\rangle\langle \breve{\varphi}(z)\breve{S}\rangle}{\langle \breve{S}\rangle^2}\right] \times G_r(t, t'|\rho) = 0. \quad (12)$$

However, we have obtained an unknown second variational derivative of $G_r(t, t'|\rho)$. Integrating once again Eq. (12), we can obtain a special equation for this derivative. Thus, we obtain a nonclosed chain of equations. The later we break such a chain, the more accurate the result. We will restrict ourselves to two equations (11) and (12). This means that more accurate solutions obtained with regard to other equations that we omitted will only improve the result. If we omit the variational derivative in Eq. (11) and restrict ourselves to a single equation, we obtain the Hartree–Fock approximation. Our system of two equations is sufficient for studying phase transitions. For example, it allows one to describe the behavior of ferromagnets in the vicinity of the Curie point [15]. When uncoupling the equations, it is not required to assume that there is a small parameter. Below, we will return once again to the question of the applicability of the results obtained.

Using Eq. (11), we can solve Eq. (12) as follows:

$$\frac{\delta G_r(t, t'|\rho)}{\delta\rho(z)} = ig\int G_r(t, t_1|\rho)\left[\frac{\langle \breve{\varphi}(t_1)\breve{\varphi}(z)\breve{S}\rangle}{\langle \breve{S}\rangle} - \frac{\langle \breve{\varphi}(t_1)\breve{S}\rangle\langle \breve{\varphi}(z)\breve{S}\rangle}{\langle \breve{S}\rangle^2}\right] \times G_r(t_1, t'|\rho)dt_1. \quad (13)$$

If Eq. (12) did not contain variational derivatives, then formula (13) would provide its exact solution. The substitution of (13) into (11) shows that one variational derivative remains uncompensated. The approximate equality (13) represents a so-called single-loop approximation. Setting $\rho = 0$ and taking into account that $\langle \breve{\varphi}(t)\rangle = \langle \breve{x}(t)\rangle = 0$, from formulas (11) and (13) we obtain a closed integrodifferential equation for the unknown function $\langle G_r(t-t')\rangle$ that is equivalent to the following integral equation:

$$\langle G_r(t-t')\rangle = G_r^0(t-t') + \int G_r^0(t-t_1)M_r(t_1-t_2)\langle G_r(t_2-t')\rangle dt_1dt_2, \quad (14)$$

$$m\frac{d^2G_r^0(t-t')}{dt^2} + \kappa G_r^0(t-t') = \delta(t-t'),$$

where

$$M_r(t-t') = g^2\langle G_r(t-t')\rangle\langle \breve{\varphi}(t-t')\breve{\varphi}(0)\rangle. \quad (15)$$

Suppose that the correlator $\langle \breve{\varphi}(t)\breve{\varphi}(t')\rangle$ decays exponentially with the constant γ as the quantity $|t-t'|$ increases,

$$\langle \breve{\varphi}(t)\breve{\varphi}(t')\rangle = \langle \breve{\varphi}^2\rangle\exp(-\gamma|t-t'|),$$
$$\langle \breve{\varphi}^2\rangle = \langle \breve{\varphi}(0)\breve{\varphi}(0)\rangle.$$

Then, for small γ, the Fourier transform

$$\langle \varphi\varphi\rangle_\omega = \int_{-\infty}^{\infty}\exp[i\omega(t-t')]\langle \breve{\varphi}(t)\breve{\varphi}(t')\rangle d(t-t') = i\langle \breve{\varphi}^2\rangle\left(\frac{1}{\omega+i\gamma} - \frac{1}{\omega-i\gamma}\right)$$

has a pronounced maximum at the point $\omega = 0$; this fact allows one to rewrite (15), after the Fourier transformation, as

$$M_r(\omega) = g^2\int G_r(\omega-\omega')\langle \breve{\varphi}\breve{\varphi}\rangle_{\omega'}\frac{d\omega'}{2\pi} \approx g^2\langle \breve{\varphi}^2\rangle G_r(\omega). \quad (16)$$

It follows from the derivation of the system of equations (14), (15) that their validity does not depend on the statistical properties of the fields considered. From the system of equations (14), (16), we obtain the required functions

$$M_r(0) = \frac{\kappa}{2} - \sqrt{\frac{\kappa^2}{4} - g^2\langle \breve{\varphi}^2\rangle},$$
$$G_r(\omega) = \frac{1}{-\omega^2 m + \kappa - M_r(0)}, \quad \omega \longrightarrow 0. \quad (17)$$

The sign before the radical is chosen so that $M_r(0) \longrightarrow 0$. When

$$\kappa > \kappa_c = \sqrt{4g^2\langle\breve{\varphi}^2\rangle},$$

the operator $M_r(0)$ is real and, according to the fluctuation–dissipation theorem, no noise is generated in the system at low frequencies. At the point $\kappa = \kappa_c$, a sui generis phase transition occurs, and the operator $M_r(0)$ acquires an imaginary part:

$$M_r(0) = \frac{\kappa}{2} + i\,\mathrm{sgn}\,\omega\sqrt{g^2\langle\breve{\varphi}^2\rangle - \frac{\kappa^2}{4}}. \tag{18}$$

The sign before the radical is chosen so that the right-hand side of the first equation in (6) is positive. According to the definition

$$\mathrm{Im}M_r(\omega) = \int_0^\infty M_r(t)\sin\omega t\,dt, \tag{19}$$

the sign of $\mathrm{Im}M_r(0)$ is changed together with the sign of the frequency ω. The substitution of relations (17) and (18) into identity (6) shows that, at low frequencies, the noise

$$\langle\breve{x}\breve{x}\rangle_\omega = \frac{2T}{\omega}\mathrm{sgn}\,\omega\frac{\sqrt{g^2\langle\breve{\varphi}^2\rangle - \frac{\kappa^2}{4}}}{g^2\langle\breve{\varphi}^2\rangle} \tag{20}$$

with the characteristic singularity 1/ω is generated in the system.

According to (19), the operator $M_r(0)$ may have a finite imaginary part as $\omega \longrightarrow 0$ only if the operator $M_r(t)$ has an asymptote $M_r(t) \propto t^{-1}$ for large times. For the same reason, the Green function has a similar asymptote for large times: $G_r(t) \propto t^{-1}$. At the same time, it is clear that the correlator $\langle\breve{x}\breve{x}\rangle_\omega$ cannot have the singularity 1/ω for arbitrarily small frequencies. This would violate the finiteness of the integral

$$\int_0^\infty \langle\breve{x}\breve{x}\rangle_\omega d\omega$$

and would lead to the infinite correlator $\langle\breve{x}(0)\breve{x}(0)\rangle$. The arising difficulty is associated with the use of the approximate equality (16). Let us explain this fact in greater detail. For finite values of γ, the correlator $\langle\breve{\varphi}(t)\breve{\varphi}(0)\rangle$ decays exponentially as the argument increases; therefore, according to (15), the quantity $\mathrm{Im}M_r(\omega)$ tends to zero as $\omega \longrightarrow 0$, rather than remains constant as was assumed above. Since the singularity 1/ω in the noise arises only for finite $\mathrm{Im}M_r(0)$ and when the constant γ is neglected, the 1/ω spectrum exists only in the frequency interval

$$\gamma \ll \omega \ll \omega_0. \tag{21}$$

Let us return once again to the question of the accuracy of the single-loop approximation. To this end, notice that the problem considered above admits an exact solution (see the Appendix) for $\gamma \longrightarrow 0$ under the assumption that the field $\breve{\varphi}$ is Gaussian. This solution can be obtained by expanding the function $G_r(\omega)$ in a series in the parameter $g^2\langle\breve{\varphi}^2\rangle/\kappa^2$ and (with regard to the identity similar to the Ward [16] identity in electrodynamics) by summing all Feynman diagrams. In place of Eq. (16) for the operator $M_r(\omega)$, we obtain

$$M_r(\omega) = g^2\langle\breve{\varphi}^2\rangle G_r(\omega)\left[1 - \frac{d}{d\kappa}M_r(\omega)\right]. \tag{22}$$

When

$$\frac{\kappa^2}{g^2\langle\breve{\varphi}^2\rangle} \ll 1, \tag{23}$$

this equation has the following asymptotic representation:

$$\begin{aligned} M_r(0) &= \frac{\kappa}{2}\left(1 - \frac{\kappa^2}{6g^2\langle\breve{\varphi}^2\rangle}\right) \\ &+ i\,\mathrm{sgn}\,\omega\sqrt{\frac{g^2\langle\breve{\varphi}^2\rangle}{2}}\left(1 - \frac{\kappa^4}{24g^2\langle\breve{\varphi}^2\rangle^2}\right). \end{aligned} \tag{24}$$

The presence of this asymptote, which indicates that $\mathrm{Im}M_r(0)$ is finite as $\omega \longrightarrow 0$ under inequality (23), clearly proves that there exists 1/ω noise in the frequency interval (21) even if the previous arguments based on the single-loop approximation seem doubtful. As regards the single-loop approximation, under inequality (23), it yields

$$M_r(0) = \frac{\kappa}{2} + i\,\mathrm{sgn}\,\omega\sqrt{g^2\langle\breve{\varphi}^2\rangle}. \tag{25}$$

A juxtaposition of the asymptotic result (25) obtained in the single-loop approximation and the asymptotic behavior of the exact solution (24) shows that, for large interaction constant g, the real part of the operator $M_r(\omega)$ in the single-loop approximation (23) coincides with the real part of the exact solution. For correct literal combination, the imaginary part of the operator $M_r(0)$ in the single-loop approximation turns out to be overstated by a factor of $\sqrt{2}$. Under the reverse inequality

$$\frac{\kappa^2}{g^2\langle\breve{\varphi}^2\rangle} \gg 1, \tag{26}$$

the single-loop approximation and the exact solution yield identical results because they both lead to the first term of perturbation theory. Thus, the single-loop approximation has a sufficiently high accuracy so that, at the first acquaintance with a system, one may judge

whether or not there is noise with a $1/\omega$ spectrum in this system. In the intermediate interval between inequalities (23) and (24), the single-loop approximation gives an interpolatory result and correctly predicts the existence of a phase transition; however, one should be cautious when dealing with the quantitative description of this phase transition.

The analysis carried out shows that one does not need an external noise field $\breve{\varphi}(t)$ to generate $1/\omega$ noise in the oscillator. A harmonic oscillator placed in a thermostat starts to fluctuate by itself. The amplitude of these fluctuations increases with temperature. If one makes it so that the stiffness coefficients of the oscillator depend on this amplitude, i.e., if one introduces feedback, then, as shown above, $1/\omega$ fluctuations arise in the oscillator. Since one type of noise feedback has already been described by Eq. (16) in determining $M_r(0)$, we can speak of the generation of $1/\omega$ noise in nonlinear systems due to a double feedback. Thus, we can argue that $1/\omega$ fluctuations may exist in any anharmonic oscillator, provided that the thermostat temperature is sufficiently high.

Indeed, consider the equation of an anharmonic oscillator

$$m\frac{d^2\breve{x}_f(t)}{dt^2} + \kappa\breve{x}_f(t) + g\breve{x}_f^2(t) = f(t). \qquad (27)$$

Suppose that the problem has been solved and a solution to (27) is known. Denote this solution by $\breve{\psi}(t)$. Let us rewrite Eq. (27) as

$$m\frac{d^2\breve{x}_f(t)}{dt^2} + \kappa\breve{x}_f(t) + g\breve{\psi}(t)\breve{x}_f(t) = f(t).$$

Since the operator $\breve{\psi}(t)$ is known, for the operator $\breve{x}(t)$, we obtain Eq. (7), which was studied above. If we assume that the field $\breve{\psi}$ is Gaussian, then, based on the system of equations (14), (22), we can find an exact solution to the problem. If we do not make such an assumption, then, we may restrict the analysis to the single-loop approximation. As is shown above, for high anharmonism, the accuracy of this approximation is quite satisfactory and the results are independent of the statistical properties of the system. According to expression (15), we obtain

$$M_r(t-t') = g^2G_r(t-t')\langle\breve{\psi}(t-t')\breve{\psi}(0)\rangle. \qquad (28)$$

In Eq. (28), we will again use the operator $\breve{x}$ in place of the operators $\breve{\psi}$ in order that the results thus obtained correspond to the equation of an anharmonic oscillator (27). After the Fourier transformation, the operator takes the form

$$M_r(\omega) = g^2\int G_r(\omega-\omega')\langle\breve{x}\breve{x}\rangle_{\omega'}\frac{d\omega'}{2\pi}. \qquad (29)$$

Just as above, we will restrict the analysis to the range of classical frequencies $\hbar\omega \ll T$. According to formulas (3) and (20), we will seek the unknown function $\langle\breve{x}\breve{x}\rangle_\omega$ in the form

$$\langle\breve{x}\breve{x}\rangle_\omega = \frac{2\pi A}{|\omega|}\theta(\omega_0-|\omega|) + 2\pi B[\delta(\omega-\omega_0)+\delta(\omega+\omega_0)], \qquad (30)$$

where $B = T/2\kappa$ and A is an unknown constant. Taking into account the singularity $1/|\omega|$ in the last expression, we can take the function G_r at the point $\omega' = 0$ in Eq. (29) outside the integral sign:

$$M_r(\omega) = g^2G_r(\omega)\int_\gamma^{\omega_0}\frac{2A}{\omega}d\omega + \frac{g^2B}{-m(\omega-\omega_0)^2+\kappa-M_r(\omega-\omega_0)} + \frac{g^2B}{-m(\omega+\omega_0)^2+\kappa-M_r(\omega+\omega_0)}. \qquad (31)$$

Here, according to (6), the integration interval is in fact the half-line $[0, \infty)$. However, if γ is small, then, for $t = 0$, the greater part of the area of the integrand is concentrated in the region of small frequencies due to the singularity $1/\omega$. Therefore, we can cut off the upper limit of integration at a frequency of ω_0, which is consistent with condition (21). The lower limit of integration cannot be set equal to zero. However, there are no parameters in the model considered from which one could construct the lower limit of integration with the dimension of frequency. This means that, in the model considered, the singularity $1/\omega$ may occur at arbitrarily small frequencies. A restriction from low frequencies arises only due to the interaction of the oscillator with external fields that guarantee, according to Eq. (21), the lower limit of integration in (31) in real situations.

Equation (31) represents a system of coupled equations. The later we break this chain, the higher the accuracy of the result. Our concern is the operator $M_r(0)$. According to (31), we have

$$M_r(0) = \frac{2g^2A\ln\dfrac{\omega_0}{\gamma}}{\kappa-M_r(0)} - \frac{g^2B}{M_r(\omega_0)} - \frac{g^2B}{M_r(-\omega_0)}. \qquad (32)$$

Now, we write out an equation for $M_r(\pm\omega_0)$ and, restricting ourselves to the diagonal approximation, obtain

$$M_r^2(\pm\omega_0) = -2g^2A\ln\frac{\omega_0}{\gamma}.$$

Since, according to (19), the function $\mathrm{Im}M_r(\omega)$ is odd, the last two terms in (32) cancel out. This means that, in the first approximation, one can neglect the effect of noise in the resonance domain of frequencies on the

formation of 1/ω noise in the oscillator. Now, Eq. (32) can easily be solved. For

$$2g^2A\ln\frac{\omega_0}{\gamma} > \frac{\kappa^2}{4}$$

we obtain

$$\langle \breve{x}\breve{x}\rangle_\omega = \frac{T}{\omega}\operatorname{sgn}\omega\frac{\sqrt{2g^2A\ln(\omega_0/\gamma)-\frac{\kappa^2}{4}}}{g^2A\ln(\omega_0/\gamma)}. \quad (33)$$

The matching equation for finding the unknown A takes the form

$$2\int_\gamma^{\omega_0}\langle \breve{x}\breve{x}\rangle_\omega\frac{d\omega}{2\pi} = \left(2A\ln\frac{\omega_0}{\gamma}\right)^2$$
$$= \frac{2T}{\pi g^2}\sqrt{2g^2A\ln\frac{\omega_0}{\gamma}-\frac{\kappa^2}{4}}\ln\frac{\omega_0}{\gamma}.$$

This equation is rewritten in dimensionless quantities as

$$z^2 = \zeta\sqrt{z-\frac{1}{4}}, \quad (34)$$

where

$$\zeta = \frac{2g^2T}{\pi\kappa^3}\ln\frac{\omega_0}{\gamma}, \quad z = \frac{2g^2A}{\kappa^2}\ln\frac{\omega_0}{\gamma}.$$

Equation (34) has a solution only when the parameter ζ is greater than a certain critical value ζ_c, which determines the critical temperature T_c. The curves z^4 and $\zeta^2(z-1/4)$ osculate at the critical point. Therefore, the derivatives of these curves coincide at this point; this allows one to determine the quantities

$$\zeta_c = \frac{2}{\sqrt{27}}, \quad z_c = \frac{1}{3}, \quad T_c = \frac{\pi\kappa^3}{g^2\sqrt{27}}\left(\ln\frac{\omega_0}{\gamma}\right)^{-1}.$$

When $T > T_c$, Eq. (34) has two solutions. The existence of one of them is certain because it falls into a domain where the single-loop approximation holds. The other solution falls into the interpolation domain and is a subject for further analysis. It is reasonable to assume that the single-loop approximation correctly points to the existence of this solution. As a result, instead of (33), we have

$$\langle \breve{x}\breve{x}\rangle_\omega = z\frac{\pi\kappa^2}{g^2\omega}\left(\ln\frac{\omega_0}{\gamma}\right)^{-1}.$$

Thus, when reaching a certain threshold temperature T_c, 1/ω noise is generated in any anharmonic oscillator. We assume that the proposed mechanism of the onset of thermal 1/ω noise quite adequately describes the origin of such noise in the spectrum of phonons in quartz, which was experimentally observed in [12] but has not yet been explained theoretically.

APPENDIX

Let us derive Eq. (22). If the function $\breve{\varphi}(t)$ describes a Gaussian random field, Eq. (9) can be solved in the following way. Rewrite this equation in the integral form

$$\breve{G}_r(t,t') = G_r^0(t-t') - g\int_0^\infty G_r^0(t-t_1)\breve{\varphi}(t_1)G_r(t_1,t')dt_1,$$

where

$$m\frac{d^2G_r^0(t-t')}{dt^2} + \kappa G_r^0(t-t') = \delta(t-t'),$$

and solve it by an iterative method. We average the arising series over an ensemble of systems and, using the properties of the Gaussian distribution, represent the higher order correlators of the field $\breve{\varphi}$ in terms of bilinear combinations of these operators. The arising Feynman series is easily summed by the Dyson method. The summation yields

$$\langle G_r(t-t')\rangle = G_r^0(t-t')$$
$$+\int G_r^0(t-t_1)M_r(t_1,t_2)\langle G_r(t_2-t')\rangle dt_1dt_2,$$

where

$$M_r(t,t') = g\int G_r(t-t_1)\langle\breve{\varphi}(t_1-t_2)\breve{\varphi}(0)\rangle \times\Gamma(t_1,t_2,t')dt_1dt_2. \quad (A.1)$$

Here, $\Gamma(t_1, t_2, t')$ is a vertex function. Taking into account the deltalike behavior of the correlator $\langle\breve{\varphi}\breve{\varphi}\rangle_\omega$, we can rewrite the operator (A.1) after the Fourier transformation as

$$M_r(\omega,\omega') = g\langle\breve{\varphi}^2\rangle \times\int d(\omega-\omega_1)G_r(\omega_1)\Gamma(\omega_1,0,\omega')d\omega_1. \quad (A.2)$$

If we apply the approximation

$$\Gamma(\omega_1,0,\omega') = 2\pi\delta(\omega_1-\omega'),$$

we arrive at the equations of the single-loop approximation.

Structurally, the series representing the propagator $\langle\breve{G}_r(\omega)\rangle$ is similar to the Feynman series for the Green

function in quantum electrodynamics. Reproducing the well-known arguments of [17], we obtain

$$\Gamma(\omega_1, 0, \omega') = 2\pi g\delta(\omega_1 - \omega') - g\frac{d}{d\kappa}M_r(\omega_1, \omega'). \quad \text{(A.3)}$$

The accuracy of this relation is determined by the accuracy of the Ward identity [16]. Introduce the notation

$$M_r(\omega, \omega') = 2\pi\delta(\omega - \omega')M_r(\omega)$$

and substitute formula (A.3) into (A.2). For the operator $M_r(\omega)$ of interest, we obtain Eq. (22). This equation can be rewritten as

$$M_r(\omega) = g^2\langle\check{\varphi}^2\rangle\frac{d}{d\kappa}\ln[-m\omega^2 + \kappa - M_r(\omega)]$$
$$= g^2\langle\check{\varphi}^2\rangle\frac{d}{d\kappa}\ln G_r^{-1}(\omega).$$

ACKNOWLEDGMENTS

I am grateful to the participants of the seminar led by A. A. Rukhadze for discussions on this paper.

REFERENCES

1. G. N. Bochkov and Yu. E. Kuzovlev, Usp. Fiz. Nauk **141**, 151 (1983) [Sov. Phys. Usp. **26**, 829 (1983)].
2. G. P. Zhigal'skiĭ, Usp. Fiz. Nauk **173**, 465 (2003) [Phys. Usp. **46**, 449 (2003)].
3. J. B. Jonson, Phys. Rev. **26**, 71 (1925).
4. P. H. Handel, Phys. Rev. A **22**, 745 (1980).
5. T. Musha, in *Proceedings of the 17th Conference on Noise in Physical System and 1/f Fluctuations*, Ed. by J. Sikula (Prague, 2003), p. 3.
6. H. Furukava, Phys. Rev. A **34**, 2315 (1986).
7. B. Pellegrini, in *Proceedings of the 15th International Conference on Noise in Physical Systems and 1/f Fluctuations*, Ed. by C. Surya (Hong Kong, 1999), p. 303.
8. Sh. M. Kogan and K. E. Nogaev, Solid State Commun. **49**, 387 (1984).
9. M. N. Mihaila, in *Proceedings of the 16th International Conference on Noise in Physical Systems and 1/f Fluctuations*, Ed. by G. Bosman (Floride, USA, 2001), p. 169.
10. V. N. Skokov, V. P. Koverda, and A. V. Reshetnikov, Zh. Éksp. Teor. Fiz. **119**, 613 (2001) [JETP **92**, 535 (2001)].
11. R. F. Voss and J. Clarke, Phys. Rev. Lett. **36**, 42 (1976).
12. T. Musha, G. Borbely, and M. Shoji, Phys. Rev. Lett. **64**, 2394 (1990).
13. H. B. Callen and T. A. Welton, Phys. Rev. **83**, 34 (1951).
14. R. Kubo, in *Thermodynamics of Irreversible Processes*, Ed. by D. N. Zubarev (Inostrannaya Literatura, Moscow, 1962), p. 345 [in Russian].
15. S. V. Tyablikov, Ukr. Mat. Zh. **11**, 287 (1959).
16. J. Ward, Phys. Rev. **78**, 182 (1950).
17. A. I. Akhiezer and V. B. Berestetskiĭ, *Quantum Electrodynamics*, 3rd ed. (Nauka, Moscow, 1969; Wiley, New York, 1965).

Translated by I. Nikitin